MULTI-SCALE MODELING AND OPTIMIZATION FOR INDUSTRIES WITH FORMULATED PRODUCTS

Borja Hernández Blázquez

VNiVERSiDAD D SALAMANCA

CAMPUS DE EXCELENCIA INTERNACIONAL

PhD. Thesis
2020

MULTI-SCALE MODELING AND OPTIMIZATION FOR INDUSTRIES WITH FORMULATED PRODUCTS

Borja Hernández Blázquez

Doctorado en Ciencia y Tecnología Química.

Departamento de Ingeniería Química y Textil.

Universidad de Salamanca, Septiembre, 2020.

FUNDING AND ACKNOWLEDGEMENTS

I would like to acknowledge Banco Santander and Universidad de Salamanca for the PhD. Fellowship. Furthermore, I also acknowledge to Procter and Gamble for economic support.

I would like to thank my supervisor Professor Mariano Martín for guiding me in the development of this thesis. He has been always open to questions and he has been supporting me in the good and bad times. I would also like to acknowledge to my industrial supervisors, Dr. Luis Martín for challenging me to do part of the work presented here, and Dr. Mark A. Pinto for his advice and patience in some of the meetings. I cannot forget about my PhD. Colleges at PSEM3 group and the people of the Modeling and Simulation department at the Newcastle Innovation Centre, in particular to Dr. Prashant Gupta for his support during the last months. Finally, I would like to thank my parents and sister for their emotional support.

STRUCTURE AND SCIENTIFIC PUBLICATIONS

The thesis is composed of two parts. The first part has been developed in collaboration with the Modeling and Simulation department at the Newcastle Innovation Centre of Procter and Gamble and the second part focuses on the use of optimization techniques for the design of processes within the waste-to-chemicals concept. The first part is divided in three modeling areas with different chapters and the second part is divided in two areas at process level. In most of the cases, each of the chapters corresponds to a formal manuscript already published in a scientific journal or to a one that can be published in the months to come. Thus, the thesis is presented as compendium of publications, where each publication corresponds to a different chapter. The relation between the chapters of the thesis and the papers published or that can be published is structured as follows:

GENERAL INTRODUCTION. This introduction provides a general overview of the scales in the chemical industry and, in particular, in the area of formulated products. Furthermore, the modeling approaches used in each of the scales is described.

PART A. MULTI-SCALE MODELING FOR SPRAY DRYERS.

INTRODUCTION TO SPRAY DRYING. This introduction only provides a general overview of the phenomena that take place within the operation of spray dryers. The aim is to provide the reader a background about the complexity involved in the unit.

1. **MODELING AT PARTICLE SCALE**

   1.1 Single droplet drying of detergents. It corresponds to a submitted manuscript, currently under review, to the journal Particuology: "Single droplet drying of detergents: Experimentation and Modelling". Hernández, B. Mondragón, R. Pinto, M.A. Hernández, L. Juliá, J.E. Jarque, J.C. Chiva, S. Martín, M.

2. **RIGUROUS MODELING AT UNIT LEVEL.**

   2.1 Geometry, meshing and numerical errors analysis in spray drying simulations. This chapter is not considered for publication but it describes how a suitable mesh, which is used in the following chapters, has been obtained.

   2.2. CFD modeling of the airflow in Industrial counter-current dryers with swirl flow pattern. This chapter corresponds to the published manuscript: Hernández, B. Fraser, B. Martín de Juan, L. Martín, M. (2018) Computational fluid dynamics (CFD) modeling of swirling flows in industrial counter-current spray-drying towers under fouling conditions. Industrial & Engineering Chemistry Research, 57 (35), 11988-12002.

2.3 Further studies of the airflow in the dryer. This chapter is structured in two sections where the first part corresponds to a manuscript submitted to the Chemical Engineering Research and Design journal that is under review as: "Numerical study of airflow regimes and instabilities produced by the swirl generation chamber in counter-current spray dryers". Hernández, B. Martín, M. Gupta, P.

2.4 Analysis of the particle residence time in industrial swirl counter-current dryers. This chapter has not been published but it can be part of a formal publication as: "Analysis of the particle residence time in industrial swirl counter-current dryers. The effective restitution coefficient."

2.5 CFD modeling of drying within the counter-current spray dryer. This chapter has not been published yet but it can be submitted in the following moths as: "CFD modelling of counter-current spray dryers following a step-by-step validation".

2.6 Characterization of agglomeration and breakage for particle-wall interactions. This chapter has not been published yet. It can be submitted as a formal publication as: "Quick CFD driven characterization of agglomeration and breakage by particle-wall interaction in spray dryers".

3. COMPARTMENT MODELING AT UNIT LEVEL.

3.1 Methodology for the generation of robust compartment models based on CFD simulations. Zones, fluxes and momentum characterization. This chapter has not been submitted to any journal yet. It can be published in the following months as: "A methodology for robust compartment model generation based on CFD. Characterization of zones flexibility and fluxes in a 2 way-coupling system."

3.2 CFD-DPM based compartment model for counter-current spray dryers. Heat and Mass transfer modeling. This chapter has not been submitted to any journal yet. It can be published in the upcoming year as: "A robust compartment model for counter-current spray dryers. Heat and mass transfer modeling".

PART B. OPTIMIZATION OF PROCESSES INVOLVING FORMULATED PRODUCTS. Bioprocessing of wastes to value-added products.

INTRODUCTION TO WASTE TREATMENT METHODS. This introduction only provides a general overview of the technologies to be used in the treatment of organic wastes.

4. PROCESS OPTIMIZATION.

4.1 Bio-waste selection and blending for the optimal production of power and fuels via anaerobic digestion. This chapter has been published as a manuscript in: "Hernández, B. León, E. Martín, M. (2017) Bio-waste selection and blending for the optimal production of power and fuels via anaerobic digestion. Chemical Engineering Research and Design, 121, 163-172."

4.2 Optimization for biogas to chemicals via tri-reforming. Analysis of Fischer-Tropsch fuels from biogas. This chapter corresponds to the published manuscript: Hernández, B. Martín, M. (2018) Optimization for biogas to chemicals via tri-reforming. Analysis of Fischer-Tropsch fuels from biogas. Energy Conversion and Management, 174, 998-1013.

4.3. Optimal production of syngas via super-dry reforming. Analysis for natural gas and biogas under different CO_2 taxes. It is a published manuscript as: "Hernández, B. Martín, M. (2019) Optimal production of syngas via super-dry reforming. Analysis for natural gas and biogas under different CO2 taxes. Chemical Engineering Research and Design, 148, 375-392."

4.4 Production of H_2 and methanol via dark fermentation. A process optimization study. This chapter has been published as scientific manuscript: Hernández, B. García-Blázquez, C. Aristizabal-Marulanda, V. Martín, M. (2020) Production of H2 and Methanol via dark fermentation. A process optimization study. Industrial & Engineering Chemistry Research, 59, 38, 16720-16729.

5.1 PROCESS INTEGRATION.

5.1. Optimal integrated process for the production of biodiesel from waste via anaerobic digestion. This chapter has been published as a scientific manuscript: Hernández, B. Martín, M. (2017) Optimal integrated plant for production of biodiesel from waste. ACS Sustainable Chemistry & Engineering, 5 (8), 6756-6767.

TABLE OF CONTENTS

2.3 Further studies of the airflow in the dryer.

Part A. Numerical study of airflow regimes and instabilities produced by the swirl generation chamber in counter-current spray dryers.

2.4. Analysis of the particle residence time in industrial swirl counter-current dryers.

2.5. CFD modeling of drying within the counter-current spray dryer.

2.6 Characterization of agglomeration and breakage for particle-wall interaction.

3. COMPARTMENT MODELING AT UNIT SCALE.

3.1 Methodology for the generation of robust compartment models based on CFD simulations. Zones, fluxes and momentum characterization.

3.2 A CFD-DPM based compartment model for counter-current spray dryers. Heat and mass transfer modeling.

4.2 Optimization for biogas to chemicals via tri-reforming. Analysis of Fischer-Tropsch fuels from biogas.

4.3 Optimal production of syngas via super-dry reforming. Analysis for natural gas and biogas under different CO_2 taxes.

NOTE: THE FIGURES, TABLES AND REFERENCES ARE LOCAL IN EACH OF THE CHAPTERS.

MULTI-SCALE MODELING AND OPTIMIZATION FOR PROCESSES WITH FORMULATED PRODUCTS

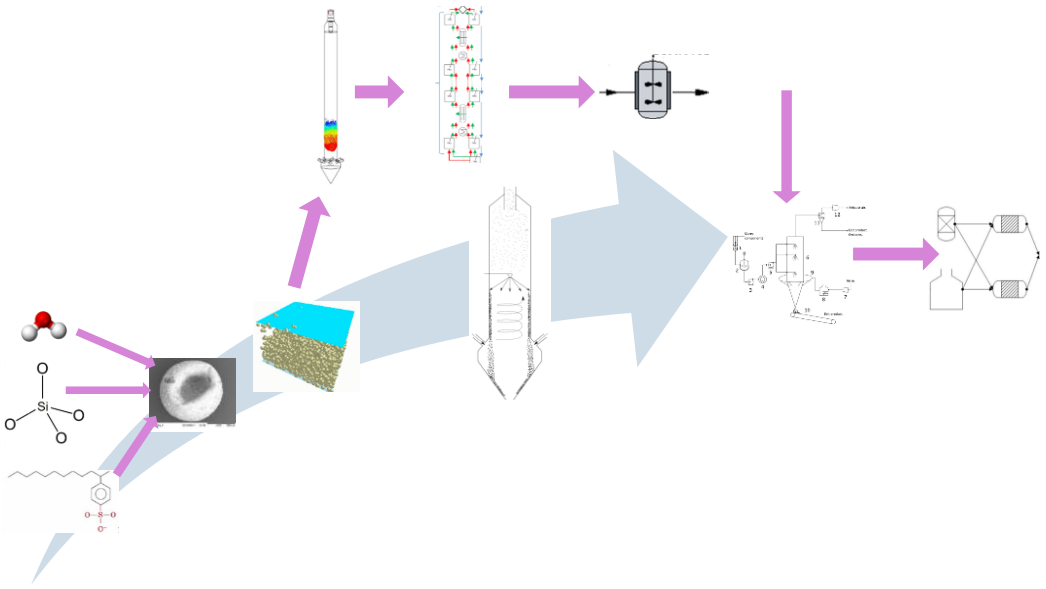

GENERAL INTRODUCTION. MULTI-SCALE MODELING AND OPTIMIZATION FOR PROCESSES WITH FORMULATED PRODUCTS.

G.1 INTRODUCTION

Formulated products cover a wide range of industries such as food, pharmaceutical, agrochemical, specialty chemicals, consumer goods, energy or materials. These products represent one of the largest and more dynamic businesses in the manufacturing sector. In United Kingdom they involve sales and exports in excess of 168 billion GBP each year [1]. In Europe, out of the 507 billion EUR traded in chemicals, 68 billion correspond to consumer chemicals (13.6%). Furthermore, pharmaceutical industry also represents a very relevant sector with a trade of 258 billion EUR [2, 3].

In contrast with bulk chemicals, these formulated products are composed by a wide range of components that influence the product characteristics and properties, including the structure. Structured products are a wide area within formulated products, where one can find very common products like as ice-cream, margarine or jam in the food industry and detergents or toothpaste in the consumer goods industry. In these structured products, the critical performance properties (critical quality attributes) are highly dependent on the product structure as well as the composition, so that the final performance of the product is very complex to predict [4]. The studies regarding the influence of the composition on the final product properties have traditionally been dominated by chemists, material scientists or food technologists. However, chemical engineers have also provided a relevant contribution in the area of product design since their traditional strengths (mass and energy balances, transport phenomena, process design, mathematical programing) complement the characterization of material properties and the marketing research [5]. These areas have different contributions in the development of a new product, which requires the next stages [5]:

1. An analysis of the consumer trends.
2. Conceptual product design.
3. Development of a physical prototype.
4. Introduction of the novel critical property into the prototype.
5. Testing the prototype product before launch it in the market.
6. Design of a production process for the production of the novel product.

The procedure in the development of a new product is sometimes iterative using as a basis a previous product launched in the market. As a result from this continuous development, the complexity of the products is also continuously growing. Several examples can be found nowadays such as the production of specialty products (e.g. yogurt with proteins or pieces of cereals) or products sold in new devices (e.g. detergent pods, coffee pods). In this procedure for the development of new products, one relevant key aspect is the “speed to market” [5, 6]. In this context, the use of computational tools is a key aspect for accelerating the development of new products as well as the decisions taken in each of the stages attending to economic or environmental criteria [7]. Examples of the

use of tools during previous stages can be found in the development of molecules by Computer-aided Molecular Design (CAMD) [8], the development and evaluation of product prototypes by means of Computer Aided Design tools based on rigorous simulations like ANSYS® [9] and COMSOL® [10] or the modeling and optimization of processes like blending [11] and pharmaceutical processing [12].

In the definition of the stages previously presented, it can be seen that the last one is where chemical engineers become critical and have the most adequate profile for carrying out that task. This development of new processes or the modification of the previous ones in order to meet new consumer requirements is a permanent need and it is preferred to be done as fast as possible. Here, as previously mentioned, the use of computational tools are key to take decisions about the novel process (e.g. units required and operating conditions of them). The use of the computational tools to be adopted will be defined by the accuracy desired and the complexity of the material to be developed. For example, the blending of different petrol fractions to obtain a gasoline with a level of octane requires simple models where the properties can be easily controlled from the bulk chemicals added [10]; however, the production of ice-cream with a desired level of creaminess is a more challenging task due to the interaction of operating conditions such as the contact time and temperature with product components such as milk proteins water content and shape of the ice crystals [13-15]. As a result, the final structure of the ice within the product is modified, so that the process is more difficult to control and optimize. The description in the modification of the ice-structure through the freezer and the impact that the operating conditions have on it at each location requires to solve a large set of partial differential equations that can involve discontinuities. This large number of equations can be solved by rigorous models but they have to be reduced in the case of making a model for optimization or control. In this reduction, some critical properties can be missed reducing the flexible utilization in the model such as its use under different scales [16-19]. Therefore, the development of new tools and their predictive capabilities can find limitations in reproducing some of the phenomena under study as well as in addressing very detailed phenomena in the optimization of the process. The difficulties in capturing the phenomena become more challenging when there is a change in the scale within the processing. It is very hard to cover particle level phenomena from an enterprise wide optimization (EWO) level. Litster and Bogle [4], remark recently this challenge as well as some of the needs such as:

- The development of flexible models that capture the uncertainty of the processing of formulated products. Especially in the area of pharmaceutical manufacturing where quality must be ensured.
- The use of models that will be able to predict very detailed phenomena with a quick response.
- Reproducing stability and security attributes under different scales and for the entire product life. This fact is especially critical in the production and distribution of pharmaceutical products.
- The development of customer models and their integration within the framework for the development of the product, the production process and the supply chain.
- Developing models that will be able to track the evolution of property distributions within the processing and the product life.

As it can be seen from these needs, the interaction between the different scales in the enterprise is a recurrent topic. The idealized objective is being able to predict and optimize with robust models very detailed properties and including them into the EWO. However, most of the studies distinguish among the different scales remarking the difficulty of scaling-up the process. This scale-up of the process properties is even more challenging in structured products since they are typically discrete and multiphase, which does not ensure continuity in distribution of properties [20]. A more detailed description of the scales that can be found in an industry with formulated structured products is provided in the following section.

G.2 SCALES IN FORMULATED PRODUCT INDUSTRY.

The different scales that one can find in a chemical company have been defined in previous works [20-22]. In the area of process system engineering, most of the works have defined the following scales [21]:

- A molecular scale where molecules are designed from their functional groups.
- Unit scale: Models are developed to simulate the role of the operating conditions and material properties in each of the units involved in a process.
- Process scale: At this level a process superstructure is modeled as a set of units, which behavior is modeled by means of first principles and rules of thumb.
- Supply chain & Enterprise scale: The models developed for the process are reduced capturing only the critical characteristics and including them into the modeling of the entire supply chain and enterprise.

However, in the area of structured products, where there is typically a discrete phase, the following scales complementing the previous ones are also defined [20]. As a result, Figure 1 is obtained including all the scales.

- Particle/droplet/bubble scale: At this scale, the role that molecules and formulation play in the particle structure and properties are studied.
- Mesoscale: This scale studies how the particles are organized within a small volume [22].
- Macro-scale: This scale studies how volumes of particles/droplets with different properties organize within a unit operation.

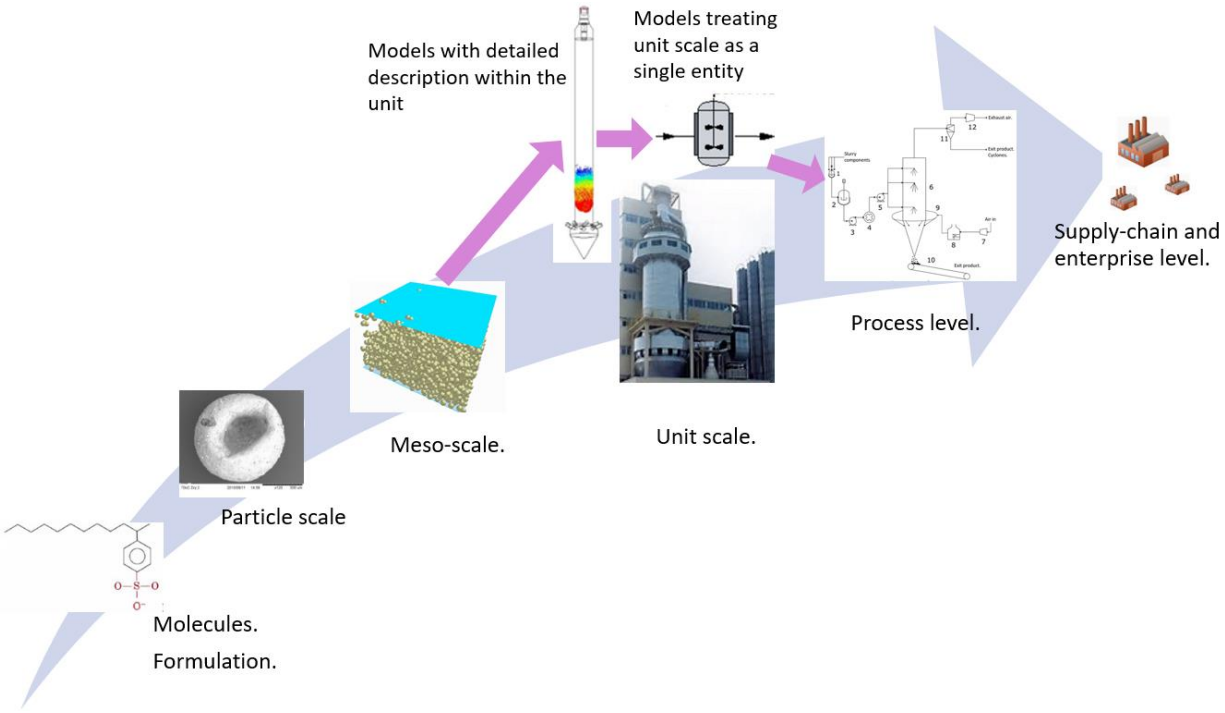

Figure 1. Scales in an enterprise with structured formulated products.

The modelling approaches followed in each of the scales is usually different and the scale-up of models for reproducing characteristics at small scale represents a challenge since, in some cases, the models tend to lose its robustness. The types of models that one can find in each of the scales are summarized in Figure 2 and described with higher detail in the following section. In Figure 2, these scales and the most common modeling approaches used are presented. Furthermore, it also shows the flux of information followed when a new formula/product is developed. The models may need to be updated across scales as presented by the arrows. The number of modifications to be performed depend on the robustness of the model. Apart from the robustness, the number of variables to be considered in the final enterprise optimization model is also a valuable attribute. Ideally, the final EWO model should consider all the product, process and supply chain attributes in order to make the best decision. If these cannot be implemented in the EWO model, at least they should be considered and the decision can be made at a different scale level, typically below. One example of the importance of developing models in each of the scales can be found in optimizing the energy consumption in an industry. From a mathematical process optimization point of view, it is possible to obtain the optimal composite curve and heat exchanger network [23]. The definition of this network is typically done using commercial heat exchangers with standard specifications, which are placed in an optimal distribution. However, with previous decisions one does not design the most efficient heat exchanger, being necessary to develop more rigorous models that address the distribution of heat transfer within the heat exchanger and suggesting, for example, the introduction of lobed pipes [24], which could be a cheaper decision. Thus, the generation of models in each of the scales is necessary since the process proficiency can be improved in different ways that need to be taken into account. Based on this fact, this thesis provides a process and modeling studies under different scales for two types of industries with formulated products. For a

better understanding of the possible models that one can find in each of the scales and the approaches followed in the modeling of processes, the following section provides a review of them.

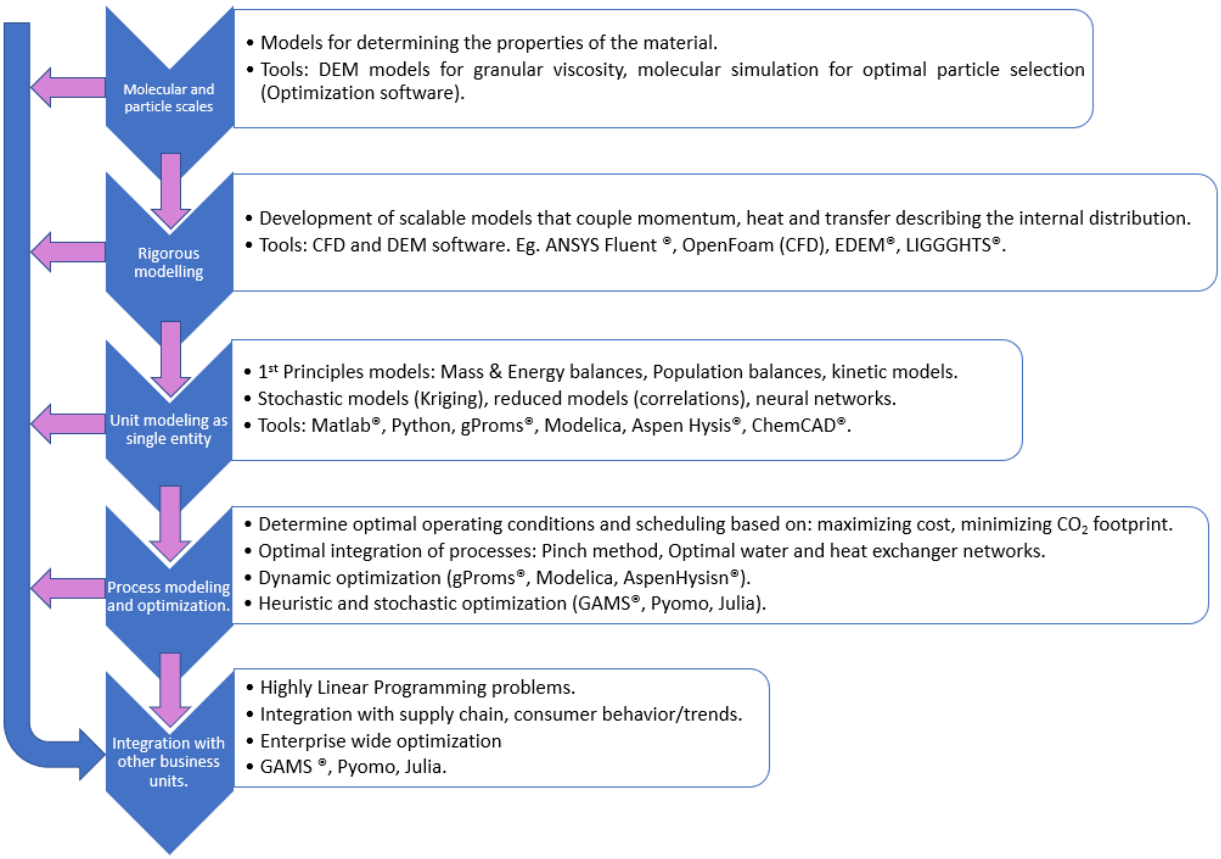

Figure 2. Types of tools and models at different scales.

G.3 MODELING APPROACHES FOR PROCESSES

In this section the modelling approaches typically used at process level are depicted. The first section 3.1 provides a description of the models used when each of the units are described as a single entity. Section 3.2 describes the rigorous models applied when modeling one unit operation of the process. In these sections most of the modeling approaches are introduced and a description of them is not repeated in the scales defined in sections 3.3 to 3.5. In section 3.3 a description of hybrid models that can be generated combining process and rigorous modelling approaches is presented. In Section 3.4 and 3.5, the types of modelling approaches that one can find within units at meso and particle scales are described. In the last section 3.6 an overview of the integration of processes with other modeling levels, is presented.

G.3.1 Process modeling assuming each unit as a single entity.

Short-cut methods

The most basic modeling approach in a real system is based on mass, momentum and energy balances. This type of models is simple and can be complemented with other models. In particular, mass balances are the most fundamental requirement and they have to be accomplished even in the least detailed scale (supply chain and enterprise scales) [21, 25].

Mechanistic models

This type of approach uses first principles to model the issues involved in each of the units. They are based on the underlying chemistry, physics or biology that governs the behavior of the system [22]. Some examples of these type of models are:

- Equilibrium models in reactions: Some chemical reactions are limited by thermodynamic constraints. In the case that the reactors ensure enough residence time, the behavior of the unit can be modelled under these conditions. Some examples of the use of the current equilibrium conditions can be found in the water-gas-shift and steam reforming reactions [26].
- Phase equilibrium: This type of approach is used to determine the distribution between two phases. One example of the equilibrium between two phases is given by Henry's law for the absorption of gases in a solution [27]. Another common example is found in the modelling of distillation system. The modeling of each of the single equilibrium stages can be done as in Eq. (1) to (4). Eq. (1) is the global mass balance and Eq. (2) is the mass balance per components. Eq. (3) presents the relation between the concentration in the gas and liquid phases. In Eq. (3), K_i is the equilibrium constant, which is computed as function of the ratio of the vapor pressure of the component and the total pressure as presented in Eq. (4). The vapor pressure can be computed from Antoine equation for each component [23].

$$F = L + V \tag{1}$$

$$F \cdot z_i = L \cdot x_i + V \cdot y_i \tag{2}$$

$$y_i = K_i x_i \tag{3}$$

$$K_i = \frac{P_{vap}^i}{P_{total}} \tag{4}$$

- Kinetic models: In many cases equilibrium conditions are not achieved due to the large residence time required. In these cases, kinetic models are required. These models are more commonly used in the description of reactors [28, 29] but they can also be used for the description of unit operations. For example, one of the main topics of the current thesis is the modeling of drying phenomena, which is modelled following different kinetic approaches, see [30].

- Population balances [31, 32]: This modeling approach is based on discretizing an entity in several bins with homogenous properties. The number of entities generated after the discretization are balanceable and they have rates of growth and death. A general formulation of a population balance in a particulate system is presented in Eq. (5) [22]. In Eq. (5) the term of the left hand side corresponds to the rate of accumulation of the number of particles for every bin, k. The first term of the right hand side accounts for the rate of generation of particles in a bin k, due to collision between particles i and j, the second term represents the rate of destruction of particles due to such collisions, the third term corresponds to the breakage closure for particles of bin k and the fourth term corresponds to the decrease in the number of particles due to breakage in the bins i, larger than k. Function $\alpha(i,j)$ corresponds to the collision efficiency, function $\beta(i,j)$ is the collision frequency and $\chi(k)$ is the breakage function.

$$\frac{dn_k}{dt} = \frac{1}{2}\sum_{i+j=k}\alpha(i,j)\beta(i,j)n_i n_j - \sum_{i=1}^{\infty}\alpha(i,j)\beta(i,j)n_i n_j - \chi(k)n_k + \sum_{i>k}^{\infty}\chi(i)n_i \quad (5)$$

Rules of thumb

This methodology based on operational data from industry provides a simple approach to model the units. Based on them, constrains that characterize the range of operation and models for the operating conditions, consumptions, etc. are obtained. Some books [33-35] collect a series of references for multiple units such as heat exchangers, compressors, distillation columns, etc.

Dimensionless analysis

The dimensionless analysis stablishes what dimensionless groups determine the performance of the system. It is based on the generation of correlations that capture the scale up/down issues [36]. Large number of applications in fluid mechanics and heat or mass transfer use these kinds of models. For example, Dittus-Boelter correlation, Eq. (6), is used in the heat transfer of fluids in pipes with fully developed turbulent regime or Ranz-Marshall equations, Eq. (7) and (8) are used to model the heat and mass transfer in spherical droplets/particles [37]. These correlations are empirical and the parameters used can be corrected. For example, in Dittus-Boelter correlation, n takes a value of 0.3 when the fluid is heated and 0.4 when the fluid is cooled down. Similarly, alternatives to Ranz-Marshall correlations have been also proposed modifying the parameters and including terms to address the role of viscosity or specific heat capacity [38].

$$Nu = 0.023 \cdot Re^{0.8} \cdot Pr^{0.3} \quad (6)$$

$$Nu = 2 + 0.6 \cdot Re^{0.5} \cdot Pr^{0.33} \quad (7)$$

$$Sh = 2 + 0.6 \cdot Re^{0.5} \cdot Sc^{0.33} \quad (8)$$

Reduced order models

In some cases such as in optimization or control, the models developed for a detailed prediction of the performance or operation of a unit are too complex to be introduced at a higher scale analysis. In these cases, the generation of reduced models is an effective alternative to be followed. The development of this type of models is typically carried out following the next steps [39]:

- Generation of a design of experiments scheme.
- Running the numerical simulations with a detailed model in each of the sampling points.
- Construction of the subrogate model.
- Validation of the model.

In the first step the use of design of experiments techniques helps to distribute the sampling point through the space of design. Generally, full factorial designs are very computational expensive and fractional methods are used. Latin Hypercube sampling is a stratified method where every portion has a representative value. This method shows problems with the uniformity of the samples through the design space [39]. The Orthogonal arrays (OA) is a method where probable subspaces are generated in the design space. These spaces are orthogonal to each other [40]. This method depends on four variables: the number of samples, the number of variables, the levels of the variables and the number of effects to be accounted for in the model [39]. In the specific case that the number of subspaces is one (the subspace is the same than the space of design), the design space obtained by OA methods is the same than Hypercube sampling. One of the problems involved in OA is the possibility of creating duplicate points. This is not desirable in surrogate models from rigorous simulations. A method that uses random sampling is the Monte Carlo simulation. In this technique, with the random sampling and the statistical inference tools, it is possible to extract information about the system [41]. Finally, the maxmin approach maximizes the minimum distance between two design points [42].

The second stage generates a set of results by running the model for the scenarios generated in the sampling. These scenarios are used in the third stage to build the subrogate model. Different methods and with various optional stages can be followed. It is possible to distinguish the two following sub-stages:

1. Characterization of principal components.
2. Determine the model with the optimal number of terms and fitting of the function.

In the first sub-stage of the subrogate model generation, the variables with higher influence on estimating the final value are determined. One of the most recurrent techniques to identify the key variables is principal component analysis (PCA). It is used with the objective of minimizing the set of input variables to the most significant ones. This analysis determines the possible correlated variables into a set of values (principal components) that are linearly uncorrelated. The use of PCA is not limited to linear models [43] and continuous variables, nonlinear models and other variables such as binary, discrete or symbolic data can be also analyzed [44]. Alternatively to

PCA, other statistical methods such as Kernel PCA, or methods based on mapping possible solutions can be also used [45].

Once the most critical components have been characterized, the terms that compose the model need to be determined. Different approaches have been followed in the generation of these models such as the use of B-splines [46], the generation of kriging models, models based on multivariate analysis or artificial neural networks. Among them, the most basic modelling approach is the use of polynomial regressions, which uses the relation between the variable using a polynomial function [47].

However, the output of the model is typically affected by more than one factor (Multivariate analysis) and one needs to evaluate the optimal variables to be addressed. With the objective of determining a model that ensures a good trade-off between accuracy and complexity, one can evaluate the model using different metrics such as Bayesian, Akaike's or Hannan-Quinn information criterion. These metrics evaluate each of the possible models generated by the combination of all the terms, introducing a penalty term for the number of parameters in the model. The model that has the lowest value of the metric represents the best trade-off between accuracy and complexity, reducing the risk of overfitting [48, 49]. The minimization of these metrics for multivariate models is available in ALAMO, which uses a global optimization solver, BARON, for determining the model that minimizes each criterion from an initially specified set of possible functions (linear, inverse, quadratic, etc.) [50-52]. This machine learning procedure based on minimizing previous criteria is useful when simple correlations are generated. However, characterizing the parameters of the model when it has highly non-linear terms (eg. $x^a y^b$, x/log(ay)) is difficult since the problem is a complex NLP with MIP in the selection of the terms. In these cases, the evaluation of possible models must be carried out by the developer, having as guide the reduction to the most significant terms obtained from PCA.

Kriging models estimate the relationship between variables as a sum of two terms, see Eq. (9). The first one is a linear model (for example a polynomial) and the second one represents the fluctuations on the mean of the data set y(x) [53-55].

$$y(x) = f(x) + Z(x) \tag{9}$$

Z(x) is a stochastic Gaussian process with a mean value of 0 and a covariance given by Eq. (10), where σ^2 is the process variance and $R(w,x)$ is a correlation function.

$$\mathrm{cov}(Z(w), Z(x)) = \sigma^2 R(w,x) \tag{10}$$

Another surrogate modelling approach is the use of Artificial Neural Networks (ANN) [56]. In this methodology, the model tries to imitate the behaviour of human neural networks in the brain. A scheme of the basic structure of a neuron is shown in Figure 2 [57]. This method is based on generating an input signal as the summation of all the weighted inputs, see Eq. (11), and send it to a transfer function as the one proposed in Eq. (12). To address the high complexity of some problems, the number of neurons can be extended, including different layers.

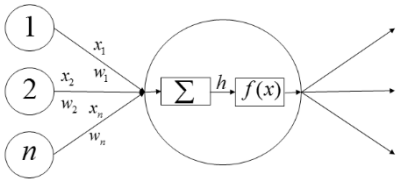

Figure3. Scheme of a neural unit.

$$x_{in} = \sum_{i=1}^{n} x_i \cdot w_i \tag{11}$$

$$f(\mathrm{x}) = \frac{1}{1+e^{h}} \tag{12}$$

G.3.2 Rigorous modeling with internal description

Previous modeling approaches and methodologies are used at process scale, assuming the units as a single entity and missing the distribution of properties within them. For addressing such distribution, more detailed methods based on solving partial differential equations are addressed, as presented in the following paragraphs.

Computational fluid dynamics

Computational fluid dynamics (CFD) modeling is based on solving the continuity, momentum and energy equations. Two approaches have been proposed to solve these equations: by means of particle elements with Lattice-Boltzmann method [58, 59] and by means of finite volume method. The second approach is the most common and it is based on dividing the fluid system in infinitesimal elements. In each of the elements the equations are solved using the finite volume method [60], which provides an approximate solution to the integral form of the equations. The accuracy of the solution is then highly dependent on the size of the elements, being necessary to ensure a sufficient small size for that solution not to change. This evaluation, named grid independence test, is typically the first stage in the development of a CFD model. Then, the models are defined. In most of the chemical processes the flow is turbulent, being necessary to include in the model turbulent components such as turbulent kinetic energy and dissipation of eddies. Different approaches can be followed depending on how the eddies of the turbulence are modelled, see Figure 4:

- Direct Numerical Simulations reproduce all eddies of the entire control volume requiring very high computational cost.
- Large Eddy Simulations uses a filter to exclusively reproduce eddies with enough size. The remaining smaller eddies are modelled by means of turbulent models.
- Reynolds Average Navier-Stokes (RANS) approach uses turbulence models for reproducing the energy contained and dissipated in eddies. This approach is the most commonly used in the modeling of industrial processes.

For further description of the approaches, models, numerical methods used in the CFD and applications to chemical engineering problems the reader is referred to the following literature [60-63].

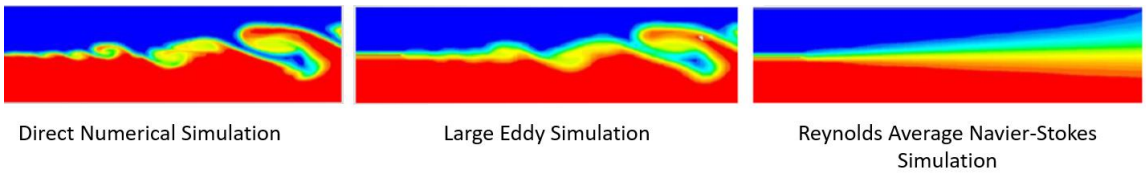

Figure 4. Comparison between Direct Numerical, Large Eddy and Reynolds Average Navier-Stokes Simulations [64].

Discrete Element Method

Discrete or Distinct Element Method (DEM) is a rigorous modeling approach used for reproducing the motion of the particles. The Newton's laws of motion are applied to describe the motion of the particles and contact mechanics are used to describe the interaction with neighbor particles. Depending on how the contact between the particles is modelled, two type of approaches are distinguished:

- Soft-sphere approach where spherical particles are allowed to have deformation and multiple contacts are allowed to occur at the same time. These deformations are used to calculate the elastic, plastic and frictional forces between the particles. Since multiple contacts can be modelled at the same time, this approach is useful in particulate systems where the solid fraction is relatively high (e.g. rotating drums, blenders).
- Hard sphere approach where one collision can occur at a time, being rarely to use an explicit definition of the forces between the particles. This method is more useful in rapid granular flows where the solid fraction is small or in systems where particle contact forces are not relevant.

For further detail in the description of the forces involved and the applications of DEM in different processes, the following literature is recommended [65-67].

Multiphase modeling

The modeling of chemical processes is not exclusively limited to previous rigorous modeling approaches. In many cases, multiphase systems are used in the processing of formulated products. For example, fluidized beds or spray dryers in pharmaceutical processes or each of trays in a distillation column. In these cases, the CFD model is typically used to model the continuous phase, meanwhile the discrete phase is modelled using other approaches such as:

- Particle source in cell method, which has resulted in the discrete parcel method (DPM), uses a parcel that involves a group of particles/droplets/bubbles with the same properties [68, 69]. The method allows implementing the models for turbulence dispersion, particle collision and motion, resulting in a parcel

tracked through the flow field. It is also important to remark that different DPM methods can be used depending on the volume fraction [70]:

  - The CFD-DPM 1-way coupling approach where the motion of the discrete phase is governed by the fluid dynamic forces, being the fluid not affected by the presence of discrete phase. This approach is only suitable for volume fractions below $1 \cdot 10^{-6}$.
  - The CFD-DPM 2-way coupling approach takes into account both the influence of the fluid dynamics on the particles and the influence of the particles on the fluid. This approach is recommended for volume fractions below $1 \cdot 10^{-3}$.
  - The CFD-Dense DPM approach where particles interactions play a significant role in the particle motion. This approach is recommended for volume fractions above $1 \cdot 10^{-3}$.

- DEM method, allowing to reproduce all the particle motion as described in previous paragraphs is another method integrated with CFD [66, 67]. The CFD-DEM resultant models have been mainly applied for fluidizations and pneumatic conveying systems [67, 71].
- Apart from the most common approaches based on coupling CFD with DPM and DEM methods, other approaches coupling CFD with population balances [72, 73] or the use of a two fluid methods are also used in multiphase systems [74,75].

G.3.3 Hybrid models

The use of rigorous models such as the previous CFD and DEM provides a detailed description of the units but requiring a high computational cost. Alternatively, process models do not ensure a description of the distribution within the unit but they are simple enough to have low computational costs and being implemented into process control and optimization. With the objective of generating a tool that combines both benefits from CFD and process models appears the use of CFD driven compartment models [76, 77]. The approach is based on dividing the geometry of the processing unit into a network of ideal reactors. Each of the reactors corresponds to a zone that can be constructed based on different criteria. Bezzo et al. proposed an automatic procedure for generating zones with similar sizes, as well as they transfer the fluxes from CFD to the compartment model [78]. The approach has been widely used in compartment models based on CFD and DEM [12,17]. Alternatively, each of the compartments can also corresponds to a zone with homogeneous phenomena [79] or properties such as flow pattern [76], turbulent components [80] or temperature distribution [81]. A methodology for characterizing these phenomena within the units have been also recently presented by Tajsoleiman et al. [82]. However, the distribution of the zones is time and operating conditions dependent, being necessary to generate flexible zones in future works. A review of the challenges, among them the previous one, methodologies and tools in the generation of compartment models has been recently presented by Jourdan et al. [83].

G.3.4 Mesoscale models

In the case of structured products, the particle and mesoscale levels are defined between the unit and molecular levels. At mesoscale level the modeling is mainly based on the use of mechanistic models that explain the physics behind a phenomena. These models focus on bridging the gap between a discrete system like a particle, which typically uses more theoretical models, and a continuous system such as a finite volume part of a unit, which mainly uses empirical models. The scale-up is not straightforward since the properties move from a heterogeneous to a homogeneous distribution depending on the finite volume selected, see Figure 5. These small finite volumes, where continuity is ensured, correspond to a level covered by mesoscale modeling [22]. This area has been widely covered in the modeling of turbulent flows, where averaging methodologies such as the RANS method have been proposed resulting in effective transport coefficients like the eddy viscosity [22, 84]. In the case of turbulence the average is computed over time, but spatial distribution also exists, especially in the area of multiphase and particle systems. In multiphase systems, one modelling approach followed is based on using empirical models. One example is the Ergun equation for the flow through a packed bed where there is an average porosity factor to be determined for every bed [85]. Another approach that provides a spatial description of a multiphase system in mesoscale is the two fluid model approach. In this approach, the discrete phase is assembled as another fluid. As in CFD, the entire flow field is divided in a number of cells to obtain the motion of both phases, where the discrete phase needs to be formulated as a fluid with average density and viscosity properties [20]. In the case of particulate systems, the scale-up from particle scale to mesoscale is not straightforward. One of the modelling approaches used nowadays is based on generating reduced models for mechanical properties from DEM models that account the motion of the single particles that compose the system [86, 87].

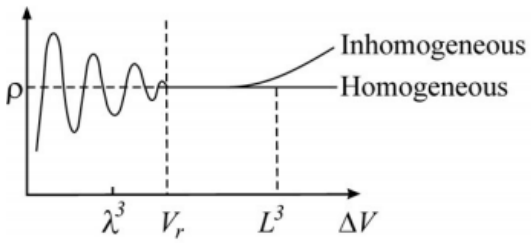

Figure 5. Concept of representative elementary volume fluid [22].

G.3.5 Particle scale models

In the modeling at particle scale level the properties are not continuous [22]. At this scale, each of the particles are treated as a discrete system. As at mesoscale level, most of the modelling approaches are mechanistic since the main focus is to describe the physics involved in the system. However, two levels can be distinguished depending on the accuracy desired. On the one hand, the particles are studied as a single entity assuming homogeneous properties, the studies are mainly based on the use of empirical models. For example, in the modeling of drying systems, a common approach is the evaluation of a single particle whose drying is modeled and later scale-up by

means of Ranz-Marshall correlations [37]. In this example, the most common models proposed for drying are empirical, where a diffusion coefficient or equivalent constants are determined for each type of droplet [30, 88].

On the other hand, the particle structure is desired to be reproduced. Revising the example of drying single droplets, one can also find examples where the droplet structure has been studied. This structure has been modeled by means of a combination of empirical models that are discretized in each internal structure [89] or by using population balances [90]. Another common example where particle structure is modeled with a different technique is the use of DEM simulations to predict the structure of particles [91, 92]. This use of DEM simulations in the modeling of structures has not been exclusively limited to particles, products from other types of industries have been also evaluated such as concrete [93] and batteries [94].

G.3.6 Integration of process models with other scales.

The models developed for processes can be combined with the models of other business units that take part of the development of the product. On the one hand, the model can be integrated with platforms dedicated to model formulations or molecules. On the other hand it can be reduced for its integration into supply chain and EWO.

Integration with molecular design

Molecular design focus on determining stable species that meet a certain set of properties. In this context, the use of Computer Aided Molecular-Mixture Design (CAMD) helps on the definition of the molecular structures and their stability. The development of CAMD tools have mainly focused on a very detailed definition of the properties for each of the functional groups and the interactions among them [8, 95]. These CAMD techniques have not only focus on bulk chemicals, formulation of solvents and polymers have been also studied [96, 97]. However, the interaction of the different products that compose a mixture is not always captured by thermodynamic models, and empirical models based on the critical quality attributes are used [98, 99]. The use of reduced models based on empirical measurements allows the optimization of this product design problem identifying the mixture of components. Furthermore, the use of these reduced models also allows the integration of the formulation characterization within a process optimization problem. These optimization problems based on simultaneous process and product design can be classified into two groups [100]:

- Blending and pooling problems where different raw materials are used for the production of a formulated product. Different examples of this type of problems have been addressed such as in the production of polymers [101] and surfactants [102].
- Design of the formulated product fed into a process. In this type of problems the composition of a product used in the entire facility is designed. This type of problem typical of refineries, can be also find in a bio-refinery [103].

Integration with supply chain and enterprise levels

Above the process, the supply chain scale of the ingredients and the products is found. The costs involved in the supply chain also affect the formulation of the products where the distance also supposes a cost. Different types of supply chains can be considered in the definition of the problem such as centralized or decentralized approaches, cooperative or non-cooperative and global or national. In the case of a decentralized approach where the manufacturer decisions affect the behavior of the supplier and costumers, two type of modeling approaches for the supply chain have been followed [100]:

- A graphical method where a hierarchical graph is used to model the interactions between the products [104].
- A multilayer model where the different actors involved are posed in different levels [105].

Both types of approaches have been used not only to evaluate the profit, but also environmental and social aspects [106]. The integration of the process variables into this supply chains have required the use of model reduction techniques based on decomposition [107], Taylor-made solution algorithms [108] or metaheuristics [109]. Nonlinearities are addressed in the models of the process as well than in the mixing of the components, hindering the integration with the MIP of the supply chain and becoming necessary the use of these techniques. Reducing to MIP, one can not only determine the optimization of the process, but it is also possible to have suggestions on the scheduling of the operations [11,110].

G.4 AIMS, SCOPE AND STRUCTURE OF THE THESIS

As it has been remarked in the first section, the use of computational tools helps in the first to market concern by accelerating and making decisions in the development of new products. In the current work, the development of these tools focuses on the modeling and optimization of processes that involve formulated products. The structure of the thesis is presented in Figure 6. On the one hand, the modeling of processes with structured formulated products, detergents, is developed. On the other hand, the second part of the thesis focuses on the optimization of processes with formulated products, wastes, where the influence of the structure is not considered.

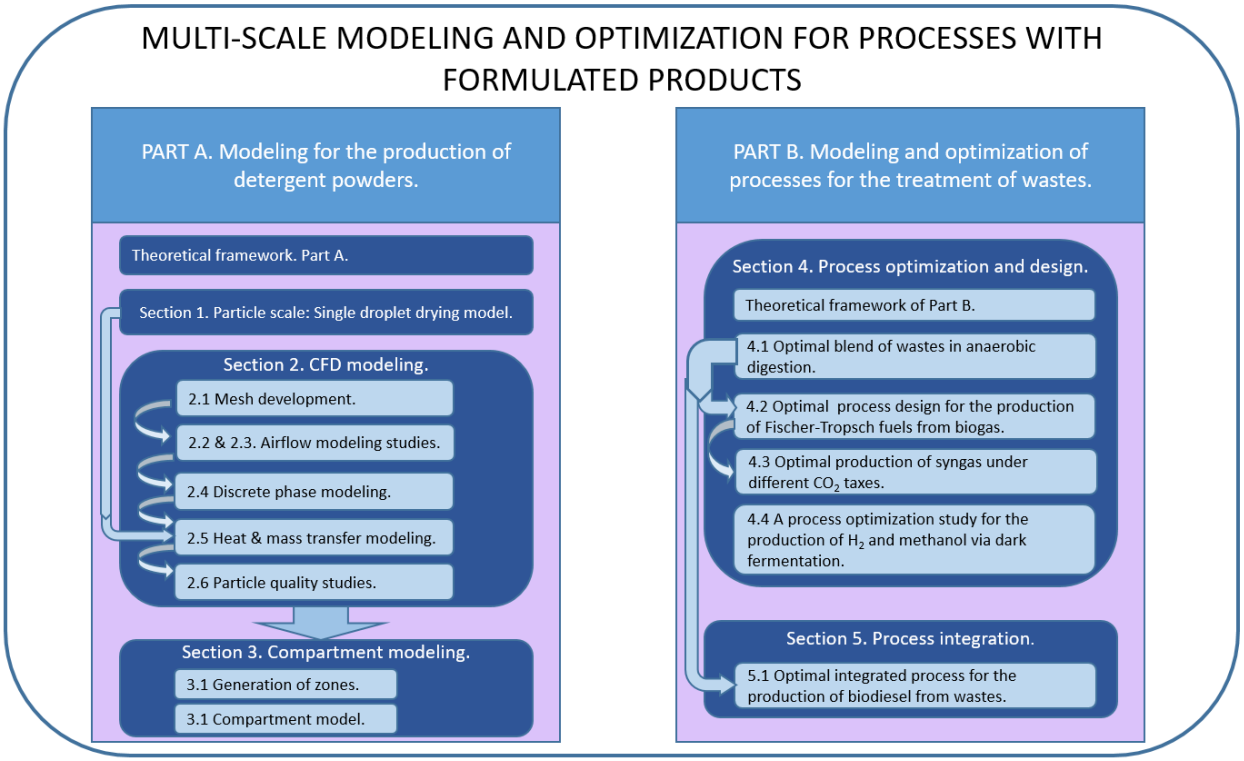

Figure 6. Structure of the thesis.

The first part of the thesis undertakes the modeling of the process for the production of powder detergents. In particular, the thesis is focus on the spray drying unit, where different modeling methodologies are applied to the process. The rigorous modeling of this unit requires the implicit evaluation of different scales. The drying has been traditionally modeled scaling up with Ranz-Marshall correlations the drying of a single droplet [37]. Therefore, in the first part of the thesis different modeling approaches are used from particle to process level. The different chapters of the first part of the thesis are divided according to these scales and approaches as:

- First, in section 1 the drying of detergent powders is evaluated at particle scale. In this chapter a comparison of different mechanistic modeling approaches are evaluated under different detergent formulations.
- Section 2 of this part focuses on the development of a rigorous model for the spray drying unit. This section is divided in the following subsections corresponding to each of the stages in the modeling of the unit.
    - Initially, in 2.1 the generation of the finite volumes is carried out. The procedure followed for the meshing is developed performing a grid independence test and comparing the solutions obtained for the modeling of the fluid in transient and steady-state operations.
    - Section 2.2 focuses on modeling the airflow in the system without the interaction of the particles. Even though particles have not been addressed, the deposits generated in the walls by previous operation of the unit have shown to have a relevant influence on the airflow dynamics [111]. Then the role of dried deposits on the airflow is studied developing a CFD model.

- In section 2.3, the model developed in the previous section is used for evaluating other studies regarding the dynamics of the airflow. In particular, the irregular distribution of the airflow at the inlets is studied distinguishing two types of airflows and providing a methodology to minimize this distribution.
- In section 2.4, the momentum of the particles interacting with the air is evaluated. In this section the previously validated model for the air is extended with a DPM approach for the modeling of the discrete phase, the particles. This CFD-DPM model is validated with the Residence Time Distribution of an injected pulse of particles.
- Section 2.5 addresses the heat and mass transfer model to the particles. The model developed for single droplets in section 1 is adapted and combined with the previous CFD-DPM model, validating the results with the operation of the unit.
- Section 2.6 performs the last study involving the use of rigorous models. In this study the agglomeration generated in the walls is obtained from the model developed in the previous section.

- Section 3 of this part focuses on the development of compartment models based on the previously validated CFD-DPM model. As it has been presented in the introduction, one of the key aspects in the development of a new product is the speed in making the decisions. In this context, the use of zonal model becomes a very useful technique to accelerate that decisions providing a similar accuracy than CFD based models. For the generation of this model, two parts are distinguished:
  - A first chapter 3.1 where the generation of the zones as a function of the momentum is evaluated as well as a procedure for generating zones that is flexible depending on the operating conditions and that are composed by different sets of equivalent reactors.
  - A second chapter 3.2 where the zonal model developed for the simulation of the dryer is evaluated in terms of heat and mass transfer.

In the second part of the thesis different modeling approaches are applied to the optimization of processes. This part focuses on the use of wastes as raw materials. The wastes used as raw materials are formulated materials composed by different chemicals such as carbon, nitrogen and oxygen. The treatment of these wastes can be performed following different thermal (incineration), thermochemical (gasification, pyrolysis, etc.) or biochemical (anaerobic digestion, fermentation, etc.) methods [112]. In the current thesis, processes involving biochemical methods are optimized for the generation of products with added value. The studies are structured as follows:

- In the first section 4, the studies focus on the development of the following process optimization problems:
  - In section 4.1 a first study where a combined product and process optimization problem is presented. The study focuses on the anaerobic digestion of wastes for the production of power and chemicals, where the optimal operating conditions of the process are optimized at the same time that the optimal blend from a given set of wastes.

- In section 4.2, the study focuses on determining the optimal process operating conditions and mixture of gases that can be used for the production of fuels via tri-reforming of methane and Fischer-Tropsch process. Among these gases, the use of biogas, which can be produced from anaerobic digestion, is also evaluated.
- In section 4.3 the operation and technology selection under different CO_2 taxes are evaluated. From this approach, it is possible to determine the optimal operating conditions as well as the CO_2 taxes for which one has to change between two technologies. Different reforming technologies and raw materials, among them biogas, are evaluated.
- Section 4.4 focuses on the modeling and optimization of dark fermentation for the treatment of biomass and wastes. Several kinetic models are compared for this process and they are later addressed in to the process optimization where two produced chemicals are studied, hydrogen and methanol.

- In the last section 5, a process integration study is evaluated. The two products obtained from anaerobic digestion, biogas and digestate, can be processed for generating products with higher value. In the current case the production of biodiesel is evaluated. On the one hand, digestate can be used as fertilizer to increase the yield in the production of algae, which are then used to produce oil. On the other hand, the biogas can be used for producing methanol, which is used later in the transesterification of the oil for the production of biodiesel.

REFERENCES

[1] The Institute of Grocery Distribution and IGD Services (2019) c2004-2019. Available in: ttp://www.igd.com/About-us/Media/Key-industry-facts/.

[2] The European Chemical Industry Council (2020). Landscape of the European Chemical Industry 2020. Available in: https://www.chemlandscape.cefic.org/

[3] The European Federation of Pharmaceutical Industries and Associations (2019) Available in: https://www.efpia.eu/

[4] Litster, J. Bogle, I.DL. (2019) Smart Process Manufacturing for Formulated Products. Engineering, 5, 1003-1009.

[5] Hill, M. (2004) Product and Process Design for Structured Products. AIChE Journal, 50 (8), 1656-1661.

[6] Cussler, E.L. Moggridge, G.D. (2011) Chemical Product Design. Cambridge University Press, 2nd Edition. ISBN: 9781139035132.

[7] Koning, A. Schowanek, D. Dewaele, J. (2010) Uncertainties in a carbon footprint model for detergents; quantifying the confidence in a comparative result. Int. J. Life Cycle Assessment, 2010; 15-79.

[8] Gani, R. (2004) Chemical product design: Challenges and opportunities. Computers and Chemical Engineering 28, 2441-2457.

[9] Byron, P.R. Hindle, M. Lange, C.F. Longest,P.W. McRobbie, D. Oldham, M.J. Olsson, B. Thiel, C.G. Wachtel, H. Finlay, W.H. (2010) In Vivo-In Vitro Correlations: Predicting Pulmonary Drug Deposition from Pharmaceutical Aerosols. Journal of Aerosol Medicine and Pulmonary Drug Delivery, Vol. 23, No. S2. S-59 – S-69.

[10] Cao, H. Jia, X. Li, Y. Amador, C. Ding, Y. (2019) CFD-DNS simulation of irregular-shaped particle dissolution. Particuology, DOI: https://doi.org/10.1016/j.partic.2019.08.003

[11] Lee, H. Pinto, J.M. Grossmann, I.E. Park, S. (1996) Mixed-Integer Linear Programming Model for Refinery Short-Term Scheduling of Crude Oil Unloading with Inventory Management. Ind. Eng. Chem. Res. 35, 5, 1630-1641.

[12] Rogers, A.J. Hashemi, A. Ierapetritou, M.G. (2013) Modeling of Particulate Processes for the Continous Manufacture of Solid-Based Pharmaceutical Dosage Forms. Processes, 2013, 1, 67-127.

[13] Lian, G. Moore, S. Heeney, L. (2006) Population balance and computational fluid dynamics modelling of ice crystallization in a scraped surface freezer. Chemical Engineering Science, 61(23), 7819-7826.

[14] Arellano, M. Benkhelifa, H. Alvarez, G. Flick, D. (2013) Coupling population balance and residence time distribution for the ice crystallization modeling in a scraped surface heat exchanger. Chemical Engineering Science,

[15] Dorneanu, B. Bildea, C.S. Grievink, J. Bongers, P.M. (2010) A reduced model for the freezing step in ice cream manufacture. Computer Aided Chemical Engineering, 28 (C), 265-270.

[16] Klatt, K-U. Marquardt, W. (2009) Perspectives for process systems engineering. Personal views from academia and industry. Computers & Chemical Engineering, 33(3), 536-550.

[17] Gernaey, K.V. Cervera-Padrell, A.E. Woodley, J.M. (2012) A perspective on PSE in pharmaceutical process development and innovation. Computers & Chemical Engineering, 42, 15-29.

[18] Bui-Thanh, T. Willcox, K. Ghattas, O. van Bloemen Waanders, B. (2007) Goal-oriented, model-constrained optimization for reduction of large-scale systems. Journal of Computational Physics, 224 (2), 880-896.

[19] Marquardt, W. (2001) Nonlinear Model Reduction for Optimization Based Control of Transient Chemical Processes. Chemical process Control – 6, Tucson, Arizona, 7-12.1.2001.

[20] Tsuji, Y. (2007) Multi-scale modeling of dense phase gas-particle flow. Chemical Engineering Science 62, 3410-3418.

[21] Guillén-Gosálbez, G. You, F. Galán-Martín, A. Pozo, C. Grossmann, I.E. (2019) Process systems engineering thinking and tools applied to sustainability problems: current landscape and future opportunities. Current Opinion in Chemical Engineering, 26, 170-179.

[22] Rasmuson, A. Andersson, B. Olsson, L. Andersson, R. (2014) Mathematical modeling in Chemical Engineering. Cambridge University Press. ISBN: 978-1-107-04969-7.

[23] Biegler, L.T. Grossmann, I.E. Westerberg, A.W. (1997) Systematic methods of Chemical Process Design. Prentice Hall.

[24] Tang, X. Dai, X. Zhu, D. (2015) Experimental and numerical investigation of convective heat transfer and fluid flow in twisted spiral tube. International Journal of Heat and Mass Transfer, 90, 523-541.

[25] Martín, M. Grossmann, I.E. (2012) BIOpt: A library of models for optimization of biofuel production process. Computer Aided Chemical Engineering, 16-20.

[26] Roh, H.S. Lee, D.K. Koo, K.Y. Jung, U.H. Yoon, W.L. (2010) Natural gas steam reforming for hydrogen production over metal monolith catalyst with efficient heat-transfer. Int. J. Hydrogen Energy, 35 (3), 1613-1619.

[27] Geankoplis, C.J. (2003) Transport processes and separation process principles. Pearson Education Inc. 4th Edition. ISBN: 978-81-203-2614-9.

[28] Fogler, H.S. (2016) Elements of Chemical Reaction Engineering. Pearson Education Inc. 5th Edition. ISBN: 978-0-13-388751-8.

[29] Levenspiel, O. (2004) Chemical Reaction Engineering. John Wiley & Sons, Inc. 3rd Edition. ISBN: 978-81-265-1000-9

[30] Mezhericher, M. Levy, A. Borde, I. (2010) Theoretical models of single droplet drying kinetics: A review. Drying Technology, Vol. 28, 278-293.

[31] Ramkrishna, D. (2000) Population balances: Theory and applications to particulate systems in engineering. Academic press. ISBN: 0-12-576970-9.

[32] Ramkrishna, D. Mahoney, A.W. (2002) Population balance modeling. Promise for the future. Chemical Engineering Science, 57 (4), 595-606.

[33] Branan, C.R. (2005). Rules of Thumb for Chemical Engineers. Elsevier. 4th edition.

[34] Couper, J.R. Penney, W.R. James, R.F. Walas, S.M. (2005) Chemical Process Equipment. Selection and Design. Second Edition. Gulf Professional Publishing. Elsevier. ISBN: 978-0-7506-7510-9.

[35] Woods, D.R. (2007) Rules of thumb in Engineering Practice. Wiley. ISBN: 9783527312207.

[36] Munson, B.R., Young, D.F., Okiishi, T.H., Huebsch, W.W. (2009). Fundamentals of Fluid Mechanics. John Wiley & sons. 6th edition.

[37] Ranz, W.E. Marshall, W.R. (1952) Evaporation from Drops. Chem. Eng. Progress. 48 (22), 141-146.

[38] Young, R.M. Pfender, E. (1987) Nusselt number correlations for heat transfer to Small Spheres in Thermal Plasma Flows. Plasma Chemistry and Plasma Processing, 7, 2, 211-227.

[39] Queipo, N. V., Haftka, R.T., Shyy, W., Goel, T., Vaidyanathan, R., Tucker, P.K. (2005). Surrogate-based analysis and optimization. Progress in Aerospace Sciences, 41, 1-28.

[40] Arora, J.S. (2017). Introduction to Optimum Design. Elsevier, 4th edition. ISBN: 9780128008065

[41] Lemieux, C. (2009). Monte Carlo and Quasi-Monte Carlo Sampling. Springer.

[42] Roshan Joseph, V. Gul, E. (2015) Maximum projection designs for computer experiments. Biometrika (2015), 1-10. DOI: 10.1093/biomet/asv002

[43] Dong, D. McAvoy, T.J. (1996) Nonlinear principal component analysis- Based on principal curves and neural networks. Computers and Chemical Engineering, 20(1), 65-78.

[44] Jolliffe, I.T. Cadima, J. (2016) Principal component analysis: a review and recent developments. Phil. Trans. R. Soc. A 374:20150202. DOI: http://dx.doi.org/10.1098/rsta.2015.0202

[45] Sorzano, COS Vargas, J. Montano, A.P. (2014) A survey of dimensionality reduction techniques. Available in: https://arxiv.org/ftp/arxiv/papers/1403/1403.2877.pdf

[46] Grimstad, B. et al. (2015) SPLINTER: a library for multivariate function approximation with splines. Available in: https://github.com/bgrimstad/splinter.

[47] Montgomery D.C., Peck, E.A., Vining, G.G. (2012). Introduction to Linear Regression Analysis. Wiley, 5th edition.

[48] Miller, A. (2002) Subset selection in Regression. Chapman & Hall. ISBN: 1-58488-171-2.

[49] Akaike, H. (1974) A new look at the statistical model identification. IEEE Transactions on Automatic Control 19 (6): 716-723.

[50] Cozad, A. Sahinidis, N.V. Miller, D.C. (2014) Learning surrogate models for simulation based optimization. AIChE Journal, 60 (6), 2211-2227.

[51] Cozad, A. Sahinidis, N.V. Miller, D.C. (2015) A combined first-principles and data-driven approach to model building. Comp. Chem. Eng. 73, 116-127.

[52] Wilson, Z.T. Sahinidis, N.V. (2017) The ALAMO approach to machine learning. Computers & Chem. Eng. 106, 785-795.

[53] Caballero, J. A. Grossmann, I.E. (2008) An algorithm for the use of surrogate models in modular flowsheet optimization. AIChE. Journal, 54(10), 2633-2650.

[54] Krige, D.G. (1951) A statistical approach to some mine valuation and allied problems on the Witwatersrand. University of Witwatersrand. South Africa University Master's thesis.

[55] Quirante, N. Javaloyes, J., Caballero, J.A. (2015). Rigorous Design of Distillation Columns Using Surrogate Models Based on Kriging Interpolation. AIChE Journal, 61(7), 2169-2187.

[56] Eason, J. Cremaschi, S. (2014) Adaptive sequential sampling for surrogate model generation with artificial neural networks. Computers & Chemical Engineering, 68, 220-232.

[57] Himmelblau, D.M. (2000). Applications of Artificial Neural Networks in Chemical Engineering. Korean Journal of Chemical Engineering, 17(4), 373-392.

[58] Chen, S. Doolen, G.D. (1998) Lattice Boltzmann method for fluid flows. Annual Review of Fluid Mechanics. Vol. 329-364.

[59] Mohamad, A.A. (2011) Lattice Boltzmann method. Springer Verlag. ISBN: 978-1-4471-7422-6.

[60] Anderson, J.D. (1995) Computational Fluid Dynamics: The Basics with Application, McGraw-Hill.

[61] Ferziger, J.H. Peric, M. (2002) Computational Methods for Fluid Dynamics. 3rd Edition. Springer-Verlag. ISBN: 3-540-42074-6.

[62] Andersson, B. Andersson, R. Hakansson, L. Mortensen, M. Sudiyo, R. Van Wachem, B. (2012) Computational Fluid Dynamics for Engineers. Cambridge University Press. ISBN: 978-1-107-01895-2.

[63] Ranade, V. K. (2002) Computational flow modeling for chemical reactor engineering. Academic Press. ISBN: 0-12-576960-1.

[64] ANSYS. (2018) ANSYS Courses. Available under customer registration.

[65] Matuttis, H.G. Chen, J. (2014) Understanding the Discrete Element Method: Simulation of Non-Spherical Particles for Granular and Multi-Body Systems. John Wiley & Sons. ISBN: 9781118567203.

[66] Zhu, H. P. Zhou, Z.Y. Yang, R.Y. Yu, A.B. (2007) Discrete Particle Simulation of Particulate Systems: Theoretical developments. Chemical Engineering Science, 62, 3378-3396.

[67] Zhu, H.P. Zhou, Z.Y. Yang, R.Y. Yu, A.B. (2008) Discrete Particle Simulation Particulate Systems: A Review of Major Applications and Findings. Chemical Engineering Science, 63, 5728-5770.

[68] Crowe, C.T. Sharma, M.P. Stock, D.E. (1977) The Particle-Source-In Cell (PSI-CELL) Model for Gas-Droplet Flows. Journal of Fluids Engineering, 99(2): 325-332.

[69] Michaelides, E. E. Crowe, C.T. Schwarzkopf, J.D. (2006) Multiphase Flow Handbook. CRC Press. ISBN: 9781498701006.

[70] Crowe, C.T. Schwarzkopf, J.D. Sommerfeld, M. Tsuji, Y. (2012) Multiphase flows with droplets and particles. 2nd Edition. CRC Press. ISBN: 9781439840511

[71] Chu, K.W. Yu,A.B. (2008) Numerical simulation of complex Particle-Fluid Flows. Powder Technology, 179, 104-114.

[72] Sanyal, J. Marchisio, D.L. Fox, R.O. Dhanasekharan, K. (2005) On the Comparison between Population Balance Models for CFD Simulation of Bubble Columns. Industrial and Engineering Chem. Res. 44 (14), 5063-5072.

[73] Zucca, A. Marchisio, D.L. Barresi, A.A. Fox, R.O. (2006) Implementation of the population balance equation in CFD codes for modelling soot formation in turbulent flames. Chemical Engineering Science, 61 (1), 87-95.

[74] Mudde, R.F. Simonin, O. (1999) Two- and three-dimensional simulations of a bubble plume using a two-fluid model. Chemical Engineering Science, 54 (21), 5061-5069.

[75] Igci, Y. Andrews, A.T. Sundaresan,S. Pannala, S. O'Brien, T. (2008) Filtered two-fluid models for fluidized gas-particle suspensions. AIChE Journal, 54(6), 1431-1448.

[76] Bermingham, S.K. Dramer, H.J.M. Neuman, A.M. Verheijen, P.T.J. (1998) Towards on-scale crystallizer design using compartmental models. Computers and Chemical Engineering, 22, 355-362.

[77] Bezzo, F. Macchietto, S. Pantealides, C. (2000) A general framework for the integration of computational fluid dynamics and process simulation. Computers and Chemical Engineering, 24 (2), 653-658.

[78] Bezzo, F. Macchietto, S. (2004) A general methodology for hybrid multizonal-cfd models: Part II. Automatic zoning. Computers and Chemical Engineering, 23 (4), 513-525.

[79] Freireich, B. Li, J. Liitster, J. Wassgren, C. (2011) Incorporating particle flow information from discrete element simulations in population balance models of mixer-coaters. Chemical Engineering Science, 66, 3592-3604.

[80] Le Moullec, Y. Gentric, C. Potier, O. Leclec, J.P. (2010) Comparison of systemic, compartmental and CFD modelling approaches: Application to the simulation of a biological reactor of wastewater treatment. Chemical Engineering Science, 65, 1, 343-350.

[81] Kougoulos, E. Jones, A.G. Wood-Kaczinar, M. (2005) CFD modeling of mixing and heat transfer in batch cooling crsytallizers. Chemical Engineering Research and Design, 83 (1), 30-39.

[82] Tajsoleiman, T. Spann, R. Bash,C. Gernaey, K.V. Huusom, J.K. Kruhne, U. (2019) A CFD based automatic method for compartmental model development. Computers and Chemical Engineering, 123, 236-245.

[83] Jourdan, N: Neveux, T. Potier, O. Kanniche, M. Wicks, J. Nopens, I. Rehman, U. Le Moullec, Y. (2019) Compartmental Modelling in Chemical Engineering: A critical review. Chemical Engineering Science, 210, 115196. DOI: https://doi.org/10.1016/j.ces.2019.115196

[84] Pope, S. (2000) Turbulent Flows. Cambridge University Press. ISBN: 9780511840531

[85] Ergun, S. (1952) Fluid flow through packed columns. Chemical Engineering Progress, 48.

[86] Luding, S. (2008) Introduction to Discrete Element Methods: Basics of Contact Force Models and how to perform the Micro-Macro Transition to Continuum Theory. European Journal of Environmental and Civil Engineering. EJECE 12, No. 7-8, 785-826.

[87] Washino, K. Tan, H.S. Hounslow, M.J. Salman, A.D. (2013) Meso-scale coupling model of DEM and CIP for nucleation processes in wet granulation. Chemical Engineering Science, 86, 25-37.

[88] Woo, M.W. Daud, W.R.W. Mujumdar, A.S. Talib, M.Z.M. Hua, W.Z. Tasirin, S.M. (2008) Comparative study of droplet drying models for CFD modelling. Chemical Engineering Research and Design, 86 (9), 1038-1048.

[89] Darvan, A. Sommerfeld. M. (2014) Modeling and numerical analysis of the drying stages during single droplet drying. 19th International Drying Symposium.

[90] Handscomb, C.S. Kraft, M. Bayly, A.E. (2009) A new model for the drying of droplets containing suspended solids. Chemical Engineering Science, 64 (4), 628-637.

[91] Moreno, R. Ghadiri, M. Antony, S.J. (2003) Effect of the impact angle on the breakage of agglomerates: a numerical study using DEM. Powder Technology, 130, 132-137.

[92] Kozhar, S. Dosta, M. Antonyuk, S. Heinrich, S. Bröckel, U. (2015) DEM simulations of amorphous irregular shaped micrometer-sized titania agglomerates at compression. Advanced Powder Technology, 26 (3), 767-777.

[93] Nitka, M. Tejchman, J. (2015) Modeling of concrete behaviour in uniaxial compression and tension with DEM. Granular matter, 17, 145-164.

[94] Sangrós Giménez, C. Finke, B. Nowak, C. Schilde, C. Kwade, A. (2018) Structural and mechanical characterization of lithium-ion battery electrodes via DEM simulations. Advanced Powder Technology, 29 (10), 2312-2321.

[95] Liu, Q. Zhang, L. Liu,L. Du,J. Kumar, A. Eden,M. Gani, R. (2013) OptCAMD: an optimization-based framework and tool for molecular and mixture product design. Computers and Chem. Engineering, 124, 285-301.

[96] Klein, J.A. Wu, D. Gani,R. (1992) Computer aided mixture design with specified property constrains. Computers and Chem. Engineering, 16, S229-S236.

[97] Zhou, T. Wang, J. McBride, K. Sundmacher,K. (2016) Optimal design of solvents for extractive reaction processes. AIChE Journal., 62, 3238-3249.

[98] Conte, E. Gani, R. Ng, KM. (2011) Design of formulated products: a systematic methodology. AIChE Journal, 57, 2431-2449.

[99] Martin, M. Martínez, A. (2013) Methodology for simultaneous process and product design in the consumer products industry: the case study of the laundry business. Chem. Eng. Research and Design, 91, 795-809.

[100] Taifouris, M. Martín, M. Martínez, A. Esquejo, N. (2020) Challenges in the design of formulated products: multiscale process and product design. Current Opinion in Chemical Engineering, 27, 1-9.

[101] Valdyanathan, R. El-Halwagi, M. (1996) Computer-aided synthesis of polymers and blends with target properties. Ind. Eng. Chem. Res. 35, 627-634.

[102] Mattei, M. Kontogeorgis, G. Gani, R. (2014) A comprehensive framework for surfactant selection and design for emulsion based chemical product design. Fluid Phase Equilibria, 362, 288-299.

[103] Martín, M. Grossmann, I.E. (2013) Optimal engineered algae composition for the integrated simultaneous production of bioethanol and biodiesel. AIChE. Journal, 59, 2872-2883.

[104] Sampat, A. Martín,E. Martín,M. Zavala, V. (2017) Optimization formulations for multi-product supply chain networks. Computers and Chem. Engineering, 104, 296-310.

[105] You, F. Grossmann, I.E. (2009) Optimal design of large-scale supply chain with multi-echelon inventory and risk pooling under demand uncertainity. Computers Aided Chemical Engineering, 26, 991-996.

[106] You, F. Ling, T. Graziano, D.J. Snyder, S.W. (2012) Optimal design of sustainable cellulosic biofuel supply chains: multiobjective optimization coupled with life cycle assessment and input-output analysis. AIChE Journal, 58, 1157-1180.

[107] Terrazas-Moreno, S. Grossmann, I.E. Wassick, J.M. Bury, S.J. Akiya, N. (2012) An efficient method for optimal design of large-scale integrated chemical production sites with endogenous uncertainty. Computers and Chemical Engineering, 37, 89-103.

[108] Quesada, I. Grossmann, I.E. (1995) Global optimization of bilinear process networks with multicomponents flows. Computers and Chemical Engineering, 19, 1219-1242.

[109] Fischer, X. Nadeau, JP. (2011) Interactive design: then and now. Research in interactive design, 3, 1-5.

[110] Jia, Z. Ierapetritou, M. (2003) Mixed-Integer Linear Programming Model for Gasoline Blending and Distribution Scheduling. Ind. Eng. Chem. Res. 42 (4), 825-835.

[111] Francia, V. Martin, L. Bayly, A.E. Simmons, M.J.H. (2015) Influence of wall friction on flow regimes and scale-up of counter-current swirl spray dryers. Chemical Engineering Science, 134, 399-413.

[112] Aristizabal-Marulanda V, Botero Gutierrez C, Cardona Alzate C, Chapter 4- Thermochemical, Biological, Biochemical and Hybrid Conversion Methods of Bio-derived Molecules into Renewable Fuels. Advanced Bioprocessing for Alternative Fuels, Biobased Chemicals and Bioproducts. 2019; DOI: https://doi.org/10.1016/B978-0-12-817941-3.00004-8.

PART A. MULTISCALE MODELING OF SPRAY DRYERS.

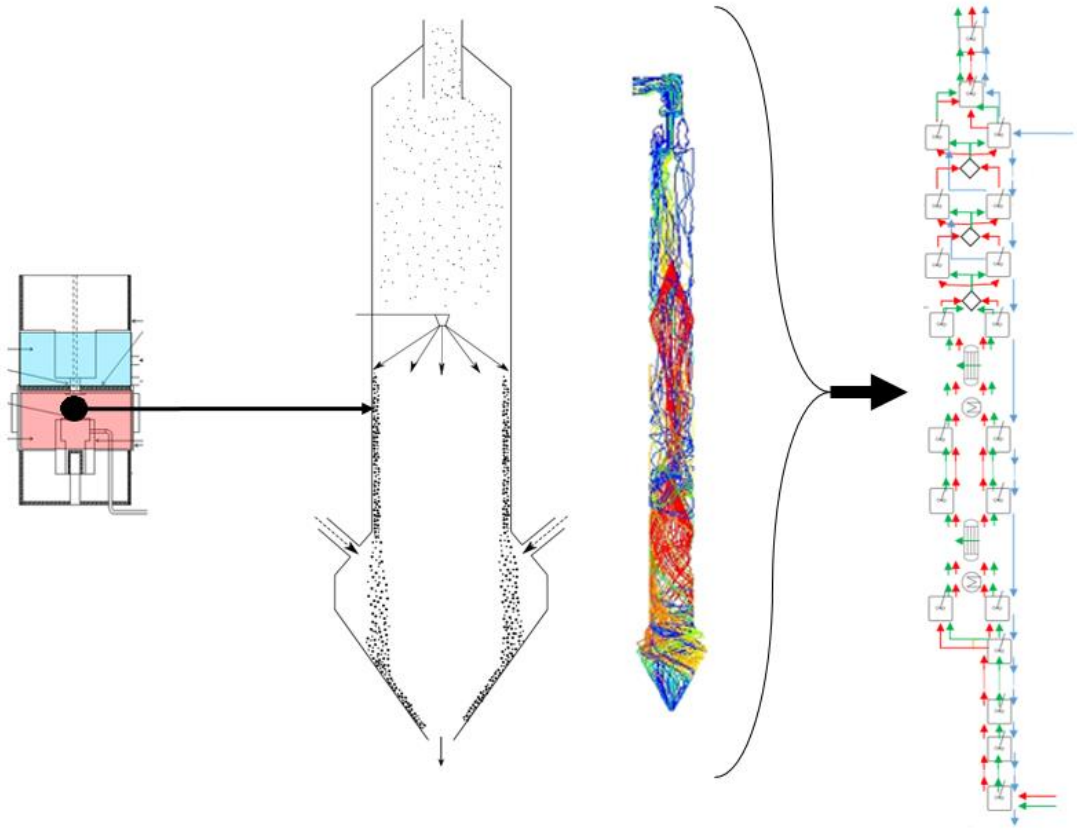

PART A. INTRODUCTION TO SPRAY DRYING.

A.1 INTRODUCTION

This first part of this thesis focuses on the modeling of the detergent powder production process by means rigorous models. It has been developed with the collaboration and sponsorship of Procter & Gamble, concretely, with the department of Modeling & Simulation located at the Newcastle Innovation Centre. One of the conventional ways to produce powder detergents of low density includes the introduction of a spray drying unit to produce the base granule. Spray drying is based on drying an atomized solution or a slurry by contact with hot gas to produce dry particles. Apart from the detergent industry, this process has also been applied in a wide range of industries like in the production of instant coffee, milk powder, pharmaceutical products, enzymes, pigments, catalysts or ceramics. The process is composed of the following four stages that are summarized in Figure 1 and described with detailed in the following sections of this chapter [1]. In particular, special focus is paid to the third stage, whose phenomena is modelled during this thesis.

- 1st Stage: Preparation of the feed, a formulated slurry mixture, in a mixer.
- 2nd Stage: Atomization of the slurry where fine droplets are formed inside the dryer.
- 3rd Stage: Contact between the droplets and the hot air in current or counter-current. During this stage, the moisture of the droplets is evaporated and dried particles are formed. Drying is not the only phenomena that takes place during this stage. At the same time particles interact among them and with the wall. As a result, other phenomena such as agglomeration [2-4] and fouling [4-6] occur simultaneously in the dryer. These phenomena modify the drying as well as other particle properties such as the particle size distribution (PSD), density and shape of the particles.
- 4th Stage: The existing dried powder in the wet air stream is separated from the gas with the use of separation units such as cyclone, scrubber or bag filters.

The presentation of the previous stages into a process diagram is sketched in Figure 2. In this figure, the flowsheet with the equipment for the production of detergent is presented. The 1st stage for the preparation of the slurry is performed into a batch mixer where the mixture is homogenized. This slurry is formed by a suspension of solids in an aqueous and organic phase. Thus, for ensuring a better homogenization in the transition to the continuous operation, a large mixer is necessary. From the mixer, the slurry is pumped at low pressure into a hammer mill that prevents the generation of agglomerates in the liquid stream sent to the atomizers. Finally, the slurry is pumped at high pressure to the atomizers that can be located at different heights in the cylindrical section of the dryer. The slurry injected in the atomizers comes into contact with the air that is introduced in the bottom of the dryer, having a counter-current contact. This air has been previously compressed and heated up in a burner, which generates air at high temperature that is introduced in the dryer by means of a distributor. Once the droplets are dried, they are recovered at the bottom of the dryer by means of a conical base where they roll until leave the tower. However, not all the slurry introduced is recovered at the bottom of the tower. Particles with small particle size, namely fines,

are elutriated with the air and obtained in the top part of the dryer. The fines recovered are separated by means of a system of cyclones in order to avoid their release to the atmosphere.

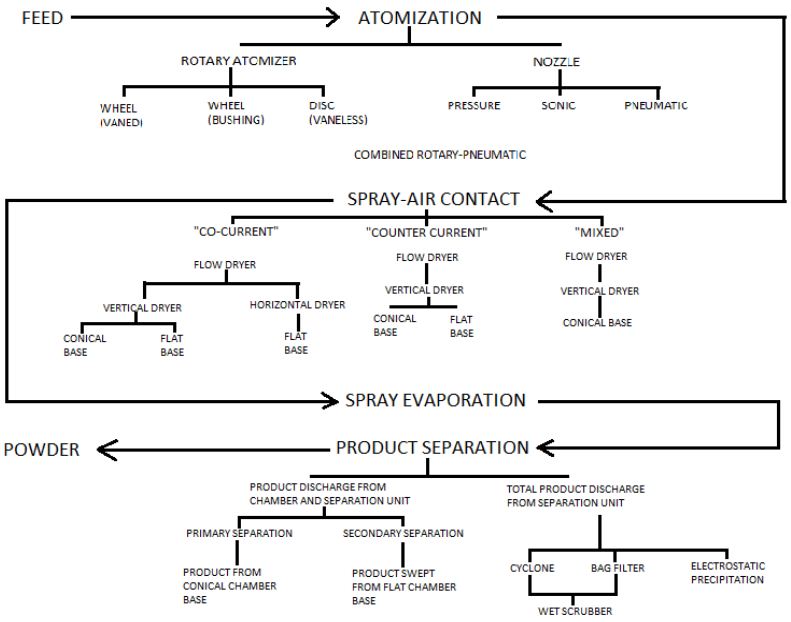

Figure 1. The features of the process stages involved in spray drying. Adapted from Masters, K. (1985) [1].

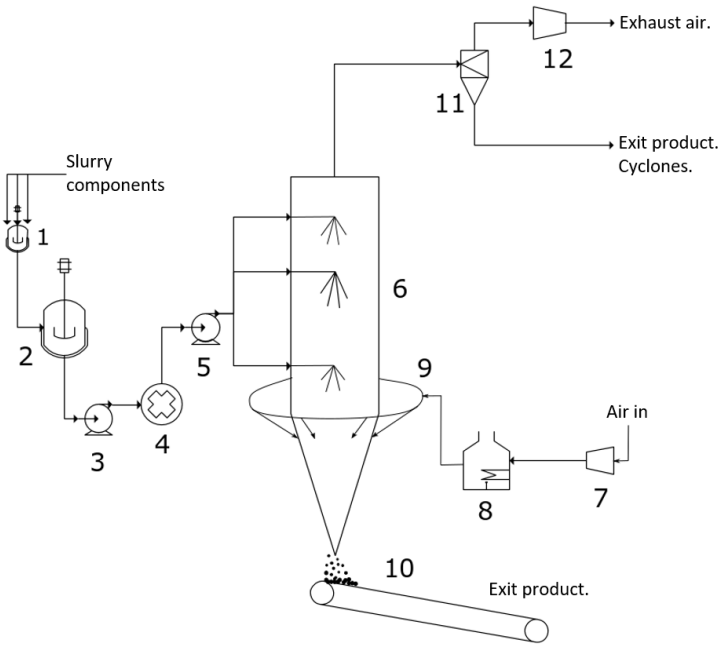

Number	Unit
1	Crutcher. Batch mixer.
2	Continuous mixer.
3	Low pressure pump.
4	Hammer mill.
5	High pressure pump.
6	Counter-current spray dryer.
7	Air fan.
8	Burner.
9	Air distributor.
10	Belt.
11	Cyclones.
12	Exhaust air fan.

Figure 2. Detergent powder production process.

A.2. PREPARATION OF THE FEED.

The slurry introduced into the atomization is a suspension that contains a solid phase (between 30-60%) dissolved in aqueous and organic liquid phases. The composition of detergents is very wide and different formulations with constant changes are developed to meet consumer requirements and achieve business profitability. For example, the range of concentrations provided in [7] and [8] are presented in Tables 1 and 2. Note that these formulations presented in Table 1 and 2 only focus on builder components, which are the ones with highest concentrations and other components such as enzymes and perfumes are also added after the generation of the structure.

Table 1. Range of concentration for the main components in dried powder detergent [7].

Component	Mass fraction (%)
Anionic surfactant	5-40
Non-ionic surfactant	1-20
Cationic surfactant	0-50
Detergent builder (with an amount of phosphate builder)	0-10 (0-5)
Polycarboxylate polymer	0-3
Optionally detergent ingredients to 100% like perfumes, silicates, etc.	

Table 2. Composition of detergent paste [8].

Ingredient	Mass fraction (%)
LAS	9
Poly-acrylate	3
Water	29
Zeolite	25
Sodium sulphate	34

A.3 ATOMIZATION

Despite the stage of atomization is carried out inside the dryer, the modeling of this part is not the main aim of this thesis, being the particle size generated by each formula and with every different atomizer determined by models internally validated in the company. This stage consists in creating a droplet distribution of the slurry. The slurry, which comes from the mixer, is pumped at high pressure to help in the generation of the droplets. To produce the droplets, a certain energy is to be provided. The way to introduce this energy classifies the atomizers into the following groups as presented in Figure 3 [1]:

- Rotary atomizer, Figure 4, A): Uses centrifugal energy to generate the droplets. They are generated with a centrifugal acceleration of the liquid before being discharged into an air-gas atmosphere. In this kind of atomizers the liquid extends over the rotating surface as a film. To prevent the slippage that can be generated at low velocities, vanes can be used. The degree of atomization obtained using this design is highly dependent on the acceleration of the wheel, the slippage between the liquid and the rotating surface, the feed rate and the physical properties of the liquid introduced. This kind of atomizers can generate a wide range of spray characteristics.
- Pressure nozzles: The liquid is discharged at high pressure through an orifice. The parts of a pressure nozzle are presented in Figure 4, B). Two sections can be identified. First, a swirl chamber that contains the slurry that has been pressured. Second, the air cone generated by the pressure difference, the orifice created where a film of the liquid flows through and the final droplet pattern. The pattern followed by the droplets can be classified in two types:
    - Solid cone profile where the droplets are distributed fairly uniformly throughout the conical pattern.
    - Hollow cone profile that contains an air core at the center of the orifice, which is generated by the rotation of the liquid within the nozzle.
- Pneumatic nozzles, Figure 4, C) and D): In this type of atomizers the liquid is broken-up by means of the kinetic energy existing due to the feed of both, liquid and gas phases, at high velocity. The frictional forces between the gas and the liquid surface cause the disintegration of the liquid phase into spray droplets. These atomizers provide more homogeneity in the droplet size distribution than the previous ones. At small liquid feed rates the air can penetrate easily in the slurry and the droplets are generated. These pneumatic nozzles can be classified in two types according to how the air comes in contact with the slurry: a) dual fluid nozzles with external introduction of the air; b) dual fluid nozzles with internal introduction of the air.
- Apart from these types other atomizers can be also found such as whistle, ultrasonic, electrostatic, effervescent and air blast atomizers [9].

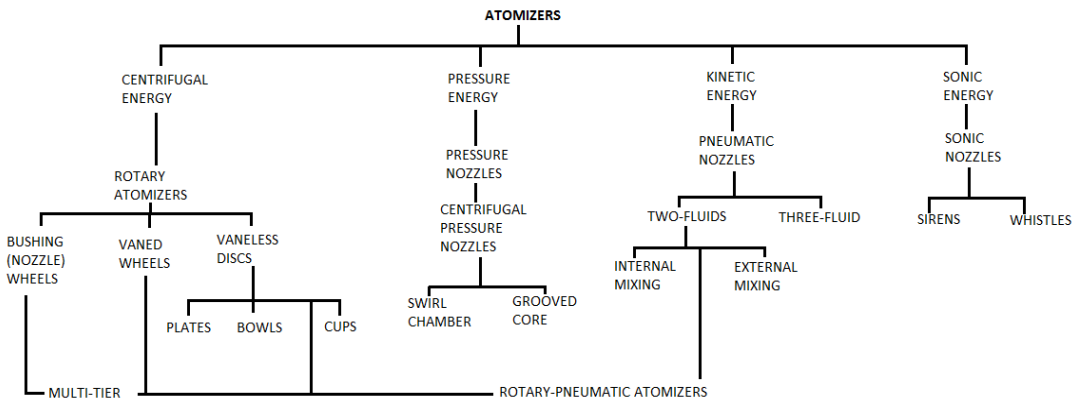

Figure 3. Classification of atomizers (Adapted from Masters,K. (1985) [1]).

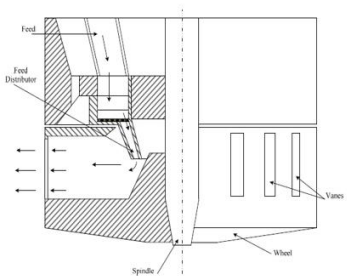

Figure 4, A)

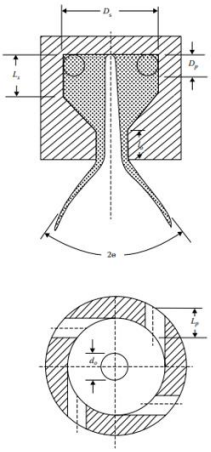

Figure 4, B)

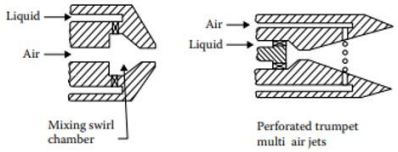

Figure 4, C)

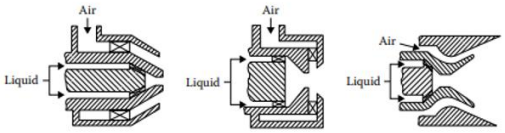

Figure 4, D)

Figure 4. Scheme of: A) a rotary atomizer [1], B) a pressure nozzle [9], C) pneumatic nozzles with internal introduction of air and D) pneumatic nozzles with external introduction of air [9].

A.4 PHENOMENA IN THE DRYER.

A.4.1. Air particle interaction

The atomized slurry is introduced into the drying chamber where hot air comes in contact with the droplets obtaining dried particles. Depending on how the contact between the droplets and the air occurs, spray dryers can be classified as [1]:

- Co-current: The feed and the gas flow in the same direction, see Figure 5, A). This arrangement is used, especially when heat sensitive products are involved, for instance, the case of the pharmaceutical industry. The evaporation is faster than in the other cases due to the initial difference of temperatures between the air and the feed is higher, consequently the residence time is low.
- Counter-current: The air enters in the opposite direction than the feed, see Figure 5, B). This layout allows reaching a better heat efficiency of the process. It suits for products with not heat sensitive components as in the case of ceramics and the detergent industry.
- Mixed flow dryers: This type combines co-current and counter-current flows. Two kinds of mixed flow spray dryers can be considered. On the one hand, the fountain type where the spray moves in two directions (from the bottom to the top and then in the opposite way) meanwhile the air only follows one, see Figure 5, D); on the other hand, upward firing type where the air is introduced by two inlets (top and bottom) and the spray is introduced in the top, see Figure 5, C).

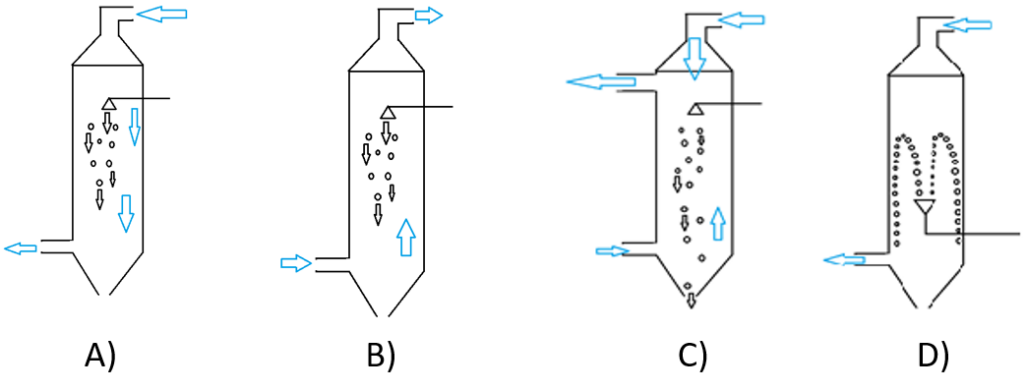

Figure 5. A) Co-current, B) counter-current, C) upward firing mixed flow spray dryer and D) fountain type spray dryers.

In the current thesis, a counter-current spray-dryer at industrial scale is considered. This dryer is characterized by a swirl flow pattern that improves the heat and mass transfer efficiency [4,10,11]. This swirl flow is achieved by the tangential arrangement of the air inlets. The swirl flow is commonly characterized by a swirl number that was defined by Kitoh [12] according to the Eq. (1) and quantifies the non-dimensional flux of angular momentum, neglecting the contribution of the Reynolds stresses and the axial flow development [12] and being normalized by the axial flux of momentum based on superficial velocity, U_{av}, and dryer radius, R.

$$S = 2\pi\rho \int_0^R \frac{\bar{U}\,\bar{W}}{\rho\pi\overline{U_{av}}R^3} r^2 dr \qquad (1)$$

As demonstrated by Kitoh in pipes and Francia et al. in swirl counter-current dryers, this flow intensity suffers a decay due to the wall shear stress with the walls [12-14]. This decay may result in significant changes in the flow pattern since at the top of the dryer the presence of a contraction results in a vortex breaker phenomena [15]. In case that the swirl flow achieved at the entrance of the vortex breaker is higher than 1, recirculation is generated. Otherwise, the flow maintains the pattern in the contraction, see Figure 6.

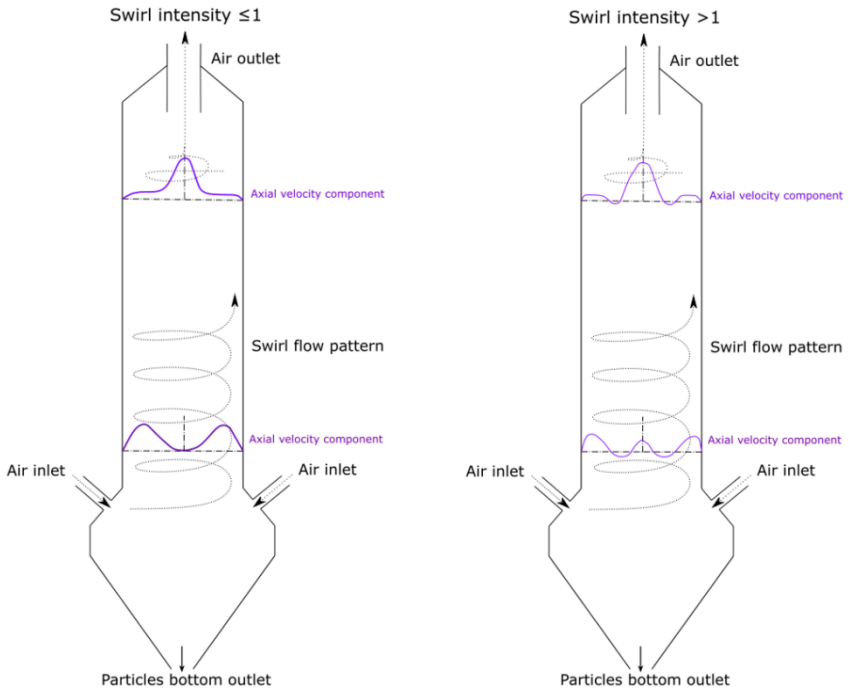

Figure 6. Axial air velocity profiles for swirl intensity at the entrance of the outlet (vortex breaker) lower or equal than one (left) and greater than one (right). Adapted from Francia et al. [14].

This characteristic swirl flow pattern of this counter-current dryer has high implications on the particle dynamics. Once the particles are injected, different trajectories can be followed generating the zones presented in Figure 7. In general terms, most of the powder flows down as a bulk but elutriates can be also generated. The path followed by each of the particles is different depending on the contact with the air, the injection properties, the impact with the wall or between the particles. Despite the dynamics of the particles look like very complex because the dependency of a large number of variables, one can split the dryer in different zones based on the dominant process in each of them [4,5]:

- Nozzle Region: It is defined as the volume of the projection of the spray cone.
    - Nozzle inertial region: Contains the recently spray droplets, commonly from the nozzle to the wall, where the droplets are drag by the swirl flow until lost their velocity.
    - Nozzle terminal region: This region is close to the wall, where the particles can flow up or down due to an influx between the elutriation and sedimentation region.
- Elutriation region: This region is characterized by the particles that flow up from the atomization region. One can expect that the particles favor to flow as elutriates are the ones with very small Stokes and Archimedes numbers, see Eq. (2) and (3). Stokes number accounts for the characteristic residence time of the particles versus the one of the air and therefore the impact of the air on the particle trajectories and Archimedes accounts the ratio between the gravity and the viscous forces. Since the elutriated particles are governed by a balance between the gravity and the drag force being this last one not much greater than the gravity, the particles move slow and the impact between them occurs at low impact velocities.

$$St = \frac{\tau_p}{\tau_f} = \frac{\rho_p d_p^2 U_{air}}{18\mu D\, C_D} \quad (2)$$

$$Ar = \frac{g d_p^3 \rho_{air}(\rho_p - \rho_{air})}{\mu^2} \quad (3)$$

- Near Wall region: The swirl pattern of the airflow concentrates the particles close to the wall. As a result, this zone is characterized by higher concentration of particles. In this zone the contacts happen at higher velocities. Depending on the particle size, one can expect more or less contacts with the wall. Big particles with high Stokes numbers are expected to have a motion close to a free fall after the impact meanwhile small particles (also with smaller Stokes number) are expected to follow the path of the vortex generated by the swirl flow and having more interactions with the wall.
- Central region of the tower: This region is mainly characterized by the low presence of particles since most of them are concentrated near the wall. The only particles that are expected to be there are the ones with very low Stokes numbers since they are transported by means of turbulent diffusion [16].
- Cone region where the air is fed and the powder is collected in the bottom part of the tower.

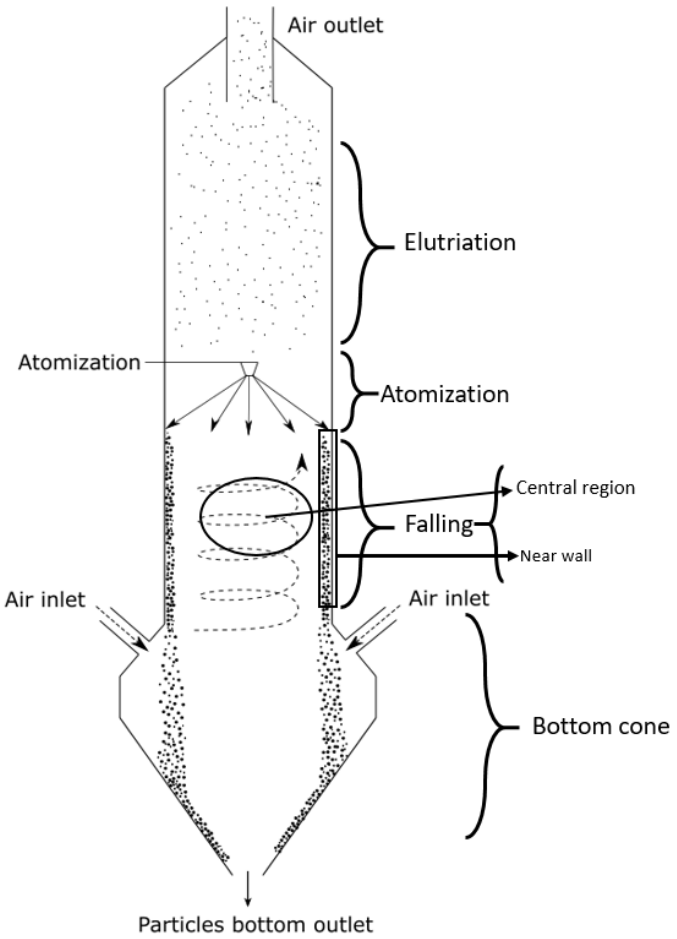

Figure 7. Distribution of regions according to previous experimental studies in particle dynamics.

A.4.2 Drying

The drying of the particles is commonly characterized by a profile of the evolution of moisture content through the time. The factors that will have an influence in the drying process are [1]:

- Difference of temperature between the droplets/particles and the continuous phase, air.
- Physico-chemical properties and geometry of the droplet.
- Dynamic characteristics of the particle.
- Residence time of the particle.

Since the discrete phase represents a very low fraction versus the air introduced into the dryer, the most recurrent approach used in the modelling of these systems is based on modelling of a single droplet. The model obtained for a single droplet can be applied to all the material injected in the atomization, ensuring it scaled-up by means of Ranz-Marshall correlations [17]. Thus, for the characterization of the material to be dried only one particle is required to be studied. The experimental characterization of the droplet can be performed using different methods such as a conventional microbalance, a balance in combination with a drying tunnel, an acoustic levitator, a magnetic suspension balance [18] or by glass filament [19]. The results obtained from the experimental characterization with a single droplet have mainly focused on the stages observed in the drying and the particle structures developed in this process, being the last ones influenced by the factors previously defined. An interesting review based on experimental characterization of the possible development of the structures was presented by Charlesworth and Marshall [20]. Due to the composition of detergents, the structures developed have been assimilated to a solution with dissolved small particles [21, 22]. The possible structures are presented in Figure 8 and the stages that generate them are:

- A first stage where drying is governed by the diffusion of water in air through the boundary layer. In this stage the droplet is heated up until achieving the wet bulb temperature (see Figure 9) and it maintains saturated conditions on the surface. The drying rate is constant and the droplet suffers a shrinkage as presented in Figure 8 [23, 24].
- The second stage begins when the flux of water that reaches the surface of the droplet does not maintain the saturated conditions generating a crust on the surface of the droplet. In this case, the diffusion through the crust starts to govern the drying rate of the droplet showing a falling of the drying rate and an increase of the temperature of the droplet (see Figure 9). [25,26].
- The third stage starts if the droplet reaches the boiling point of the moisture. During this stage the evaporation rate is governed by an equilibrium between the heat transferred to the droplet and the vaporization enthalpy of a dynamic boiling point. This boiling point is modified by the concentration of solids [27]. Different structures can be developed once the particles achieve this boiling condition. The final structure of the dried particle has been showed to be highly dependent on the drying temperature. In the case that a dry shell is formed, the final particle may result in a solid particle when temperature is low or in a decomposed particle if the temperature is high. In the case that the crust is partially wet, which

corresponds to the most common case in detergents, bubbles are assumed to be generated internally. The mechanisms and models proposed in the description of this stage for wet droplets assume a bubble located in the center of the droplet. This bubble can expand and/or shrink generating different shapes. For example, as presented in Figure 8 the bubble can suffer small expansions resulting in a hollow particle with similar shape to the original one, or it can be dried at high temperature generating a puffed or blistered particle. As it has been defined in most of the previous works, the drying temperature plays an important role during this boiling stage, governing the expansion of the droplet generated. Different particle behaviors have been experimentally characterized and modelled with a single bubble [27-30] but the focus on the origin of the bubbles that promotes the boiling and subsequently the expansions is still an area to be covered in single droplet drying. The generation of these bubbles has been studied in boiling studies, which have mainly focused on characterizing the different regimes of boiling described in Figure 10. These regimes can be identified by the overheating temperature provided. At low over-temperatures, natural convection takes place and no bubbles are generated. An increase of the temperature results in a nucleate boiling regime, first generating isolated non-stable bubbles and then generating columns of stable bubbles. The boiling nucleation regime ends at a critical point suffering a depletion of the heat transfer during the transition regime until the Leidenfrost point. Finally, at very high superheated surfaces, the film regime takes place where the increase of the temperature difference results in an increase of the heat flux. The role of this temperature difference in the definition of the regimes as well as the effect that the roughness of the surface has on the generation of the generation of the nucleation bubbles and their stability have focused most of the attention of the studies regarding boiling [31-34]. However, the connection of this bubble nucleation regime with the effect that it has on the drying of the droplet is still an area to be covered in future works.

- In the last stage, the moisture of the particle has been removed and the temperature of the droplets increases very quick reaching the temperature of the surrounding air.

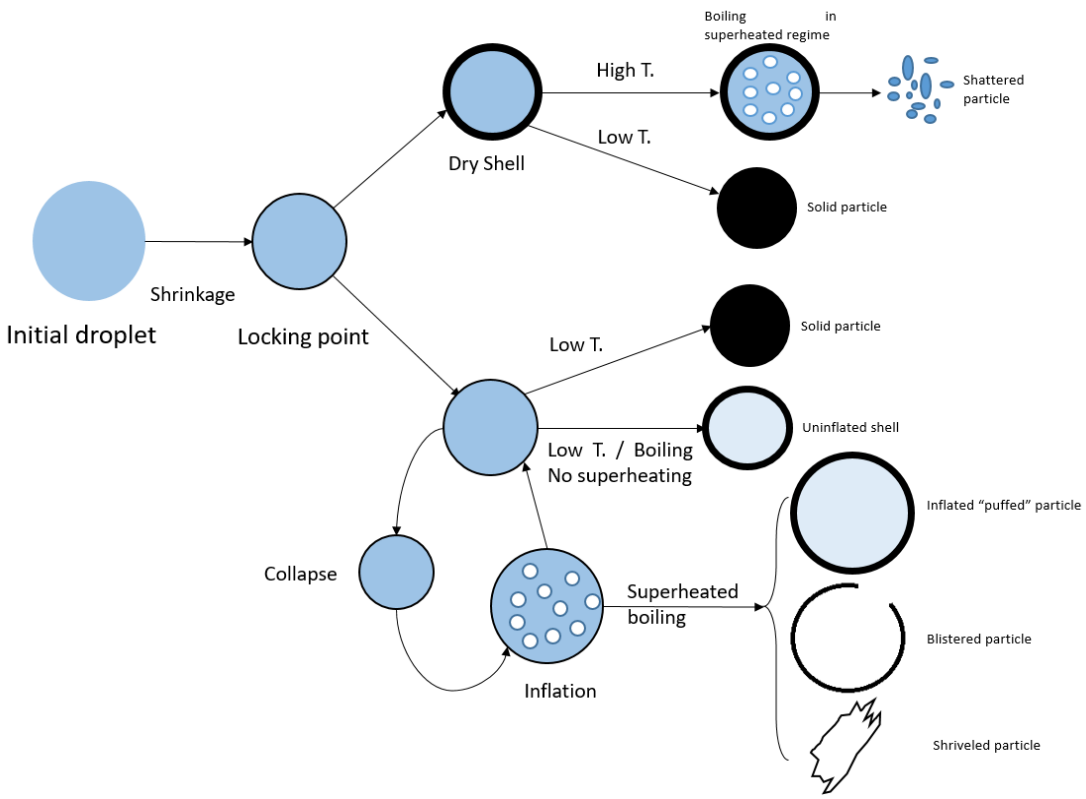

Figure 8. Possible single droplet drying mechanisms including the role of the boiling regime.

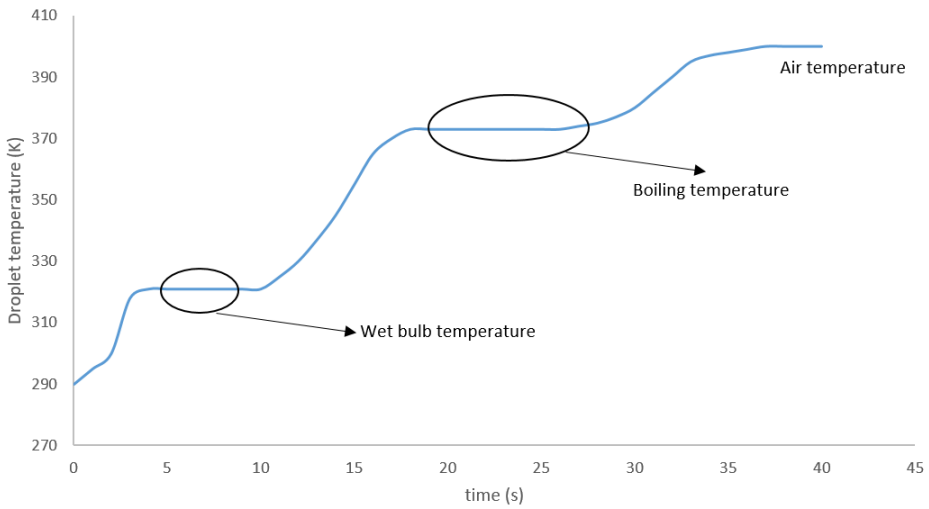

Figure 9. Example of droplet temperature profile during single droplet drying including diffusion and boiling mechanisms.

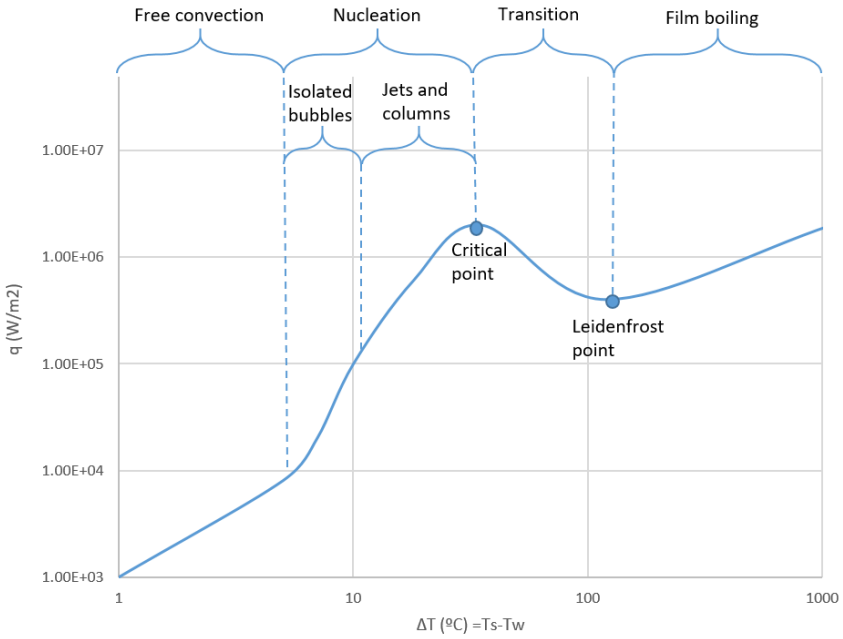

Figure 10. Example of boiling regimes.

A.4.3 Particle-particle interactions

One of the first studies regarding this phenomena independently from heat and mass transfer was developed by Podvysotsky and Shraiber in 1984, obtaining empirical models for the interaction as a function of the Reynolds, Laplace and Weber numbers, Eq. (4) to (6) [35]. Lately, equation based models were developed by Quian and Law (1997) [36]. They identified 3 collision regimes for the water and 5 collision regimes for hydrocarbon droplets as a function of the Weber number and the impact parameter, B (see Eq. (7)), defined by Ashgriz and Poo (1990) [37]. These collision regimes are represented in a collision map. A typical characteristic collision map indicating the different regimes is presented in Figure 11. The generation of these maps has been studied in droplets with similar and different liquids [36-38], showing that properties such as the difference in the viscosity may influence in the region of coalescence [38]. Furthermore, other factors such as the ambient gas composition and the size ratio of the impact droplets have also shown to be significant in the modification of the droplet maps. Some of these changes in the maps can be characterized from non-dimensionless groups derived from Weber number such as the Ohnesorge and Capillarity numbers, see Eq. (8) and (9) [39]. These numbers influence on some of the characteristic points that one can find in the map, which are:

- Transition from bouncing to coalescence.
- The critical Weber number that is a function of the Ohnesorge number [36] and it indicates the transition from coalescence to reflexive separation at B=0.
- The triple point where bouncing, coalescence and stretching separation regimes meet. This point is indicated by We_t and it is function of the Capillarity and Weber numbers [39].
- The intersection of the boundary line between coalescence and stretching separation at B=1.

The modelling of these collisions within a multiphase system has been typically evaluated by means of a Lagrangian framework. Three approaches such as the fully deterministic, the deterministic-stochastic parcel model and the stochastic collision model can be used [38]. Among them, the second one has the best application in spray systems since it considers the tracking of multiphase droplets. In this approach the probability of collisions is determined as a function of the kinetic theory of gases from the diameters and velocity components of the parcel [2, 40, 41].

Figure 11, A)

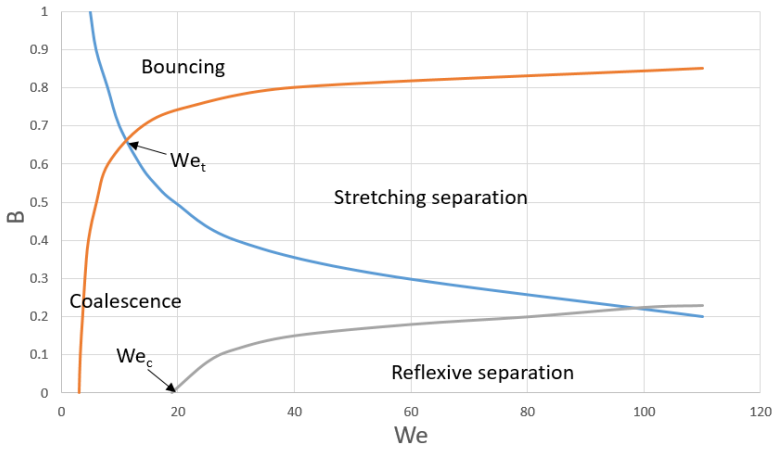

Figure 11, B)

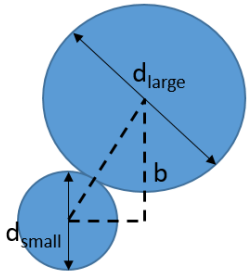

Figure 11. A) Example of typical collision map and B) definition of the diameters in the computation of B.

$$Re_p = \frac{\rho d_{small\ droplet} v_{rel}}{\mu} \quad (4)$$

$$La = \frac{\sigma \rho d_{small\ droplet}}{\mu^2} \quad (5)$$

$$We = \frac{\rho v_{rel}^2 d_{small\ droplet}}{\sigma} \quad (6)$$

$$B = \frac{2b}{d_{small\ droplet} + d_{large\ droplet}} \quad (7)$$

$$Oh = \frac{\mu}{\sqrt{\rho \sigma d_{small\ droplet}}} \quad (8)$$

$$Ca = \sqrt{We} Oh = \frac{\mu}{\sigma} v_{rel} \quad (9)$$

The interaction between particles or droplets can result in two types of phenomena, agglomeration/coalescence or breakage. The first one is the phenomena with higher chances to take place in particle-particle interactions within the dryer since the higher velocities are obtained in the atomization region where the particles are wet. The second one can also occur, but it is favored in the falling region and the cone, where the particles are dried, and they can take place between the particles and in particle-wall interactions.

Agglomeration

As it has been described in previous paragraphs, the properties of the droplets have a high influence on the collisions maps. The characterization of the collision maps is typically performed independently from heat and mass transfer. However, in the case of a spray dryer this phenomena takes place at the same time. In the drying process of the droplets it is possible to distinguish sticky droplets/particles when the surface of the particle is wet (the surface tension similar to the liquid content) and non-sticky particles when the surface is dry. A common approach in the identification of this transition is the use of the glass transition temperature [2, 42-45], which has been described to be highly influenced by material properties such as the crystallinity of the matrix and the polarity of the solvent of the droplet [46]. Apart from the influence of the glass transition temperature, Palzer also described the agglomeration process for two particles contacted by a liquid bridge [42]. Complementing this theory with the coalesce between droplets and considering the observations of Huntington [3], the agglomeration in a counter-current dryer by particle/droplet collisions can follow one of the following mechanisms:

- Coalescence of wet droplets, which are more expected to be favor in the atomization region when the surface of the injected droplets is still wet. In the case that these droplets impact with enough energy the coalescence takes place but if the energy in the collision among them is not that large, they come in contact forming liquid bridges and the final droplet.
- Collision between two droplets or a particle and a droplet forming a liquid bridge connection that sinters with sufficient drying time. This agglomeration process can take place when the jets of several sprays overlap or near the wall where interactions are given between particles with different sizes, free falling velocities and drying rates.
- Contact by a liquid bridge between droplet-particle or particle-particle and its sintering with sufficient drying time, which can take place in the same regions than the previous ones.

A more detailed study than the one of Huntington [3], was developed by Verdumen et al. [2]. In that work, a design tool was developed for co-current dryers dedicated to the production of milk powder and it was validated with the final PSD. The tool was composed by means of CFD that included a drying model and a post-processing analysis based on a deterministic-stochastic parcel model. Similar approach was also developed by the group at University of Sidney [41, 46], who also developed the study for a co-current spray dryer and based the validation on characteristic particle size diameters. In more recent studies Francia et al. [47], characterized the agglomeration in counter-current dryers indicating the influence of the nozzle height [48] and introducing the relevant influence of the particle-wall [49] contacts in the agglomeration as presented in the sections below. In this type of counter-current spray dryers, the modeling has also developed introduced by the group of Lodz university [50], who followed a similar procedure to the one developed by Verdumen et al. [2] for predicting the agglomeration given by droplet-droplet interactions in the dryer.

A.4.4 Particle-wall interactions

As a result from the swirl pattern of the airflow, the particles injected in the atomizer tend to move near the wall, becoming of special interest the particle-wall impacts since they modify the dynamics of the particles and also the mass transfer occurred on the wall. This particle-wall interaction behaves as a dynamic equilibrium that is composed of three stages [51-53]:

- Deposition of the particles and droplets. The particles can be deposited on the wall by impaction, when they have enough momentum, or by diffusion through the viscous layer [52]. The mechanism that governs this deposition is highly influenced by the particle size and inertia. If the particle size and inertia is large enough deposition takes place by impaction. Otherwise, if turbulence governs, it takes place by diffusion through the viscous sub-layer. Several studies have focused on the interactions between particles and near wall-boundary layers [52, 54], describing the action that turbulence in this near wall region has on this deposition and the re-entrainment mechanism described below.
- Aging. The particles or droplets deposited on the wall spend some time until they can be re-entrained into the air system. During this time the droplets can dry and sinter with the hot air. As a result, a layer is generated on the wall being not only influenced by the particle-wall forces but also by the particle-particle forces that governs the growing of the deposits by agglomeration. These deposits grow until achieving a limit where the re-entrainment of particles is equal to the deposition, which is known as blocking effect [55].
- Re-entrainment. The material on the layer may interact with the entrained material resulting in a re-suspension to the system. A wide range of work describing this phenomena has been provided by the group at Newcastle University proposing models based on the impact energy of particles for mono and multilayer deposits [56, 57]. This re-entrainment process is not only generated by the inertia of the particles. Other forces such as Van der Waals, thermophoretic or electrostatics of the particles and the turbulence of the air are also associated to the re-entrainment [55].

In the area of spray drying, fouling is relevant due to 3 main issues: First, the product degradation, safety and quality concerns; second, the connection with the yield and process efficiency and third because of the maintenance costs [6, 58]. This reduction of the yield due to the wall agglomeration has been studied emphasized by the group of Langrish in co-current spray dryers to produce food [59,60]. Because of the negative effect on the operation of the dryer, some methodologies have been developed to reduce the deposition as the modification of the nozzles location [61], varying the swirl [6], or replacing the wall using Teflon instead of stainless steel [61]. In the case of counter-current spray dryers, the number of works is less. Hassall [5] showed that high amount of powder concentrates near the wall due to the swirl pattern introduced to increase the particle residence time. Then, Francia performed an experimental characterization of the different stages of the fouling process [53] providing a description of the fluxes and age distributions of the stages and the possible particle structures that can be developed during the particle-wall interaction.

A.4.5 Breakage

The last phenomenon that can take place into the dryers is the breakage and attrition of the particles, generating elutriates and dust that represent a health and safety risk. The generation of airborne material can increase the concentration up to achieving the explosive region. Attrition can be characterized following different methods based on single or multiple number of particles [62]. For example, one can characterize the fragmentation by impact with vibrational tester or the fraction lost by breakage by means of impact tests with single particles or one can characterize the size reduction in a rotor mill [62, 63]. Similar to particle-particle contacts, Subero and Ghadiri proposed a map of breaking regimes for agglomerates, see Figure 12 [64]. Three regimes are identified in the map for localized damage, local fragmentation and multiple fragmentation. These regimes are dependent on the agglomerate structure and the impact velocity. This impact velocity and subsequently the energy during this impact has been included in most of the modelling works regarding attrition [65]. The types of models used can be classified in the following groups according to the type of models described in [63]: Stochastic and monte-carlo based models where the attrition can be modeled as function of the particle size distribution [66, 67], mechanistic and population balance based models [68]. Apart from this modelling approaches, the use of DEM simulations has also covered a high relevance in the analysis of single particle, being this simulated as a set of smaller particles [69].

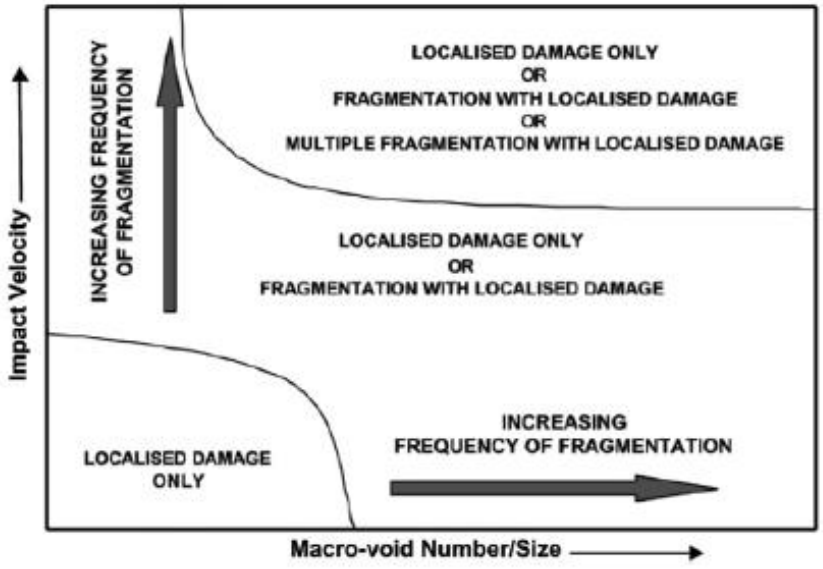

Figure 12. Map of breakage for agglomerates. [64].

A.5 PRODUCT SEPARATION

In this final stage, the product is separated from the gas phase. The aim of this separation is not only to increase the economic the performance of the process by recovering part of the product, but also to avoid the release of powder to the atmosphere resulting in health and environment issues. The recovery of the product can be carried out first at the chamber (collecting the final product) and second using other recovery unit. The amount of the primary product obtained depends on the design and operating conditions of the dryer. In most of the cases this

primary product is recovered by a conical section in both co-current and counter-dryers. However, designs with a flat base can be also found [1,44]. Whatever method of collection is used in the primary recovery, a secondary recovery is necessary to reduce the release of material to the atmosphere and the recovery of it. The selection of the second recovery method. A comparison based on collection efficiency and relative costs is provided in Tables 3 and 4. In Table 3 it can be seen that the highest recovery is achieved by means of bag filters but they are also more expensive than other options such as the cyclones. After this secondary recovery, the resultant air can be released to the atmosphere or it can be partially recirculated to the dryer. Instead of the recycle to the dryer is the most profitable option limitations in that recycle are presented due to the cost of removing the moisture content in the drying media.

Table 3. Collection efficiency of Separators on low and high powder-air loadings [1].

Type	Recovery operating on low powder-air loadings	Recovery operating on high powder-air loadings.
Cyclones	90-96%	95-99%
Bag filters	95-99.5%	97-99.9%
Electrostatic precipitators	90-99%	95-99%

Table 4. Relative Costs of Separation Equipment in Spray Dryers [1].

Type	Capital costs	Operating costs.
Cyclones	1	1
Bag filters	4-5	5-6
Spray chamber scrubber	1.5-2	4-4.5
Venturi scrubber	2	7-8
Impingement scrubber	4-5	2.5-3
Electrostatic precipitator	5-6	1

A.6 AIMS AND OUTLINE OF THIS PART

Even though the process involves a reduced number of units, spray drying has been demonstrated to be a very complex process due to all the phenomena involved and described in previous sections. The characterization and modelling of the phenomena involved in spray dryers have taken decades in the research groups dedicated to this area. For example, the group of Professor Langrish at University of Sidney has been working during the last 3 decades [59] being able to characterise and generate models in all the phenomenological areas defined [6, 41, 60]. Other groups such as the ones at University of Lodz [54, 59] and Monash University [70, 71] have also been able to reproduce most of the phenomena involved in the dryer. In all of these cases, due to the complexity of the phenomena evaluated and the spatial distribution of it within the unit, rigorous simulations of the dryer have been

carried out by means of CFD simulations and particle tracking methods. The approach followed by these research groups has been also used in industry. During the last decade, several analysis and CFD simulations have been developed for industrial dryers at Procter and Gamble [5, 72]. Most of these studies were developed in collaboration with the University of Leeds in the framework of a thesis project [72]. In this project, several models for air flow, particle dynamics and heat and mass balances were developed by means of CFD simulations and validated against experimental data. In this validation, the final model including heat and mass balances showed to reproduce the temperature profile within the dryer [73]. However, previous validations performed for particle dynamics showed to have a huge error in the prediction of the particle residence times [74], which suggests a wrong distribution of the errors between the momentum and mass transfer. As a result from this fact, the model is hard to be trusted in the application of such cases where no experimental data is provided and it necessary the development of a new CFD framework that has to be validated in each of the stages defined in Figure 13. Therefore, the first aim of this part focuses on developing a similar industrial project introducing new methodologies for the modelling, calibration and validation of the CFD framework in each of the stages presented in Figure 13. The rigorous models are developed at two scales, corresponding with sections 1 and 2:

- On the one hand, the modelling of drying of single droplets is studied at particle scale since it needs to be validated independently before its scale-up to the dryer.
- On the other hand, section 2 focus on the rigorous modelling by means of CFD simulations at unit level. The CFD modelling and validation procedure followed during this section 2 is based on the one described in Figure 13, being modified for the introduction of fouling as presented in section 2.2.

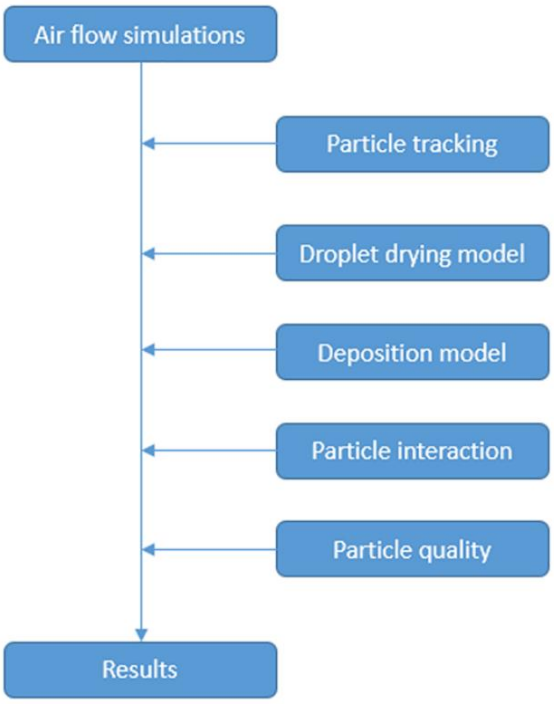

Figure 13. Systematic methodology for the development of CFD models in spray dryers. Adapted from [70].

Once the CFD framework has been developed, the second part of this project focuses on the development of compartment models that will allow reducing the high computational cost required by CFD simulations. Similar than in previous section, this area has been also developed in two previous projects: On the one hand, a project developed by Process System Enterprise ® where the generation of the zones based on the framework developed by Bezzo and Machieto [75] was applied. As a result from this project, a tool commercialized within the gFormulate ® package was developed [76]. On the other hand, a zonal model based on phenomenological regions was developed by Ali, M. et al. [77] but, as it was also occurring with the CFD framework, this zonal model is based on a previous validated CFD model with wrong results in the residence time predictions, which reduces its application in the prediction of other cases within the dryer. Furthermore, the compartmentalization process in the two previous cases is not robust enough. In the first case, the zones are homogenously distributed, not dealing with the particle distribution within the dryer, which result in a wrong prediction of the fluxes and subsequently the drying. As a result the use of the multi-zonal tool ® [78] is required for every new operating conditions. In the second case, the zones are fixed from a unique operating conditions and it has been only validated with one case, which does not ensure the application of the model under other operating conditions. Thus, for the generation of a more robust model, a new methodology has to be developed. This methodology and the final compartment model obtained are presented in section 3 of the current thesis.

NOMENCLATURE

Ar	Archimedes number.
b	Axial distance between the center of the large droplet and the projected line of the relative velocity vector of the small droplet (m).
B	Bond parameter in droplet interaction.
Ca	Capillarity number.
C_D	Drag coefficient.
$d_{large\ droplet}$	Diameter of the large particle (m).
$d_{small\ droplet}$	Diameter of the small particle (m).
D	Diameter of the dryer (m).
g	Gravity constant, 9.8 m/s^2.
La	Laplace number of the particle.
Oh	Ohnesorge number.
r	coordinate in the radial direction (m).
R	Radius of the dryer (m).
Re_p	Reynolds number of the particle.
S	Swirl intensity.
St	Stokes number.

$\overline{U}$	Axial velocity (m/s).
U_{air}	Average air velocity (m/s).
$\overline{U_{av}}$	Average axial velocity, normalized for the entire cross-sectional area (m/s)
v_{rel}	Relative velocity of the small particle referred to the large particle (m/s).
$\overline{W}$	Average tangential velocity (m/s).
We	Weber number.
ρ	Density of the fluid (kg/m^3).
ρ_p	Density of the particle (kg/m^3).
σ	Surface tension (N/m).
μ	Dynamic viscosity (Pa·s).
τ_f	Characteristic time of the fluid (m/s).
τ_p	Characteristic time of the particle (m/s)

REFERENCES

[1] Masters, K. (1985) Spray Drying Handbook. 5th Edition. ISBN: 0-582-06266-7

[2] Verdumen, R.E.M., Menn, P., Ritzert,J. Blei, S. Nhumaio, G.C.S., Sorensen,T.S. Gunsing,M. Straatsma,J. Verschueren,M. Sibeijn,M. Schulte,G. Fritsching,U. Bauckhage,K. Tropea,C. Sommerfeld,M. Watkins,A.P. Yule,A.J. Schonfeldt,H. (2004). Simulation of agglomeration in spray drying installations: The EDECAD project. Drying technology, 22, 6, 1403-1461.

[3] Huntington, D. H. (2004). The influence of the spray drying process on product properties. Drying technology, 22, 6, 1261-1287.

[4] Francia, V. (2014) Spray drying of detergents in counter-current towers: A study of turbulent swirling flows, fouling and agglomeration.

[5] Hassall, G.J. (2011). Wall build-up in spray dryers. Eng.D. thesis. School of Chemical Engineering. University of Birmingham. United Kingdom.

[6] Ozmen,L. and Langrish, T.A.G. (2003). An experimental investigation of the wall deposition of milk powder in a pilot-scale spray dryer. Drying technology, 21, 7, 1235-1252.

[7] PATENT US7078373 B2 (Burrows, J. Crawford, R.J. Norris, P.J. Thorley,D.C. (2006) Laundry detergent composition)

[8] Griffith, J.D. Bayly, A.E. Johns, M.L. (2008) Magnetic resonance studies of detergent drop drying. Chemical Engineering Science, Vol. 63, 13, 3449-3456.

[9] Lefebvre, A. H. McDonell, V.G. (2017) Atomization and Sprays. CRC Press. ISBN: 13:978-1-4987-3625-1.

[10] Sharma, S. (1990) Spray dryer simulation and air flow pattern studies, Ph. D. thesis. The University of Astom. Birmingham. United Kingdom.

[11] Chang,F. and Dhir, V.K. (1995). Mechanisms of heat transfer enhancement and slow decay of swirl in tubes using tangential injection. International journal of heat and fluid flow, 16, 2, 78-87.

[12] Kitoh,O. (1991) Experimental study of turbulent swirling flow in a straight pipe. Journal of fluid mechanics, 225, 445-479.

[13] Steenbergen,W. and Voskamp,J. (1998). The rate of decay of swirl in turbulent pipe flow. Flow measurement and Instrumentation, 9, 67-78.

[14] Francia, V. Martin, L. Bayly, A.E. Simmons, M.J.H. (2015) Influence of wall friction on flow regimes and scale-up of counter-current swirl spray dryers. Chemical Engineering Science, Vol. 134, 2015, 399-413.

[15] Scudier, M.P. and Keller, J.J. (1985) Recirculation in Swirling Flow: A manifestation of vortex breakdown. AIAA Journal, 23, 1, 111-116.

[16] Crowe, C.T. Schwarzkopf, J.D. Sommerfeld, M. Tsuji, Y. (2011) Multiphase flows with droplets and particles. 2nd Edition. ISBN: 9781439840504

[17] Ranz, W. Marshall, W. (1952) Evaporation from drops. Chemical Engineering Progress, 48 (141), 173.

[18] Tsotsas, E. Mujumdar, A.S. (2009) Modern Drying Techonology. Volume 2: Experimental Techniques. Wiley-VCH Verlag GmbH & Co. ISBN: 978-3-527-31557-4.

[19] Fu, N. Woo, M.W., Chen, X.D. (2012) Single Droplet Drying Technique to Study Drying kinetics measurement and particle functionality: A Review. Drying Technology, 30: 1771-1785, 2012.

[20] Charlesworth, D.H. Marshall, W.R. (1960) Evaporation from drops containing dissolved solids. AIChE J. 6, 9-23. DOI: 10.1002/aic.690060104.

[21] Ali, M. Mahmud, T. Heggs, P.J. Ghadiri, M. Djurdjevic, D. Ahmadian, H. Juan, L.M. Amador, C. Bayly , A. (2014) A one-dimensional plug-flow model of a counter-current spray drying tower. Chem. Eng. Res. Des. 92, 826-841. DOI: 10.1016/j.cherd.2013.08.010

[22] Handscomb, C.S. Kraft,M. Bayly,A.E. (2009) A new model for the drying of droplets containing suspended solids. Chemical Engineering Science 64, 628-637.

[23] Efremov, G. I. (2007) Drying kinetics derived from diffusion equation with flux-type boundary conditions. Drying Technology, 20(1), 55-66, Taylor & Francis. ISSN: 0737-3937

[24] Farid, M. (2003). A new approach to modeling of single droplet drying. Chemical Engineering Science, 58 (2003) 2985-2993.

[25] Cheong, H. Jeffreys, G. Mumford, C. (1986) A receding interface model for the drying of slurry droplets. AIChE. Journal 32 (8), 1334-1346.

[26] Nesic, S. Vodnik, J. (1991) Kinetics of droplet evaporation. Chem. Eng. Sci. 46, 527-537. DOI: 10.1016/0009-2509(91)80013-O

[27] Hecht, J.P. King, C.J. (2000) Spray Drying: Influence of Developing drop morphology on Drying Rates and retention of volatile substances. 2. Modeling. Ind. Eng. Chem. Res. 39, 1766-1774.

[28] Sano, Y. Keey, (1982) The drying of a spherical particle containing colloidal material into a hollow sphere. Chemical Engineering Science. 37 (6), 2985-2993.

[29] Tran, T.T.H. Jaskulski, M. Avila-Acevedo, J.G. Tsotsas, E. (2017) Model parameters for single-droplet drying of skim milk and its constituents at moderate and elevated temperatures. Drying Tecnology, 35:4, 444-464.

[30] Lewandowski, A. Jaskulski, M. Zbicinski, I. (2018) Effect of foam spray drying process parameters on powder morphology. Drying Technology, 37:5, 353-545.

[31] Chesters, A. K. (1978) Modes of bubble growth in the slow-formation regime of nucleate pool boiling. Int. J. of Multiphase Flow, 4, 3, 279-302.

[32]Auracher, H. Marquardt, W. (2002) Experimental studies of boiling mechanisms in all boiling regimes under steady-state and transient conditions. Int. J. of Thermal Sciences. 41, 586-598.

[33] Ramaswamy, C. Joshi, Y. Nakayama, W. Johnson, W.B. (2002) High-speed visualization of boiling from an enhanced structure. International Journal of Heat and Mass Transfer, 45, 24, 4761-4771.

[34] Peyghambarzadeh, S.M. Vatani, A. Jamialahmadi, M. (2013) Influence of bubble formation on different types of heat exchanger fouling. Applied Thermal Engineering, 50, 1, 848-856.

[35] Podvysotsky,A.M. and Shraiber,A.A. (1984). Coalescence and break-up of drops in two-phase flows. Int. J. Multiphase Flow. Vol. 10, No. 2, pp. 195-209.

[36] Qian, J. and Law,C.K. (1997), Regimes of coalescence and separation in droplet collision. Journal of Fluid Mechanics, vol. 331, pp.59-80.

[37] Ashgriz,N. and Poo, J.Y. (1990), Coalescence and separation in binary collision of liquid drops. Journal of Fluid Mechanics,, 221, 183.

[38] Sommerfeld, M. Pasternak, L. (2019) Advances in modelling of binary droplet collision outcomes in Sprays: A review of available knowledge.

[39] Sommerfeld, M. Kuschel, M. (2016) Modelling droplet collision outcomes for different substances and viscosities. Exp. Fluids, 57: 187. DOI: 10.1007/s00348-016-2249-y

[40] Sommerfeld, M. (2001) Validation of a stochastic Lagrangian modelling approach for inter-particle collisions in homogeneous isotropic turbulence. Int. J. Multiphase Flows, 27, 1828-1858.

[41] Guo, B. Fletcher, D.F. Langrish T.A.G. (2004). Simulation of the agglomeration in a spray using Lagrangian particle tracking.

[42] Palzer, S. (2005) The effect of glass transition on the desired and undesired agglomeration of amorphous food powders. Chemical Engineering Science, 60, 3959-3968.

[43] Ozmen, L. Langrish, T.A.G. (2002) Comparison of glass transition temperature and sticky point temperature for skim milk powder. Drying Technology, 20:6, 1177-1192.

[44] Malafronte, L. Ahrné, L. Innings, F. Jongsma, A. Rasmuson, A. (2015) Prediction of regions of coalescence and agglomeration along a spray dryer – Application to skim milk powder. Chem. Eng. Res & Design, Vol. 104, 703-712.

[44] Jubaer, H. Xiao, J. Chen, X.D. Selomulya, C. Woo, M.W. (2019) Identification of regions in a spray dryer susceptible to forced agglomeration by CFD simulations. Powder Technology, 346, 23-37.

[45] Palzer, S. (2009) Influence of material properties on the agglomeration of water-soluble amorphous particles. Powder Technology, 189, 318-326.

[46] Nijdam, J.J. Guo,B. Fletcher, D.F. and Langrish,T.A. (2006). Lagrangian and Eulerian models for simulating turbulent dispersion and coalescence of droplets within a spray. Applied Mathematical Modelling, 30, 1196-1211.

[47] Francia, V. Martín, L. Bayly, A.E. Simmons, M.J.H. (2015) Particle aggregation in large counter-current spray drying towers: Nozzle configuration, vortex momentum and temperature. Procedia Engineering, 102, 668-675.

[48] Francia, V. Martín, L. Bayly, A.E. Simmons, M.J.H. (2016) Agglomeration in counter-current spray drying towers. Part A: Particle growth and the effect of nozzle height. Vol. 301, 1330-1343.

[49] Francia, V. Martín, L. Bayly, A.E. Simmons, M.J.H. (2017) Agglomeration during spray drying: Airborne clusters of breakage at the walls? Chemical Engineering Science, 162, 284-299.

[50] Jaskulski, M. Wawrzyniak, P. Zbicinski, I. (2015) CFD Model of Particle Agglomeration in Spray Drying. Drying Technology, 33:15-16,1971-1980.

[51] Fiedlander, S.K. and Johnstone, H.F. (1957). Deposition of suspended particles from turbulent gas streams, Ind. Eng. Chem. Res. 49, 1151-1156.

[52] Soldati, A. Marchioli, C. (2009). Physics and modelling of turbulent particle deposition and entrainment: Review of a systematic study. International Journal of Multiphase Flow, 35, 827-839.

[53] Francia, V. Martín, L. Bayly, A.E. Simmons, M.J.H. (2015) The role of wall deposition and re-entrainment in swirl spray dryers. AIChE Journal, Vol. 61, 6, 1804-1821.

[54] Papavergos, P.G. and Hedley, A.B. (1984). Particle deposition behaviour from turbulent flows. Chemical Engineering Research and Design, 62, 5, 275-295.

[55] Henry,C. Minier,J.P. and Lefevre,G. (2012) Towards a description of particulate fouling: From single particle deposition to clogging. Advances in colloid and interface science, 185-186, 34-76.

[56] Reeks, M.W. Reed, J. Hall, D. (1988) The resuspension of small particles by a turbulent flow. Journal of physics, 21, 574-589.

[57] Zhang, F. Reeks, M. W. Kissane, M. Perkins, R.J. (2013) Resuspension of small particles from multilayer deposits in turbulent boundary layers. Journal of Aerosol Science, Vol. 66, 31-61.

[58] Kota, K. and Langrish,T.A.G. (2006). Fluxes and patterns of wall deposits for skim milk in a pilot-scale spray dryer. Drying technology, 24, 8, 993-1001.

[59] Langrish, T.A.G. and Zbicinski,I. (1994). The effects of air inlet geometry and spray cone angle on the wall deposition rate in spray dryers. Chemical engineering research and design. 72, A3, 420-430.

[60] Kota,K. and Langrish,T.A.G. (2007). Prediction of wall deposition behaviour in a pilot-scale spray dryer using deposition correlations for pipe flows. Journal of Zhejiang University Science A, 8, 301-312.

[61] Woo, M.W. Daud, W.R.W. Mujumdar, A.S. Tasirin,S.M. and Talib,M.Z.M. (2010). Role of rheological characteristics in amorphous food particle-wall collisions in spray drying. Powder technology, 198, 252-257.

[62] Bemrose and Bridgwater (1987) A review of attrition and attrition test methods. Powder Technology, 49, 97-126.

[63] Salman, A. Hounslow, M.J. Ghadiri, M. (2007) Handbook of powder technology. Vol. 12. ISBN: 9780444530806

[64] Subero, J. Ghadiri, M. (2001) Breakage patterns of agglomerates. Powder Technology 120, 232-243.

[65] Ghadiri, M. Zhang, Z. (2002) Impact attrition of particulate solids. Part I: A theoretical model of chipping. Chem. Eng. Science, 57(17), 3659-3669.

[66] Austin, L.G. (1971) Introduction to the mathematical description of grinding as a rate process. Powder Technology, 5(1), 1-17.

[67] Shah, B.H. Ramkrishna, D. Borwanker, J.D. (1977) Simulation of particulate systems using the concept of the interval of Quiescence. AIChE Journal, Vol. 23, 6, 897-904.

[68] Patruno, L.E. Dorao, C.A. Svendsen, H.F. Jakobsen, H.A. (2009) Analysis of breakage kernels for population balance modelling. Chemical Engineering Science, Vol. 64 (3), 501-508.

[69] Hassanpour, A Antony,S.J. Ghadiri, M. (2007) Effect of size ratio on the behaviour of agglomerates embedded in a bed of particles subjected to shearing: DEM analysis. Chemical Engineering Science 62(4), 935-942.

[70] Woo, M.W. (2019) Computational Fluid Dynamics Simulation of Spray Dryers: An Engineers Guide. ISBN: 9780367873172.

[71] Jubaer, H. Xiao, J. Chen, X.D. Selomulya, C. Woo, M.W. (2019) Identification of regions in a spray dryer susceptible to forced agglomeration by CFD simulations. Powder Technology, 346, 23-37.

[72] Ali, M. (2014) Numerical modelling of a counter-current spray drying tower. Ph.D. thesis. Institute of Particle Science and Engineering. University of Leeds. United Kingdom.

[73] Ali, M. Mahmud, T. Heggs, P.J. Ghadiri, M. Bayly, A.E. Ahmadian, H. Martin de Juan, L. (2014) CFD modeling of a pilot-scale countercurrent spray drying tower for the manufacture of detergent powder. Drying Technology, 35 (3), 281-299.

[74] Residence time distribution of glass ballotini in isothermal swirling flows in a counter-current spray drying tower. Powder Technology, 305, 809-815.

[75] Bezzo, F. Macchietto, S. (2004) A general methodology for hybrid multizonal/CFD models: Part II. Automatic zoning. Computers & Chemical Engineering, 28 (4), 513-525.

[76] Process System Enterprise. (2020) gFormulate. Available at: https://www.psenterprise.com/products/gproms/formulatedproducts Last access: April, 2020.

[77] Ali, M. Mahmud, T. Heggs, P.J. Ghadiri, M. (2020) Zonal modelling of a counter-current spray drying tower. Chemical Engineering Research and Design, Vol. 155, 180-199.

[78] Process System Enterprise. (2020) Hybrid Multizonal gProms-CFD. Available at: https://www.psenterprise.com/products/gproms/hybrid-multizonal. Last access: April, 2020.

CHAPTER 1.1. SINGLE DROPLET DRYING MODELING OF DETERGENTS.

This chapter evaluates the single droplet drying (SDD) of detergents. Experimental data are used to validate a theoretical multistage model. The experiments are carried out in an acoustic levitator analysing 6 different detergent formulations at 393 K. The work is completed by developing a model based on conservation equations. The model is composed of the three stages observed in the drying curve. In the first stage an external surface drying stage occurs until the surface is saturated and the crust is formed. In the next stage the drying rate is governed by diffusion through the pores. At the same time, the particle heats up until boiling conditions are achieved in the core of the particle. At this point, the third stage begins. In the final stage, the droplet core is in boiling conditions which are governed by the pressure drop through the crust and the concentration of salts. This model has been evaluated for the different formulations being flexible to predict the drying of different mixtures with good accuracy.

Acknowledgements: The author acknowledges the group of Professor Rosa Mondragón for the experimental characterization of the droplets.

Note: The supplementary material is attached in the physical edition of the thesis and it is also available in: https://drive.google.com/drive/folders/1_EkYTjaqQYkP_okY1ckLG9DMSdbt8gRt?usp=sharing

1.1.1 INTRODUCTION.

Many particulate products such as pharmaceuticals, foodstuffs (milk powder, instant coffee, etc.) and powder detergents are manufactured by spray drying [1]. Spray drying works by contacting an atomised slurry with hot air in a chamber. The operation is a complex process that includes aspects from many areas such as fluid mechanics, heat and mass transfer, particle technology and reaction engineering. The understanding of these phenomena is critical for scaling-up and optimizing the production of the particles [1-3]. The use of validated computational models has helped in these areas by reducing the cost and time involved in experimental trials. The first models were based on heat and mass balances, involving assumptions such as uniform gas conditions and perfect-mixing inside the dryer [4]. The improvement in computational capabilities and the rapid expansion of the interest in spray drying has led to the development of more complex models in the last three decades [2, 5]. One of the most recurrent technologies in this area is computational fluid dynamics (CFD) [3, 6-8]. CFD models developed for spray drying towers are structured in different blocks such as airflow modelling, discrete phase momentum modelling, drying or particle quality [3, 7, 9]. The modelling of the particles within the dryer has traditionally been performed by means of a discrete particle method that assumes a low concentration of particles. This allows the scale-up of the drying phenomena by studying the single droplet drying (SDD) of the material processed in the system. A range of approaches have been used to model SDD. Langrish [2] recently classified the most popular approaches in four groups: The use of characteristic drying curves (CDC) [10, 11], shortcut models based on the diffusion equation [12-14], receding-plane type of models that include diffusion and convection mechanisms [15-17] and reaction engineering approaches (REA) [18, 19]. Apart from these types used in CFD, a more detailed approach based on population balances has also been developed for the description of the particle formation [20, 21].

The CDC approach has been used in many works for modelling drying in spray dryers due to its simplicity [6, 11, 22]. This type of model is semi-empirical and is represented by a set of simplified equations allowing fast computations with good predictions for small particle sizes [23, 24] and industrial units. In this type of model, a first stage is simplified by analogy with evaporation of a small pure liquid droplet and a second stage shows a falling rate that is dependent on the critical, equilibrium and current moisture content values [24]. Similarly, the reaction engineering approach developed by [18] also uses simplified semi-empirical correlations for the modelling of SDD. This approach resembles the drying of the droplet by a kinetic model where the evaporation of water is an activation process having to overcome an energy barrier, whereas condensation or adsorption is assumed not to have an energy barrier [25]. The application of this type of model is limited by experimental characterization of the material since the activation energy and drying constant need to be estimated for each material under different moisture contents [22]. However, this has not stopped REA, being applied to different droplet materials such as milk droplets [25] and maltodextrin [26, 27]. Small differences of around 5% between this approach and the CDC are found when comparing both [22].

Contrary to the simplicity of the two previous approaches, deterministic models based on mass, momentum, and energy conservation equations provide a more detailed explanation of the phenomena involved and, in some

cases, the droplet structure. As with the two previous types, these models are based on the characterisation of the transport of water in the boundary layers of spherical droplets as proposed by Ranz and Marshall [28, 29]. These studies, which assumed infinite thermal conductivity in the droplet, were extended in the study of Abramzon and Sirignano [30], who suggested the use of an effective thermal conductivity for the liquid of the droplet to improve the prediction of the drying rate. Another first principles-based model that modifies the drying rate as function of the droplet properties was proposed by Nesic and Vodnik [31]. This model includes the shrinkage of the droplet and the formation of a crust so that water diffusion is affected by its thickness. If the pores created in that crust have lower effective diffusion coefficient than the water in the boundary layer, the global diffusion coefficient decreases [31]. These first principles-based models assume a uniform temperature for the entire droplet. Newer models have been developed to include the temperature distribution for some specific cases. In the case where Biot and Lewis numbers were very low and droplet temperatures were below the boiling temperature, Farid [32] developed a model that includes the temperature distribution within the droplet. A model considering the temperature distribution, the influence of the concentration and the formation of the crust was recently developed by Darvan and Sommerfeld [33]. In addition to defining a new model, their study provided more accurate predictions were provided in the stage transitions for milk droplets.

All these previous models mainly focused on milk droplets evaluated at low temperatures. A few studies such as the ones performed by Sano and Keey [34] and Mezhericher et al. [35] have used temperatures above the boiling temperature of water for the SDD of milk. In both cases, higher temperatures were only observed at the end of the drying curve without showing boiling phenomena within the droplet. One of the first works including boiling in drying was developed by Hecht and King [36] for sucrose droplets. Their work proposed a model for boiling based on the energy balance and a correlation for the boiling temperature as a function of the moisture content in the droplet. Apart from the focus on boiling, previous works also focused on the crust behaviour observing that it could be deformed at high temperatures depending on the flexibility and capillarity forces. In a recent work, Tran et al. [37] studied this deformation observing the rupture of milk particles for temperatures above 413 K and proposed a model to estimate the final diameter and drying rates of such droplets.

Even though boiling rarely takes place in the production of milk powders since denaturalization of the proteins appears at 345 K [38], the study of Tran et al. [37] provides relevant description of drying at high temperature and it is relevant to more stable materials such as detergents and ceramics that are processed at high temperatures. Focusing on the drying of detergent droplets, two studies have developed SDD models for the CFD modelling of spray drying towers. Jaskulski, et al. [39] proposed a CDC model. The model was validated using the temperature distribution within the tower and was applied to predict agglomeration. The second study by Ali et al. [40] used a variation based on experimental fittings of the model of Hecht and King [36]. In these two studies the drying curves were not validated either for different formulations or with direct analysis of the drying of the droplet. The Hecht and King model was initially developed and validated for the drying of sucrose powders [36] but it has not been validated for detergents with direct analysis of single droplets. Detergent formulations are created by the mixing of the large numbers of ingredients, which affects the shape of drying curve. Therefore, this work provides a

comparison of the SDD of different detergent formulations. Furthermore, a simple but flexible SDD model, which combines concepts from previous studies, is developed allowing the prediction of the drying curves of different detergent formulation. This model can also be implemented in CFD codes.

The rest of the paper is structured as follows. In section 1.1.2, the experimental methodology consisting on the use of a levitator is presented. In section 1.1.3, the theoretical model based on experimental observations is developed. In section 1.1.4, the experimental results are presented together with the evaluation of the model. Conclusions are presented in section 1.1.5.

1.1.2 EXPERIMENTAL METHODOLOGY

This section presents the experiments performed to validate the model. It is divided into the following parts. In section 1.1.2.1 the modified acoustic levitator is described. In section 1.1.2.2 the procedure to perform the experiments is presented.

1.1.2.1 Experimental apparatus

The study of drying kinetics of particles can be performed using different methods such as a conventional microbalance, a balance in combination with a drying tunnel, an acoustic levitator, a magnetic suspension balance or by glass filament [41]. Previous works have also shown the application of some of these techniques to the characterization of single droplet drying at elevated temperatures. For example, Mondragón et al. [42] and Tran et al. [37] used a non-intrusive method such as acoustic levitator but that does not allow to predict the particle temperature or Ebrahim, W. [43] used a microbalance that allow the prediction of the temperature but it lightly modify the structure of it. In the present work the acoustic levitator is used. It is composed of three systems as presented in Figure 1: the acoustic levitator itself consisting of an ultrasonic 58 kHz horn and a concave reflector; an optical system consisting of a white light source with a CCD camera; and an air conditioning system.

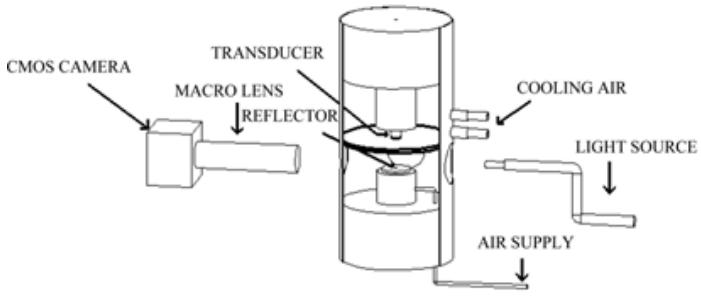

Figure 1. Ultra-sonic levitator used for the experiments.

The levitator has been modified to be used with higher temperatures, up to 423 K, than the initial specifications allowed by the supplier, 333 K. Previous works that used this modified levitator reported stability for the drying of multiphase droplets at 393 K [42, 44]. The modification has been performed as presented in Figure 2. Two metallic chambers separated by the insulator can be found. The first is identified as the “cold chamber” and contains the

ultrasonic transducer of the levitator. The temperature of this chamber cannot be higher than 333 K to prevent damage to the piezoelectric transducer. This temperature is controlled by forced convection using a flow of cold air. The second “hot chamber” contains the lower part of the levitator. The temperature of this chamber is controlled by an electric heater, see Figure 2. The ultra-sonic levitator uses an air stream that enters the levitator tube through an array of holes located in the reflector [42].

The air conditioning system is composed of a dierite air-drying cartridge, two-mass flow controllers and an evaporator/mixer unit. This system allows temperatures up to 473 K and humidity up to a dew point of 353 K. To prevent the cooling down of the air stream from the conditioning system to the levitator, the tube that connects both devices, as well as the reflector, needs to be heated using electric heaters.

A CMOS camera with a back-light illumination is used to measure the droplet cross sectional area and the vertical position of the droplet during the drying process. A resolution of 500 pixels/mm and a recording speed of 87 fps are set for all experimental conditions. The recorded images are analysed later to determine the drying curve.

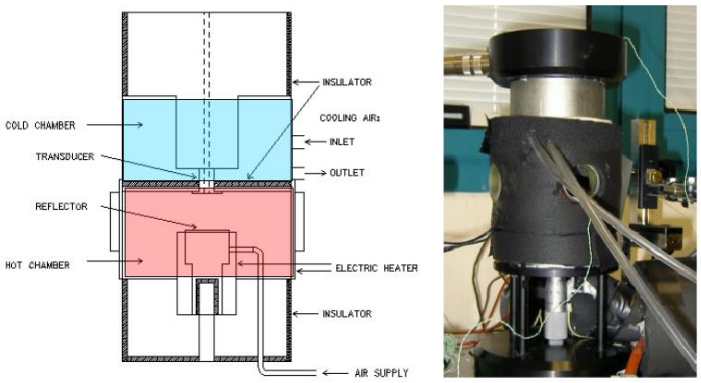

Figure 2. Modified acoustic levitator used for the experiments.

1.1.2.2 Experimental procedure

In this study, six formulations have been analysed. The formulation of these detergents is complex involving different species such as crystalline and amorphous salts, polymers, surfactants and water [45]. The droplets are introduced with a syringe into the hot chamber of the levitator. The droplet size selected for the study is around 800 µm in diameter. The exact size is captured by the camera to avoid errors in the modelling part of this work.

The flow rate and temperature of the air stream are set to 0.5 l/min and 393 K, above the boiling temperature of the formulations at atmospheric conditions (between 368 K and 381 K), to ensure constant drying conditions around the droplet, to ventilate the acoustically induced vortex system around the droplet from liquid vapour and avoid the blow out of the droplet [42, 44]. The estimated flow velocity at the droplet based on the analysis from Yarin et al. [46] was 0.7 cm/s. The drying air is introduced in the levitator hot chamber after flowing through the

drierite air-drying cartridge to remove the initial moisture content and to minimize relative humidity for the drying tests.

The drying of the droplet is recorded by the CMOS camera. The images reported are subsequently analysed by Matlab®'s Image Processing Toolbox, which reports the particle cross-sectional area of the droplet and the position of the droplet.

1.1.3 MODELLING APPROACH

Historically, the modelling of particle drying in CFD simulations for spray drying towers has been performed using one of the 4 theoretical approaches presented in the introduction. In this study a first-principle based model including diffusion and convection mechanisms is developed. The mechanism and the equations used to model them are discussed in this section.

1.1.3.1 Theoretical description of the model

The drying mechanism described in Figure 3 is used. It is composed of the following 3 stages:

- A surface drying stage where the surface water diffuses into the surrounding air and results in a shrinkage of the droplet. This stage occurs until the locking point is achieved. At this point, the surface is dry and the generation of the crust begins.
- In the second stage drying is governed by the diffusive resistance of water through the pores formed in the crust that grows from the surface to the centre of the droplet. Apart from controlling diffusive mass transfer, the crust is also assumed to govern the transition to boiling. The droplet heats up until it reaches boiling conditions. This happens when the vapour pressure within the droplet is equal to the pressure in the wet core, is the latter given by the atmospheric pressure plus the pressure drop through the crust.
- Once the boiling conditions are achieved in the wet core, the drying rate increases by vapour convection through the pores. Since the evaporation rate within the droplet increases due to boiling, the flow through the pores also suffers an increase and the droplet behaves as a "pressure cooker" where the pores are the "valve" that control the internal pressure. Apart from the change in the drying rate, it is also important to remark the influence of the nucleation regime expected for boiling. In the extreme case, where the crust reaches the gas temperature quickly, the maximum difference between the boiling temperature of the core (373 K at atmospheric conditions) and the temperature of the crust (temperature of 393 K in the air) is never higher than 20 K. In practice, smaller temperature differences are generated because (1) the salts dissolved in the core increase the boiling temperature and (2) because the crust presents a pressure drop, allowing higher boiling temperatures to be achieved inside the core. These two effects combined result in a smaller temperature difference between the boiling conditions and the crust. Since this difference is small, it is assumed that the boiling regime does not generate stable bubbles [47], see Figure S-1 in the supplementary material. As a result the pressure within the droplet is not higher than the rupture strength of the material and the droplet does not result in bursting. The pores can maintain their shape or

they can only suffer a plastic deformation by the pressure increasing their size. The characterization of these pores is extremely challenging during drying and the only concern observed is that bursting does not occur as presented in the videos attached as supplementary material. Therefore, the modelling of this third stage is carried out dividing the third stage is two parts:

- A first sub-stage where the boiling is governed by the pressure drop through the pores. The pores formed in the previous stage still present a resistance, maintaining the boiling temperature at higher conditions than the boiling temperature at atmospheric conditions.
- A second sub-stage where the boiling temperature is governed by the moisture content of the droplet. In this second stage, the concentration of solids in the core increases. This results in a decrease in the activity coefficient and an increase in the boiling temperature, increasing the likelihood that equilibrium is eventually reached. This stage is assumed to last until the final equilibrium moisture content is achieved.

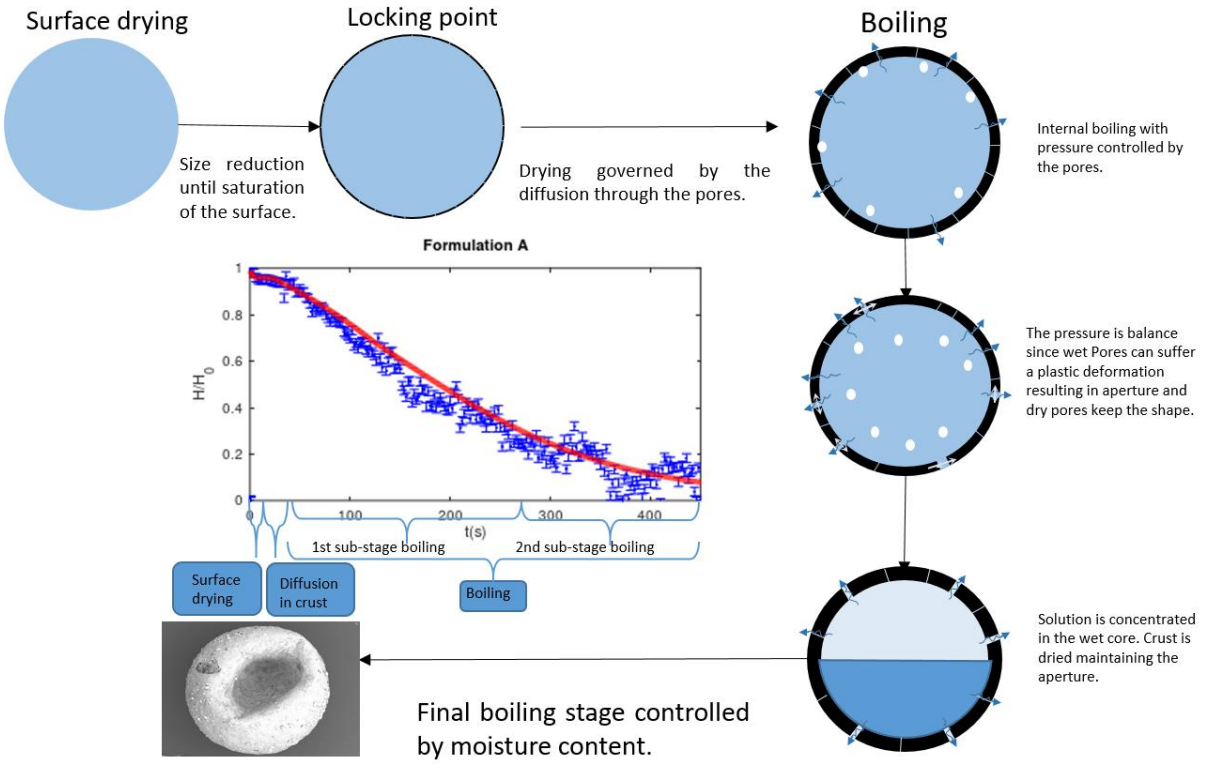

Figure 3. Droplet drying mechanism.

1.1.3.2 Mathematical modelling

The model has been developed in gProms®, ModelBuilder® v.5.1 and the stages previously described are modelled as presented in the following paragraphs.

Modelling of the 1st drying stage

The first stage is modelled with the equations presented below. The mass balance for the drying of the droplet during this stage is modelled with Eq. (1), which corresponds to a system controlled by mass transfer through a boundary layer.

$$\frac{dm}{dt} = 4\pi R^2 \cdot K \cdot \frac{(P_{v,s} - P_{v,\infty}) MW_w}{RT} \quad (1)$$

In Eq. (1), P_v is the vapour pressure. The subscript s refers to the droplet-air interface and the subscript ∞ refers to the air-bulk phase. The vapour pressure is computed by Eq. (2) as a function of the moisture concentration in the droplet, C_l, the activity coefficient, γ_l, and the saturation pressure of the vapour, P_l^0. The activity coefficient, γ_l, is modelled using Eq. (3) as a function of the moisture content. The parameters in Eq. (3) are experimentally determined from the desorption isotherm of each formulation at 323 K. The saturation pressure is computed by Eq. (4).

$$P_{v,s} = C_l \cdot \gamma_l \cdot P_l^0 \quad (2)$$

$$\gamma_l = a \cdot C_l^b \quad (3)$$

$$P_l^0 = 10^{8.07131 - \frac{1730.63}{T_d - 28.515}} \cdot \left(\frac{1.01325 \cdot 10^{-5}}{760}\right) \quad (4)$$

The mass transfer coefficient, K, in Eq. (1) is computed using Eq. (5) as a function of the particle radius, R, the mass diffusivity, D_w, and the Sherwood number for acoustically driven levitation, Sh_{ac}.

$$K = \frac{Sh_{ac} \cdot D_w}{2R} \quad (5)$$

The water-air diffusivity is computed using Eq. (6) [35].

$$D_w = 3.564 \cdot 10^{-10} \cdot (T_d + T_\infty)^{1.75} \quad (6)$$

The Sherwood number,Sh_{ac}, is computed using Eq. (7) as reported by Yarin et al. [44].

$$Sh_{ac} = \left(\frac{45}{4\pi}\right) \cdot \frac{B}{(\omega D_w)^{1/2}} \quad (7)$$

Where the angular velocity, ω, is determined from the oscillation frequency of the levitator (f_{lev}) by Eq. (8). The gas-particle velocity amplitude in the acoustic wave, B, is computed using Eq. (9). In Eq. (9), ρ_∞ is the density of the air at 393 K, c_o is the gas sound velocity, which takes a value of 397 m/s at 393 K, and A_o is the effective pressure amplitude of the acoustic field. The value of the pressure amplitude of the acoustic field is a parameter

determined with the first formulation and subsequently used in the remaining experiments. The value obtained for A_o from the first experiment is 1.2 x 10^3 Pa. This value finally results in a Sherwood number between 2.3 and 2.6, in the range reported in [44].

$$\omega = 2 \cdot \pi \cdot f_{lev} \tag{8}$$

$$B = \frac{A_o}{\rho_\infty c_o} \tag{9}$$

In the same way, a heat balance is also performed during this stage as presented in Eq. (10).

$$\frac{dT}{dt} = \frac{1}{m\,(C_s C_{ps} + C_l C_{pl})}\left[\, 4\pi R^2 \cdot h \cdot (T_\infty - T_s) + L_H \frac{dm}{dt}\right] \tag{10}$$

The heat transfer coefficient through the boundary layer, h , is computed using Eq. (11) as a function of the Nusselt number for acoustically driven levitation, Nu_{ac}, and the thermal conductivity of the air, k_{air}. The Nusselt number for acoustically driven levitation is determined from the thermal diffusivity of the air, α_o, and the Sherwood number as presented in Eq. (12).

$$h = \frac{k_{air} \cdot Nu_{ac}}{2R} \tag{11}$$

$$Nu_{ac} = \left(\frac{D_w}{\alpha_o}\right)^{\frac{1}{2}} Sh_{ac} \tag{12}$$

Apart from the parameters defined in the previous equations, the rest of parameters have been assumed to be constant with the values presented in Table 1.

Table 1. Variables defined for the modelling.

Variable	Value
$\boldsymbol{L_H}$ (J/kg)	2,264,760
$\boldsymbol{C_{psolid}}$ (J/kg K) [40]	700
$\boldsymbol{C_{pl}}$ (J/kg)	4,185
$\boldsymbol{k_{air\,(393K)}}$ (W/m K)	0.033
$\boldsymbol{\alpha_{o\,(393\,K)}}$ (m^2/s)	3.75 x 10^{-5}

Modelling of the 2nd drying stage

The second stage begins with the locking point, which is achieved when the droplet surface gets dried and the crust starts to be generated. This locking point is defined as a function of a critical moisture content,C_{lcr}, This is a parameter in the drying curve determined for each formulation. After achieving the locking point, the crust grows and presents a resistance to mass transfer. Despite the low porosity of the particle, the diameter of the pores are assumed to be much greater than the vapour molecular free path. As a result, the Knudsen number is much smaller

than unity [48] and the overall mass transfer rate is computed as the sum of two resistances as defined in Eq. (13). In the denominator of Eq. (13), the first term corresponds to the resistance due to the diffusion across the boundary layer, which is obtained from Eq. (5), and the second term is the resistance given by the diffusion through the crust. R_c is the droplet radius that remains constant once the crust has been formed. Sh_{ac} is computed as presented in Eq. (7) and D_w is the diffusivity of water in air. In the second term, D_{cr} is the diffusion coefficient across the crust pores and δ is the crust thickness, which grows as presented in Eq. (14). In Eq. (14) the crust thickness is shown to be dependent on its porosity, ε. This porosity is covered by the vapour generated from the core with a flow rate that can be computed using Eq. (15).

$$\frac{dm}{dt} = \frac{MW_w}{RT} \cdot \frac{2\pi \left(P_{v,s} - P_{v,\infty}\right)}{\frac{1}{R_c\, Sh_{ac}\, D_w} + \frac{\delta}{2D_{cr} R_c (R_c - \delta)}} \tag{13}$$

$$\frac{d\delta}{dt} = \frac{1}{(1-\varepsilon)\cdot\rho_{solid}\cdot 4\cdot\pi\cdot R_C^2} \frac{dm}{dt} \tag{14}$$

$$\left(\frac{dm}{dt}\right)_d = \frac{dm}{dt} \frac{\varepsilon\cdot\rho_v}{(1-\varepsilon)\rho_d} \tag{15}$$

A heat balance is also formulated on the droplet core as presented in Eq. (16). The resistance to the heat transfer into the droplet is defined in the denominator of the first term in brackets. It represents the resistance to the heat transfer in the boundary layer and the resistance in the crust. The second term within the brackets corresponds to the energy consumed to evaporate the solvent. The third term is the vapour required to cover the pore of the crust. The fourth term is the energy absorbed by the crust, which is assumed to be heated until it achieves the external gas temperature.

$$\frac{dT}{dt} = \frac{1}{(m_{s_{core}} C_{psolid} + m_l C_{pl})} \left[\frac{2\pi R_c Nu_{ac} k_{air} (T_\infty - T)}{1 + \frac{Nu_{ac} k_{cr}}{2k_{cr}} \frac{\delta}{R_c - \delta}} + L_H \frac{dm}{dt} + L_H \left(\frac{dm}{dt}\right)_p - m_{s\,cr} C_{psolid} (T_\infty - T) \right] \tag{16}$$

In addition to the critical moisture content,C_{lcr}, the diffusivity through the crust is estimated from SDD experiments. The rest of the parameters involved in this second stage have been defined in Table 1, except for the thermal conductivity of the crust, which is assumed to be 0.7 W/mK [49], the conductivity of the main dried component [45].

In defining the transition to the third stage, it is assumed that there is a vapour-liquid equilibrium within the droplet given by Eq. (17). Boiling conditions in the wet core are achieved when the saturation pressure of the vapour in this equilibrium is equal to the pressure within the core. The pressure within the core is computed as the sum of the atmospheric pressure and the pressure drop across the crust, which is obtained from the Carman-Kozeny equation, Eq. (18). In this equation, the viscosity of the steam, μ, is taken to be 1.4 x 10^{-5} Pa·s, the superficial velocity, v_{cs}, is computed from the drying rate as presented in Eq. (19), the mean diameter of the particles that compose the crust, d_{mpc}, is assumed to be 1 μm, the porosity of the crust, ε, is a parameter characterized for every formulation.

$$\frac{dP_{wc}}{dt} = \frac{dP_{cr}}{dt} \tag{17}$$

$$\frac{\partial P_{cr}}{\partial \delta} = -\frac{180\mu}{d_{mpc}^2}\frac{(1-\varepsilon)^2}{\varepsilon^3} v_{cs} \quad (18)$$

$$\frac{dm}{dt} = \frac{1}{v_{cs}\cdot\rho_v\cdot 4\cdot\pi\cdot R_c^2} \quad (19)$$

Modelling of the 3rd drying stage

In this stage of the drying of the droplet, a hollow core is assumed to be formed. The drying rate is controlled by two mechanisms: First, an equilibrium between the heat and mass transfer is achieved. Water activity in the core is 1 and the pressure in the core, which is also influenced by the pressure drop across the crust, is equal to the vapour pressure defined by the Antoine equation for water. As a result, the temperature in the droplet core, where boiling occurs, is constant. Thus, due to the equilibrium reached at boiling, during this period the drying rate of the droplet is computed from the energy balance, Eq. (20) and the temperature is assumed to be constant, see Eq. (21).

$$\frac{dm}{dt} = \frac{hA_d(T_\infty - T_p)}{L_H\cdot\left(1+\frac{\rho_v}{\rho_{wc}}\right)} \quad (20)$$

$$\frac{dT}{dt} = 0 \quad (21)$$

This first period of the third stage lasts until a critical moisture content is achieved. Below this critical moisture content, the solids concentration in the droplet core reduces the activity of the water and part of the energy provided to the droplet is retained. Therefore, mass transfer in this stage is characterised by multiple equilibria between mass and heat transfer that follows the boiling temperature equation, Eq. (22), corresponding to the composition at the core. Apart from this equation, the energy balance is computed by Eq. (23) [36]. One way to determine the boiling temperature as a function of the moisture content, Eq. (22), was provided by Ali et al. [40]. They used a modified Antoine correlation as presented in Eq. (22). However, the values of the factors used in Eq. (22) change for every formulation.

$$T_d = \exp\left(\frac{ANTA}{ANTB+ANTC\cdot C_l} - ANTD\right) + T_{bo} \quad (22)$$

$$\frac{dm}{dt} = \frac{hA_d(T_\infty - T_p)}{\lambda*\left(1+\frac{\rho_v}{\rho_{wc}}\right)-\left(C_{s_{core}}C_{ps}+C_lC_{pl}\right)C_s\frac{dT_d}{dC_l}} \quad (23)$$

1.1.4. EXPERIMENTAL RESULTS AND MODEL EVALUATION

This section presents the experimental results in section 1.1.4.1 together with a validation of the model developed in this work in section 1.1.4.2.

1.1.4.1 Experimental results

The analysis of measurements by Matlab®'s Image Processing Toolbox provides the projected area of the particle and its relative position. One example of these measurements is provided in Figure 4 for formulation A. Data for the remaining formulations are presented in Figure S-1 to S-6 of the supplementary material. They show the two following periods:

- A first period showing a shrinkage of the area together with a rapid increment of the relative position. In Figure 4, this period corresponds to the first 20 seconds of drying.
- A second period where the cross-sectional area of the droplet remains constant and the relative position increases until the droplet reaches an equilibrium position.

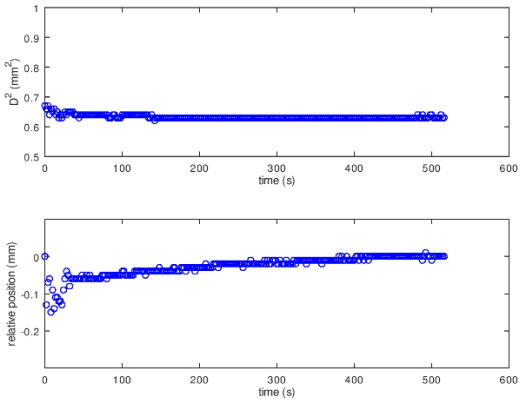

Figure 4. Square diameter (top) and particle relative position (bottom) for the drying of a droplet of formulation A.

During the first period, the shrinkage of the droplet is due to the evaporation of the moisture on the surface. In order to compute the mass transfer rates during this first period ($m_{L,1}$), d²-law is applied [50], as presented in Eq. (24). ρ_w is the density of the water, d_{t1} and d_{t2} are the diameters between two subsequent time-steps and t_{t1} and t_{t2} are the time between two time-steps.

$$\frac{dm_{L,1}}{dt} = \frac{\pi}{6}\rho_w \frac{d_{t1}^3 - d_{t2}^3}{t_{t1} - t_{t2}} \quad (24)$$

During the second period, the droplet diameter is constant and the droplet position varies. The variation of the droplet position is due to the change in its density and mass. In this period, the mass is computed by Eq. (25) [50]. In this equation, y_{21} and y_{22} are the droplet positions at the beginning and end of the second drying stage, respectively, $y(t)$ is the instantaneous position of the droplet, t is the time, which is subtracted from the time at

the beginning of the second stage, t_{21}, and m_{21} is the liquid mass content in the droplet at the beginning of the second drying period, which is computed by Eq. (26):

$$m_{L,2} = \frac{m_{21}}{t-t_{21}} \frac{y(t)-y_{21}}{y_{22}-y_{21}} \quad (25)$$

$$m_{21} = \frac{\pi}{6} d_0^3 \rho_d (1 - C_{solid}) - \frac{\pi}{6} \rho_l (d_0^3 - d_{12}^3) \quad (26)$$

As a result, a drying curve can be obtained from this analysis as presented by the blue dots in the plot of Figure 5. In this Figure 5 the blue dots correspond to the experiments and the red lines correspond to the results of the model presented in section 1.1.3. The modelling results are described in the following section 1.1.4.2. The experimental results of Figure 5 show three stages: A brief first stage where the moisture evaporates by diffusion, a second stage where the drying rate is reduced and a third stage that shows another increase in the drying rate. It is also observed from the analysis of the radius presented in Figure S-2 to S-7 of the supplementary material that the droplet radius remains constant after the second stage has been reached. The surface of the droplet is dried and further drying only occurs for the moisture within the droplet. Thus, for the droplets studied in this work, the droplet radius can be determined fitting the transition from the first to the second stages in the drying curve. This second stage does not take a long time and it can be very short as in formulation E, see Figure 5, which is the most similar to the one presented in the work of Griffith et al. [45]. In that work, only one detergent formulation was analysed and drying was carried out at 355 K, below the boiling temperature. In order to quantify the length of this second stage, the percentage of time of each stage is shown in Table 2. The results show that the first stage corresponding to drying governed by diffusion, is the shortest. On the contrary, the third stage is the longest. In this stage, the drying is governed by boiling. Hence, most of the drying of the particles occurs during the third stage, while the structure of the droplet and its transition to having a dry surface occurs during the two first stages.

Another observation from the experimental results is that there are oscillations in the moisture content in some of the formulations. Looking at the drying curves for formulations B, E and F in Figure 5, oscillations appear in the moisture content during the third stage. These oscillations can be explained by the heterogeneous drying of the droplet which results in a loss of sphericity in the droplet and makes the droplet rotate. The videos attached in the supplementary material show the drying of two formulations. In those videos, and from the drying curves, it can be observed that the rotation tends to increase (even causing the oscillation of the droplet) when the droplet is reaching its equilibrium moisture content. This fact is promoted by the distribution of material within the droplet when it is getting dried. As can be seen in Figure 6, most of the material in the droplet is concentrated in the external crust of the droplets, which is unbalanced, and makes the droplet oscillate.

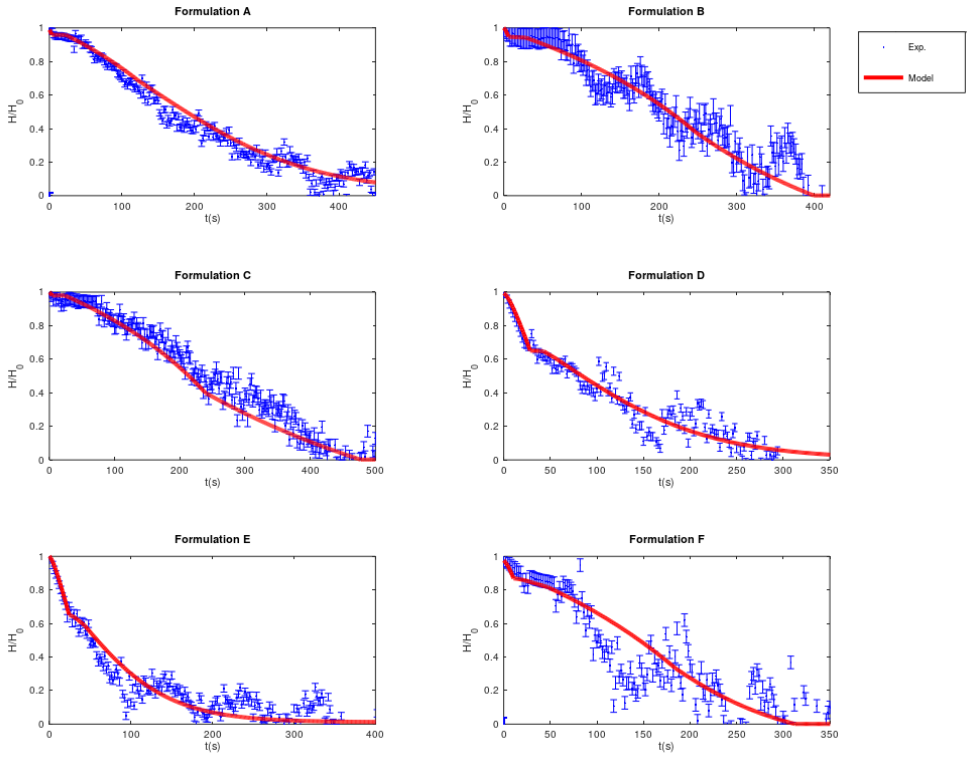

Figure 5. Experimental data and model predictions of the drying curves for each of the six formulation evaluated in this study (experimental data ·, model —).

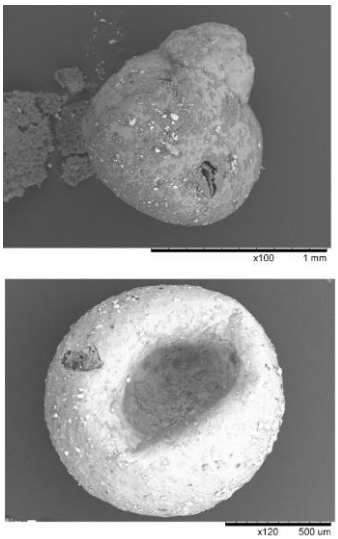

Figure 6. Final droplet structure observed from SEM analysis for two different formulations.

Table 2. Percentages of time per stage.

Formulation	1st Stage (%)	2nd Stage (%)	3rd Stage (%)
A	6.4	25.6	68
B	6.9	16.5	76.6
C	1.8	15.3	82.9
D	8.6	4.3	87.1
E	11.2	2	86.8
F	5	14.4	80.6

1.1.4.2 Model validation and evaluation

In this section, the drying curves of the formulations are used to validate the model described in section 1.1.3 against the experimental moisture content, radius and density.

Drying curves evaluation

The prediction of the moisture content is presented in Figure 5. The model proposed accurately fits the moisture observed experimentally. Deviations are primarily due to the rotation of the droplet generated in the experiment, being more apparent in formulations B, E and F.

Analysing the prediction in each of the stages, the first stage is captured well for most of the formulations. The use of the Sherwood and Nusselt numbers based on the acoustic field reduces the error in the prediction as also observed by Yarin et al. [44]. For formulation F, small differences exist with the experimental data. The model estimates a higher drying rate than that measured. However, these differences do not impact the estimation of the locking point as it is predicted well for all the formulations.

Analysing the second stage, the moisture content during this stage is predicted with reasonable accuracy for all the formulations. As previously mentioned, formulation B is the one that shows a poorer match with experimental data due to the oscillations of the droplet. The transition from this second stage to the third one is characterised by the pressure drop generated in the crust. The computed pressures inside of the droplet are presented in Table 3 for all the formulations. Even that they cannot be characterised since temperature in the core cannot be measured with this technique they are estimated to be higher. It can be seen that the pressure for the transition to boiling, determined from the crust porosity and thickness, tends to be higher for formulations with a longer second stage. However, formulation F shows a pressure of 1.42×10^5 Pa which is as high as formulations A and B. This pressure is obtained because the pressure for the transition to the third stage is determined as a parameter for each formulation. The parameter estimation not only takes into account the values of the second stage, but also considers the values from the third stage. As a result, the pressure obtained by the parameter estimation is also influenced by the experimental data of both stages. It is important to consider the data from the third stage in the parameter estimation because the pressure achieved at the end of the second stage is the same as the pressure

at the beginning of the third stage where the drying rate is governed by the temperature difference between the droplet and the bulk. For example, if higher pressures had been achieved within the droplet during the second stage, the wet core would have had higher temperatures and the drying rate in boiling conditions would have been too small to predict the moisture content of the droplet. Thus, the model suggests a better prediction in the third stage, which is more relevant in terms of drying time (it represents between 68 % and 87% of the drying time), instead of an accurate transition from the second to the third stage.

The high fraction of time that this third stage represents over the whole drying time can also explain why previous researchers [39, 40] have obtained good results when they validate the SDD model with temperature measurements in the tower. However, comparing with the work of Ali et al. [40], where a polynomial was used for the modelling of the second stage, the current work provides a physical explanation for the phenomena that generate these stages. It also addresses the fact that higher pressures and temperatures can be achieved within the core at the end of the second stage and that these temperatures are governed by the crust's thickness and the pores that it contains.

Table 3. Calculated pressures inside the droplet achieved at the end of the second stage when boiling starts.

Formulation	Pressure in the transition from second to third stage (Pa)
A	1.45×10^5
B	1.49×10^5
C	1.8×10^5
D	1.24×10^5
E	1.02×10^5
F	1.42×10^5

Radius evaluation

Figure 7 presents the validation of the radius profile. It can be seen that the radius is predicted correctly for some formulations but not for formulations A, D and F. The experimental results show an initial decrease in the size due to the evaporation of the moisture in the surface until it gets saturated and the formation of the crust begins. In the second stage, the radius behaves differently for some of the formulations studied. In cases A, D and F, this radius continues to show a slight decrease resulting in a small lack of accuracy in the final prediction of the droplet size. Although this lack of accuracy may cause errors in the evaluation of other phenomena such as drying in boiling conditions, particle density or agglomeration [51], the average error only reaches 4.8% of the total particle radius in the worst case, formulation D.

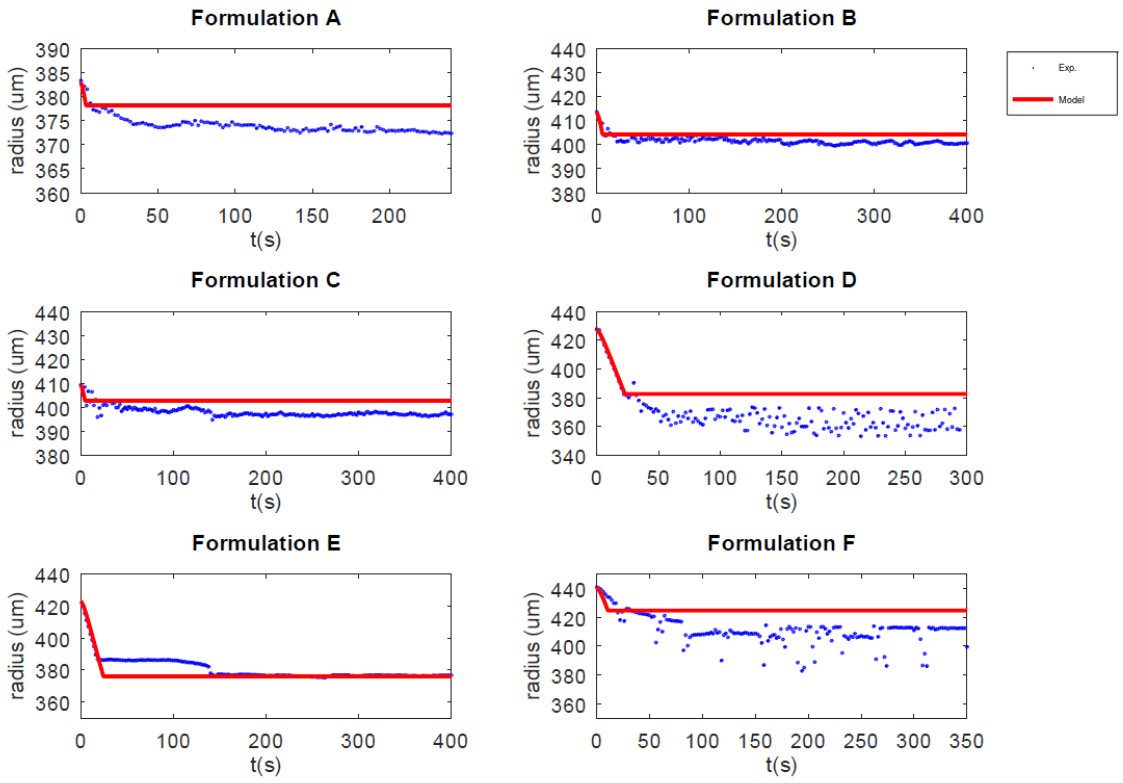

Figure 7. Experimental data and model predictions of droplet radius for each of the six formulations evaluated in this study (experimental data ·, model —).

Other variables computed by the model.

Another variable that can be used for validation of the experiments is the droplet density. This variable is derived from the radius and the particle moisture content. A lack of prediction in either the droplet's radius or its moisture content results in an inaccurate prediction of its density. It is presented in Figure 8 and the final value is shown to be predicted well for all the formulations except D where the higher radius predicted by the model results in a lower density. There is also an error in predicting the density at the end of the second stage for formulation B, for which a shorter second stage was predicted by the model. However, this lack of accuracy in the prediction of the droplet density is finally corrected during the third stage, which takes most of the total drying time, and the final density of the particle is predicted well.

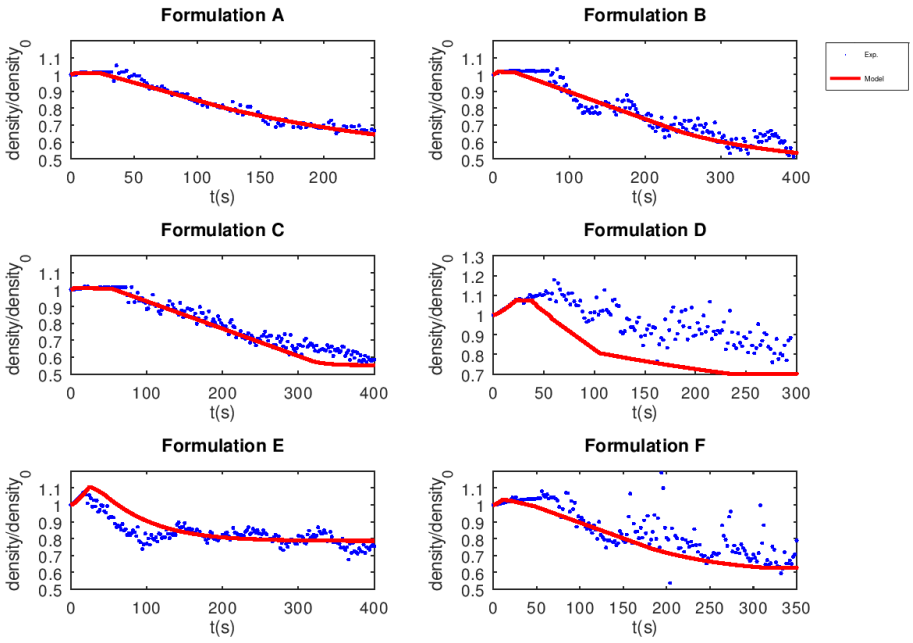

Figure 8. Experimental data and model predictions of relative droplet density for each of the six formulations evaluated in this study (experimental data ·, model —).

Another critical variable in SDD is the droplet temperature. The temperature computed by the model is presented in Figure 9. The method used to measure the SDD of the particles does not provide the particle temperatures and their validation cannot be carried out. However, the use of alternative single droplet drying methods that measure the particle temperature are intrusive and modify the structure of the crust favouring apertures near the thread used for the thermocouple and subsequently a lower boiling temperature than the real one. The only non-intrusive alternative is the use of a thermographic camera. It can allow the determination of the surface temperature [52]. However, for the formulations evaluated in this study a crust is formed and such methods do not allow the prediction of the temperature in the wet core of the particle. Therefore, these predictions could not be validated. Their validation will be more relevant for the third stage where the drying is governed by boiling and the drying rates depends on the boiling temperature reached by the droplet.

Analysing the temperature estimated for the droplets during this third stage, it can be seen that boiling conditions are achieved above the boiling temperature of water at atmospheric conditions. As a result of this higher temperature, the temperature difference between the heat transfer media, the crust, and the core is small and the nucleate boiling regime, where bubbles are generated, is not achieved. The droplet is then in the free convection regime of boiling, see Figure S-1 of the supplementary material. Thus, as presented in Figure 5 for the experimental humidity of the droplet and the videos attached in the supplementary material, there is no bursting in the droplet. To identify the temperature where this bursting takes place for every formulation, in addition to evaluating the SDD under different temperatures, future work should also study the transition to the bubble nucleation regime. Such a study will help to understand the temperature difference at which stable bubble jets are generated under different concentrations and for every formulation.

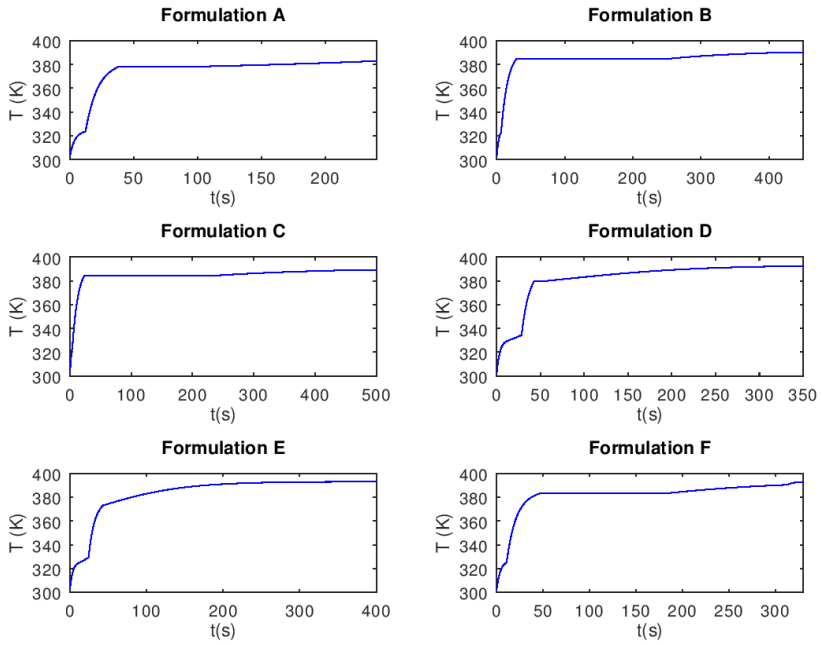

Figure 9. Temperatures computed by the model.

1.1.5 CONCLUSIONS

In the current work, the drying curves for six different detergent formulations have been presented. The experiments are performed by mean of an acoustic levitator at 393 K. For these experiments, drying appears to take place in 3 stages:

- A surface drying stage with a shrinkage of the droplet until the surface gets saturated.
- A second stage where the where the drying is governed by the diffusive resistance of water through the pores. This stage lasts until boiling conditions are achieved. Since the temperature difference between the bulk and the droplet core is not big enough, stable bubbles are not generated within the core and no bursting is observed in the droplet. Thus, it has been showed that boiling can occur during the drying of the droplet but does not always result in bursting.
- A third stage controlled by boiling temperature until the final equilibrium moisture content is achieved.

To shred light into the drying mechanism, a first principles-based model is proposed. The model has been used to study the SDD experiments described in this work. It is capable of predicting the moisture content for all the formulations studied in this work and is also implementable in CFD codes for the scale-up of drying. Furthermore, this model also provides a physical basis to explain: first, the controlled drying in the second stage where the pores in the crust govern the drying and it is not exclusively a function of the time until boiling as proposed by Ali et al. (2017); and second, the transition to the third stage obtained at pressures higher than atmospheric due to the pressure drop in the crust thickness. In the third stage, two periods are distinguished. In the first period, accumulation of heat within the core does not occur and the temperature in the core is only control by the pressure

drop through the pores. In the second period, the temperature in the core increases partly due to an increase in the concentration of the solids and partly because higher pressures are necessary to achieve the equilibrium in the core.

NOMENCLATURE

Symbols

A	Area (m^2)
A_o	Amplitude of acoustic wave
ANTA	Antoine correlation constant A.
ANTB	Antoine correlation constant B.
ANTC	Antoine correlation constant C.
ANTD	Antoine correlation constant D.
B	Particle velocity amplitude in the acoustic wave.
C	Concentration (kg/m^3)
C_p	Specific heat capacity (J/kgK)
c_o	Gas sound velocity (m/s)
D	Diffusivity (m^2/s)
f_{lev}	oscillation frequency of the levitator (Hz)
h	Heat transfer convective coefficient (W/Km^2)
H	Moisture content of the droplet (%)
K	mass transfer coefficient (m/s)
k	Thermal conductivity (W/Km)
L_H	Vaporization enthalpy (J/kg)
m	mass (kg)
Mw	Molecular weight.
Nu	Nusselt number
P	Pressure (Pa)
y	droplet position (m)
R	Absolute radio (m)
Sh	Sherwood number
T	Temperature (K)
t	time (s)
α_o	Thermal diffusivity (m^2/s)
γ	activity coefficient (kg/m^3)
δ	Crust length (m)
ε	Porosity.
ρ	Density (kg/m^3)
ω	Angular velocity (s^{-1})

Super-index

o	Saturation conditions.

Sub-index

1	1st Drying period in experiments
2	2nd Drying period in experiments
12	End of first period of drying.
21	Beginning of second period of drying
22	End of second period of drying
ac	Referred to the acoustic levitator.
bo	Boiling at atmospheric conditions.
c	Critical
cs	Cross-sectional

cr	Crust
d	Droplet
dm	Dried matter
eq	Equilibrium
l	Liquid
o	Initial conditions
sat	Saturation
solid	solid phase
$t1$	Instant 1.
$t2$	Instant 2.
v	vapour
w	Water
∞	Air

REFERENCES

[1] Masters, K. 1992 Spray Drying Handbook, 5th Ed. Longman Scientific and Technical, UK.

[2] Langrish, T.A.G. 2009. Multi-scale mathematical modelling of spray dryers. Journal of Food Engineering 93 (2009) 218-228.

[3] Woo, M. W. 2017. Computational Fluid Dynamics Simulation of Spray Dryers. An Engineer's Guide; CRC Press, Taylor & Francis Group:Boca Raton, FL, ISBN: 978-1-4987-2464-7.
[4] Strumillo, C. Kudra, T. 1986. In: Drying: Principle. Application and Design. Gordon and Breach, New York, pp. 45-54.

[5] Mujumdar, A.S. Huang, L.X. 2007. Global R&D needs in drying. Drying Technology 25 (4), 647-658.

[6] Harvie, D. J. E.; Langrish, T. A. G.; Fletcher, D. F. 2002. A Computational Fluid Dynamics Study of a tall-form Spray Dryer. Food Bioprod. Process. 80, 163−175.

[7] Jaskulski, M.; Zbicinski, I.; Wawrzyniak, P. 2015. CFD simulation of particle agglomeration in industrial counter-current spray drying tower. Presented at the 1st Nordic Baltic Drying Conference, Gdansk, Poland, 2015.

[8] Zbicinski, I. 2017. Modeling and Scaling Up of Industrial Spray Dryers: A Review. Journal of Chemical Engineering of Japan. DOI: https://doi.org/10.1252/jcej.16we350

[9] Hernández, B. Fraser, B. Martin de Juan, L. Martin, M. 2018. Computational Fluid Dynamics (CFD) Modeling of Swirling Flows in Industrial Counter-Current Spray Drying Towers under Fouling Conditions. Ind. Eng. Chem. Res., 57 (35), 11988-12002.

[10] Zbicinski, I. Li, X. 2006. Conditions for Accurate CFD Modeling of Spray-Drying Process. Drying Technology, Vol. 24, 2006, 1109-1114.

[11] Langrish, T.A.G. Kockel, T.K. 2001. The assessment of a characteristic drying curve for milk powder for use in computational fluid dynamics modelling. Chemical Engineering Journal 84, 69-74.

[12] Liou, J.K. Bruin, S. 1981. An approximate method for the nonlinear diffusion problem with a power relation between diffusion coefficient and concentration- I. Computation of desorption times.

[13] Kieviet, F. G. 1997 Modelling quality in spray drying. PhD. Thesis, T.U. Eindhoven, The Netherlands

[14] Adhikari, B. Howes, T. Bhandari, B.R. Troung,V. 2003. Surface Stickiness of drops of carbohydrate and organic acid solutions during convective drying: experiments and modelling. Drying Technology, Vol. 21, 2003, 839-873.

[15] Keey, R.B. and Suzuki, M. 1974. On the characteristic drying curve. Int. J. Heat Mass Transfer. Vol. 17, 1455-1464.

[16] Chen, X.D. Farid, M. Reid, D. Fletcher, A. Pearce,D. Chen, N.X. 1997. A new model for the drying of milk droplets for fast computation purposes. In: Jebson, R.S. Chong, R. Ozilgen, M. (Eds.), Proceedings Chemeca'97, Institution of Professional Engineers New Zealand, Rotorua, New Zealand, 29 September-1Octuber, vol. 1, pp. 825-830.

[17] Seydel, P. Sengespeick, A. Blomer, J. Bertling, J. 2004. Experiment and mathematical modelling of solid formation at spray drying. Chemical Engineering Technology, 27, (5), 505-510.
[18] Chen, X.D. Xie, G.Z. 1997. Fingerprints of the drying behaviour of particulate or thin layer food materials established using a reaction engineering model. Trans. IChemE. C. ;75:213-222.

[19] Lin, S.X. Chen, X.D. 2005. Air drying of milk droplet under constant and time-dependent conditions. AIChE Journal 2005, 51 (6), 1790-1799.

[20] Seydel, P. Blomer, J. Bertling, J. 2004. Experiment and mathematical modelling of solid formation at spray drying. Chemical Engineering and Technology, 27 (5), 505-510.
[21] Handscomb, C.S. Kraft, M. Bayly, A.E. 2009. A new model for the drying of droplets containing suspended solids after shell formation. Chem. Eng. Science 2009, 64 (2), 228-246.

[22] Woo, M.W. Daud, M.R.W., Mujumdar, A.S. Talib, M.Z.M. Hua, W.Z. Tasirin, S.T. 2008 Comparative study of droplet drying models for CFD modelling. Chemical Engineering Research and Design, 86, 1038-1048.
[23] Keey, R.B. 1992. Drying of Loose and Particulate Materials; Hemisphere Publishing, New York, 1992.

[24] Mezhericher, M. Levy, A. Borde, I. 2010 Theoretical models of Single Droplet Drying Kinetics: A Review. Drying Technology, 28:2, 278-293.

[25] Lin, S.X.Q. Chen, X.D. 2002. Improving the Glass-Filament Method for Accurate Measurement of Drying Kinetics of Liquid Droplets. Chem. Eng. Research and Design, 80, 4, 401-410.

[26] Patel, K. C. Chen, X.D. Lin, S.X.Q. Adhikari, B. 2009. A composite reaction engineering approach to drying of aqueous droplets containing sucrose, maltodextrin (DE6) and their mixture. AIChE Journal, 55(1), 217-231.

[27] Chen, X.D. Putranto, A..2013. Modeling Drying Processes: A reaction Engineering Approach, Cambridge: Cambridge University Press. ISBN: 9781107012103.

[28] Ranz, W.E. Marshall, W.R. 1952a. Evaporation from Drops Part 1. Chemical Engineering Progress, 48 (3), 141-146.

[29] Ranz, W.E. Marshall, W.R. 1952b. Evaporation from Drops Part 2. Chemical Engineering Progress, 48 (4), 173-180.

[30] Abramzon, B. and Sirignano, W.A. 1989. Droplet vaporization model for spray combustion calculations. Int. J. Heat Mass Transfer. 32: 1605-1618.

[31] Nesic, S. Vodnik, J. 1991. Kinetics of droplet evaporation. Chemical Engineering Science, Vol. 46, No. 2, pp. 527-537.

[32] Farid, M. M. 2003. A new approach to modelling of single droplet drying. Chem. Eng. Science. 58, 2985-2993.

[33] Darvan, A. Sommerfeld, M. 2014. Modeling and numerical analysis of the drying stages during single droplet drying. 19th International drying Symposium, IDS 2014.

[34] Sano, Y. Keey, R.B. 1982. The drying of a spherical particle containing colloidal material into a hollow sphere. Chem. Eng. Science, 37 (6), 881-889.

[35] Mezhericher, M. Levy, A. Borde, I. 2008. Modelling of particle breakage during drying. Chemical Engineering and Processing 47, 1404-1411.

[36] Hecht, J.P. King, C.J. 2000. Spray drying: Influence of developing drop morphology on drying rates and retention of volatile substances. 2: Modeling. Ind. Eng. Chem. Res., 2000, 39, 1766-1774.

[37] Tran, T. T.H. Jaskulski, M. Avila-Acevedo, J.G. Tsotsas,E. 2017. Model parameters for single-droplet drying of skim milk and its constituents at moderate and elevated temperatures. Drying Technology, 2017,35, 444-464.

[38] Dannenberg, F. Kessler, H. 1988. Reaction Kinetics of the Denaturation of Whey Proteins in Milk. Journal of Food Science. Vol. 53, No. 1, 258-263.

[39] Jaskulski,M. Wawrzyniak, P. Zbicinski, I. 2016. CFD prediction of powder particle size distribution in the industrial scale spray drying process. 20th International Drying Symposium (IDS 2016) Gifu, Japan.

[40] Ali, M. Mahmud, T. Heggs, P.J. Ghadiri, M. Bayly, A.E. Ahmadian, H. Martin de Juan, L. 2017. CFD modelling of a pilot-scale counter-current spray drying tower for the manufacture of detergent powder. Drying Technology, Vol. 35, No. 3, 281-299.

[41] Tsotsas, E. Mujumdar, A.S. 2009. Modern Drying Techonology. Volume 2: Experimental Techniques. Wiley-VCH Verlag GmbH & Co. ISBN: 978-3-527-31557-4.

[42] Mondragon, R. Hernandez, L. Enrique Julia, J. Jarque, J.C. Chiva, S. Zaitone, B. Tropea, C. 2011. Study of the drying behaviour of high load multiphase droplets in an acoustic levitator at high temperature conditions. Chem. Eng. Science 66, 2734-2744.

[43] Ebrahim, W.A.M. (2019) Single droplet drying at high temperatures. PhD thesis, University of Leeds.

[44] Yarin, A.L. Brenn, G. Kastner, O. Tropea, C. 2002. Drying of acoustically levitated droplets of liquid-solid suspensions: Evaporation and crust formation. Phy. Fluids 14, 2289; doi: 10.1063/1.1483308. Doi: 10.1063/1.1483308.

[45] Griffith, J.D. Bayly, A.E. Johns, M.L. 2008. Magnetic resonance studies of detergent drop drying. Chem. Eng. Science 63, 3449-3456.

[46] Yarin, A.L. Brenn, B. Kastner, O. Rensink, D. Tropea, C. 1999. Evaporation of acoustically levitated droplets. J. Fluid Mech. 399, 151-204.

[47] Incropera, F.P. Dewitt, D.P. Bergman, T.L. 2006. Fundamentals of Heat and Mass Transfer. 6th Edition. ISBN: 978-0-471-45728-2.

[48] Minoshima, H. Matsushima, K. Liang, H. Shinohara, K. 2002. Estimation of diameter of granule pepared by spray drying of slurry with fast and easy evaporation. J. Chem. Eng. Jpn. 35, 880-885.

[49] Koniorczyk, M. Konca, P. 2013 Experimental and numerical investigation of sodium sulphate crystallization in porous materials. Heat and mass transfer, 49:437-449.

[50] Kastner, O. Brenn, G. Rensink, D. Tropea,C. 2000. Mass transfer from multiphase droplets during drying in a tube levitator. In: Proceedings of the 8th International Conference on Liquid Atomization and Spray Systems, Pasadena.

[51] Jubaer, H. Afshar, S. Xiao, J. Chen, X.D., Selomulya, C. Woo, M.W. 2017. On the importance of droplet shrinkage in CFD modelling of Spray Drying. Drying Technology, 2017, 36, 1785-1801.

[52] Wulsten, E. Lee, G. 2008. Surface temperature of acoustically levitated water microdroplets measured using infra-red thermography. Chem. Eng. Science 63, 5420-5424.

CHAPTER 2.1. GEOMETRY, MESHING AND NUMERICAL ERRORS ANALYSIS IN SPRAY DRYING SIMULATIONS.

ABSTRACT

In this chapter we develop a screening methodology for the error analysis of meshes in swirl flow systems. In CFD modeling, meshing is one of the most time-consuming tasks due to the large number of prototypes that must be evaluated in industry. The development of a procedure may simplify future works within a company. This procedure is based on the evaluation of numerical errors involved in the simulation such as iteration and discretization errors. Apart from mesh evaluation, the solver algorithms are also evaluated since each of them discretizes the equations differently. Finally, using the error analysis procedure developed, a comparison between steady-state and transient simulations is provided in order to evaluate if the precessing vortex core, characteristic of swirl flow patterns, may be significant enough for opposing the reduction of the simulation to a steady-state approach. As result from this study, it is obtained that transient simulations show a convergent GCI curve for all the range of cell sizes studied, which ensures its feasibility for reproducing the physics of the system. However, steady-state simulations do not show that convergence for the GCI index in the current system. Therefore, while steady-state simulations can provide a quick screening of the solutions, they cannot always be trusted. Its use is limited for simulating the airflow patterns of the system with a maximum accuracy of 65 mm.

2.1.1 INTRODUCTION

For years, the use of transient simulations has occupied most of the development of units with swirl flow since it allows higher accuracy. However, transient simulations have larger computational cost conflicting with business objectives in terms of speed and "first in the market" principles. The development of CFD models has been historically divided in three stages: pre-processing, processing and post-processing [1]. The preprocessing stage is the one that requires a larger involvement from the user since most of the current software computes the solution and contains large amount of post-processing tools for visualization and data extraction. Preprocessing stage includes geometry definition, grid generation, models definition and the properties and boundary conditions setting [2]. Among them, the most time consuming stages are the definition of the geometry and the grid generation for 3D geometries since at company level the models used to simulate a specific system only need to be developed once, meanwhile the number of geometries and prototypes change every time. In fact, in the case of industrial equipment with swirling flows such as cyclones [3] and spray drying towers [4], the number of publications related to the modelling is much larger than those focusing on the meshing and the error analysis. In most of the cases, meshing is only roughly described, or no mesh error analysis is provided [5-7].

This study focuses on spray drying towers. Spray drying is a common unit operation in industries such as the production of food (milk and coffee powder), pharmaceuticals or detergents [8]. However, literature lacks a detailed analysis of meshing procedures for this kind of units unlike the case of cyclones [9]. For some time, spray dryers were modelled in steady-state. After the work of Langrish et al. [10], who perceived a coherent behavior of the flow patterns inside the dryers generated by the precessing vortex (PV) [11], transient simulations started to be adopted. Other authors continue the comparison between steady-state and transient in co-current spray drying towers [12] [13]. Ullum assumed steady-state since quasi-steady solutions were also obtained in transient [12]. However, Woo et al. remarked again the importance of using transient simulations to reproduce the periodic oscillations of the vortexes. These oscillations of the vortex showed to result in instabilities of the steady-state solution [13]. Thus, aiming at ensuring the stability [14], capturing the dynamic nature of PV [15] and improving accuracy of CFD simulations has led to the use of transient simulations in the last years [7] [14] [16]. However, the comparisons between the work of Woo et al. and Ullum presented stable solutions for large geometries when co-current towers were solved in steady-state [13].

Thus, it is expected that for industrial scale the simulation could be simplified as steady-state. In addition, the computational cost involved in running a transient simulation is typically 3 to 5 times larger than for steady-state, which is key when first to market principles want to be achieved in industry. In this work we continue the work of Woo et al. [14] applying it to industrial scale. The work is not only extended, but also a procedure is proposed to quantify the differences between the steady-state and transient in terms of solution stability. The procedure is based on an error analysis using convergence curves together with the standard deviation of the measurements. Furthermore, the stability of the grids is compared from a numerical discretization point of view, showing the

number of cells where the transient and steady-state solutions have closer solutions and the reduction can be applied to further modelling.

In this chapter we develop an error analysis based method for quick screening procedure of different meshes in order to ensure convergent and stable solutions. It becomes useful to save time in the cell size selection without compromising the accuracy of the solution. The chapter is structured according to the meshing procedure as follows: mesh topology generation, evaluation of mesh quality and error analysis of the mesh. They correspond to an iterative procedure until an adequate mesh for the CFD simulation is obtained. Each of these stages is described in section 2. Furthermore, section 2 is completed with an analysis of the models and solvers used to run the simulation. In section 3, the results of the analysis are explained and a comparison between running the simulation in transient and steady-state. The possibility of reducing the problem to steady-state is provided. Finally, in section 4, the conclusions are presented.

2.1.2 MESHING PROCEDURE

The selection of an appropriate mesh is an iterative procedure where a grid is initially implemented and then its quality is evaluated. If the system passes this check, then an error analysis needs to be performed in order to evaluate each of the error sources and quantify them. Once the error analysis is carried out, the user knows the error that is assumed with the current mesh and how the error is reduced when the mesh is finer. Finally, it is also recommendable to check the y+ at the geometry walls since some of the approaches defined later such as the wall functions are dependent on the y+. In Figure 1, a summary of the mesh selection procedure is presented.

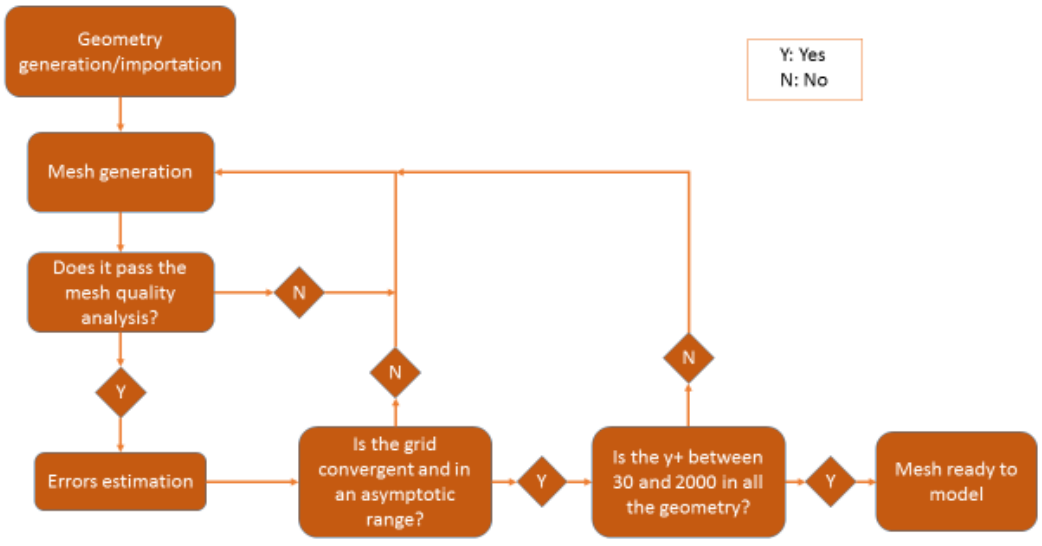

Figure 1. Stages on the development and selection of a mesh.

2.1.2.1 Mesh topology generation

The geometry of the tower is complex, as it is showed in Figure 2, and large at industrial scale. Therefore, the use of structured meshes that provide a high level of accuracy for all the geometry becomes difficult or even impossible task, involving a large time of development because of the cones and elbows of the geometry. A common approach used to generate the mesh in order to implement structured meshes, is the multi-block generation. This procedure has different variants such as medial axis transformations [17] or lines adaption according to the velocity profiles [18]. However, the development with axis transformation is not straightforward since the geometry is in 3D and the axis can interact each other. The second method requires a larger number of simulations to develop a mesh, and also the flow patterns change with the deposition level so the number will be larger [4]. Therefore, according to the flow patterns in the work developed by Ali et al. [19], the geometry can be sliced into the following bodies represented in Figure 2:

- The air inlets: This section is not as relevant as the other ones since no drying of the particles is happening there. The mesh applied here can be hexahedral or tetrahedral. In our case the hexahedral mesh with inflation in the walls was used.
- Bottom cone: Where a tetrahedral mesh is applied because the hexahedral cannot be easily implemented due to the change in the radius.
- Outlet elbow. In this section inflation is also not selected and a tetrahedral mesh is applied because of the irregularity and the product quality is not highly affected since the particles in this region are fines that leave the tower.
- Internal cylinder: With the size of the outlet since a central recirculation zone may exist [4]. In further modelling stages, this region may require larger accuracy to capture the recirculation by mean of dynamic meshes. However, with the actual methodology, it is considered to have the same size than other parts of the geometry.
- External cylinder: It is meshed as a sweepeable body in order make easier the computation of the swirling flow inside locating the cells in the direction of the flow.

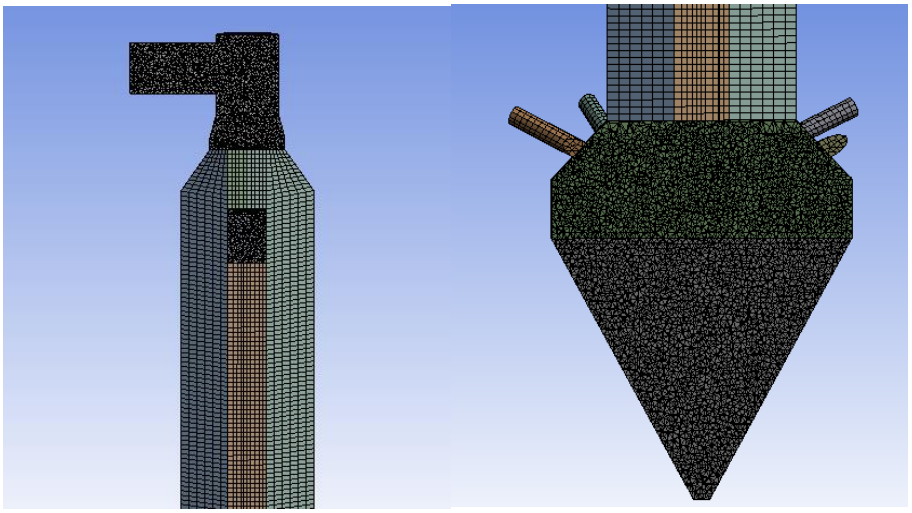

Figure 2. Top (left) and bottom zones of the tower (right).

Furthermore, in order to check how the multi-block mesh (M-1) reduces the discretization error [20], another two meshes are proposed: A full unstructured mesh that involves tetrahedral for the entire the geometry (M-2) and an intermediate mesh (M-3) that uses tetrahedral in the inlet, outlet and bottom cone, meanwhile in the cylinder hexahedral mesh is applied.

The initial mesh size used as reference for the simulation is computed using Eq. (1) [21]. Furthermore, larger sizes have been also defined for the mesh since a y+ lower than 30 is not recommended because the wall functions need to bridge until a region out of the buffer layer. The use of wall functions is required since the geometry is complex and with them use we can introduce the roughness at industrial scale.

$$y = \frac{y^{+}\mu}{U_{\tau}\rho} \tag{1}$$

Where y+ is aimed for a value of 165 as average value between the initial recommendation of a minimum y+ of 30 and a maximum of 300. μ is the dynamic viscosity and ρ the density of the air, both defined on section 2.4.2. U_{τ} is known as friction velocity and it is computed by Eq. (2),

$$U_{\tau} = \sqrt{\frac{\tau_w}{\rho}} \tag{2}$$

Where the wall shear stress, τ_w, can be initially estimated for internal flows using Eq. (3):

$$\tau_w = \frac{1}{2} C_f \rho U_{\infty}^2 \tag{3}$$

Where the velocity is in the free shear flow region, U_{∞} and C_f is computed as follows:

$$C_f = 0.079 Re_d^{-0.25} \tag{4}$$

2.1.2.2 Mesh quality

Once the mesh is developed, its quality must be evaluated. The mesh is usually evaluated according to two parameters, the orthogonal quality and the skewness [22]. Some authors have proposed that the maximum skewness should be smaller than 0.95 and the average is recommended below 0.33 [2]. Meanwhile, the minimum orthogonal quality is recommended to be larger than 0.05 and the average not larger than 0.66 [22]. Furthermore, other parameters such as the aspect ratio are studied in this checking step to provide more confidence on the mesh selection. The aspect ratio is recommended to be lower than 5.

2.1.2.3 Error estimation

The next stage in the development of a reliable mesh is the error estimation. The errors involved in a CFD simulation is a recurrent topic since the simulations are based on numerical methods for solving the Navier-Stokes equation in every finite volume. A classification of these errors was given by Ferziger and Peric [23], who propose the following four groups attending to the source: modelling errors, discretization errors, iteration errors and programming-user errors. In the present paper we focus on each of the three first errors for the simulation of a spray drying swirling tower for industrial scale simulations. The programming-user errors are not considered due to the simulations are performed with a commercial software, ANSYS® Fluent 17.2, and only the mesh conditions are changed for the same models and solvers. Another error also described in literature is the computer round-off error but due to its low significance with the actual computers resources, it is discarded [1].

2.1.2.3.1 Iteration error

The iterative process that solves the model of the system given by the Navier-Stokes equations has to be stopped at some point that is fixed by the user. In our case, in order to quantify the iteration error for each mesh in steady state, the system is simulated as pseudo-convergent, obtaining the residuals associated to the continuity equation straightforward [23]; meanwhile solving in transient simulation, an acceptance error is defined for the convergence of the solution.

2.1.2.3.2 Discretization error

It accounts for the difference between the solution of the numerical method and the analytical solution. It can be evaluated using the Grid Convergence Index (GCI) method described by Roache [24]. Other authors such as Roy [25] proposed a more detailed analysis of the error when the mesh is generated as multi-block and each of the blocks are discretized differently. However, in order to provide consistency for the entire geometry we consider the geometry as a whole, discretizing every block that composes the tower proportionally in every block of the mesh.

The GCI method used in this study helps quantify the grid convergence and indicates how much the solution would change with a further refinement of the grid. It can be computed from two mesh sizes to estimate the convergence and its order. However, three mesh sizes are required to check that the grid is within an asymptotic range of convergence [23]. Therefore, with 3 sizes it is possible to identify if the user is working with convergent and stable

solutions on the range of grid operation. Each level is indicated from finer to coarser with the sub-index 1 to 3. GCI index is defined for the fine following Eq. (5) and for the coarse mesh as Eq. (6):

$$GCI_{fine} = \frac{F_s|\epsilon|}{r^p - 1} \quad (5)$$

$$GCI_{coarse} = \frac{F_s|\epsilon|r^p}{r^p - 1} \quad (6)$$

Where F_s is a safety factor and it will take a value of 3 for the comparison of two grids. ϵ is the relative error measure of the key variable, f, between the coarse, f_2, and fine, f_1, solutions of the grid.

$$\epsilon = \frac{f_2 - f_1}{f_1} \quad (7)$$

The coarse grid has a space of $h_2 f_1$, meanwhile for the fine grid is $h_1 r$, where r is the refinement ratio defined as $r = h_{coarse}/h_{fine}$, that in the case of complex 3D geometries it is defined by Eq. (8) for the comparison of the two finest meshes [24]:

$$r_{12} = \left(\frac{N_1}{N_2}\right)^{1/3} \quad (8)$$

p is the order of the discretization method, being 2 when second order discretization is used for all the geometry [24] and when $r_{12} \neq r_{23}$ it is computed iterating the Eq. (9):

$$\frac{e_{23}}{(r_{23}^p - 1)} = r_{12}^p \left[\frac{e_{12}}{r_{12}^p - 1}\right] \quad (9)$$

Furthermore, the asymptotic range,α, which needs to be near 1, is computed according to Eq. (10) [23]:

$$\alpha = \frac{r_{12} GCI_{fine}^{12}}{GCI_{fine}^{23}} \quad (10)$$

Finally, a ratio of errors, R, is used to monitor the error reduction for finer meshes, Eq. (11):

$$R = \frac{\epsilon_{12}}{\epsilon_{23}} \quad (11)$$

2.1.2.3.3 Modelling errors

Modelling errors are the ones generated when the models selected to solve the system are not the appropriate ones. These modelling errors need experimental results to be identified, which is out of the scope of this chapter. The models used to reproduce the flow and the boundary conditions are based on literature and described in section 2.1.2.5.

The modeling error in the current work can only be given to the turbulence and its interactions with other defined inputs such as the boundary conditions. A relevant aspect in the modelling of turbulent flow, it is the use of logarithmic wall functions that extend the viscous sublayer until a distance given by the mesh size. Different

approaches have been proposed for the selection of a y+ value to extend that layer: Andersson et al. recommends a y+ between 30 and 300 [2], meanwhile Pope recommends a value between 30 and 2000 [26]. The difference in the upper boundary is not as exact due to the logarithmic tend followed. The value used in our evaluation is in agreement with the proposal suggested by the commercial packages such as ANSYS ® Fluent, which is the same provided in [2].

Moreover, in this chapter the error involved when the system is solved as steady-state (internal transient behavior is not modeled) and as transient flow (transient components are modeled) is evaluated. It is remarked again that the modelling errors generated by solving steady-state versus transient are not covered since it is not compared with experimental data. However, this error can also influence on the iteration and discretization errors as shown by Woo et al. [13]. Therefore, the comparison of the discretization errors by GCI between steady-state and transient models is expected to show the differences by solving with each methodology.

2.1.2.4 Flow & model solvers

In order to analyze the errors, the simulation needs to be completed defining the models applied to the flow, the boundary conditions and the solvers selected to simulate the problem. The use of these solvers and boundary conditions is always the same for each of the cases ran in order to avoid the modelling errors. The selections correspond to previous CFD studies to simulate the continuous phase in the tower.

2.1.2.4.1 Turbulence modelling

In order to model the flow, continuity (Eq. 12) and Navier-Stokes (Eq. 13) equations are solved:

$$\frac{\partial \rho}{\partial t} + \nabla \cdot (\rho U) = 0 \tag{12}$$

$$\frac{\rho D U_j}{Dt} = \mu \frac{\partial^2 U_j}{\partial x \partial y} - \frac{\partial P}{\partial x_j} - \rho \frac{\partial \Phi}{\partial x_j} \tag{13}$$

The flow in the dryer was experimentally identified as a turbulent anisotropic swirling flow [20]. Therefore, the Reynolds stresses have to be resolved independently and the turbulence is modelled in CFD with the Reynolds Stress model (RSM). RSM is defined from the Navier-Stokes equation when the Reynolds average theorem is applied obtaining Eq. (14) and, contrary to the k-ε or k-ω models, the turbulent kinetic energy (TKE) does not involve all the Reynolds stresses. The terms that compose Eq. (14) are: Reynolds-stress flux,R_{ij}, mean flow convection, C_{ij}, turbulence production tensor, P_{ij}, transport by diffusion, D_{ij}, turbulence dissipation rate, ε_{ij}, pressure rate of strain tensor, Φ_{ij}, and transport due to rotation, Ω_{ij}.

$$\frac{DR_{ij}}{Dt} = \frac{\partial R_{ij}}{\partial t} + C_{ij} = P_{ij} + D_{ij} - \varepsilon_{ij} + \Phi_{ij} + \Omega_{ij} \tag{14}$$

The diffusion term of the equation is modeled through a gradient-diffusion approximation [27]. The kinetic energy dissipation is modelled in terms of rate of dissipation as presented in Eq. (15), where ε is the dissipation rate and δ_{ij} is the Knoecker's delta. The pressure rate of strain is modelled using the linear decomposition described by

Gibson and Launder [28] (Eq. 16), which decomposes the pressure strain into three terms, the slow pressure-strain term $\Phi_{ij,1}$, the rapid pressure-strain term $\Phi_{ij,2}$ and the wall reflection term, $\Phi_{ij,w}$.

$$\varepsilon_{ij} = \frac{2}{3}\delta_{ij}\varepsilon \tag{15}$$

$$\Phi_{ij} = \Phi_{ij,1} + \Phi_{ij,2} + \Phi_{ij,w} \tag{16}$$

Furthermore, the model requires the following constants to be defined, which are taking as the defaults ones since the modelling error is not the focus of this paper:

$$C_{\mu} = 0.09 \quad C_{\varepsilon 1} = 1.44 \;\; C_{\varepsilon 2} = 1.92 \;\; C_{\varphi 1} = 1.8$$

$$C'_{\varphi 1} = 0.5 \;\; C_{\varphi 2} = 0.6 \;\; C'_{\varphi 2} = 0.3 \;\; \sigma_k = 1 \;\; \sigma_{\varepsilon} = 1.3$$

2.1.2.4.2 Boundary conditions and properties

An additional requirement for every CFD simulation is the definition of the boundary conditions for the system. The boundary conditions of our system are classified into three types: inlets, outlets and walls. Since boundary conditions can be used to model the flow and introduce modelling errors, its use needs to be simple and the interaction with the mesh needs to be avoided. Inlets and outlets are straightforward defined using a common operation mass flow (Re=1.48x10^5) previously used in experiments [4]. Walls are defined with the use of wall functions since the geometry is complex and viscous sub-layer cannot be solved easily keeping a stability for the convergence.

Other aspect required to run the simulation is the specification of the properties of the flow. In order to simplify the simulation, the air is considered at 25 Celsius and the properties at this temperature are set with a density of 1.25 kg/m^3 and a viscosity of 1.78x10^{-5} kg/ms.

2.1.2.4.3 Solvers

The system is solved using the SIMPLE and PISO schemes, which are compared using default values in each of them for the skewness and neighbour corrections. The SIMPLE scheme is based on the use of a pressure correction instead of the real pressure as it is presented in Eq. (17) [29].

$$p^m = p^{m-1} + p' \tag{17}$$

Discretizing the velocity similarly and substituting into the momentum equations, the correlation between the velocity and pressure corrections is obtained as follows, see Eq. (18):

$$u'_{i,P} = \tilde{u}'_{i,P} - \frac{1}{A_P}\left(\frac{\delta p'}{\delta x_i}\right)_P \tag{18}$$

Where the variable $\tilde{u}'_{i,P}$ is defined as Eq. (19):

$$\tilde{u}'_{i,P} = -\frac{\sum_l A_l^{u_i} u'_{i,l}}{A_P^{u_i}} \tag{19}$$

The SIMPLE scheme defined in previous equations has been modified, with the development of SIMPLEC [30] and PISO that address a second correction [31]. In this second correction, a relation between velocity and pressure is followed as presented in Eq. (20).

$$u''_{i,P} = \tilde{u}'_{i,P} - \frac{1}{A_P^{u_i}}\left(\frac{\delta(\rho\tilde{u}'_{i,P})}{\delta x_i}\right) \tag{20}$$

From the introduction of this second correction one can expect that PISO requires more CPU time but the solutions is expected to converge faster. Furthermore, the PISO scheme performs corrections for the skewness and neighbor cells that can modify our results in comparison with SIMPLE [32]. Thus, it is required to check how the different discretizations applied, can modify the results obtained.

To complete the solver definition, the gradient method used to determine the value in each cell is the 'Least Squares Cell Based' since the use of the cell centroid is preferred versus face or cell averaging methods. Furthermore, the discretization method needs to be selected for each of the variables calculation (velocity, k, Reynolds stresses, ε) which have been solved using the QUICK scheme that uses a second order discretization in tetrahedral cells and first order in the hexahedral ones. The algorithm reduces the computational cost versus other second orders combining the second order with central interpolation for hexahedral cells computation. One special case is the pressure discretization method. The method required is PRESTO! because of the swirling flow simulated [32].

2.1.3 RESULTS

The results are divided in four parts. First, the evaluation of the mesh quality parameters for the three mesh types (multi-block, intermediate and tetra) is described. Second, each of the errors are described comparing the three type of meshes for the iteration and discretization error. A special case of this section is the modeling error due to the assumption of steady-state, which has been carried out applying the multi-block mesh. In the third section, the solver algorithms are compared and evaluated. Finally, in the fourth section, the steady-state solver and transient solutions are compared in order to check the improvement that the transient simulation has over the error.

2.1.3.1 Mesh quality

This analysis proves which meshes should not be used based on two parameters, maximum skewness and orthogonal quality, since the geometry coupling of the cells is not adequate.

Meshing quality is evaluated according to the parameters described on section 2.1.2.2 and summarized for each mesh in Table 1. It is possible to see that the requirements described previously for the mesh restrictions are achieved in most of the cases. Only one exception, the finest multi-block mesh of 20 mm does not pass the initial

test in terms of skewness. Even though, for the sake of a comprehensive comparison we also consider this mesh for further stages in the analysis.

Table 1. Mesh quality parameters evaluation.

Mesh type	Mesh size (mm)	N. of elements	Minimun Orth. Quality	Avg. Orth. Quality	Std dev.	Maximun Skewness	Avg. Skewness	Std. Dev.	Aspect ratio
Multi-block	20	14,226,816	0.141	0.915	0.091	0.996	0.157	0.127	20.6
	30	4,444,816	0.170	0.914	0.0924	0.922	0.168	0.131	16.7
	37.5	3,301,578	0.176	0.918	0.0918	0.947	0.169	0.131	13.9
	45	2,298,175	0.141	0.898	0.0945	0.920	0.185	0.132	19.7
	55	1,488,820	0.159	0.922	0.0929	0.913	0.181	0.136	14.1
	65	1,088,983	0.093	0.923	0.0942	0.912	0.188	0.139	15.4
	75	823,185	0.150	0.924	0.0976	0.895	0.194	0.146	17.3
Interm.	40	1,151,009	0.225	0.895	0.0959	0.841	0.191	0.128	18.8
	50	692,815	0.200	0.893	0.0098	0.849	0.195	0.129	20.9
	60	452,512	0.188	0.891	0.102	0.850	0.202	0.131	18.8
Full tetra	50	2,194,474	0.182	0.864	0.083	0.897	0.259	0.138	24.3
	60	1,393,973	0.219	0.842	0.088	0.897	0.264	0.138	20.9
	70	933,692	0.199	0.862	0.083	0.893	0.218	0.117	18.9

2.1.3.2 Error analysis

The errors described previously in section 2.1.2 are presented for each of the meshes. Furthermore, the case of the multiblock mesh (M-1) has also been used to make a comparison between steady state and transient solutions.

2.1.3.2.1 Iteration error

The iteration error can be extracted straightforward from Fluent, where the residuals of the continuity equation are the ones used to evaluate each of the meshes in pseudo-convergent solution. A summary of the iteration error results is provided in Table 2. The average iteration error per mesh size is computed from 15 iteration samples. Moreover, for each mesh type the average iteration error for a mesh between a size of 35mm and 75 mm is computed. It is possible to see that the use of multiblock mesh reduces the iteration error as it is described in [20].

Table 2. Iteration error for different meshes.

Mesh type	Mesh size (mm)	Average Iteration error
Multi-block (M-1)	20	0.182
	30	0.205
	37.5	0.205
	45	0.195
	54	0.178
	65	0.205
	75	0.0793
	Average 35-75	0.172
Intermediate (M-3)	40	0.264
	50	0.108
	60	0.256
	Average	0.209
Full tetra (M-2)	50	0.233
	60	0.188
	70	0.203
	Average	0.208

As it has been described in section 2.1.2.1, the mesh structure has larger influence on the iteration error. The multi-block mesh shows lower iteration error than the tetra, helping that the solution converges and reducing the possibilities of divergence when the particles will be introduced in further stages of the simulation.

2.1.3.2.2 Discretization error

The discretization error is computed according to the GCI method explained in section 2.1.2.3.2. The physical variable used to quantify the discretization error with the GCI is the velocity. The velocity profiles have been extracted at 8 heights of the tower and 2 normal diameters (4 radius) are used in each height extracting 100 points per diameter. For the multi-block mesh, the mesh with a size of 30 mm is used as the finest one and it is compared with the ones of 45 mm and 75 mm for general range analysis and in small ranges to analyze the change in the rate of convergence. Meanwhile, for the intermediate and tetra the sizes described on previous tables are used. In all the cases, one can appreciate that the relative error of the finest mesh is lower than the coarse one and consequently the convergence ratio, R, is always lower than 1, ensuring the convergence of the mesh in the range of sizes studied, see Table 3.

Table 3. Discretization error analysis for each of the meshes in steady-state.

Mesh type	Mesh sizes compared (mm)	ε_{12}	ε_{23}	GCI_{12}	GCI_{23}	α	R
Multi-block (M-1)	30-45-65	0.091	0.126	0.465	0.561	1.033	0.722
	30-45-75	0.091	0.232	0.230	0.333	1.033	0.393
	30-45-54	0.091	0.150	0.050	0.159	1.033	0.607
Interm. (M-3)	40-50-60	0.075	0.089	0.287	0.416	0.914	0.841
Full tetra (M-2)	50-60-70	0.074	0.097	0.151	0.232	1.056	0.763

Apart from the GCI study, the relative discretization error can be studied within the entire number of sizes. The finest mesh is taken as the exact solution and relative errors are computed for each mesh geometry comparing the errors with it. For the multi-block mesh, the curve obtained is presented in Figure 3. In this convergence curve, the statistical distribution of the velocity near the wall (since it is a swirling flow and most of the momentum is concentrated in the wall region) is also included for the error representation. The values are considered up to a dimensionless radius of 0.6. In these plots, the error bars represent the 95% confident intervals for the discretization error according to a Student's distribution. They are computed from the standard deviation of the 4 radius and averaging for the 8 heights. This deviation covered as distribution has physical explanation due to there are irregularities depending on the degree of mixing in the inlets.

The reader can see in Figure 3 that the system diverges at 55mm and 30mm. However, the confidence intervals in these two points are large enough and convergence exists if the error bars are considered. Thus, the solutions cannot be discarded, but according to this analysis is better to avoid cell sizes smaller than 37.5mm.

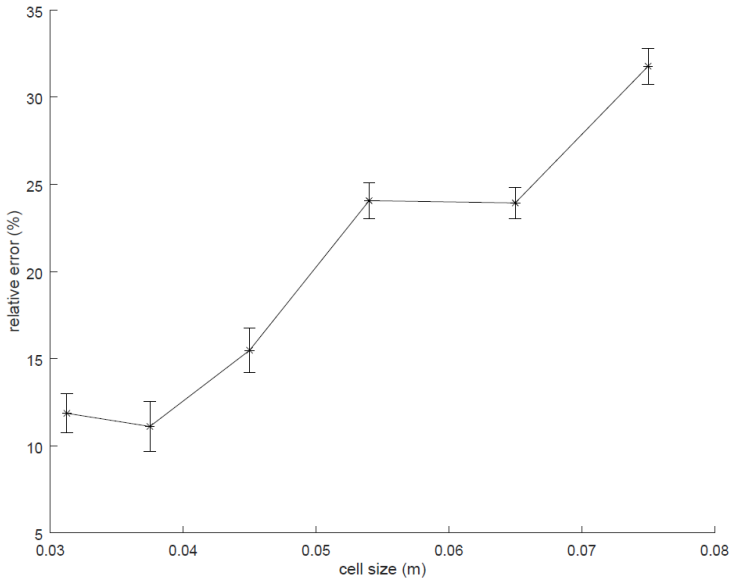

Figure 3. Discretization error refer to the finest mesh of 20mm with PISO solver.

2.1.3.2.3. Effect of solver algorithm

The numerical solver algorithm also affects the solution reported since the discretization is performed in two different ways as it is explained in section 2.1.2.4.3. The two algorithms compared are PISO and SIMPLE. The PISO scheme has an additional term for the discretization so it is expected to be a more accurate solver [31].

As it can be seen in Figure 4, the differences are especially significant for meshes larger than 55 mm where the differences in the discretization start to be significant for the average cell size. It can be seen that the axial velocity in the center and near to the wall, which is a region with large amount of momentum, are different. For the two larger sizes, the loss of tangential momentum from SIMPLE to PISO is translated in an increase of tangential momentum. In terms of iteration error, the two solvers compared do not show large differences, increasing also with the mesh size, as with the PISO does (see Table 4). Meanwhile, the discretization error curve, see Figure 5, shows convergence for all the sizes smaller than 65mm, contrary to the PISO solver, see Figure 3.

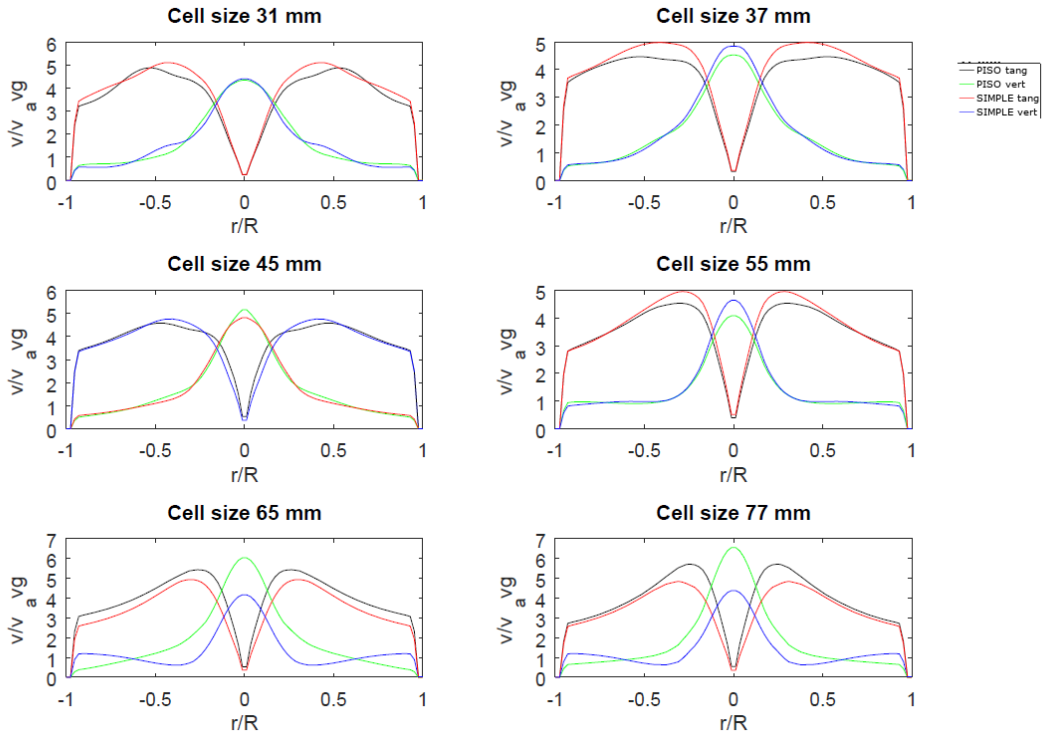

Figure 4. Differences in the velocity profiles for PISO and SIMPLE solver algorithms.

Table 4. Iteration error using SIMPLE algorithm.

Mesh type	Mesh size (mm)	Average Iteration error
Multi-block	20	0.2175
	30	0.1590
	37.5	0.1463
	45	0.1184
	54	0.0589
	65	0.0176
	75	0.0155

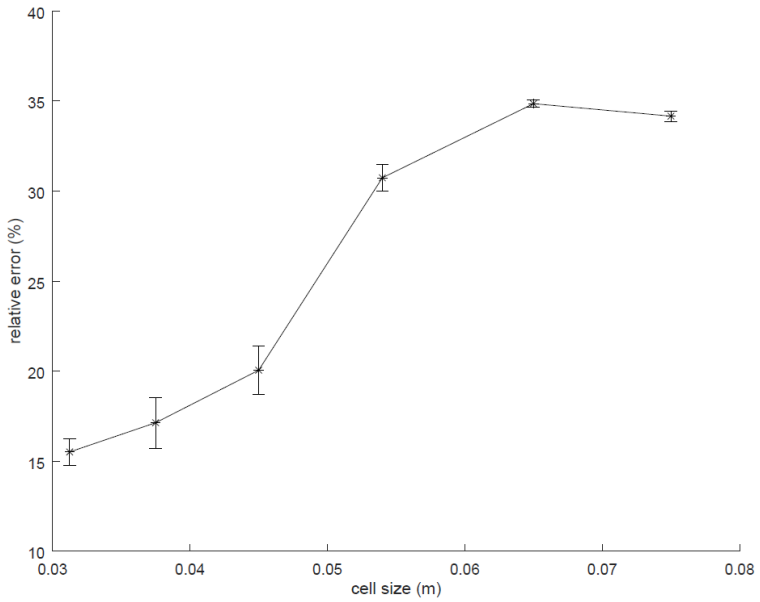

Figure 5. Discretization error referred to the finest mesh of 20mm with SIMPLE solver.

2.1.3.3 y+ Checking

Finally, completing the procedure described in Figure 1, the y+ values extracted from the results are presented in Table 5. As the 20 mm mesh size has two zones in the tower with a y+ lower than 30, the mesh needs to be discarded and the relative error needs to be computed using the 30 mm mesh size as reference. The other meshes show y+ values larger than 30 except the size of 45 mm in the cone. Since the y+ reported is also influenced by the velocity, the conditions of velocity and distance can complement with each other resulting in a very low y+ in only one cell meanwhile the remaining cells of that cone may have higher values than 30. Thus, the size of 45 mm is not discarded.

The convergence curve plotted in Figure 6 shows that the mesh is convergent for all the meshes larger than 30 with PISO solver. In this new convergence curve, two asymptotic regions can be identified for 37mm and 54mm where more stable solutions in terms of mesh size are expected. Meanwhile in the analysis with the SIMPLE solver the mesh is convergent between 30mm until 60mm, reaching more stability when it becomes smaller.

Comparing this Figure 6 with the one shown in Figures 3 and 5, it is possible to note some of the modelling anomalies as in this case the use of y+ distances lower than 30, which generates non convergence in previous curves (Figures 3 and 5). Therefore, in the following stages, the comparison is based on the cell size of 30 mm.

Table 5. y+ for multi-block mesh.

Mesh type	Mesh size (mm)	y+ min cone	y+ max cone	y+ min heap	y+ max heap	y+ min donut	y+ max donut
Multi-block	20	29.8303	104.575	23.8297	155.746	61.558	349.364
	30	31.2909	143.45	37.1687	154.977	83.6915	302.857
	37.5	35.2066	161.606	38.6628	176.134	92.1579	278.593
	45	25.6128	136.156	36.6396	154.102	93.9595	296.019
	54	30.7785	218.802	56.0224	204.639	83.2135	285.664
	65	30.3514	237.969	59.4338	225.834	87.8406	281.769
	75	36.5498	286.195	63.795	255.692	94.1855	277.402

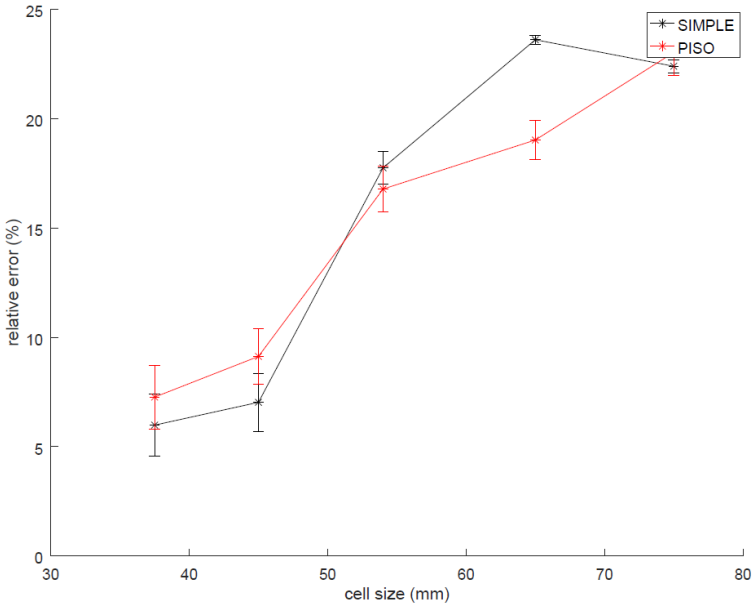

Figure 6. Discretization error for PISO and SIMPLE solvers base on 30mm cell size.

2.1.3.4 Transient vs steady-state solver

The residuals obtained when running steady-state simulations show a coherent oscillation behavior. It suggests that the simulation needs to be solved with an unsteady solver [33]. However, depending on the accuracy desired and the characteristics of the vortex, the same results can be obtained with steady-state and transient solution [34]. Thus, a comparison between the transient and steady-state solutions is required to be performed before using the mesh in further stages of the model and check if the momentum components are equivalent in some of the cases studied.

To run the transient simulations, it is required to get stable solutions. For its fast stability, the problem is initialized from the steady state solution and it is run for 40 s using the PISO scheme. The time-step size is set to 0.1s and each of them end when the residuals get under $1x10^{-3}$.

In order to validate that the stability is achieved, the velocity is extracted using points at different locations in the dryer. From Figure 7, it is possible to see that velocity oscillations exist. In addition, these oscillations become stable earlier for the bottom of the tower, at 25 s, than in the top, at 30 s.

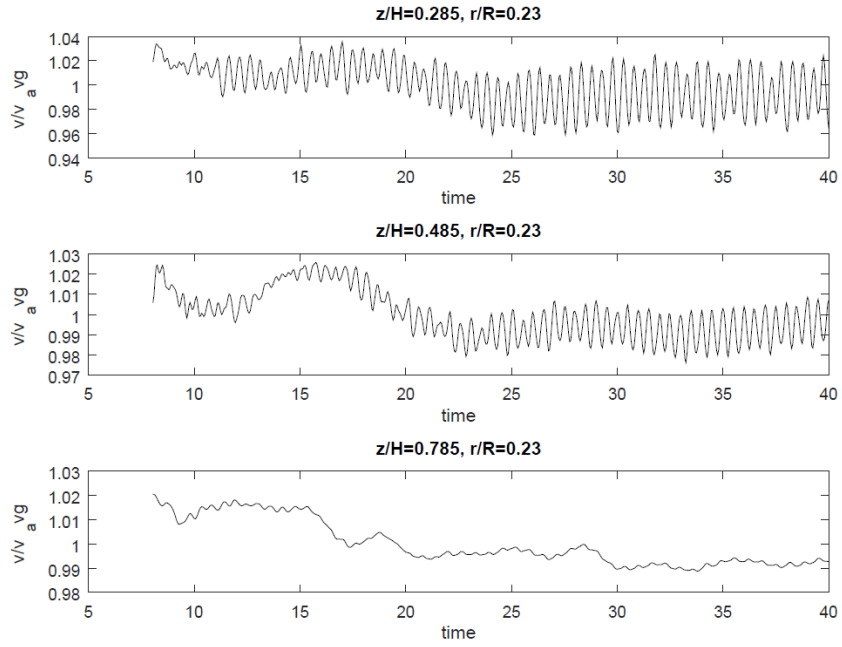

Figure 7. Velocity distribution in time.

The analysis of this velocity evolution, provides a point where the analysis for the transient simulations can be started since the variables reach a steady-state solution and the transient solver can be compared in equal conditions with the steady-state solver. The comparisons are performed with the velocity profiles and the discretization errors that will ensure a convergent solution. 12 velocity profiles are used for the comparison and are extracted every 0.2 s, which roughly suppose 2 profiles in a wave for 6 waves, averaging the error per wave and between waves. The use of 0.2 s is a rough value for the frequency because there is a frequency axial decay in the tower (average frequency of 0.42) that needs to be considered, as it was reviewed by Luca-Negro and O'Doherty [11]. This frequency axial decay distribution is plotted in Figure 8 where the frequency plotted is the area weight average extracted from 7 radial points, assuming the same frequency for all the circumference.

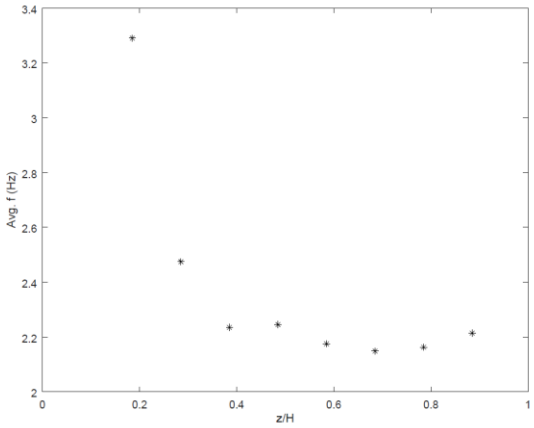

Figure 8. Frequency axial decay in the tower.

In Figure 9 the comparison of the velocity profiles, between steady and transient cases, in two wave periods are reported for tangential and axial velocities. The cases have been run using the PISO algorithm for which it is possible to observe that the solutions reported maintain more constant than in the steady state case with larger sizes. Furthermore, it can be clearly observed that for larger mesh sizes the values reported by the transient and steady-state simulations become more similar. This fact suggests that a threshold exists for a mesh size from which equivalent solutions are obtained. For the system of this work, the mesh size where both solutions are similar is identified for cells with a size of at least 60 mm.

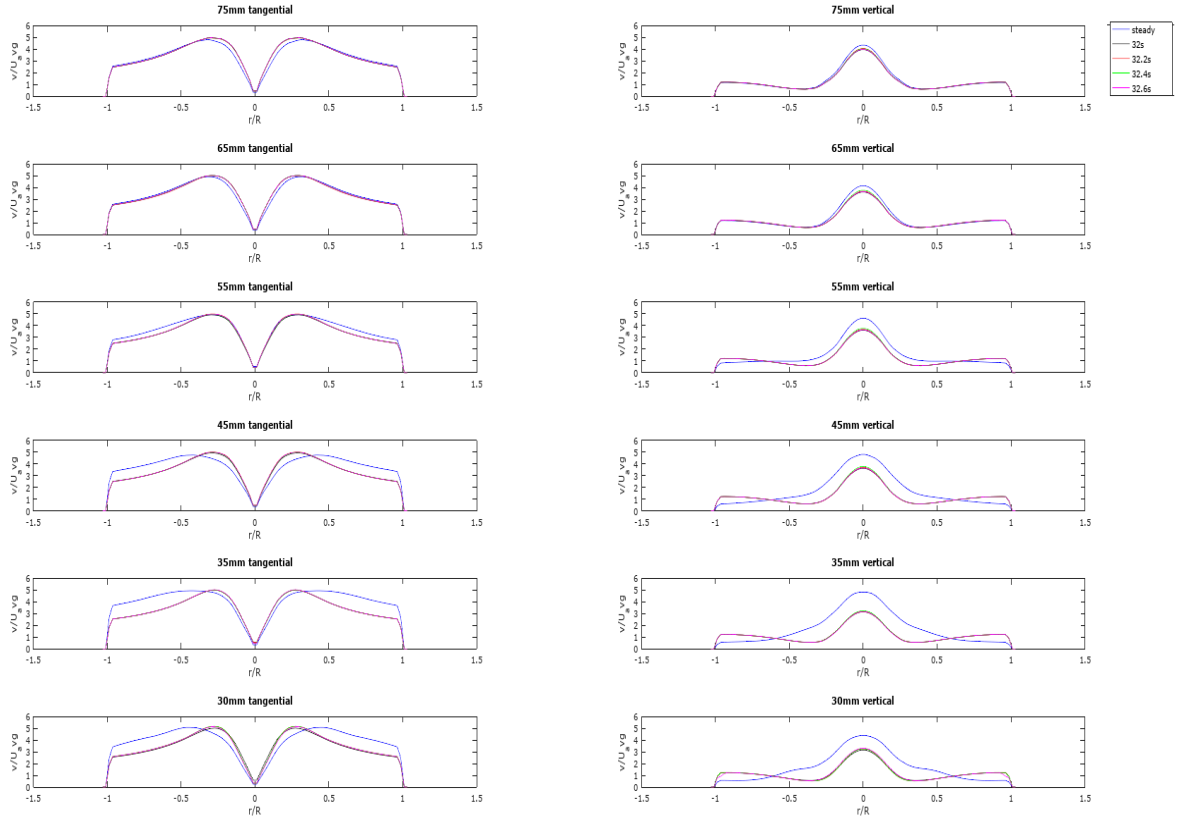

Figure 9. Comparison of velocity profiles for tangential (left) and axial (right) velocities.

For the analysis of the discretization error, the velocity profiles have been also extracted in the same locations as for the steady-state one, being averaged in time for each point extracted. In Figure 10 the discretization is represented for steady-state and transient solutions, based on the minimum size for each case. It is possible to see that the discretization error is smaller in comparison with the error given by the steady-state solver so the solution is less dependent on the mesh size. From this discretization error analysis, the solution shows a divergence interval between 55mm and 65mm where it is not recommendable to operate but where this interval cannot be discarded since the confident interval of the adjacent smaller size is larger than the difference between the two points. Furthermore, the confidence interval for the radial extractions is lower since more points have been extracted and there are more similarity between them.

Thus, if the transient solution is taken as the ideal one, it is possible to appreciate from Figures 9 and 10 that this transient solution remains stable for a wide range of cell sizes. Therefore, the transient solution is adequate for all the cell sizes. However, if the solution wants to be simplified with the use of a steady-state simulation, the minimum cell size that can be achieved is 60 mm. In order to check that for larger mesh sizes, the steady-state solution is more similar to the ideal transient solution, Figure 11 is presented.

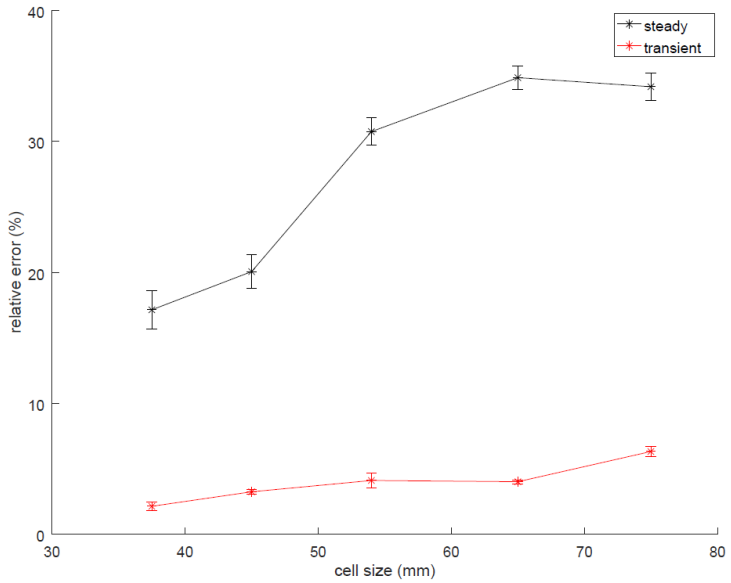

Figure 10. Comparison between discretization errors with steady-state and transient solutions. Steady-state uses a cell size of 37.5 mm run in steady-state as reference and transient uses the results of the transient simulation with a cell size of 37.5 mm as reference.

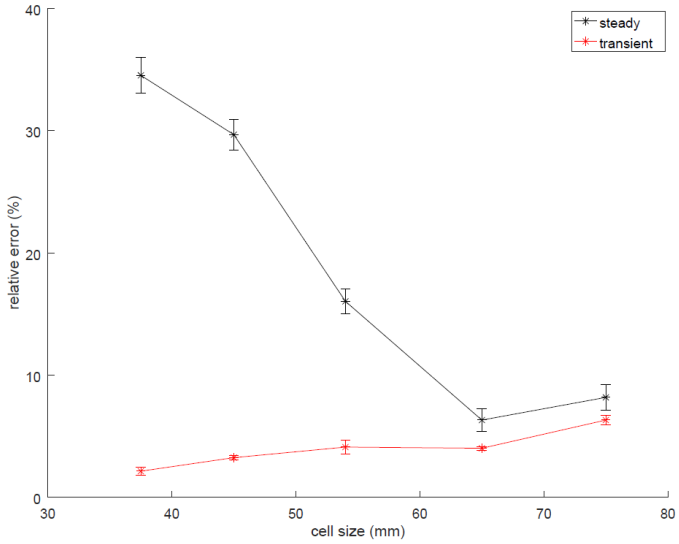

Figure 11. Comparison of the discretization errors taken the finest transient solution as reference.

In Figure 11 the discretization errors are referred to the finest transient solution for the steady-state and transient simulations. The discretization error becomes larger when the mesh is smaller. Therefore, taking into account that the transient is the right one since it reproduces the oscillating behavior of the vortex [10, 13], the steady-state solution must be only used for mesh sizes larger than 60mm.

The differences between steady-state and transient observed in Figure 11 are hypothesized to be generated by the turbulence filtered for each of the cell sizes. The energy cascade is divided in two ranges: the universal equilibrium range and the energy-containing range. In transient simulations the isotropic eddies of the equilibrium are resolved but in steady-state their energy and dissipation are included in the TKE, k, and dissipation terms, ε, respectively [26]. The filter for the eddies to be included inside of the TKE depend on the cell size. Only eddies smaller than the cell size are included in the TKE. Thus, if the cell size is smaller than a certain value that shows large quantity of eddies, the TKE resolved in steady-state drops and the velocity is modified. This behavior is presented from Figure 12 to 14, where it can be seen that for a mesh size of 55mm the transient solution keeps constant values, meanwhile the steady-state is lower for smaller meshes.

Figures 12 to 14, present the TKE reported by steady-state and two TKE for the transient solution. $transient_g$ is the TKE contained in the eddies of the equilibrium range, meanwhile $transient_t$ is the TKE contained in the equilibrium range plus the TKE generated by the eddies resolved. It can be seen than in Figure 12 the contribution of the resolved eddies is larger than in Figure 14, which shows that large percentage of eddies are solved and the oscillations increases in the solution provided for the velocity.

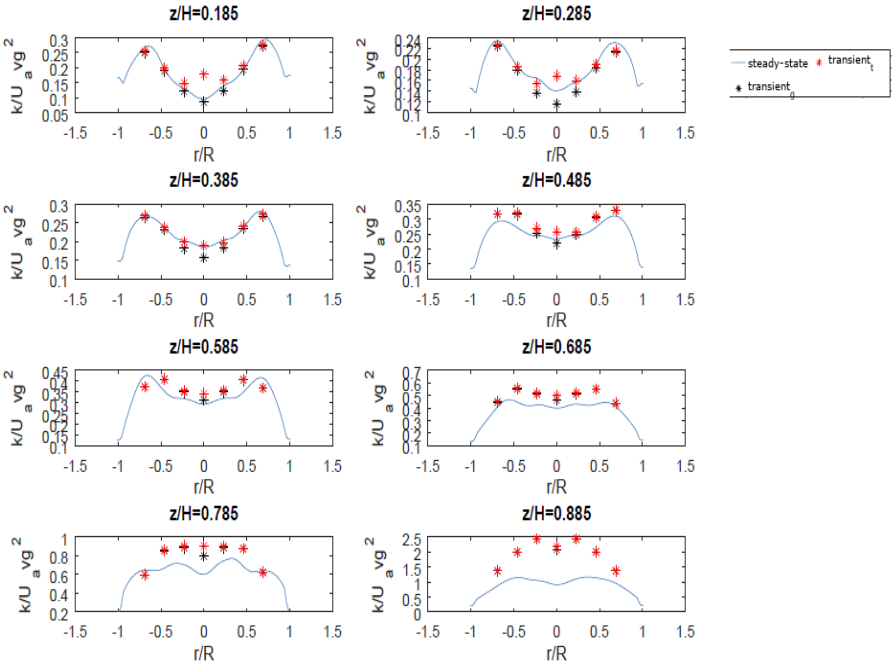

Figure 12. Comparison of TKE between steady-state, transient considering only small isotropic eddies and transient considering small and large eddies contributions for a mesh size of 55mm.

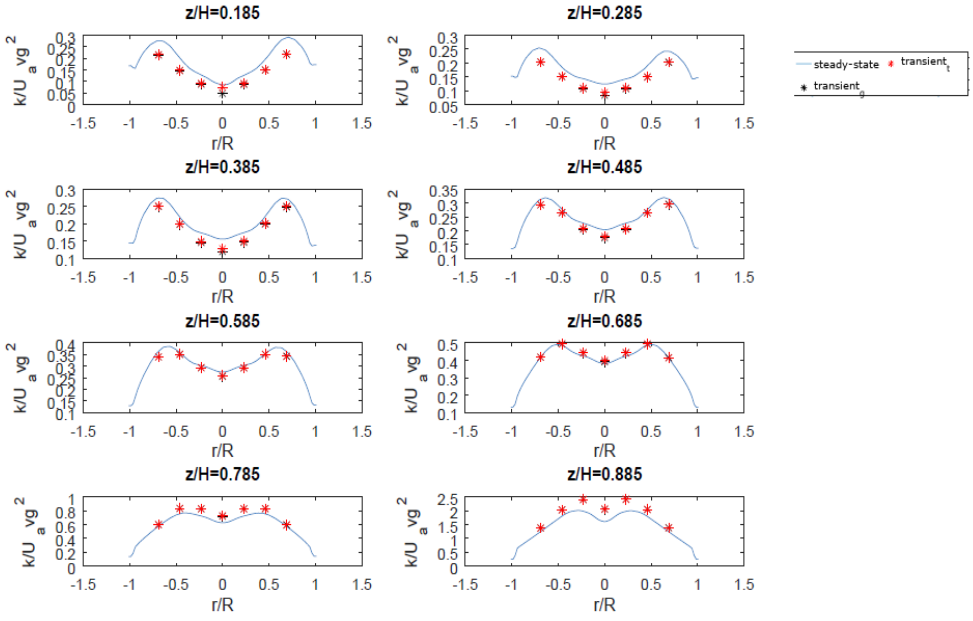

Figure 13. Comparison of TKE between steady-state, transient considering only small isotropic eddies and transient considering small and large eddies contributions for a mesh size of 65mm.

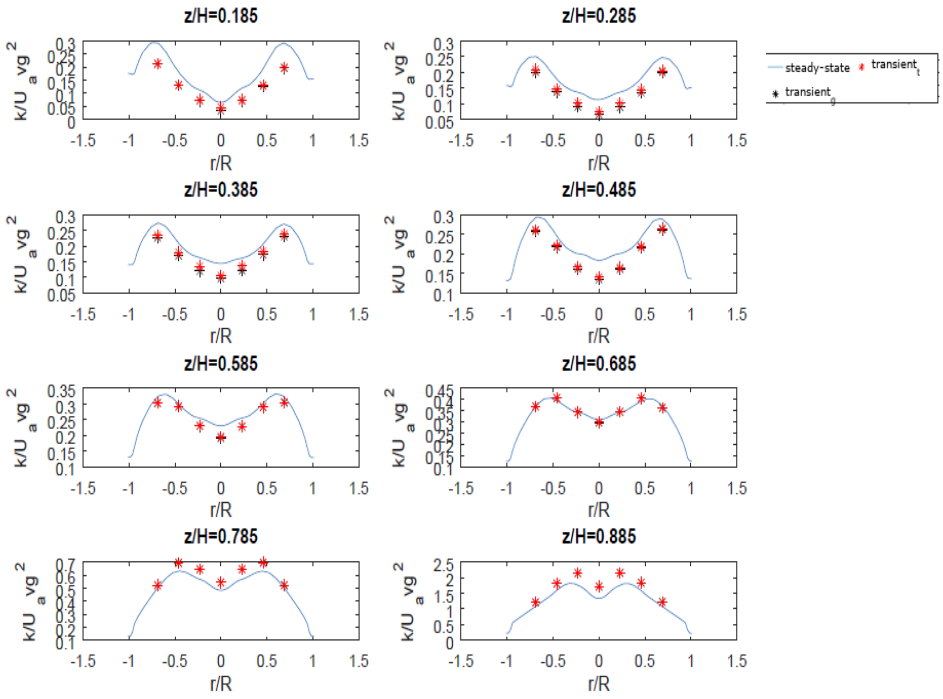

Figure 14. Comparison of TKE between steady-state, transient considering only small isotropic eddies and transient considering small and large eddies contributions for a mesh size of 75mm.

2.1.4 CONCLUSIONS

In this chapter a procedure for the selection of the mesh size for complex geometries with swirling flow is presented. The procedure is based on the error analysis of various simulations changing only the mesh size once a type of mesh has been generated. The convergence curve shows the ranges of sizes that can be applied for the final simulation and/or the modelling. One of the values of the procedure is its easily automation, reducing the amount of time that the user needs to be paying attention to the simulation and receiving a report of the convergence curve, which is an extension of the GCI method widely applied in the area of CFD.

The use of GCI curves to analyze the discretization error allows us to predict the ranges of sizes that we can use for future modelling. From all the comparisons performed for the discretization error, it is observed that the use of PISO or SIMPLE discretization method only shown differences for sizes larger than 55mm. Thus, it is required to define the discretization method applied in further stages of the modelling since it can generate different solutions when the system is solved in steady-state. Meanwhile, comparing the steady-state and transient solutions large differences are appreciated for small sizes. It is possible to see that the solution provided for larger cell sizes with steady state is similar to the transient. Thus, it is possible to find a minimum cell size from which the steady-state and transient solutions are equivalent. This approach allows reducing the CPU time between 3 and 5 times providing fast prediction and being first in the market when new prototypes are developed.

However, in this work, the approach of using a steady-state solution instead of a transient is only applicable to cells of 65mm. In that case, the problem can be reduced to steady-state since the solutions provided are similar than in the transient case. The use of the cell size needs to be also completed in order stages of the simulation that depend on the application (material to be processed and operation conditions) since restrictions appear due to a minimum cell size to predict representatives tracks with Discrete Phase Model [35]or maximum cell size that predicts the eddies that affect the particles [36]. For the analysis of our case, selecting as threshold the mean particle size recovered as fines in the elutriated particles and the maximum air to be introduced, the value of minimum size required to capture the eddies that affects the particles is 140mm, which is still higher than the threshold obtained for steady-state solutions to be equivalent to transient solutions.

Therefore, if one needs to determine the transient behavior such as the processing oscillations or capture very accurate phenomena (with cell sizes below 65mm), the transient simulation has to be used. However, if the phenomena desired to be capture does not require the use of cells below 65mm, steady-state simulations can be used. For business needs, where time is first, the steady-state solution is enough since it allows to predict all the final product with lower involvement of computational cost.

REFERENCES

[1] Anderson, J.D. (1995) Computational Fluid Dynamics. The Basics with Applications. McGraw-Hill. ISBN: 0-07-001685-2.

[2] Andersson, B. Andersson R. Hakansson, L. Sudiyo, R. van Wachem, B. (2012) Computational Fluid Dynamics for Engineers. Cambridge, United Kingdom. ISBN: 978-1-107-01895-2.

[3] Hoffmann, A.C. Stein, L.E. (2008) Gas Cyclones and Swirl Tubes: Principles, Design and Operation. 2nd Edition Springer Berlin Heidelberg New York. ISBN: 978-3-540-74694-2.

[4] Francia, V. Martin, L. Bayly, A.E. Simmons, M.J.H. (2015) Influence of Wall friction on flow regimes and scale-up of counter-current swirl spray dryers. Chemical Engineering Science 134 (2015) 399-413.

[5] Ali, M. (2017) Residence time distribution of glass ballotini in isothermal swirling flows in a counter-current spray drying tower. Powder Technology 305 (2017) 809-815.

[6] Langrish,T.A.G. (2009) Multi-scale mathematical modelling of spray dryers. Journal of Food Engineering 93 (2009) 218-228.

[7] Wawrzyniak,P. Podyma,M. Zbicinski,I. Bartezak,Z. Rabaeva,J. (2012) Modeling of air flow in an industrial countercurrent spray-drying tower. Drying Technology, 30: 217-224, 2012.

[8] Masters, K. (1972) Spray Drying: An introduction to Principles, Operational Practice and Applications. London: Leonard Hill Books.

[9] Elsayed, K. Lacor,C. (2011) Numerical modeling of the flow field and performance in cyclones of different cone-tip diameters. Comp. & Fluids 51 (2011) 48-59.

[10] Langrish, T.A.G. Oakley, D.E. Keey, R.B. BAhu, R.E. Hutchinson, C.A. (1993). Time-dependent flow patterns in spray dryers. Transactions of the Institution of Chemical Engineers 71 (A), 355-360.

[11] Lucca-Negro, O. O'Doherty,T. (2001) Vortex breakdown: a review. Progress in Energy and Combustion Science 27 (2001) 431-481.

[12] Ullum, T. (2006) Simulation of a spray dryer with rotary atomizer: The appearance of vortex breakdown. Proceedings of the 15th International Drying Symposium, 2006, 20-23th August, Budapest, Hungary, 251-257.

[13] Woo, M.W. Daud, W.R.W. Mujumdar, A.S. Wu, Z. Talib, M.Z.M. Tasirin,S.M. (2009) Non-swirling steady and transient flow simulations in short-form spray dryers. Chemical product and process modeling: Vol.4: Iss.1,Article20.

[14] Woo, M. W. (2017) Computational Fluid Dynamics simulation of Spray Dryers. An Engineer's Guide. CRC Press. Taylor & Francis Group. ISBN: 978-1-4987-2464-7.

[15] Guo, B. Langrish, T.A.G. Fletcher,D.F. Simulation of gas flow instability in a spray dryer. Trans IChemE, 2003, Vol. 81 (A) 631-638.

[16] Langrish, T.A.G. (2009) Multi-scale mathematical modelling of spray dryers. Journal of Food Engineering 93 (2009) 218-228.

[17] Tam, T.K. H. and Armstrong, C. G. (1991) 2D Finite Element Mesh Generation by Medial Axis Subdivision. Advances in Engineering Software 13: 313-324.

[18] Ali, Z. Dhanasekaran, C. Tucker, P.G. Watson,R. Shahpar, S. (2017) Optimal multi-block mesh generation for CFD. Internantional Journal of Computational Fluid Dynamics, 2017. DOI: 10.1080/10618562.2017.1339351

[19] Ali,M. (2014). Numerical Modelling of a Counter-Current Spray Drying Tower. PhD Thesis. The University of Leeds.

[20] Armstrong, C.G. Fogg,H.J. Tierney, C.M. Robinson,T. (2015) Common themes in multi-block structured quad/hex mesh generation. Procedia Engineering 00 (2015) 000-000.

[21] https://www.computationalfluiddynamics.com.au/tips-tricks-cfd-estimate-first-cell-height/

[22] Ansys meshing course.

[23] Ferziger, J. H. Peric, M. (2002) Computational Methods for Fluid Dynamics. Springer-Verlag Berlin Heidelberg New York. ISBN: 3-540-42074-6

[24] Roache, P.J. (1994) Perspective: A Method for Uniform Reporting of Grid Refinement Studies. J. Fluids Eng. 116 (3), 405-413 (Sep 01,1994).

[25] Roy, C.J. (2010) Review of Discretization Error Estimators in Scientific Computing AIAA Paper No. 2010-126.

[26] Pope, S.B. (2015) Turbulent Flows. 15th Edition. Cambridge University Press. Cambridge, United Kingdom.

[27] Shir, C.C. A preliminary numerical study of atmospheric turbulent flows in the idealized planetary boundary layer. Journal of Atmospheric Sciences 1973, 30, 1327-1339.

[28] Gibson, M.M. Launder,B.E. (1978) Ground Effects on Pressure Fluctuations in the Atmospheric Boundary Layer. Journal of Fluid Mechanics, 86:491-511, 1978.

[29] Caretto, L.S. Gosman, A.D. Patankar, S.V. Spalding, D.B. (1972) Two calculation procedures for steady, three-dimensional flows with recirculation. Proc. Third Int. Conf. Numer. Methods Fluid Dyn., Paris

[30] van Doormal, J.P. Raithby, G.D. (1984) Enhancements of the SIMPLE method for predicting incompressible fluid flows. Numer. Heat Transfer, 7, 147-163.

[31] Issa, R.I. (1986) Solution of implicitly discretized fluid flow equations by operator-splitting. J. Comput. Phys., 62, 40-65.

[32] Fluent User's guide. Ansys Inc. (2009) Available at: http://www.ansys.com

[33] http://www.symscape.com/steady-state-or-unsteady-cfd-simulation

[34] Bayly, A.E. Jukes, P. Groombridge,M. McNally,C. (2004) Airflow patterns in a counter-current spray drying tower. Simulation and measurement. Proceedings of the 14th International Drying Symposium, 2004.

[35] Crowe, C.T. Schwarzkopf, J.D. Sommerfeld, M. Tsuji,Y. (2012) Multiphase flows with droplets and particles. 2nd Edition. CRC Press. Taylor & Francis Group. ISBN: 978-1-4398-4051-1.

[36] Sommerfeld, M. (2001) Validation of a stochastic Lagrangian modelling approach for inter-particle collision in homogeneous isotropic turbulence. International Journal of Multiphase Flow 27 (2001) 1829-1858.

CHAPTER 2.2. CFD MODELING OF THE AIRFLOW IN INDUSTRIAL COUNTER-CURRENT DRYERS WITH SWIRL FLOW PATTERN.

ABSTRACT

This chapter presents a procedure for the modeling of the airflow in a swirling flow counter-current dryer. The model has been evaluated under steady-state and transient simulations being able to predict the swirl intensity decay within the tower under different Reynolds number and levels of deposition. The model predicts the swirl intensity with an average error of 2.8% and a maximum error of 18%. Apart from the swirl intensity, the model is also validated with the axial, tangential and radial velocity components as well as with the turbulent components under different heights. In this comparison the model shows a good agreement in most of the locations. Only the axial component in the center of the dryer is not predicted with enough accuracy before the top of the tower for the case with clean walls. Similarly, the turbulent components show low accuracy in the center of the tower, specially in the top locations of the tower.

Once the model is validated, it is applied to evaluate the effect of diameter reduction by deposition. As a result, it shows that the main reduction of the swirl intensity is due to the roughness of the wall surface and not to the contraction generated by the deposits. Furthermore, the characteristic parameters of the vortex braking phenomena and the swirl flow decay are evaluated under different Reynolds numbers. In the analysis of the swirl decay parameters, it is obtained that they are only stable when the flow is in fully developed turbulent regime. For Reynolds numbers below 10^5 the parameters show oscillations. The analysis of the vortex breakage phenomena is performed by means of the Rossby number at this location. It is obtained that the vortex breakage behaves similar in fully developed turbulent regime. However, for Reynolds numbers below 10^5 the Rossby number increases promoting the generation of recirculation phenomena in the dryer.

Note: This chapter has been published as manuscript and the supplementary material is available in: https://pubs.acs.org/doi/abs/10.1021/acs.iecr.8b02202

2.2.1 INTRODUCTION

Spray drying is a common unit operation to manufacture a wide range of particulate products such as pharmaceuticals, detergents and food, by which a solution is atomized so drops are dried in contact with hot gas. According to the contact, spray dryers are classified as: co-current, counter-current or mixed flows [1]. Co-current dryers are the most analysed type in CFD modelling, at small [2] and large scale [3]. However, CFD research applied to counter-current towers is not as extensive since the number of industrial relevant cases is lower [4]. In particular, the flow inside the counter-current towers of the present study is characterized by a swirl pattern. This flow pattern presents a more complex fluid dynamics, but it improves the heat and mass transfer efficiency [5]. The benefits provided by swirl flows have also been applied to other operations such as combustion [6], centrifugal separation [7-9], or heat exchangers with lobed pipes [10] or internal swirl generators [11, 12].

Most of the studies on swirl flows have focused on the instabilities associated, such as the presence of periodical structures [13] or the existence of vortex breakdown (VBD) [14]. VBD induces the formation of recirculation regions that depend on the effect of the downstream boundaries, especially, when the flow suffers a contraction [15]. The presence of these instabilities is observed in both swirl co-current [16] and counter-current drying towers [17]. The generation of recirculation regions in large scale counter current towers has been experimentally studied by Francia et al. [5]. They described the influence of the wall deposits on the modification of the swirl intensity and the existence of recirculation according to the criteria proposed by Escudier et al. [15]. Furthermore, Francia et al. [5] also described the structure, momentum, velocity and turbulence components of the vortex at different Reynolds numbers and deposition levels. The structure is composed of two vortexes: one internal dominated by the pull towards the low pressure in the top outlet and an external structure across the dead regions, controlled by interactions with the wall. The friction generated in this external vortex depends on the wall deposit levels and it produces a decay in the swirl intensity from the bottom to the top of the tower [5,17]. The swirl decay changes according to the deposits within a range of 200% [5]. Previous studies in CFD modelling did not consider the friction generated by the deposits at different levels of deposition, resulting in a lack of accuracy in the simulations under certain conditions for particle dispersion and momentum prediction [20]. The addition of roughness given by the deposits requires the entire modelling procedure for spray drying towers [18, 19] to be changed, because the deposits modify the airflow and the same airflow core-model should not always be used for different levels of deposition. Therefore, in this work a new methodology for the modelling of spray drying towers is presented. However, including this phenomenon is not straightforward. A procedure is developed to account it for and include the effect of deposits in the modelling of the flow inside spray drying towers.

The validation of CFD models for spray drying towers has traditionally been carried out based on the study of velocity profiles [21-23]. However, the momentum distribution is not regular along the radius, concentrating the mass and momentum at large radial positions. Fluid momentum governs the particle momentum, concentrating them near the wall. Because of this irregular momentum distribution and its direct influence in further modelling stages, a calibration based on swirl intensity is proposed in this work. In fact, since it accounts for the momentum

distribution, swirl intensity has been recognized as a more robust method to estimate the momentum of the continuous phase in industrial towers [5].

The rest of the paper is structured as follows. In section 2.2.2 a physical description of the flow is provided. In section 2.2.3, the CFD modelling methodology to include the effect of the deposits is described. In section 2.2.4 the results for the model are reported. This section is completed by applying the CFD model to study vortex characteristics. Finally, in section 2.2.5, the conclusions of the work are presented as well as some lines for future work in the area.

2.2.2 PHYSICAL DESCRIPTION OF THE FLOW

The airflow pattern in the tower was identified as an anisotropic swirling flow [5]. In this section we describe the physical laws that model the swirl flow such as the swirl intensity, the VBD and the turbulent components like the Reynolds stresses and anisotropy.

2.2.2.1 Swirl intensity

Swirling flows are commonly characterized by the swirl intensity or swirl number, S, that quantifies their degree or strength. The swirl intensity was defined by Kitoh [25] as the non-dimensional flux of angular momentum, neglecting the contribution of the Reynolds stress and the axial flow development [26]. It is normalized by the axial flux of momentum based on superficial velocity, U_{av}, and tower radius, R, as in eq. (1).

$$S = 2\pi\rho \int_0^R \frac{\bar{U}\,\bar{W}}{\rho\pi\overline{U_{av}^2}R^3} r^2 dr \quad (1)$$

2.2.2.2 Swirl decay

In the case of a flow passing through the tower, the fluid experiences a decay on the swirl intensity due to the wall shear stress (WSS) generated. Kitoh determined the tangential wall shear from the Reynolds averaged angular momentum equation for incompressible, stationary and axially symmetric flow as follows [25]:

$$\tau_{w\theta}(z) = \frac{\rho}{R^2}\int_0^R r^2 \frac{\partial}{\partial z}\left(\bar{U}\bar{W} + \overline{u'w'} - \mu\frac{\partial \bar{W}}{\partial z}\right) dr \quad (2)$$

Where U and W are the time averaged values of the axial and tangential velocity components respectively, $\overline{u'w'}$ are the instantaneous fluctuations, μ is the dynamic viscosity, x and r are the axial and radial positions, $r^2\bar{U}\bar{W}$ is the flux density of angular momentum per unit mass at radial position r.

Turbulent shear stress, $\overline{uw}$, and viscous shear stress, $\mu\frac{\partial \bar{W}}{\partial z}$, can be neglected assuming symmetry, steady state and incompressibility. Thus, for a slow axial development eq. (3) is obtained:

$$\tau_{w\theta} = \frac{\rho}{R^2}\frac{\partial}{\partial z}\int_0^R r^2\,\bar{U}\bar{W}\,dr \quad (3)$$

Eq. (3) can be written in dimensionless form using the following transformations: z⟶ z/D, r⟶r/D, U⟶U/U_{av} and W ⟶ W/U_{av}. Now, the non-dimensional tangential WSS is rearranged as eq. (4):

$$\tau'_{w\theta}(z) = \frac{\tau_{w\theta}(z)}{0.5\rho U_m^2} = \frac{1}{2}\frac{dS}{d\left(\frac{z}{D}\right)} \quad (4)$$

Eq. (4) indicates that the non-dimensional tangential WSS is a linear function of the axial gradient of swirl intensity. Steenbergen and Voskamp [26] concluded that the existence of tangential WSS in the swirl flow causes reduction of the swirl intensity. This explanation justifies the decay predicted by Kitoh [25] in pipes and by Francia et al. [5] in swirling flow towers, which is defined as eq. (5):

$$S = S_{ref} \cdot e^{-\lambda\left(\frac{z-z_{ref}}{D}\right)} \quad (5)$$

Thus, the decay rate is a function of the tangential WSS generated. The total shear stress is composed of two terms: the viscous stress and the Reynolds stress. At the wall, the velocity is zero and consequently all the Reynolds stress components are also zero. Meanwhile in free-shear flow the viscous stress is non-significant compared to the Reynolds stresses. In turbulent flow, the connection of the two regimes is usually modelled by wall functions composed of two regions: A viscous sub-layer near the wall, where the dimensionless velocity and length are equal ($u^+ = y^+$); and a logarithmic region which follows eq. (6) [27]:

$$u^+ = \frac{1}{\kappa}\ln(y^+) - B \quad (6)$$

In eq. (6), u^+ is the non-dimensional velocity (see eq. (8)) defined as the ratio between the velocity parallel to the wall, u_t, and the friction velocity u_τ, see eq. (7). τ_w is the shear stress, κ is the von-Karman constant with a value of 0.41 and y^+ is the dimensionless length from the wall described as eq. (9).

$$u_\tau = \sqrt{\tau_w/\rho} \quad (7)$$

$$u^+ = \frac{u_t}{u_\tau} \quad (8)$$

$$y^+ = \frac{\rho u_\tau y}{\mu} \quad (9)$$

B is an independent parameter that is influenced by the level of roughness and commonly named additive constant [28].

2.2.2.3 Vortex breakdown and recirculation

One of the first observations of this phenomena was reported by Harvey [29], who described it as 'the effect that an imaginary spherical body placed on the axis of the vortex generates over the surrounding fluid that is obligated to flow.

VBD existence is related to recirculation phenomena [15, 30]. This means that the VBD characterization is critical to understand the flow behaviour and the generation of recirculation in the tower. Therefore, validated CFD models

are useful to characterize the flow pattern in the unit at industrial scale. Recirculation can be explained using wave theory for axisymmetric, inviscid and steady vortexes where there is a critical state separating two regimes [31]. The first state consists of a subcritical flow with disturbances that can propagate upstream and downstream. In this state standing waves are supported. The second state is the supercritical flow where only downstream propagation is possible. This supercritical state is the one where breakdown occurs and recirculation is generated in the tower since the waves are compressed in the vortex breaker and are only reflected downstream [32]. Squire [31], Lambourne [33] and Benjamin [34] also quantified the maximum swirl level that still supports standing waves, with a value between 1 and 1.2 for Rankine vortex, or 0.8 for Rossby number (defined as the inverse of Swirl intensity). Swirl flow spray drying towers are comparable to these cases since a Rankine vortex is obtained in the top. A Rankine vortex is generated by the contraction that the flow suffers in the vortex breaker in the top of the tower. Thus, the prediction of swirl intensity at the entrance of the vortex breaker is critical in the prediction of the recirculation.

2.2.2.4 Turbulent components and anisotropy

Internal swirling flows in cylindrical geometries are described by their anisotropy for the Reynolds stresses [35-37]. The Reynolds stresses are defined as follows:

$$\zeta_{ij} = \overline{u_i' u_j'} \tag{10}$$

Where u'_i and u'_j are the turbulence components of the velocity in the directions x and y. From the sum of the normal Reynolds stresses, the turbulence kinetic energy (TKE), k, is defined as in eq. (11):

$$k = \frac{1}{2}\left(\overline{v'^2} + \overline{w'^2} + \overline{u'^2}\right) \tag{11}$$

Meanwhile the anisotropy of the Reynolds stresses is described following eq. (12) where the first term defines the Reynolds stress contribution and the second term is the dissipation of turbulence. $\delta_{ij}$is the Kronecker's delta so that for $i \neq j$, $\delta_{ij} = 0$. However, the normalized anisotropy is provided by Francia et al. [5] following eq. (13), as shown in the results to be comparable with experimental measurements.

$$a_{ij} = < u_i u_j > \ -\frac{2}{3} k \delta_{ij} \tag{12}$$

$$\overline{a_{ij}} = \frac{\overline{u_r u_z}^2 + \overline{u_r u_\theta}^2}{2k} \tag{13}$$

2.2.3. CFD MODELING

Spray dryers are typically modelled using a sequential procedure [19, 38], including air flow models, as the core of the simulation. The air flow is extended with the air-particle momentum interaction, the energy balance with the drying model and finally the deposition model, the particle-particle interaction and particle quality predictions as it is described in Figure 1, A). However, the level of deposits modifies the air flow core model [5]. Therefore, the

modelling methodology needs to include this phenomena as in Figure 1, B). In addition, the omission of deposits results in an under-estimation of the swirl intensity between 40% and 186% [5].

However, in this work we only model the flow pattern under steady-state conditions. This assumption can be used as the air experiments were performed after achieving the dynamic equilibrium in the deposits [5, 39]. In Figure 2, a theoretical plot of the growth of deposits is presented. The deposits increase within a logarithmic trend every time that the tower is ran. As there is no cleaning between runs, during the second cycle of production the deposits grow on the deposits of the first cycle. These depositions overlap each other until the tower is cleaned. Furthermore, since the deposits are not equally distributed, for every cycle of production the deposition becomes more irregular. The red point from Figure 2 indicates the air measurement at the end of cycle 1 when the deposits have reached equilibrium and have dried. Therefore, measuring only the air flow at that moment, we can capture the air behaviour under the deposition conditions achieved in the dynamic equilibrium of the previous cycle 1. This measurement methodology allows to simplify Figure 1, B) to Figure 1, C).

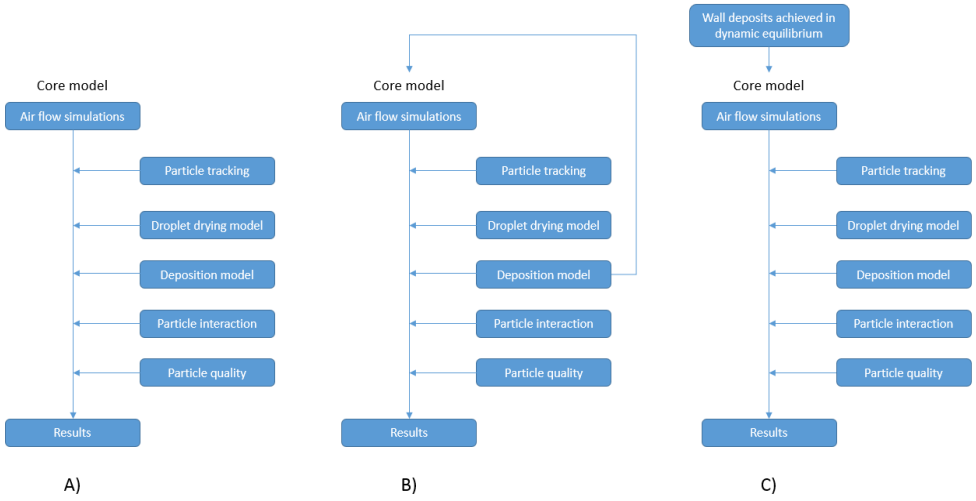

Figure 1. Modeling procedure of Woo et al. [19] (a) compared with the behavior observed (b) and the new procedure presented (c).

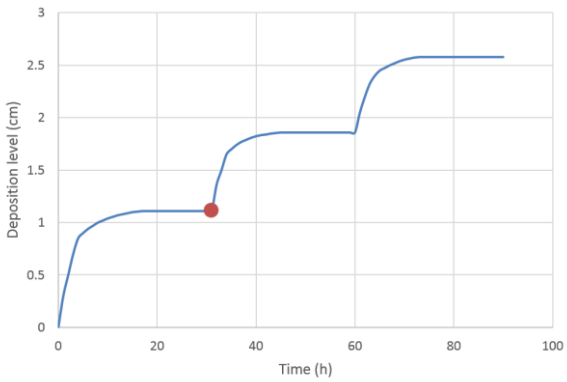

Figure 2. Theoretical example of deposits growth.

In the following paragraphs, the CFD modelling procedure is described. First, the mesh methodology and the geometry are briefly outlined. Second, the transient and steady-state simulations are compared to evaluate if the simulation can be simplified. Third, the CFD model implemented is presented focusing on the turbulent model and the wall boundary conditions. In the fourth section the numerical solvers are discussed. In the fifth section, the modelling procedure is briefly defined.

2.2.3.1 Geometry and meshing

The geometry used in this work has been previously presented by Francia et al. [5, 39]. The mesh used for the simulations is composed of different blocks as presented in the supplementary material, Figure S-1. Hexahedral and sweepable elements have been used for the cylindrical part of the tower and tetrahedral for the irregular parts (bottom cone and outlet).

The y+ of the mesh is initially studied ensuring that it is larger than 30 for all the regions [28]. From this study, a minimum cell size of 40 mm is required. In addition, for the mesh size lower limit it is important to consider that in further stages the mesh will be applied to track particles, which is performed using a Discrete Phase Model (DPM). According to Crowe et al., DPM requires a minimum cell size to predict the track of the particles with enough confidence. For the mean particle size introduced in our simulations a minimum cell size of 45 mm is required [40]. Finally, the Grid Convergence Index (GCI) method [41] and convergence curves are evaluated using a homogeneous cell size.

The results obtained from the GCI method and the convergence curves are presented in the supplementary material (Table S1 and Figures S2 and S3). Applying the GCI method to different cell sizes of the same solution (steady-state), the mesh converges asymptotically (Table S1 and Figure S2). However, the results obtained from transient and steady-state simulations are different at small cell sizes. Thus, the smallest cell size used for the comparison needs to be adequately selected. As precessing vortices are characterized by their transient behaviour, the transient results with the finest cell size must be used for the comparison. Comparing the results with the transient solution using a cell size of 45mm, Figure S3 in the supplementary material is obtained. The steady-state solution is only convergent for meshes larger than 70 mm. Thus, the finest mesh size that ensures convergent results in steady-state is 70 mm.

2.2.3.2 Transient versus steady-state solutions.

Spray dryers have been typically modelled in transient since Langrish et al. perceived a coherent behaviour of the flow patterns generated by the precessing vortex [42].[42] Other authors also provided comparisons between steady-state and transient in co-current spray drying towers [2, 43].[2,43] Woo used transient simulations since the steady-state provided unsteady solutions [2]. However, Ullum [43] and Bayly et al. [44] assumed steady-state since quasi-steady solutions were also obtained as transient. The comparisons between the work of Woo et al. [2] and Ullum [43] presented stable solutions for large geometries when co-current towers were solved in steady state [2]. Thus,

it is expected that for industrial scale towers the simulation could be simplified as steady-state. This simplification is evaluated in this section.

The comparison between transient and steady-state is performed as follows:

- The steady-state simulation is computed for 15,000 iterations extracting 3 samples of velocity profiles in the last 3,000 iterations.
- The transient simulations are computed in two stages starting from a steady-state solution. First, from the steady-state solution, the model is run in transient for 40 s with a time-step of 0.1 s in order to ensure that stability is achieved (as presented in Figure S4 in the supplementary material). The frequency is analysed for the last 5 s of the first stage obtaining a frequency axial decay (average frequency of 2.42 Hz) that needs to be considered, as it was reviewed by Syred [13]. The area weight average of the frequency, extracted from 7 radial points per height, is presented in Figure S5 of the supplementary material.

  In a second stage the simulation is run for 5s extracting the velocity profiles every 0.2 s for the last 0.8 s. It roughly evaluates the profiles contained in 2 waves, according to the previous evaluation of the frequency. This analysis is presented in Figure 3. It can be seen that the steady-state and transient solutions are not equivalent for meshes smaller than 70 mm where a divergence exists. Transient behaviours for cell sizes smaller than 70mm are not captured by the steady-state solution, which is not mesh independent for all the range of sizes studied. However, comparing the steady-state solution with the one of the finest mesh of the transient simulation, only differences up to 7% exist in the prediction of the velocity profiles, see Figure S6 for direct comparison of velocity profiles. Taking into account this small lack of accuracy in the prediction together with the important amount of computational time saved (around 60 times less), the steady-state solution with 70mm is selected.

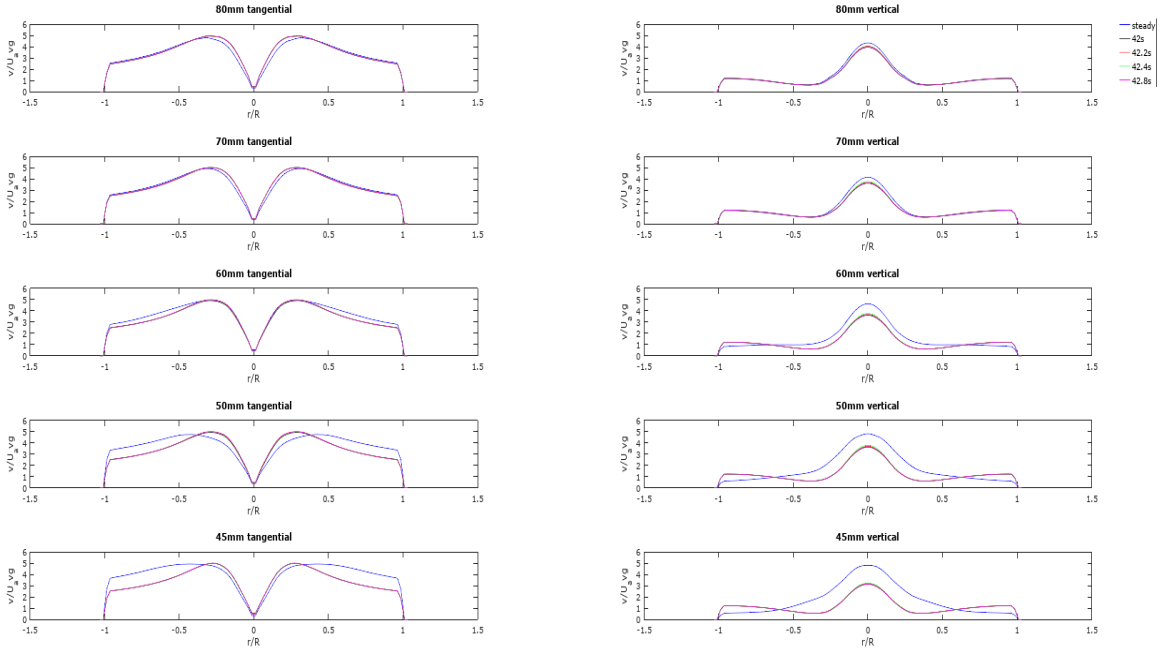

Figure 3. Comparison between transient and steady-state results of tangential and axial velocity profiles at different mesh sizes (45 mm, 50 mm, 60 mm, 70 mm and 80mm).

It is thought that the differences observed between steady-state and transient solutions are generated by the turbulence filtered for each of the cell sizes. The energy cascade for turbulence is divided in two ranges: the universal equilibrium range and the energy-containing range. In transient simulations the isotropic eddies of the equilibrium are resolved but in steady-state their energy and dissipation are included in the TKE, k, and dissipation terms, ε, respectively [28]. The filter for the eddies to be included within the TKE depends on the cell size. Only eddies smaller than the cell size are included in the TKE. Thus, if the cell size is smaller than a certain value that shows large quantity of eddies, the TKE resolved in steady-state drops and the velocity is modified. This behavior is presented in Figures S7 and S8 in the supplementary material, where it can be seen that the transient solution provides similar results for both meshes but the steady-state ones are different.

Figures S7 and S8 present the TKE reported by the steady-state solution and two TKE components for the transient solution. Transient$_g$ is the TKE contained in the eddies of the equilibrium range, meanwhile transient$_t$ is the TKE contained in the equilibrium range plus the TKE generated by the eddies resolved. It can be seen that in Figure S7 (60 mm of cell size) the contribution of the resolved eddies is larger than in Figure S8 (80 mm of cell size), which shows that large percentage of eddies are solved and the oscillations increases in the solution provided for the velocity.

2.2.3.3 Air Modelling

The air flow is modelled using an Eulerian approach where the continuity eq. (14) and Navier-Stokes eq. (15) are solved using the finite volume approach in Ansys ® Fluent 17.2.

$$\frac{\partial \rho}{\partial t} + \nabla \cdot (\rho U) = 0 \tag{14}$$

$$\frac{\rho D U_j}{Dt} = \mu \nabla^2 U - \nabla P + \frac{1}{3}\mu \nabla(\nabla \cdot \mathrm{U}) - \rho g \tag{15}$$

2.2.3.3.1 Turbulent model.

The flow was characterized experimentally as a turbulent anisotropic swirl [5]. Therefore, in the following paragraphs we present some considerations for the selection of the turbulent model.

The approach selected to solve the problem is Reynolds-averaged Navier-Stokes (RANS). It has been previously used in the literature for spray drying modelling [19, 22, 23]. Another alternative, aiming to provide a better accuracy than RANS is the use of large eddy simulations (LES). LES have been recently applied to model only the continuous phase in co-current towers [45], but it has not been used for particulate flows and in swirling counter-current towers, where the flow is highly anisotropic near the wall.

The turbulent model selected to reproduce the anisotropy is the Reynolds Stress Model (RSM). RSM is selected since it includes a deviatoric rate of strain tensor. This model is based on the transport equation for the Reynolds stresses obtained from Navier-Stokes equation, see eq. (16). It considers 7 terms: Reynolds-stress flux (R_{ij}), mean flow convection (C_{ij}), turbulence production tensor (P_{ij}), transport by diffusion (D_{ij}), turbulence dissipation rate (ε_{ij}), pressure rate of strain tensor (Φ_{ij}) and transport due to rotation (Ω_{ij}) [28].

$$\frac{DR_{ij}}{Dt} = \frac{\partial R_{ij}}{\partial t} + C_{ij} = P_{ij} + D_{ij} - \varepsilon_{ij} + \Phi_{ij} + \Omega_{ij} \tag{16}$$

The pressure rate of strain tensor is modeled according to the decomposition described by Gibson and Launder [46], which presents three contributions. The slow pressure-strain term, the rapid pressure-strain term and the wall-reflection term.

The following constants are used to compute the model:

$$C_{\varphi 1} = 1.8 \;\; C_{\varphi 2} = 0.6 \;\; C'_{\varphi 1} = 0.5 \quad C'_{\varphi 2} = 0.3$$

$$C_{\mu} = 0.09 \quad C_{\varepsilon 1} = 1.44 \quad C_{\varepsilon 2} = 1.92 \;\; \sigma_{\varepsilon} = 1.3 \;\; \sigma_{k} = 1$$

Note that the diffusion term, modeled as gradient-diffusion approximation [47], has the constant σ_k set to 1 to be in agreement with the experiments performed by Francia et. al. [5] where diffusion was not included in the TKE calculation.

2.2.3.3.2 Modelling the effect of the deposits with wall functions.

In order to model the effect generated by the deposits for industrial scale towers, wall functions are required because of the dimensions of the system and the high Reynolds numbers of operation. Deposits are so heterogeneous that they cannot be implemented as part of the geometry [5, 28]. Thus, the use of an appropriate wall function in terms of momentum and turbulent components is key for an accurate prediction of the flow. In fact, for experiments at small scale it was observed that the turbulence kinetic energy [48] and the anisotropy [49-51] are much larger near the wall.

Previous studies for swirl towers used standard wall functions [21]. However, standard wall functions are not robust under strong pressure gradients [52] and the turbulent components are highly dependent on the y+. Thus, some authors have discarded standard wall functions for modelling swirl flows of small scale experiments. Najafi et al. [11] used scalable wall function because of the robustness in turbulent components and Li [53] used non-equilibrium wall function because of the pressure gradients generated by the swirl pattern near the wall. Attending to these considerations, the following set of recommendations are defined:

- Scalable and standard wall functions are not recommended under strong pressure gradients [54-56]. The pressure gradients may be significant at large swirl intensities, providing inconsistent results. The effect of the swirl intensity needs to be analysed, comparing these two wall functions with the non-equilibrium one.
- Scalable wall functions are recommended for 3D geometries [54-56]. They are similar to standard wall functions but with a reduced mesh dependency for the turbulence terms because diffusion is avoided in the turbulence balance and the y+ is not considered lower than 11.225 since eq. (17) is applied.

$$\tilde{y} = MAX\ (y^*, y^*_{limit}) \tag{17}$$

- Non-equilibrium wall functions are recommended for flows with large pressure gradients. However, they include the effect of diffusion in the turbulence balance near the wall, avoiding the turbulence closure [54].

Considering these recommendations, a comparison is performed for the current study. The results are shown in the supplementary material, Figures S9 to S14. It can be seen that scalable and standard wall functions provide similar results since a y+ larger than 30 has been ensured from the mesh analysis. Furthermore, differences are also observed between the non-equilibrium and the other two wall functions. In the vertical profiles of the standard deposition case, higher accuracy is provided by the scalable and standard wall functions at heights lower than z/D=5.7. We focus the comparisons on the operation under standard conditions because it is the most common operation regime for the tower. The improvement of accuracy given by the scalable and standard wall functions versus the non-equilibrium is because:

- The first tower parts that the air contacts are the heap and the bottom cone.
- Swirl intensities achieved in the tower are not very large. The maximum is 2 when the tower is clean, meanwhile the dirty case works with swirl intensities lower than 1 in most of the tower.

From these results and the recommendations described, the scalable wall function is selected. It provides higher accuracy than non-equilibrium and is more robust than the use of standard wall functions.

Once the scalable wall function is selected, the roughness generated by the deposits is introduced by means of the roughness defined in Fluent. The method introduced in Fluent considers the roughness as packed sand grains over the surface [24]. It computes an increment on the additive constant over 5.5 following eq. (18), which is expressed as eq. (19) when the system works in rough regime. The definition is based on the first cell conditions, including turbulent components as it is shown in eq. (20) [54].

$$\Delta B = f(C_s \cdot s^+_{Fluent}) \tag{18}$$

$$\Delta B = \frac{1}{k} * \ln\left(1 + \frac{C_s \rho s_{Fluent} u^*}{\mu}\right) \tag{19}$$

$$u^* = C_\mu^{1/4} k^{1/2} \tag{20}$$

C_s is a constant of roughness set to 1, s_{Fluent} is the roughness introduced in ANSYS ® *Fluent*, which is calibrated using the swirl intensity decay. ρ is the density and μ is the dynamic viscosity of the system. u^* is the nominal friction velocity set at the boundary condition which is defined following eq. (19), where k is the turbulence kinetic energy and C_μ is the constant for eddy viscosity computation [54].

The calibration of the roughness is performed using the swirl intensity decay. The swirl intensity is selected as the calibrating variable, instead of velocity profiles, since it accounts for the distribution of momentum, which is more significant at large radial positions. Hence, the prediction of the velocity profiles in the centre of the tower is not as significant as for large radial positions. In addition, this calibration according to the momentum distribution allows accurate prediction of the particle dispersion since the particles are governed by the air flow momentum and concentrated near the wall.

2.2.3.4 Solver settings for CFD modelling

The model is initialized using a hybrid procedure. The system is solved as 'pressure based' considering two PISO scheme. PISO is selected because it includes one term to correct the discretization and more accurate results are expected [54]. The gradient option is Least Square Cell since the use of the cell centroid is preferred versus face averaging methods.

For the discretization of the terms that compose the system such as velocity, Reynolds stresses and turbulence dissipation and kinetic energy, the QUICK scheme is used since it reduces the computational cost for the hexahedral cells, meanwhile the tetra are computed with two discretization orders. The PREssure Staggering Option (PRESTO!) Solver is also needed because of the swirling flow generated inside of the tower [54]. Finally, the system is solved as pseudo-convergent using the default relaxation factors for 15,000 iterations.

2.2.3.5 Procedure proposed for the modelling

The procedure to determine a roughness in Fluent uses the calibration based on the swirl intensity to fit the three roughness scenarios. The swirl is selected as the fitting parameter since it ensures the distribution of momentum that affects the particle dispersion. Furthermore, it has been recognised as a more robust parameter for the scale-up of spray drying towers since the momentum shows less oscillations in the prediction than the velocity measurements. Swirl intensity considers the momentum distribution when the fitting is carried out, giving higher weight at large radius, where the momentum is higher and the particles are also concentrated [5]. Once the swirl intensity is calibrated, the CFD model is validated for different Reynolds number of operation.

2.2.4. RESULTS

In this section, the modelling results of the air flow are presented. In section 2.2.4.1 the results of the calibration and validation of the model are presented for every case of deposition and at different Reynolds numbers. In section 2.2.4.2 other applications of the model are shown such as the determination of WSS and the vortex characterization under different Reynolds numbers of operation.

2.2.4.1 Validation of the model

In this section we validate the model using the experimental data in Francia et al. [5]. In section 2.2.4.1.1 we calibrate the roughness in Fluent with the use of the swirl intensity decay for different levels of deposition. Then, in section 2.2.4.1.2, we validate the model under different Reynolds number. In section 2.2.4.1.3, the velocity profiles predicted by the model are compared with the experimental ones. In section 2.2.4.1.4, the comparison for the turbulence components is also provided.

2.2.4.1.1 Prediction of Swirl decay at different deposition levels.

In the following paragraphs, the results from the modeling procedure described in section 2.2.3.5 are shown. The variable used to calibrate the momentum predicted by the model is the swirl intensity decay. This swirling behavior is ensured as shown in Figure 4, where the streamlines are plotted.

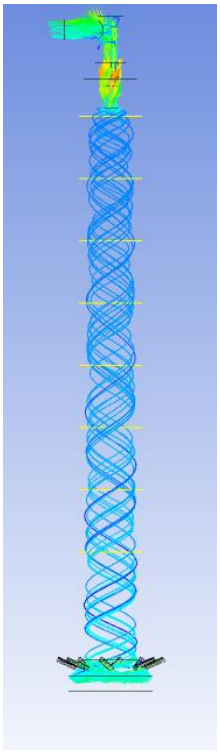

Figure 4. Streamlines of the airflow in the tower.

The roughness of the CFD model has been calibrated for the same Reynolds number ($1.4 \cdot 10^5$) and at three different levels of deposition: clean case without deposits, standard deposits and dirty conditions of deposition. The results for the roughness to be introduced in Fluent are summarized in Table 1. Meanwhile the plots comparing the experimental swirl decay and that predicted by the model are plotted in Figure 5. We can see that the simulation matches accurately the swirl intensity decay for the three deposition regimes.

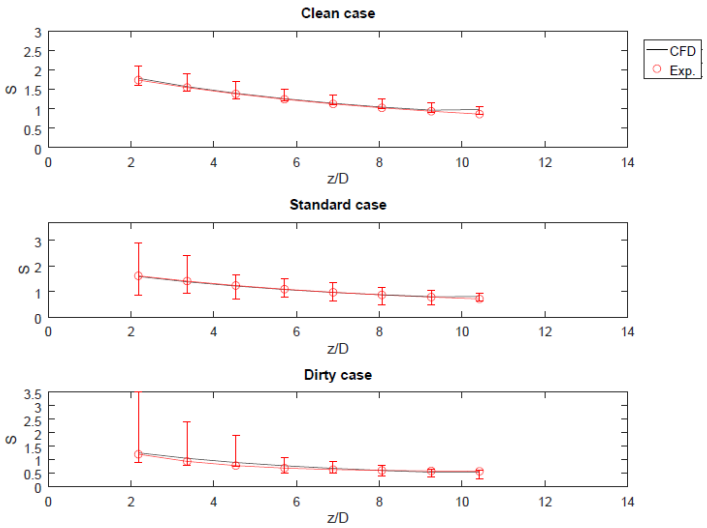

Figure 5. Prediction of swirl decay under different levels of deposition.

Table 1. Roughness required in ANSYS ® Fluent for each deposition level.

CASE	Roughness (mm)
CLEAN	7
STANDARD	12
DIRTY	30

2.2.4.1.2 Swirl decay at different Reynolds numbers.

The previously calibrated model is validated against different Reynolds numbers of operation. Francia et al. [5] also performed experiments for the swirl decay with standard levels of deposition and at three different Reynolds numbers of operation, obtaining the same swirl decay profile for all of them. We validate our model for the three Reynolds numbers. The model predicts the same swirl decay for the three Reynolds numbers evaluated, maintaining the roughness constant. In Figure 6 the swirl decay curves for the three Reynolds are showed.

The same swirl decay is obtained in these experiments because they were performed in fully developed turbulent regime. In section 2.2.4.2.2 it is shown how the decay curve changes when the Reynolds number is reduced.

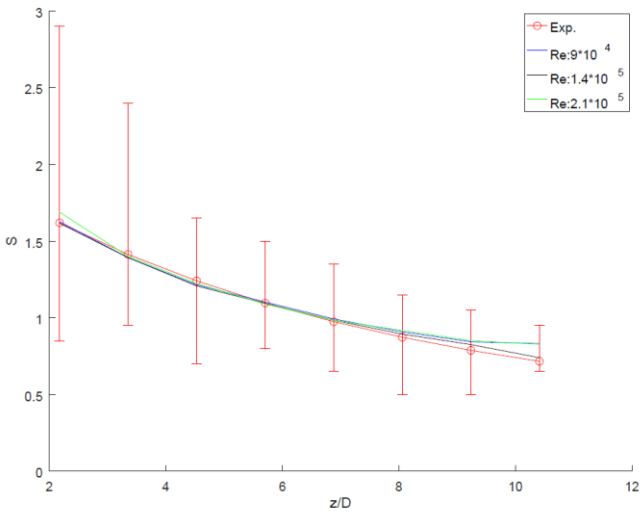

Figure 6. Swirl decay prediction at different Reynolds number.

2.2.4.1.3 Comparison of velocity profiles

To ensure that the new method of validation using the swirl intensity decay is accurate enough, the velocity profiles are also validated as previous authors have done [18, 23]. This study corroborates that our assumptions on the use of swirl and the model predictions are correct.

First, we compare the experimental velocity profiles for standard conditions, see Figure 7 (vertical component) and Figure 8 (tangential component). The radial component is not compared since it is nearly zero and less significant in momentum [5]. It is possible to see that the tangential and axial velocities are accurately predicted by the model.

The only section with lack of accuracy is the central axis, between a height of 6.8 z/D and 10.4z/D. This region corresponds to the center, where the momentum is lower and the particle concentration is also lower, having low relevance for the modeling of the particle motion of that particles obtained as products, which are the ones that govern the drying. The velocity of the droplets leaving a nozzle located in the center that spray to the walls is large enough that the droplets reach the tower very quickly and their momentum is governed by the air at large radius.

However, this lack of accuracy in the center may introduce further discrepancies in the modeling of the fines since if they get to the central axis, the momentum and eddies are not solve accurate enough. Furthermore, it would also influence if an atomization ring would be used to spray onto that center. In that cases, instead of the transient solution with finest mesh involves larger computational cost, it should be used since it allows reproducing finer the central jet, see Figure S6. In further works of CFD modelling, the influence of simplifying to the steady-state mesh can be studied with the introduction of particles and drying.

Second, the model has also been evaluated for different levels of deposition. It is possible to check that the correct velocity is also estimated for the clean and dirty cases, see supplementary material from Figures S15 to S22. The velocity profiles are accurately determined for the dirty case, meanwhile for the clean case, the vertical velocity is predicted correctly except near the vertical axis at a height of 9.2z/D, as well as the tangential in the central axis in the bottom of the tower.

Furthermore, the velocity profiles allow us to determine the type of swirl in the tower following the classification provided by Steenbergen and Voskamp [27]. The three types of swirl that they provide are observed. In the bottom, the flow follows a wall jet, then a solid body is generated and in the top of the tower the flow is like a concentrated vortex.

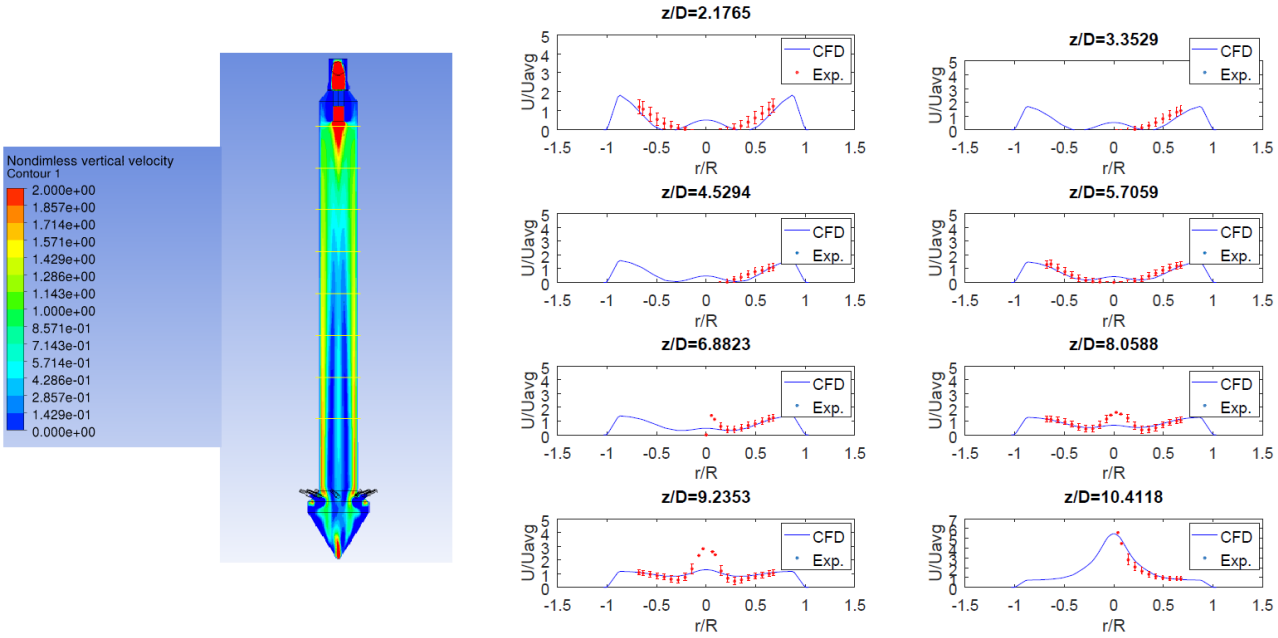

Figure 7. Standard case, dimensionless vertical velocity.

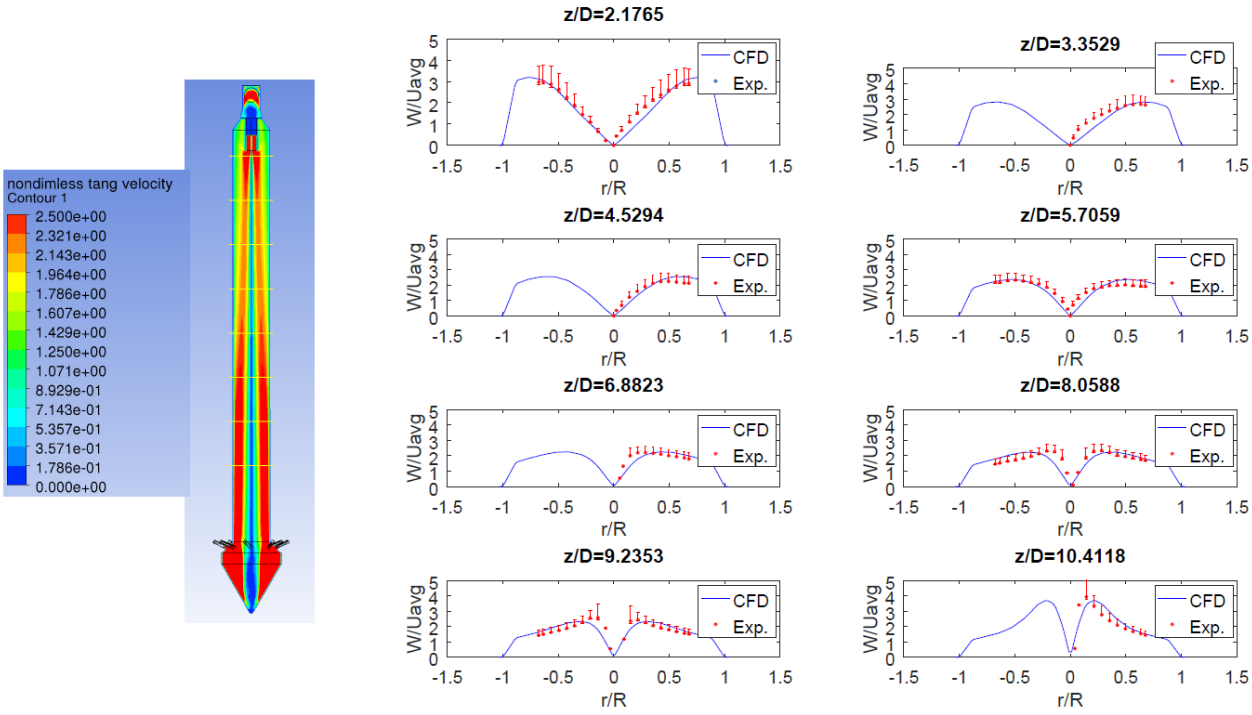

Figure 8. Standard case, dimensionless tangential velocity.

2.2.4.1.4 Prediction of turbulent components

The turbulence components are also analyzed. Here, we present the TKE prediction for the standard case of deposition. For dirty and clean cases the turbulence kinetic energy is presented in the supplementary material.

As it can be seen in Figure 9, the TKE predicted maintains the trend followed by the experimental data, except in the top measurement. The model predicts more accurately the experimental data for larger radius than in the center of the tower. However, in the center there is not a pattern of increment or reduction from the bottom to the top of the tower. It is thought that these irregular large values observed in the center for some heights are due to the torsion generated in the vortex. This torsion makes the vortex oscillate and consequently increase the TKE. The model developed does not include torsion in the vortex. This torsion phenomena must be studied in further modelling stages.

In addition, other turbulence components such as the Reynolds stresses and the anisotropy defined in section 2.2.2.4 have also been studied. They are presented in the supplementary material from Figures S23 to S31. Considering the size of the tower, all the components are predicted with a high degree of accuracy. The component with the least accuracy is the normal Reynolds stress for the radial component, which predicts a higher value than the measured experimentally for the entire geometry. The rest of the components only show lower accuracy for the central axis, attending to radial distribution. Meanwhile for axial distribution, the top height is the least accurate in the predictions.

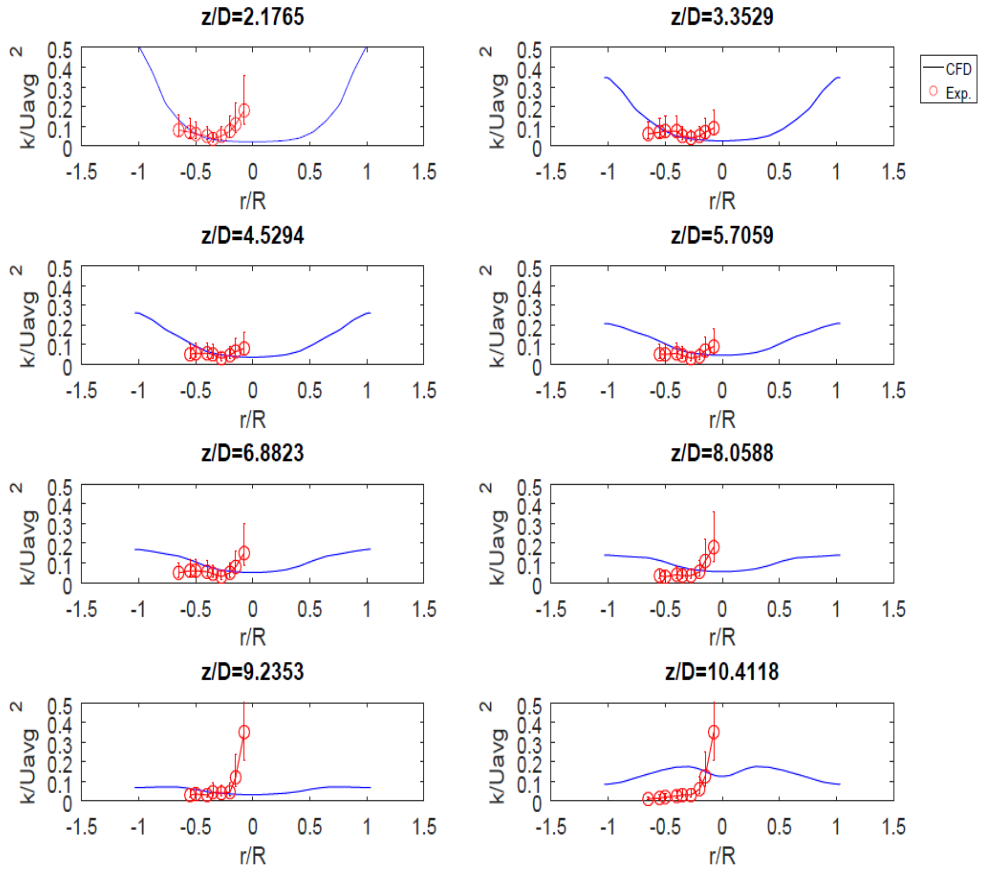

Figure 9. Comparison of turbulent kinetic energy.

2.2.4.1.5 Vortex Breaker characterization & effect of Reynolds and Swirl numbers.

The tower used for the modelling does not present recirculation [5]. However, the modelling procedure has also been validated in other towers where recirculation occurs. In addition, as explained in section 2.2.2.3, the proper prediction of the swirl at the entrance of the vortex breaker ensures the prediction of the recirculation phenomena. The study of the recirculation is extended in section 2.2.4.2.2 where the CFD model is applied to study the effect that different Reynolds of operation have on the Rossby number in the outlet.

2.2.4.2. Further studies with the model developed

In this section we apply the validated model developed for the study of the WSS in section 2.2.4.2.1. In section 2.2.4.2.2, the influence of different Reynolds numbers are studied over the swirl decay curve parameters as well as for the study of the Rossby numbers in the vortex breaker. Finally, in section 2.2.4.2.3 the influence of the contraction for the swirl prediction due to the deposits is also studied.

2.2.4.2.1 Wall shear stress determination

The tangential wall shear stress must be proportional to the decay rate, λ, from the swirl decay curve. To check that the decay rate agrees with this statement, it is first necessary to extract the WSS for the different conditions studied. The total dimensionless WSS is mainly governed by the one given by the angular velocity (Dimensionless tangential WSS) as it can be seen in Figure 10 for clean conditions. The angular component of the flow is the main component in the generation of WSS. It controls the WSS generation in the regions where the swirl intensity is very large.

As it can be also seen in this Figure 10, the WSS represented follows a logarithmic decay and it is fitted following eq. (23). The parameters that characterize the logarithmic curve are summarized in Table 2 for the 5 different operation conditions.

$$WSS_{dimless} = B - A \cdot ln\left(\frac{z}{D}\right) \quad (23)$$

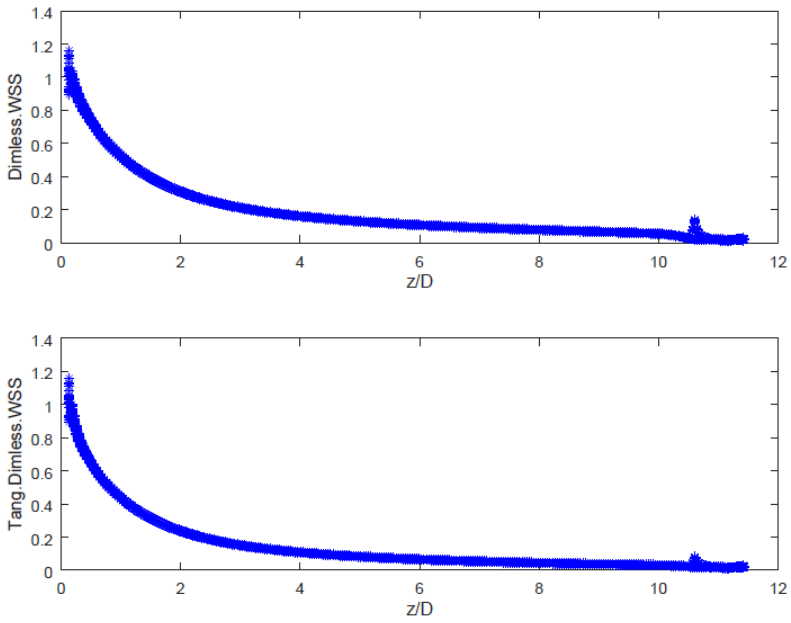

Figure 10. Dimensionless tangential WSS through the tower.

From the data, it can be seen that the level of deposition influences the decay ratio since, due to the swirl, the tangential component has larger contact with the wall in this region than at the cone and heap sections. It can be also seen in Table 2 that the dimensionless WSS is only controlled by the level of deposition as it also occurs with the Swirl intensity.

Table 2. Parameters of the logarithmic decay of dimensionless WSS in the tower.

Case	A	B	R^2
Clean – Re $1.4 \cdot 10^5$	-0.036	0.407	0.95
Standard – Re $1.4 \cdot 10^5$	-0.169	0.409	0.95
Dirty – Re $1.4 \cdot 10^5$	-0.187	0.424	0.92
Standard – Re $9 \cdot 10^4$	-0.169	0.408	0.95
Standard – Re $2.1 \cdot 10^5$	-0.169	0.409	0.95

Finally, in order to provide further validation, the link between the dimensionless WSS generated by the angular component and the decay rate presented in eq. (4) is evaluated. The average WSS and the decay rate of the 5 cases studied are plotted in Figure 11. It shows that the linear correlation between the decay rate and the dimensionless WSS generated by the angular component of the velocity exits.

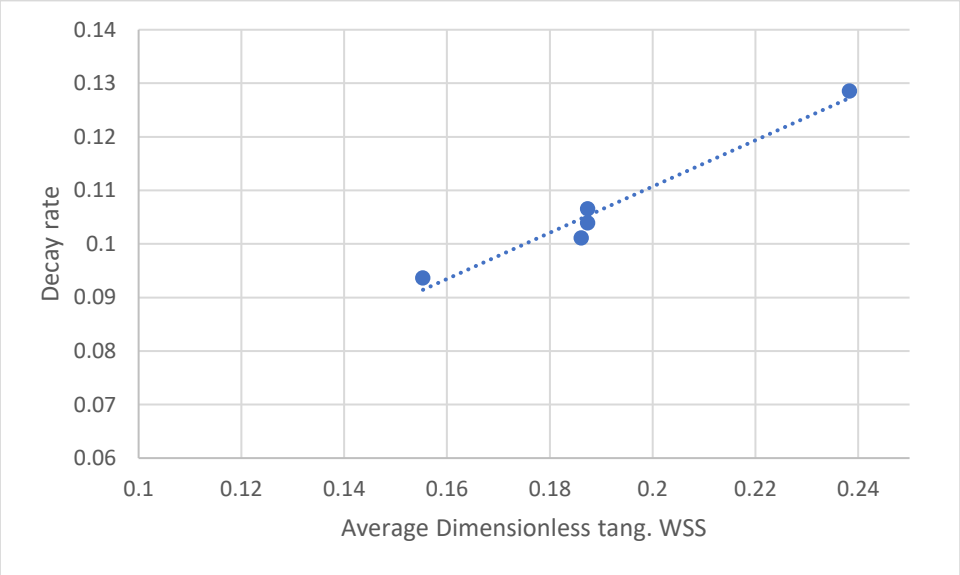

Figure 11. Decay rate as function of the dimensionless WSS.

2.2.4.2.2 Vortex stability and operation for different Reynolds numbers.

The model has also been used to predict the flow pattern at different Reynolds numbers. The experiments [5] for validation were performed at high Reynolds where the flow behaves as fully developed turbulent flow and the parameters do not change. However, the flow was not experimentally studied for smaller Reynolds numbers where the tower can also operate. Thus, the characteristic parameters of the swirl decay curve, eq. (5), have been studied for Reynolds numbers from $2.45 \cdot 10^4$ to $4.41 \cdot 10^5$. The results are summarized in Figure 12.

A reduction in the decay rate is predicted for Reynolds numbers smaller than $7 \cdot 10^4$. An oscillation of the vortex parameters can be observed since the flow leaves the fully developed turbulent regime and enters the transition regime. This Reynolds number becomes a constrain in the operation conditions if flow stability needs to be ensured for the swirl decay behaviour. In addition, this decay is studied for the three levels of deposition, where it can be seen that the dirty case has a larger decay rate. Moreover, it is also noted that this dirty case has large stability on the characteristic parameters of the decay curve, meanwhile the standard and clean curves oscillate for a Reynolds number of $7 \cdot 10^4$, reducing its decay contribution.

Figure 12 is similar to Nikuradse and Moody's diagrams. Comparing with these diagrams, it can be observed that the dirty case, with a large roughness, shows a behaviour closer to fully rough pipes.

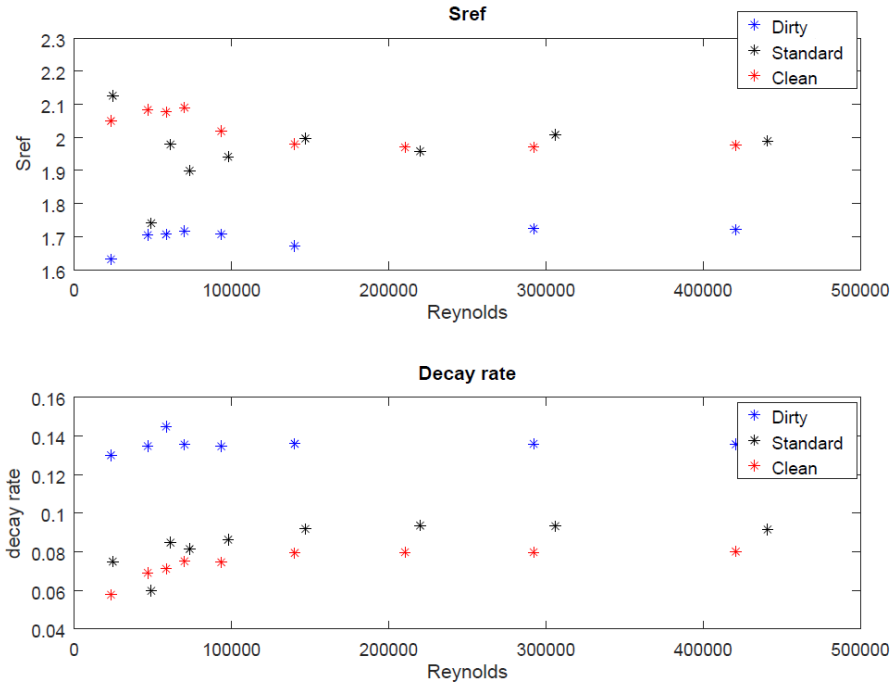

Figure 12. Swirl Decay curve parameters at different Reynolds numbers, initial swirl intensity (a) and decay rate (b).

Moreover, the Rossby number has been evaluated at the entrance of the vortex breaker for different Reynolds numbers. When the tower is dirty, no influence is perceived, but when the tower operates at clean or at standard conditions a plot similar to the ones predicted by Leibovich [32] are obtained, as it is represented in Figure 13. From Figure 13, it is also possible to see that a constant value is achieved for large Reynolds numbers, which corresponds with the constant section described by Garg & Leibovich. As it can be seen, this value is largely dependent on the deposition level, with the deposits being the factor that controls the swirl intensity in this geometry. For all the cases the flow results in subcritical conditions at the entrance of the vortex breaker. No recirculation is generated by standing waves at the entrance of the vortex breaker. The subcritical conditions are

characterized since the Rossby number is always larger than 0.8 or the swirl intensity before the entrance lower than 1.

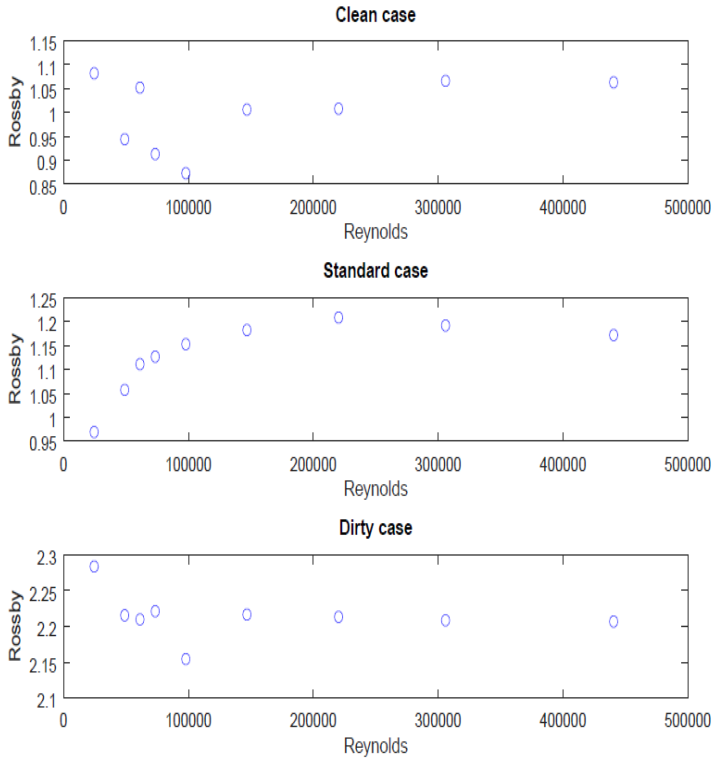

Figure 13. Determination of the characteristic Rossby number at the entrance of the vortex breaker for clean tower, standard deposits and dirty tower.

2.2.4.2.3 Evaluation of the effect of tower diameter reduction by deposition.

The deposition of the powder in the wall does not only increase the roughness of the wall, but it also reduces the diameter. From the definition of the swirl intensity and the average velocity, it is expected that a reduction in the radius results in a reduction of the swirl intensity. The deposition observed experimentally in dirty conditions is not estimated to be larger than 7% of the radius in some specific regions and 4% of the radius as average. Assuming a reduction of 4% in the radius, the swirl is estimated to decay 18% when eq. (1) is used and the velocity distribution between the axial and angular component is assumed constant. However, the distribution between velocity components may change because of the reduction and it needs to be evaluated by mean of the CFD model previously calibrated.

Thus, from the calibrated clean model, a reduction of 4% in the radius is evaluated, obtaining the results presented in Table 3. Together with the reduction of 4%, other two cases have been evaluated in order to check if the swirl intensity could be predicted. These cases use larger reductions of 12% and 20% respectively, which are not physically feasible.

Table 3. Comparison of swirl intensity predicted by different Radius contractions.

z/H	Swirl clean. No radius reduction.	Swirl Intensity. Radius reduction 4%	Swirl Intensity. Radius reduction 12%	Swirl Intensity. Radius reduction 20%
2.18	1.97	1.77	1.42	1.32
3.35	1.73	1.56	1.28	1.19
4.53	1.55	1.41	1.18	1.10
5.71	1.39	1.31	1.09	1.02
6.88	1.26	1.22	1.02	0.95
8.06	1.15	1.16	0.97	0.91
9.23	1.07	1.11	1.06	0.89
10.41	1.08	1.17	1.06	0.98

As it can be seen in Table 3, the use of the reduction in the radius decreases the swirl intensity in the bottom of the tower, but it does not decrease the swirl at the top of the tower. Thus, the contraction cannot be individually used to model the swirl intensity decay observed in the tower. Other sources such as the roughness and the irregular distribution of the deposits manage the momentum reduction in the top part and they allow predicting the swirl intensity decay. If it is desired to integrate the reduction of the tower radius in the modelling, further knowledge about the size and characterization of the deposits needs to be developed. The study of the deposits is easier to be carried out at small scale since the dimensions in industrial towers difficult their characterization. These further studies may allow quantifying how much loss of momentum is given by the radius reduction and how much by the irregularities.

2.2.5. CONCLUSIONS

In this work a new procedure has been presented together with a mesh study comparing steady-state and transient simulations for industrial scale spray drying towers. The mesh study shows that instead of the transient solution does not provide a mesh independent solution for the entire range of cell sizes, a steady-state solution with larger size provides similar results (differences up to 7%) than the finest transient one but with an important reduction of computational cost, being the steady-state used to perform the modelling.

The procedure presented is a general methodology to model the air flow pattern of swirling flow spray drying towers under different levels of deposition in steady-state operations. It is demonstrated how the roughness defined in a wall function can be used to model the airflow pattern. This roughness involves the effect that the roughness of the wall and the irregular distribution of deposits have on the air flow pattern. Furthermore, it has been identified to allow the fitting of the swirl decay since other phenomena such as the radius reduction given by the accumulation of deposit is not able to predict the complete swirl decay pattern. This first methodology developed using the

roughness is only applicable to steady-state since the dynamic equilibrium between deposition and re-entrainment is achieved and the deposits are constant in terms of time. It does not consider the simultaneous interaction between the deposits generated and the effect that they create on the flow. Hence, the transition when deposits increase such as in the start-ups of the towers for every new cycle of operation is not predicted.

To complement this modelling procedure, a novel calibration based on the swirl intensity decay has been proposed for industrial scales. This calibration is accurate in the prediction of the swirl intensity decay profile under different deposition conditions but lacks accuracy in the prediction of the velocity profiles near the axis. The use of this procedure based on the swirl decay ensures the prediction of momentum distribution in the tower, which is responsible of the control of particle dispersion in the tower. In further works, this methodology can be complemented evaluating the prediction on the discrete phase motion.

REFERENCES

[1] Masters, K. *Spray Drying: An introduction to Principles, Operational Practice and Applications.* **1972**. London: Leonard Hill Books.

[2] Woo, M. W. Daud, W.R.W. Mujumdar, A.S. Wu, Z.H. Talib, M.Z.M. Tasirin, S.M. Steady and transient flow simulations in short-form spray dryers. *Chem. Prod. Process Model.* **2009**, 4(1), Article 20.

[3] Harvie, D.J.E. Langrish,T.A.G. Fletcher, D.F. A Computational Fluid Dynamics Study of a tall-form Spray Dryer. *Trans. Inst. Chem. Eng.* **2002**, 80©, 163-175.

[4] Jaskulski, M. Zbicinski,I. Wawrzyniak, P. CFD simulation of particle agglomeration in industrial counter-current spray drying tower. *1st Nordic Baltic Drying Conference – Gdansk, Poland*, **2015**.

[5] Francia, V. Martin, L. Bayly, A.E. Simmons, M.J.H. Influence of Wall friction on flow regimes and scale-up of counter-current swirl spray dryers. *Chem. Eng. Sci.* **2015,** 134, 399-413.

[6] Najim, S.E. Styles, A.C. Syred, N. A study of modulatable cyclone combustors, ii, premixed combustión. *J. Energy Inst.,* **1982**, 55(422): 19-27.

[7] Andoh, R.Y.G., Hides,S.P., Saul, A.J. Improving Water Quality Using Hydrodynamic Vortex Separators and Screening Systems. *9th International Conference on Urban Drainage, Portland, Oregon, USA, 8-13 September,* **2002**.

[8] Hoffmann, A.C. Stein,L.E. *Gas Cyclones and Swirl Tubes. Principles, Design and Operation.* 2nd Edition. Springer Berlin Heidelberg New York. **2008**. ISBN 978-3-540-74694-2.

[9] Chang, F. Dhir, V.K. Turbulent flow field in tangentially injected swirl flows in tubes. *Int. J. Heat Fluid Flow* **1994** , 15 (5), 346-356.

[10] Fokeer, S. Lowndes,I. Kingman,S. An experimental investigation of pneumatic swirl flow induced by a three lobed helical pipe*. Int. J. Heat Fluid Flow* **2009,** 30, 369-379.

[11] Najafi,A.F. Mousavian,S.M. Amini,K. Numerical investigations on swirl intensity decay rate for turbulent swirling flow in a fixed pipe. I*nt. J. Mech. Sci.* **2011,** 53, 801-811.

[12] Gul,H. Evin,D. Heat transfer enhancement in circular tubes using helical swirl generator insert at the entrance. *Int. J. Therm. Sci.* **2007**, 46, 1297-1303.

[13] Syred, N. A review of oscillation mechanisms and the role of the precessing vortex core (PVC) in swirl combustión systems. *Prog. Energy Combust. Sci.* **2006**, 32, 93-161.

[14] Lucca-Negro, O. O'Doherty,T. Vortex breakdown: a review. *Prog. Energy Combust. Sci.* **2001**, 27, 431-481.

[15] Escudier, M.P. Keller, J.J. Recirculation in swirling flow: a manifestation of vortex breakdown. *AIAA J.* **1985**, 23 (1), 111-116.

[16] Southwell, D.B. Langrish, TAG The effect of swirl on flow stability in spray dryers. *Chem. Eng. Res. Des.* **2001**, 79, 222-234.

[17] Francia,V. Martin,L. Bayly,A.E. Simmons,M.J.H. An experimental investigation of the swirling flow in a tall-form counter current spray dryer. *Exp. Therm. Fluid Sci*. **2015**, 65, 52-64.

[18] Woo, M.H. Huang,L.X. Mujumdar, A.S. Daud,W.R.W. *CFD simulation of spray dryers – Volume 1*, **2010**, Ed. Woo,MW, Mujumdar,A.S. and Daud,W.R.W, ISBN-978-981-08-6270-1, Published in Singapore, pp. 1-36

[19] Woo, M. W. *Computational Fluid Dynamics Simulation of Spray Dryers. An Engineer´s guide.* **2017** CRC Press. Taylor&Francis Group. Boca Raton,FL. ISBN: 978-1-4987-2464-7.

[20] Ali, M. Mahmud, T. Heggs, P. Ghadiri, M. Bayly, A. Crosby, M. Ahmadian, H. Martindejuan, L. Alam,Z.. Residence time distribution of glass ballotini in isothermal swirling flows in a counter-current spray drying tower. *Powder Technol*. **2017**. 305, 809-815.

[21] Ali, M. Numerical Modelling of a Counter-Current Spray Drying Tower. University of Leeds (Ph.D. thesis) **2014**.

[22] Wawrzyniak,P. Podyma,M. Zbicinski,I. Bartezak,Z. Rabaeva,J. Modeling of air flow in an industrial countercurrent spray-drying tower. *Drying Technol.* **2012**, 30: 217-224, 2012.

[23] Langrish, T.A.G. Williams, J. Fletcher, D. F. Simulation of the effects of inlet swirl on gas flow patterns in a pilot-scale dryer. *Chem. Eng. Res. Des.* **2004**, 82 (A7): 821-833.

[24] Schlichting, H. Boundary-Layer Theory **1979** (7th. Ed.) McGraw-Hill. New York.

[25] Kitoh, O. Experimental study of turbulent swirling flow in a straight pipe. *J. Fluid Mech*. **1991** 225, 445-479.

[26] Steenbergen, W. Voskamp, J. The rate of decay of swirl in turbulent pipe flow. *Flow Meas. Instrum*. **1998** 9, 67-78.

[27] von Karman Mechanische Ahnlichkeit und Turbulenz. In Proc. *Third Int. Cong. Applied Mechanics* **1930**, Stockholm, pp. 85-105.

[28] Pope, S.B. *Turbulent Flows*. **2015** 15th Edition. Cambridge University Press. Cambridge, United Kingdom.

[29] Harvey, J.K. Some observations of the vortex breakdown phenomenon. *J. Fluid Mech*. **1962**; 14: 585-92

[30] Gore, R.W. Ranz, W.E. Backflows in Rotating Fluids Moving Axially through Expanding Cross Sections, *AIChE J.* **1974**, Vol. 10, No. 1, Jan. 1964, pp. 1069-1078.

[31] Squire, HB. Analysis of the vortex breakdown phenomenon. Part 1. Department Report no. 102, Imperial College of Science and Technology Aeronautics, **1960**.

[32] Leibovich, S. The structure of vortex breakdown. *Annu Rev. Fluid Mech.* **1978**;10:221-46.

[33] Lambourne, N.C. The breakdown of certain types of vortex. Aeronautical Research Council – Current paper 915, **1967**.

[34] Benjamin, TB. Theory of the vortex breakdown phenomenon. *J. Fluid Mech*. **1962**;14: 593-629.

[35] Najafi, A.F. Saidi, M.H. Sadeghipour, M.S. Souhar,M. Numerical analysis of turbulent swirling decay pipe flow. *Int. Commun. Heat Mass Transfer* **2005,** 32,627-638.

[36] Maddahian,R. Kebriae,A. Frarhanleh,B. Firoozabadi,B. Analytical investigation of boundary layer growth and swirl intensity decay rate in a pipe. *Archive of Applied Mechanics.* **2011**, 81:489-501.

[37] Derksen, J.J. Van den Akker, H.E.A. Simulation of vortex core precession in a reverse-flow cyclone. *AIChE J*. **2000**, Vol. 45. No. 7.

[38] Jaskulski, M. Wawrzyniak, P. Zbicinski,I. CFD Model of Paricle agglomeration in Spray Drying. *19th International Drying Symposium* August **2014**, Lyon, France.

[39] Francia, V. Martin, L. Bayly, A.E. Simmons, M.J.H. The role of wall deposition and re-entrainment in swirl spray dryers. *AIChE J.* **2015**, Vol. 61, 6, 1804-1821.

[40] Crowe, C.T. Schwarzkopf, J.D. Sommerfeld, M. Tsuji,Y. *Multiphase flows with droplets and particles*. **2012**, 2nd Edition. CRC Press. Taylor & Francis Group. ISBN: 978-1-4398-4051-1.

[41] Roache, P.J. Perspective: A Method for Uniform Reporting of Grid Refinement Studies. *J. Fluids Eng.* **1994**, 116 (3), 405-413.

[42] Langrish, T.A.G. Oakley, D.E. Keey, R.B. Bahu, R.E. Hutchinson, C.A. (1993). Time-dependent flow patterns in spray dryers. *Trans. Inst. Chem. Eng.* 71 (A), 355-360.

[43] Ullum, T. (2006) Simulation of a spray dryer with rotary atomizer: The appearance of vortex breakdown. *Proc. of the 15th Int. Drying Symp.* 2006, 20-23th August, Budapest, Hungary, 251-257.

[44] Bayly, A.E. Jukes, P. Groombridge,M. McNally,C. (2004) Airflow patterns in a counter-current spray drying tower. Simulation and measurement. *Proc. of the 14th Int. Drying Symp*, 2004.

[45] Jongsma,F.J. Innings,F. Olsson,M. Carlsson,F. Large eddy simulation of unsteady turbulent flow in a semi-industrial size spray dryer. *Dairy Sci. Technol*. **2013**, 93:373-386.

[46] Gibson, M.M. Launder, B. E. Ground Effects on Pressure Fluctuations in the Atmospheric Boundary Layer. *J. Fluid Mech*, **1978**, 86:491-511.

[47] F. S. Lien and M. A. Leschziner. "Assessment of Turbulent Transport Models Including Non-Linear RNG Eddy-Viscosity Formulation and Second-Moment Closure". *Comput. Fluids*. **1994** 23(8). 983–1004.

[48] Pashtrapanska,M. Jovanovic, J. Lienhart,H. Durst, F. Turbulence measurements in a swirling pipe flow. *Exp. Fluids* **2006** 41: 813-827.

[49] Foroutan, H. Yavuzkurt,S. A partially-averaged Navier-Stokes model for the simulation of turbulent swirling flow with vortex breakdown. *Int. J. Heat Fluid Flow* **2014**, 50, 402-416.

[50] Pashtrapanska, M. Jovanovic, J. Lienhart, H. Turbulence measurements in a swirling pipe flow. *Exp. Fluids* **2006** 41:813-827.

[51] Oyewola, O. Djenidi, L. Antonia, R.A. Influence of localized wall suction on the anisotropy of the Reynolds stress tensor in a turbulent boundary layer. *Exp. Fluids* **2004**, 37, 187-193.

[52] Wilcox, D. C. Turbulence modelling for CFD. **1993** La Canada, CA: DCW Industries.

[53] Li, G. Hall, P. Miles, N. Wu,T. Improving the efficiency of 'Clean-In-Place' procedures using a four-lobed swirl pipe: A numerical investigation. *Comput. Fluids* 2015, 108, 116-128.

[54] Fluent User's guide. Ansys Inc. **2009** Available at: http://www.ansys.com

[55] Leap Australia Computational Fluid Dynamics blog (CFD) (2013) Turbulence Part 3 – Selection of wall functions and Y+ to best capture the Turbulent Boundary Layer. Available in: https://www.computationalfluiddynamics.com.au/turbulence-part-3-selection-of-wall-functions-and-y-to-best-capture-the-turbulent-boundary-layer/

[56] Moukalled, F. Mangani, L. Darwish, M. (2016) *The finite volume method in Computational Fluid Dynamics. An advanced introduction with OpenFOAM and Matlab*. Ed. Springer. ISBN 978-3-319-16873-9.

CHAPTER 2.3 FURTHER STUDIES OF THE AIRFLOW IN THE DRYER.

This chapter presents a most detailed analysis of the components of the airflow. The chapter is divided in two sections. The first part (addressed as a submitted paper) focuses on the role that the geometrical parameters of the inlet ports have on the vortex behaviour, the swirl intensity and the instabilities addressed. As a result from the study, the contraction between the zone dedicated to generate the swirl and the cylindrical region has been observed to be critical. Two critical swirl intensities are determined. The first critical swirl intensity makes a distinction between a free and a wall governed vortex. In a free vortex the instabilities addressed to the flow pattern decrease when the swirl intensity is increased showing a negative power correlation between them. However, in a wall governed vortex the instabilities do not show a correlation with the swirl intensity, tending to a slight increase when the swirl is increased. The second critical swirl intensity indicates the presence of a breakdown of the vortex at the bottom zone of the dryer. In the case that the swirl intensity is higher than the critical recirculation is generated at the bottom of the chamber but without impact in a top cylindrical part of the chamber.

One of the results obtained from the first study is the uncontrolled instabilities in the wall governed regime. One of the reasons of these instabilities can be the generation of small eddies at the end of the smooth contraction by the formation of a stagnation region. However, this stagnation region is not observed in the CFD simulations with a Reynolds Stress turbulence model. Thus, the use of most detailed Dettached Eddy simulations have been also explored under different turbulent models. As a result, it has been obtained that only the Spalart-Allmaras turbulence models is robust enough to reproduce the momentum distribution under different Reynolds numbers and level of roughness. This model shows a good prediction in both the swirl intensity decay and the velocity components through the dryer. Even though the velocity components have shown very good results, this modelling approach still requires of further validation in terms of anisotropy and in the prediction of the particle momentum in further stages of the modelling process.

Note: The supplementary material is attached in the physical version of the thesis and it is also available in: https://drive.google.com/drive/folders/1_EkYTjaqQYkP_okY1ckLG9DMSdbt8gRt?usp=sharing

PART 2.3.A - NUMERICAL STUDY OF AIRFLOW REGIMES AND INSTABILITIES PRODUCED BY THE SWIRL GENERATION CHAMBER IN COUNTER-CURRENT SPRAY DRYERS.

2.3.A.1 INTRODUCTION

Spray drying is a common unit operation to manufacture a wide range of particulate products (e.g. pharmaceuticals, food powders, detergents). It consists on atomizing a solution in the form of drops that are dried in contact with hot gas. According to the contact, spray dryers are classified as: co-current, counter-current or mixed flows [A1]. Co-current dryers are the most studied type of spray dryers since they are applied to most added value and sensitive materials such as pharmaceuticals and food; meanwhile counter-current dryers, applied to most stable materials such as ceramics or detergents, provide higher energy efficiency. Apart from the type of contact, the intensification of spray drying process with the objective of improving the efficiency has resulted in the modification and the introduction of novel designs [A2-A5], among them the use of swirl flow patterns [A6, A7]. This type of pattern, used in other units including cyclones [A8-A11], has been applied in either counter-current [A6, A12] or co-current [A13-15] spray dryers. Its use increases the residence time of the air and the particles within the chamber, improving the heat transfer efficiency and reducing the size of the chamber. However, swirl flows involve high complexity since phenomena such as precession and vortex breakdown (VBD) result in the generation of instabilities. VBD phenomena has been reviewed by several authors [A16-A18]. It is favoured when a vortex with enough rotation rate suffers a narrow contraction or expansion [A18]. Under this VBD, the fluid gives the impression to flow under an axisymmetric bubble placed on the axis of the vortex [A17]. Around the bubble, the air can form up to 7 different types of breakdown as reported in [A17]. The type generated (typically in form of bubbles or spirals) is highly dependent on the Reynolds number, the swirl intensity and the degree of contraction/expansion [A16]. In particular, the effect of the swirl intensity number at the contraction (also defined as the inverse of the Rossby number) has been widely studied since it governs the presence of airflow recirculation [A17]. Under sufficient swirl intensity, the adverse pressure at the centre is high enough that contract the cores of the vortex, generating recirculation regions [A19]. The phenomena, identified in combustion chambers [A19] has also been observed in swirl flow spray dryers [A20]. Another characteristic of the VBD is its time dependency generated by the precessing vortex core (PVC) at the forced vortex region of the flow [A21]. The vortex flow is unstable and starts to precess about its axis of symmetry forming the PVC [A17]. The nature of this PVC is highly influenced by the Reynolds number. An increase in the Reynolds favours the pressure oscillations and subsequently an increase of the characteristic frequency of the process [A22, A23]. Apart from the influence of the flow rate in the frequency, other contributions such as the one given by the curvature, the one given by the torsion of the vortex and the influence of the walls have been also analytically described for PVC's [A24, A25].

The vibrations and noise generated by these phenomena have been studied in cyclones showing a reduction in the separation efficiency [A26]. In co-current spray dryers, the swirl flow is generated by means of swirl vanes located close to the atomizer in the top part of the dryer [A2, A14]. At the inlet, the flow keeps the

swirl motion generated by the vanes and it shows a vortex with stable precession. However, the development of the swirl in the chamber showed different behaviours depending on the tangential angle. In the case that the tangential angle is high enough, VBD is generated and the vortex maintains the PVC with a central recirculation zone and its stable oscillations. However, for low swirl conditions the vortex becomes unstable generating irregular airflow patterns with external recirculation zones near the wall and eddies rolling in all directions. These unstable oscillations are more irregular and require the use of transient simulations to reproduce the flow patterns [A2]. By using very large eddy (VLE) simulations and suggesting modifications in the chamber, numerical analysis have been performed in co-current spray dryers to evaluate the presence, stability and characteristic parameters of the vortex [A14, A27]. In the case of counter-current dryers, the generation of the vortex does not respond directly to the tangential injection, being carried out by the tangential arrangement of the inlets at the bottom of the dryer. Huntington [A6] lists the typical designs of large swirl counter-current dryers describing the difficulties to obtain stable patterns, for which attaining a good balance between the pressures at all inlet ports is paramount. The control of the pressure in each of the inlet ports is straightforward in the case that each of them is individually fed. However, an alternative design is the use of a single feed followed by a distributor that sends the air to each of the ports. In this second case, the generation of a stable vortex is more challenging since asymmetry is always presented, even under placing enough inlet ports [A20]. The pressure drop in the distributor results in the asymmetrical distribution of the air, which can be avoided by using asymmetrical ports with different diameters or internal elements that generate a pressure drop in that ports with higher airflows. After the tangential parts, a smooth contraction can be introduced in the system before the cylindrical part of the chamber [A12, A20]. In the cylindrical part, where asymmetries have been also observed [A12, A20], the vortex is mainly governed by the contact with the wall observing a decay of the swirl intensity in the drying chamber. This decay, observed in the swirl counter-current dryer [A20], was previously evaluated in pipes showing that the existence of angular wall shear stress (WSS) in the swirl causes a reduction of the swirl intensity [A28, A29]. This WSS is highly dependent on the roughness of the wall and in counter-current dryers is given by the different levels of depositions achieved, which are highly heterogeneously distributed. The modelling of the airflow including the influence of the deposits on the air was carried out in a previous work [A30], showing to predict the swirl intensity through the dryer under different levels of deposits with average errors of 2.8% and a maximum error of 12%. The validated CFD model is applied to this study to evaluate the role of the geometry at the bottom of the dryer. Even though previous experimental and modelling work paid attention to the effect of the deposits on the flow and the effect of a top contraction where a VBD is generated [A20, A30], the bottom section is the responsible for generating the vortex pattern. These structures of the vortex and their behaviour are highly dependent on the geometry of the chamber at the bottom, which has not been modified before due to experimental constraints. Thus, the validated CFD model is used instead in this work to understand the different types of vortices that can be generated as well as the instabilities related to them with the objective of determining how future designs can minimize the instabilities in counter-current spray dryers.

The following sections of the paper are structured as follows: section 2.3.A.2 provides a description of the unit used for the study and the airflow pattern within it. Section 2.3.A.3 describes the numerical analysis performed, which results are analysed in section 2.3.A.4. The last section 2.3.A.5 summarizes the conclusions.

2.3.A.2 DESCRIPTION OF THE MATERIALS AND FLOW IN THE UNIT

This work uses the semi-industrial scale counter-current dryer property of Procter and Gamble Co. as a basis for the computational studies, see Figure 1, a) to Figure 1, c). The air is introduced into the counter-current dryer by means of a ring distributor, which is composed by only one feed that separates the air into the 8 inlet ports connected to the dryer, see Figure 1, d). The ports located farther from the entrance suffer a higher pressure drop, which results in less flow through them as it can be seen in Figure 2. In this figure an example of an asymmetric distribution of mass per inlet port is compared with the ideal case of balanced inlets. It should be noted that asymmetric distribution in the ports does not correspond to the one in the industrial dryer to protect the confidential information of the sponsoring company. The orientation of these ports, together with the hip and the cone sections of the dryer result in the generation of the vortex. Each of the inlet ports are tangentially and vertically oriented with the subsequent α and β angles showed in Figures 3, a) and b). As a result from the angular momentum introduced by the ports, the vortex is generated in the dryer, which is characterized by the swirl intensity defined in Eq. (1) [A28]. However, this swirl intensity depends on the radius at each location. The dependence on the radius can be avoided by using a dimensionless flux of angular momentum normalized by the axial momentum referred to the cylinder (subscript c) as proposed by [A31], see Eq. (2). This ratio of momentums shows a dependency of the inlet angles as presented in Eq. (3).

$$S = \frac{G_\theta}{G_z \cdot R} = 2\pi\rho \int_0^R \frac{\overline{U}\,\overline{W}}{\rho\pi\overline{U_{avg}}R^3} r^2 dr \quad (1)$$

$$\Omega_i = \frac{G_{\theta i}}{R \cdot G_{z_{av}}} = \frac{\overline{M_i} \cdot \overline{U_{i,\theta}} R_i / \pi R_C^2}{\overline{M_c} \cdot \overline{U_{av}} R_C / \pi R_c^2} \quad (2)$$

$$\Omega_i = \frac{\overline{M_i^2} \cdot A_c \cdot R_i}{\overline{M_c^2} \cdot A_i \cdot R_c} \cdot \sin\alpha \cdot \cos\beta \quad (3)$$

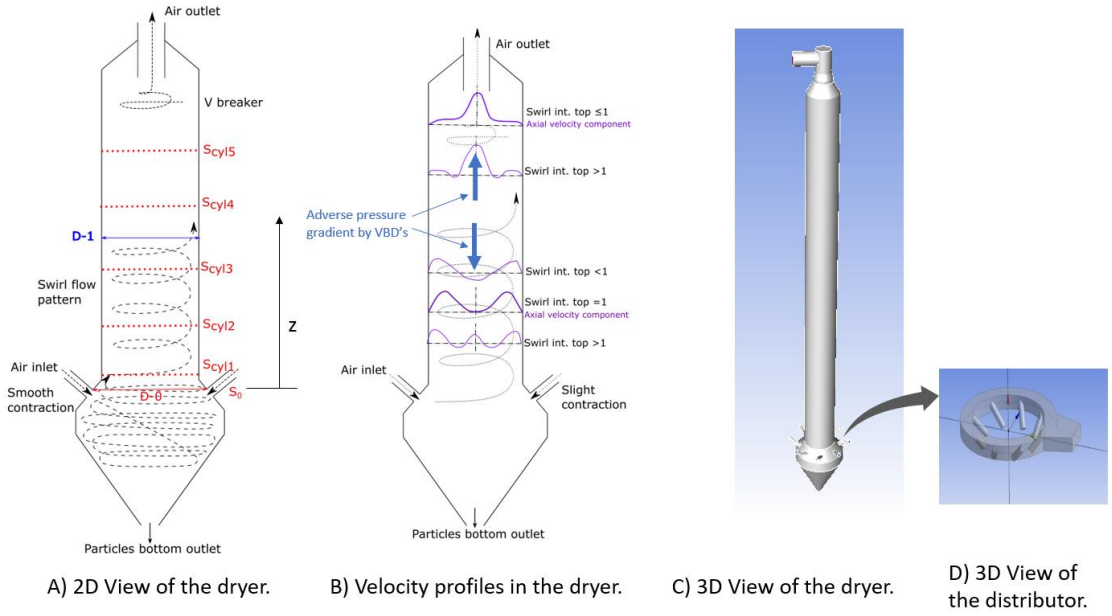

A) 2D View of the dryer. B) Velocity profiles in the dryer. C) 3D View of the dryer. D) 3D View of the distributor.

Figure 1. A) 2D view of the dryer and location of measurements. B) Velocity profiles in the dryer [A20], C) 3D view of the dryer. D) 3D View of an air distributor.

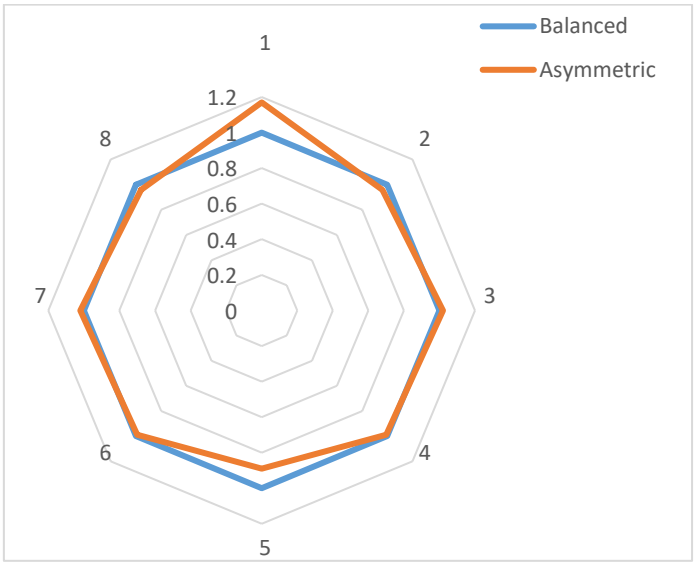

Figure 2. Relative mass flow rate per inlet port comparing a balanced distribution through the ports with a created example with asymmetric distribution.

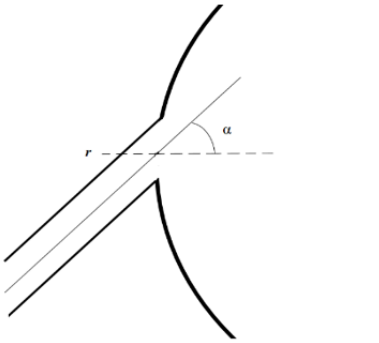

A) Top View of the ports.

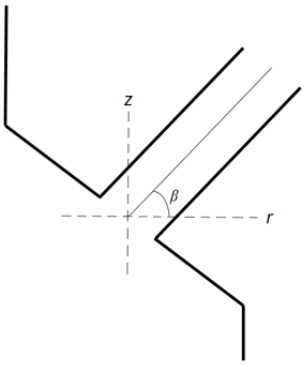

B) Lateral View of the ports.

Figure 3. Top (A) and lateral (B) views of the inlet ports.

The swirl motion generated in the bottom part of the chamber suffers a smooth contraction in the hip before moving into the cylindrical part of the dryer. Even though no experimental characterization has been performed, previous studies of swirl flow in similar systems have shown that the swirl intensity and the degree of contraction can generate different flow states in the vortex. From a theoretical study Rusak and Meder [A32] identified two critical swirl intensity levels. First, a critical swirl intensity was identified for the formation of the wall separation phenomena. In addition, a second critical swirl, typically higher than the first one, was observed for the generation of VBD [A18]. These theoretical regimes were experimentally observed by Leclaire and Jacquin [A33] by using a contraction and evaluating the fluid in an open duct exit the contraction. In this work they observed that under a smooth contraction, an increase of the swirl intensity at the entrance results in an increase of the tangential velocity in the centre and the presence of eddies in the near wall section. Furthermore, they also suggested a contraction parameter, defined as Eq. (4). Under no-friction conditions, this parameter was demonstrated to predict the modification of Reynolds and Swirl intensity numbers as proposed in Eq. (5) and (12) [A33, A34]. Eq. (5) can be obtained from mass and momentum definition meanwhile Eq. (6) is obtained assuming the conservation of the angular momentum. However, it has not been evaluated with friction, which should result in even lower swirl intensities than the one given by Eq. (6).

$$\chi = \left(\frac{R_0}{R_1}\right)^2 \quad (4)$$

$$Re_1 = Re_0\sqrt{\chi} \quad (5)$$

$$S_1 = \frac{S_0}{\sqrt{\chi}} \quad (6)$$

In the cylindrical chamber, the vortex has been experimentally analyzed in previous works [A20, A31]. The vortex was observed to be governed by the contact with the wall along the cylinder and free, in the form of a Rankine vortex, near the contraction in the top of the dryer, see Figure 1, A). However, at the bottom of the cylinder alternative types to the wall governed vortex can be generated depending on the distribution of the tangential velocity and subsequently the swirl intensity [A29]. In the case that the swirl intensity is low, concentrated and solid body vortices could be formed. These vortices are free and more difficult to control suggesting more unstable oscillations as showed in some of the dryers reported in [A20]. The generation of the free or wall governed vortex is highly dependent on the flow after the smooth contraction. In case that the swirl intensity before the contraction is low, the contact with the wall is expected to be low and free vortices are generated. On the contrary, under high swirl intensities the contact with the wall takes place generating wall jets [A20, A29]. Once the vortex is governed by the wall, the non-dimensionless angular momentum or swirl intensity decays through the cylindrical section due to the tangential wall shear stress (WSS). Assuming symmetry, steady-state and incompressibility, the dimensionless WSS generated by the angular component is defined as Eq. (7):

$$\tau'_{w\theta}(z) = \frac{\tau_{w\theta}(z)}{0.5\rho U_{avg}^2} = \frac{1}{2}\frac{d\Omega}{d\left(\frac{z}{D}\right)} \quad (7)$$

Eq. (7) indicates that the dimensionless angular WSS is a linear function of the axial gradient of Ω. Integrating Eq. (7), Eq. (8) is obtained where the decay rate, λ, represents the effect of the wall shear stress in the reduction of Ω as proposed by Steenbergen and Voskamp [A29] and observed by Kitoh [A28] in pipes and in a dimensionless form by Francia et al. [A31] in the spray dryer under study. Eq. (7) and (8) are only realistic for low swirl intensity or Ω values. At higher Ω, the relation between the WSS and Ω requires experimental characterization or other estimations (e.g. [A35]), that have more complex functions as the one presented in (9) [A36]. Further modifications of this scalable equation have been also carried out including the effect of Re or the number of tangential injectors [A37, A38] but Eq. (9) showed a good correlation for the case of study across different scales and levels of wall deposition [A20, A31].

$$\Omega = \Omega_{ref} \cdot e^{-\lambda\left(\frac{z-z_{ref}}{D}\right)} \quad (8)$$

$$\Omega = \left(\Omega_{ref} + \frac{B}{A}\right) \cdot e^{2A\left(\frac{z-z_{ref}}{D}\right)-\frac{B}{A}} \quad (9)$$

At the end of the cylindrical section, a narrow contraction is placed for the outlet of the air. Because of the high degree of contraction, the Rankine vortex formed before the outlet suffers a VBD phenomena resulting in a decrease of the pressure at the centre and subsequently in an increase of the axial velocity. The increase of the axial velocity is extended to lower locations of the dryer avoiding a central recirculation if the

swirl intensity at this contraction is equal to 1. In the case of the swirl intensity is below 1, the adverse pressure is not that high, the flow is dominated by a second VBD at the bottom of dryer that generates a central recirculation region, see Figure 1, B). However, for swirl intensities above 1 at the top contraction, the pressure rises and new recirculation zones are generated modifying the axial velocity profiles [A20].

2.3.A.3 NUMERICAL ANALYSIS.

This section describes the CFD model used and the numerical analysis performed to evaluate the effect of the geometrical parameters of the inlet in the presence of instabilities. The modelling of spray dryers is commonly performed in a series of sequential stages [A30, A39]: First, the airflow is modelled and validated. Second, the momentum of the discrete phase is introduced in the model. Finally, the heat and mass transfer mechanisms are modelled. For a better understanding of the instabilities in the airflow and the influence of the geometry of the ports on them, the current study only focuses on the airflow system.

2.3.A.3.1 CFD Model.

To model the dryer, a mesh screening has been performed evaluating the quality by the Grid Convergence Index (GCI) [A40] method as applied in previous work. As a result, a convergent and stable mesh is obtained ensuring the minimum scale to capture the discrete phase in future works [A30]. The air flow is modelled using the finite volume approach where the continuity, Eq. (10), and Navier-Stokes, Eq. (11), are solved using in Ansys ® Fluent 18.2.

$$\frac{\partial \rho}{\partial t} + \nabla \cdot (\rho U) = 0 \tag{10}$$

$$\frac{\rho D U_j}{Dt} = \mu \nabla^2 U - \nabla P + \frac{1}{3}\mu \nabla(\nabla \cdot \mathrm{U}) - \rho g \tag{11}$$

2.3.A.3.1.1 Turbulent model

Even though different default turbulent models have shown to reproduce the air velocity profiles in swirling flows [A41], the characteristic anisotropy of the swirling flow in the current system [A31], requires the use of the Reynolds Stress Model (RSM) as turbulent model. It is composed of 7 terms as presented in Eq. (12): Reynolds-stress flux (R_{ij}), mean flow convection (C_{ij}), turbulence production tensor (P_{ij}), transport by diffusion (D_{ij}), turbulence dissipation rate (ε_{ij}), pressure rate of strain tensor (Φ_{ij}) and transport due to rotation (ψ_{ij}). The constants required in the RSM are defined in the Appendix.

$$\frac{DR_{ij}}{Dt} = \frac{\partial R_{ij}}{\partial t} + C_{ij} = P_{ij} + D_{ij} - \varepsilon_{ij} + \Phi_{ij} + \psi_{ij} \tag{12}$$

2.3.A.3.1.2 Boundary conditions for the walls.

The deposits covering the walls of industrial counter-current dryers are very heterogeneous and have a significant impact on the momentum distribution within the dryer [A20]. The effect that the deposits have on the airflow pattern is modelled by means of the additive constant included in a scalable wall logarithmic

function [A30]. This additive constant is defined as in Eq. (13). The values of the constants required (C_s and s_{Fluent}) are specified considering the standard conditions of deposition as presented by [A30].

$$\Delta B = \frac{1}{k} * \ln\left(1 + \frac{C_s \rho s_{Fluent} u^*}{\mu}\right) \quad (13)$$

2.3.A.3.1.3 Solver settings

The model is initialized using a hybrid procedure. Following the best practice for swirling flows, the PRESTO! scheme is used for the discretization of the pressure. The solver PISO is selected since it includes one term to correct the pressure, expecting a fast convergence, and QUICK scheme is used for the spatial discretization since it provides a good trade-off between computational cost and discretization order. These specifications are used to solve each of the simulations, which are computed in two steps: First, the system is solved as pseudo-steady for 10,000 iterations. Second, the transient simulation is started from the pseudo-steady solution and computed for 50 s with a time-step of 0.1 s. This time-step is used since it provides stability on the solution and it also ensures to reproduce the characteristic frequency of the PVC (between 0.2 Hz and 1.6 Hz [A31]. Each of the simulations is computed in a High Processor Computer with 3 parallel Intel-Xeon E5-2698 ® and takes approximately 20 h.

2.3.A.3.2 Numerical analysis of the inlets.

Two numerical analysis are performed to understand the influence of the geometrical parameters of the ports that introduce the air on the airflow regime at the bottom of the dryer and on the stability of the vortex generated in the chamber. First, an analysis is performed including all the geometrical parameters and the asymmetrical distribution of the air in the ports. Second, a more detailed study with the most relevant geometrical parameters of the first analysis is carried out evaluating the swirl intensity and its influence on the instabilities and the decay that suffers before achieving the cylindrical part of the dryer. These variables, which have been shown to be highly correlated with the different regimes in pipes, have not been evaluated within counter-current dryers.

2.3.A.3.2.1 Numerical analysis of geometrical parameters in the bottom part of the chamber.

Different geometrical parameters regarding the ports and the structure can be studied in the generation of the airflow pattern. In a first stage, a screening design of experiments (DOE) is used to evaluate the following parameters, see Table 1: The tangential angle of the ports, α, is evaluated for zero (non-swirling) and swirling conditions. The axial angle, β, is evaluated under two positions, in both cases with a certain axial orientation. The number of ports and the size of the inlets is also modified as well as the distribution of the airflow per inlet, which distinguishes two cases: one case with regular distribution and another case with the irregular distribution. Apart from the changes in the ports, their distance to the axial axis is also modified but always ensuring that the ports are introduced into the hip. All these computational experiments have been simulated

as defined in section 2.3.A.3.1 with a Reynolds number of $2.1x10^5$ that ensures the fully developed turbulent regime and under standard conditions of deposition as defined in previous works [A20, A30, A31].

Table 1. Screening design of experiments for evaluating the role of each geometrical parameter on the instabilities of the airflow.

Experiment	α	β	N. Inlets	Size	Flow in ports	Contraction
1	Non-swirling	Low	8	Small	Homogeneous	High
2	Swirling	High	8	Big	Homogeneous	High
3	Non-swirling	High	8	Small	Irregular	High
4	Swirling	Low	4	Small	Irregular	Low
5	Non-swirling	High	4	Big	Homogeneous	Low
6	Swirling	High	8	Big	Irregular	Low
7	Non-swirling	High	4	Small	Homogeneous	Low
8	Non-swirling	Low	8	Big	Irregular	Low
9	Swirling	High	4	Small	Irregular	High
10	Swirling	Low	8	Small	Homogeneous	Low
11	Swirling	Low	4	Big	Homogeneous	High
12	Non-swirling	Low	4	Big	Irregular	High

2.3.A.3.2.2 DOE for the detailed study of vortex regimes and instabilities.

The second study focuses on characterising the regimes that can be generated at the bottom of the dryer, the swirl intensity, its decay and its influence on the instabilities in the cylinder. In the previous DOE, a comparison is carried out between swirling and non-swirling patterns. However, different tangential angles are not used. Thus, a new Box-Behnken DOE with three central points is proposed since the aim is not only to understand the influence but also to generate simplified models that represent some of the behaviours and determine the operating conditions at which the unstable oscillations of the airflow are minimized. The new DOE uses different tangential angles, which are expected to be the main driver in increasing the swirl intensity, and different size of the inlet ports and axial angles, which are the other two parameters with higher influence on the swirl intensity introduced, see Eq. (3), and that have shown a higher influence on the study carried out in section 2.3.A.3.2.1. Table 2 presents all the computational cases of the Box-Behnken DOE.

Table 2. Box-Behnken DOE for characterization of critical swirl parameters.

Experiment	α	β	Inlet Size
HαMβLSize	High	Medium	Low
MαMβMSize	Medium	Medium	Medium
MαHβLSize	Medium	High	Low
LαMβLSize	Low	Medium	Low
MαHβHSize	Medium	High	High
HαMβHSize	High	Medium	High
HαHβMSize	High	High	Medium
MαLβLSize	Medium	Low	Low
MαMβMSize	Medium	Medium	Medium
HαLβMSize	High	Low	Medium
LαMβHSize	Low	Medium	High
LαLβMSize	Low	Low	Medium
MαLβHSize	Medium	Low	High
LαHβMSize	Low	High	Medium
MαMβMSize	Medium	Medium	Medium

2.3.A.4 RESULTS

This section presents the results obtained from running the simulations of the DOE's presented in the previous section. The analysis of the results focuses on: the unstable oscillations of the airflow in the cylindrical part of the chamber, cyl1 and cyl2, and the swirl intensity at the generation, which can govern the regime of the air, and at the cylindrical region.

2.3.A.4.1 Screening study of instabilities of the airflow in the dryer.

Analysis of instabilities in the airflow pattern

This first section presents the results for the screening study focused on evaluating the role of the geometrical parameters on generating unstable oscillations in the dryer. The unstable oscillations have been shown to generate irregular flow patterns [A13]. For quantifying this irregular airflow pattern, the parameter φ_u is used for the axial velocity, see Eq. (14). It computes the irregularities of the axial velocity component over time and across locations. 4 radial locations, each of them with 50 points and at 2 different heights, are extracted. In the case of a symmetrical vortex, at each height the axial and tangential velocities extracted along the radius should be very similar and only modified by the precessing frequency of the vortex. Thus, one radius is taken as reference and the difference is computed from the three remaining ones. Similar to φ_u, the parameter φ_w is used to compute the asymmetries of the tangential velocity, see Eq. (15). The

results obtained for these parameters in each experiment are presented in Table 3. A statistical analysis (SA) of the results obtained in Table 3 is carried out by means of Kendall's method showing that the geometrical parameters with highest influence are the size and angles of the inlets (see Table S-1 of supplementary material for further details). The size of the inlets is responsible for the core of the flow patterns, suggesting that bigger inlets have more dispersed cores and more homogeneity in the pattern. The second variable with the largest impact is the tangential angle, α. As observed in co-current dryers [A13], the analysis of α shows that the experiments with non-swirling flow pattern are more instable that the ones with swirl flow. The use of normal angles does not achieve air mixing before the cylindrical part forming irregular patterns in which the cores of the ports can be distinguished. On the contrary, larger β angles generate higher irregularities. An axial orientation does not favour the homogenization of the airflow by impact with the walls, maintaining irregular patterns in the cylindrical chamber.

$$\varphi_u = \frac{\sum_{z=1}^{z=2}\sum_{r=2}^{r=4}\sum_{i=1}^{i=50} u_{irz} - u_{i1z}}{U_{avg}} \quad (14)$$

$$\varphi_w = \frac{\sum_{z=1}^{z=2}\sum_{r=2}^{r=4}\sum_{i=1}^{i=50} w_{irz} - w_{i1z}}{U_{avg}} \quad (15)$$

For a better understanding of the results and considering the differences in the airflow pattern, the analysis of the results is also performed independently for swirling and non-swirling flows. In the case of non-swirling flows (α=0), the SA shows that the size of the inlets is also the most relevant geometrical parameter in the instabilities followed by β and the asymmetric distribution at the inlets (see Table S-2 of the supplementary material for further details). The size of the inlets shows to increase the instabilities when it is reduced meanwhile β shows to increase them when it is also increased as in the previous case. With regards to the asymmetry in the ports, the instabilities of the vortex increase when their distribution is more irregular. This effect is generated because of the low mixing achieved under non-swirling airflow. The cores of the vortex correspond to the inlet ports and an increase in the irregular distribution in the ports results in an increase in the instability of the flow in the upper cylindrical region.

The importance of promoting mixing in the non-swirling flows is also observed in swirling flows. However, the geometrical parameters that have a higher impact in swirling flows are slightly different, see Table S-3 of the supplementary material. Together with the size of the inlets, the number of inlets also has a significant impact. The influence of placing more inlets favours the homogeneity of the flow, reducing the instabilities. In this case, the mixing achieved by using the tangential angle is high enough. In fact, in some cases the swirl intensity is so high that the vortex has a higher contact with the wall even before the contraction, see experiment 10 of Figure S-1 of the supplementary. For a better understanding of the different behaviours of the flow and the impact that they have on the instabilities, the experiments performed in the study of section 2.3.A.3.2.1 are analysed in the following section.

Table 3. Results for the analysis of the instabilities of the vortex.

Experiment	φ_u	φ_w	$\varphi = \varphi_u + \varphi_w$
1	13.18	167.87	181.05
2	26.39	31.20	57.59
3	220.73	68.93	289.66
4	65.47	86.16	151.64
5	69.52	33.24	102.76
6	20.68	25.88	46.56
7	191.79	100.25	292.04
8	45.80	22.48	68.29
9	63.63	83.72	147.35
10	44.98	56.42	101.40
11	28.44	32.32	60.76
12	13.18	11.91	25.09

Analysis of swirl intensity.

Apart from the study of the asymmetries, the role that the geometrical parameters have on the swirl intensity before and after the contraction for the swirling experiments is also analysed at locations 0 and cyl1 from Figure 1, A). The results for these swirl intensities are presented in Table 4 and a SA has been also carried out to determine the most significant geometrical parameters. It is obtained that under the same tangential angle, the geometrical parameter with the highest impact on the swirl intensity is the size of the inlets (see Table S-4 of the supplementary material), which has been shown to take part on the swirl intensity introduced, Eq. (3). The study of the swirl is completed evaluating if Eq. (6) holds. For the validation, the measurements have been carried out under a contraction degree of χ=1.1715, which should correspond to a swirl ratio (S_{cyl}/S_o) of 0.924 as presented in Eq. (6). In experiments 2 and 6 similar values are obtained even considering that the flow has oscillations and it is affected by the WSS generated by the deposits. This effect of the roughness is more relevant in the remaining experiments with swirl flow, which show a substantial reduction of the swirl intensity in the contraction. The reduction is more significant with smaller inlets and with a higher tangential momentum. As a result from the higher swirl intensity introduced in the chamber, the air has more contact with the deposits of the walls resulting in a much greater drop. Therefore, it can be deduced that there must be a critical swirl intensity where the vortex starts to be governed by the wall generating higher WSS in the contraction. A most detailed analysis with intermediate swirl intensities is also provided in the following section.

Table 4. Swirl intensity results.

Experiment	S_o	S_{cyl}	S_{cyl}/S_o
2	3.38698	3.183	0.93967
4	15.9095	6.754	0.4245
6	2.09875	2.253	1.0735
9	13.20235	6.486	0.4913
10	9.1375	4.950	0.5418
11	4.9405	3.414	0.6911

The swirl intensity obtained in the previous cases is high enough to show recirculation in the centre. Furthermore, in experiment 4 two recirculation regions are observed, see Figure S-2 of the supplementary material. The first one corresponds to recirculation in the central axis and the other region is located near the walls. The recirculation in the centre is generated by the VBD of the vortex that even takes place in the cylindrical region and it is also observed for experiments 9 (this one have similar S_{cyl1}) and 10. However, the origin of a recirculation region near the wall is only observed in experiment 4, which is the one with the highest S_0. In experiment 9, which is the one with the second highest S_0, a decrease of the velocity in the same zones where recirculation takes place in experiment 4 is also observed. This decrease suggests that the swirl intensity is close to the critical level, which is approximately 14, to generate a second recirculation region as observed in the top contraction of the dryer. The velocity profiles of experiment 4 have also been evaluated in the cylindrical chamber, and the second recirculation zone is not found at the height of cyl1, see Figure S-3 of the supplementary material. This observation at cyl1, which corresponds to the lowest height in the cylinder, justifies the no observation of a second recirculation at the bottom in previous works of this dryer chamber [A20]. However, it should not be forgotten in the design or modification of future chambers since it could explain part of the instabilities observed in the airflow pattern at the bottom part of similar chambers such as the one presented by Wawryzniak et al. [A12]. In the case that high operating swirl intensities will be desired, the presence of this second region or recirculation can be avoided by the suppression/reduction of the hip, resulting in a free swirl, whose stability can be improved by increasing the swirl intensity forcing the contact with the walls.

Analysis of the precessing frequency in the cylinder

Another characteristic variable always related to PVC is the precessing frequency, which is analysed as follows. Different points are located in a relative height of 2.2 (cyl1) and 3.35 (cyl2) z/D and a relative radius of 0, 0.23, 0.47 and 0.7 r/R respectively. The velocity is sampled at these points with a time-step of 0.2 s. The frequency for the velocity is computed using the fast Fourier transform algorithm. The power spectrum of the frequency, P_{DFT}, is finally computed from the discrete Fourier transform of the data as presented in Eq. (16). One example of the power spectrum is shown in Figure S-4 of the supplementary material. The

characteristic frequency of the PVC is determined as the maximum from the power spectrum. Furthermore, the characteristic Strouhal number, which is self-similar to the Reynolds number and can be applied to estimate the frequency under different Re [A25, A42], is also computed. A summary of the results for f_{PVC} and St in z/D=2.2 and r/R=0.47 are presented in Table 5. As for the irregularities of the flow pattern, a SA to understand the influence of the geometrical parameters on f_{PVC} is carried out showing that an increase in all the terms results in a reduction of f_{PVC}, see Table S-5 of the supplementary material. These terms are compared in the following lines with the terms that influence in its definition, see Eq. (A-1) to (A-4) of the appendix and the different contributions in the frequency of the PVC, see Eq. (A-5) [A24].

$$P_{DFT}(i) = abs\left(F\left(v(i)\right)\right)^{2/n} \tag{16}$$

$$St = f_{PVC} \cdot D/U_{avg} \tag{17}$$

Apart from the tangential angle, α, the geometrical parameter with the highest influence on the precessing frequency is the angle β. An increase of β results in lower swirl intensities, which also reduces the frequency since the bi-normal velocity of the vortex, $\widehat{u_b}$, and the vortex intensity, Γ, are also smaller. A similar trend, and with the same justification, is also observed with respect to the size of the ports. Their increase results in lower swirl intensities and subsequently in lower vortex intensities that reduce the characteristic frequency. The parameter with the second highest influence after the angle β is the location of the inlet ports. Even though the locations farther from the central axis can generate higher swirl intensities and subsequently higher frequencies, there is no evidence about the influence of this parameter and the modification in the frequency can also be due to the modification of the centre of the precessing core and its width. The point of measurement is fixed and the core centre and width change with the geometrical parameters. The last parameter studied is the irregular distribution of the air through the inlet ports. In the cases where the air is introduced homogenously, a lower frequency is obtained. The influence of this irregular distribution can be obtained from the decomposition of f_{PVC} in different terms. In that decomposition the terms of curvature and torsion, which depend on the radius and pitch of the helix [A24], can be influenced by the asymmetric distribution of the inlets.

Table 5. Frequency of the PVC and Strouhal number.

Experiment	f_{PVC} (Hz)	St
2	1.1	1.73
4	3.2	4.63
6	1.4	0.5788
9	1	1.447
10	2	2.894
11	1.6	2.315

2.3.A.4.2 Results for the detailed study of vortex regimes and instabilities

The analysis of the previous section has identified that the angles and the size of the inlet ports have the highest influence on the unstable oscillations of the vortex and the swirl intensity introduced in the dryer. For a better understanding of the influence of these parameters, the DOE presented in section 2.3.A.3.2.2 is evaluated in this section.

Analysis of the swirl intensity.

The first study focuses on characterising the swirl intensity and the dimensionless angular flux, Ω, at the entrance and the influence that the geometrical parameters have on them. The results obtained for both at the entrance are presented in Table 6. This table also presents a comparison with the theoretical definition of Ω given by Eq. (3). It can be seen that the definition provides a good estimation of the angular momentum introduced in the dryer, see also the parity plot in Figure S-5 of the supplementary material. Furthermore, a SA of the geometrical parameters defined in Eq. (3) is also carried out, obtaining that the size of the inlets has as much influence as the tangential angle in increasing the swirl intensity for the range of angles studied, see Table S-6 of the supplementary material. Thus, with sufficient tangential angle, an easier way to increase the swirl intensity can be done by reducing the size of the ports.

Apart from the analysis on the generation of the swirl intensity, its decay in the contraction and through the cylinder is also analysed. The change of swirl intensity in the contraction is presented in Table 6. In the cases with low swirl intensity at the bottom of the dryer, it is maintained or even increased along the contraction. In these cases, the vortex at the bottom of the dryer is "free", without having significant contact with the wall. In fact, in some cases the cores of the vortex are still expanding and they show an increase of the swirl intensity. On the contrary, for high S_o this behaviour of the vortex is not observed, showing that the swirl intensity after the contraction follows a logarithmic function with respect to the swirl in the bottom, see Figure S-6 of the supplementary material. This function suggests the influence of the logarithmic law used for modelling the near wall flow, which generates a WSS reducing the swirl intensity. A similar analysis can be carried out by evaluating the swirl ratio, S_{cyl}/S_o, which shows to be correlated by a negative power with the initial swirl intensity, see Eq. (18) and Figure 4. This correlation also shows that the reduction of the swirl intensity is a function of the initial swirl intensity. At higher S_o, the contact with the wall is favoured increasing the WSS generated and it subsequently shows a low increase of S_{cyl}.

$$\frac{S_{cyl}}{S_o} = aS_0^{-b} = 1.1446 * S_0^{-0.2815} \quad (18)$$

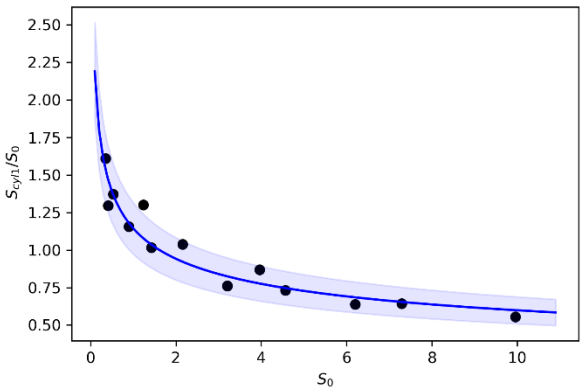

Figure 4. Influence of swirl intensity on the ratio of swirl intensities.

The distinction of the two regimes (free and wall governed) for the vortices is also observed from the analysis of the WSS, see Figure S-7 in the supplementary material, showing:

- A Free vortex in which low swirl intensities have a low increase in the WSS because of the low contact of the air with the wall. The swirl is shown to be less controlled by the wall, being highly influenced by the smooth contraction and the acceleration resulting from that.
- Wall governed vortex: At high swirl intensities, the WSS shows a linear relationship with S_{cyl}. In this second regime, the core of the vortex is closer to the wall, being more influenced and governed by the contact with the wall. Furthermore, the reduction of the swirl in the contraction is much more significant having values below 1, S_{cyl}/S_o <1, and tending to an asymptotic value of 0.5, see previous Figure 4.

The identification of these two type of regimes in the vortices, may modify the effects that each geometrical parameter have on the swirl intensity generation. Independent SA's have been performed for each regime showing that:

- In the case that the vortex is free, the tangential angle is the main driver for modifying the swirl intensity, see Tables S-7 and S-8 of the supplementary material.
- However, in the case that the vortex is governed by the contact with the wall in the contraction, the main driver is the size of the inlets, see Tables S-9 and S-10. Under these conditions the tangential angle is enough for providing a tangential component and the swirl is easier to be increased by reducing the inlet size.

Apart from the two previous regimes, another distinction within the free vortex is also observed. The analysis of the velocity profiles show that after the contraction a central recirculation region is observed for swirl intensities higher than 1. This central recirculation region indicates the formation of a VBD as also remarked by other authors in swirling flows under contraction [A32]. Further details are provided in Figure S-8 of the

supplementary material comparing experiments MαHβHSize ($\Omega_i = 0.918$) and HαMβHSize ($\Omega_i = 1.598$).

The last analysis of the swirl intensity evaluates the decay of the swirl intensity along the cylinder (measuring from cyl1 to cyl5 of Figure 1, A)) determining the parameters of Eq. (8) and (9). Once the parameters are determined for each case, the robustness of the equations is evaluated extrapolating the equations to the inlet ($z\text{-}z_{ref}/D=0$) and obtaining the results presented in Table 6 for Ω_{ref}. Comparing the estimated values of Eqs. (8) and (9) with the one measured at the ports, Ω_i, it can be seen that the best estimation of the initial swirl is given by Eq. (8). Even though Eq. (9) have more parameters to be fitted and it have shown less error in the prediction of the swirl intensity at different heights; it should be carefully used when the swirl intensity wants to be predicted by extrapolating to different heights and a best estimation can be carried out by using Eq. (8). The errors in the extrapolation to the inlet are especially significant at low swirl numbers. However, as it has been reported in previous works [A20, A36] the model is not designed for low swirl intensities and in these cases the error can be understood. Nevertheless, it can be seen that Eq. (9) also have higher errors on extrapolating the swirl intensity for high swirl intensities, remarking again that Eq. (8) is a best method to extrapolate the Swirl intensity.

Table 6. Swirl intensity obtained from the CFD simulations and reduced models of the experiments in the response surface DOE.

Experiment	S_o	S_{cyl}	S_{cyl}/S_o	Ω_i	Estimated Ω_i from Eq. (3)	Ω_{ref} Eq. (8)	Ω_{ref}Eq.(9)
HαMβLSize	9.96	5.52	0.55	7.362	7.338	5.762	4.73
MαMβMSize	3.20	2.44	0.76	2.366	1.313	2.507	5.17
MαHβLSize	7.29	4.69	0.64	5.388	2.760	4.926	4.49
LαMβLSize	0.90	1.04	1.16	0.665	1.279	1.121	2.81
MαHβHSize	1.24	1.61	1.30	0.918	0.388	1.669	1.56
HαMβHSize	2.16	2.25	1.04	1.598	1.032	2.358	1.87
HαHβMSize	3.96	3.44	0.87	2.931	1.366	3.567	3.78
MαLβLSize	6.21	3.97	0.64	4.587	5.657	4.094	3.84
MαMβMSize	3.20	2.44	0.76	2.366	1.313	2.507	3.08
HαLβMSize	4.57	3.34	0.73	3.378	2.798	3.459	9.44
LαMβHSize	0.41	0.54	1.29	0.307	0.180	0.537	1.68
LαLβMSize	0.35	0.56	1.61	0.258	0.488	0.554	10.96
MαLβHSize	1.43	1.45	1.02	1.054	0.795	1.496	3.23
LαHβMSize	0.53	0.72	1.37	0.390	0.238	0.724	6.73
MαMβMSize	3.20	2.44	0.76	2.366	1.313	2.507	3.08

Analysis of instabilities in the airflow pattern

The two regimes identified result in different behaviours of the unstable oscillations within the cylindrical chamber. The results of the irregularities of the airflow pattern generated by the unstable oscillations in each of the experiments are presented in Table 7. The influence of the geometrical parameters in the generation of irregularities has been evaluated including all the experiments, Table S-11, and making a distinction per regime, Tables S-12 and S-13 of the supplementary material. In the case that all experiments are included, the tangential angle and the size of the inlets have the largest impacts suggesting more stable patterns when they are increased. However, if one makes a distinction by regime, the results obtained for the free regime with low Swirl intensity and low WSS (see Table S-12 of the supplementary material) show that the irregularities are mainly governed by the size of the inlets. In the case of high swirl intensities these irregularities are mainly governed by the tangential angle.

With the objective of understanding the influence by means of a scalable parameter, the irregularities are also analysed as a function of the swirl intensity, S_0. Evaluating all the experiments, a slight decrease as the swirl intensity increases is shown, see Figure S-9 and S-10 of the supplementary material. However, the correlation between both involves high uncertainty. The analysis of the influence of the swirl intensity on the irregularities of the airflow patterns for each regime also shows that in free regime the irregularities decrease with an increase of the swirl intensity as observed in co-current swirl spray dryers. However, in wall governed vortex they do not show a correlation with the swirl. They show high uncertainty when they are compared with the swirl, showing a slight increase when they are compared with S_0 and S_{cyl1}, see Figure S-11 and S-12 in the supplementary material. These high oscillations could be due to the existence of stagnation regions after the contraction, which are not shown by the RANS approach but are accounted in the turbulence energy balance and a modification of the turbulent dissipation rate, ε_{ij}, is observed, see description and Figure S-13 in the supplementary material for further detail. The wall governed regime with higher swirl intensities show a higher turbulent dissipation that suggest higher number of small uncontrollable eddies meanwhile the free regime shows bigger stable eddies in the stagnation region. Therefore, less and more controlled patterns are expected within the transition from the free to wall governed vortex. Between this transition, it is preferred that the system operates with a swirl in the free regime since the degree of irregularity can be estimated from the swirl intensity as presented in Eq. (19) and Figure 5. However, in the case of wall governed regime, it does not show a correlation with either the S_0. This impact that the swirl intensity and the contraction play on homogenising the vortex explains the instabilities observed by Francia et al. [A20] in the different counter-current swirl dryers. The geometries that have higher contraction ratio, χ, and less swirl intensity tend to favour the instabilities.

$$\varphi = 22.534 \cdot S_0^{-0.4205} \quad (19)$$

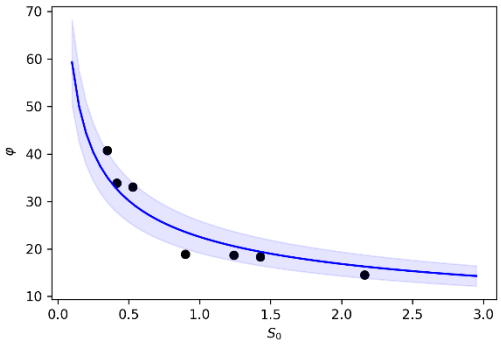

Figure 5. Decay of φ as function of swirl intensity. Validation of Eq. (19).

Table 7. Instabilities obtained from the CFD simulations of the response surface DOE.

Experiment	φ_u	φ_w	$\varphi = \varphi_u + \varphi_w$
HαMβLSize	4.66	8.45	13.1
MαMβMSize	26.23	18.88	45.1
MαHβLSize	27.57	33.81	61.4
LαMβLSize	16.11	30.95	47.1
MαHβHSize	12.28	6.42	18.7
HαMβHSize	9.26	5.25	14.5
HαHβMSize	6.23	6.76	13.0
MαLβLSize	12.67	16.09	28.8
MαMβMSize	26.23	18.88	45.1
HαLβMSize	10.69	11.33	22.0
LαMβHSize	21.90	11.95	33.8
LαLβMSize	15.02	25.75	40.8
MαLβHSize	10.35	8.01	18.4
LαHβMSize	19.12	13.94	33.1
MαMβMSize	26.23	18.88	45.1

Analysis of the precessing frequency in the cylinder

The last study carries out an analysis of the precessing frequency at cyl1. The results obtained for the frequency and the Strouhal number are presented in Table S-14 of the supplementary material. As observed in the screening analysis, the geometrical parameters that increase the swirl intensity also have an increase on the precessing frequency since the vortex intensity, Γ, is increased. Based on this fact, the Strouhal number is analysed as a function of the swirl intensity, obtaining the correlation presented in Eq. (S-2) and Figure S-14. The comparison between both numbers show a linear correlation but with high dispersion.

From the analytical model of the precessing frequency, see Appendix, it is shown that the tangential component of the velocity increases the frequency, but it is not the only one that modifies it. Other variables such as the radius and pitch of the vortex also modify the frequency. For a most detailed of the influence of each of the parameters an analytical reconstruction of the vortex within the dryer can be performed in future works.

The analysis of the effect of the swirl intensity on the frequency is complemented with an analysis between the frequency and the irregularities of the airflow pattern. The analysis is only carried out for the cases with a free vortex since in wall governed regime the irregularities are highly modified by the contact with the wall. The trend observed for a free vortex is presented in Figure S-15 of the supplementary material, suggesting a decrease of the instabilities when the frequency is increased. This trend is expected since high swirl intensities have shown higher frequencies and less instabilities. However, the trend between the frequency and the instabilities does not show the source of the frequency that mainly affects the instabilities. Each of the terms of the frequency (Eq. A-5) can balance between them and the conclusions obtained for this trend cannot be generalized for all the contributions of the frequency and the geometrical parameters of the ports. For example, in the previous screening analysis it has been shown that the frequency increases when the distribution of the air in the port is asymmetric, which have also shown to increase the instabilities in the air.

2.3.A.4. CONCLUSIONS

This work has presented a CFD based numerical study focused on the instabilities generated in the swirl flow of counter-current spray dryers. Special attention has been paid to the swirl generation system, where the different geometrical parameters involved in the ports have been evaluated. As a result from the numerical analysis, a deeper understanding of the vortex within the dryer is obtained defining the regimes as presented in Figure 6. The regimes are separated by three critical swirl intensities. The first critical swirl, S_{cr1}, identifies the formation of the VBD as proposed by previous researchers. If the Swirl intensity after the contraction is above 1, the central recirculation starts to be generated at the bottom of the dryer.

The second swirl intensity, S_{cr2}, identified here separates the behaviour of the vortex in:

- A free vortex regime where the vortex has low contact with the smooth contraction used in the counter-current dryer. In this regime, the swirl intensity is mainly governed by the angle and the irregularities caused by uncontrolled instabilities of the airflow show a decay when the swirl intensity is increased. This pattern shows a minimum in the instabilities in the transition from this free vortex to the wall governed vortex.
- A wall governed vortex for swirl intensities higher than S_{cr1}. Under this regime, it has been observed that the instabilities generated do not correlate with the swirl intensity, being more difficult to control since wall separation phenomena takes place generating stagnation regions after the smooth contraction. In the current work, a RANS approach has been used for the modelling and eddies generated in those stagnation regions are not captured but modifications in the turbulent dissipation

are observed. In future works, more detailed approaches such as large eddy simulations (LES) or Detached Eddy simulations can be used to reproduce the eddies. However, the inclusion of a roughness mechanism in LES should not be forgotten since the roughness generated by the deposits has been demonstrated to also govern the flow pattern.

The third critical swirl, S_{cr3}, governs the presence of recirculation at the bottom of the chamber, where swirl is generated. In the case that the swirl intensity is smaller than S_{cr2}, no recirculation is observed. However, in the case than $S>S_{cr2}$, the VBD in the generation chamber generates that recirculation. Apart from the swirl intensity, the generation of this recirculation is also governed by the contraction ratio, χ, at the smooth contraction of the bottom part. In future works, different contraction ratios can be evaluated with the objective of generating a map for the two swirl intensities as it has been done in analytical studies for lab scale cases (Leclaire and Jacquin, 2012).

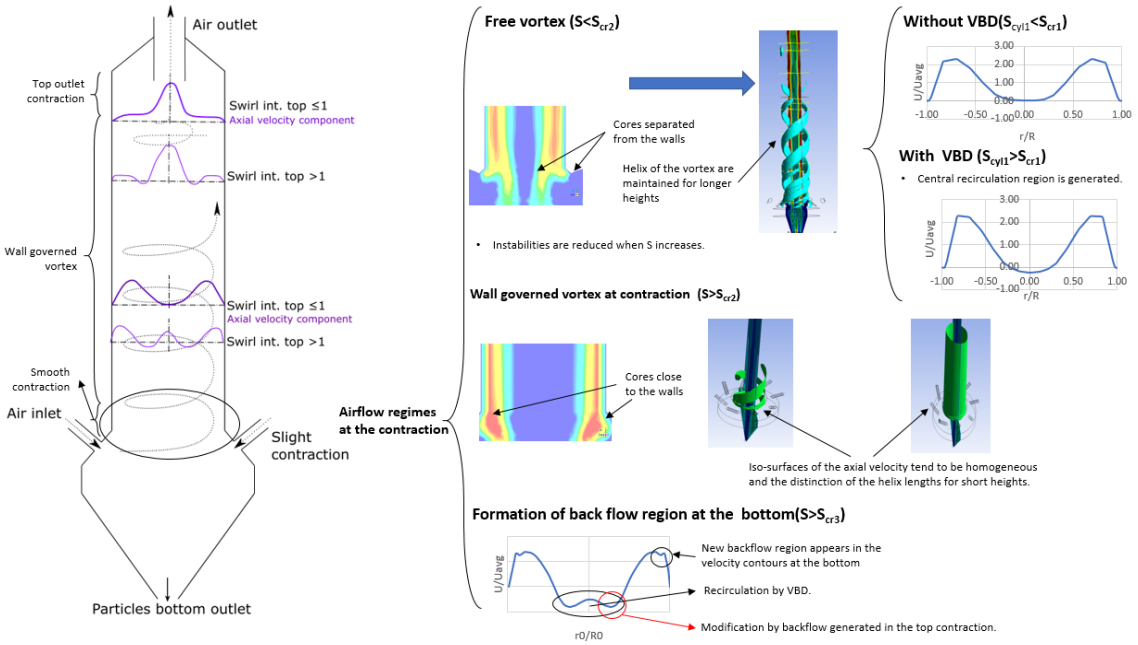

Figure 6. Summary of flux states in each of the sections of the counter-current dryer with swirl flow.

Taking into account the current study of the irregularities carried out and assuming that the angle of the inlet will be flexible, the airflow in the dryer is suggested to operate as free vortex near the transition to wall governed vortex. Considering that the presence of deposits reduces the swirl intensity but they are low in the contraction section, it is recommended to start the operation in the transition from free to wall governed regime. At the beginning of the operation the deposits grow until achieving a dynamic equilibrium [A20, A43]. As a result, the swirl intensity will be reduced by an increase of the WSS generated by the deposits and the vortex will be favoured to operate in the free regime but with low and controllable irregularities in its pattern.

APENDIX

Constants of the RSM turbulent model

$$C_{\varphi 1} = 1.8 \;\; C_{\varphi 2} = 0.6 \;\; C'_{\varphi 1} = 0.5 \;\; C'_{\varphi 2} = 0.3$$
$$C_{\mu} = 0.09 \;\; C_{\varepsilon 1} = 1.44 \;\; C_{\varepsilon 2} = 1.92 \;\; \sigma_{\varepsilon} = 1.3 \;\; \sigma_{k} = 1$$

Definition of the precessing frequency used in the analysis.

In Eq. (A-1) an analytical definition of the precessing frequency is given as function of the characteristic parameters of the vortex core. In Eq. (A-1) Γ is the vortex intensity defined as eq. (A-2), a is the radious of helical structure, τ is defined according to eq. (A-3), dependent on the pitch of the helix (l) and the radius of the helical structure, a. The pitch can be computed from the velocities as presented in Eq. (A-4). Finally, u_b is the dimensionless bi-normal velocity for a helical vortex (Alekseenko et al. 1999).

$$f = \frac{\Gamma}{8\pi^2 a^2} \frac{\widehat{u_b}}{\tau(1+\tau^2)^{1/2}} \quad \text{(A-1)}$$

$$\tau = l/a \quad \text{(A-2)}$$

$$\Gamma = 2\pi \cdot W_{max} \cdot r|_{W-W_{max}} \quad \text{(A-3)}$$

$$\frac{1}{l} = \frac{U_{ax}-\overline{U}}{W \cdot r} \quad \text{(A-4)}$$

Furthermore, the frequency is decomposed in structure dependent terms as in eq. (A-5), where f_c is the contribution of the curvature, f_t is the torsion, f_r is the contribution generated by the walls and f_β is the frequency generated by the velocity at the axis. The formula assumes that the helical vortex has a nonzero velocity of its own motion along the nozzle axis.

$$f = f_{cu} + f_t + f_r + f_\beta \quad \text{(A-5)}$$

NOMENCLATURE

Symbols

a	Radius of the helix (m).
A	Area (m^2)
C_{ij}	Mean flow of convection (m^2//s^2)
C_s	Roughness constant
D	Diameter from the axial axis to the wall (m).
D_{ij}	Transport by diffusion (m^2/s^2)
f	Frequency.
g	Gravity constant (9.81 m/s^2).
G	Mass flow rate (kg/s)
k	von-Karman constant (0.41).
l	Pitch of the helix (m).
P	Pressure (Pa)
P_{DFT}	Power spectrum function of the frequency.
P_{ij}	Turbulence production tensor (m^2/s^2).
r	Radial position (m).
R	Radius from the axial axis to the wall (m).
R_{core}	Radial location of the centre of the Vortex core (m).

R_{ij}	Reynolds stress flux (m^2/s^2).
Re	Reynolds number.
S	Local Swirl intensity.
St	Strouhal number.
s_{Fluent}	Roughness height (m).
$\overline{U}$	Axial velocity (m/s).
U_{av}	Average axial velocity (m/s).
u^*	Dimensionless velocity in the logarithmic law in the wall.
$\widehat{u_b}$	Bi-normal velocity of the vortex core (m/s).
V	Global velocity (m/s).
W	Tangential velocity (m/s).
z	Axial distance from the ports (m)
α	Tangential angle of the port.
β	Axial angle of the port.
χ	Contraction ratio.
ε_{ij}	Turbulence dissipation rate (m^2/s^2).
σ	Size of the core in the calculation of the frequency terms (m).
ΔB	Additive constant of the logarithmic law.
λ	Decay rate for the swirl intensity.
φ	Instabilities (m/s).
Ω	Swirl intensity using the cylinder as reference.
Φ_{ij}	Pressure rate of strain tensor (m^2/s^2).
μ	Viscosity (Pa·s)
ρ	Density (kg/m^3).
τ	Relative pitch.
$\tau_{w\theta}$	Tangential WSS (Pa).
$\tau'_{w\theta}$	Dimensionless tangential WSS.
Γ	Vortex intensity (m^2).
ψ_{ij}	Transport due to rotation (m^2/s^2).

Subscripts

0	Location at the smooth contraction.
C	Referred to the cylinder.
cu	Curvature
Cyl1	Location at the cylindrical chamber (z/D=0.45)
Cyl2	Location at the cylindrical chamber (z/D=2.2)
Cyl3	Location at the cylindrical chamber (z/D=7.4)
Cyl4	Location at the cylindrical chamber (z/D=8.6)
Cyl5	Location at the cylindrical chamber (z/D=9.8)
i	Referred to the inlets.
Max	Referred to the maximum tangential velocity of the vortex.
ref	Height of reference for swirl decay evaluation.
t	Torsion.
r	Frequency generated by the walls.
u	Referred to axial velocity.
v	Referred to tangential velocity.
z	Referred to the axial component.
β	Frequency generated by the velocity at the axis.
θ	Referred to the angular component.

Abbreviations

CFD	Computational Fluid Dynamics.
DOE	Design of experiments.
PISO	Pressure-Implicit with Splitting of Operatiors.

PRESTO!	PREssure STaggering option.
PVC	Precessing vortex core.
RSM	Reynolds-Stress Model of turbulence
SA	Statistical analysis.
VBD	Vortex breakdown.
WSS	Wall shear-stress.

REFERENCES

[A1] Masters, K., 1972. Spray Drying: An introduction to Principles, Operational Practice and Applications. London: Leonard Hill Books.

[A2] Southwell, D.B. Langrish, T.A.G., 2001. The Effect of swirl on flow stability in spray dryers. Trans. IChemE, Vol. 79, Part A, 2001.

[A3] Huang, L. Kumar, K. Mujumdar, A.S.. 2003a Use of Computational Fluid Dynamics to Evaluate Alternative Spray Dryer Chamber Configurations, Drying Technology, 21 (3), 385-412.

[A4] Huang, L. Kumar, K. Mujumdar, A.S., 2003b. A Parametric Study of the Gas Flow Patterns and Drying Performance of Co-current Spray Dryer: Results of a Computational Fluid Dynamics Study. Drying Technology, 21, 957-978.

[A5] Soltani, S. Gerde, P. Acevedo, F. Rasmuson, A., 2015. Counter-current spray drying with stream separation: Computational modeling of a novel dryer design. Chem. Eng. Res. Design, 93, 163-173.

[A6] Huntington, D. H., 2004. The influence of the Spray Drying Process on Product Properties. Drying Technology, Vol. 22, No. 6, 1261-1287.

[A7] Rahman, U.J.U. Baiazitov, I. Pozarlik, A.K. Brem, G., 2018. CFD study of air flow patterns and droplet trajectories in a vortex chamber spray dryer. 21st International Drying Symposium.

[A8] Chang, F. Dhir, V.K., 1994. Turbulent flow field in tangentially injected swirl flows in tubes. *Int. J. Heat Fluid Flow*, 15 (5), 346-356.

[A9] Derksen,J. Van den Akker, H.E.A., 2000. Simulation of vortex core precession in a reverse-flow cyclone. AIChe J. 46 (7), 1317-1331.

[A10] Andoh,R.Y.G. Hides, S.P. Saul, A.J., 2002. Improving Water Quality Using Hydrodynamic Vortex Separators and Screening Systems. 9th International Conference on Urban Drainage, Portland, Oregon, USA.

[A11] Dulin, V. M. Lobasov, A. S. Chikishev, L.M. Markovich, D. M. Hanjalic, K., 2019. On the impact of helical structures on stabilization of swirling flames with Vortex Breakdown. Flow, Turbulence and Combustion, 103, 887-911.

[A12] Wawrzyniak, P. Podyma,M. Zbicinski,I. Barczak,Z. Rabaeva, J., 2012. Modeling of Air Flow in an Industrial Countercurrent Spray-Drying Tower. Drying Technology, 30:217-224, 2012.

[A13] Southwell, D.B. Langrish, T.A.G. Fletcher, D.F. 2001. Use of Computational Fluid Dynamics Techniques to assess design alternatives for the plenum chamber of a small spray dryer. Drying Technology, Vol. 19 (2), 257-268.

[A14] Guo, B. Langrish, T.A.G. Fletcher, D.F., 2001. Numerical simulation of unsteady turbulent flow in axisymmetric sudden expansions. J. Fluids Engineering., 123, 574:587.

[A15] Langrish, T.A.G. Williams, J. Fletcher, D.F., 2004. Simulation of the effects of inlet swirl on gas flow patterns in a pilot-scale spray dryer. Chemical Eng. Research and Design, 82 (A7): 821-833.

[A16] Leibovich, S., 1984. Vortex stability and breakdown: survey and extension. AIAA, J. 22 (9), 1192-1206.

[A17] Lucca-Negro, O. O'Doherty, T., 2001. Vortex breakdown: a review. Progress in Energy and Combustion Science 27 (2001) 431-481.

[A18] Rusak, Z. Zhang, Y. Lee, H. Wang, S., 2017. Swirling flow states in finite-length diverging or contracting circular pipes. J. Fluid Mech. (2017), 819, 678-712.

[A19] Escudier, M.P. and Keller, J.J., 1985. Recirculation on Swirling Flow: A Manifestation of Vortex Breakdown. AIAA Journal, 23, 1, 111-116.

[A20] Francia, V. Martin, L. Bayly, A.E. Simmons, M.J.H., 2015. Influence of Wall friction on flow regimes and scale-up of counter-current swirl spray dryers. Chemical Engineering Science, 134, 399-413.

[A21] Syred, N., 2006. A review of oscillation mechanisms and the role of the Precessing Vortex Core (PVC) in Swirl Combustion Systems, Prog. Energy Combust. Sci. vol. 32, 2, 93-161, 2006.

[A22] Chanaud, RC., 1965. Observations of oscillatory in certain swirling flows. J. Fluid Mech 21:111-127.

[A23] Alekseenko, SV. Kuibin, PA. Okulov, VL. Shtork, SI., 1999. Helical vortices in swirl flow. J. Fluid Mech 382: 195-243.

[A24] Alekseenko, S.V. Kuibin, P.A. Okulov, V.L., 2007.Theory of Concentrated Vortices: An Introduction. Springer Science & Bussiness Media.

[A25] Litvinov, I.V. Shtork,S.I. Kuibin,P.A. Alekseenko, S.V. Hanjalic, K., 2013. Experimental study and analytical reconstruction of precessing vortex in a tangential swirler. Int. J. Heat and Fluid Flow.

[A26] Hreiz, R. Gentric, N. Midoux, 2011. Numerical investigation of swirling flow in cylindrical cyclones. Chem. Eng. Res. Des. 89, 2521-2539.

[A27] Woo, M.W. Daud, W.R.W. Mujumdar, A.S. Wu, Z. Talib, M.Z.M. Tasirin,S.M., 2009. Non-swirling steady and transient flow simulations in short-form spray dryers. Chemical product and process modeling.

[A28] Kitoh, O., 1991. Experimental study of turbulent swirling flow in a straight pipe. *J. Fluid Mech*. 1991 225, 445-479.

[A29] Steenbergen, W. Voskamp, J., 1998. The rate of decay of swirl in turbulent pipe flow. *Flow Meas. Instru*. 1998 9, 67-78.

[A30] Hernández, B. Fraser, B. Martin de Juan, L. Martin, M., 2018. Computational Fluid Dynamics (CFD) Modeling of swirling Flows in Industrial Counter-Current Spray-Drying Towers under Fouling Conditions. Ind. Eng. Chem. Res. 57, 35, 11988-12002.

[A31] Francia, V. Martín, L. Bayly, A.E. Simmons, M.J.H., 2015b. An experimental investigation of the swirling flow in a tall-form counter-current spray dryer. Experimental Thermal and Fluid Science, 65, 52-64.

[A32] Rusak, Z. Meder, C.C., 2004. Near-critical Swirling Flow in a Slightly Contracting Pipe. AIAA Journal, 42 (11), 2284-2293.

[A33] Leclaire, B. Jacquin, L., 2012. On the generation of swirling jets: high-Reynolds-number rotating flow in a pipe with a final contraction. Journal of Fluid Mechanics, 692, 78-111.

[A34] Mclelland, G. MacManus, D. Sheaf, C., 2015. The effect of streamtube contraction on the characteristics of a streamwise vortex. Journal of Fluids Engineering, 137.

[A35] Najafi, A.F. Mousavian, S.M. Amini, K. 2011, Numerical investigations on swirl intensity decay rate for turbulent swirling flow in a fixed pipe. Int. J. Mech. Sci. 53, 801-811.

[A36] Senoo, Y. Nagata, T. (1972) Swirl flow in long pipes with different roughness. Bullet. JSME, 5 (90), 1514

[A37] Erdal, F. 2001. Local measurements and computational fluid dynamics simulations in a gas-liquid cylindrical cyclone separator. Ph.D. Thesis, The University of Tulsa.

[A38] Gomez, L. Mohan, R. Shoham, O. 2004. Swirling gas-liquid two-phase flow. Experiment and modeling. Part II: Turbulent quantities and core stability. J. Fluids Eng. 126, 943-959.

[A39] Woo, M.W., 2017. Computational Fluid Dynamics Simulation of Spray Dryers. An Engineer's Guide. CRC Press. Taylor & Francis Group. ISBN: 978-1-4987-2464-7.

[A40] Roache, P.J., 1994. Perspective: A Method for Uniform Reporting of Grid Refinement Studies. Journal of Fluids Engineering, 116 (3), 405-413.

[A41] Miltner, M. Jordan, C. Harasek, M., 2015. CFD simulation of straight and slightly swirling turbulent free jets using different RANS-turbulence models. Applied Thermal Engineering, 89, 1117-1126.

[A42] Malalasekera, W. Ranga,-Dinesh, K.K.J. Ibrahim, S.S. Masri, A.R. 2008. LES of recirculation and vortex breakdown in swirling flames. Combustion Sci. Tech. vol. 180, pp. 809-832, 2008.

[A43] Francia, V. Martín, L. Bayly, A.E. Simmons, M.J.H., 2015. The role of wall deposition and re-entrainment in swirl spray dryers. AIChE Journal, 61 (6), 1804-1821.

PART 2.3.B) NUMERICAL STUDY OF INESTABILITIES IN SWIRLING FLOW COUNTER-CURRENT DRYERS.

2.3.B.1 INTRODUCTION.

One of the results obtained from the first study is the uncontrolled instabilities in the wall governed regime. One of the reasons of these instabilities can be the generation of small eddies at the end of the smooth contraction by the formation of a stagnation region. However, this stagnation region is not observed in the CFD simulations with a Reynolds Stress turbulence model, also known as Very Large Eddy Simulation [B-1]. In order to reproduce the stagnation regions, the use of Large Eddy Simulations (LES) can be required to reproduce a large number of systems. However, this approach is very high computational cost consuming. An intermediate solution between LES and the Reynolds Average Navier Stokes (RANS) approach is the use of Dettached Eddy Simulation (DES) [B-2]. The use of this DES approach assumes a RANS approach surrounding boundary layers and free flows with a LES approach [B-3]. The methodology have shown good predictions in free-flows impacting solid bodies. Two interesting reviews of the DES approach and its applications in the last years are given in [B-4] and [B-5]. However, the use of DES in flows through internal systems has not been extensively explored even though LES have been performed in units such as cyclones [B-6], co-current spray dryers [B-7] or agitation tanks [B-8].Therefore, the aim of this part is to evaluate the possibilities of using DES in the modelling of the counter-current swirl dryer. Furthermore, this combination of both approaches is highly relevant for our case of study since the near wall region has been shown to require the use of logarithmic laws to attach the influence of the deposits in generating the wall shear stress that reduced the swirl intensity through the dryer. Thus, the first aim before using the DES approach for predicting eddies in the stagnation regions of the contraction is to validate the swirl intensity decay through the dryer and the velocity profiles. The use of the DES simulation approach has been evaluated under the default turbulence models available in ANSYS® Fluent. In the following section the DES approach is defined in a better detailed as well as the turbulent models available.

2.3.B.2 EVALUATION OF MODELS.

DES was developed to avoid the difficulties that standard LES simulation models had on computing the flow near the walls. In this wall bounded region the LES methodology is substituted by the RANS framework, which is faster and robust, generating the hybrid DES technique. The integration of both models is formulated by means of a distance function, $\tilde{d}$, as presented in Eq. (B-1). In this Eq. (B-1), d is the distance of the RANS model, C_{DES} is a constant and Δ is the largest dimension of the grid cell. As a result from this function, the model behaves as RANS in regions close the walls and like an LES away from them. In this LES is remarked that the flow is modelled with a Smagorinsky model in which eddies are computed until a filter-width length scale [B-9, B-10].

$$\tilde{d} = \min(d, C_{DES} \cdot \Delta) \quad \text{(B-1).}$$

Even though the concept of DES can be initially applied to any RANS model, the presence of damping functions in some models difficult the integration with LES since the solution of DES is not stable [B-5].In the current case, the RANS turbulence models to be evaluated for its integration in the DES simulation are limited to the ones available in ANSYS®, which are summarized in the following lines.

Spalart-Allmaras

This is a one equation turbulence model in which the eddy viscosity is computed as function of other viscosity-like variable, Eq. (B-2). This model includes a rotation tensor that can be used to reproduce the vortex. However, it has been mainly used in free shear flows for systems with low viscosity (e.g. aerofoils) [B-4, B-11]. Another advantage of the model is that it allows the use of logarithmic wall functions with a term for the roughness. This is highly necessary since the vortex is governed by the contact with the wall.

$$\nu = f_{\nu}\tilde{\nu} \tag{B-2}$$

Realizable k-ε

This turbulent model is a modification of the most popular k-ε model based on two equations (one for k and other one for ε) for the eddy viscosity, see Eq. (B-3). Furthermore, contrary to standard k-ε, in which C_μ is a constant, in the current realizable k-ε model C_μ is dependent of a relative velocity that includes the rotation tensor [B-12]. This inclusion of the rotation tensor allows the use of the model into rotating flows as it has been done for agitation tanks. However, it has been demonstrated to fail in the prediction of swirling free jets [B-13] and it does not allow to include the walls shear stress proportional to the roughness. Thus, it is possible that it will not have accurate predictions of the vortex within the dryer.

$$\nu_t = \frac{C_\mu k^2}{\varepsilon} \tag{B-3}$$

SST k-w

The Shear Stress Transport (SST) turbulence model is also a two equation model. In the current case the turbulent kinetic energy, k, and the turbulent dissipation ratio are used for modelling the eddy viscosity, see Eq. (B-4). The use of the turbulent dissipation ratio, ω, instead of the turbulent dissipation, ε, determines the scale of the turbulence in each of the cells allowing to achieve better description of eddies in the free regime [B-9]. The use of this SST k-w turbulence model have shown good results in separating flows and with adverse pressure gradients [B-14], among them swirling free jets [B-13]. However, it has the problem on the implementation of the logarithmic law in the near wall region. In the current case the model is designed for low Reynolds with stable wall shear stress and in the case of the swirl dryer the Reynolds number of operation is high, being necessary the use of a logarithmic function to implement the wall shear stress as function of the velocity and the characteristic roughness.

$$\nu_t = \frac{ak}{\max(aw,\Omega F)} \tag{B-4}$$

2.3.B.3 RESULTS.

The models presented in the previous section have been evaluated obtaining the results presented in this section. A summary of the possibilities of modelling the swirl flow patter of the dryer by a screening evaluation of the models is provided in Figure B-1. This figure shows that the Realizable k-ε model is the one that have more difficulties in reproducing the swirl flow pattern. In particular, the main difficulties are given by the specification of the roughness given by the deposits. This model only allows implementing the wall shear stress directly as boundary condition. For its implementation, this wall shear stress has been previously read from the validated Very Large Eddy simulation at different heights. Then it has been specified in the dryer but it shows negative velocity in some of the parts. The behaviour of the swirl flow pattern is dynamic resulting then in changes of the shear stress. Thus, this Realizable k-ε cannot be addressed in the DES for simulating the vortex of the dryer. Another model with unsatisfactory results is the SST k-w. The model does not allow to predict the swirl intensity decay through the dryer. The decay of the swirl intensity is too low. As previously defined, the coupling in the near wall region is designed for low Reynolds numbers and in the current case the dryer operates in the order of $Re=10^5$.

The best RANS model to be considered in the DES from the default ones Spalart-Allmaras. The model allows introducing the effect of the deposits as a roughness constant in the logarithmic law. Apart from this advantage, it also allows to solve the model including the vorticity and with a correction of the curvature. In order to introduce that effects, the following selections have been done:

- The Delayed DES is selected for running the model.
- The Production in the Spalart-Allmaras is defined as Vorticity-Based.
- Curvature correction is selected in the options.

Including the selection of previous terms, the swirl intensity decay is obtained as presented in Figure B-2 for two time extractions and different Reynolds numbers. The prediction of the swirl intensity in the dryer is slightly worse than the one obtained by the Reynolds Stress turbulence model but still good, within the experimental error bars. Furthermore, the velocity profiles obtained in each of the relative heights also show a good accuracy of the results, see Figure B-3 and B-4 for the tangential and axial compoents.

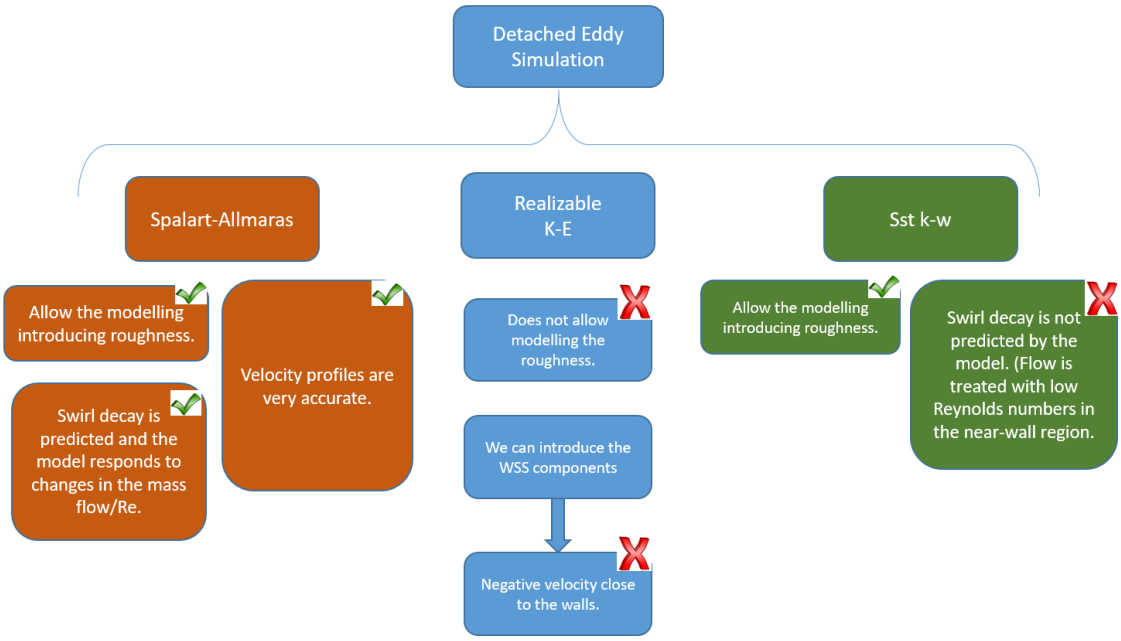

Figure B-1. Summary of RANS turbulence models used in the DES with the best and worst points extracted.

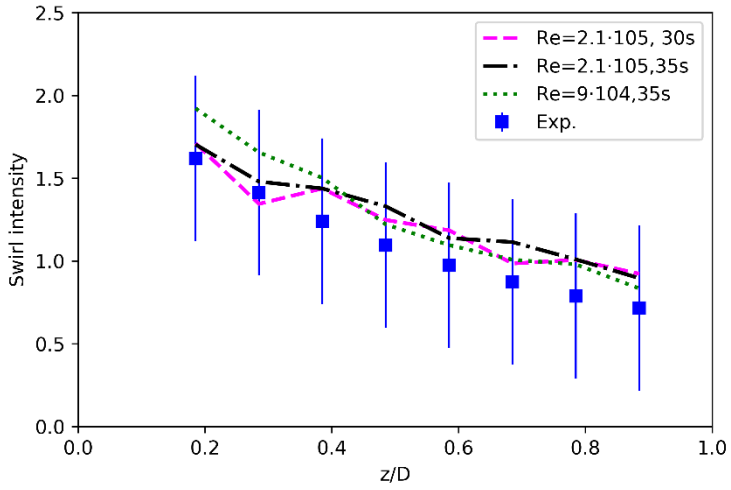

Figure B-2. Prediction of the swirl intensity decay in the dryer by the DES with Spalart-Allmaras model.

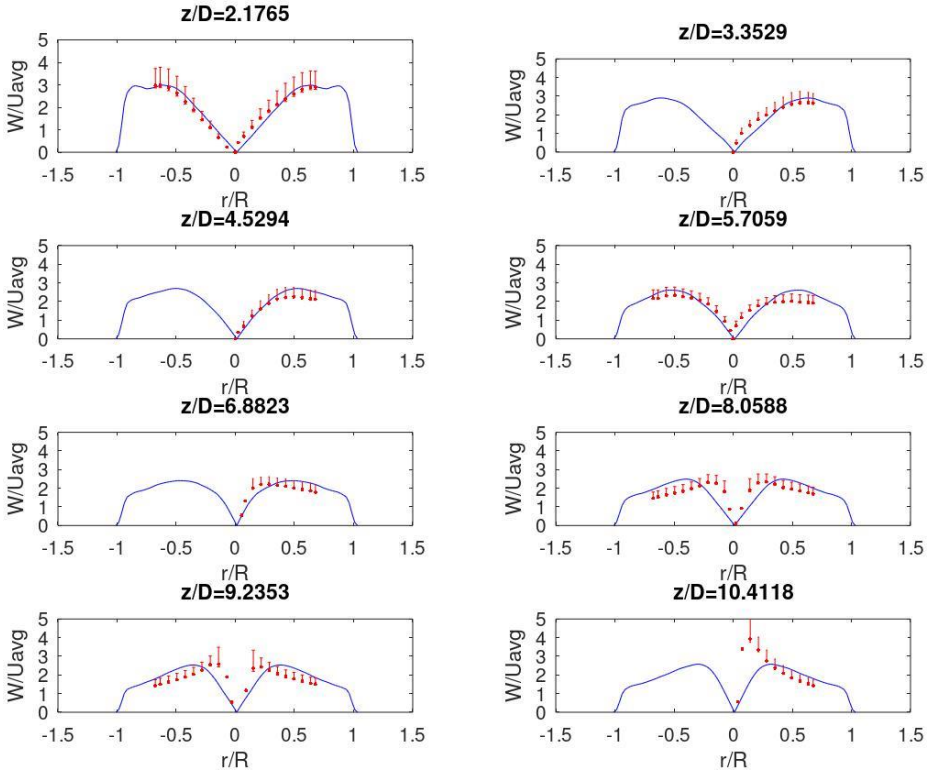

Figure B-3 Tangential velocity profiles for DES with Re=2.1·10^5.

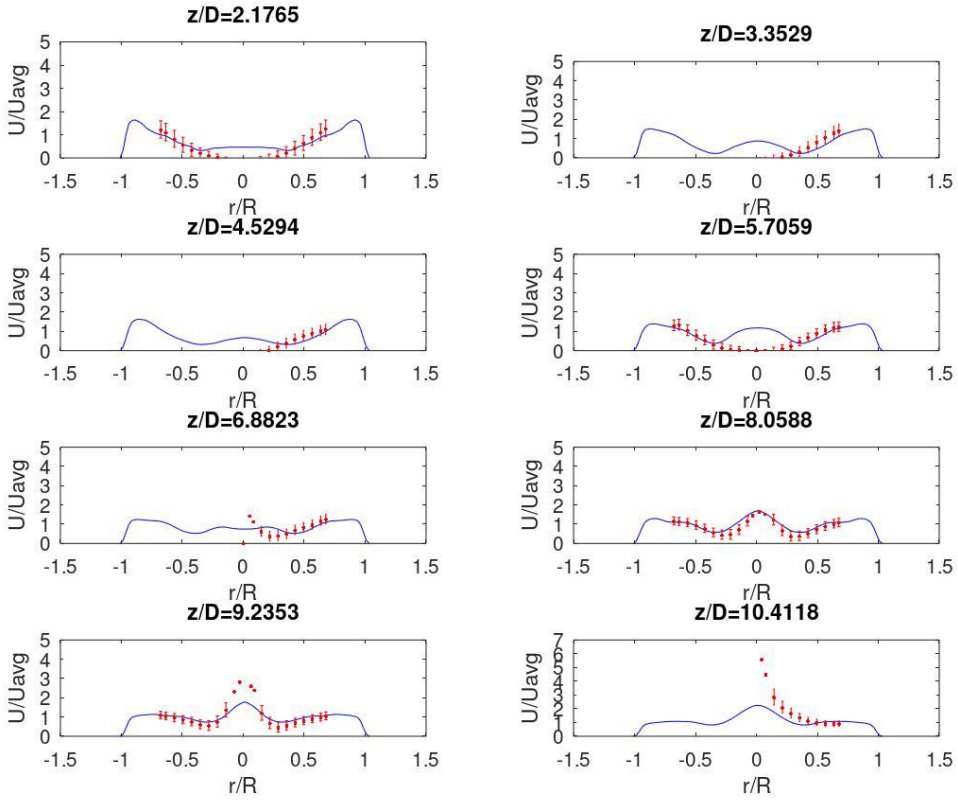

Figure B-4. Axial velocity profiles for DES with Re=2.1·10^5.

2.3.B.4 CONCLUSIONS

This part has presented a comparison of different modelling approaches for implementing Large Eddy Simulations in counter-current Spray Dryers with swirling flow. As a result, it has been obtained that only the Spalart-Allmaras turbulence models is robust enough to reproduce the momentum distribution under different Reynolds numbers and level of roughness. This models shows a good prediction in both the swirl intensity decay and the velocity components through the dryer. Even though the velocity components have shown very good results, this work only provides an insight for now and it still requires of further validation in terms of anisotropy and in the prediction of the particle momentum in further stages of the modelling process.

NOMENCLATURE

a	Constant for the SST k-w turbulent model.
C_μ	Turbulence model constant.
F2	Parameter of the SST-k-w turbulent model.
ε	Turbulence dissipation rate (m^2/s^2)
k	Turbulent kinetic energy (m^2/s^2)
w	Turbulence dissipation ratio.
ν_t	Kinematic eddy viscosity (m/s).
Ω	Rotation tensor (m^2/s^2).

REFERENCES

[B-1] Fletcher, D.F. Guo, B. Harvie, D.J.E. Langrish, T.A.G. Nijdam, J.J. Williams, J. (2006) What is important in the simulation of spray dryer performance and how do current CFD models perform?. Applied Mathematical Modeling, 30 (11), 1281-1292.

[B-2] Jamshed, S. (2015) Chapter 4 – High Reynolds Number Flows. Using HPC for Computational Fluid Dynamics. A Guide to High Performance Computing for CFD Engineers. 81-100

[B-3] Almaras, P.R. Jou, W.H. Stretlets, M. Allmaras, S.R. (1997) Comments on the Feasibility of LES for Wings and on the Hybrid RANS/LES Approach. Advances in DNS/LES. Proceedings of the First AFOSR International Conference on DNS/LES.

[B-4] Spalart, P.R. (2009) Detached-Eddy Simulation. Annual Reviews of Fluid Mechanics. 41, 181-202.

[B-5] Strelets, M. (2001) Detached eddy simulation of massively separated flows. AIAA 2001-0879.

[B-6] Derksen, J.J. Van den Akker, H.E.A. Sundaresan, S. (2008) Two –way coupled large-eddy simulations of the gas-solid flow in cyclone separators. AIChE Journal, 54 (4), 872-885.

[B-7] Jongsma, F.J. Innings, F. Olsson, M. Carlsson, F. (2013) Large eddy simulation of unsteady turbulent flow in a semi-industrial size spray dryer. Dairy Science & Technology, 93, 373-386.

[B-8] Delafosse, A. Line, A. Morchain, J. Guiraud, P. (2008) LES and URANS simulations of hydrodynamics in mixing tank: Comparison to PIV experiments.

[B-9] Pope, S. (2001) Turbulent Flows. Cambridge University Press. ISBN: 9780511840531

[B-10] Blazek, J. (2015) Computational Fluid Dynamics: Principles and Applications. Butterworth-Heinemann. ISBN: 978-0-08-099995-1

[B-11] Caruele, B. Ducros, F. (2003) Dettached-Eddy Simulations of Attached and Detached Boundary Layers. Int. J. of Computational Fluid Dynamics, 17 (6), 433-451.

[B-12] CFD-Online (2020) Realisable k-epsilon model. Available in: https://www.cfd-online.com/Wiki/Realisable_k-epsilon_model

[B-13] Miltner, M. Jordan, C. Harasek, M. (2015) CFD simulation of straight and slightly swirling turbulent free jets using different RANS-turbulence models. Applied Thermal Engineering, 89, 1117-1126.

[B-14] CFD-Online (2020) Realisable k-epsilon model. Available in: https://www.cfd-online.com/Wiki/Realisable_k-epsilon_model

CHAPTER 2.4. ANALYSIS OF THE PARTICLE RESIDENCE TIME IN INDUSTRIAL SWIRL COUNTER-CURRENT DRYERS.

ABSTRACT

This chapter studies particle dispersion in a strong turbulent vortex flow at a large scale and evaluates the accuracy of computational platforms used in the design of spray dryers. The analysis is done in the absence of heat and mass transport to provide an independent validation of the multi-phase flow model. Particle residence time distributions (RTD) are obtained from pulse injections of glass beads and detergent particle at various location of an industrial counter-current dryer using an isothermal swirling air flow. As expected, they are highly influenced by the operating Reynolds and the particle Archimedes and Stokes numbers. However, the influence of complex physics cannot be reproduced from the analysis of the inputs. A sensitivity analysis of a CFD-DPM model shows that in detailed simulations, the particle-wall contact is a critical factor determining the solids RTD. CFD-DPM models typically simplify these contacts to a single restitution coefficient. However, the contacts in a complex unit are much more complex. They are not only determined by the properties of the particles but also by the type and level of deposits at the wall. Deposits do not distribute structure and mechanical properties with sufficient detail to inform a CFD model. Furthermore, the functionality of a restitution coefficient of non-spherical granules colliding an heterogeneous surface of varying properties would be very complex. To address these limitations, here we propose to use a hybrid model that makes use of a simple machine learning approach to estimate an "effective restitution coefficient" at the unit walls. A learning procedure is given to determine this parameter according to the behaviour of a given material in a given dryer. The use of a single (pair) of restitution coefficients lumps the complex wall phenomena into a simplified wall model. While rudimentary, this approach shows a drastic improvement in the prediction of RDT prediction under isothermal conditions. In contrast to the deficiency of existing CFD tools, a hybrid model is able to capture accurately the mean residence time to a quantitative level in every case and reproduce the shape of the distributions in reasonable manner. A comparative study of an equivalent set of reactors is also evaluated to predict the experimental RTD. Equivalent number of CSTR, PFR with axial diffusion and their combination are evaluated, where the best performance is obtained by the combination of both.

Note: Author acknowledges the experimental characterization carried out by Dr. Hossein Ahmadian at Procter & Gamble.

The supplementary material of the chapter is available in: https://drive.google.com/drive/folders/1_EkYTjaqQYkP_okY1ckLG9DMSdbt8gRt?usp=sharing

2.4.1 INTRODUCTION

Spray drying involves the production of powder by drying an atomized solution or a slurry into dry particles by contact with hot gas. According to how the contact between the droplets and the air is carried out, spray dryers can be classified in two types: co-current and counter-current [1]. High sensitive materials such as pharmaceutics or food powders are manufactured in co-current units to avoid the degradation of key ingredients when they are exposed to high temperatures. Thermally stable products such as detergents or ceramics are confronted with higher temperatures in counter-current dryers to improve heat transfer and reduce external mass transfer limitations. However, the drying rates are often limited by the diffusion of the solvent i.e. water, and the residence time droplets and particles spend in the chamber [1]. An excessive residence time (RT) may lead to charring and thermal degradation of the product causing safety hazards and the potential for unexpected plant shut-down [2]. On the contrary, insufficient RT causes insufficient drying and as a result agglomeration and caking [1, 3].

Rigorous modelling of a spray dryer must follow a sequential procedure [4-7] whereas a validated model for the continuous phase is developed first. Then, it is sequentially extended to validate the different multiphase transport terms individually, starting with momentum, followed by heat and mass (e.g. include a single droplet drying model, equation of state and energy equation) and finally the study of particle interactions (i.e. fouling and agglomeration leading to key particle quality properties such as size and density [8,9]). However, the collection of data inside a drying chamber is very difficult and comprehensive experimental studies are scarce. In most of the previous works momentum, heat and mass transport sub-models are commonly validated in a qualitative manner using a limited set of data such as the outlet temperatures or compositions claiming a good agreement [9]. This approach is not ideal because it is difficult to unveil of the origin of errors because the inaccuracies in the prediction of particle dispersion, heat and mass transfer, agglomeration or deposition are unknown and cannot be decoupled from an integral measurement such as the exit moisture content. In this work we focus on studying the particle RT in the absence of heat and mass transfer rates or particle interactions (deposition or agglomeration).

There exists an extensive literature studying the residence time distribution (RTD) of the discrete phase in co-current spray dryers. One of the first studies reported for a tall-form dryer concluded that the mean RT of water droplets [10] was smaller than the mean air residence time due to the important contribution of gravity. A more comprehensive study was carried out by Kieviet [11] with the use of a tracer combined with the development of a CFD frame. They showed that the RT's predicted with a CFD framework were shorter than the experimental ones, and attributed the differences to the interactions between the wall and the particles causing deposition. Furthermore, it was found that particles spent a large amount of time in the bottom conical section where they had a notable interaction with the wall. Another validation of CFD models with an experimental RTD was developed by Ducept et al. in a superheated steam dryer [12]. They observed that the RTD was strongly affected by the circulation of the fluid and the particle size distribution (PSD), which was linked to the final product quality. The objective of these studies was to relate the RTD of the product to its properties. However, the RTD is also a key aspect in the design and optimization of the drying chamber [13]. For example, Huang et al. used CFD simulations

to evaluate alternative chamber configurations, using the particle RTD as critical variable [11]. Alternative to the use of CFD models in RTD characterization, the equivalent number of continuous stirred-tank reactors (CSTR) in series has also been shown to be a good method for characterizing the RTD in particle processes [12]. In a recent work Ruprecht and Kohlus characterized the particles dispersion of a co-current spray dryer by means of scattered light technique and generate a model based on a series of plug flow (PFR) and CSTR reactors [13].

In contrast to the extensive literature in co-current dryers, the knowledge of swirl counter-current units is by far less extensive. Even in a single phase flow, the scalability of turbulent vortex flows under rough walls is not trivial [14]. In multiphase systems, the sedimentation velocity and the centrifugal inertia of the solids scale differently with size complicating the design. As a result, the operation and optimization of counter-current swirl towers is mainly empirical. Many experiments are required to evaluate the effects of the operating conditions (e.g. airflow rate and temperature, slurry flow rate, temperature and pressure) and the design parameters (e.g. dryer diameter and height, swirl intensity) in the performance. Because of the large scale of these drying towers, experimentation is very expensive and time consuming. Thus, the use of a computational fluid dynamics (CFD) framework based on the Reynolds Average Navier-Stokes equations (RANS) to study the operation and design of dryers is a useful tool to reduce the operational costs. However, most of these studies in counter-current towers do not follow a rigorous sequential validation of the momentum, heat and mass transports being hardly difficult to distinguish the origin of the errors in the model. To the best of the authors' knowledge, only one recent study provides information on modelling the dispersion independently from drying. Ali et al. [15] studied the RTD of glass beads in a cold isothermal system. They injected 0.5 kg of particles in the drying chamber at a determined location and weighted the mass recovered at the exit of the tower. Experiments were carried out at different heights, radial positions and airflows, and compared with the results from a RANS-CFD model. However, this initial numerical strategy was unable to predict the mean RT with a reasonable accuracy using commercial CFD packages. The single phase, air, model used in the evaluation of the dispersion, was not previously validated under different fouling regimes. It showed an average error or 2.8% and maximum of 12% in the prediction of the swirl intensity, which accounts for the tangential and axial distribution of momentum, under standard conditions of fouling. The uncertainty addressed in the prediction of the single phase plays an important role in the prediction of momentum of the disperse phase that then results in exponential errors into the drying rate. Therefore, in this work we introduce a new modelling approach based on a CFD-RANS model that has previously validated the momentum distribution of the single phase. Such a model is not only used to study the dispersion of the particles with different operation of Reynolds numbers, Re, and injection locations [15], but also under different particle sizes and materials, glass beads and detergent powder. The development of the CFD-RANS framework is also completed with the development of equivalent reactors models. The only work known reported the use of a PFR was developed by Ali et al. showing relatively a good agreement in the prediction of the temperature distribution within the dryer. However, the dispersion of the particles was not considered [16]. To determine if the use of a PFR without dispersion is the best method, this work also evaluate the two most common approaches based on a set of CSTR and a PFR with diffusion [12]. Furthermore, it is also completed with a combined PFR+CSTR model.

The rest of the manuscript is organised as follows: section 2.4.2 reports the set of experiments used for the experimental characterization of the RTD. Section 2.4.3 presents a new modelling methodology generated for the CFD-RANS framework. Section 2.4.4 describes the equations used for modelling the residence time as an equivalent network of CSTR and PFR reactors. Section 2.4.5 discusses the experimental and modelling results, leading to conclusions summarized in section 2.4.6.

2.4.2 EXPERIMENTAL CHARACTERIZATION OF RESIDENCE TIME DISTRIBUTIONS.

The experiments are conducted in the semi-industrial scale counter-current spray drying tower property of Procter & Gamble Co. Figure 1 presents the design, nomenclature of the chamber, and it sketches the flow pattern and the device used for injecting the particles. Since the current study only focuses on the characterization of the particles RTD, the air is introduced at ambient temperature at the bottom part of the dryer via a series of tangential inlets flowing into the conical region generating the swirling motion. After the cone, the flow undergoes a smooth contraction in the hip section before entering the cylinder. The distribution of angular and axial momentums, quantified by the swirl intensity defined in Eq. (1), depends on the values given by the design of the unit and the friction exerted by the walls [14]. Kitoh [17] described how the non-dimensional angular momentum or swirl intensity decays axially in a pipe due to the action of the wall shear stress (WSS). Francia et al. extended the analysis to the design of counter-current swirl dryers demonstrating that the swirl intensity of a vortex decays exponentially in the cylindrical chamber, Eq. (2) [18]. The experimental characterization of the flow field in a range of counter-current units led to the formulation of a new design and scale-up procedure based on the initial swirl intensity, Ω_i, which is defined in Eq. (3) and it is exclusively a function of the design of the chamber and the size and orientation of the inlets (See figure 1,b) [18], and the rate of decay, λ ,function of the wall conditions. λ is determined by the presence of deposits on the walls of the chamber. A large level of deposition involves more irregularities on the wall surface of a large scale, which generates a higher roughness and consequently, an increase in the WSS [14]. Previous experimental and computational works have studied the influence of the wall conditions and the level of deposition on the rate of decay and subsequently on the swirl intensity [14], demonstrating a reasonable ability to predict the decay of the swirl intensity under varying deposition levels [5]. This work focuses on studying the dispersion of particles in a typical flow field, therefore it will exclusively use standard deposition conditions. After the cylinder, in the upper part of the chamber the air flows through a narrow contraction that can lead to a vortex breakdown if the swirl intensity is high enough. This phenomenon is highly significant when the swirl intensity is larger than 1 since the breakdown results in areas of coaxial recirculation. However, in the dryer and under the conditions studied the swirl intensity at the top of the chamber is 0.7 and recirculation does not take place. Only at the bottom of the dryer, where the swirl intensity is 1.7, a central recirculation appears [14].

$$\Omega = 2\pi\rho_A \int_0^R \frac{\bar{U}\,\bar{W}}{\rho_A \pi \overline{U_{av}^2} R_T^3} r^2 dr \quad (1)$$

$$\Omega = \Omega_i \cdot e^{-\lambda\left(\frac{z-z_{ref}}{D_T}\right)} \quad (2)$$

$$\Omega_i = \frac{\overline{M_i^2} \cdot A_c \cdot R_i}{\overline{M_c^2} \cdot A_i \cdot R_T} \cdot \sin\varphi \cdot \cos\xi \qquad (3)$$

The residence time distribution of the particles is measured in a so-called pulse experiment, injecting a known quantity of particles at a point in the dryer and measuring the exit rate. The unit is operated in isothermal conditions using a flow of ambient air with the required rate. Once stable flow field is achieved, an in-house cone feeder (see Figure 1, c) is used to inject 0.5 kg of powder, either glass beads or detergent powder into the swirling flow. The cone is initially filled with the sample, facing upwards in an upright position and it is placed at a given position in the dryer while the air is continuously fed into the chamber. Then at the desired location the powder sample is dropped down into the upwards flowing air by activating a trigger that inverts the feeder and starts timing. The cone does not fully invert immediately, but it provides enough time to allow the particles to freely discharge from the feeder. High speed camera analysis demonstrate that the injection takes place over 0.65 s [15]. At the bottom part of the dryer, an in-line weighing balance records the weight of the exit mass powder, which can be used to reconstruct the residence time distribution of the sample in the dryer.

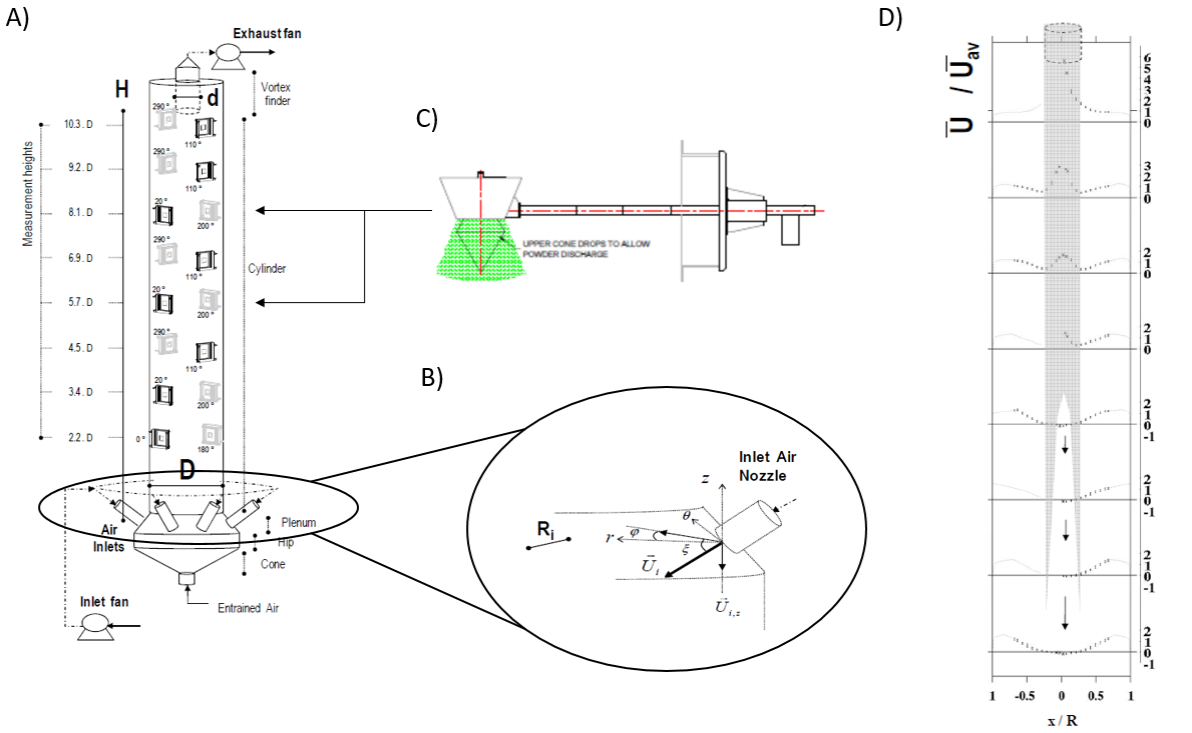

Figure 1. Schematic description of the swirling flow counter current spray dryer (A), the inlets of the airflow (B), the device used for the injecting the particles (C) and the airflow pattern in the dryer (D). Figures (A), (B) and (D) are taken from [6] with permission of the author.

Table 1 summarizes the design of a set of experiments to screen the effect of particle size, shape and injection location in the residence time distributions under different operating Re numbers. In order to avoid any effect stemming from changes in the particle density or size (e.g. drying and agglomeration), the experiments are carried out in isothermal conditions and employing dry non-agglomerating powder. Table 1 includes the both materials

used: glass beads and granular detergent from a standard detergent formulation manufactured in this unit. The characteristic size of a detergent formulation and two different sizes for glass beads in a similar order of magnitude. Different injection heights and radial positions are also studied in order to understand the effect that the main flow features in the vortex have in the dispersion of the solids. Previous works have described preeminent flow structures in the dryer. Under the conditions studied, the central region shows recirculation at the bottom of the cylinder and an upwards jet that extends to the exit. The axial velocity develops a minimum in the midpoint of the radius and then increases towards the wall. Furthermore, the tangential velocity shows a strong intensity at the bottom part and a Rankine vortex at the top whereby the magnitude decreases as the vortex rises in the tower due to the friction on the walls [14, 18].

Table 1. Summary of experiments performed.

Experiment	Material	Re	d_{mean} (μm)	d_{min}-d_{max}	z/D_T	r/R_T
G9_360_LC	Glass beads	$9.5 \cdot 10^4$	360	300-425	5	0
G9_360_HC					7.5	
G9_360_HM						0.5
G1_360_HC		$1.5 \cdot 10^5$				0
G1_360_HM						0.5
G9_610_HC		$9.5 \cdot 10^4$	610	425-800		0
G9_610_HM						0.5
G1_610_HM		$1.5 \cdot 10^5$				
D9_425_HC	Detergent	$9.5 \cdot 10^4$	425	350-500	7.5	0
D9_425_HM						0.5
D9_425_LC					5	0
D9_425_LM						0.5
D1_425_HC		$1.5 \cdot 10^5$			7.5	0
D1_425_HM						0.5
D1_425_LC					5	0
D1_425_LM						0.5

2.4.3 CFD-DPM MODELING

An Eulerian-Langrangian RANS CFD platform is employed for the modelling approach presented here. The continuity and momentum equations for the continuous and discrete phases are computed using a commercial package, Ansys Fluent® v.17.2. The computational description of the continuous phase is briefly described in section 2.4.3.1. Section 2.4.3.2 discusses the formulation of the discrete phase momentum equations. Section 2.4.3.3 shows the procedure followed to model the experiments presented where a combined CFD-DPM and machine learning framework has been developed.

2.4.3.1 Air flow modelling

The system is modelled computing the continuity and momentum balance for the air are by means of a finite volume approach. Given the characteristic strong anisotropy of swirl flows, experimentally observed in these units [14], the turbulence is closed with a Reynolds Stress Model (RSM) where the pressure rate of strain tensor involved in RSM is solved according to the decomposition described by Gibson and Launder [19]. Table A-1 in the Appendix summarizes the equations and parameters used for computing this model.

Wall effects however play a major role in industrial dryers that needs to be addressed. The friction caused at the walls reduces the angular momentum of the vortex and leads to major changes in the flow and turbulence structure. In our previous work [5], we presented a methodology do so in a large scale counter-current unit utilising the swirl intensity decay rates reported by Francia et al. [14] as a source of validation. This procedure showed a significant improvement of the simulations and a reasonable quantitative agreement with the experimental velocity profiles under different levels of deposition and Re numbers. The current study follows the same procedure to ensure a correct description of the angular and axial momentum flux in the dryer. The influence of the deposits in the WSS is introduced by means of the additive constant in the logarithmic law, Eq. (4). The additive constant is a function of the roughness defined in the wall, s, as presented in Eq. (5).

$$u^+ = \frac{1}{\kappa}\ln(y^+) - B \tag{4}$$

$$\Delta B = \frac{1}{\kappa} \cdot \ln\left(1 + \frac{C_s \rho_A s u^*}{\mu_A}\right) \tag{5}$$

As a standard practice for swirling flows, the continuous phase is solved using the PRESTO! Scheme for the discretization of the pressure whereas QUICK is selected for the momentum since it provides a good balance between accuracy and computational cost [20].

2.4.3.2 Disperse phase modelling

A Lagrangian framework with linear momentum coupling is used to describe the motion of the solids, following the traditional approach in spray drying [2, 4]. Particle tracking is performed using the non-dense discrete parcel model (DPM). It is selected since the low volume fraction of particles implies that for most of them the motion is controlled by fluid dynamic forces.

The analysis of the particle Stokes number (St), defined in Eq. (6) and formulated for the chamber, provides a guide to evaluate the type of coupling between the discrete and continuous phases. For St<<1, the solid phase causes a negligible disruption to the continuous phase and there is no need for a momentum exchange and one-way coupling is appropriate [21]. However, for higher numbers, the effect that the solid phase has on the momentum of the air must be taken into account and two-way coupling is necessary. Given that the tangential motion is dominant, for simplification, the Stokes number in a swirl dryer can be assimilated to that of cyclones [22, 23], Eq. (7), where St is a function of the particle mean diameter and density, the unit diameter and the air properties. The Stokes number in the dryer studied ranges between 0.3 and 2.4 across all the experiments described, and thus, a two-way coupling formulation is required. This is particularly true in two regions, at the walls where it could reach higher values and at the injection area given that the injection of all the particles in a short length of time would tend to dilute as the particles disperse in the chamber.

$$St = \frac{\tau_p}{\tau_f} \tag{6}$$

$$St_{50} = \frac{d_{mean}^2 \rho_p Q}{\mu_A D_T^3} * \frac{2}{9\pi} \tag{7}$$

The injected mass of powder in the CFD-DPM model is discretized into a series of parcels of the specified mass but representing a collection of real particles. The total number of parcels required to comply with the continuity equation is computed following Eq. (8) [21].

$$N_p = \dot{N}_p \Delta t \tag{8}$$

The time-step, Δt, must be smaller than other relevant time scales of the flow, such as the particle relaxation time and the integral time scale of turbulence [24, 25]. Furthermore, it must comply with sufficiently small Courant numbers to guarantee that any parcel travels a distance much shorter than the cell dimension in one-time step [21]. In a geometry as complex as the dryer described, a theoretical characterization of each time scale is not straightforward and a sensitivity analysis of the time-step has to be carried out. As a result from this analysis, a stable solution for the particle residence time distribution is obtained only for time steps below 10^{-3} s, see Figure S-1 of the supplementary material.

2.4.3.2.1 Air-particle interaction

The equation of motion of each parcel is integrated to obtain its trajectory, and the linear momentum coupling is used in line with standard practice in spray drying [2, 4]. The particles density is found to be high enough to allow neglecting pressure buoyant, virtual mass and Basset terms [26] (see Table S-1 of the supplementary material for further information). The general equation of motion, BBO (Basset-Boussinesq-Ossen), Eq. (9), is then simplified to Eq. (10) containing only the main driver, gravity, and drag terms.

$$\frac{du_p}{dt} = F_g + F_D - F_{und} + F_{vm} + F_B \tag{9}$$

$$\frac{du_p}{dt} = F_g + F_D \tag{10}$$

The drag force acting on a particle at high Re numbers is computed according to Eq. (11), where C_D denotes the drag coefficient. Different empirical correlations are available to estimate the drag coefficient under a varying Re [27] and particle shapes [28, 29]. The correlation proposed by Haider and Levenspiel [28], Eq. (12) is employed here in order to describe both spherical and non-spherical particles under different Re, and to evaluate the influence of different sphericity of glass beads and detergent particles in the dispersion. The parameters A, B, C and D in Eq. (13) to (17) are functions of the sphericity defined as in Eq. (31) from 2D digital image analysis of powder samples.

$$F_D = \frac{18\mu_A}{\rho_P d^2}\frac{C_D Re_p}{24}(u_F - u_P) \tag{11}$$

$$C_D = \frac{24}{Re_p}\left(1 + D_A \cdot Re_p^{D_B}\right) + \frac{D_C}{1+\frac{D_D}{Re_p}} \tag{12}$$

$$D_A = \exp(2.3288 - 6.4581\psi + 2.4486\psi^2) \tag{13}$$

$$D_B = 0.0964 + 0.5565\psi \tag{14}$$

$$D_C = \exp(4.905 - 13.8944\psi + 18.4222\psi^2 - 10.2599\psi^3) \tag{15}$$

$$D_D = \exp(1.4681 + 12.2584\psi - 20.7322\psi^2 + 15.8855\psi^3) \tag{16}$$

$$\psi = \frac{A_{sphere}}{A_p} \tag{17}$$

Turbulence dispersion is also taken into account and it is introduced in the simulation by means of an isotropic discrete random walk using the model of Hutchinson et al. [30] to compute the dispersion of the particles in every cell as a function of the characteristic eddy lifetime defined by the ratio between the turbulence kinetic energy and the turbulence dissipation rate.

2.4.3.2.2 Particle-wall interaction

The swirling motion concentrates the solids close to the walls [31, 32]. As a result, a swirl dryer shows an important level of deposition. In the context of these experiments, the deposits form an irregular surface that conditions the way in which particles impact and rebound from the walls, particularly at the bottom conical section where the impacts occur at high velocity and lower impact angles. Due to this phenomena, recent works have implemented the effect of the wall roughness in the context of spray drying towers using a stochastic approach [33].

Particle-wall collisions are described by means of the restitution coefficients for the normal, Eq. (18), and tangential, Eq. (19), components. As proposed by Sommerfeld and Huber [34], the behavior of the wall collisions is sampled from a predefined distribution rebound angles. The influence of the wall roughness on the distribution of rebound angles is described with a modified impact angle, α', which is composed by the particle trajectory angle and the stochastic contribution due to wall roughness s, $\Delta\gamma$, see Eq. (20). The stochastic term, $\Delta\gamma$, is computed as a function of the width, R_w, and height deviation, R_d, of the elements that compose the roughness, see Eq. (21).

$$e_n = \frac{v_{out}}{v_{in}} \quad (18)$$

$$e_{tg} = \frac{u_{out}}{u_{in}} \quad (19)$$

$$\alpha' = \alpha + \Delta\gamma_w \quad (20)$$

$$\Delta\gamma_w = \text{arctg}(2R_d/R_w) \quad (21)$$

Such modelling approaches including the rebound angle and its stochastic distribution have shown accurate results at laboratory scale. However, the characterization of the deposits within an industrial dryer is extremely challenging due to a near impossible visualization inside the whole dryer and their dynamic nature constantly growing and breaking [31]. Deposits are constantly changing as they dry, new particles deposit and agglomerates break off, and they exhibit different mechanical properties across different sections of the dryer [32]. However, given the limitations of the system, the simulations performed in the following computational study will simplify particle-wall interactions with a single set of parameters given by particle-wall restitution coefficients, Eqs. (18) and (19).

2.4.3.3 Computational set up

The model described in previous sections is simulated with setting summarized in Table A-1 of the appendix. It is initialized in steady-state conditions. A period of 50 s is then solved in transient conditions ensuring the stability and convergence of the solution [5]. Once the single-phase simulation is found to be stable, the state of the airflow is taken as a reference. For a direct comparison, in the study of particle dispersion, particles are injected always in this reference. A time step of 10^{-3} s is selected for the solution of the particle phase since it has been shown to ensure the stability of the residence time distribution computed with the lower computational cost. The incoming particle size distribution is discretized in 100 streams. Thus, given in Eq. (8), the total number of parcels account for 65,000. Each of the discrete phase simulations takes between 15 h and 30 h and they are solved in a High Processor Computer using 6 parallel processors Intel-Xeon E5-2698 ®.

2.4.3.4 Hybrid CFD-DPM and machine learning framework. Modelling procedure.

A sensitivity of the solids RTDs to changes in the particle-wall contact and the particle-fluid forces in has been studied independently. A screening design of computational experiments has been employed to evaluate the effect of sphericity (that only modifies the drag coefficient in the model) and restitution coefficients in the RTDs (details are available in the supplementary material, Tables S-2 and S-3). The analysis shows that the restitution coefficients have a stronger impact on the overall residence time than the drag model and highlight the importance of an accurate evaluation of the particle-wall restitution coefficients. In the case of glass beads, which density is set to 2,500 kg/m3 [15], Sommerfeld and Huber described how the restitution coefficients depend on particle and wall materials [34]. They reported values for the normal restitution coefficient of glass beads, ranging from 0.9 (100

μm glass beads impaction on polish steel with an angle of 20º) to 0.5 (100 μm glass beads impaction on a rubber wall with an angle of 18º) whereas the tangential restitution could range from 0 to 1 [34]. In the case of detergent powders, the experiments performed by Hassall [35] showed that the restitution coefficients of detergent powder impacting on iron walls have values between 0.1 and 0.6. Furthermore, Hassall showed that these restitution coefficients depend on the detergent formulation. The analysis by Hassall [35] has been repeated for the formulations used in this study using two type of walls: an iron wall and an iron wall with deposits of detergent powder. A normal restitution coefficient of 0.323 ± 0.11 is obtained for clean walls and 0.3 ± 0.07 for layered wall. No data is available for tangential restitution coefficients.

Even though characterization of the restitution coefficients is performed for the restitution coefficients, this characterization is far to represent all the different deposits in the dryer. The walls of the dryer are covered by very irregular deposits of detergent powder [7] that modify the nature of the contacts and the torque of the particles. The restitution coefficients depend also on the impact angle, the interaction with an irregular layer of deposits will modify the restitution coefficient through both routes, via the energy exchange with the detergent layer and its possible consolidation, and through modification of the distribution of impact and rebound angles. Thus, one cannot rely on experimentally reported values for the impact with cleaned walls or with a characteristic layer. The experiments can be used as an estimator but they can involve significant errors since all the different distributions of deposits cannot be studied. Alternatively, one may use the RTD of the glass beads as an indirect indication of the nature of particle-wall collisions.

Given the limitations of the industrial system studied here and the difficulties on characterizing the deposits on the wall experimentally, the CFD-DPM model presented in previous section is completed with a machine learning framework to determine the effective restitution coefficients. Two methodologies are presented here to employ a hybrid machine learning and CFD-DPM framework to generate a model able to predict the RTD of the particles within the dryer in any condition.

Minimization of the error in the probability density function.

The first methodology is the most from the two proposed and it is based on minimizing the error of the mass fraction in the RTD curve. The methodology is presented in Figure 2, a) and it consists on the following stages, which are deeply described in the supplementary material:

1. First, one experiment is randomly selected and the pair of restitution coefficients that minimizes the error defined by Eq. (22) is determined. The procedure for minimizing the error is presented in Figure 2, b). It is important to remark that at the initialization of the procedure, we have to parameters: normal (e_n) and tangential (e_{tg}) restitution coefficients to be determined and one variable used (error to RTD). Thus one restitution coefficient must be fixed.

$$\varepsilon = \frac{\sum_{t=0}^{n} \sqrt{(w_{CFD} - w_{exp})^2}}{2} \tag{22}$$

2. Second, the solution obtained using an initial random experiment is modified according to the remaining experiments. Thus, the tangential restitution coefficient is determined for a second experiment.
3. The system is train averaging the value of the second experiment with the value of the first experiment.
4. The training remains with more experiments until a threshold variance is achieved. In the current work the variance has been set to $5x10^{-3}$. Furthermore it is important to define a minimum number of experiments, which restitution coefficient must be determined. In the current work we have set this minimum number of experiments to be 3.

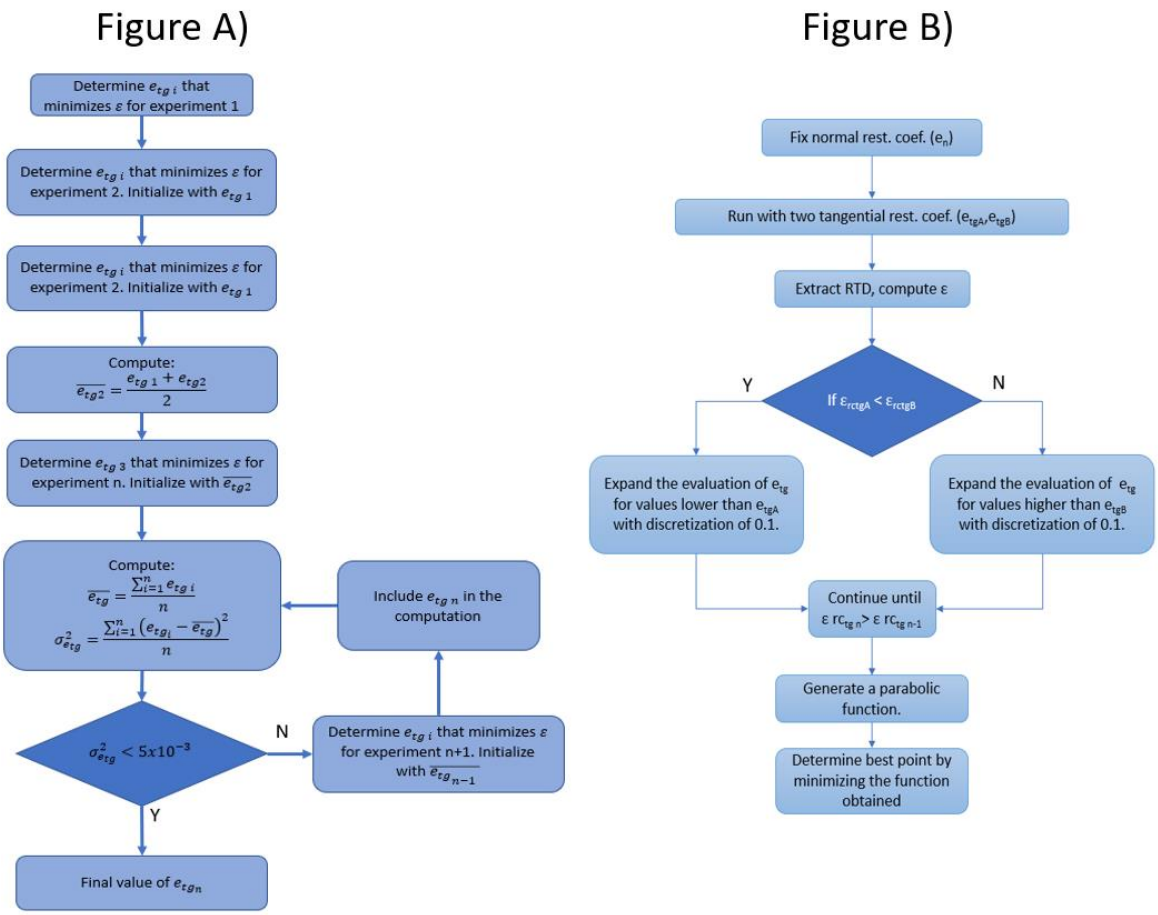

Figure 2. Procedure followed for the estimation of tangential restitution coefficient. A) For the entire set of experiments. B) For a single experiment.

Minimization of the error in the mean RT.

The previous methodology is based on capturing the complete RTD curve of the pulse, but it may require large number of simulations to determine the restitution coefficient with the threshold variance set. In order to minimize the computational cost, an alternative approach is proposed here. It assumes that the RTD of all the experiments follow the same distribution and variance, and it is restricted to minimize the error of its mean RT. The methodology is presented in Figure 3 and it is composed of the following stages, which are deeply described in the supplementary material:

1. Initially one experiment is randomly selected as a fitting subset. The normal restitution coefficient, e_n, is fixed and the tangential, e_{tg}, is left as a variable with the objective of minimize the error given by the norm as in Eq. (23). The procedure followed to minimize $\varepsilon_{rt_{mean}}$ is similar to the one presented in Figure 2, b).

$$\varepsilon_{rt_{mean}} = \sum_{t=0}^{n} \sqrt{(\bar{t}_{CFD} - \bar{t}_{exp})^2} \quad (23)$$

2. A subset of experiments is selected and they are run with the restitution coefficient determined in previous step.
3. The relative difference in the mean RT computed between the simulation run in the previous case and the experiments is computed as in Eq. (24). As a result, three type of experiments can be distinguished over a mean: the ones that tend to over-estimate the time, the ones close to the mean and the ones that under-estimate. One case of each is selected. (Note that the first experiment can be classified in one of the three types).

$$relative\ distance = \frac{(rt_{CFD} - rt_{exp})}{rt_{exp}} \quad (24)$$

4. From the other two experiments, a characterization of the tangential restitution coefficient for each of them is required following the procedure presented in Figure 2, b). As a result two new tangential restitution coefficients.
5. The three cases selected are now run again with each restitution coefficient.
6. The cumulative $\varepsilon_{rt_{mean}}$ including the three simulations is fitted to parabolic function that can be minimized reporting the tangential restitution coefficient with the lowest error.

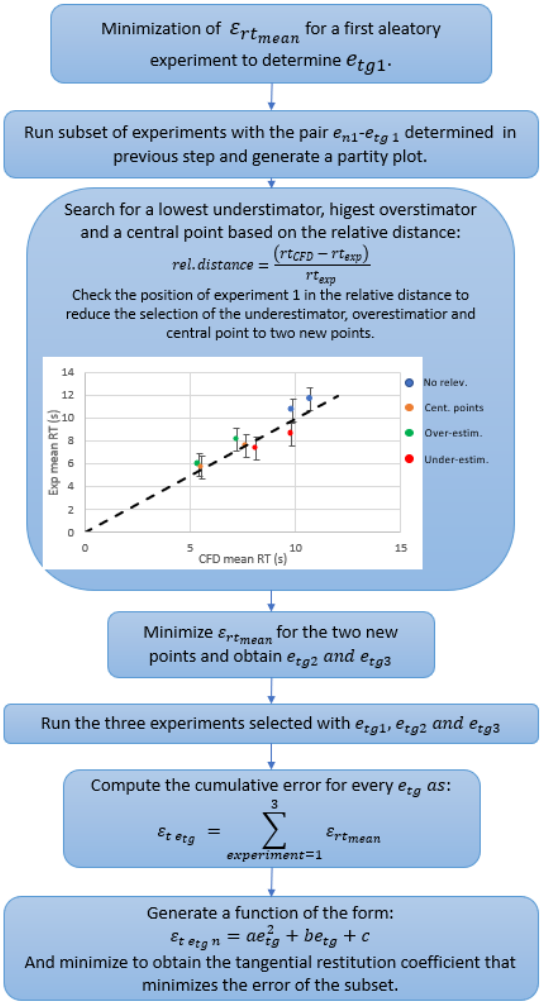

Figure 3. Procedure followed for the characterization of the pair of restitution coefficients for minimizing the error in the prediction of the mean RT.

2.4.4 EQUIVALENT NUMBER OF CSTR AND PFR MODELS.

An alternative simpler modelling approach used in particle processing technologies is the use of equivalent number of Continuous Stirred-Tanks Reactors (CSTR) or plug-flow reactors (PFR) with dispersion [12]. Even though the approach is very simple and unable to describe complex structures and particle interactions, it has shown an accuracy in the prediction of RTD curves for a wide range of particulate processes [36-38], among them co-current spray dryers [13].

In this work, we will compare this approach to experimental residence time distributions to elucidate whether a simple surrogate model based on a set of reactors can be used to characterize the RTD of the solid phase in swirl counter-current spray dryers, and what limitations this entails. It should be noted that in the current work the device presented in Figure 1 has been used instead of a pressure nozzle. Thus, the aim of this work exclusively focus on evaluating different reactor configurations to check if a model simpler than CFD can be constructed and

understanding their limitations for reproducing the RTD. In later works, the approach can be evaluated from CFD simulations that use a nozzle for the injection of the discrete phase.

The RTD of an equivalent number of CSTR's in series is described in Eq. (25) to Eq. (28). The 1st and 2nd moments of the RTD are subsequently computed as Eq. (25) and (26). With the mean RT and the variance, the dimensionless variance, $\sigma_{\bar{\theta}^2}$, is computed as presented in Eq. (27). The equivalent number of CSTR's, N_t, is computed as the inverse of the dimensionless variance. The age curve is computed as presented in Eq. (29), where θ is the relative residence time defined as in Eq. (30) [12].

$$\bar{t} = \sum_0^\infty t\, E(t) \tag{25}$$

$$\sigma^2 = \sum_0^\infty t^2 E(t) \; - \bar{t}^2 \tag{26}$$

$$\sigma_\theta = \frac{\sigma^2}{\bar{t}^2} \tag{27}$$

$$N_t = \frac{1}{\sigma_\theta} \tag{28}$$

$$E(\theta) = \frac{N_t (N_t \theta)^{N_t - 1}}{(N_t - 1)!} \exp(-N_t \theta) \tag{29}$$

$$\theta = \frac{t}{\bar{t}} \tag{30}$$

A different idealised approach consists of the use of a PFR with axial dispersion. In this case, the RTD curve is computed from the Taylor dispersion model, see Eq. (31). In this case the relative time, θ, and the Peclet numbers are the two parameters that characterise each system [12].

$$E(\theta) = \frac{1}{2\sqrt{\pi\theta/Pe}} \exp\left(\frac{-Pe(1-\theta)^2}{4\theta}\right) \tag{31}$$

Another way to deal with dispersion is to combine both ideal systems including a PFR reactor without dispersion followed by a set of equivalent CSTR's to address the dispersion of the solids. The residence time of at the CSTR reactor corresponds to a delay that the particles take to reach the PFR. The residence time age curve for a single CSTR is given as presented in Eq. (32) [38, 39]. For the Nth tank, the residence time distribution referred to the mean residence time of the tank, t_{react}, in Eq. (33). Eq. (33) can be used to obtain the probability density of the age distribution curve. The age distribution curve defined in Eq. (34) has been finally obtained considering the following definitions:

- The time spent in the series of CSTR's is equal to the number of tanks multiply by the mean RT in every tank, see Eq. (35).
- The relative time defined in Eq. (30).
- A relative delay defined in Eq. (36).

$$E(t) = \begin{cases} 0 & \tau < t_{del} \\ \frac{e^{-(t-t_{del})/t_{react}}}{t_{react}} & t \geq t_{del} \end{cases} \quad (32)$$

$$E(t) = \begin{cases} 0 & t < \tau_{del} \\ \frac{(t-t_{del})^{N-1}}{t_{react}^{N}} \frac{e^{(t-t_{del})/t_{react}}}{(N-1)!} & t \geq \tau_{del} \end{cases} \quad (33)$$

$$E(\theta) = \begin{cases} 0 & \theta < \theta_{del} \\ \left(\frac{N}{(1-\theta_{del})}\right)^{N} \cdot \frac{(\theta-\theta_{del})^{N-1}}{(N-1)!} \cdot e^{\left(-\frac{N}{1-\theta_{del}}(\theta-\theta_{del})\right)} & \theta \geq \theta_{del} \end{cases} \quad (34)$$

$$N \cdot t_{react} = (\bar{t} - t_{del}) \quad (35)$$

$$\theta_{del} = \frac{t_{del}}{\bar{t}} \quad (36)$$

2.4.5 RESULTS

Section 2.4.5.1 introduces the experimental results along an empirical model. Section 2.4.5.2 shows the results for the hybrid CFD-DPM and machine learning platform. Finally, section 2.4.5.3 shows the results for the equivalent CSTR and PFR modelling approach.

2.4.5.1 Experimental results

The mass recovery is recorded every second, providing large amount of data. For simplicity, an example of the mass recovery curve for one experiment is given in Figure 4, meanwhile the results for all experiments are available in the supplementary material (datasheet and Figure S-3). The overall mass recovery of the initial pulse varies from -14.3% to +20.93% for glass beads and from -69.7% to -16.3% for detergent powder. Further details of the overall mass gains and losses for each experiment are provided in the supplementary material, Table S-4. An interesting phenomenon linked to the deposition and erosion of deposits from the walls leads in some cases to overall loses and gains of mass (more or less mass than the initial injected is obtained). This is the case for example of experiment G9_610_HC that shows a gain of mass associated to deposit removal. The walls of the tower are never completely cleaned. Before performing the experiments some patches of detergent were present at the walls, and detergent material was obtained when the glass beads were recovered at the bottom, see for example experiment 4 of the supplementary material. This observation is in agreement with studies of agglomeration in swirl dryers that indicate the importance of growth and breakage of deposit structures [31, 32, 40]. Contrary to the experiments using glass beads, the injections of detergent powders show mass losses. Despite the injected detergent powder was dried, it retains a certain level of stickiness and being non-spherical is more prompt to interlock in the structure of the deposits, making the loss of mass due to deposition higher than in the case of spherical glass beads. Detergent has also a longer residence time increasing the number of contacts to the wall and the chances for deposition, and of course, being lighter suffers a higher level of elutriation. The low amount of

mass recovered in detergent powders makes more prominent the error of the inline balance. Figure 4, b) shows that under some time intervals the mass recovered is negative. The oscillations in the belt, which includes the in-line balance and it has to be initially tar to zero in an initial location, is responsible of the error that is observed and takes values up to 12.9 g, which correspond to a 2.58 % of the total injected mass, see Table S-5 for further details. This maximum error in the mass measured per second is used to define the experimental error defined by the error bars in the following figures presented in this work.

In most of the following cases, the mass is presented as a distribution function. The experimental points corresponding to the distribution function are computed based on the mass released at the exit of the dryer. The experimental measurements with negative mass are assumed to be zero and aggregated in the following second. However, this negative values generated by oscillations involve experimental error, which is accounted in the error bars by dividing the maximum error obtained in the intervals (12.9 g) by the total mass obtained at the exit of the dryer.

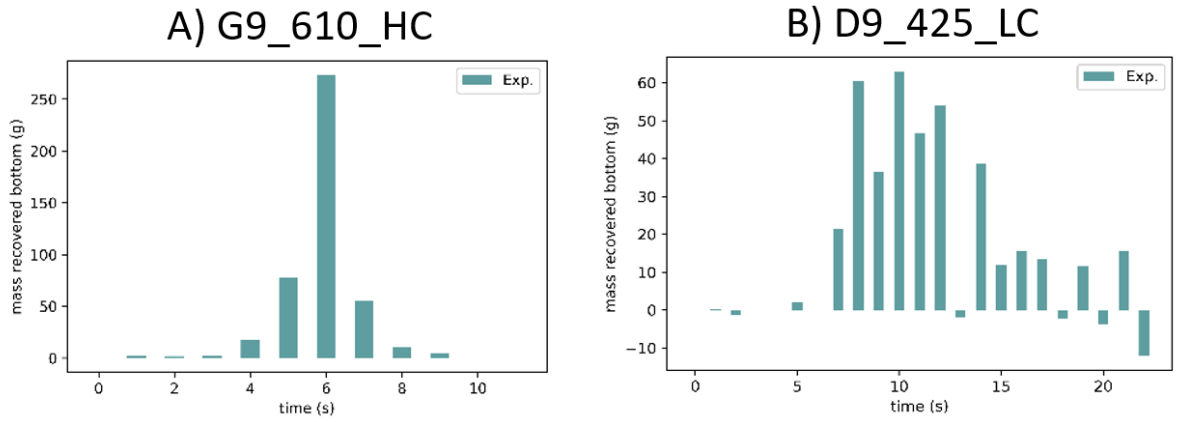

Figure 4. Mass recovered (g) in every second for glass beads (A) and detergent powder (B).

2.4.5.1 Statistical analysis of experimental results.

The data measured by the in-line balance are analysed obtaining the mass recovery curves presented in Figure 4 for experiment G9_610_HC (glass beads) and D9_425_LC (detergent powder). The measurements obtained for the remaining experiments are available in Figure S-3 of the supplementary material. Each of the cases show different mass distribution profiles that are characterised with the 1st and 2nd moments and the dimensionless variance. Table 2 presents the summary of the moments of distribution for all experiments. The mean RT is found to be smaller than the RT of the air in the dryer (roughly 30 s), in a similar way to the observations in co-current dryers [11]. In order to understand the influence of each input variables in Table 1 (i.e. Re, dp, sphericity, injection location) a statistical analysis is conducted. The analysis is also extended including additional characteristic magnitudes that are expected to drive the physics, such as the Reynolds number (Re_t), Eq. (37), based on the

terminal velocity of the particles, Eq. (38), the Reynolds number of the dryer, Eq. (39), the Stokes number of the particles defined in Eq. (7), and the Archimedes number, Eq. (40).

$$Re = \frac{d_{p50} U_{avg} \rho_A}{\mu_A} \tag{37}$$

$$v_{t50} = \sqrt{\frac{2m_{p50} g}{\rho A_{pr}}} \tag{38}$$

$$Re = \frac{D_T U_{avg} \rho_A}{\mu_A} \tag{39}$$

$$Ar = \frac{d_{p50}^3 \cdot g \cdot \rho_A \cdot (\rho_p - \rho_A)}{\mu_A^2} \tag{40}$$

Table 2. Characteristic moments of the distribution for the experiments performed.

Experiment	Mean RT, $\bar{t}$, (s)	σ^2 (s)	σ_θ
G9_360_LC	7.55	0.5	0.01
G9_360_HC	8.59	2.8	0.04
G9_360_HM	7.33	2.2	0.04
G1_360_HC	11.64	21.1	0.16
G1_360_HM	10.67	18.1	0.16
G9_610_HC	5.89	0.9	0.03
G9_610_HM	5.71	0.4	0.01
G1_610_HM	8.1	1.9	0.03
D9_425_HC	13.03	3.9	0.02
D9_425_LC	11.79	16.3	0.12
D9_425_LC	11.21	9.5	0.08
D9_425_HC	10.31	13.9	0.13
D1_425_HC	18.71	5.3	0.02
D1_425_HM	16.59	28	0.10
D1_425_LC	13.29	13.4	0.08
D1_425_LM	14.69	29.7	0.14

Table 3 reports the results of the Pearson coefficient of each term. The variables with a higher impact on modifying the mean RT are the St of the particles, the Re of the dryer and the Ar. The location of the injection shows no apparent significance, which is not expected. A contrast with a minimization of the Bayesian Information Criteria is then performed determining the optimal number of significant variables. In addition to the mentioned Re, St and

Ar, the BIC analysis points to the dimensionless height for the injection location, although as indicated by the p-values in Table 3, its influence is orders of magnitude lower. As a result from the BIC minimization a reduced linear model is also obtained including only the terms that affects the mean RT. The linear model generated is presented in Eq. (41), the p-values of this model are presented in Table 3 and the prediction of this reduced model is presented in Figure 5. It should be noted that the expression obtained in Eq. (41) is not developed for design or modelling purposes. One must recognise the limitations of any type of linearization to describe effects that are likely to be highly non-linear. The main objective of this study is simply to find the strongest contributors to the mean RT. Furthermore, a detailed characterization of the particle size distribution must be carried out. Even though the particle size introduced is very narrow, the distribution between d_{max} and d_{min} is not known and it can either modify the mean RT and the dispersion.

$$\bar{t}\,(s) = -5.31127 + 1.33 \cdot 10^{-4} Re + 0.871 \cdot \frac{h}{D} - 16.45 \cdot St + 1.51 \cdot Ar \qquad (41)$$

Table 3. Pearson coefficients for all the inputs and P-values for the reduced order linear model generated by BIC minimization.

Variable	Pearson coefficient	P-Value from BIC
Re	0.5956	$1x10^{-5}$
St	-0.6726	$2x10^{-5}$
Ar	-0.6613	$1x10^{-4}$
h/D	-0.0870	$1.335x10^{-2}$
Re_{pterm}	-0.5076	Not selected by min(BIC)
r/R	-0.0919	Not selected by min(BIC)

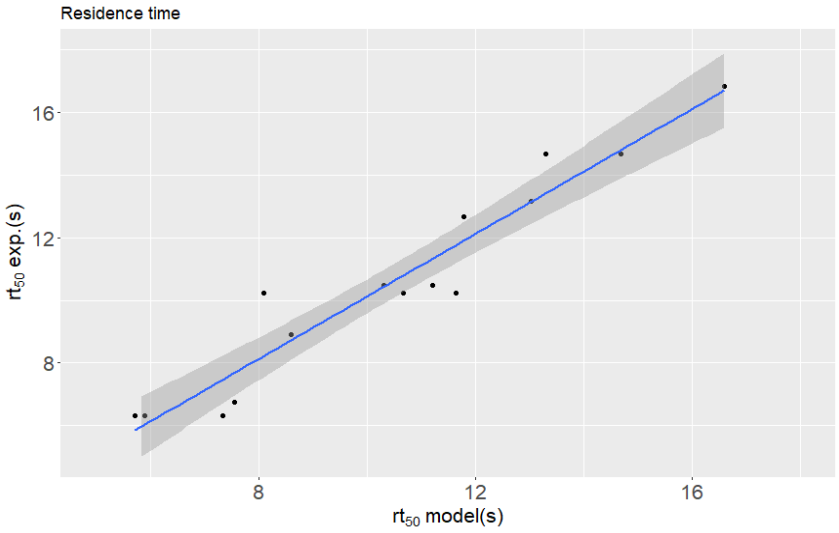

Figure 5. Estimation of the mean RT of the particles by mean of a reduced model based on BIC minimization of dimensionless numbers.

A second analysis is performed to evaluate the influence of the inputs on the dimensionless variance of the RTD, $\overline{\boldsymbol{\theta}}^{\boldsymbol{2}}$. The Pearson coefficients suggest that none of the variables have a strong effect on $\overline{\boldsymbol{\theta}}^{\boldsymbol{2}}$**.** Those with a higher influence are the Re and Ar numbers, see Table 4. The BIC minimization does not suggest to remove any of the variables for generating a reduced linear model, which is shown in Eq. (42). The p-values associated to this Eq. (42) are also presented in Table 4. All the terms are higher than 0.01 indicating that there is not a term with higher significant than the others and a low relevance of the linear model proposed, see also Figure 6 for the prediction. In fact, the R^2 of the model is limited to 0.53. Of course, due to potential highly non-linear effects this model is not developed for design or modelling purposes.

$$\sigma_\theta = -0.286 - 0.0017 \cdot \frac{h}{D} - 2.37 \cdot 10^{-6} \cdot Re + 0.0227 \cdot \frac{r}{R} + 0.5449 \cdot St - 1.03 \cdot 10^{-4} \cdot Ar + 0.303 \cdot Re_{tvel} \quad (42)$$

Table 4. P-values for the estimation of σ_θ as function of dimensionless numbers of the inputs.

Variable	Pearson coefficient	P-Value
Ar	-0.4141	0.05023
St	-0.3339	0.05802
Re_{pterm}	-0.3675	0.05804
Re	0.4216	0.1343
r/R	0.1000	0.72929
h/D	-0.1884	0.89114

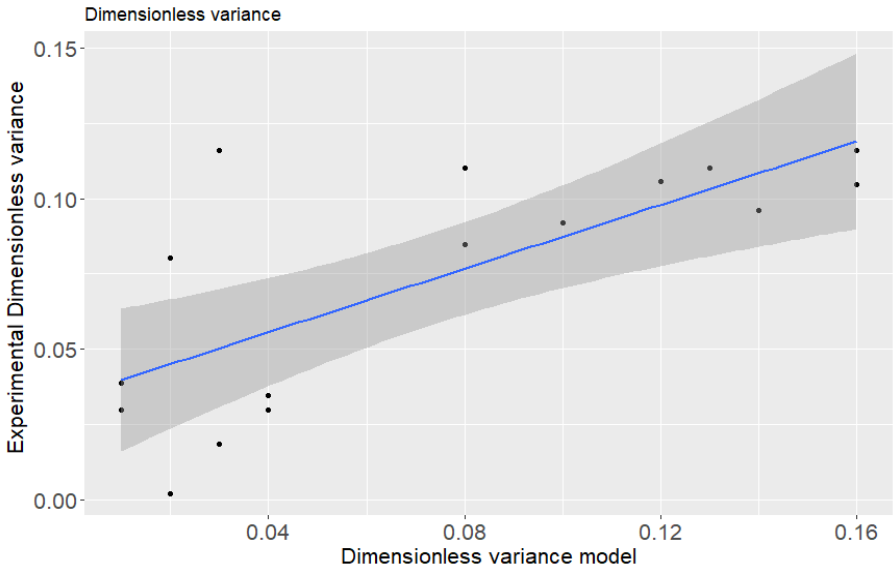

Figure 6. Reduced statistical model. Estimation of $\boldsymbol{\sigma_\theta}$ by BIC minimization of dimensionless numbers.

2.4.5.2 Results from the CFD-DPM model of particle residence time.

This section presents the results of the hybrid CFD-DPM and machine learning modelling presented in section 2.4.4. The results are divided in the analysis of the predicted, mean RT and RTD for glass beads and detergent powder.

2.4.5.2.1 Residence time distributions of a pulse of glass beads.

Minimization of the error in the probability density function RTD.

The minimization the cumulative error of the RTD, ε, results in a characteristic pair of restitution coefficients of e_n=0.7 and e_{tg}=0.17. The characteristic value is obtained with a set of five experiments included in the learning scheme. At this iteration, the mean e_{tg} is 0.172 and the variance is 4.48×10^{-3}, meeting the threshold to finish the learning process set as variance below 5×10^{-3}. This result is very close to the value one would obtain including every single experiment in the minimization process (e_{tg}=0.15). Further details of the results obtained for e_{tg} in each experiment are given in Table S-6 of the supplementary material. The fact that the suggested methodology incurs in a ± 0.02 of error in comparison to the final optimal supports the validity of setting a threshold for the variance of e_{tg} to drastically reduce the number of computational simulations required in future datasets.

The prediction of the mean RT and the RTD is given in Figures 7, a) and 8, a). Figure 7, a) shows that the prediction of the mean RT is not balanced, having more experiments with an under-prediction of the mean RT. This bias in the mean RT prediction is due to the differences in the distribution of the mass recovered. The experimental distributions show a bit higher dispersion and they tend to concentrate most of the mass released at the beginning. The procedure favours to cover the intervals with higher release of mass, even that the mean RT is not capture. Analysing the errors, it is obtained an average value of ε=0.342. Comparing the experiments between them, it is observed that the higher errors are linked to experiments G9_610_HC, G9_360_HC, G1_360_HM, G1_610_HM. Experiments G9_610_HC, G9_360_HC and G1_610_HM exhibit very narrow RTDs and thus, a small deviation in the mean RT prediction results in a large cumulative error. In experiment G1_360_HM, the model is not able to predict the qualitative features of the RTD, characterised by narrow release of particles at the beginning and a long plateau thereafter. The model provides a much more homogenously distributed RT curve than observed experimentally.

Table 5. Cumulative error of the hybrid CFD-DPM and machine learning model for glass beads.

Experiment	ε, Method A) Minimizing ε	ε, Method B) minimizing error with mean RT
G9_360_LC	0.1580	0.3102
G9_360_HC	0.3642	0.5653
G9_360_HM	0.2507	0.3932
G1_360_HC	0.3237	0.3206
G1_360_HM	0.4985	0.5322
G9_610_HC	0.4253	0.4335
G9_610_HM	0.2888	0.3523
G1_610_HM	0.4264	0.3345
Average	0.3419	0.4052

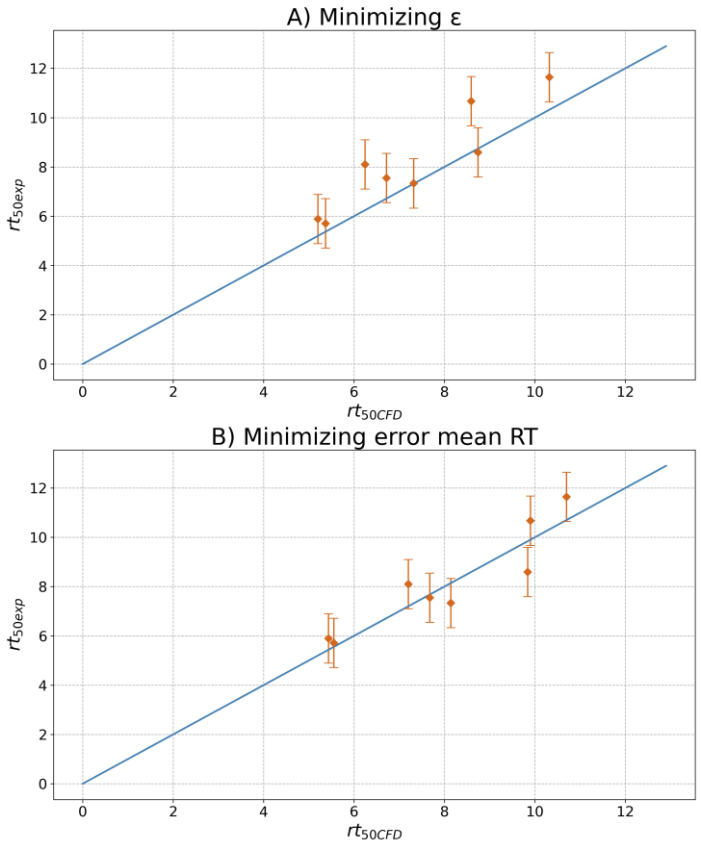

Figure 7. Mean residence time prediction A) minimizing the error of the cumulative RTD and B) minimizing the error of the mean RT. The error bars represent the experimental error addressed in each experiment.

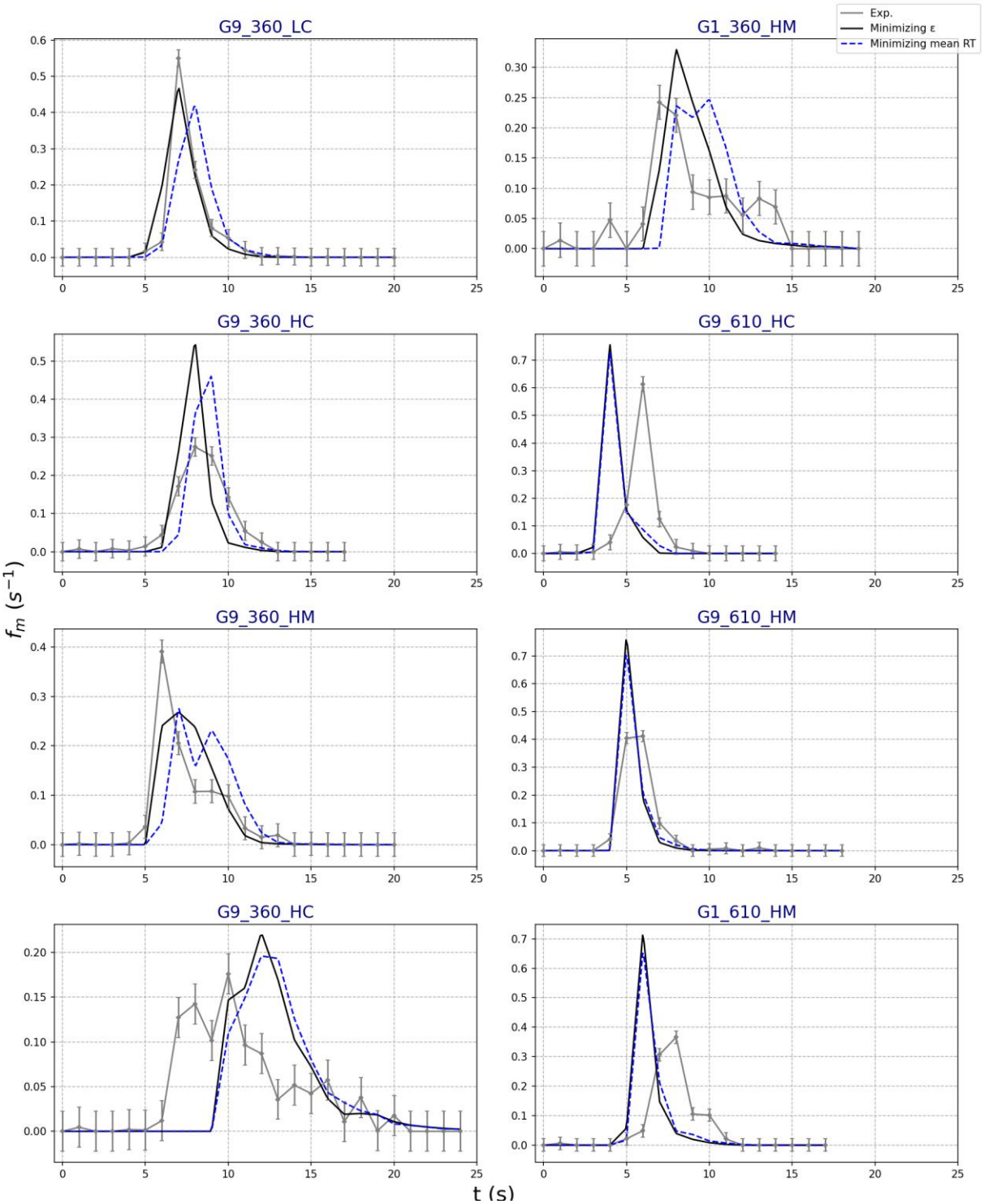

Figure 8. RTD curves obtained for glass beads by minimizing ε (-) and by minimizing the error with the mean RT (- -).

Minimization of the error in the mean RT

Alternatively, the estimation of the tangential restitution coefficient can be done on the basis of minimizing the error in the prediction of the mean RT. In this case, e_{tg}, is estimate to be 0.07, 0.1 smaller than with the minimization of the cumulative error. The results for the prediction of the mean RT and the RTDs are given in Figures 7, b) and 8. Figure 7, b) shows that the prediction of the mean RT improves, with predictions laying within the experimental error. However, as expected they exhibit a worse prediction of the full body on the RTD, whereby the average value of ε for all experiments increases to 0.4025 (see Table 5). Thus, this method captures better the mean RT than the previous one but it fails to capture the nuances of the sharp picks and long tails observed in the experiments, see for example experiment G9_360_HM.

Further analysis.

In the procedure presented one must question the effects of fixing the role of the normal restitution coefficient, e_n, to a given value to estimate the corresponding tangential restitution coefficient, e_{tg}. In order to evaluate if the accuracy of the methodology proposed is independent of the value of the e_{tg} selected, a sensitivity analysis has been carried out by conducting an entire new set of simulations fixing e_n to 0.6 instead of 0.7. The new e_{tg} obtained following the methodology of minimizing ε is 0.34. A comparison of the pairs 0.7-0.17 and 0.6-0.34 is available in Figure S-4 of the supplementary material, which only shows minor changes in the variance of the RTD. In experiments G9_360_LC and G9_610_HC, the curves obtained are wider for a lower e_{tg} but in experiments G1_360_HC, G1_360_HM and G9_360_HM they are narrower. The average cumulative error of the RTD for the new pair 0.6-0.34 is ε=0.384, which is very near to the pair 0.7-0.17 (ε=0.3419). Furthermore, the comparison based on the estimation of the mean RT also gives similar results, see Figure S-5 of the supplementary material. Thus, within the range of values studied, the approach presented can be considered independent of the selected value of e_n.

The results obtained by the methodology developed in the current work can be directly compared to the ones provided by Ali et al. [15], see Figure 9. A direct comparison of experiment G9_610_HC of the current work is presented in Figure 9, a). It shows that in previous work, the RT computed by the CFD model was between 2 and 3 seconds higher than the experimental values. In the new procedure, the error in the prediction of the RT is lower than 0.5 s. A second comparison is applied to another experiment with glass beads, G1_360_HC in the current work that could not be fitted in the previous work [15]. While previous models were unable to qualitatively describe it, the current methodology has an error of 0.9 s for the mean RT. Two main reasons explains the improvements observed:

- Prediction of the vortex momentum flux. Instead of the air velocity profiles used in [15], this work uses the swirl intensity as calibrating parameter to predict the air momentum in the tower. A calibration based on the swirl intensity ensures a better overall prediction of the momentum flow and takes into account the importance of error distribution in the modelling of the airflow. Furthermore, the model is able to include the influence of the deposition conditions, ensuring a better definition of the flow pattern [5].

- Functionality of the restitution coefficients. In previous works [15] the contact between glass beads and walls were described with a constant value of 0.7 for the restitution coefficient. The restitution coefficient was combined with two roughness wall models: smooth with only impact and rough with an stochastic effect, leading to the profiles presented in Figure 9, a) where the use of a rough wall collision model increases the RT and worsens the prediction [15]. Furthermore, even though an stochastic rebound model was implemented according to the roughness, the restitution coefficient was still taken as 0.7 in contradiction with the observations of Huber and Sommerfeld [34]. As we have mentioned, the restitution coefficients depend on a wide range of variables among them the impact angle and the material of the wall. Despite these two attributes cannot be easily characterized in the tower under study, their influence has to be taken into to account since the impact of the particles in the tower and the material of the wall are not the same than in the value obtained from external experiments. Thus, instead of a fixed value obtained from experiments, this study proposes the use of an effective pair of restitution coefficients for the entire tower that lumps the effects concerning the particle-wall contacts and ensures a good prediction of the RT.

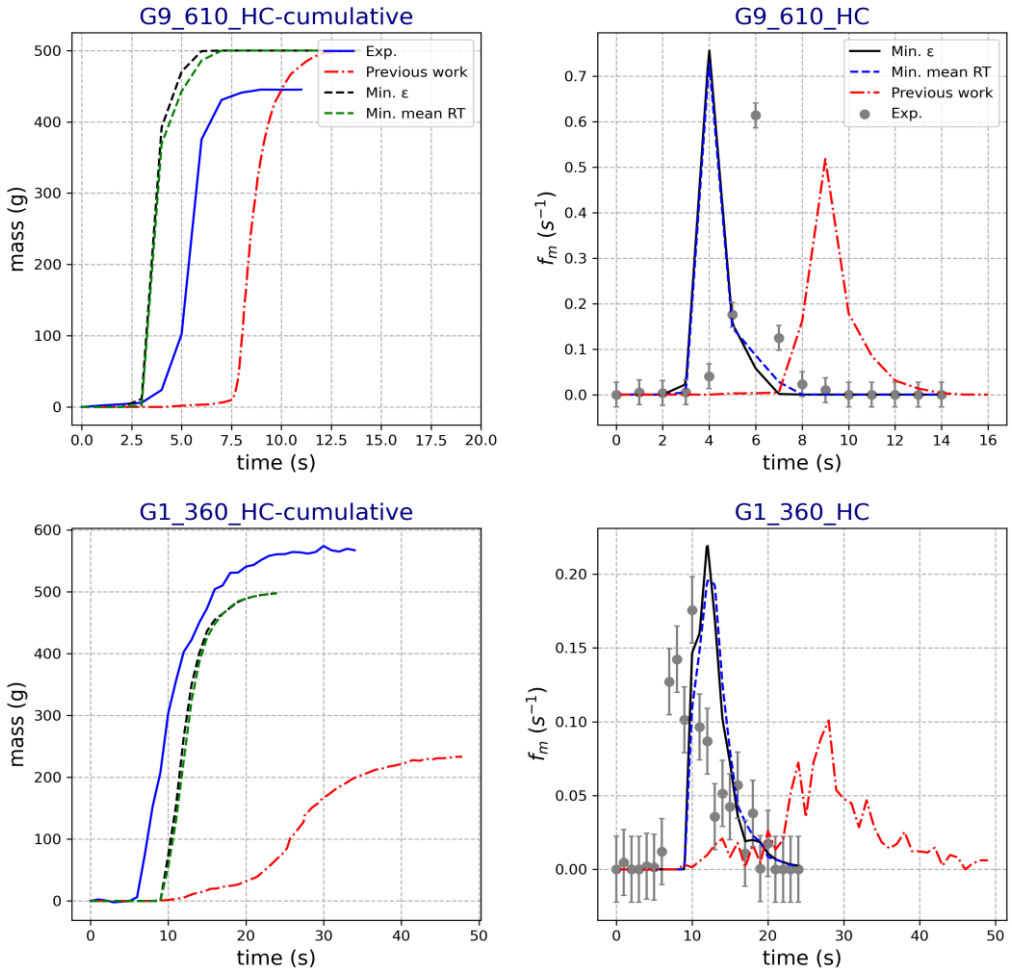

Figure 9. Comparison between the RT predicted by [15] and the current methodology in G9_610_HC (a) and G1_360_HC (b).

2.4.5.2.2 Residence time distributions of a pulse of detergent powder.

Minimization of the error in the cumulative RTD.

The minimization of the cumulative error in the RTDs results in a pair of restitution coefficients e_n-e_{tg} of 0.504-0.504. Since the restitution coefficients were not independently characterized and demonstrating in previous section that the solution is independently of the fixed e_{tg}, the minimization was carried out constraining that both restitution coefficients have to be equal. The average value of e_{tg}, including all the experiments is 0.45, which is 10% below the one estimated by a threshold in the minimization (further details are given in Table S-7 of the supplementary material). However, include all the values is much more costly in terms of computation and such a low errors enforces the validity of using the variance as a threshold to limit the computational cost. This method has an error of ±0.05 in estimating the optimal e_{tg}, for detergent powder reducing the computational cost to one half.

The results obtained for the mean RT and the RTD are subsequently presented in Figures 10, a) and 11, a). Figure 10, a) shows that the mean RT is underestimated, particularly in experiments D9_425_HC, D9_425_LM, D1_425_LM where the prediction is beyond the bounds of the experimental uncertainty. Analysing the fir of the RTD, the average cumulative error is 0.3849 (see Table 6), slightly higher than in the case of the glass beads (ε=0.3419). In particular, experiments D9_425_HC, D9_425_LC, D1_425_HC and D1_425_HM are the ones with the highest errors. In the case of D9_425_HC and D9_425_LC the model shows an over-estimation of the dispersion, obtaining a wider curve. In experiments D1_425_HC and D1_425_HM the model underestimate the mean RT beginning the release of particles too early. With the exception of experiment D9_425_LC, the other three cases share the same height of the injection. It seems for injections in a higher location and with detergent powder (low St and Ar numbers), the model tends to underperform by overestimating the level of dispersion. Note that the particles with worst prediction have been shown to be the ones with low St numbers (detergent powder) and subsequently the ones more affected by the eddies. Therefore, even though particle-wall interaction have the greater impact on the modelling of the RT, in future works the model must be extended to include more detailed physics. Particularly, in regards to the turbulence and the effect of the flow on the particles near the wall.

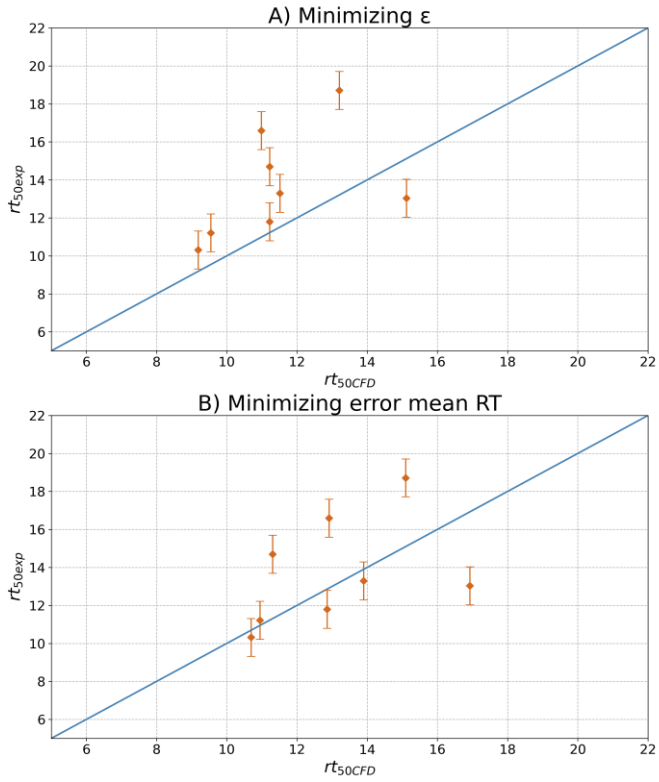

Figure 10. Mean RT predicted for detergent powder based on minimizing ε and minimizing the error with the mean RT.

Table 6. Cumulative error of the hybrid CFD-DPM and machine learning model for detergent powders.

Experiment	**ε, Method A) Minimizing ε**	**ε, Method B) minimizing error with mean RT.**
D9_425_HC	0.4023	0.4410
D9_425_HM	0.2789	0.4127
D9_425_LC	0.3986	0.3494
D9_425_LM	0.2347	0.2933
D1_425_HC	0.5837	0.4714
D1_425_HM	0.4423	0.3822
D1_425_LC	0.3673	0.3456
D1_425_LM	0.3716	0.4061
Average	0.3849	0.3877

Minimization of the error in the mean RT

Following this second procedure, the estimated restitution coefficient e_{tg} is obtained to be 0.39, which is 25% lower than the one obtained by minimizing the cumulative error. The predictions are given in Figures 10, b) and 11. As expected, the prediction of the mean RT improves that of the minimization of the cumulative error. In the later RTD curves are delayed in comparison causing the prediction in some cases (see for example experiment D1_425_LM) to miss the main pick of the release. In this case the cumulative error is 0.3877, almost identical to the minimization of the cumulative error itself. Such small difference in the error between both methods can be due to the higher dispersion of the detergent. The RTD curves of glass beads were narrower and more different one to another requiring the model to track many picks, while in detergent they are wider and more homogeneous, fulfilling the assumption required in the minimization of their average instead of the distribution (variance is similar in all the cases).

Apart from the comparison between both methods, the restitution coefficient obtained can be also compared with the one measured experimentally. The current effective restitution coefficient for all the unit is higher than the one characterised experimentally for layered walls (0.3 ± 0.07). However, it is important to remark that in the dryer the contacts are by far much more irregular in the dryer (modified by the impact angle and irregular level of deposition) than in a single experiment, which difficult any further comparison or scalability between them.

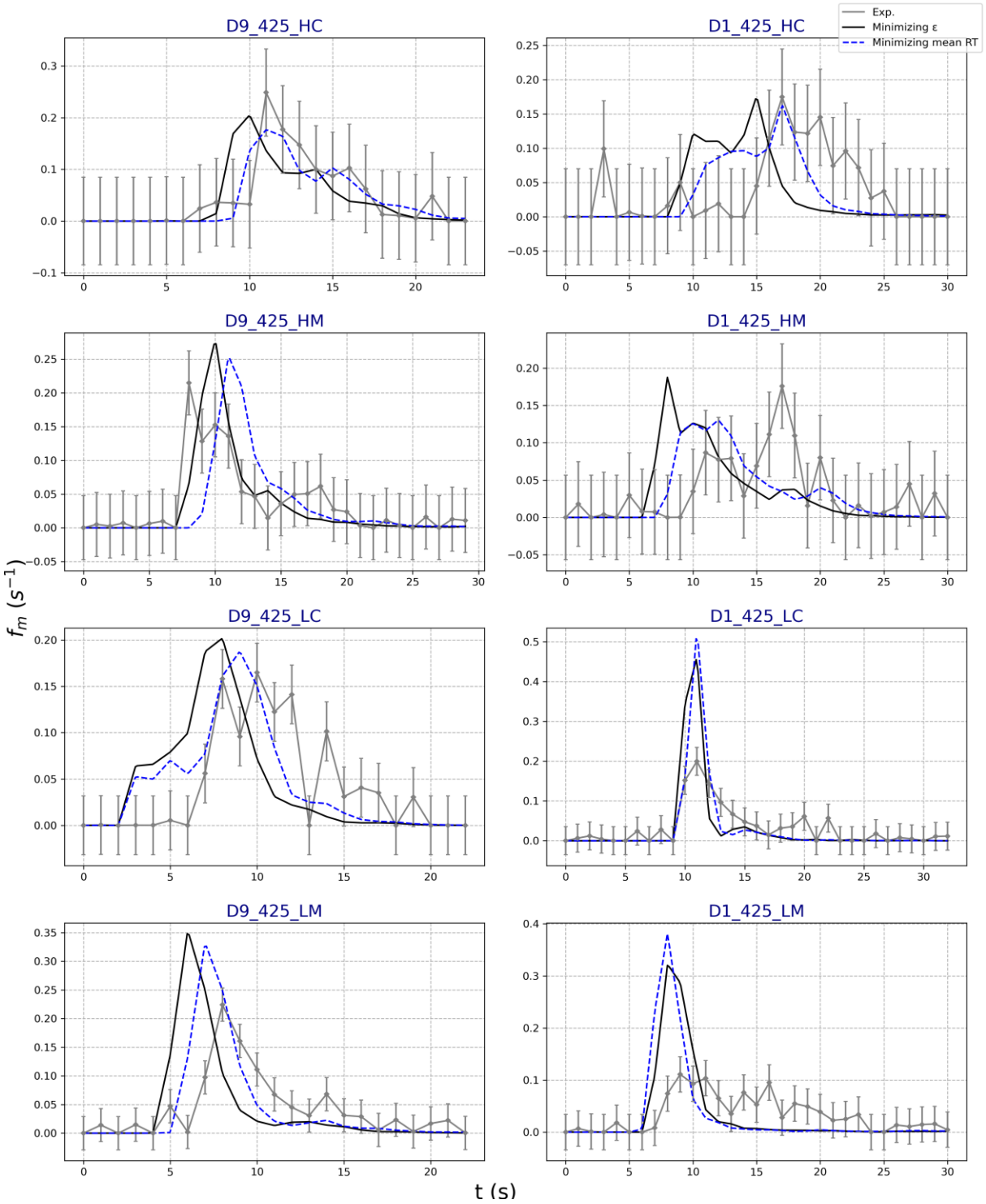

Figure 11. RTD curves obtained for detergent powder by minimizing ε (-) and by minimizing the error with the mean RT (- -).

2.4.5.3 Results for the analysis of equivalent reactors

As an example, Figure 12 presents the comparison of experimental data with an ideal system of reactors. The estimated number of equivalent CSTR in series and the Peclet, Pe, numbers are given in Table 7. Pe numbers are higher than 10 in every experiment, suggesting a low dispersion overall [12]. Comparing both materials however, the average number of equivalent CSTR's for detergent powder is 21 (Pe=43) whereas it is 48 (Pe=97) for glass beads, in an indication that detergent powder has more dispersive behaviour. Thus, modelling it as a PFR without dispersion would cause significant issues which may explain the errors reported by other researchers [16], modelling the same dryer as a PFR.

Despite lower Pe are observed for detergents, most of the experiments with glass beads show values well over 10, which suggests that the equivalence between the number of CSTR and the Pe can be achieved by modelling the PFR as an open system (Pe_{open}), see Eq. (43). However, there are some cases (e.g. Experiments G1_360_HC, G1_360_HM, D9_425_LM and D1_425_LM) in which the Pe number is close to 10 and the open boundary conditions model, Eq. (43) cannot reproduce the system. A more detailed comparison between the estimated Pe and Pe_{open} is available in the supplementary material, Table S-8.

$$\sigma_\theta = \frac{1}{N_t} = \frac{2}{Pe_{open}} - \frac{8}{Pe_{open}^2} \tag{43}$$

A final alternative is to combine a PFR followed by a set of CSTR to address the dispersion. Table 7 shows the estimation of the parameters in this model (delayed relative residence time, , θ_{del} , and number of CSTR after the PFR). In most of the cases only one CSTR is required to deal the dispersion. In these cases, the PFR+CSTR model should be reduced to Eq. (34) as shown in other studies [38, 39]. The influence of each inputs in the number of CSTR's computed has been analysed. As a result, the variables with higher influence in the number in the number of CSTR's required are the Ar, St and Re_{pterm} (the cross correlations are available in the supplementary material, Figure S-6). The increase in all these three numbers results in an increase in the number of tanks. In the case of the Ar and $Re_{pterm,}$ an increase represents a higher influence of gravity versus the drag force so a lower dispersion through turbulence, resulting then in a low number of tanks. Similarly, an increase of the particle St implies lower chances of the particle to be captured by the flow pattern of the air. The second model parameter is the relative RT of the delay, θ_{del}. None of the inputs appear to have a significant correlation (see Figure S-7 of the supplementary material). The variables with higher influence are the Re_{pterm} and the height of the injection. Re_{pterm} is an indicator of the velocity of the particles in free-fall and consequently the time these particles spent in the dryer. Thus, for higher Re_{pterm}, lower values of θ_{del} are obtained. With a similar effect, a higher injection point increases the delay of the particles to get the CSTR.

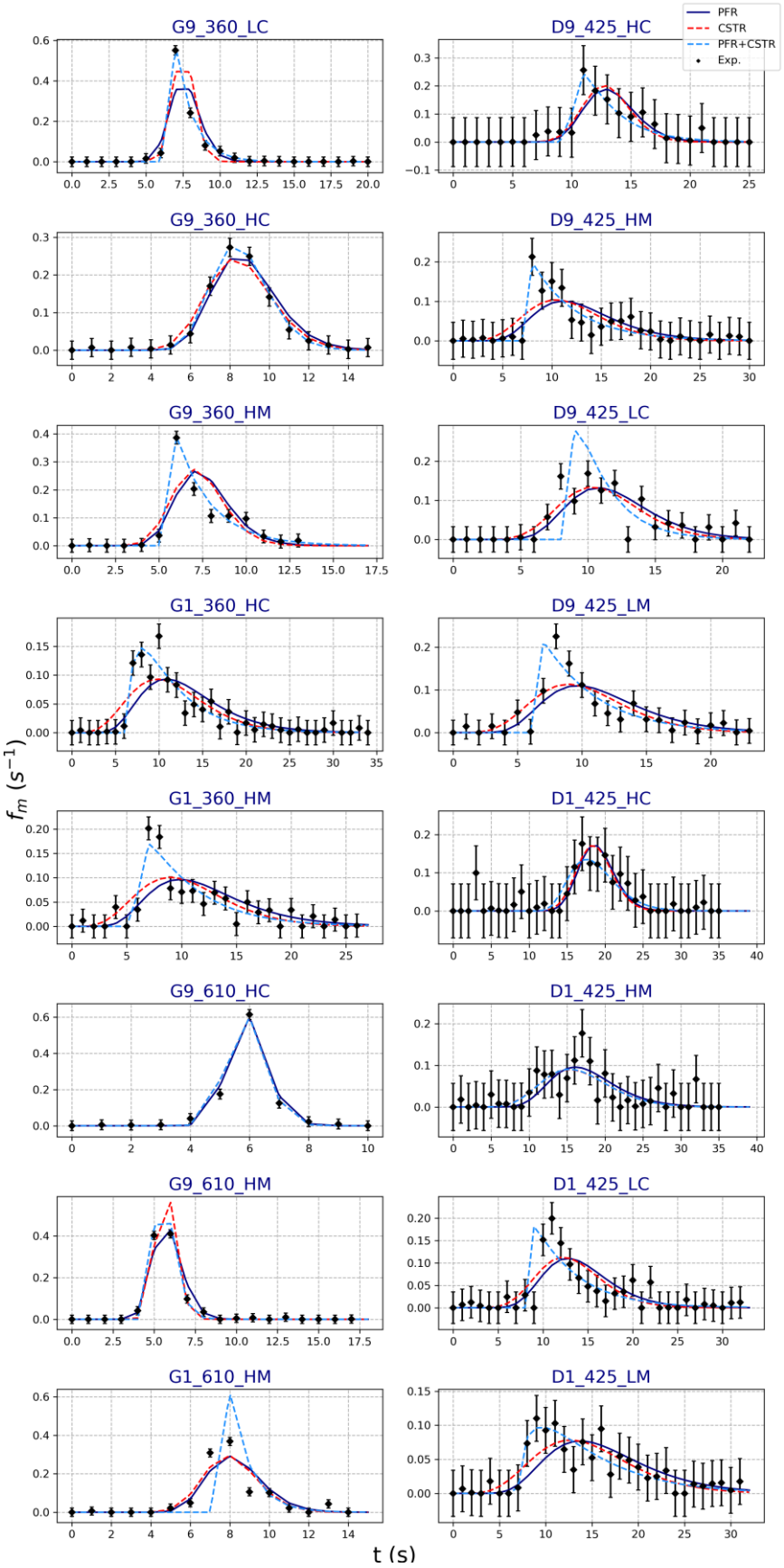

Figure 12. Comparison of mass fraction recovered at the bottom by the experiments and the estimated by CSTR, PFR and PFR+CSTR models.

Table 7. Number of CSTR in series and Peclet number of a PFR for each experiment.

Experiment	Number CSTR	Pe	$CSTR_{PFR+CSRT}$	θ_{del}
G9_360_LC	120	240.65	1.02	0.843
G9_360_HC	26.7	53.45	22.18	0.211
G9_360_HM	24.6	49.15	1	0.723
G1_360_HC	6.4	12.93	1.32	0.575
G1_360_HM	6.3	12.67	1.15	0.562
G9_610_HC	83.8	165	83.8	0
G9_610_HM	88.2	176.41	4.63	0.768
G1_610_HM	35.4	70.85	1.16	0.864
D9_425_HC	43.2	86.40	1.22	0.767
D9_425_HM	8.5	17.10	1	0.616
D9_425_LC	13.3	26.56	4.17	0.357
D9_425_LM	7.6	15.29	1.05	0.596
D1_425_HC	65.4	130.85	7.2	0.554
D1_425_HM	13	31.18	12.66	0.020
D1_425_LC	13.2	26.47	1.06	0.642
D1_425_LM	7.3	14.61	1.49	0.476

The use of a system of reactors have shown to reproduce with high accuracy the shape of the residence time distributions. A quantitate evaluation of the error of each model is carried out by integrating the age curve of each reactor model with a discretization of 1s and computing the cumulative differences as in Eq. (22). The results of the cumulative error are presented in Table 8 showing higher errors for the cases with higher residence times. Thus, a relative cumulative error based on the mean RT is also defined as in Eq. (44). The results for this relative error are also presented in Table 8 showing that the equivalent reactor network with the lowest error is the one that combines a PFR and a set of CSTRs since it contains one parameter more in the fitting. However, the reactor network is highly dependent of the operating conditions. For proposing a general model that adapt the reactor network to the inputs in the operating conditions more accurate reduced models (including non-linear terms) have to be developed for the dispersion as well as the CFD-DPM model must include the use of a nozzle for injecting the particles, which can be carried out in future works. The quality as well as the robustness of the models for determining the parameters as a function of the inputs will be critical to determine the best reactor network approach.

$$\varepsilon_t = \frac{\sum_{t=0}^{n} \sqrt{(w_{CFD} - w_{exp})^2}}{2 \cdot \bar{t}} \tag{44}$$

Table 8. Cumulative error for equivalent PFR and CSTR models.

Experiment	ε_{PFR}	ε_{CSTR}	$\varepsilon_{PFR+CSTR}$	$\varepsilon_{t\,PFR}\,(s^{-1})$	$\varepsilon_{t\,CSTR}\,(s^{-1})$	$\varepsilon_{t_{PFR+CSTR}}(s^{-1})$
G9_360_LC	0.2653	0.2314	0.0639	0.0351	0.0307	0.0085
G9_360_HC	0.1053	0.0823	0.0400	0.0123	0.0096	0.0046
G9_360_HM	0.2557	0.2657	0.0955	0.0349	0.0362	0.0130
G1_360_HC	0.2472	0.2314	0.1433	0.0212	0.0199	0.0123
G1_360_HM	0.2562	0.2821	0.2052	0.0240	0.0264	0.0192
G9_610_HC	0.0889	0.0889	0.0889	0.0151	0.0151	0.0151
G9_610_HM	0.1685	0.1532	0.1071	0.0295	0.0268	0.0188
G1_610_HM	0.2070	0.1841	0.4201	0.0255	0.0227	0.0519
D9_425_HC	0.2551	0.2559	0.2261	0.0196	0.0196	0.0173
D9_425_HM	0.3021	0.2993	0.1926	0.0256	0.0254	0.0163
D9_425_LC	0.1575	0.1651	0.1853	0.0140	0.0147	0.0165
D9_425_LM	0.2698	0.2278	0.3015	0.0262	0.0221	0.0292
D1_425_HC	0.3103	0.3097	0.2711	0.0166	0.0165	0.0145
D1_425_HM	0.3492	0.3328	0.3235	0.0210	0.0201	0.0195
D1_425_LC	0.3091	0.2864	0.2007	0.0233	0.0215	0.0151
D1_425_LM	0.2166	0.1964	0.1495	0.0147	0.0134	0.0102

2.4.6 CONCLUSIONS

This study has presented two modelling approaches and a statistical analysis of the RTD in a spray drying counter-current dryers independently from drying and agglomeration phenomena. The analysis of the RT of the particles is reported under different operating parameters such as Re, injection locations (radial and axial), particle size and surface properties varying hardness and sphericity (glass beads and detergent powder). The differences observed in the mean RT are associated to four dimensionless groups, primarily the operating Re of the dryer and the Ar number, and to a lower degree the particle Stokes number and the particle Re_{pterm} referred to terminal velocity. The particle Stokes number does not only mean RT, but drives most of variance of the RTD, which is expected for a strong turbulent flow.

A detailed modelling approach has been proposed, making use of a CFD-DPM model and experimental data to estimate the effective pair of restitution coefficient by an iterative learning procedure. Analysis of CFD-DPM simulations has shown a high sensitivity in the prediction of the RT to the treatment of the particle-wall interactions. Modelling particle-wall interaction is not a trivial task in a detergent spray dryer where the walls are covered by irregular deposits, difficult to characterise experimentally and to reproduce and scale-up numerically. The

procedure proposed here has addressed these limitations by using a machine learning framework to determine the pair of restitution coefficients that minimize the error in the prediction of the RTD of the solid phase. Under the new methodology, the error for the CFD-DPM methodology is far lower than previous computational works focus on modelling these units [15]. However, it is higher than the one of an ideal system of reactors. One must notice that a series of equivalent reactors utilises 2 or 3 fitting parameters whereas the CFD-DPM uses a single parameter (fully correlated) pair of restitution coefficients to minimise the errors. The need to estimate the restitution coefficients is based on the irregular levels of deposition observed experimentally and the difficulty to characterise them. Furthermore, other physics (eg. rolling of the particles in the bottom cylindrical region) can be highly relevant since the particle-wall contact at this bottom region is also significant. In further works more detailed models can be developed but due to the high complexity and heterogeneity of the momentum in the particle-wall contact, it is recommended to study the particle dynamics by regions. For example, DEM simulations can be used to reproduce the dynamics in the bottom conical section.

A second modelling approach evaluates the use of an equivalent system of reactors to model the dispersion. Three models based on an equivalent set of CSTRs, PFR with dispersion and PFR+CSTR were evaluated. The PFR followed by a CSTR that address the dispersion shows to be the one with the best accuracy. However, the network of equivalent reactors is not generalized to make adaptable the reactor network to the input properties. In the current work only the three systems have been evaluated but they cannot be used for the modelling of a spray dryer in current operation since the nozzle is not included in the injection of the particles. Thus, for an appropriate characterization of a robust reactor based model, it has to be developed in future stages based on CFD-DPM simulations based on the current CFD-DPM model but with the inclusion of a nozzle to inject the particles.

APPENDIX.

Table A-1. Summary of the computational settings and models for the CFD-DPM model.

Number of mesh elements	1.08×10^6
Mesh size	60 mm
Continuity equation (A-1)	$\frac{\partial \rho}{\partial t} + \nabla \cdot (\rho U) = 0$
Navier-Stokes equation (A-2)	$\frac{\rho D U_j}{Dt} = \mu \nabla^2 U - \nabla P + \frac{1}{3}\mu \nabla(\nabla \cdot \mathrm{U}) - \rho g$
Reynolds Stress Model (A-3)	$\frac{DR_{ij}}{Dt} = \frac{\partial R_{ij}}{\partial t} + C_{ij} = P_{ij} + D_{ij} - \varepsilon_{ij} + \Phi_{ij} + S_{ij}$
Constants in Reynolds Stress model	$C_{\varphi 1} = 1.8$
	$C_{\varphi 2} = 0.6$
	$C'_{\varphi 1} = 0.5$
	$C'_{\varphi 2} = 0.3$
	$C_{\mu} = 0.09$
	$C_{\varepsilon 1} = 1.44$
	$C_{\varepsilon 2} = 1.92$
	$\sigma_{\varepsilon} = 1.3$
	$\sigma_k = 1$

ACKNOWLEDGEMENTS

Authors would like to acknowledge financial support from P&G.

NOMENCLATURE

A_c	Area of the cylindrical part of the dryer (m^2).
A_i	Area of the air flow inlets (m^2).
A_p	Area of the particle (m^2).
A_{pr}	Projected area of the particle (m^2).
A_{sphere}	Area of the particle as a sphere (m^2).
Ar	Archimedes number.
B	Additive constant of the logarithmic law.
C_D	Drag coefficient.
C_{ij}	Mean flow convection (m^2/s^2)
C_s	Roughness constant (1).
d	Particle diameter (μm).
d_{min}	Minimum diameter of the particle size distribution (μm).
d_{mean}	Particle mean diameter in a Rosin Rammler distribution (μm).
d_{max}	Maximum diameter of the particle size distribution (μm).

D_A	Constant of the drag coefficient computation.
D_B	Constant of the drag coefficient computation.
D_C	Constant of the drag coefficient computation.
D_D	Constant of the drag coefficient computation.
D_T	Tower diameter (m).
D_{ij}	Transport by diffusion (m^2/s^2).
e_n	Normal restitution coefficient.
e_{tg}	Tangential restitution coefficient.
E	Age curve.
f_m	Mass frequency distribution (s^{-1})
F_B	Basset force (N/s).
F_D	Drag force term acting on the particle (m/s^2).
F_g	Gravity force term acting on the particle (m/s^2).
$F_{p,s}$	Pressure bouyant force term on the particle (m/s^2).
F_{und}	Force term that accounts the force of the undisturbed flow on the particle (m/s^2).
F_{vm}	Virtual mass force term (m/s^2).
g	Gravity constant (9.81 m/s^2).
M_c	Mass flowrate of air at the cylindrical region of the dryer (kg/s).
M_i	Mass flowrate of air at the airflow inlets (kg/s)
m_p	Mass of the particle (kg).
m_{p50}	Mass of the particle with the mean diameter.
N	Number of CSTR.
N_p	Total number of parcels.
$\dot{N}_p$	Number of parcels per second.
P	Pressure force of the air (N/s).
P_{ij}	Turbulence production tensor (m^2/s^2).
Pe	Peclet number
Pe_{open}	Peclet number for a PFR with open-open boundary conditions.
Q	Volume flow rate of the air (m^3/s)
r	Radial location in the dryer (m).
rt	Residence time of the particles (s)
Ra	Wall mean roughness (m).
R_{ij}	Reynolds stress produced by velocity components i and j (m^2/s^2).
R_T	Tower radius in the cylindrical region (m).
R_i	Tower radius at the inlets (m).
R_w	Mean profile width in the wall (m).
Re	Reynolds number of the dryer.
Re_p	Reynolds number of the particle.
s	Roughness height (m).
S_{ij}	Transport due to rotation (m^2/s^2).
St	Stokes number.
St_{50}	Stokes number for the mean diameter.
t	Time (s).
$\bar{t}$	Mean Residence Time (s).
t_{react}	Average Residence Time of a reactor (s).
t_{del}	Time of delay (s)
u_{in}	Tangential inlet velocity to the wall (m/s).
u_{out}	Tangential outlet velocity from the wall (m/s).
u_F	Velocity of the air (m/s).
u_p	Velocity of the particle (m/s).
u^+	Dimensionless velocity in logarithmic law of the wall.
w_{CFD}	Mass fraction obtained from the CFD model for every second.

w_{exp}	Mass fraction measured experimentally for every second.
$\overline{U}$	Average time axial velocity of the air in a point (m/s).
$\overline{U_{avg}}$	Average time axial velocity for the entire cross-sectional area (m/s).
v_{in}	Normal inlet velocity to the wall (m/s).
v_{out}	Normal outlet velocity from the wall (m/s).
v_{t50}	Terminal velocity of the particles with the mean diameter (m/s).
$\overline{W}$	Average time tangential velocity of the air in a point (m/s).
y^+	Dimensionless distance in the logarithmic law of the wall.
z	Height location in the tower (m).
z_{ref}	Height location of reference in the tower (m).

Symbols

α	Angle of rebound after particle-wall impact.
λ	Decay rate of the swirl intensity.
$\Delta\gamma$	Stochastic contribution due to wall roughness.
Ω	Swirl intensity.
Ω_i	Swirl intensity at the height of reference.
ξ	Axial alignment of the air inlets (rad).
ε	Cumulative error of the model in the RTD prediction.
ε_t	Cumulative error of the model in the RTD prediction divided by the average RT.
ε_{ij}	Turbulence dissipation rate (m^2/s^2).
κ	Von-Karman constant (0.41).
σ^2	Variance of the residence time distribution.
σ_θ	Dimensionless variance of the residence time distribution.
θ_{del}	Dimensionless residence time of delay for a PFR reactor.
ρ_A	Density of the air (kg/m^3).
ρ_p	Density of the particles (kg/m^3).
μ_A	Dynamic viscosity of the air ($kg\ m^{-1}\ s^{-1}$).
ψ	Sphericity.
Φ_{ij}	Pressure rate of strain tensor (m^2/s^2).
φ	Radial alignment of the air inlets (rad).
τ_f	Characteristic time of the fluid (s).
τ_p	Response time of the particle (s).
τ	Wall shear stress (Pa).

REFERENCES

[1] Masters, K. Spray Drying: An introduction to Principles, Operational Practice and Applications. **1972**. London: Leonard Hill Books.

[2] Fletcher, D.F. Guo, B. Harvie, D.J.E. Langrish, T.A.G. Nijdam, J.J. Williams, J. (2006) What is important in the simulation of spray dryer performance and how do current CFD models perform? Applied Mathematical Modelling, Vol. 30, 11, 1281-1292.

[3] Huntington, D.H. (2004) The influence of the Spray Drying Process on Product Properties. Drying Technology. Vol. 22, No. 6, pp. 1261-1287, 2004.

[4] Woo, M. W. (2017) Computational Fluid Dynamics Simulation of Spray Dryers. An Engineer's Guide. CRC Press. Taylor & Francis Group. ISBN: 978-1-4987-2464-7.

[5] Hernandez, B. Fraser, B. Martin de Juan, L. Martin,M. (2018) Computational Fluid Dynamics (CFD) Modeling of Swirling Flows in Industrial Counter-Current Spray-Drying Towers under Fouling Conditions. Ind. Eng. Chem. Res. DOI: 10.1021/acs.iecr.8b02202

[6] Francia, V. Spray drying of detergents in counter current towers: a study of turbulent swirling flows, fouling and agglomeration. EngD. Thesis. University of Birmingham.
[7] Francia et al. (2016) Francia V, Martin L, Bayly AE, Simmons MJH. 2016. Agglomeration in counter-current spray drying towers. Part A: Particle growth and the effect of nozzle height. Powder Technology 301 : 1330-134

[8] Jaskulski, M. Wawrzyniak, P. Zbicinski, I. (2015) CFD Model of Particle Agglomeration in Spray Drying. Drying Technology. 33: 1971-1980, 2015.

[9] Harvie, D.J.E. Langrish, T.A.G Fletcher, D.F. (2002) A Computational Fluid Dynamics Study of a Tall-Form Spray Dryer. Food and Bioproducts Processing, 80, 2002, 163-175.
[10] Pham, Q.T. Keey, R.B. (1977) Some Experiments on the Residence Time Distribution of Droplets in a Cocurrently Worked Spray Chamber. The Canadian Journal of Chemical Engineering, Vol. 33, August, 1977.
[11] Kieviet, F. G. (1997) Modelling Quality in Spray Drying. PhD Thesis, Eindhoven University of Technology.
[12] Ducept, F. Sionneau, M. Vasseur, J. (2002) Superheated steam dryer: Simulations and experiments on product drying. Chemical Engineering Journal 86 (2002) 75-83
[13] Huang, L. Kumar, K. Mujumdar, A.S. (2003) Use of Computational Fluid Dynamics to Evaluate Alternative Spray Dryer Chamber Configurations, Drying Technology, 21:3, 385-412.
[12] Gao, Y. Muzzio, J. Ierapetritou, M. G. (2012) A review of the Residence Time Distribution (RTD) applications in solid unit operations. Powder Technology, 228, 2012, 416-423.
[13] Ruprecht, N. Kohlus, R. (2018) Determination and modelling of the particle size dependent residence time distributions in a pilot plant spray dryer. 21st International Drying Symposium Proceedings. DOI: 10.4995/IDS2018.2018.7740
[14] Francia, V. Martin, L. Bayly, A.E., Simmons, M.J.H. (2015) Influence of wall friction on flow regimes and scale-up of counter-current swirl spray dryers. Chemical Engineering Science, 134, 2015, 399-413.
[15] Ali, M. Mahmud, T. Heggs, P. Ghadiri, M. Bayly, A. Crosby, M. Ahmadian, H. Martindejuan, L. Alam, Z. (2017) Residence time distribution of glass ballotini in isothermal swirling flows in a counter-current spray drying tower. Powder Technology 305 (2017) 809-815.
[16] Ali, M. Mahmud, T. Heggs, P.J. Ghadiri, M. Djurdjevic, D. Ahmadian, H. Martín de Juan, L. Amador, C. Bayly, A. (2014) A one-dimensional plug-flow model of a counter-current spray drying tower. Chemical Engineering Research and Design, 92 (5), 826-841.
[17] Kitoh, O. Experimental study of turbulent swirling flow in a straight pipe. *J. Fluid Mech*. **1991** 225, 445-479.
[18] Francia, V. Martín, L. Bayly, A.E. Simmons, M.J.H. (2015) An experimental investigation of the swirling flow in a tall-form counter current spray dryer. Experimental Thermal and Fluid Science. Vol. 65, 52-64.
[19] Gibson, M.M. Launder, B. E. Ground Effects on Pressure Fluctuations in the Atmospheric Boundary Layer. *J. Fluid Mech*, 1978, 86:491-511.
[20] Fluent User's Guide; Ansys, Inc., 2009; available via the Internet at: http://www.ansys.com.
[21] Crowe, C.T. Schwarzkopf, J.D. Sommerfeld, M. Tsuji, Y. (2011) Multiphase Flows with droplets and particles. 2nd Edition. ISBN: 9781439840504
[22] Soltani, S. Gerde, P. Acevedo, F. Rasmuson,A. (2015) Counter-current spray drying with stream separation: Computational modeling of a novel dryer design. Chem. Eng. R&D, 93 (2015) 163-173.
[23] Seville, J.P.K. (1997) Gas cleaning in demanding applications. Springer-Science + Business Media Dordrecht. ISBN: 978-94-011-7665-1.
[24]] Lain, S. (2010) On Modelling and Numerical Computation of Industrial Disperse Two-Phase Flow with the Euler-Lagrange Approach, Shaker Verlag, Aachen, Germany, 2010.
[25] Goz, M.F. Lain, S. Sommerfeld, M. (2004) Study of the numerical instabilities in Lagrangian tracking of bubbles and particles in two-phase flow. Computers & Chemical Engineering 28 (2004) 2727-2733.
[26] Sommerfeld, M. (2016) Forces on Particles, Droplets and Bubbles and their Importance. CFD for Dispersed Multi-Phase Flows Best Practice Guidelines. ERCOFTAC.
[27] Turton, R. Levenspiel, O. (1986) A short note on the drag correlation for spheres. Powder Technology, 47, 1,1986, 83-86.
[28] Haider, A. Levenspiel, O. (1989) Drag coefficient and terminal velocity of spherical and non-spherical particles. 58, 1, 1989, 63-70
[29] Ganser, G. (1993) A rational approach to drag prediction of spherical and non-spherical particles. Powder Technology, 77, 1993, 143-152.

[30] Hutchinson, P. Hewitt, G.F. Dukler, A.E. (1971) Deposition of liquid or solid dispersions from turbulent gas streams: a stochastic model, Chem. Eng. Sci. 26 (1971), 419-439.
[31] Francia, V. Martin, L. Bayly, A.E. Simmons, M.J.H. (2015). The Role of Wall Deposition and Re-Entrainment in Swirl Spray Dryers. AIChE Journal. Vol. 61, No. 6, 1804-1821.
[32] Francia, V. Martin, L. Bayly, A.E. Simmons, M. J. H. (2017) Agglomeration during spray drying: Airborne clusters or breakage at the walls? Chemical Engineering Science, 162, 2017, 284-299.
[33] Ali, M. Mahmud, T. Heggs, P.H. Ghadiri, M. Bayly, A. Ahmadian, H. Martin de Juan, L. (2015) CFD Simulation of a counter-current Spray Drying Tower with Stochastic Treatmetn of Particle-wall Collision. Procedia Engineering, Vol. 102, 2015, 1284-1294.
[34] Sommerfeld, M. Huber, N. (1999) Experimental analysis and modelling of particle-wall collisions. International Journal of Multiphase Flow, 25 (1999) 1457-1489.
[35] Hassall, G. (2011) Wall Build up in spray dryers. EngD. Thesis, University of Birmingham.
[36] Kumar, A. Vercruysse, J. Vanhoorne, V. Toiviainen, M. Pierre-Emmanuel, P. Juuti, M. Vervaet, C. Remon, J.P. Gernaey, K.V. De Beer, T. Nopens, I. (2015) Conceptual framework for model-based analysis of residence time distribution in twin-screw granulation. European Journal of Pharmaceutical Sciences, Vol. 71, 2015, 25-34.
[37] Hua, L. Wang, J. (2018) Residence time distribution of particles in circulating fluidized bed risers. Chemical Engineering Science, 186, 2018, 168-190.
[38] Escotet-Espinoza, M.S. Moghtadernejad, S. Oka, S. Wang,Z. Wang, Y. Roman-Ospiro, A. Schäfer, E. Cappuyns, P. Van Assche, I. Futran, M. Muzzio, F. Ierapetritou, M. (2019) Effect of material properties on the residence time distribution (RTD) characterization of powder blending unit operations. Part II of II: Application of models.
[39] Rodríguez-Rojo, S. López-Valdezate, N. Cocero, M.J. (2008) Residence time distribution studies of high pressure fluidized bed of microparticles. The Journal of Supercritical Fluids. Vol. 44, 3, 2008, 433-440.
[40] Wawrzyniak, P. Jaskkulski, M. Piatkowski, M. Sobulska, M. Zbicinski, I. Egan, S. (2019) Experimental detergent drying analysis in a counter-current spray dryer with swirling air flow. Drying Technology, 38, 108-116.

CHAPTER 2.5 CFD MODELING OF DRYING WITHIN THE COUNTER CURRENT SPRAY DRYER.

ABSTRACT

This chapter presents the rigorous modeling of the heat and mass transfer phenomena in the counter-current spray dryer used in previous chapters. Even though the strategy for developing CFD models for spray dryers is based on model first the momentum of continuous and discrete phases independently from heat and mass balance, in previous studies from other research groups this methodology has not been followed, validating straightforward the energy balance, and when the momentum of the discrete phase has been independently studied, high differences have been reported between the CFD model and the experiments, suggesting that in previous studies the errors are balance each other and a wrong scale-up have been carried out. Thus, in the current chapter a CFD-DPM model validated independently from heat and mass transfer is applied for the first time in a counter-current dryer. The model is validated for wide range of operating conditions, including different detergent formulations, Reynolds numbers and temperatures of the air, heights of the injection and mass loadings; showing a good prediction of the temperature profiles through the dryer but still failing on predicting the particle properties indicating the importance of implementing agglomeration mechanisms in future works.

Note: The supplementary material is attached in the physical version of the thesis and also available in: https://drive.google.com/drive/folders/1_EkYTjaqQYkP_okY1ckLG9DMSdbt8gRt?usp=sharing

2.5.1 SCOPE OF THE CHAPTER.

The modeling of heat and mass transfer phenomena in either rigorous or reactor based models [1] has been carried out by scaling-up the drying of a single droplet by means of Ranz-Marshall correlations [2]. In the case of a rigorous modeling based on CFD simulations, the solution must be carried out in a subsequent series of steps as described in [3,4]. In the two first steps, the momentum of the continuum and discrete phases is independently modeled and validated. In the third step, the heat and mass transfer models are included in the model. Even though this procedure is widely accepted in the community, in most of the cases the CFD model is straightforward validated in the mass and energy balances, which does not allow to understand the source of error (continuous or discrete phase momentum models or heat and mass transfer model). These errors can balance each other and the physics behind will have problems to be reapplied in the modeling of other operating conditions. Several research groups report work which neither validation of the air nor particle dispersion is carried out independently [5, 6] even they talk of the residence time of the discrete phase in the simulation [7]. In some cases the air is validated, missing the particle dispersion [8-10]. The only studies that follow a step by step comparison were carried out by Kieviet [11] and Ali et al. [12, 13]. In the first case Kieviet observed an important difference between the CFD and experimental residence time. In the second case, Ali et al. [12, 13] were able to predict the temperature distribution within the dryer but the model could not capture the particle dispersion. This fact suggests a possible interaction of errors between the momentum model and the heat and mass transfer ones, making the model not trustable. In the view of previous observations, the thesis has developed novel methodologies to ensure that in each of the stages the model is validated. Previous chapters have focused on the modeling and validation of the air and particle momentum and this chapter glance at the heat and mass balances in the dryer. The validation of the heat and mass balances, either straightforward or going step by step, has been traditionally carried out by means of an indirect measurement such as the temperature distribution within the unit [3, 9]. In the first section of the current thesis different single droplet drying models have been developed and validated with single droplet experiments. This chapter adapts the multistage model developed for single droplets and include it into the CFD-DPM model of the counter-current dryer developed in through this thesis. This CFD-DPM model has been sequentially validated in previous chapters and here the modeling and validation corresponds to the heat and mass transfer model. The validation is carried out using experiments developed in previous experimental works that include different detergent formulations (it has been performed internally at company level), several initial air and detergent temperatures and different mass loadings (mass detergent/mass of air).

2.5.2 MODELING

2.5.2.1 Droplet drying model

The scale-up of the drying model from the single droplet drying model evaluated in an acoustic levitator is carried out by means of the Ranz-Marshall correlations [2] for spheres, see Eq. (1) and (2). This scale-up

can be performed since the droplets and particles are dilute enough (with volume fractions below 10^{-3}) assuming that they do no interact sufficiently between them to modify the drying. The assumption has been carried out in different types of dryers where particle-particle interactions have been traditionally evaluated in later stages after performing a particle tracking of the dilute phase previously dried [14-16]. The use of these Ranz-Marshall correlations is also used in the current work for substituting the Sherwood and Nusselt numbers referred to the acoustic levitator, see chapter 1 for single droplet drying. Furthermore, the first stage of drying is also adapted including the variables that are experimentally characterized within the collaborating company. The novel model for the first stage of drying as well as a summary of the second and third stages is provided in the following lines.

$$Sh = 2 + 0.6Re^{0.5}Sc^{0.33} \quad (1)$$

$$Nu = 2 + 0.6Re^{0.5}Pr^{0.33} \quad (2)$$

1st Stage-Drying by the diffusion of water with shrinking droplet.

In the first stage the water of the surface diffuses into the surrounding air and results in a shrinkage of the droplet. This stage occurs until the locking point is achieved and the surface gets dried. In the study of chapter 1, the drying rate during this stage was computed from the general equation of mass transfer, Eq. (3).

$$\frac{dm_w}{dt} = 4\pi R^2 \cdot K \cdot k_c\left(C^g_{equil} - C_{surface}\right) \quad (3)$$

Even though the previous mass transfer equation has been the most widely used in modeling the drying of the droplets, it does not describe the dynamics of the concentration profile. Thus, an alternative solution can be performed based on Fick's second law [17, 18]. According to this law, the mass diffusion mechanism is defined as presented in Eq. (4). Assuming isotropic diffusion in one direction, Eq. (5) is obtained.

$$\frac{\partial C}{\partial t} = \nabla(D \cdot \nabla C) \quad (4)$$

$$\frac{\partial C}{\partial t} = D\frac{\partial^2 C}{\partial r^2} \quad (5)$$

The boundary and initial conditions to solve this equation are presented from Eq. (6) and (7). The boundary condition at the surface of the droplet is presented in the form of a mass flux, which is proportional to the drying rate computed per unit of area from the mass transfer equation, Eq. (6). Since the concentration of water in the liquid and vapor phases are different, a "partition coefficient" is defined to relate the gas-phase water concentration to the liquid-phase concentration in the drop, see Eq. (8). As initial condition, the concentration of the particle is assumed to be equal to the initial introduced as an input, see Eq. (7).

r=0: $$-D\frac{\partial C}{\partial r} = K \cdot k_c\left(C^g_{equil} - C_{surface}\right) \quad (6)$$

t=0: $$C = C_{init} \quad (7)$$

$$K = \frac{C_w^g}{C_w^l} \cong \frac{H \cdot \rho_{air}}{w_{init} \cdot \rho_{slurry}} \quad (8)$$

By applying Laplace transform, an analytical solution is obtained through time as presented in Eq. (10) [17]:

$$\frac{C - C_{init}}{C_{equil} - C_{init}} = \operatorname{erf}\left(\frac{r}{2\sqrt{D_{Deterg} t}}\right) - \exp\left(\frac{K \cdot k_c}{D_{Deterg}} r + \left(\frac{K \cdot k_c}{D_{deterg}}\right)^2 D_{Deterg} t\right) \operatorname{erf}\left(\frac{r}{2\sqrt{D_{Deterg} t}} + \frac{K \cdot k_c}{D_{Deterg}} \sqrt{D_{Deterg} t}\right) \quad (10)$$

From this Eq. (10), the mass flux can be computed at the surface (r=0) as presented in Eq. (11):

$$\frac{C - C_{init}}{C_{equil} - C_{init}} = 1 - \exp\left(\left(\frac{K \cdot k_c}{D_{Deterg}}\right)^2 Dt\right) \operatorname{erf}\left(\frac{K \cdot k_c}{D_{Deterg}} \sqrt{D_{Deterg} t}\right) \quad (11)$$

The term $\frac{K \cdot k_c}{D_{Deterg}} \sqrt{D_{Deterg} t}$ can be given in the form of a modified Fourier number, Fo', see Eq. (12). As a result, Eq. (13) is obtained. The value selected for this number modifies the solution of Eq. (11) since the moisture at which equilibrium is achieved (C_{equil}) it is defined by the Fo' selected, see Eq. (13). Efremov [18] showed that the solution of Eq. (13) is only stable for 1/Fo' below 25, which corresponds to the time for the surface of a drop to reach 98% of the equilibrium moisture content. The approach was also used for detergents by Ali, M. [13, 19]. They assumed that the moisture in which locking point takes place corresponds to 90% of the equilibrium. In this second case, by solving Eq. (14), the value obtained for 1/Fo' is 5.5. The use of this value was introduced with the following stages of the model and validated with the temperature profiles through the dryer by using a CFD model and a plug flow reactor model [13, 19]. However, the value was taken without any experimental concern. Furthermore, the CFD model was not able to reproduce the momentum of the discrete phase suggesting that errors can balance between the momentum and the heat and mass transfer. Therefore, the Fo' number has been characterized as presented in the following paragraph.

$$\frac{1}{Fo'} = \frac{K \cdot k_c}{D_{Deterg}} \sqrt{D_{Deterg} \cdot t} \quad (12)$$

$$\frac{C - C_{init}}{C_{equil} - C_{init}} = 1 - \exp\left(\frac{1}{Fo'^2}\right) \operatorname{erf}\left(\frac{1}{Fo'}\right) \quad (13)$$

$$\exp\left(\frac{1}{Fo'^2}\right) \operatorname{erf}\left(\frac{1}{Fo'}\right) = 0.1 \quad (14)$$

The current methodology for the characterization of the properties within the company and presented in [13, 19] is based on determining the partition and diffusion coefficients and applying them straightforward to the CFD model. The methodology used is faster and cheaper since the intermediate validation of a single droplet is not carried out. However, the characterization of the Fourier number to be used (which determines the locking point) is missed and a value of 5.5 for the Fo' number was selected without any concern [13, 19].To minimize the error given by assuming Fo'=5.5, the following procedure have been followed to estimate this Fourier number from the single droplet drying experiments of chapter 1:

- First, it is assumed that the partition coefficient used is assumed to be the average reported in different internal formulations; meanwhile the diffusion coefficient of the dried detergent, D_{Deterg}, is assumed to be the one generated by crust, D_{cr}, which is obtained from the single droplet drying model in the first chapter.
- Considering these assumptions, the model of the first stage defined in the current section has been run with the experiments performed in the chapter 1 of the thesis obtaining an average value of 13.7 for 1/Fo'. This value is used in the CFD modeling of the remaining formulations, which have been characterized following the methodologies of the company.
- Finally, the drying model, with this Fourier number is implemented by means of a User Defined Function (UDF) in the CFD model for the different cases studied in the current chapter.

Apart from the mass balance, the heat balance is also computed in the droplet as presented in Eq. (15). In this Eq. (15), the first term of the right hand side corresponds to the heat transferred from the bulk to the droplet, where h is the convection heat coefficient computed from the Ranz-Marshall correlation, and the second term corresponds to the water evaporated in the time that the particle spends in each cell.

$$\frac{dT}{dt} = \frac{1}{(C_{dm}C_{psolid}+C_wC_{pl})}\left[h \cdot 4\pi R^2 \cdot (T_\infty - T_d) + L_H \frac{dm_w}{dt}\right] \quad (15)$$

2nd Stage-Drying by diffusion limited by the external crust

The second stage begins with the locking point, which is achieved when the droplet surface becomes dried and the crust starts to be generated. This locking point is defined as a function of a critical moisture content,C_{lcr}, This is a parameter in the drying curve determined for each formulation. After achieving the locking point, the crust grows and presents a resistance to the mass transfer. As a result, the overall mass transfer rate is computed as the sum of two resistances as defined in Eq. (16) [20]. The first term of Eq. (16) corresponds to the resistance due to the diffusion across the boundary layer and the second term is the resistance given by the diffusion through the crust.

$$\frac{dm_w}{dt} = \frac{2\pi K\left(C^g_{equil} - C_{surface}\right)}{\frac{1}{R_c\, Sh\, D_w} + \frac{\delta}{2D_{Deterg}R_c(R_c-\delta)}} \quad (16)$$

In Eq. (16), R_c is the droplet radius that remains constant once the crust has been formed. Sh is computed as presented in Eq. (1) and D_w is the diffusivity of water in air. In the second term, D_{cr} is the diffusion coefficient across the crust pores and δ is the crust thickness. The growth of the crust is simplified from the SDD model presented in chapter 1 to an integrated form as presented in Eq. (17).

$$\delta = R_c\left[1 - \left(\frac{m_d - m_{dm}}{m_c - m_{dm}}\right)\right] \quad (17)$$

The last equation to be solved during this second stage corresponds to the energy balance, which is computed as presented in Eq. (15). As a result from this energy balance, the particle temperature is

obtained. This temperature is used as a criterion for the transition to the third stage. When the particle temperature achieves the one obtained for the transition to boiling in the experiments of chapter 1, the next stage of boiling begins.

3rd Stage-Boiling

In this stage of the drying of the droplet, a hollow core is assumed to be formed. The drying rate in this stage is controlled by two mechanisms as described in the single droplet drying model: First, an equilibrium between the heat and mass transfer is achieved. Water activity in the core is 1 and the pressure in the core, which is also influenced by the pressure drop across the crust, is equal to the vapor pressure defined by the Antoine equation for water. Second, the concentration of solids increases in the droplet core reducing the activity of the water and part of the energy provided to the droplet is retained. The detergent formulations evaluated in the current study contain higher concentrations than the ones evaluated in the first chapter. Thus, the modeling during the boiling regime is reduced to the second mechanism. The mass transfer rate in this stage is characterized by assuming multiple equilibria between mass and heat transfer, resulting in Eq. (18) [8]. In this Eq. (18), the droplet temperature is assumed to the boiling one, which is computed from the modified Antoine equation presented in Eq. (19) [21].

$$\frac{dm_w}{dt} = \frac{h4\pi R^2(T_\infty - T_d)}{L_H \cdot \left(1+\frac{\rho_v}{\rho_{wc}}\right) - \left(C_{dm}C_{ps} + C_w C_{pl}\right)C_{dm}\frac{dT_d}{dC_l}} \tag{18}$$

$$T_d = \exp\left(\frac{ANTA}{ANTB + ANTC \cdot C_l} - ANTD\right) + T_{bo} \tag{19}$$

2.5.2.2 Experimental cases studied

The model presented in the previous section has been validated with the experiments presented in [4]. The experimental conditions for the cases with formulation A are presented in Table 1. Furthermore, the following properties are defined in the formulation used:

- The moisture content of the formulation is 30.4%.
- The density of the droplets introduced is 1560 kg/m^3.
- The diffusion coefficient of the formulation is: 2x10^{-10} m^2/s
- The partition coefficient is: 10.5
- The formulation is injected as a Rosin-Rammler distribution in the dryer by means of a pressure nozzle, which has been internally characterized, obtaining the angles and velocity specified in the CFD simulation. See supplementary material for further details.

Table 1. Summary of operating conditions for mass flow rates, temperature and injection locations used for Formulation A.

Exp.	z_{inj}/Z	Re_{Air}	T_{in} (K)	F_{slurry}/F_{air}
A-HL-HF	0.7	$6.61x10^4$ (High Flow)	493	0.171
A-HL-LF	(High Level)	$4.06x10^4$ (Low Flow)	564	0.254
A-ML-HF	0.5	$5.97x10^4$ (High Flow)	492	0.179
A-ML-LF	(Middle Level)	$3.95x10^4$ (Low Flow)	564	0.247
A-LL-HF	0.3	$6.59x10^4$ (High Flow)	493	0.166
A-LL-MF	(Low Level)	$4.87x10^4$ (Middle Flow)	530	0.214
A-LL-LF		$4.09x10^4$ (Low Flow)	564	0.245
A-2N-HF	0.3 and 0.7	$9.57x10^4$ (High Flow)	526	0.219
A-2N-LF	(2 Nozzles)	$5.87x10^4$ (Low Flow)	598	0.323

2.5.2.3 Computation and solver settings.

Modification with previous cases.

The cases defined in the previous sections have been modeled using ANSYS Fluent® as CFD software with different versions (17.2 to 2019R3). The computation of the airflow and discrete phases has been performed as presented in the previous sections except for the following changes:

- The restitution coefficient is changed based on the droplet/particle stage of drying. In the case that the surface of the particles is dried, the discrete phase should be in the form of a droplet and stick to the walls surface. However, at the same time material is obtained from the wall due to the dynamic equilibrium on the walls surface. Thus, the material incoming into the drier has nearly zero velocity. Assuming steady-state conditions, the mass rate reaching the wall must be the same that the one leaving the wall. In order to ensure the mass balance and consider that the particles left the wall with nearly zero velocity, the restitution coefficient is assumed to be 0.01. Even though this modification in the momentum is considered, it can be noted that the agglomeration is not included and the mass flow rate per parcel of the DPM model before and after the wall contact is the same.
- The air is introduced at high temperature and heat losses through the walls of the dryer have to be defined based on internal characterizations such as the ones presented in [22].

Simulation set-ups.

The numerical solvers have been also defined as in previous sections. However, in the current case the computational cost is much higher since mass and heat balances need also to be computed in every parcel of the CFD model. The computational cost corresponding to simulating the discrete phase has been

observed in the previous chapter to be much higher in transient simulation than in the steady-state one. The simulation of a release of detergent powder (injected in only 0.65 s) in transient and without drying takes approximately 30 h meanwhile the steady-state modeling of the dryer including the UDF for drying takes between 40 h and 90 h, both of them run with 4 parallel processors Intel-Xeon E5-2698 ®. This steady-state simulation has been run ensuring a cell size of at least 70 mm as presented in Chapter 2.1.

Taking into account these observations from previous chapters it can be seen that the simulation of the current spray dryer in transient takes much longer than the steady-state one. Thus, a screening evaluation of the transient simulation has been performed as presented in the supplementary material. The simulation is carried out ensuring the minimum conditions for obtaining a stable solution without numerical errors as defined in previous chapters (Eg. cell size of at least 90 mm for the elutriated particles to be captured, time step of the particles of at least 0.001 s). As a result, the simulation takes approximately 20 days using a High Processor Computer with 6 parallel processors Intel-Xeon E5-2698 ®. The time of the computation is so high because of two reasons: First, the particles are not injected as a release. They are required to be injected continuously until achieving the steady-state operation. Second, some particles take long residence times in the dryer. For example, the fines that are elutriated take long residence times to leave the dryer and other fraction of particles can stay suspended in the dryer for long residence times since no agglomeration mechanism is implemented. The impact of this second problem has been reduced by defining in a UDF the removal of the particles after 50 s, which is approximately 1.5 the residence time of the air in the dryer and it could be sufficient for the finest particles to leave the system. Further information of the study carried out with the transient simulation is provided in the supplementary material.

Considering the high computational cost of this study, each of the cases presented in section 2.2 has been run using steady-state simulations with 7,500 parcels. The validation of the steady-state model is provided in the supplementary material, showing good accuracy in the prediction of the volume fraction of the particles near the wall. The procedure to run the simulations is sequential with the following steps: first 10,000 iterations for computing only the air and then the particles are introduced in three steps to avoid numerical divergences: first, 1,000 iterations are run with a maximum number of iterations of the parcel per cell of 30,000; second, another 1,000 iterations are run with a maximum number of iterations of the parcel per cell of 50,000; third, the last 1,000 iterations with a maximum number of iterations of the parcel per cell of 70,000 is used. Each of the simulations takes between 30 h and 90 h using a High Processor Computer with 6 parallel processors Intel-Xeon E5-2698 ®.

2.5.3 RESULTS

The simulations performed for each of the experiments of the previous section are compared with the experimental results reported by Francia [4]. The temperature at each of the heights has been determined from the CFD model generating a surface and extracting its mass-weight average temperature. The results of the temperature at the different heights for formulation A are presented in Figure 1. As it can be seen, the

temperatures obtained at different heights of the dryer are very accurately predicted, within the error bars of ±5 K in most of the cases. The case with the worst prediction corresponds to experiment A-HL-LF. In this case the temperature is not predicted at the bottom of the dryer, showing up to 50 K below the measured temperature at the location of 0.3. However, after the injection the temperature is within the error bars ensuring the coupling of the energy balance. The second and third cases with one point with high error correspond to experiments A-ML-LF and A-LL-LF. In experiment A-LL-LF, one point shows an error of 27 K and in experiment A-ML-LF another point shows an error of 21 K. However, the remaining points of experiments A-ML-LF and A-LL-LF are very accurately predicted, with most of their points within the error of ±5 K. Even though the validation against other formulations is not presented here, the model has been also validated internally showing similar accuracies in the prediction of the temperature distribution within the dryer.

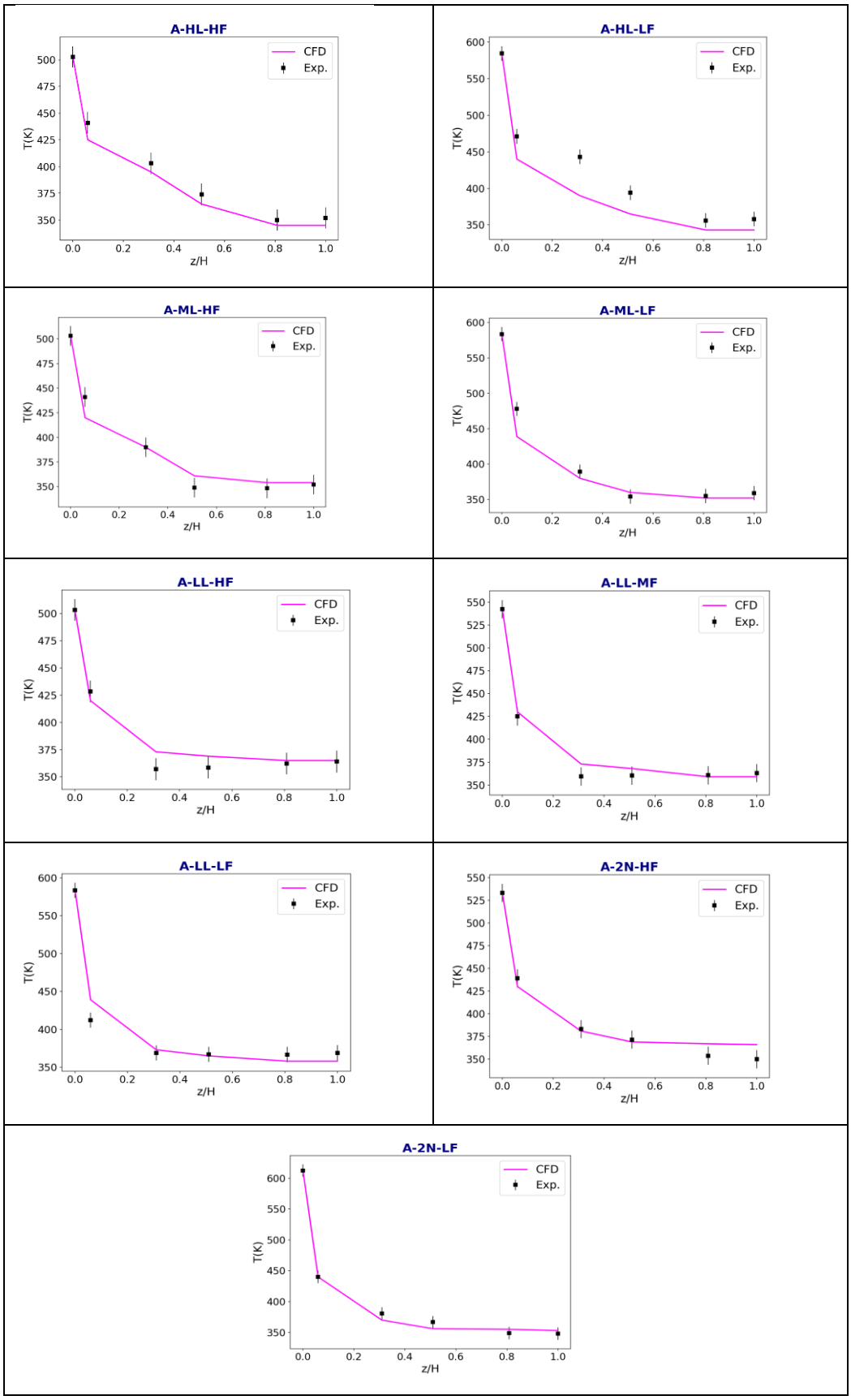

Figure 1. Summary of experimental and CFD temperatures with Formulation A.

Complementing the temperature profiles, the analysis of the results obtained from the CFD model also provides the distributions of other properties within the dryer. For example, the moisture content and the particle concentration of the air within the dryer are obtained as presented in Figures 2 and 3 for experiments A-HL-HF and A-2N-HF respectively. Furthermore, other properties such as the moisture content of the particles and the stage of drying of each of the particles can also be obtained as presented in Figures 4 and 5. From this analysis of the moisture content in the air, the regions described in previous sections of the are observed:

- A nozzle region where most of the particles maintain the projection of the angle of the nozzle used (See Figure 2). In this region the moisture content is also greater since all the particles introduced are under evaporation by diffusion, stage 1. This first stage of diffusion shows different lengths in each of the cases studied. For example, in experiment A-HL-HF some of the particles projected to the bottom impact with the wall as droplets (stage 1); meanwhile in experiment A-2N-HF the particles sprayed at the bottom suffer a quick drying to stage 2 and the particles sprayed at the top (where the moisture content is higher) suffer a slower drying but in this case is still sufficient for the particles to get dried to the wall.
- A region of elutriated particles: The small droplets elutriate following different paths until they leave the dryer by the top exhaust as described in other experimental works [4]. Furthermore, some them sill have high moisture content when they left the dryer. Most of these particles left the dryer in the second stage (which involves high moisture content) since the low temperatures achieved in this top part of the dryer do not allow them to achieve boiling conditions and the drying by diffusion is much slower than the one by boiling.
- A falling region with different behaviors: The droplets that reach the bottom of the dryer and are obtained as product shown two different behaviors in the first impact with the wall. The ones that arrive with a dried surface to the wall rebound forming a very disperse distribution through the radius. This region tends to disappear by the effect of the vortex that concentrates the particles near the wall at the bottom of the dryer. Furthermore, the swirl intensity of the vortex makes that in the bottom part of the cylinder some of the particles will follow the vortex motion having helical trajectories, see Figure 4, A). Apart from these observations in the motion of the particles, it is also observed that most of them are not completely dried when they leave the dryer. It can be seen that the 3rd stage of drying still takes place for the parcels presented, yellow color in Figure 5.
- In the case with 2 nozzles, the region of elutriated particles from the bottom nozzle interact with the ones from falling region of the top nozzle. However, the interaction between both zones is highly complex and it will be different for each of the cases and operating conditions studied. The elutriated particles, have a non-structured distribution; meanwhile the falling particles from the top dryer also show the two types of motion described in the previous paragraph. As a result, the interactions between them can be different for each of the cases. Only the two following trends,

which can modify the agglomeration mechanisms, are observed: the interactions will be favored in those cases where the particles get with dry surface at the wall in the top injection. However, these interactions will be less effective for generating agglomeration since the surfaces of both discrete phases, elutriated and falling particles, are dried.

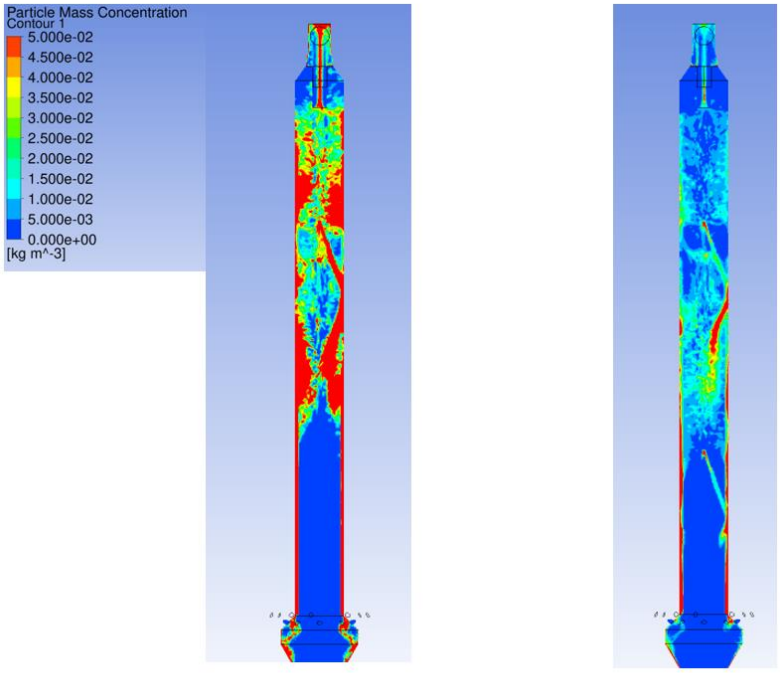

A) A-HL-HF B) A-2N-HF

Figure 2. Particle concentration (kg/m^3) for experiments A-HL-HF and A-2N-HF.

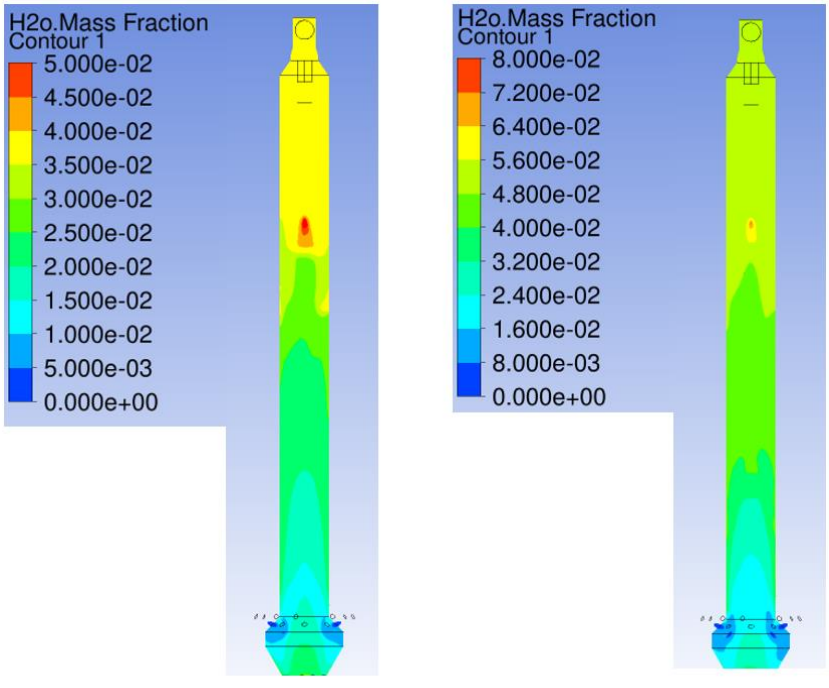

A) A-HL-HF B) A-2N-HF

Figure 3. Mass fraction of water in the air for experiments A-HL-HF and A-2N-HF.

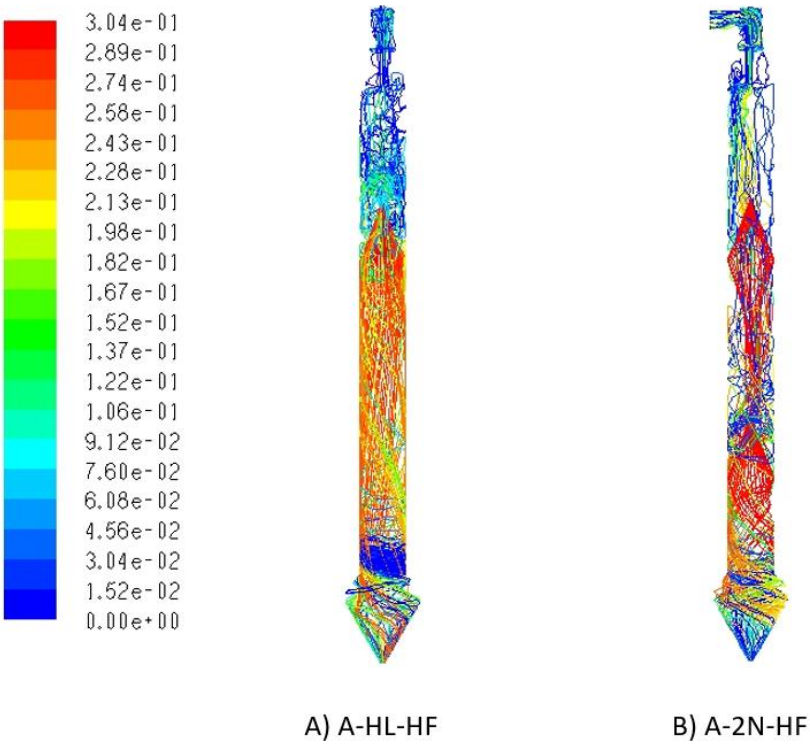

Figure 4. Mass fraction of moisture for the particles for experiments A-HL-HF and A-2N-HF.

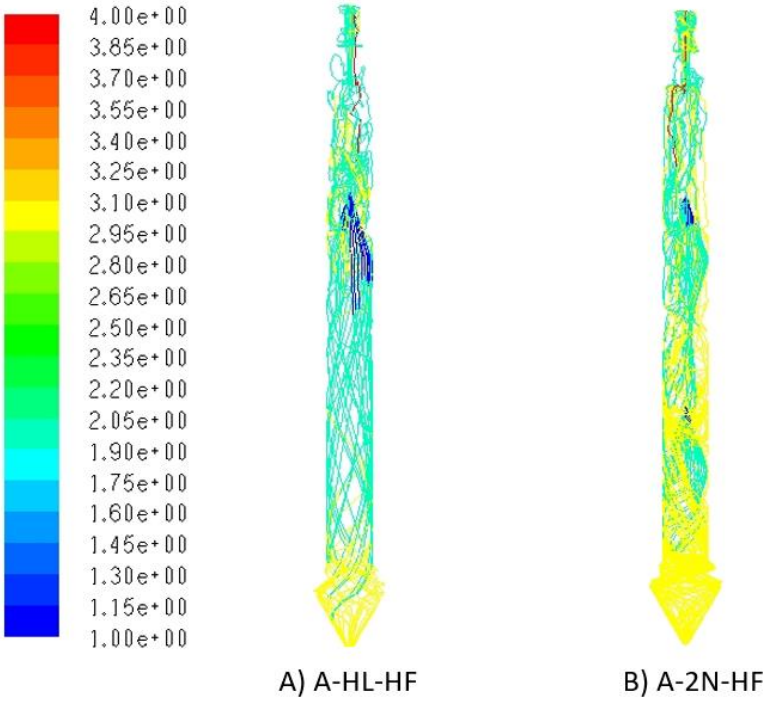

Figure 5. Stages of drying for experiments A-HL-HF and A-2N-HF (1-surface drying, 2-drying governed by diffusion through the crust, 3-boiling, 4-Particles fully dried).

Other variables that can be extracted from the CFD model are the moisture content of the product and the elutriated particles. Considering both, the average mass weight distribution of the moisture content is obtained as presented in Figure 6. This moisture is presented for CFD and experimental studies for the range of droplet sizes, up to 1100 μm. As it is shown in Figure 6, the simulated moisture content for the large particles show high disagreements with the experimental one. In particular, the large particles of the CFD model spent a very few time in the dryer. Two main reasons are expected to generate this difference in the prediction of the moisture content for the different particle sizes:

- First, an agglomeration mechanism between the particles has not been included in the CFD model. The particle size changes in the dryer due to droplet and particle interactions, obtaining a different distribution as presented in Figure 7. It can be seen that both fines and agglomerates are promoted dispersing the initial droplet distribution introduced. As a result from the different interactions between the particles, the distribution of the moisture in the final particles is also modified. For example, the big droplets, which are wet for longer times, can collide with smaller particles distributing the moisture to smaller particles that are easier to be dried. Furthermore, in the collision they can also breakage in smaller droplets that can then agglomerate with bigger particles.
- Second, agglomeration and breakage mechanisms between the particles/droplets and the wall are not included. As it has been described in the previous section, all the particles are assumed to rebound instantaneously. However, the droplets stick to the wall, then they sinter with other incoming material and dry on it until the material growths enough to fall in the form of big particles.

Therefore, as described in the literature of spray drying [3, 4, 23], for determining particle properties accurately, the agglomeration mechanism must be included. However, its introduction cannot be straightforward performed in CFD. The high computational resources required to track every parcel together with the air as well as it is defined in commercial codes such as kinetic growth does not allow to implement the agglomeration mechanism easily into the CFD model and it is commonly carried out by means of particle tracking [14-16].

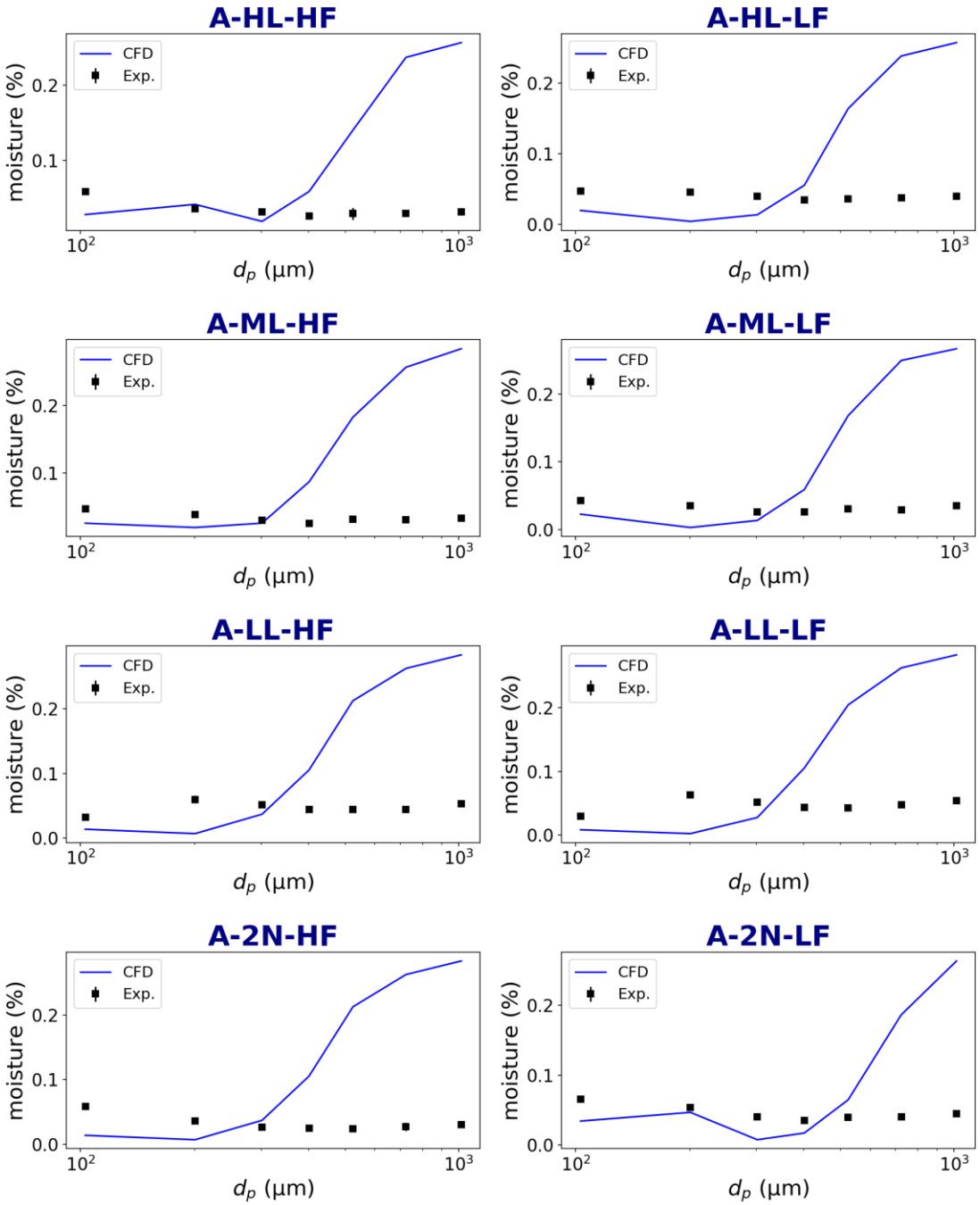

Figure 6. Cumulative moisture as function of the diameter for experiments (■) and CFD (-). Note: No characterization of the moisture distribution was carried out for experiment A-LL-MF.

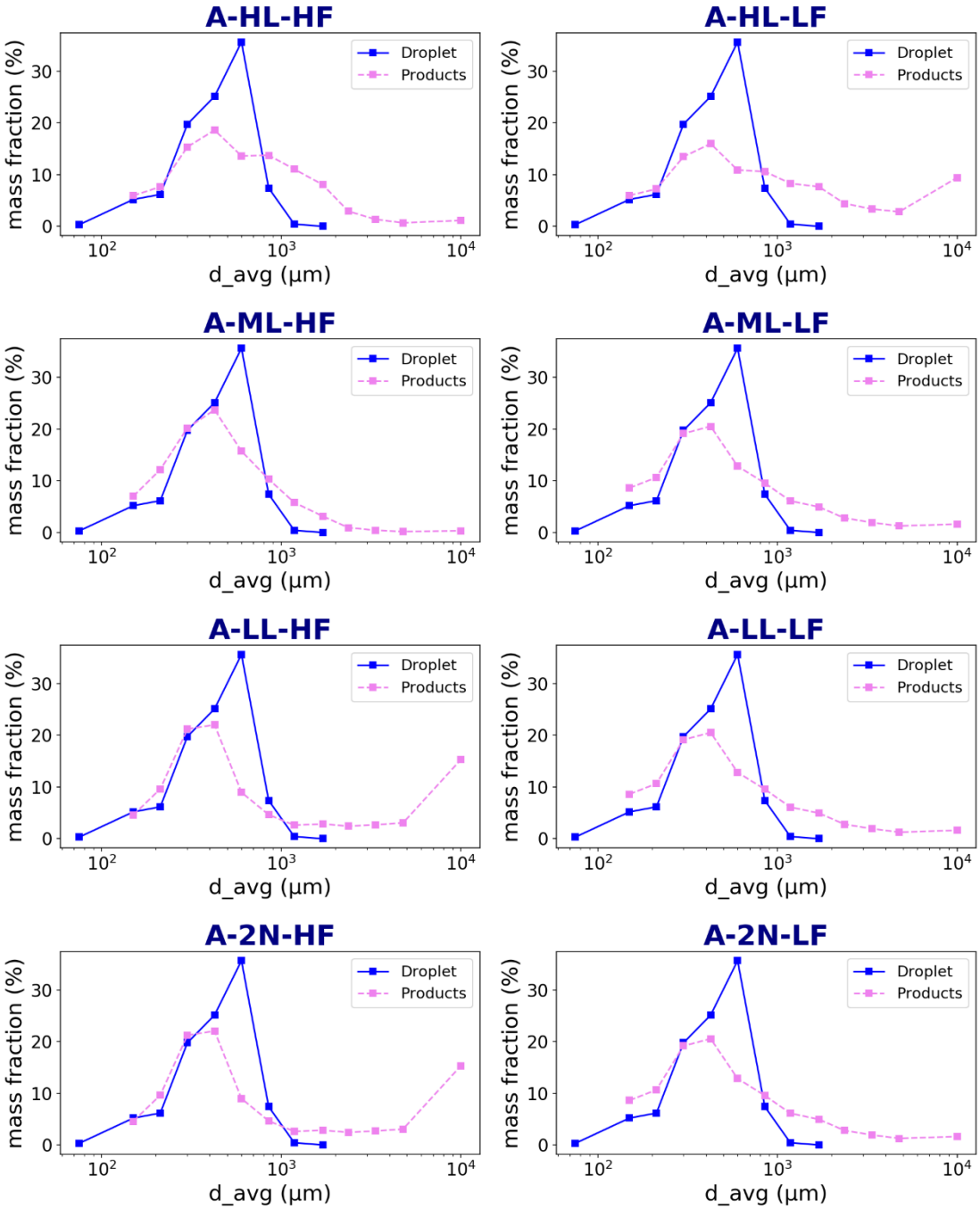

Figure 7. Comparison between the droplet and particle size distributions. Note: No characterization of the moisture distribution was carried out for experiment A-LL-MF.

2.5.4 CONCLUSIONS

This chapter has presented the rigorous modeling of the heat and mass transfer phenomena in the counter-current spray dryer by means of a CFD-DPM framework. The model combines an adaption of the heat and mass transfer model of a single droplet developed in the first chapter together with the validated air and

discrete phase models developed from chapters 2.1 to 2.4. The resultant model is validated using different detergent formulations, Reynolds numbers and temperatures of the air, heights of the injection and mass loadings. The validation of the model shows a good prediction of the temperature profiles through the dryer in most of the cases. However, it fails to predict the distributed properties of the particles such as the moisture content through the different particle sizes. This observation remarks the need of including agglomeration and breakage mechanisms on the future modeling stages of the dryer.

SYMBOLS

Symbols

$ANTA$ 1st Antoine Coefficient.
$ANTB$ 2nd Antoine Coefficent
$ANTC$ 3rd Antoine Coefficient.
C Water concentration (kg/m^3).
C_{equil}^{g} Equilibrium moisture content of water in equilibrium with the gas phase (kg/m^3).
C_{init} Initial water concentration (kg/m^3).
$C_{surface}$ Surface water concentration (kg/m^3).
C_{psolid} Specific heat coefficient of the dried matter in the particle (J/kgK)
C_{pl} Specific heat coefficient of water (J/kgK).
D Water diffusivity (m^2/s).
D_{deterg} Detergent diffusivity (m^2/s).
d_{dryer} Dryer diameter (m)
d_p Droplet diameter (m)
d_{mean1} Mean diameter of the 1st Rosin-Rammler distribution (m).
d_{mean2} Mean diameter of the 2nd Rosin-Rammler distribution (m).
F_{air} Mass flux of air (kg/s)
F_{slurry} Mass flux of slurry (kg/s)
Fo' Modified Fourier number ($Fo' = \frac{K \cdot k_c}{D_{Deterg}} \sqrt{D_{Deterg}\, t}$)
h Convective coefficient (W/m^2).
H Absolute humidity of the air.
K Partition coefficient
k_c Mass transfer coefficient (m/s)
L_H Latent heat of water (J/kg)
m_d Mass of the droplet (kg).
$n1$ Size distribution parameter of the first Rosin-Rammler distribution.
$n2$ Size distribution parameter of the second Rosin-Rammler distribution.
r Differential radius of the particle (m).
R Particle radius (m).
R_c Particle radius in the locking point (m).
T_{amb} Ambient temperature, reference 293 K.
T_{bo} Reference boiling temperature (K).
T_{ex} Exhaust temperature of the air in the dryer (K).
T_d Temperature of the droplet (K).
T_{in} Inlet temperature of the air in the dryer (K).
T_∞ Temperature of the air (K).
t Time (s).
U_{Avg} Average axial velocity of the air in the dryer (m/s).
w_1 Mass fraction corresponding to the first Rosin-Rammler distribution.
w_2 Mass fraction corresponding to the second Rosin-Rammler distribution.
w_{dm} Mass fraction of dried matter in the particle.
w_{init} Initial moisture content.
w_w Mass fraction of water in the droplet.
Y_d Mass fraction of droplets with diameter greater than d.

z_{inj}	Height of the injection (m).
Z	Height of the dryer (m).
δ	Crust thickness (m)
η_t	Thermal efficiency of the dryer.
ρ_{air}	Density of the air (kg/m^3).
ρ_{slurry}	Density of the slurry (kg/m^3).
μ	Air viscosity (Pa·s)

Dimensionless groups

Nu	Nusselt number ($Nu = \frac{hd_p}{k_t}$)
Pr	Prandtl number ($Pr = \frac{c_p \cdot \mu}{k_t}$)
Sh	Sherwood number ($Sh = \frac{k_c}{D \cdot R}$)
Re	Reynolds number ($Re = \frac{\rho \cdot v_p \cdot d_p}{\mu}$)
Re_{Air}	Reynolds number of the air in the dryer ($Re = \frac{\rho_{air} \cdot U_{Avg} \cdot d_{dryer}}{\mu}$)
Sc	Schmidt number ($Sc = \frac{\mu}{\rho D}$)

REFERENCES

[1] Langrish, T.A.G. (2009) Multi-scale mathematical modelling of spray dryers. J. of Food Engineering. Vol. 93 (2), 218-228.

[2] Ranz, W.E. Marshall, W.R. (1952) Evaporation from Drops. Chemical Eng. Prog. 48, 22, 141-146.

[3] Woo, M.W. (2017) Computational Fluid Dynamics Simulation of Spray Dryers. An Engineer's Guide. CRC Press. Taylor & Francis Group. ISBN: 978-1-4987-2464-7.

[4] Francia, V. (2014) Spray drying of detergents in counter-current towers: a study of turbulent swirling flows, fouling and agglomeration. U. of Birmingham.

[5] Rahman, U.J. Baiazitov, I. Pozarlik, A.K. Brem, G. (2018) CFD study of air flow patterns and droplet trajectories in a lab scale vortex chamber spray dryer. 20th International Drying Symposim.

[6] Malafronte, L. Ahrné, L. Innings, F. Jongsma, A. Rasmuson, A. (2015) Prediction of regions of coalescence and agglomeration along a spray dryer – Application to skim milk powder. Chem. Res & Design. 104, 703-712.

[7] Anandharamakrishnan, C. Gumbun, J. Stapley, A.G.F. Rielly, C.D. (2010) A study of particle histories during spray drying using computational Fluid Dynamic Simulations. Drying Technology, 28:566-576.

[8] Woo, MW. Daud, W.R.W. Mujumdar, A.S. Talib, MZM. Hua, WZ. Tasirin, SM. (2008) Comparative study of droplet drying models for CFD modelling. Chem. Eng. Res and Design, 86(9), 1038-1048.

[9] Harvie, DJE. Langrish, T.A.G. Fletcher, DF. (2002) A computational fluid dynamics study of a tall-form spray dryer. Food and Bioproducts Processing.

[10] Jaskulski, M. Wawrzyniak, P. Zbicinski, I. (2015) CFD model of particle agglomeration in Spray Drying. Drying Technology, 33, 1971-1980.

[11] Kieviet, F. G. (1997) Modelling Quality in Spray Drying. PhD Thesis, Eindhoven University of Technology.

[12] Ali, M. Mahmud, T. Heggs, P. Ghadiri, M. Bayly, A. Crosby, M. Ahmadian, H. Martindejuan, L. Alam, Z. (2017) Residence time distribution of glass ballotini in isothermal swirling flows in a counter-current spray drying tower. Powder Technology, 305, 809-815.

[13] Ali, M. Mahmud, T. Heggs, P.J. Ghadiri, M. Bayly, A. Ahmadian, H. Martin de Juan, L. (2016) CFD modelling of a pilot-scale counter-current spray drying tower for the manufacture of detergent powder. Drying Technology, 35 (3), 281-299.

[14] Guo, B. Fletcher, D.F. Langrish, T.A.G. (2004) Simulation of the agglomeration in a spray using Lagrangian particle tracking. 28, 273-290.

[15] Verdurmen, R.E.M. Menn, P. Ritzert, J. Blei, S. Nhumaio, C.S. Sonne Sorensen, T. Gunsing, M. Straatsma, J. Verschueren, M. Sibeijn, M. Sulte, G. Frisching,U. Bauckhage, K. Tropea, C. Sommerfeld, M. Watkins, A.P. Yule, A.J. Schonfeldt, H. (2004) Simulation of Agglomeration in Spray Drying Installations: The Edecad Project, 22, 1403-1461.

[16] Verdumen, R.E.M. van Houwelingen, G. Gunsing,M. Verschueren,M. Straatsma, J. (2007) Agglomeration in Spray Drying Installations (The EDECAD Project): Stickiness Measurements and Simulation Results. Drying Technology, 24,6, 721-726.

[17] Crank, J. (1975) The Mathematics of Diffusion. Clarendon Press, Oxford.

[18] Efremov, G.I. (2002) Drying kinetics derived from diffusion equation with flux-type boundary conditions. Drying Technology, 20:1,55-66.

[19] Ali, M. Mahmud, T. Heggs, P.J. Ghadiri, M. Djurdjevic, D. Ahmadian, H. Martin de Juan, L. Amador, C. Bayly, A. (2014) A one-dimensional plug flow model of a counter-current spray drying tower. Chem. Eng. Res and Design, 92 (5),826-841.

[20] Nesic, S. Vodnik, J. (1991) Kinetics of droplet evaporation. Chemical Engineering Science, 46 (2), 527-537.

[21] Hetch, J.P. King, C.J. (2000) Spray drying: Influence of developing drop morphology on drying rates and retention of volatile substances. 2: Modeling. Ind. Eng. Chem. 39, 1766-1774.

[22] Ali, M. Mahmud, T. Heggs, P.J. Ghadiri, M. Davidson, A. Ahmadian, H. MartindeJuan, L. Djurdjevic, D. Bayly, A. (2013). Heat losses from a pilot-scale counter-current spray drying tower. 13th UK Heat Transfer Conference.

[23] Langrish, T.A.G. (2010) New Engineered Particles from Spray Dryers: Research Needs in Spray Drying. Drying Technology, 25, 971-983.

CHAPTER 2.6 CHARACTERIZATION OF AGGLOMERATION AND BREAKAGE FOR PARTICLE-WALL INTERACTION

ABSTRACT

This chapter presents the use of the computational fluid dynamic model for evaluating the agglomeration and breakage generated by particle-wall interactions. On the one hand, the agglomeration generated by particle-wall interactions, which is the responsible of generating most of the agglomerates with sizes above the initial droplet size distributions, is determined to be a function of the material that reaches the wall as droplets (with sticky surface). A correlation has been developed and validated under different formulations, injection locations and airflow operating conditions showing only to fail when a bit more wet formulations are injected at the bottom part of the dryer. On the other hand, the breakage generated by particle-wall interactions is also determined. This mechanism is responsible of an increase of the elutriates recovered in the top part of dryer. The amount of elutriates generated by particle-wall interaction is determined to be a function of the kinetic energy of the fluxes of dry particles that reach the wall above a threshold velocity.

Note: The supplementary material is attached in the physical version of the thesis and it is also available in: https://drive.google.com/drive/folders/1_EkYTjaqQYkP_okY1ckLG9DMSdbt8gRt?usp=sharing

2.6.1 SCOPE OF THE CHAPTER

Inside spray dryers, interactions take place between droplets, particles and these ones with the boundaries of the dryer. As a result from the particle interactions, the properties of each one of the bins/parcels of the particle size distribution are modified since agglomeration and breakage occur. The influence of these interactions was demonstrated in the previous chapter, where the distributed properties such as the particle size distribution or the moisture content for each bin of the particle size distribution were not predicted. Previous experimental works identified two mechanisms for the agglomeration in spray dryers [1-3]. The one generated by droplet-particle or droplet-droplet interactions and the one generated by the interaction between the discrete phase and the wall.

On the one hand, agglomeration takes place as a result from the interaction of the droplets or the particles with droplets. This agglomeration mechanism has been widely studied at laboratory scale, providing a detailed description of the regimes that can be generated as a result of the materials of the droplets and the physics of the impact [4]. In industrial processes, the agglomeration mechanism cannot be described as accurate as at laboratory scale, focusing mainly on the change of the distributed properties (particle size distribution, moisture distribution at different particle sizes, etc.) at different locations (entrance, outlets) and/or times in the units (eg. spray dryers [1], fluidize bed [5], granulators [6], co-current spray dryers [7]). In this context, the modeling of agglomeration due to discrete phase interactions can been carried out following different strategies such as parcel interaction methods based on Lagrangian tracking of CFD-DPM simulations [8-10], population balances [11] or hybrid CFD-population balance methods [12]. In the area of spray drying, the studies have mainly focused on the use of Lagrangian based tracking methods of the parcels, which have been applied to co-current [8, 9] and counter-current spray dryers [10]. Alternatively, other methods have been also studied such as the implementation of probabilistic models into CFD codes [13] or the characterization of kernels in atomizers that can be implemented in future Eulerian-Eulerian frameworks [14].

On the other hand, the particles and droplets also contact with the wall where they agglomerate and break depending on the physical properties at the impact. This mechanism, treated as deposition for years, showed to lead the degradation of the particles in the case of milk powders and increase the risk of fire hazard since there is a self-heating in the decomposition of the deposits [15, 16]. In order to understand the problem several experimental works focused on identifying the location of the deposition [17] and quantifying the mass lost as a result of it [16]. However, the interaction with the wall does not only result in a loss of mass by the deposition, re-entrainment also occurs [1]. From previous experimental characterization and taking into account the detailed mechanisms [1, 18, 19], the particle-wall agglomeration mechanism was described as a dynamic equilibrium in which the droplets follow the next stages, see Figure 1:

- The wet and deformable droplets deposit on the wall upon impact.
- After the deposition, the droplets sinter on the wall forming large clusters that form part of the walls.

- The clusters can re-entrain in the airflow due to the action of the gravity, after attrition with other particles or due to the effect of the drag of the air on the wall. Furthermore, they can also re-entrained in the form of fine particles due to the attrition caused by the impact of other particles.

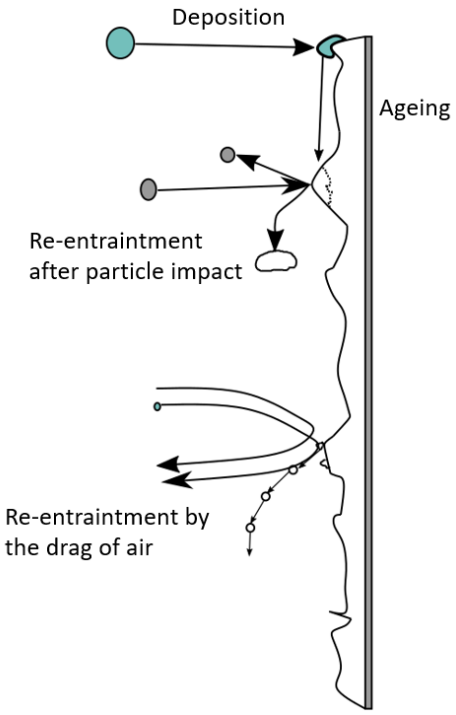

Figure 1. Dynamic equilibrium between the deposition and re-entrainment of material in the wall.

In the area of spray dryers modeling, one of the first works was carried out by Langrish and Zbicinski [20] who used a CFD model to minimize the wall deposition. Decisions such as the reduction of the spray cone and a modification of the air inlet were shown to help to reduce that deposition. Apart from this work, Kota and Langrish [19] also evaluated the deposition, predicting the patters by means of CFD modeling, while Jin and Chen [21] also developed a CFD model to address a more detailed model in which the deposited particles can reenter the air due to drag and turbulence effects as it have been also described in [1, 22, 23].

Apart from agglomeration, breakage also takes place in the dryer. Even though the breakage of particles has been deeply studied at laboratory scale and in other processes such as mixers [24] or fluidized beds [25]; it has not been evaluated in spray dryers. The aim of the current work focuses on proposing a methodology for estimating the generation of elutriated particles and agglomerates due to particle-wall interaction in counter-current spray dryers.

The two types of particle sizes generated from particle-wall interaction represent the most relevant in terms of material efficiency in the dryer. The elutriated particles is the material lost that can only be recovered after the dryer in a cyclone and that cannot ensure an improved efficiency when the fines are higher. The agglomeration due to particle-wall interaction results in particles with very high density and with sizes that can be more than 10 times larger than the d_{90} of the injection at the nozzle. These agglomerates do not

dissolve as well as the finer particles and they need to be removed before selling the product in the market. Furthermore, the large agglomerates of the generated by particle-wall interaction have a highly heterogeneous composition since it is overlapped on the detergent formula processed before and it also supposes a risk due to the auto-thermal heating of the particles [15].

The following parts of the chapter are structured as follows. Section 2.6.2 provides a description of the methodology followed to characterize the generation of these particle sizes due to particle-wall contact. Section 2.6.3 provides the results obtained. Section 2.6.4 applies the characterization method to explore the influence of the operating parameters on the generation of agglomerates and the results obtained by integrating this method with the particle-particle interaction for the prediction of particle size distribution at the bottom of the dryer. Finally, Section 2.6.5 summarizes the conclusions of the work.

2.6.2 CHARACTERIZATION METHODOLOGY.

The validated CFD-DPM framework developed in previous chapters is used in this work for determining the generation of particles sizes above the d_{90} introduced as droplet size distribution in the nozzle (oversize fraction) and the elutriated particles generated in the dryer. The methodologies for the characterization of each sizes (oversize fraction and elutriates) is provided below.

2.6.2.1 Characterization of the agglomeration given by particle-wall interaction.

The agglomeration of particles at the wall has been shown to follow a dynamic equilibrium which will require of dynamic simulations as it has been used in the work of Jin and Chen [21]. However, the presence of suspended particles with its resulting accumulation has required the use of steady-state simulations for simulating the counter-current dryer with sufficient time. Due to this computational limitation, this work only focuses on determining the change on the particle size distribution due to the input properties of the fluxes of particles on the wall. The three stages of the mechanism (impact, ageing and re-entrainment) are not modeled. Among all the incoming properties, the main precursors for the generation are expected to be the moisture content, and particularly the moisture of the surface since it governs the Ohnesorge number [4], and the amount of material that gets into the agglomeration region. The characterization of the moisture in the surface has been defined in the previous drying model of chapter 2.5, where the transition from the first (surface drying with a shrinking core) to the second (drying controlled by the crust) drying stages is given by the modified Fourier number. This Fourier number is the same for every composition and it allows determining the percentage of moisture content, referred to the initial one of the surface, at which transition occurs. Previous cases have been modeled using a Fourier number of 13.7 based on the transition determined from single droplet drying experiments.

Since the agglomeration generated by particle-wall interaction is also based on determining the amount of mass that reaches the wall in the form of droplets, this modified Fourier number has a significant impact on the characterization of the mass of over-sizes (mass with particle sizes above the initial droplet size

distribution) generated. Furthermore, this particle-wall mechanism has shown a contact time of the wet material on the wall is by far much larger (up to 2000 s [1]) than in discrete phase (particle-droplet) interactions, which allows the particles to grow more and being the main responsible for these large particles. This contact takes place until the material growths sufficiently to be released back into the airflow system, which requires the particles to be heavy enough or being affected by the turbulent eddies near the wall.

Taking into account these concerns, the characterization of the mass of discrete phase that reaches as droplets in the first impact on the walls should be useful to understand the amount of large agglomerates generated. However, particle-droplet interactions can be significant enough so that the Fourier number may not correspond with the one characterized from single droplet drying experiments. In this context, a methodology based on re-calibrating the modified Fourier number is proposed in this work. As a result, a correlation (ideally linear) can be generated for determining the mass of over-sizes produced by the particle-wall interaction. This correlation can be then introduced into a Lagrangian tracking model or population balance model as agglomeration kernel. The procedure to predict this amount of oversize material as a function of the droplets that reaches the wall is presented in Figure 2 and it is composed of the following stages:

- First, a set of experiments characterized experimentally in the spray dryer is selected and simulated with the initial Fourier number defined for drying in previous chapter 2.5.
- Then, using the CFD simulation results the fluxes of the particles to the wall and their properties are determined by reading the parcels that get to them with a User Defined Function.
- A third stage consists on data curation. The data of the fluxes to the wall is filtered taking only into account the first impact that each of the parcels has with the wall. A second filter is carried out for determining only the parcels that reach the wall as droplets (in the 1st stage of the droplet drying kinetic mechanism). From the sum of the mass of wet particles, a fraction from the initial mass introduced in the dryer is computed.
- Once all the cases of the set of experiments have been processed, the mass fraction of wet droplets is evaluated as a function of the over-sizes obtained experimentally for each case in order to determine if there is a correlation between them. Ideally, a linear correlation is desired and also expected since the mass of droplet should be proportional to the mass of agglomerates released.
- If there is not a clear linear correlation, the Fourier number that determines the transition is re-calibrated until obtaining the case with lowest dispersion in the results. The re-calibration is checked in both ways: to lower and upper values of the Fourier number.

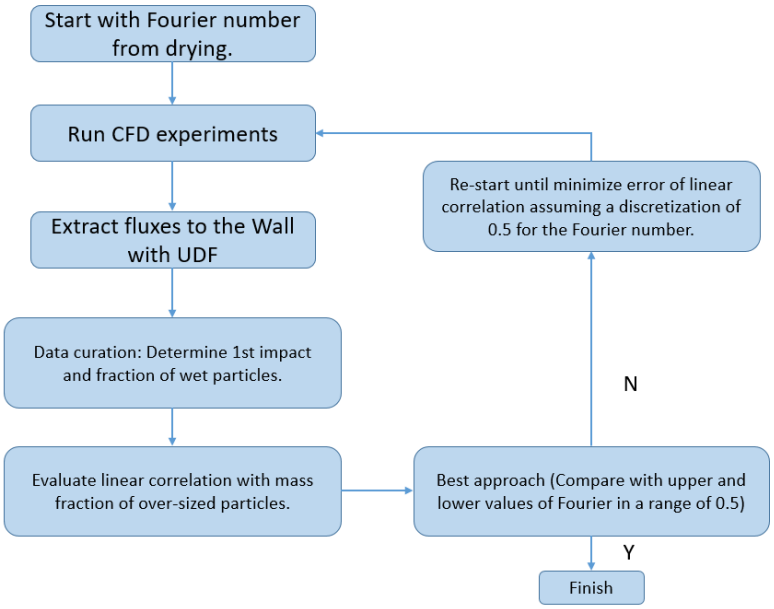

Figure 2. Procedure for the characterization of the oversized particles generated by particle/droplet-wall interaction.

2.6.2.2 Characterization of the breakage given by particle-wall interaction.

Similar to the characterization of the oversize fraction generated, the characterization of breakage kernel can be also studied to determine the fraction of elutriated particles that are generated by the impact of the particles with the wall. The breakage of particles due to attritionwas determined by Zhang and Ghadiri [26] to be proportional to the kinetic energy of the impacting particles, see Eq. (1). In Eq. (1), the dimensionless propensity to attrition, γ, is proportional to the kinetic energy multiply by the hardness of the particle (H) and divided by the fracture toughness, K_c. The hardness and fracture toughness are characteristic parameters of the detergent material (which can be assumed to be the same for all the formulations) meanwhile the kinetic energy of the particles impacting the wall can be extracted from the CFD model.

$$\gamma = \frac{\rho v^2 d_p H}{K_c} \quad (1)$$

For a characterization of this kernel, the impact velocity of the particles on the wall needs to be extracted from CFD following a similar procedure to the one presented for agglomeration. This procedure is composed of the following stages:

- First, from the previous calibrated Fourier number of the agglomeration procedure, the experiments have been simulated in CFD. After running them, the mass in the upper outlet and the fluxes to the wall are extracted. By population balances comparing the mass recovered in the experiments and the one obtained from CFD, one can determine the amount of elutriated particles that are generated by breakage in particle-wall interaction (all the difference in mass is assumed to be generated by particle-wall interaction).

- Second, the fluxes of the parcels to the wall are extracted in a similar way than for the study of the oversize fraction. In this case, the interesting variables are the fluxes of particles and the velocity components that they have when they reach the wall. The data extracted is analyzed as follows:
    - First, a distinction is made between the particles and the droplets. The droplets are assumed to stick on the wall and generate agglomerates and the particles are the ones with higher possibilities to break by impact with the wall.
    - Second, the radial component of the velocity is computed (it corresponds to the normal velocity of the particle with the wall and subsequently the one with highest opportunities to break).
    - A threshold is defined to identify the impact velocity at which the particle can break. As a result, one can determine the number of impacts and the average velocity of them. From the mass that impact on the wall, one can determine a group similar to the one of Eq. (1) as presented in Eq. (2). This group that includes the kinetic energy of the impact must be proportional (and in principle linear as in Eq. (1)) to the amount of particles breakage. The linear correlation between this group and the elutriated particles generated is validated.

$$\Delta m_{elut} \approx Km_{p\ impact} \cdot v_{p\ radial\ impact}^{2} \quad (2)$$

2.6.3 RESULTS.

The experiments presented in chapter 2.5 have been used for evaluating the quality of the modeling procedure for the agglomerates with sizes higher than initial droplet size distribution and for the elutriated particles. These experiments, together with an extension with two intermediate airflows at higher and upper locations of the injections are presented in Table 1.

Table 1. Experiments used for the validation of the agglomerates and elutriated particles.

Exp.	Formula	z_{inj}/Z	Re_{Air}	T_{in} (K)	F_{slurry}/F_{air}
A-HL-HF	A	0.7 (High Level)	6.61×10^4 (High Flow)	493	0.171
A-HL-MF			4.87×10^4 (Middle Flow)	530	0.214
A-HL-LF			4.06×10^4 (Low Flow)	564	0.254
A-ML-HF		0.5 (Middle Level)	5.97×10^4 (High Flow)	492	0.179
A-ML-MF			4.87×10^4 (Middle Flow)	530	0.214
A-ML-LF			3.95×10^4 (Low Flow)	564	0.247
A-LL-HF		0.3 (Low Level)	6.59×10^4 (High Flow)	493	0.166
A-LL-MF			4.87×10^4 (Middle Flow)	530	0.214
A-LL-LF			4.09×10^4 (Low Flow)	564	0.245

2.6.3.1 Agglomeration given by particle-wall interactions.

The procedure for determining the agglomeration generated by particle-wall interaction involves the assumption of modifying one parameter of the drying model. Therefore, before having the final solution it is necessary to evaluate if the distribution of temperature in the dryer is not significantly influenced by the modification of the Fourier number. A comparison of the temperature profiles using an intermediate experiment, A-ML-LF, from Chapter 2.5 is presented in Figure 3. This experiment is used because has an intermediate location and low Reynolds number (higher impact on the temperature).It can be seen that no significant changes are observed in the temperature distribution in the dryer for the highest and lowest value of Fourier number used. The temperature is still predicted in those locations at which the CFD shows accurate prediction in comparison with the experimental result.

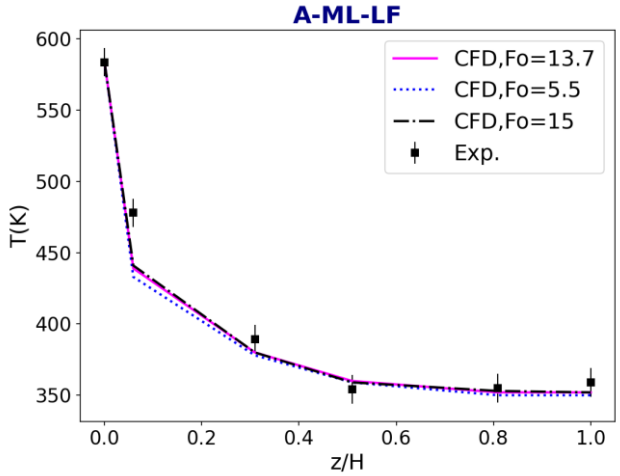

Figure 3. Comparison of temperatures with different values of the modified Fourier number in the transition from 1st to 2nd stage of drying.

The Fourier number that minimizes the error in predicting the mass of particles with sizes higher than the initial droplet size distribution is determined to be 12.5. This number shows to minimize the value for most of the experiments and it is determined with a larger set of experiments than the ones presented here. Further evaluations with other Fourier numbers are presented in the supplementary material. Here the values corresponding to the experiments used in Chapter 2.5 are presented. The remaining values are not included due to confidential information of the formula and particle sizes of the final product. The result for the formulation of the experiments presented in Table 1.

It can be seen that most of the cases a linear trend is followed. As a result, the correlation presented in Eq. (3) can be used to determine the fraction of particles with sizes higher than the initial droplet distribution. However, there are three cases studied that are by far not predicted. The three cases correspond to the experiments in which the detergent is injected at the lowest location in the dryer. However, injecting at that location and using other formulations that significant error has not been observed. This deviation found at

this location can be a consequence of the formulation studied, the amount of water content is a bit higher than the one used in other formulations. As a result, the high amount of particles with big sizes is not captured. This higher agglomeration can be given as a result of two mechanisms:

- On the one hand, the surface of the droplet can dry but still the discrete phase has enough water content that when it achieves the wall in the first impact, the particle is broken by the impact releasing the water contained. As a result, part of the material sticks there generating particles with over-sizes. This fact is the most probable since at the end of the nozzle, the particles contained the highest velocity of impact on the wall (see following section 3.3) and they subsequently have more possibilities to be broken.
- On the other hand, a second alternative can be given at the bottom cone where the particles also have a significant impact velocity and they can break releasing high amounts of water.

$$\Delta fraction_{overs} = 0.40197 \cdot fraction_{droplets\ 1st\ impact} \quad (2)$$

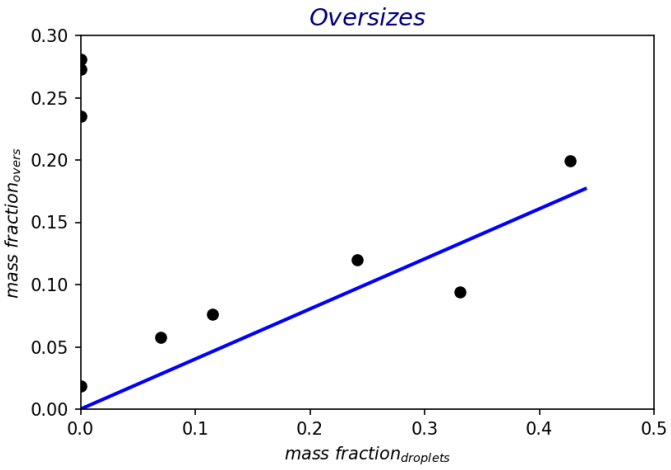

Figure 4. Prediction of the mass of agglomerates with sizes higher than the droplet size distribution as a function of the number of droplets.

2.6.3.2 Breakage

The results for determining the fluxes of elutriated particles generated by impact with the wall as a function of the kinetic energy on the impact are presented in Figure 5. The resultant equation that computes the elutriated particles generated by particle-wall impact as a function of the modified kinetic energy of the impact is presented in Eq. (3). In order to determine when the impact is a source of breakage, a threshold has to be defined for the velocity. The threshold velocity for which the particles start to break by impacting the wall is determined to be 0.1 m/s. A more detailed comparison is provided in the supplementary material evaluating the accuracy of a linear correlation such as the one presented in Eq. (3) with different thresholds. Furthermore, a comparison between using the total velocity of the particles or using the normal velocity of the particles to the wall is also compared.

$$\Delta fraction_{elut} = 3.1332 \cdot \frac{m_{p\,impact}}{m_{injected}} \cdot v^2_{p\,radial\,impact} \quad (3)$$

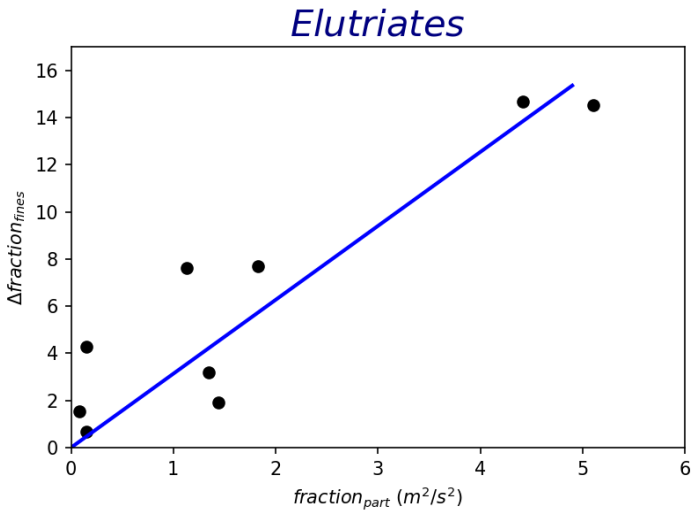

Figure 5. Prediction of the generation of elutriated particles by particle-wall interaction.

From the characterization of the mass that reaches the walls and their impact, it has been showed the possibility of obtaining the increase in the amount of elutriated particles. However, the mass ratio of the particles that impact on the wall with a velocity higher than 0.1 m/s (threshold used for the correlation and at which breakage occur) have to be determined. A simple correlation for estimating this ratio of mass with impacts at velocities higher than 0.1 m/s can be obtained in later works for simplifying the inclusion of agglomerates and address them into a single unit.

For this case, with a single particle size distribution, a simpler analysis of the data is carried out. The difference between the elutriated particles obtained experimentally and the ones obtained by the CFD model is higher at the bottom locations. This fact is not expected since lower injections should have less amount of material contacting with the wall (the number of elutriated particles should remain the same than in other locations). In the same way, and this time expected, the number of impacts predicted is also higher when the injection corresponds to upper locations, see the supplementary material for further details. However, the average impact velocity of the particles is much higher for those cases when the nozzle is in the lower locations. This velocity can be up to 10 times higher at bottom locations (partially because the particles with high velocity have also higher weight on the average) than in upper ones. Thus, instead of the method does not take into account the cumulative impacts of the particle, the average impact velocity helps to describe the influence of the nozzle location. In fact, if we exclusively focus on the impact velocity and a threshold for the velocity at which breakage starts is increased (to those particles with at least a velocity of 10 m/s), the analysis tends to exclusively focus on the impact in the nozzle region. By following a similar approach to the one proposed (based on the kinetic energy of the impact) the correlation is not obtained to be as good as

the current one. An exponential trend is only observed between the generation of elutriated particles and the fraction of impact multiplied by the velocity as it is presented in the supplementary material.

Apart from the injection location, the generation of particles due to particle-wall interaction is also determined to be highly influenced by the Reynolds number of the dryer. When the dryer is supplied with higher velocities, the generation of elutriates by particle wall interaction also tend to show a smooth increase. This fact is in agreement with the theory presented in [1] for which the air can re-suspend material from the wall (by impact of smaller particles). For evaluating the effect that the drag of air has on the deposits more detailed models are needed to studying the adhesion forces of the particles.

2.6.3.3 Distribution of impacts.

In the analysis of the agglomeration and breakage generated by particle-wall interaction, the fluxes of the particles to the wall have been evaluated. In order to determine the location at which those fluxes have more significance, an analysis of them is carried out below the nozzle. The distribution of fluxes on the axial axis is presented in Figure 6 for the experiments at which the particles are injected on the highest location. It can be seen that the majority of impacts below the nozzle occur behind the injection. This fact helps to verify the assumption taken in the estimation of the agglomeration: droplets are only considered to generate agglomerates by contact with the wall in their first impact). Therefore, an agglomeration reactor could be implemented in future works after the particles leave the nozzle and the remaining impacts does not require of other reactors since they are not shown to be sufficiently significant. In this reactor a splitter could be also added for sending a fraction of elutriates based on the correlation determined for the fines in previous section 3.2.

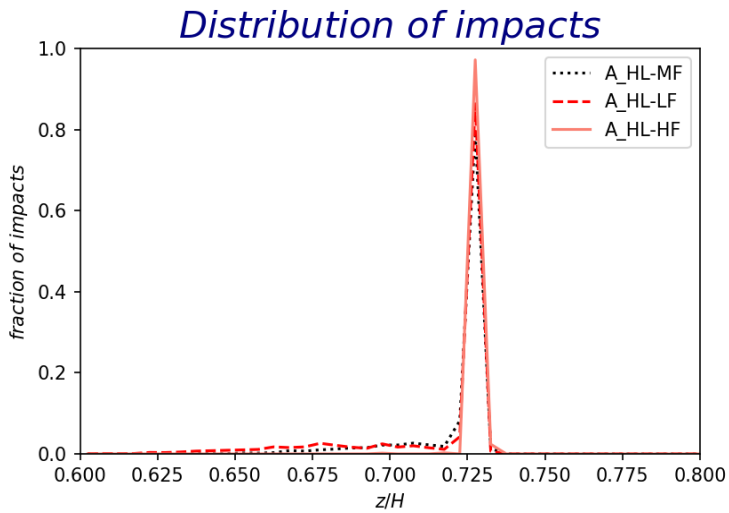

Figure 6. Axial distribution of impacts in the dryer.

2.6.4 FURTHER EVALUATIONS BASED ON AGGLOMERATION.

2.6.4.1 Efficiency in the mass recovered and heat transfer efficiency

The characterized agglomerates and fines can be also used for taking decisions on the operation of the dryer. As previously presented, the agglomerates generated by particle-wall interaction represent a high cost since a significant amount of material is lost. Several variables can have significant influence on the drying and agglomeration performance such as the geometries of the atomization regions generated by the nozzle, the properties of the material or the role of the air. The influence of the air properties (Temperature VS mass flow) on the amount of agglomerates and the drying efficiency is evaluated in the current case for the case A-HL. In this evaluation, the energy supplied in the form of dry air (enthalpy of the air) is maintained. To evaluate the dryer thermal efficiency, η_t, Eq. (4) is used. This thermal efficiency is a function of the temperatures of the dryer at the inlets, T_{in}, and at the exhaust, T_{ex}, and the ambient temperature, T_{amb}. The results of the evaluation are presented in Figure 7. It can be seen that a trade-off between the agglomerates generated and the energy efficiency of the dryer must be accomplished. When the dryer operates with Reynolds number below $7x10^4$, agglomeration by particle-wall interaction starts to take place. However, at low Reynolds numbers the thermal efficiency is also improved. Assuming that the geometries of the spray nozzle are maintained and assuming that the air will be the only possible factor to modify, the data presented in Figure 7 could be used to generate a surrogate model and introduced it into a most comprehensive model that takes into account higher number of variables. This evaluation of the airflow should be also done for other variables such as the detergent properties. The evaluation of the entire set of properties requires to run a high number of cases and subsequently a very high computational cost, which does not allow the CFD model to be applicable and adapt the decisions to the quick changes on the market. Thus, the construction of a compartment model such as the one presented for other units [27, 28] can become a very useful tool to allow the optimization of the process in short periods of time.

$$\eta_t = \frac{T_{in} - T_{ex}}{T_{in} - T_{amb}} \quad (4)$$

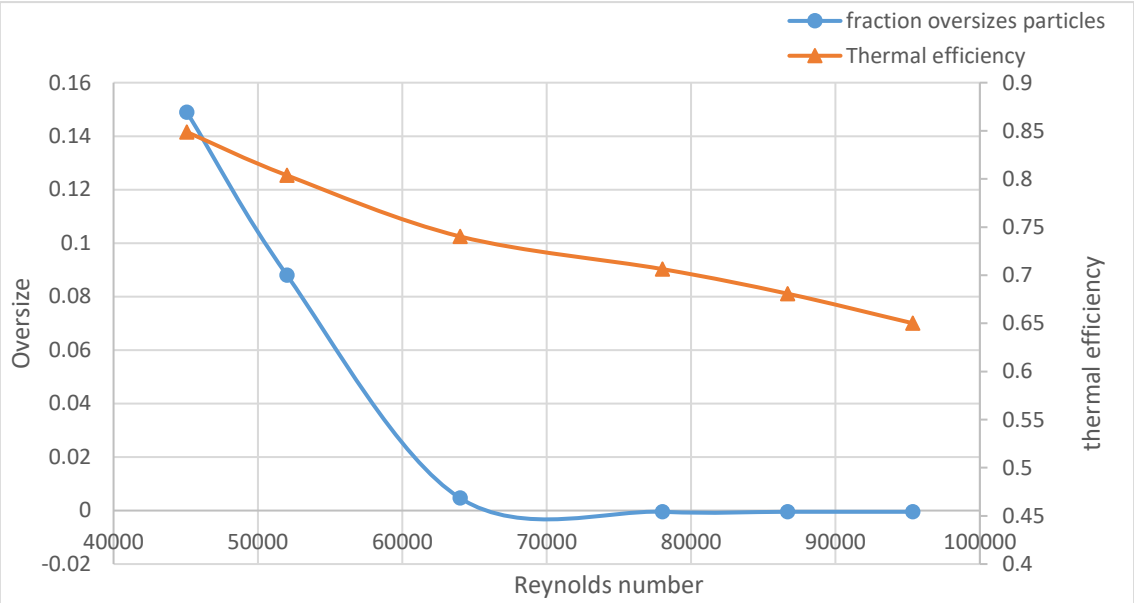

Figure 7. Oversize and thermal efficiency as a function of the Reynolds number in the dryer under constant heat capacity (enthalpy of the incoming air is the same in all the cases).

2.6.4.2 Evaluation of the particle size distribution combining particle-wall and particle-particle interactions.

Apart from the characterization of the agglomeration and breakage generated by particle-wall interactions, the agglomeration study can be also complemented with a model that determines the agglomeration generated by particle-droplet or droplet-droplet interactions. Based on the CFD model developed in the current thesis and the agglomeration method presented in [8], a Lagrangian particle tracking based method has been parallel developed in the company for determining the agglomeration generated by discrete phase interactions in the dryer. Applying that method to the current work, it can be seen that the particle size distribution is captured for low and high flows and under the different locations, see Figure 8. The main error is given again at the bottom location for the oversize fraction.

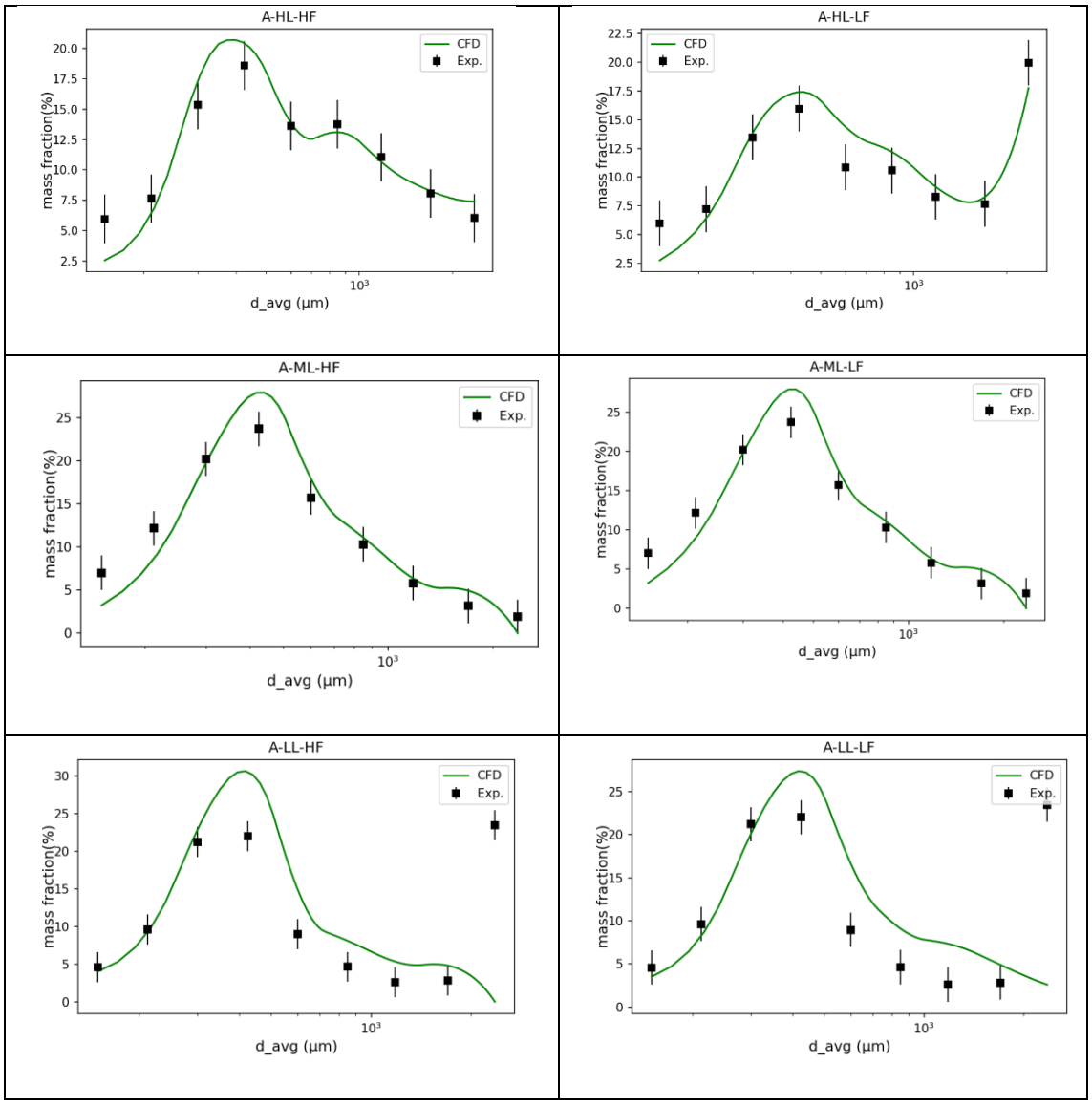

Figure 8. Prediction of particle size distribution by combining the Lagrangian based particle tracking method and the agglomeration given by particle wall.

2.6.5 CONCLUSIONS.

This section has proposed a data driven CFD based procedure for the quick characterization of the agglomerates and fines generated by particle-wall interaction. The agglomerates generated by particle-wall interaction are in particular highly significant since its size can be up to 10 times higher than the detergent introduced in the droplet size distribution and they cannot be sold in the market due to their low quality (big sizes require much more time of dissolution). The procedure proposed has shown to be able to predict the agglomerates for a wide range of injection locations, formulations and operating conditions of the air. This procedure only fails in those cases of formulations with relative high moisture content and when they can

reach the wall in the first impact with a very thin crust that breaks and stick the material. Apart from the evaluation of the agglomeration, this chapter has also characterized the elutriated particles generated by the impact of dry particles on the wall. As a result from the characterization of both, agglomerates and elutriates, two linear correlations are determined, which can be implemented in future compartment models as simple agglomeration kernels.

The correlations can be applied based on the tracking of the impacts of the particles from CFD data or they can be also introduced as agglomeration and breakage kernels in future compartment models. An evaluation based on the CFD model is carried out for studying the influence that the airflow shows on the generation of agglomeration. However, this evaluation requires a lot of computational cost in each of the CFD simulations, which does not allow to evaluate all of them. A most efficient way to study all the possible operating conditions can be carried out by developing a compartment model based on the current CFD model.

REFERENCES

[1] Francia, V. Martín, L. Bayly, A.E. Simmons, M.J.H. (2015) The role of wall deposition and re-entrainment in swirl spray dryers. AIChE Journal, 61, 6, 1804-1821.

[2] Francia, V. Martín, L. Bayly, A.E. Simmons, M.J.H. (2016) Agglomeration in counter-current spray drying towers. Part A: Particle growth and the effect of nozzle height. Powder Technology, 301, 1330-1343.

[3] Francia, V. Martín, L. Bayly, A.E. Simmons, M.J.H. (2016) Agglomeration in counter-current spray drying towers. Part B: Interaction between multiple spraying levels. Powder Technology, 301, 1344-1358.

[4] Sommerfeld, M. Pasternak, L. (2019) Advances in modelling of binary droplet collision outcomes in Sprays: A review of available knowledge. Int. Journal of Multiphase Flow, 117, 182-205.

[5] Parveen, F. Briens, C. Berruti, F. McMillan, J. (2013) Effect of particle size, liquid content and location on the stabiltiy of agglomerates in a fludized bed. Powder Technology, 237, 376-385.

[6] Hoornaert, F. Wauters, P.A.L. Meesters, G.M.H. Pratsinis, S.E. Scarlett, B. (1998) Agglomeration behaviour of powders in a Lödige mixer granulator. Powder Technology, 96, 2, 116-128.

[7] Gianfrancesco, A. Turchiuli, C. Dumoulin, E. (2008) Powder agglomeration during the spray drying process: measurements of air properties. Dayry Science & Technology, 88, 53-64.

[8] Verdumen, R.E.M., Menn, P., Ritzert,J. Blei, S. Nhumaio, G.C.S., Sorensen,T.S. Gunsing,M. Straatsma,J. Verschueren,M. Sibeijn,M. Schulte,G. Fritsching,U. Bauckhage,K. Tropea,C. Sommerfeld,M. Watkins,A.P. Yule,A.J. Schonfeldt,H. (2004). Simulation of agglomeration in spray drying installations: The EDECAD project. Drying technology, 22, 6, 1403-1461.

[9] Nijdam, J.J. Guo,B. Fletcher, D.F. and Langrish,T.A. (2006). Lagrangian and Eulerian models for simulating turbulent dispersion and coalescence of droplets within a spray. Applied Mathematical Modelling, 30, 1196-1211.

[10] Jaskulski, M. Wawrzyniak, P. Zbicinski, I. (2015) CFD Model of Particle Agglomeration in Spray Drying. Drying Technology, 33:15-16,1971-1980.

[11] Hussain, M. Kumar, J. Peglow, M. Tsotsas, E. (2014) On two-compartment population balance modeling of spray fluidized bed agglomeration. Computers & Chemical Engineering, 61, 185-202.

[12] Chen, X. Zheng-Hong, L. Wei-Cheng, Y. Ying-Hua, L. I-Song, N. (2011) Three-dimensional CFD-PBM coupled model of the temperature fields in fluidized-bed polymerization reactors. AIChE. Journal, 57, 12, 3351-3366.

[13] Mezhericher, M. Levy, A. Borde, I. (2012) Probabilistic hard-sphere model of binary particle-particle interactions in multiphase flow of spray dryers. Int. Journal of Multiphase Flow, 43, 22-38.

[14] Langrish, T.A.G. Kota, K. (2007) A comparison of collision and kernels for sprays from one and two-nozzle atomization systems. Chemical Engineering Journal, 126, 2-3, 131-138.

[15] Maxfield, L. Martindejuan, L. Bayly, A.E. (2019) Prediction of self-heating in detergent powders for application to spray dryer wall accumulations. Drying Technology, 1-15.

[16] Chong, L.V. Chen, X.D. Mackereth, A.R. Effect of ageing and composition on the ignition tendency of dairy powders. Journal of Food Engineering, 1999, 39, 269-276.

[17] Reay, D. Fluid flow, residence time simulation and energy efficiency in industrial dryers. 6th International Drying Symposium, Versailles, France, 1988.

[18] Henry,C. Minier,J.P. and Lefevre,G. (2012) Towards a description of particulate fouling: From single particle deposition to clogging. Advances in colloid and interface science, 185-186, 34-76.

[19] Kota, K. Langrish, T.A.G. (2006) Fluxes and Patterns of Wall Deposits for Skim Milk in a Pilot-Scale Spray Dryer. Drying Technology, 24, 993-1001.

[20] Langrish, T.A.G. Zbicinski, I. (1994) The effects of air inlet geometry and spray cone angle on the wall deposition rate in spray dryers. Transactions of the Institution of Chemical Engineers, 1994, 72, 420-430.

[21] Jin, Y. Chen, X.D. (2010) A Fundamental Model of Particle Deposition Incorporated in CFD Simulations of an Industrial Milk Spray Dryer. Drying Technology, 28: 960-971.

[22] Soldati, A. Marchioli, C. (2009). Physics and modelling of turbulent particle deposition and entrainment: Review of a systematic study. International Journal of Multiphase Flow, 35, 827-839.

[23] Zhang, F. Reeks, M. W. Kissane, M. Perkins, R.J. (2013) Resuspension of small particles from multilayer deposits in turbulent boundary layers. Journal of Aerosol Science, Vol. 66, 31-61.

[24] Sen, M. Ramachandran, R. (2013) A multi-dimensional population balance model approach to continuous powder mixing processes. Advanced Powder Technology, 24, 1, 51-59.

[25] Dosta, M. Antonyuk, S. Heinrich, S. (2013) Multiscale Simulation of Agglomerate Breakage in Fluidized Beds. Ind. Eng. Chem.Res. 52, 33, 11275-11281.

[26] Ghadiri, M. Zhang, Z. (2002) Impact attrition of particulate solids. Part 1: A theoretical model of chipping. Chemical Engineering Science, 57, 3659-3669.

[27] Li, J. Freireich, B. Wassgren, C. Litster, J.D. (2011) A general compartment-based population balance model for particle coating and layered granulation. AIChE Journal, 58,5, 1397-1408.

[28] Peglow, M. Kumar, J. Heinrich, S. Warnecke, G. Tsotsas, E. Mörl, L. Wolf, B. (2007) A generic population balance model for simultaneous agglomeration and drying in fluidized beds. Chemical Engineering Science, 62,1-2,513-532.

CHAPTER 3.1 METHODOLOGY FOR THE GENERATION OF ROBUST COMPARTMENT MODELS BASED ON CFD SIMULATIONS. ZONES, FLUXES AND MOMENTUM CHARACTERIZATION.

ABSTRACT

This chapter presents the generation of a robust compartment model with internal description of the fluxes. It combines principles from CFD driven and systematic compartment models. On the one hand, the data is extracted from the CFD simulations, as in a CFD driven model, to understand how the zones (based on the discrete phase concentration) are distributed within the dryer and the fluxes between each of them. On the other hand, reduced models for determining the residence time distribution as a set of equivalent reactors is used within each phenomenological region. The use of reduced models is not only applied to the residence time distribution of the particles but also to the zones. Their location and distribution within the unit is flexible and they adapt to every operating condition. The mean residence time is predicted with high accuracy in most of the regions. Taking into account the dispersion the errors are most relevant at the beginning of the injection of particles where it is low and a small error in the mean residence time supposes to capture less fraction of the mass distribution.

The work is completed with an analysis on how the number of zones affects on the prediction of the reduced models generated for the momentum. It was found that increasing the number of zones provides more accuracy under the cases studied but a significant loss of the model robustness is involved. For generating a sufficiently robust model very high number of experiments will be required and they are particular of every operating condition. This fact suggests why CFD-driven local compartment models are typically used when a system governed by the flow has to be internally cut.

Note: The supplementary material is attached in the physical version of the thesis and it is also available in: https://drive.google.com/drive/folders/1_EkYTjaqQYkP_okY1ckLG9DMSdbt8gRt?usp=sharing

3.1.1 INTRODUCTION

Multiphase and particulate processes in chemical engineering have been traditionally modelled using detailed methods such as CFD-DPM (Computational Fluid Dynamics coupled with Discrete Particle Dynamics) or DEM (Discrete Element Method). Besides helping to understand the mass and energy fluxes in the unit, they provide details of (1) the dispersion of momentum and (2) the spatial variation of phase properties for the continuous and discrete phases [1]. However, CFD-DPM and DEM methods involve a high computational cost, being not recommended for process optimization, or when a complex process phenomenon is considered. In this context, the use of compartment models becomes an interesting tool for reproducing the momentum of the discrete phase with low computational cost. These compartment models can be classified in two groups: Systematic compartment models based on an equivalent reactor network and CFD driven local compartment models.

The first systematic approach, based on generating a "virtual" reactor network for the global system dynamics, is generally used in process modeling or scale-up in order to screen among a large set of scenarios and rapidly obtain a first design with sufficient accurate results [2-5]. This approach, typically used for tracing, has been applied to a wide range of systems such as water treatment [6] combustion [7] and particulate processes [8]. The reactor network does not always have to be fixed and it can be dependent on the set operating conditions [9, 10]. Even though the reactors are flexible, this approach is not able to reproduce the local fluxes within the unit, being necessary the use of CFD driven local compartments.

The second local approach is based on extracting information of the fluxes within a unit to generate a model based on reactor networks that are equivalent to the finite volumes of the CFD model. This approach can be computationally costly depending on the accuracy desired and it requires of local experimental or CFD based measurements for generating the mapping of the zones and the fluxes between them [5,11]. Different construction methods have been used for the development of CFD driven compartment models. One of the first works was developed by Bermingham et al. [12] who modeled a crystallizer using the hydrodynamics from CFD simulations. A slightly more evolved approach was proposed by Bauer and Eigenberger [13], who introduced an iterative process between the CFD model, that provides the fluxes, and the multi-zonal model ,that computes the discrete phase (bubbles). The iteration between the CFD model and the compartments was further developed by Bezzo et al. [14, 15] who proposed a cell aggregation method after cutting them homogenously. Extending the cell aggregation method of Bezzo et al. [15] and reading the distribution of properties within the unit other methods have been evaluated for generating the zones based on different properties such as gas fractions [16], turbulent components [17,18], reaction regions [19] or reaction scales [20]. An alternative approach combining the systematic and CFD driven method was proposed by Alvarado et al. [21]. The system was divided in different zones according to the airflow velocity and each of the zones was divided in an equivalent reactor network. Even though a wide range of application and tools have been developed, there are also limitations in CFD driven compartment models. The use of this type of models is limited by the influence of the operating conditions on the distribution of fluxes [5]. If the operating conditions

modify the zones, a CFD simulation is required for every different case of study. Similarly, the kinetics and the discrete phase (in particular in 2-way coupling or dense systems) also have a significant influence on the distribution of air fluxes and a simulation is required every time. Thus, the use of this approach is only effective if the aim of the work is to implement a phenomenon that has complex kinetics and will not affect the momentum and air-fluxes but it does not provide any computational benefit since the bottle-neck in terms of computation is still the CFD simulation.

The systematic compartment modelling approach has been the most commonly used to capture the interaction between the discrete and continuous phases in particulate systems, where the momentum is characterized as a set of equivalent reactors [8]. The construction of this type of models typically requires low number of zones [22, 23], which are based on the different predominant phenomena within the unit. This framework can be based on experimental characterization or on CFD or DEM simulations. Some methodologies for addressing the momentum based on DEM simulations were reported by Freireich et al. [24] in a coater and based on CFD-DEM simulations by Tsotsas' group in fluidized beds [25, 26].

In the area of counter-current spray dryers the two previous approaches have been studied. On the one hand, a systematic compartment model has been generated for the entire unit assuming that it behaves as a plug-flow reactor, PFR [27]. On the other hand, a project between Process System Enterprise ® and Procter and Gamble has developed a CFD driven compartment model, which can be only used for obtaining quick results for an already studied case since the distributions of the fluxes are fixed.

Even though the systematic compartment model provided reasonable accuracy in the prediction of the particle attributes, it also involved errors since neither the drying nor the momentum can be considered homogeneous within the dryer. Thus, the aim of the current work is to develop a new systematic compartment model that includes some concepts of the CFD driven models to identify the distribution of zones and fluxes within the dryer. The extraction of the particle momentum within each phenomenological regions can be carried out as it has been demonstrated in the work of [24]. In that case the airflow was not internally divided (it was assumed as a plug-flow with only axial cuts). However, in our methodology, the air fluxes are as important as the discrete phase and the cut of them must be carried out. Furthermore, the work also focuses on proposing a methodology for integrating an equivalent set of reactors within each phenomenological zone that will be able to reproduce the mean residence time and the dispersion of the discrete phase. For simplicity, this first part only presents the studies of the momentum components, the zones in which the dryer can be distributed and how these zones can be made flexible. The resultant model is expected to be accurate enough in the description of the zones, momentum and flux components but also robust enough to capture them under different operating conditions.

The rest of the chapter is structured as follows: section 3.1.2 provides a deeper description of the types of compartment models. In section 3.1.3, the methodology developed is described. In section 3.1.4, the methodology is applied to a multiphase system, a counter-current spray dryer, with highly influence between

the momentum of both phases. In section 3.1.5 the results for the case of study are presented. Section 3.1.6 presents an evaluation for determining the role of the number zones on the accuracy of the prediction. Finally, section 3.1.7 summarizes the conclusions of the work.

3.1.2 REVIEW OF COMPARTMENT MODELS AND ITS APPLICABILITY TO SPRAY DRYING.

Two well defined types of compartment models can be found in the study of chemical units: Systematic compartment and CFD driven compartment models with local descriptions. Understanding the characteristics, applications and limitations of each compartmentalization method is important to understand the approaches that can be used in the current system under study and which of them is more successful in determining the different desired properties. Table 1 presents a summary of these aspects for each of the two modeling methodologies, which are defined as follows.

3.1.2.1 Systematic compartment methods

This approach is based on the modeling of a system or a phase of the system as a set of equivalent "virtual" reactors. The unit, which can be divided in regions with different phenomena (e.g. drying and agglomeration regions in a coater [28]), is modeled as a set of equivalent reactors based on the residence time distribution of the phase under study. To provide robustness to these frameworks, reduced models for determining the residence time needs to be developed based on experiments or in CFD or DEM simulations and the accuracy will be then governed by the accuracy of these models. As a result, no further need of experiments or CFD simulations is required and the computational cost for further uses is highly reduced since the bottle-neck in computational cost (The CFD or DEM simulations are not needed). The possibility of using this approach for tracing a discrete phase within other systems have promoted the use of this approach in the modeling of particulate systems. Several examples can be found applied to different systems such as fluidized beds [23], blenders [10] or coaters [28].

The application of this approach in different systems has demonstrated a good accuracy for reproducing both the particle residence time and the changes in their properties due to several phenomena. Even though some phenomena are affected by the interaction with other phases (eg. drying of particles is also affected by the moisture content of the air), the continuous phase at the entrance and outlet of the phenomenological region is not always described, which does not always ensure that the models for both phases are correctly defined. (eg. temperature of the air is only described at the entrance and outlet of the drying system in different dryers [10, 29]). As a result, some of the parameters of the model regarding the kinetics or the agglomeration may need to be calibrated for the system [30]. If the calibration is needed, it has to be carefully carried out since it cannot be done for every new case of study.

3.1.2.2 CFD and DEM driven compartment models for local description

These compartment models are based on generating a network of reactors that provide a description of the spatial distribution of the properties within a unit, see Figure 1 as example. Contrary to systematic compartment models, the use of CFD or DEM driven models with local description are computationally very expensive since they require a CFD or DEM simulation every time the operating conditions modify the momentum and/or the fluxes of the tracked phases.

Even though this approach is more detailed since the error is only given by the accuracy in the discretization, it also has limitations:

- The number of compartments required (typically modelled as CSTR's) may need to be very high. As a result from the discretization of the zones and the aggregation between them, the compartment model can also show errors in reproducing some properties within the zones. In cell aggregation, the properties within a zone are averaged. Thus, identifying such regions with constant properties is critical to avoid numerical errors in the generation of this type of compartment. In the remaining regions, as the number of zones increases so does its accuracy to predict the properties. Yang et al. [31] carried out a trial and error analysis until determining that the number of zones must be discretized until the kinetic is not modified.
- The approach is also limited to be used when the properties to be computed in the compartment model does not influence the momentum of the system [5]. The approach is useful in single phase or 1 way coupling systems but not for 2-way or dense systems.
- In case that the compartment model is constructed based on a CFD model that includes a kinetic model and this takes place very fast, the kinetic determines the number of zones. In this case, the number of zones must be high enough so that the discretization of the kinetics will not result in significant errors. A trial and error approach was evaluated by using the tool based on cell aggregation and developed in [15] for a reactor with a high heterogeneous distribution in which all the zones were equally distributed.

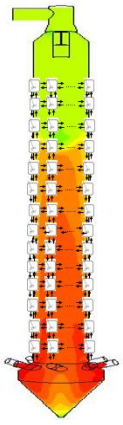

Figure 1. Example of CFD driven compartment model.

Table 1. Summary of compartment models, applications and limitations.

	Systematic compartment models	CFD driven local compartment models
Fundamentals	Compartments are divided in zones according to the phenomena and an equivalent set of reactors is generated in each of the compartments based on residence time distributions of discrete phase.	A CFD model is divided in zones that can be generated geometrically or according to the distribution of a set of properties with significant spatial changes. As a result, a set of CSTR reactors is generated.
Applications	Widely used in particle processing systems.	Typically used in flow or multiphase systems with one way coupling (bubbles).
Accuracy	• Depends on the quality of the models used and their robustness. • The accuracy is limited to the phenomenological region as whole. **No spatial definition within the region.** • In multiphase flows. The airflow is assumed as an entity without local fluxes. • Kinetic models may need to be calibrated in each case (not adaptable from CFD).	• Driven by number of zones. In kinetic governed models must be high enough to minimize the error by discretization. • Constraints must be included to avoid the transition between phenomenological regions that result in error due to property averaging within the reactor. • Limited in the extrapolation of phenomena. Fluxes are fixed and the application to phenomena that modify the fluxes may result in significant errors. • Dispersion in the Residence Time distribution is not captured.
Computational cost	**LOW**. A model independent from the CFD or DEM simulation can be generated.	**HIGH**. It requires to use the CFD model every time that the operating conditions modify the fluxes.

Assessment of methodologies for a CFD-DPM 2-way coupling system.

The two methodologies for generating a compartment model can be applied to any 2-way coupling system. However, depending on the objective and use given by the final user, the type of model used for constructing the compartment model will be different. On the one hand, a systematic compartment model can be generated based on experimental of CFD simulations. The model generated following this methodology can offer a good prediction if the aim is to determine some attributes of the particles but it can be limited in providing an accurate description of the spatial distribution of a phenomena within the unit (e.g. particle distribution and drying). On the other hand, CFD driven local compartment models can be also developed but they need a new CFD simulation for every operating condition. Taking into account these limitations and accomplishing the sequential generation of a multiphase model (first validate momentum, then mass and energy transfer and finally quality properties of the discrete phase) the following possibilities, summarized in Figure 2, can be used:

- Generating a CFD driven compartment model based on the momentum of the discrete phase as developed in [21] and evaluate if the kinetic is accurate or calibrate it to address the mass and energy balances. This approach, useful in multiphase systems with one-way coupling for the momentum [5], must be carefully used in 2 way coupling systems, especially if the concentrations are irregular within the system. The kinetic models (e.g. single droplet drying for a particle) can result in significant changes on the discrete phase momentum (density of the particle suffers significant changes) and the kinetic model determined independently is not able to reproduce the mass and energy distribution within the unit. To avoid these errors the kinetics can be calibrated for each operating condition or unit, which is far to be practical.
- The errors that can be addressed in the compartment model following previous approach, can be avoided by generating the compartment model from a CFD-DPM model that includes the kinetics. In this case the only error included is due to the averaging of the properties in the generation of the zones [31]. However, it is important to remark that for each operating condition the internal distribution of the fluxes and momentum is modified a new compartmentalization is required. This method is useful for applications focused on the control of a system under very limited operating conditions. Furthermore, it can be also applied to compute properties of the discrete phase that will not have significant impact on the momentum fluxes. For example, in the area of counter-current spray drying it can be equivalent to CFD driven models developed for addressing agglomeration, which are based on particle tracking [32, 33].

Apart from the limitations in the model applicability, the construction of the CFD driven compartment model must be also analyzed for a CFD-DPM 2-way coupling system. The extraction of the fluxes of the continuous phase (air) between the compartments has been widely studied and automatized [15, 34]. They can be extracted in the Fluent ® or in the Post-processing application of ANSYS Workbench ®. In ANSYS Fluent

®, the zones can be generated by cutting the geometry with *Mark/Adapt Cells* and selecting the Shape and geometry of the cuts. As a result, new boundaries are generated and the fluxes of air are read on them. For determining the momentum and fluxes of particles, a particle tracking is then required from a boundary condition (In ANSYS Fluent ® go to: *Reports →Discrete Phase → Sample,* select all the internal boundaries and create a suitable User Defined Function for selecting the properties to be extracted). This method is the one used by the compartmentalization tool commercialized by Process System Enterprise ® and it is similar to the CFD driven models for agglomeration of previous chapter. In both cases the particles are tracked and the only difference is the simultaneous extraction of the air. However, the air is not real since it is affected by the changes on the particles as defined in previous sections. Thus, the only use is limited to determine some properties without considering the changes in the air, being equivalent to the studies of previous chapter and in other data driven studies [32, 33].

Alternatively to previous procedure, one can firstly generate the homogeneous regions in ANSYS Fluent ® and translate them to the ANSYS Post-processing ® tool in which the fluxes in the cells are extracted by accessing to: *File → Export*. In the new panel the boundaries and properties are selected generating a new .csv file with all the properties. Even though the method has been used to extract the properties in fluid systems and introduce the cell aggregation method, the discrete phase cannot be extracted. The only variable regarding the discrete phase is the concentration in each of the boundaries. Thus, this method for extraction must be discarded for the current case since it does not provide the information of the momentum of the discrete phase.

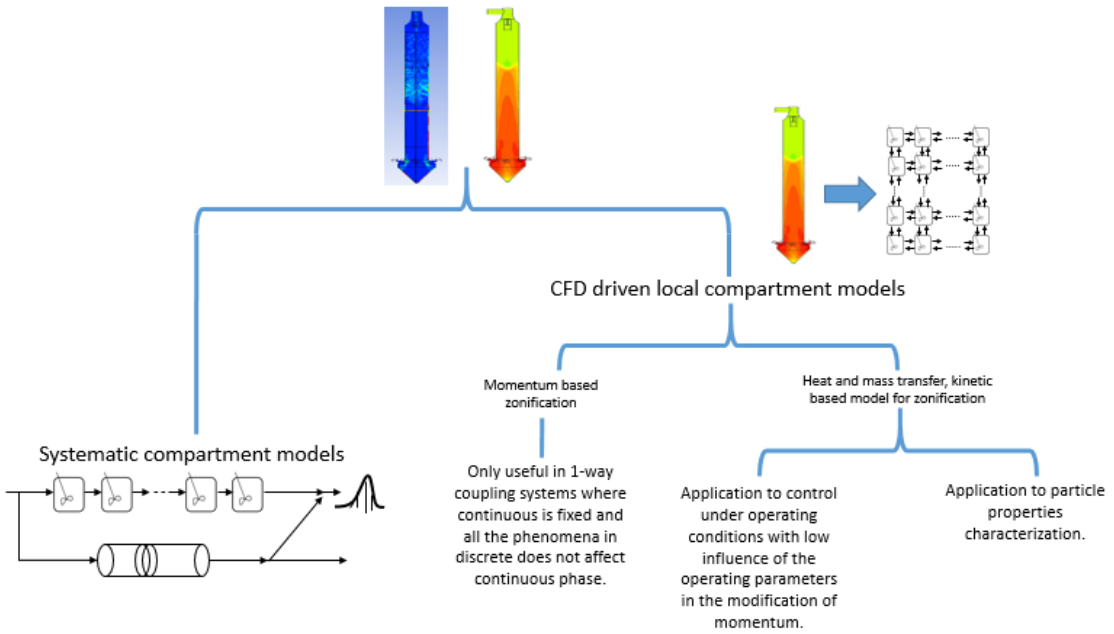

Figure 2. Summary of computational assessments for compartment models.

3.1.3. METHODOLOGY FOR ADDRESSING MOMENTUM AND FLUXES IN A ROBUST COMPARTMENT MODEL.

The methodology followed for generating the reduced models for the fluxes, zones, momentum and dispersion of the particles in each of the different phenomenological compartments is presented in Figure 3. It is divided in two parts: In the first part, the fluxes and momentum are characterized for monodispersed particles. In the second part, a comparison is provided with different characteristic diameters (e.g. mean diameter (d_{50}), Sauter diameter (d_{32}) or d_{90}) of the particle size distribution. The description of the stages required in the methodology is provided in the following lines.

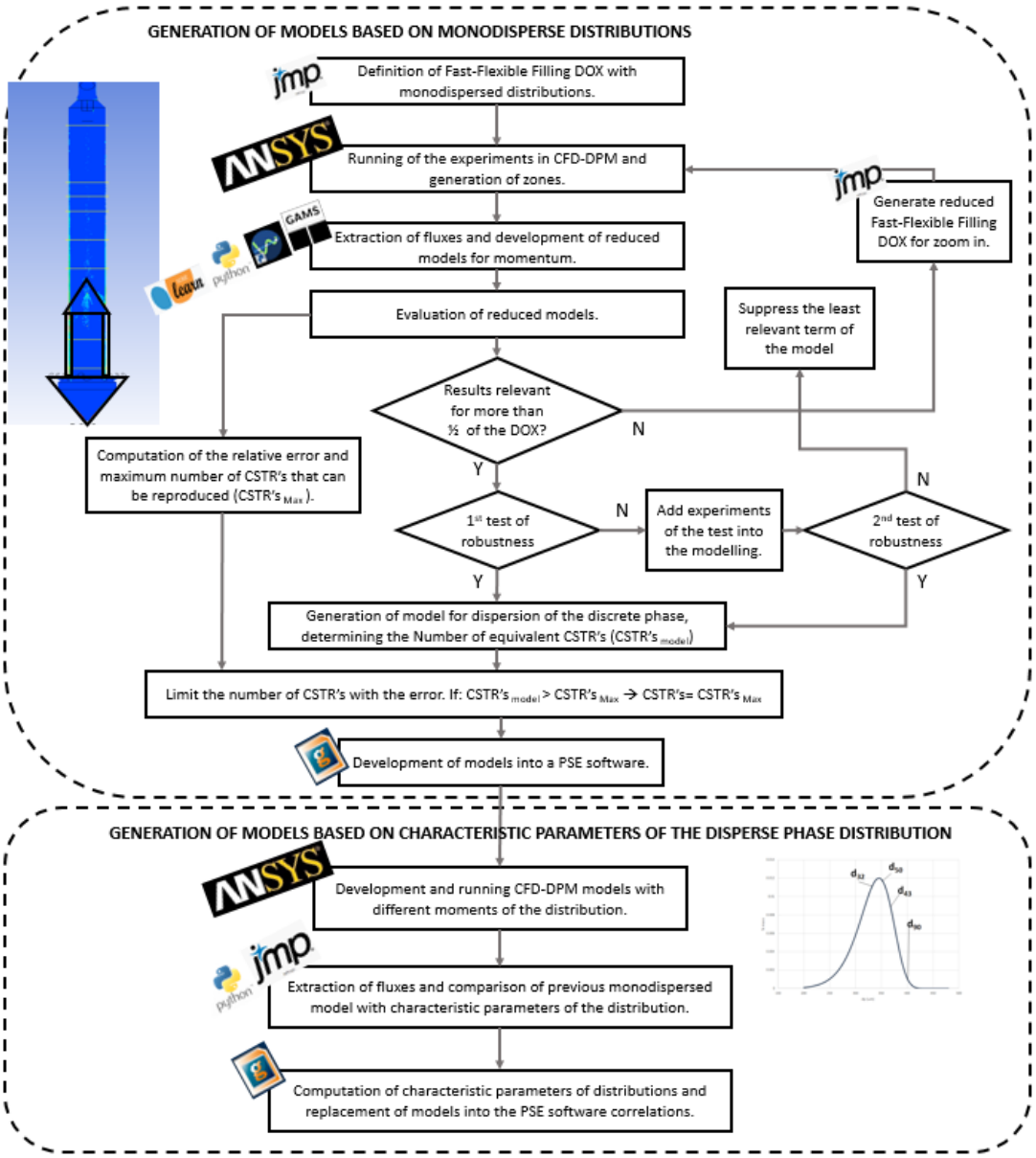

Figure 3. Methodology for the generation of a robust compartment model for multiphase flows based on CFD fluxes.

3.1.3.1 Generation of models based on monodispersed distribution.

The generation of the models in the first stage are specified in Figure 3. The methodology for generating the model combines different mathematical modeling techniques which are specified as follows.

1) Generation of experiments for process modeling

In the first stage a design of experiments (DOX) is generated. Even though traditional response surface methods such as Central Composite and Box-Behnken designs have been widely used for modeling purposes, alternative space-filling designs such as sphere-packing or Latin hypercubes have been more used in computational methods since they allow to generate a model with high number of variables and less number of computational experiments. Interesting reviews of space-filling DOX are available in the literature [35-37]. Among space-filling designs, the generation of experiments within the design space can be carried out in different ways: Latin-Hypercube DOX distribute the experiments minimizing the relative distance between the design points. Sphere-packing maximizes the minimum distance between pairs of design points. Fast-flexible filling designs determines the centroid of a cluster of random possible experiments based on the factors projected and then maximizes the products of the distances between the projections, identifying the potential design points from a number of experiments and factors given [38]. This last criterion is selected since it does not discriminate the interactions and it also has a good efficiency in the number of experiments required for constructing the reduced model. The generation of this type of DOX is available in the SLHD package of R and also in JMP®.

2) Computation of the simulation and characterization of the zones.

In the second stage the experiments are run in a rigorous modelling software. For example ANSYS Fluent®, Comsol Multiphysics ® or OpenFoam for CFD, EDEM® for DEM or LIGGGHTS® for CFD-DEM. The simulations are computed differently depending on the physics and complexity of the system, where step by step validating procedures are necessary to have a robust and rigorous model. Once the simulations have been run, the identification of the zones is required. In previous studies with similar processes, the definition has been simpler since distinctions between the zones are clear and correspond to the predominating phenomena. For example, multi-stage dryers where drying occurs at the nozzle and agglomeration in the bed of particles [28] or coater with drying and agglomeration regions [29]. However, in this case various phenomena can interact with each other increasing the complexity. The number of phenomenological regions in this case is a bit larger and the know-how from the user is needed in order to determine what properties and interactions between them are needed for the generation of the zones.
In this work, the volume fraction is selected as defined in the following section. Once the characteristic property is selected, the unit is cut based on this property following a 2-stage procedure:

- 1st) The limits in the distribution of the property that defines the zone within the unit are determined based on geometrical constraints.

- 2nd) A homogeneous sampling within those limits is developed with the objective of determining the distribution of the zone in the unit and if the zone could also have internal sub-regions.

Once the location of the zones has been determined, reduced models based on dimensionless groups and operating inputs of the unit are generated for predicting their distribution under different operating conditions.

3) Extraction of fluxes and generation of models.

In the third stage, the extraction of the fluxes and the generation of predictive models for them is carried out. The fluxes are extracted in the bounds of the zones defined from the previous section. If the data needs post-processing, a data science software such as Python or Matlab ® can be used. The fluxes and momentum components are then modeled as a function of the operating conditions and dimensionless groups defined for the unit as a whole and for the properties within the region. The use of dimensionless groups in the modelling procedure is preferred since once they are characterized, they can be re-applied to units with similar geometries and fluxes. These dimensionless groups are limited to the ones that affect each type of flux. However, the relations between the magnitudes of the groups are not constrained (e.g. by Vaschy-Buckingham π theorem), being determined by machine learning methods. In the following lines some of these machine learning methods are defined:

- A characterization based on the minimization of the Bayesian Information Criteria (BIC) or the Arkaike's Information Criteria (AIC). These machine learning methods provide the "best" trade-off between the number of terms in the model and its accuracy. However, they are not useful when terms with high non-linearities are included in the model (eg. power functions). The modeling by this method can be performed using Alamo [39].
- Sequential reduction and parameter estimation. This is a standard methodology in machine learning and statistical analysis and libraries are available in statistical packages (e.g. Scikit-learn in Python) for some methods. First, the large set of variables is reduced and then the model is fitted. The reduction can be developed following different methods:
    - Principal Component Analysis in which the terms with the most relevant variables are determined. The variables are projected to a reduced dimension (typically 2D) and the components that have a higher influence on the factor and their variance can be determined. Each of the principal components can be then decomposed to determine the variables embedded in each of them [40].
    - Filter methods. This is a multivariate analysis and fixing a threshold for number of variables selected based on statistic parameters such as the Pearson coefficient or τ from Kendall's method for a linear correlation. Even though this method proposes a model at the same time, it can be used for determining the key components, which in linear models capture the degree of effect on the output of the model. For a similar purpose, BIC and AIC minimization can also be used to identify the most relevant terms and then they can be used for fitting the model.

- Alternative techniques, not used in the current work but that can be also useful in the dimensionality reduction are: Locally Linear Embedding method in which the variables are not projected and the values are grouping taking into the neighbors before the reduction. Variations of the Principal Component Analysis like the Kernel-Principal Component Analysis or the Independent Component Analysis [40].

- Embedded optimization for parameter estimation based on the models developed. In some cases, a model includes an embedded parameter that needs to be fitted as a function of the inputs and dimensionless groups. Here specific purpose optimization models have to be defined with the objective of minimizing the Root Mean Square Error (RMSE). Similar to the two previous cases. The problem can be defined in a single optimization model including binary variables and without using highly non-linear terms using a suitable solver such as BARON. Alternatively, a filter of the variables can be done and a model with terms with high non-linearity can be fitted using a non-linear solver such as CONOPT or IPOPT.

4) Validation of reduced models.

The reduced models generated in the previous section are validated in two steps. First, the significance of the model is evaluated in order to check that a sufficient number of experiments have been used in the modelling. If there are not sufficient experiments, a new DOX is generated for zoom-in. A threshold for quantifying the significance must be defined. Here it is assumed to be ½ of the original DOX but other values can be used. The experiments of the new DOX can be then analyzed as presented in stages 2) and 3). As a result, a more robust model or an adaptable piece-wise model can be generated. In case that in the analysis of the new DOX, some experiments will have close results to the ones of the first DOX, the experiment can be added to the previous DOX since it can help to have a more robust model. The zoom-in with new DOX can be carried out until the threshold proposed by the user is achieved.

The second validation evaluates the robustness of the reduced model. A minimum of two experiments are recommended. One of them randomly selected within the operating space and other one in the bounds of the space. In the case that the RMSE error is similar when the two experiments are introduced, the model is valid. On the contrary, the experiments are added and the validation of the robustness is carried out for a second time. If the system fails in the second validation of the robustness, the model has to be reduced eliminating the least relevant term and its associated parameter. The iterative procedure is carried out until obtaining model that it is robust enough to adapt the desired variables under the entire space of operating conditions.

The modeling and validation steps are performed for the fluxes for the continuous and discrete phases. Since the dispersion can be also significant in the discrete phase (See chapter 2.4), the variance of the residence time distribution is also modelled in order to determine the number of equivalent CSTR's that have to be addressed in each of the phenomenological regions. Here, it is important to remark that the number of equivalent CSTR's used to reproduce the dispersion is limited by the accuracy of the model in the

prediction of the mean residence time. If the variance of the model for the residence times is higher than the model used for reproducing the dispersion, the maximum number of reactors is limited to the variance of the model.

5) Implementation into a modeling software.

Once the reduced models for the distribution of the zones, the fluxes, momentum and dispersion of the discrete phase have been developed. The last stage is the development of the model into a modeling software (e.g. Matlab®, gProms®, Python or Modelica).

3.1.3.2 Characterization of general fluxes and distributions based on particle size distributions.

The second part of the study focuses on determining the characteristic diameter of the particle size distribution that governs the air fluxes and structures of the zones within the unit. For example, the influence of the discrete phase on the air fluxes between different regions can be governed by a dimensionless number like the Archimedes (Ar) number, which has to be referred to a single diameter. In order to determine the characteristic diameter, a comparative analysis is carried out as follows:

- First, simulations are run with different characteristic diameters. Depending on property under study, a screening of the characteristic diameter can be done before the simulation. For example, the length of the zone dedicated to atomization has to be characterized by the maximum diameter since it is the less affected by the drag and has the largest path. Other example is the effect of the particles on the air fluxes. The study can be then reduced to the Sauter (d_{32}) the mean (d_{50}) diameters. Since the typical diameters are initially pre-screened, the number of experiments is not that large and direct comparison including several cases can be carried out.
- Second, the zone sizes, air fluxes and equivalent number of tanks in each zone are extracted and the parameters of the models for them are determined again. The diameter that shows the lowest RMSE, including monodispersed and particle size distribution experiments, is selected. These new modified parameters are updated into the process model of stage (5).

3.1.3.3 Model structure.

After all these stages, the final compartment model is obtained. It is structured using a multi-level approach as presented in Figure 4. The first layer contains the phenomenological zones, the core model for computing the size of such zones and the number of equivalent reactors within each of them. In the second layer, the equivalent number of CSTR tanks are modelled. They are modeled with an internal by-pass in case the CSTR equivalent is less than one. The maximum number of tanks is also limited by the accuracy of the model of the momentum in each region. Each tank contains the general mass and energy balances for the air and the population balances for the particles. In order to address the individual phenomena such as drying, lower levels are defined within each CSTR. In this study, the models in the third level are the continuous and discrete phase property models and the momentum model.

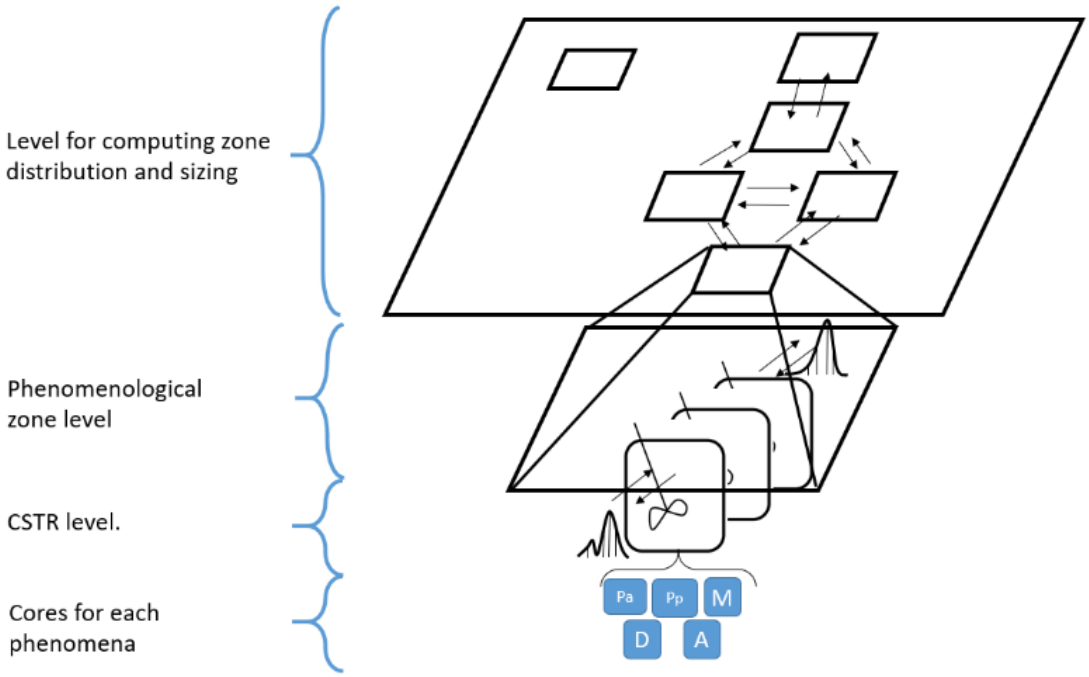

Figure 4. Structure of the compartment model for a 2 way coupling multiphase system.

3.1.4 CASE OF STUDY.

The stages defined in the previous section are applied here to model a counter-current spray dryer with swirl flow.

3.1.4.1 DOX generated and simulation.

In the first stage, the design of experiments for studying the system is developed. A Fast-Flexible-Filling method is used for generating the experiments to be run in ANSYS® Fluent. Further details of the DOX are provided in Table S-1 of the supplementary material. The simulation of each experiment uses the parameters developed in previous work, see Chapter 2.4. Each of the simulations has been run in steady-state operation with a multi-stage initialization: 10,000 iterations for the continuous phase and then another 10,000 involving the continuous and discrete phases in which the maximum number of iterations allowed for the continuous phase is increased up to 70,000. The simulations are run in a High Processor Computer with 4 parallel processors Inter-Xeon E5-2698 ® and take between 40 h and 100 h each. Even though the swirl pattern of the air has a characteristic precessing vortex core that can be only described with transient simulations, the use of transient simulations is highly computational expensive, around 20 days with the same computational resources (For simulating the entire DOX and being able to run 4 simulations at the same time, simulating the entire DOX would have require around 5 months and with the extra experiments around 11 months). As described in Chapter 2.5, the main limitation in the modeling is found in the particles that are suspended in the system.

3.1.4.2 Zone distribution and characterization

Once the simulations are run, the following phenomenological zones are defined based on the concentration of particles within the system, see Figure 5:

- A **nozzle region** where the particles move at high speed and drying occurs. Furthermore, the droplets are wet and agglomeration between them is also significant.
- A **region with the elutriated** particles from the nozzle and after the impact with the wall.
- A **falling region** near the wall in which the particles are concentrated due to the tangential momentum of the swirl flow in the dryer.
- A **central region** below the nozzle region composed by air and that does not contain particles.
- A **region** near the **inlets** where the particles can follow very different behaviors, from falling with a zone similar to the falling region or they can be highly dispersed by the inlets and having a more random movement until they get the cone, see Figure 6 for different behaviors.
- A final **cone region** in which the particles are highly concentrated on the wall and they move bumping and rolling until they are recovered at the bottom of the dryer.

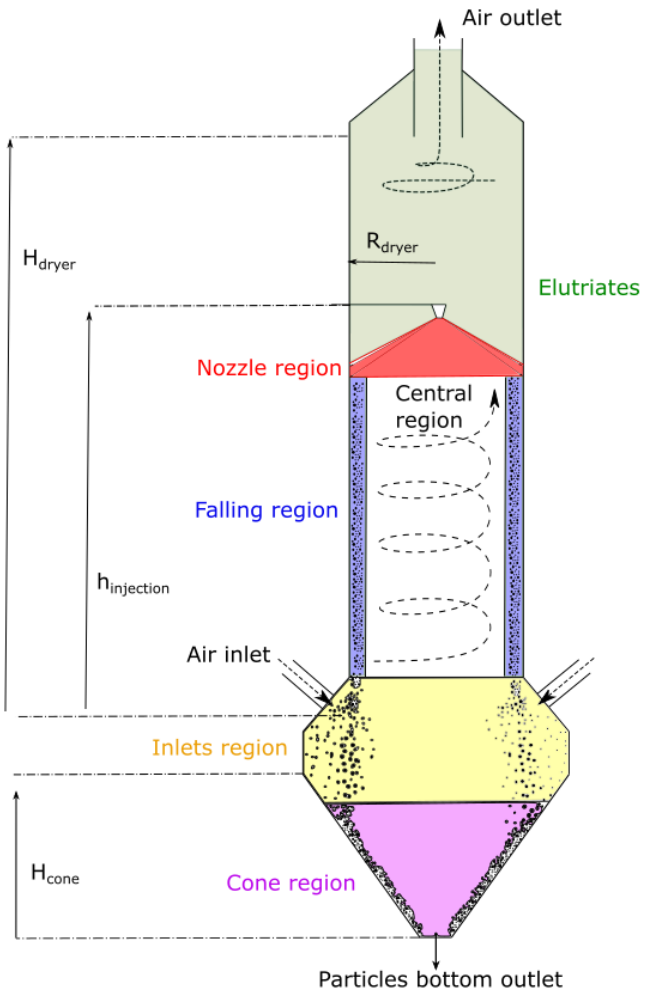

Figure 5. Distribution of phenomenological regions within the dryer and geometrical regions.

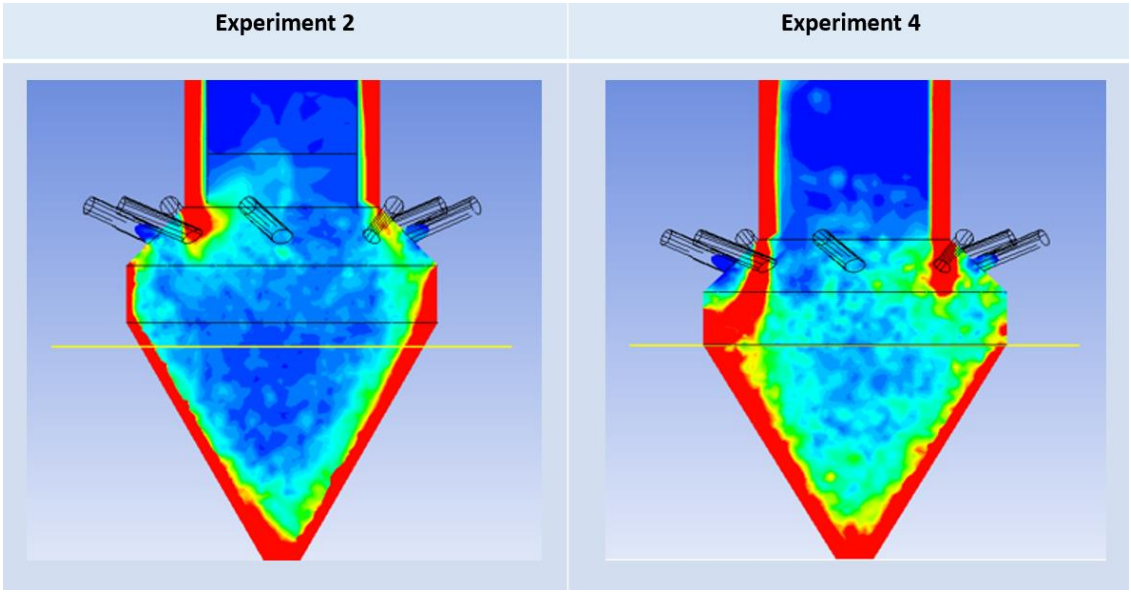

Figure 6. Examples of distribution of particles in the inlets region.

The size and distribution of the zones have geometrical limits known beforehand. The main constraint is given by the atomizer. The height of the injection cone generated by the atomizer is limited by the wall. The maximum height that the particles covers is computed as presented in Eq. (1). Once this height is known, an internal exploration (from the injection until this height) with different layers is carried out for determining the real height and if there are another sub-regions based on the volume fraction and air velocity. For further details, see Figure S-3 of the supplementary material, which shows how internal layers for are generated.

$$h_{\text{nozzle theorical max}} = \frac{R_{dryer}}{sen(\alpha_{nozzle})} \quad (1)$$

From the characterization of the location of the injection, the height of its hollow-cone and its thickness; the zone of elutriates can be defined, which accounts for the upper part of the dryer and the height of the zones below the nozzle. However, to make a distinction between the falling and central regions characterization is needed, which is extracted by reading the volume fraction at different heights. Finally, the characterization of when the inlets region finish and the cone starts is carried out. At the inlets, the particle concentration through the radial axis is highly heterogeneous as shown in Figure 6. Thus, it is considered as a unique regions but the transition to the cone region has to be determined. The cone region, in which the particles are also concentrated can be distinguished from the central part. However, the air in the central part is also difficult to model and it rarely affects the particles bed in terms of momentum and in terms of heat and mass transfer, the particles are very high concentrated that the contact can only occur on such particles in the upper layer.

Once the zones have been defined, the internal distribution of the volume fraction and other air properties (e.g. air velocity) is read and the size of them is modelled based on the inputs and dimensionless groups for

the continuous and discrete phases. The BIC minimization method is used to obtain the models for the distribution of the zones since they are mainly empirical.

3.1.4.3 Modeling of fluxes and residence time

A) Air fluxes

The modeling of the air fluxes between the phenomenological regions must be carried out remarking a very important assumption. The use of CFD steady-state simulations does not allow to provide a radial description of the air fluxes between the falling and central regions. The Precessing vortex core with a transient behavior is not reproduced by steady-state simulations and the fluxes obtained between these regions only show the net value, see Figure 7. In fact, by reading the fluxes, the radial flow in steady-state between a height of 0.185 h/H and 0.285h/H in the cylinder supposes an increase in the flux in the center between 22.19% (trend from falling to center region) and -22.7% (from center to falling region), see Table S-2 of the supplementary material for further details. This fact is very significant in the construction of the model. Supposing the case in which energy transfer will not occur between this two regions; the air in the falling region will not be able to extract all the moisture of the particles and there also will be high temperature differences between the central region and the falling one. To avoid this fact, mixers combined with separators or heat exchangers will have to be used for the mass and energy transfer in the systematic compartment model of the zone.

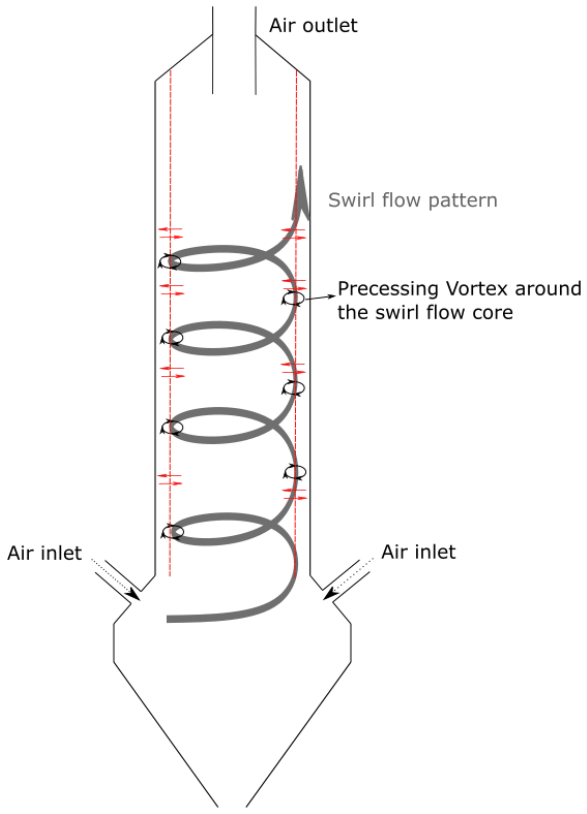

Figure 7. Example of Precessing Vortex Core cut by the zone.

Taking into account these assumptions and the observations for the radial air fluxes, only the axial distribution of the air is modelled since it could also affect the momentum of the particles. The model for the axial distribution is constructed combining a filter based on the Pearson coefficient and a parameter estimation for the model as the form presented in Eq. (2).

$$f_{Air} = a \cdot St^b \cdot Ar^c \cdot \ldots \cdot Re^d \quad (2)$$

B) Particle residence time in the nozzle region

The particles are assumed to follow the zones defined in previous paragraphs. However, the residence time spent in each zone is different. In the nozzle region, the mean residence time is modelled determining a series of parameters within a given model. Taking into account that the particles move with a velocity in the axial axis given by Eq. (3), the Reynolds number in that axis can be computed as Eq. (4). Due to drag forces, the Reynolds number decreases from an original layer, Re_{p0y} , to the following one, Re_{p1y}. The decrease is given by a drag factor as presented in Eq. (5) divided by the ratio between the layer and the nozzle, see Eq. (6) and Figure 8 for the dimensions. Since the factor is multiplied by the Reynolds number of the particles at the entrance of every layer, it needs to be elevated to the inverse of the relative height (or number of layers) to ensure that the final value is independent of the number of layers, see Eq. (7) for the Reynolds number in the last layer. The drag factor can be then determined as a function of the inputs and different dimensionless groups as well as non-linear terms including them (eg. exponential, power or logarithmic functions) and interactions, see for example Eq. (8). To determine the most relevant dimensionless groups of Eq. (8) a screening analysis needs to be performed by using a filter. Then, the parameters of the model can be determined by solving an optimization problem that minimizes the cumulative square error (CSE), Eq. (9), between the experimental Reynolds number at each of the internal cuts of the nozzle region and the one computed by the set of equations for all the "n" experiments. The optimization problem is solved in GAMS ®.

$$v_{py} = v_p \cdot \cos(\alpha_{nozzle}) = \frac{\Delta y}{\Delta t} \quad (3)$$

$$Re_{py} = \frac{\Delta y \cdot \rho_{Air} \cdot d_p}{\Delta t \cdot \mu} \quad (4)$$

$$Re_{p1y} = \left(\frac{f_{drag}}{1-ratioH}\right)^{1/N_{layers}} \cdot Re_{p0y} \quad (5)$$

$$ratioH = \frac{h_{layer}}{h_{nozzle}} \quad (6)$$

$$Re_{pn} = \left(\frac{f_{drag}}{1-ratioH}\right)^{1/N_{layers}} \cdot Re_{pn-1} = \left(\frac{f_{drag}}{1-ratioH}\right)^{2/N_{layers}} \cdot Re_{pn-2} = \cdots = \left(\frac{f_{drag}}{1-ratioH}\right)^{N_{layers}/N_{layers}} \cdot Re_{p0y} \quad (7)$$

$$f_{drag} = a \cdot St + b \cdot \ln(St) + c \cdot Ar + d \cdot \exp(Ar) + e \cdot \ln(Ar) + \cdots + z \cdot \ln(Re) \quad (8)$$

$$CSE = \sum_{n=1}^{n=nexperiment} \sum_{y=0}^{y=H_{nozzle\ cone}} \left(Re_{py\ exp} - Re_{py\ model}\right)_{n_{experiment}}^{2} \quad (9)$$

As a result of the reduction in the velocity, particles can elutriate. The fraction of elutriated particles at each of the heights is computed as a function of the dimensionless numbers at each height in the nozzle region. The model is determined by BIC minimization without independent term and including non-linear terms such logarithmic and exponential functions.

The last term to characterize it is the dispersion of the residence time. However, it is assumed that in this case the dispersion is null for that particles obtained as products (go to the bottom) and in the case of elutriates, each of the fractions separated are having different residence times that actually involves a dispersion.

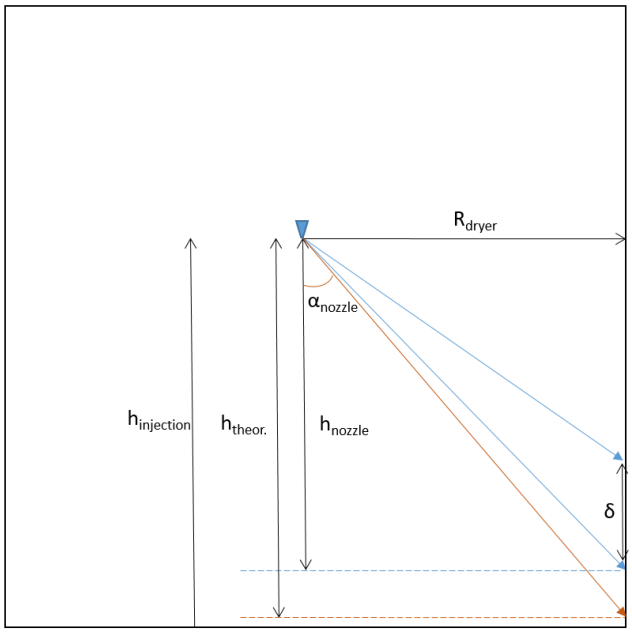

Figure 8. Geometry and characteristic values of the nozzle.

C) Particle residence time in the elutriates region

The mean residence time of the particles in the region of elutriates is determined by computing a Reynolds number for the particles with the experimental measurements. The transformation of the residence time into the Reynolds number of the particles is presented in the Appendix. Then, a model is determined for the Reynolds as a function of different dimensionless groups of the particles, air-particle interaction and air. The aim of using this approach is the scalability of it in systems with similar behaviors where only the parameters will need to be fitted but maintaining the same expression. The model for this mean residence time is determined by combining a filter of the Pearson coefficients and a parameter estimation of a non-linear function in the form of powers as presented in Eq. (10).

$$Re_{py} = \frac{\Delta y \cdot \rho \cdot d_p}{\Delta t \cdot \mu} = a \cdot St^b \cdot Ar^c \cdot \ldots \cdot Re^d \qquad (10)$$

The number of equivalent CSTR's that reproduce the dispersion of the residence time in this region is also determined by combining a filter and parameter estimation of a power function as proposed in Eq. (10).

D) Particle residence time in the falling region

As proposed in the elutriates region, the residence time is also computed determining first the Reynolds number of the particles in the axial axis from the experiments of the CFD models and then determining a model as a function of different dimensionless groups. To determine the final expression, the approach followed is the same as before: first, with a filter and then by estimating the parameters of an equation in the form of Eq. (9). The only novelty introduced is the use of local numbers for the airflow. Since the air can distribute between two regions, the dimensionless groups related to the air and the particles-air interaction in the phenomenological region are considered together with the ones of the whole unit. Since the unit is similar to cyclones, the dimensionless groups used can be as in this unit. Some examples are available in [41, 42]. Similarly, the number of equivalent CSTR's that accounts the dispersion is also determined as the mean residence time.

E) Particle residence time in the inlets region

The approach followed is also the same than the one proposed in the two previous regions. Both the particles and the equivalent number of tanks is modelled by combining a filter and a parameter estimation.

F) Particle residence time in the cone region.

This region also follows the same approach than in previous sections but with a very limited number of dimensionless groups to be used. All the numbers involving the air system or the particle-air interaction cannot be used since the particles are moved by bumping and rolling in the bottom cone compared to a silo discharge and Archimedes number is only used since it is expected to be the one with the highest influence [43].

3.1.4.4 Validation and further experiments

The last stage of the model generation from monodispersed distributions is the validation of the model and the generation of further experiments in the case that they are needed. The number of relevant experiments is observed to be low in the characterization of elutriates and the momentum modeling for small particles in the nozzle region. Two new DOX are needed which are provided in the Supplementary material, Table S-3 and S-4. Since the axial location of the nozzle was not observed to have influence in each of the models proposed for the zones, it has been fixed in the generation of the new experiments. The models finally obtained addressing all these experiments and their validation are provided in the following results section.

3.1.4.5 Characterization of fluxes based on particle size distributions

The last stage in the generation of the models is the characterization of the diameter that governs the distribution of zones within the dryer, the fluxes of air and the number of reactors. In the case of the nozzle location, the height is governed by the d_{90} since the biggest particles are the ones that show less reduction by drag forces. In the remaining cases, a comparison must be carried out between the Sauter diameter (d_{32})

typically used for particle flows and the d_{50}, which represents the average properties in terms of mass. The experiments used are provided in the supplementary material Table S-5. The selected characteristic diameter in each global flux is given in the following section.

3.1.5 RESULTS

3.1.5.1 Resulting models obtained from the methodology

Injection zone

The first set of models generated attempt to determine the distribution and size of the zones within the dryer. In the previous section, the first zone to be defined is the one generated by the nozzle. The characteristic lengths to be determined in the nozzle region are presented in Figure 8. The reduced model obtained for the height of the nozzle region has the form of Eq. (11). The model parameters are not given due to confidential property with the collaborating company. The height obtained by the reduced model is substituted by the maximum, which is given by Eq. (1) for those cases where the result of Eq. (11) is higher than the maximum. The validation of the model is presented in Figure S-1 of the supplementary material.

$$\frac{h_{nozzle}}{h_{\text{nozzle theorical max}}} = a \cdot Ar_{d90}^{b} \cdot \ln(Ar_{d90})^{c} \cdot St_{d90}^{d} \cdot Fr^{e} \quad (11)$$

Similarly, the thickness of the nozzle sheet, δ, is computed based on a reduced model, which has the form of Eq. (12).

$$\delta = a \cdot St_{d50}^{b} \cdot \alpha_{nozzle}^{c} \cdot Ar_{d50}^{d} \cdot Fr^{e} \cdot vf^{f} \quad (12)$$

The prediction of the mean residence time of the discrete phase within this region is computed based on a piece-wise model. Three intervals have been used for different particle diameters. The parameters of each of them have been independently determined by an optimization problem as defined in the previous section. The drag factor, f_{drag} , is computed for each particle size as a function of the reduced models presented as follows and validated in the supplementary material:

- For d_p < 300 μm, the factor is modelled as:

$$f_{drag\ nozzle} = 3.5813e-3 \cdot Ar^{0.6317342} \cdot St^{-0.70093} \cdot Fr^{0.15665} \cdot \alpha_{nozzle}^{-0.0816} \quad (13)$$

- For 300 μm < d_p < 450 μm:

$$f_{drag\ nozzle} = 168486 \cdot Ar^{-2.9521} \cdot St^{3.9741} \cdot Fr^{-1.50532} \cdot \alpha_{nozzle}^{-0.8247796} \quad (14)$$

- For d_p > 450 μm:

$$f_{drag\ nozzle} = 4.921097 \cdot 10^{-5} \cdot Ar^{-2.9521} \cdot St^{3.9741} \cdot Fr^{-1.50532} \cdot \alpha_{nozzle}^{-0.8247796} \quad (15)$$

The values obtained for $f_{drag\ nozzle}$ require a correction. In those cases where values higher than 0.85 are obtained the factor is fixed to 0.85 since it is the maximum obtained in the CFD simulations. The validation of the models is presented in the supplementary material.

Elutriates are generated due to the effect of drag forces. Eq. (16) computes the fraction of elutriated particles in each of the layers. Further validation about the accuracy of the model is available in the supplementary material. The factor is made independent of the intervals in a similar way to the drag factor. Furthermore, following corrections are also carried out:

- For Rep <10, the factor is assumed to be 1. All the particles elutriate.
- The model is corrected to avoid values above 1 and below zero as for the drag factor.

$$f_{elutriates} = 8.2287e-5 \cdot Ar - 0.909193 \cdot \frac{\ln(St)}{Re_{pin}} \quad (16)$$

Complementing the particles residence time, the airflow in this region is also modelled and divided in three sub-regions as presented in Figure 9. At the bottom of the nozzle the airflow is highly unstable and it can be assumed to behave as a PFR. However, due to the drag force of the particles acting on the air, there is a back-flow region near the injection. The relative distance of this back-flow region can be determined by a correlation of the form of Eq. (17). The flux entering in the back-flow region and that it is in recirculation can be computed as presented in Eq. (18). The supplementary material, Figure S-8 and S-9 shows the validation of both correlations.

$$\frac{h_{back\ flow}}{h_{nozzle}} = 0.8179 \cdot \alpha_{nozzle}^{0.4585} \cdot vf^{0.282} \cdot Ar^{-0.278398} \cdot St^{0.3506} \cdot vel_{nozzle}^{0.5483} \quad (17)$$

$$\dot{m} = \rho_{Air} \cdot A_{zone} \cdot (-4754) \cdot vf^{0.6053} \cdot Ar^{-0.55033} \cdot vel_{nozzle}^{0.567282} \cdot St^{0.4841} \quad (18)$$

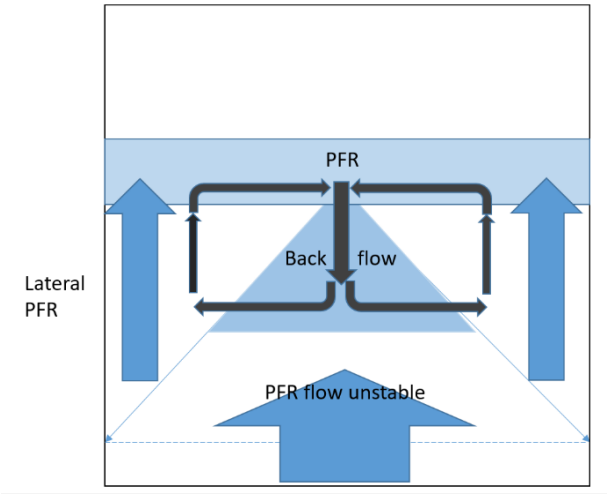

Figure 9. Airflow regions in the nozzle region.

Elutriates region

The residence time of the elutriated particles in the top region of the dryer is obtained to be a function of particle and airflow characteristic dimensionless groups. The residence time of each of the bins of the particle size distribution is modelled as presented in Eq. (19) where the Archimedes number accounts for the ratio between the gravity and drag forces and it is found to have a positive power higher than 1. However, it is corrected by the Stokes number, which is elevated to a negative power lower than the one of the Archimedes number. This fact suggests that the error for both models can be the lowest for the predictions, but a balance of the errors exist between both. Then, the Froude number has a positive exponential. This result is expected since at higher air velocities elutriates spend less time in the zone. The validation of the model is presented in Figure S-10 of the supplementary material.

$$Re_p = 4.906414e-5 \cdot Ar^{2.719125} \cdot Fr^{1.84564} \cdot St^{-3.63357} \quad (19).$$

The dispersion in this region is modelled as a set of equivalent CSTR's. The number of tanks per meter, is proportional to the dimensionless variance as presented in the Appendix. In our case it is computed as a function of the Reynolds number of the air in the dryer, and the Archimedes and Stokes numbers of using the Sauter diameter, see Eq. (20). In case that the model suggests a number of tanks below 1, a CSTR with dead zones is assumed as presented in the Appendix. The validation of the model is provided in the supplementary material, figure S-11.

$$\frac{N_{tanks}}{m} = 1.3e-8 \cdot Re^{1.6844} \cdot Ar_{d32}^{-0.3247875} \cdot St_{d32}^{1.195} \quad (20)$$

Falling and central region

Two regions are defined below the injection: Falling region with concentrated particles and central region. The division of the zone is shown to be at 0.77 r/R_{dryer} for most of the cases. Only small particles are captured by the precessing vortex of the swirl pattern and sent to the center (See supplementary material for further analysis of the comparison). The cut at 0.77 is selected and the fluxes at both zones need to be accounted. First, the airflow is determined. As steady-state simulations have been used for generating the model, only the axial fluxes are evaluated, which are modelled as a function of a fraction of the total air as presented in Eq. (21). The reduced model obtained for the fraction used to divide the fluxes is obtained to be as presented in Eq. (22). The fraction is observed to be highly influenced by the level of deposition in the walls that modifies the decay of the swirl intensity, $\frac{\Omega}{\Omega_0}$, and the Stokes number of the characteristic Sauter diameter of the particle size distribution.

$$\dot{m}_{airTotal} = \dot{m}_{airTotal} \cdot f_{Air} + (1 - f_{Air}) \cdot \dot{m}_{airTotal} = \dot{m}_{air\,Falling} + \dot{m}_{air\,Central} \quad (21)$$

$$f_{Air} = 0.4387639 \cdot \left(\frac{\Omega}{\Omega_0}\right)^{-0.37743536} \cdot \ln(St_{d32})^{-0.1802539} \quad (22)$$

A parity plot of the prediction of the model obtained by Eq. (25) is presented in Figure 10. It can be seen that the accuracy is not that good, R^2=0.44. Alternatively, a more complex model can be used, see Eq. (23). However, it only shows a slight improvement in the accuracy, R^2=0.47, but having a loss of robustness. The comparison of the axial velocity profiles shows that they are by far highly irregular for each of the operating conditions studied. Furthermore, the definition of the zone (which is based on the discrete phase concentration) is cutting the air velocity profiles in a zone of transition. The velocity profiles are very irregular, see figures S-17 and S-18 of the supplementary material for further information. The irregularities of the velocity profiles reduces the quality of the model and the definition of higher number of cuts will not improve the quality of the prediction since the error is in the model, not in the extraction of the properties. It only re-distribute the error differently between the internal zones. The distribution of air is influenced for a wide range of variables (velocity, swirl intensity, turbulent components, nozzle characteristics, volume fraction) that cannot provide a robust reduced model with the accuracy of a CFD model. In particular, the nozzle also plays a role as presented in the comparative DOX in the supplementary material, where particles are released from the wall.

$$f_{Air} = 0.5623096 \cdot \left(\frac{\Omega}{\Omega_0}\right)^{-0.374} \cdot \ln(St_{d32})^{-0.225769} \cdot vf^{0.0233} \quad (23)$$

Another evaluation has been also carried out by checking if the zone can be understood separately without the influence of the nozzle. However, the model shows very high errors and a recalibration of the parameters of Eq. (26) is required. This remarks why systematic compartment models have not been cut internally multiphase systems with compressible continuous phase for generating correlations for the air (In all the cases such as fluidized beds [25] or furnaces [44] the air is only cut axially assuming plug flow. It is compressible and, contrary to non-compressible like agitation tanks, a small change in the geometry can play a significant change in the whole fluid dynamics). One can determine the zones correctly but the correlations for the air are very weak and with poor quality in the prediction due to high instabilities that it addressed. These correlations only provide a rough estimation of the air distribution. Furthermore, it is important to remark that a very simple change in one part of the geometry modifies the fluid dynamics of the entire system, which makes the zones non-scalable.

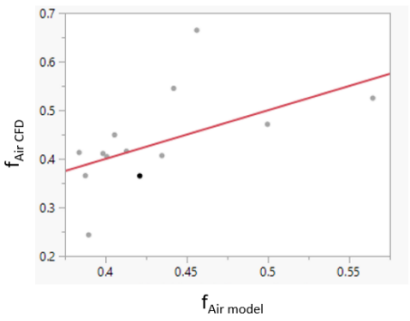

Figure 10. Parity plot for the comparison between the fraction of air predicted by the reduced model and the one obtained from CFD.

The particles are concentrated in the falling region near the wall. The residence time of the particles in this falling region is determined by the Reynolds number of each of them as presented in the Appendix. This Reynolds number of the particles is determined by means of a reduced model from other dimensionless groups. The resultant model obtained for the Reynolds number in this falling region is presented in Eq. (24) as a function of the Froude number in the region of falling, the Reynolds number of terminal velocity and the ratio of swirl intensity that accounts the effect of wall roughness on the tangential momentum decrease of the air. Further details of the modeling and a parity plot of the model validation is provided in the supplementary material, Figure S-20, where the model shows very good accuracy on predicting the Reynolds number.

$$Re_p = 0.60984205 \cdot Fr_{local\ falling}^{-0.61279} \cdot Re_{pterm}^{0.9362} \cdot \left(\frac{\Omega}{\Omega_0}\right)^{-1.1372} \quad (24)$$

The Reynolds number of the particles is dependent on the Reynolds number of the particles at terminal velocity, Re_{pterm},with a power of 0.93. Forcing Re_{pterm} to have a power of 1, a most physically based model based on the ratios of them is proposed as presented in Eq. (24). The accuracy of the model is not significantly affected, R^2 of the prediction drops from 0.9480 to 0.9479. The model presented in Eq. (25) shows that the Reynolds of the number of the particles can be computed by the one of the terminal velocity corrected by the air components. The Froude has a negative exponential remarking that with higher air fluxes, the particles will spent longer times. Similarly, with low decay in the swirl intensity, the tangential component of the air will be higher and the particles will also spend more time since they roll around for longer times.

$$\frac{Re_p}{Re_{pterm}} = 0.4397969 \cdot Fr_{local\ falling}^{-0.66207} \cdot \left(\frac{\Omega}{\Omega_0}\right)^{-1.28546} \quad (25)$$

The last model generated corresponds to the dispersion of the discrete phase that determines the number of equivalent reactors to be used in the zone. Here it is important to remark that the maximum number of CSTR's in the region is limited by the variance of the model of the mean RT and in the current case the limit is 24 CSTR's per meter. The model used to compute the number of equivalent tanks in this region is presented in Eq. (26), which is given as a function of the Archimedes and the Stokes numbers of the particles in the falling region. The validation of the prediction of the equivalent number of tanks per meter is given in Figure S-23 of the supplementary material.

$$\frac{N_{tanks}}{m} = 807.05 \cdot Ar_{d32}^{-1.02462} \cdot St_{d32\ local_{falling}}^{2.085} \quad (26)$$

Inlets region

The following region corresponds to the one where the air inlets enter the dryer. Since the air velocity after the inlets in the chamber is nearly normal to the falling of the particles, it generates a dispersion, showing different trajectories and regimes as presented in Figure 6. The particles and air characteristics are different,

tending the big particles to be lower dispersed than the smaller ones. However, the location at which the particles accumulate in the form of a bed tends to be similar in most of the cases, at a height of 0.85h/H_{cone} as further detailed in Table S-7 of the supplementary material. In this region the air is assumed to be homogeneous. The particles residence time does not show to be highly influenced by any of the input variables and dimensionless groups. The most robust model but with small accuracy is the one reported in Eq. (27) and the accuracy of the model is given in Figure 11. Since the model involves high uncertainty, the maximum number of tanks to be reproduced is also limited. In our case a maximum of 1.72 is allowed for the entire region. Thus, a maximum of 2 tanks is allowed and in the case that the value of variance is below 1, a CSTR with dead zones is assumed. The number of tanks is determined as presented in Eq. (28).

$$Re_p = 9.4102 \cdot 10^{-3} \cdot \left(\frac{\Omega}{\Omega_0}\right)^{0.59164} \cdot Re^{0.245467} \cdot St^{-0.58847} \cdot Ar^{0.822044} \quad (27)$$

$$N_{tanks} = 0.3407 \cdot Ar^{0.1282} \cdot \left(\frac{\Omega}{\Omega_0}\right)^{-3.471657} \cdot Fr^{2.1722} \quad (28)$$

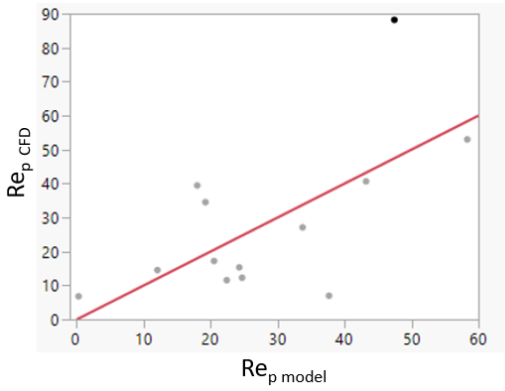

Figure 11. Parity plot of the model comparing the Reynolds number of the particles (it determines the mean residence time) for the CFD and the one estimated from the reduced model. RMSE=17.06.

Cone region

The last region corresponds to the rolling of the particles at the bottom of the dryer. The residence time of the particles in this system is similar to a silo in which the Reynolds number of the particles has shown to be dependent of the Archimedes number [43]. The model used for predicting the residence time of the particles and subsequently their Reynolds number is the one given in Eq. (29). The validation of the model is provided in Figure S-26 of the supplementary material. The number of tanks in this region is determined by Eq. (30) and the accuracy of the mean residence time model does not represent a limit (maximum allowed by the variance of the model for the mean residence time is 9) since the number of tanks determined is never higher than 4, see supplementary material for further information. Despite the momentum (mean residence time and its dispersion) is expected to be only influenced by the Archimedes number, the model dispersion does not show to be accurate enough only with this term. Better results are obtained including dimensionless groups used also in the previous regions. It suggests that the particles are influenced by

previous zones. In fact, the transition in the dynamics of the particles is not fixed in a given distance. The first impact is governed by the velocity at which the particles fall.

$$Re_p = 0.19023 \cdot Ar^{0.25623} \quad (29)$$

$$N_{tanks} = 0.23575 \cdot Ar^{0.140186} \cdot Fr^{-0.0958} \cdot \left(\frac{\Omega}{\Omega_0}\right)^{-1.797547} \quad (30)$$

3.1.5.2 Results for the case of study with monodispersed injections.

A final validation of the residence time for the entire system is carried out by developing the model into a Process Modeling software. For this work gProms® has been selected. The structure of the dynamic model developed has been presented in Figure 4 where each of the zones is composed by a set of CSTR's. The models for airflow and the fluxes within each CSTR are defined in the Appendix.

The cases previously studied have been implemented into the compartment model. As a result, the validation of the mean residence time from previous models is validated together with the dispersion. The RTD curves before the inlets region and at the bottom part of the dryer are presented in Figure 12 for experiments 2 and 10, which represents the most accurate and worst predictions. The remaining cases can be seen in the supplementary material. The accuracy of the predictions is quantified by the cumulative error in the RTD of the particles is used, ε. The error is computed with the differences between the mass fraction predicted by the compartment model, w_{comp}, and the mass fraction predicted by the CFD-DPM model, $w_{CFD-DPM}$, as presented in Eq. (31) for intervals of 0.1 s. The average cumulative error is measured before the cone and at the bottom of the dryer. The average value of ε before the particles access the inlets region is 0.2552 and the maximum is 0.55. At the bottom of the dryer, the value of ε has an average value of 0.1224 and the maximum is 0.2079. Note that these values of ε include an original DOX used for generating the model and experiments from the DOX's used for zoom-in. Further details for every experiment are provided in Table S-8 of the supplementary material.

In most of the cases it is observed that the models show flatter curves than the one observed in the CFD. Despite the main part of the release is very concentrated, there is also a long tail in the distribution that favours the introduction of low number of tanks to address the dispersion and that can account for higher fraction of the mass recovered. In fact, the high dispersion is finally able to capture higher fractions of mass even though the trend of the curve is not always captured. On the contrary, in regions with low dispersion the prediction of the mean residence time is critical since all the mass released is concentrated near the mean. Furthermore, the maximum number of tanks is limited by the accuracy of the model of the mean residence time. Both lacks of accuracy make that for low residence times and low dispersion the model can have significant errors of the cumulative distribution of the mass even that the accuracy of the models is significantly good as presented in previous sections. At the beginning of the release the dispersion is low and very small errors in capturing the mean residence time supposes a huge error in capturing the mass

distribution. In the current work, it can be also shown in Experiment 13 where the shape shows to be more accurately reproduced before the inlets section. However, ε is 0.55 before the inlets section and 0.115 at the bottom of the dryer.

$$\varepsilon = \sqrt{\sum_{t=0}^{t=t}\left(w_{comp} - w_{CFD-DPM}\right)^2} \quad (31)$$

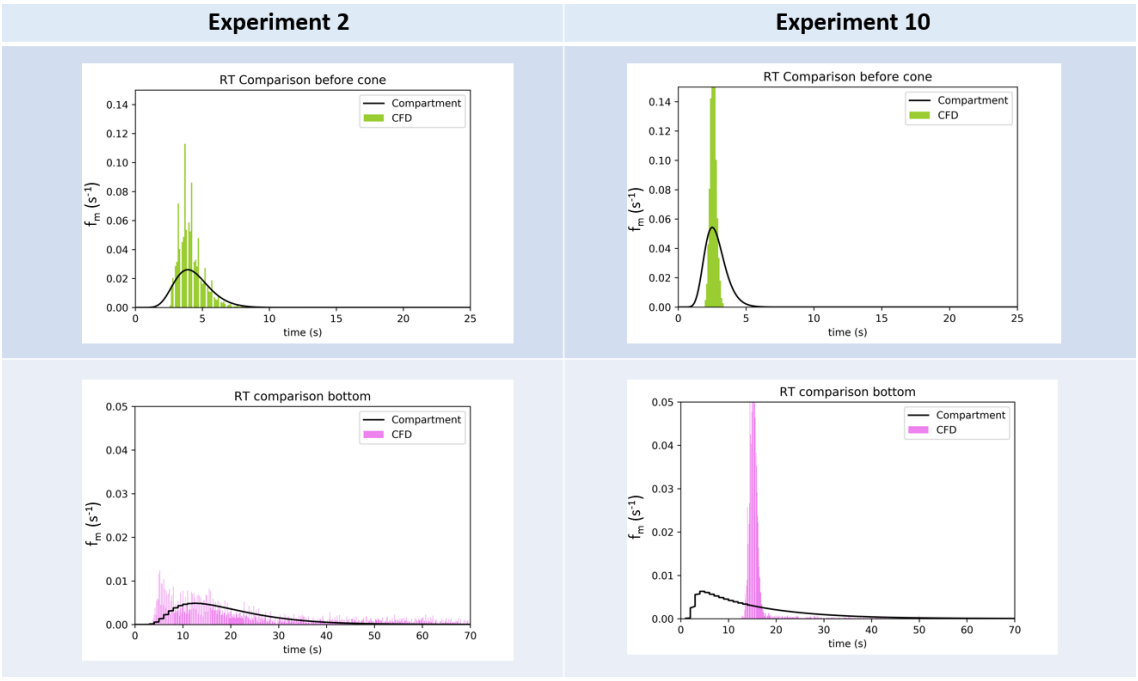

Figure 12. Comparison of the residence time distribution from CFD and from the compartment model for experiments 2 and 10 before the inlets region and at the bottom of the dryer.

3.1.5.3 Results for the case of study with particle size distributions.

A second analysis of the prediction of the mass distribution is carried out using particle size distributions. In these cases, the error computed by the parameter ε is obtained to be lower that with monodispersed distributions, with values up to 21% of ε before the inlets region (average of 14.7%) and up to 9% at the bottom of the dryer (average of 7.9%). The lower error obtained is due to a balance of the error between the different particle sizes. Thus, the use of monodispersed particles proves more reliable for validation of the momentum of the particles.

3.1.6 THE ROLE OF THE NUMBER OF ZONES IN THE MOMENTUM PREDICTION.

The validation of some models has not shown to be accurate enough in some of the regions. In CFD driven models, it has been shown that generating more zones can improve the accuracy of the prediction. However, the error involved in that methodology is different than the one here. In CFD-driven local models, the error is only given by averaging the discretization carried out by the zone definition and in this case is given by

the discretization and the accuracy of the reduced models generated. In order to check if the model could improve by re-defining the zones in the dryer, the following studies are carried out.

The first comparison is carried out with the simplest case of systematic compartment model: Modelling the whole unit as a set of CSTR's. The resulting model to predict the mean residence time is presented in Eq. (33) and the model for predicting the number of CSTR's that introduces the dispersion is presented in Eq. (34). The validation of both models is given in Figure 13, where it is shown that the prediction of the mean residence time is very accurate. However, the dispersion shows higher errors even though the model is highly non-linear and includes a large number of terms. Other approaches of the reduce model are presented in the supplementary material including other terms but they even show worst results. To compare the accuracy of the systematic model with the systematic model defined in the current work, the cumulative error of the distribution, ε, is used for only the experiments of the original DOX used in the methodology, see further details in the supplementary material Table S-10. The original case with multiple zones has an error of 10.3% and the use of a single reactor, has an error of 9.9%. Thus, it is very difficult to differentiate the effect that generating more zones has on the prediction of the residence time distribution since both are similar.

$$Re_p = 492.108 \cdot Re_{pterm}^{1.4431} \cdot St^{-0.24834} \cdot Ar^{-0.66138} \cdot vf^{0.39659} \quad (33)$$

$$\frac{N_{Tanks}}{m} = 5.709 \cdot 10^{-10} \cdot Re^{0.668646} \cdot \left(\frac{\Omega}{\Omega_0}\right)^{0.231} \cdot Ar^{1.058756} \cdot vf^{-0.77156} \cdot St^{-1.241} \quad (34)$$

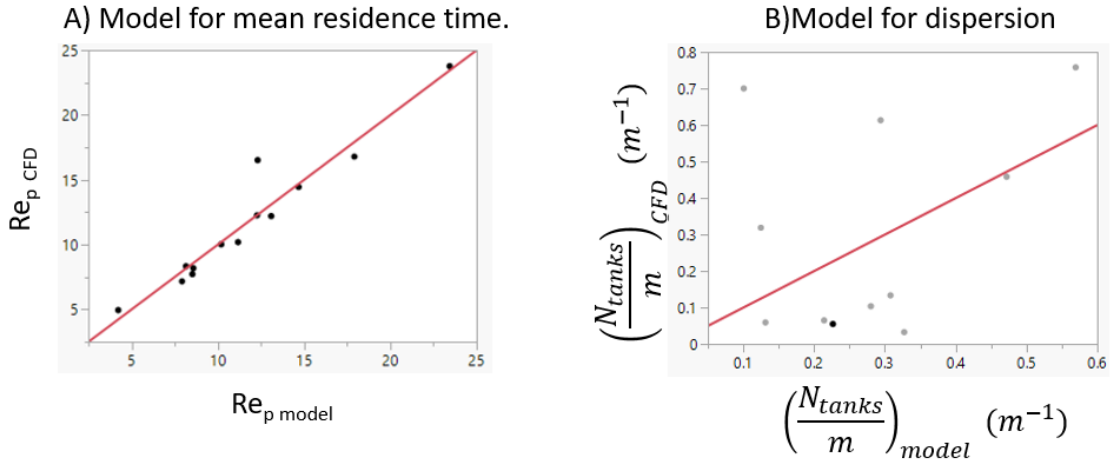

Figure 13. Validation of models for the Reynolds number (it addresses the mean residence time) and the dispersion considering the dryer as a unique system.

A second study is carried out comparing the mean residence time predicted by using different approaches: The case A) of modeling the residence time of the entire dryer with one equation, Eq. (33), a case B) where the inlets region that shows the highest errors is aggregated with the cone region, a case C) where the cone is modelled with a purely empirical equation (it includes dimensionless groups from particles in falling on air) and a case D) where the cone is only modelled with the Archimedes number, current assumption.

The RMSE's obtained for each case before and after using the experiments for validating the model are presented in Table 2, see the supplementary material for further information of the models used and their validation. It can be seen that if no validation is carried out, a larger number of zones implies a larger number of parameters and subsequently a most accurate model. Similarly, limiting the model in the cone to only the physical parameters of the zone results in an increase of the error. However, if one takes into account the error after the validation it can be seen that the model is more robust in the simplest cases (with lower number of zones). In particular, in the case with the original zones but with an empirical model, the RMSE increases so much having a less significant model that with a single region.

Table 2. Summary of RMSE before and after the validation for the case of modelling the dryer as a single unit, the case where aggregation between inlets and cone regions, the original case of the cone with same parameters (purely empirical as A) and B)) and D) the original case where the cone is only modelled as function of the Archimedes.

Case of study	**Based on**	**RMSE (s)**
A) All reactor with 1 model (1 zone)	Experiments of the model	3.0885
	Experiments of the model and of the validation	2.7929
B) Aggregation of inlets and cone zones	Experiments of the model	2.0853
	Experiments of the model and of the validation	2.3249
C) Original zones with empirical model in the cone	Experiments of the model	1.7649
	Experiments of the model and of the validation	3.1676
D) Original zones with model in the cone limited by physics (only Archimedes)	Experiments of the model	3.4619
	Experiments of the model and of the validation	4.5744

3.1.7 CONCLUSIONS

This work has presented a methodology for generating a robust compartment model. The model is able to adapt the zones and the momentum under the entire space of operating conditions. The phenomenological zones primarily characterized are based on the discrete phase distributions and the physical phenomena that acts on it. The zones not only have to ensure similar properties such as in CFD driven models, they also has to be robust in order to be fitted with a reduced model. Within the region, other sub-regions can be generated for including the different air characteristics as defined in the nozzle region. Apart from the limitations in the robustness or stability of the zone under different operating conditions, the compatibility between all the phases is also necessary (The transition between zones must ideally be at the same location). One of the largest errors is given because a zone is generated based on particle distributions, the air is also cut when it is unstable and the model of the air has large errors. In all the previous known systematic compartment models for particulate processes, the air is not cut and distributed in two regions (it is typically assumed homogeneous) [23, 28, 29]. However, in this case it is necessary since the particles are accumulated there and the moisture due to evaporation will be highly different in the falling region than in the central region. This need of having compatible regions between properties supposes one of the biggest limitations to generate the systematic model with correlations that predict the fluxes. Furthermore, the generation of more and smaller regions does not improve the accuracy. It only re-distributes the error of the reduced model and the model becomes less robust. The error of the correlation for the flow can be avoided by using a CFD driven for each case of study but it does not provide any computational benefit.

As it has been described for the air, the use of reduced models is useful in most of the regions but it fails when a region with high instabilities wants to be modeled. In the modeling of the particles momentum, this fact is observed at the inlets region. The residence time and dispersion of the particles in this region is highly irregular it does not show to be fitted by a reduced set of terms. The equation with the highest number of dimensionless groups can be used but when it is validated with new experiments the model does not show to be robust increasing significantly the error. Thus, the number of terms is reduced until having a reduced model robust enough. The final robust model reduces the accuracy. In fact it has been obtained that for having robust models in each of the regions, the accuracy of the all residence time has to be compromised. Similarly, it has been obtained that a higher number of zones increases slightly the accuracy but it reduces the robustness of the model. Based on these observations for the number of zones, the following conclusions have been obtained, which can help in the construction of future systematic compartment models:

- First, the momentum is better captured by generating more regions but the model is by far less robust which can result that the compartments generated cannot be extrapolated to other units. Therefore, if one wants to ensure the scalability of the correlations developed in systematic compartment models the number of regions must be exclusively limited to the ones with very well distinct phenomena and robust under the highest number of cases studied. Furthermore, the

models only show to be accurate in such experiments studied and intermediate operating conditions can be even missed under the same operating space. In order to balance the loss of robustness simpler models (with less number of parameters) have to be generated. However, these models will finally increase the errors of the model. In fact, a reduction of the zones can increase the error in the case that a high unstable zone wants to be modelled. The model for the unstable region will provide a value with high error (a very simple correlation is needed to ensure the robustness) that cannot be balanced with other regions in the case that the model will be generated independently for the zone and also validated independently. This is the reason why CFD driven models are typically used to reproduce the momentum when smaller compartments are generated. However, no correlations are generated in those smaller regions since some regions cannot always exist or they can be very unstable. The alternative is to generate low number of compartments but bigger (In other works 2 or 3) as proposed in other particulate processes

- Second, the error can increase more by the physical constraints to make a scalable model than by the number of zones. One example is given in the cone where the only significant term is the Archimedes number but introducing other non-reliable terms improve the prediction, even after performing the validation.

Apart from these conclusions, it is also important to take into account that in the current methodology the best overall model for the prediction of the final residence time is not developed. The objective has been the generation of a model for each of the regions independently and they do not consider the influence of each region in the parameters of the following ones. The fitting can be improved in future works by generating an embedded model (as done in the nozzle) that will be optimized but the parameters to be used must be determined before since the high non-linearity involved is not compatible at the same time with the selection of the terms to be used. Furthermore, the use of this method will give more weight in the error reduction (imaging that we minimize the sum of errors at all the layers as in the nozzle region) to the reactors with higher residence times (actually the ones of the cone) and they are actually the ones with lowest relative error, ε, from all the regions.

Finally, it is important to remark that the learnings extracted from this study are not only limited to the systematic compartment models. The tool also provides a model to understand where the zones must be cut in CFD driven models (the geometries of the robust zones has been determined and modeled). In the remaining regions, the cuts must be higher in such sections where the transition is also occurring to minimize the interpolation (eg. cut at 0.77 r/R_{dryer} but the transition is between 0.75 and 0.80. Thus, the cut must be as finer as possible between 0.75 and 0.80). Similarly, if the model is then applied to implement a kinetic model a construction wants to be implemented from the kinetic model the number of cuts will need to be high enough until the discretization of the kinetic will not be affected as evaluated by a trial and error such as the Grid convergence as shown in [31].

APENDIX.

Computation of the mean residence time based on the Reynolds number of the particle

The mean residence time of the particles in a CSTR can be computed by multiplying the length of the zone by the velocity of the particle, (A-1).

$$\bar{t} = v_p \cdot \Delta l \tag{A-1}$$

The velocity of the particle is determined from the Reynolds number of the particle in the zones as in Eq. (A-2).

$$v_p = Re_p \cdot \frac{\mu}{\rho_{Air} \cdot d_p} \tag{A-2}$$

Computation of number of equivalent CSTR's.

The number of equivalent CSTR's can be computed from the dimensionless variance as given in Eq. (A-3).

$$N_{tanks} = \frac{1}{\theta} = \frac{\overline{t^2}}{\sigma^2} \tag{A-3}$$

Model used for computing the momentum in each of the reactors

The modelling of the discrete phase has been carried out following a CSTR model that for every bin follows Eq. (A-4). The total volume of the zone is determined from the CFD model and the flux of particles coming in is obtained from the previous reactor.

$$\frac{dC_{pi}}{dt} = \frac{1}{V_T}\left(\dot{m}_{in\ pi} - \dot{m}_{out\ pi}\right) \tag{A-4}$$

The flux of particles leaving the zone is computed dependent on the concentration of particles and it is determined as presented in Eq. (A-5). Eq. (A-5) is for such cases in which the number of tanks is 1 or higher (For values higher than 1, discrete values for the number of tanks is assumed). In such cases where the number of tanks is below 1, a CSTR approach with dead zones (Fogler, 2016) is used, where a dead zones factor is used, see Eq. (A-6). In these equations, the characteristic residence time of each bin in the reactor is computed as function of the Reynolds number and the equivalent height of the reactor. The volume fraction of the particles is computed from the concentration of particles as presented in Eq. (A-7). In the current case the density of the particles is assumed to be constant in the CSTR.

$$\dot{m}_{out\ pi} = \frac{v_{fpi} \cdot \rho_{out\ pi} \cdot V_T}{\bar{t}} \tag{A-5}$$

$$\dot{m}_{out\ pi} = \frac{v_{fpi} \cdot \rho_{out\ pi} \cdot V_T}{\bar{t} \cdot factor_{DZ}} \tag{A-6}$$

$$vf_{pi} = C_{pi}/\rho_{out\ pi} \tag{A-7}$$

Since the volume of each of the zones remains constant, the volume flowrate coming in is the same that lefts the reactor.

$$V_{Pin} + V_{airin} = V_{pout} + V_{airout} \tag{A-8}$$

Where the total volume of particles at the entrance and outlet is the sum of all the bins as Eq. (A-9).

$$V_p = \sum_{i=1}^{n=bins} V_{pi} \tag{A-9}$$

NOMENCLATURE

Dimensionless groups

$Ar = \frac{g \cdot d_p^3 \cdot \rho_{air} \cdot (\rho_p - \rho_{air})}{\mu^2}$	Archimedes number of the particles
$Fr = \frac{U_{avg}}{\sqrt{g \cdot D_{dryer}}}$	Froude number of the air
$Re = \frac{\rho_{air} \cdot D_{dryer} \cdot U_{avg}}{\mu}$	Reynolds number of the air in the dryer.
$Re_p = \frac{\rho_{air} \cdot d_p \cdot v_p}{\mu}$	Reynolds number of the particles
$Re_{pterm} = \frac{\rho_{air} \cdot d_p \cdot v_{pterm}}{\mu}$	Reynolds number of particles with terminal velocity.
$St = \frac{d_p^2 \cdot \rho_p \cdot M_{air}}{\mu D_{dryer}^3 \rho_{Air}}$	Stokes number of the particles in the dryer.
$vf = \frac{V_p}{V_{air}}$	Volume fraction of particles.
$\Omega = 2 \cdot \pi \rho_{Air} \int_0^{R_{dryer}} \frac{U_y \cdot U_\theta}{\rho_{Air} \cdot \pi \cdot U_{avg}^2 R_{dryer}^3} r^2 dr$	Swirl intensity of the air in the dryer at z=0.2.

Variables

C_{pi}	Concentration of particles in the reactor (kg/m^3).
d_p	Diameter of the particle (m)
d_{32}	Sauter diameter of particle size distributions (m).
d_{50}	Mean diameter of particle size distributions (m).
d_{90}	d_{90} of particle size distributions (m).
D_{dryer}	Diameter of the dryer (m).
f_{Air}	Fraction of air sent to the falling region.
$f_{elutriates}$	Mass fraction of elutriated particles.
f_{drag}	Drag factor for reducing the velocity in the nozzle.
g	Gravity (9.8 m^2/s).
$h_{back\ flow}$	Height of the backflow region in the nozzle (m).
h_{layer}	Height of the layers in the nozzle (m).
h_{nozzle}	Height of the nozzle (m).
h_{theor}	Maximum theoretical height of the nozzle region (m).
$\dot{m}$	Mass flux of air (kg/s).
N_{layers}	Number of layers/Cuts in the nozzle region.
N_{tanks}	Equivalent number of CSTR's.
R_{dryer}	Radius of the dryer (m)
$ratioH$	Ratio of layer and nozzle height. Defined as: $ratioH = \frac{h_{layer}}{h_{nozzle}}$
t	Time (s).
$\bar{t}$	Mean residence time of the reactor (s).
T_{air}	Air temperature (K).
U_{avg}	Average velocity of the air in the zone (m/s).
v_p	Velocity of the particles (m/s).
$v_{p\ term}$	Terminal velocity of the particles (m/s).
v_{py}	Velocity of the particles in the axial axis (m/s).
vel_{nozzle}	Velocity of the particles at the injection (m/s).
V_T	Total volume of the reactor (m^3).
V_p	Volume of particles in the reactor.
$w_{CFD-DPM}$	Mass fraction released by the CFD-DPM model.
w_{comp}	Mass fraction released by the compartment model.
α_{Nozzle}	Angle of the nozzle.
σ^2	Variance of the residence time (s^2).
Ω_o	Swirl intensity of the air in the dryer at the inlets. Defined as Ω.
ρ_{air}	Density of the air (kg/m^3).
ρ_p	Density of the particles (kg/m^3).

μ	Viscosity of the air (Pa·s).
θ	Dimensionless variance of the residence time.

Abbreviations

CSE	Cumulative square error.
RMSE	Root mean square error.

Subscripts

air	Refered to the air.
i	Bins.
p	Particles
y	Axial axis.
θ	Tangential component.

REFERENCES

[1] Bezzo, F. Macchietto, S. Pantelides, C. 2003, General hybrid multizonal/CFD approach for bioreactor modeling. AIChE Journal. 49,8, 2133-2148.

[2] Danckwerts, P.V. (1953) Continuous flow systems: distribution of residence times. Chemical Engineering Science, 2 (1), 1-13.

[3] Levenspiel, O. 2004, Chemical Reaction Engineering. John Wiley & Sons. ISBN: 978-81-265-1000-9.

[4] Fogler, H.S. (2016) Elements of Chemical Reaction Engineering. 5th Edition. Prentice Hall. ISBN: 978-0-13-388751-8.

[5] Jourdan,N. Neveux, T. Potier,O. Kanniche,M. Wicks,J. Nopens,I. Rehman,U. Le Moullec,Y. 2020, Compartmental Modelling in chemical engineering: A critical review. Chemical Engineering Science 210, 115196.

[6] Laurent, Bois, P. Nuel, M. Wanko, A. (2015) Systemic models of full-scale surface flow tratment wetlands: determination by application of fluorescent tracers. Chem. Eng. J. 264, 389-398.

[7] Faravelli, T. Bua, L. Frassoldati, A. Antifota, A. Tognotti, L. Ranz, E. (2001) A new procedure fnox emissions from furnaces. Comp. Chem. Eng. 25 (4), 613-618.

[8] Gao, Y. Muzzio, F.J. Ierapetritou, M.G. (2012) A review of the Residece Time Distribution (RTD) applications in solid unit operations. Powder Technology 228, 416-423.

[9] Portillo, P.M. Vanarase, A.U. Ingram, A. Seville, J.K. Ierapetritou, M.G. Muzzio, F.J. (2010) Chemical Engineering Science, 65, 5658-5668.

[10] Escotet-Espinoza, M.S. Moghtadernejad, S. Oka, S. Wang,Z. Wang, Y. Roman-Ospino, A. Schäfer, E. Cappuyns, P. Van Assche, I. futran, M. Muzzio, F. Ierapetritou, M. (2019) Effect of material properties on the residence time distribution (RTD) characterization of powder blending unit operations. Part II of II: Application of models. Powder Technology, 344, 525-544.

[11] Haag, J. Gentric, C. Lemaitre, C. Leclerc, J.P. 2018. Modelling of chemical reactors: from systematic approach to compartmental modelling. Int. J. Chem. React. Eng.

[12] Bermingham, S.K. Dramer, H.J.M. van Rosmalen, G.M. 1998. Towards on-scale crystalliser design using compartmental models. Computers and Chemical Engineering. 22, 355-362.

[13] Bauer, M. Eigenberger, G. (1999) A concept for multi-scale modeling of bubble columns and loop reactors. Chemical Engineering Science, 54 (21).

[14] Bezzo, F. Macchietto, S. 2004, A general methodology for hybrid multizonal-cfd models: Part I. Theoretical framework. Comp. Chem. Eng. 23 (4), 501-511.

[15] Bezzo, F. Macchietto, S. 2004, A general methodology for hybrid multizonal-cfd models: Part II. Automatic zoning. Comp. Chem. Eng. 23 (4), 513-525.

[16] Nauha, E.K. Kalal, Z. All, J.M. Alopaeus, V. (2018) Compartmental modelling of large stirred tank bioreactors with high gas volume fraction. Chem. Eng. J. 334, 2319-2334.

[17] Le Moullec, Y. Gentric, C. Potier, O. Leclec, J.P. 2010, Comparison of systemic, compartmental and CFD modelling approaches: Application to the simulation of a biological reactor of wastewater treatment. Chemical Engineering Science, 65, 1, 343-350.

[18] Le Moullec, Y. Potier, O. Gentric, C. Leclerc, J.P. (2011) Activated sludge pilot plant: comparison between experimental and predicted concentration profiles using three different modelling approaches. Water Res. 45 (10) 3035-3097.

[19] Rehman, U. (2016) Next generation bioreactor models for wastewater treatment systems. PhD Thesis. Genth University.

[20] Guha, D. Dudukovic, M.P. Ramachandran, P.A. Mehta, S. Alvare, J. (2006) CFD-based compartmental modelling of single phase stirred-tank reactors. AICheJ. 52 (5), 1836-1846.

[21] Alvarado, A. Vedantam, S. Goethals, P. Nopens, I. (2012) A compartmental model to describe hydraulics in a full-scale waaste stabilization pond. Water Res. 46 (2), 521-530.

[22] Pinto, M. A. Kemp, I. Bermingham, S. Hartwig, T. Bisten, A. (2014) Development of an axisymmetric population balance model for spray drying and validation against experimental data and CFD simulations. Chemical Engineering Research and Design, 92 (4), 619-634.

[23] Peglow, M. Kumar, J. Heinrich, S. Warnecke,G. Tsotsas, E. Mörl, L. Wolf, B. (2007) A generic population balance model for simultaneous agglomeration and drying in fluidized beds. Chemical Engineering Science, 62, 513-532.

[24] Freireich, B. Li, J. Lister, J. C. Wassgren,C. 2011, Incorporating particle flow information from discrete element simulations in population balance models of mixer-coaters. Chemical Engineering Science, 66, 3592-3604.

[25] Börner, M. Peglow, M. Tsotsas, E. (2013) Derivation of parameters for a two comparment population balance model of Wurster fluidised bed granulation. Powder Technology, 238, 122-131.

[26] Börner, M. Peglow, M. Tsotsas, E. (2011) Particle Residence Times in Fluidized Bed Granulation Equipments. Chemical Engineering & Technology, 34,7, 1116-1122.

[27] Ali, M. Mahmud, T. Heggs, P.J. Ghadiri, M. Djurdjevic, D. Ahmadian, H. Martín de Juan, L. Amador, C. Bayly, A. (2014) A one-dimensional plug-flow model of a counter-current spray drying tower. Chemical Engineering Researh and Design, 92 (5), 826-841.

[28] Li, J. Freireich, B. Wassgren, C. Litster, J.D. (2012) A general comparment-based population balance model for particle coating and layered granulation. AIChE Journal, 58 (5), 1397-1408.

[29] Mielke, L. Bück, A. Tsotsas, E. (2019) Muti-stage and multi-compartment model for dynamic simulation of horizontal fluidized bed granulator. Drying Technology.

[30] Van Hauwermeiren, D. Verstraeten, M. Doshi, P. Ende. M.T. Turnbull, N. Lee, K. De Beer, T. Nopens, I. (2019) On the modelling of granule size distributions in twin-screw wet granulation: Calibration of a novel compartmental population balance model. Powder Technology, 341, 116-125.

[31] Yang, S. Kiang, S. Farzan, P. Ierapetritou, M.G., 2019, Optimization of Reaction Selectivity using CFD-Based Compartmental Modeling and Surrogate-Based Optimization. Processes, 7(1), 9.

[32] Verdumen, R.E.M. Menn,P. Ritzert, J. Blei, S. Nhumaio, G.C.S. Sorense, T.S. Gunsing, M. Straatsma, J. Verschueren, M. Sibeijn, M. Schulte, G. Fritsching, U. Bauckhage, K. Tropea, C. Sommerfeld, M. Watkins, A.P. Yule, A.J. Schonfeld, H. (2007) Simulation of Agglomeration in Spray Drying Installations: The EDECAD Project. Drying Technology, 22 (6), 1403-1461.

[33] Guo, B. Fletcher, D.F. Langrish, T.A.G. (2004) Simulation of the agglomeration in a spray using Lagrangian particle tracking. Applied Mathimatical Modelling, 28, 3, 273-290.

[34] Tajsoleiman, T. Spann, R. Bach, C. Gernaey, K.V. Huusom,J.K. Krühne, U, 2019, A CFD based automatic method for compartment model development. Computers and Chemical Engineering, 123, 236-245.

[35] Roshan, V. (2016) Space-filling designs for computer experiments: A review. Quality Engineering, 28, 28-35.

[36] Garud, S.S. Karimi, I.A. Kraft, M. (2017) Design of computer experiments: A review. Computers and Chemical Engineering. 106, 71-95.

[37] Pronzato, L. Müller, W.G. (2012) Design of computer experiments: space filling and beyond. Statistics and Computing, 22, 681-701.

[38] Roshan, V. Gul, E. Ba, S. (2015) Maximum projection designs for computer experiments. Biometrika, 1-10. DOI: 10.1093/biomet/asv002

[39] Cozad, A. Sahinidis, N.V. Miller, D.C. (2014) Learning surrogate models for simulation-based optimization. AIChE J. 60 (6), 2211-2227.

[40] Gerón, A. (2019) Hands-on Machine Learning with Scikit-Learn, Keras and TensorFlow. 2nd Edition. Ed. O'Reilly.

[41] Overcamp, T.J. Scarlett, S.E. (1993) Effect of Reynolds Number on the Stokes Number of Cyclones. Aerosol Science and Technology, 19 (3), 362-370.

[42] Hoffman, A.C. Stein, L.E. (2008) Gas Cyclones and Swirl Tubes. Principles, Design and Operation. 2nd Edition. Springer Berlin. ISBN: 978-3-540-74694-2.

[43] Muite, B.K. Hunt, M.L. Joseph, G.G. (2004) The effects of a counter-current interstitial flow on a discharging hourglass. Physiscs of Fluids, 16,3415.

[44] Ma, J. Eason, J.P. Dowling, A.W. Biegler, L.T. Miller, D.C. (2016) Development of a first-principles hybrid boiler model for oxy-combustion power generation system. International Journal of Greehouse Gas Control, 46, 136-157.

CHAPTER 3.2 A CFD-DPM BASED COMPARTMENT MODEL FOR COUNTER-CURRENT SPRAY DRYERS. HEAT AND MASS TRANSFER MODELING.

ABSTRACT

This chapter presents the use of a systematic compartment model for computing the heat and mass transfer within spray dryers. The drying model used for implementing the kinetics in the CFD model is implemented in this case to maintain the scalability of the model. Furthermore, the CFD model is also used to extract the heat and mass transfer fluxes and generating surrogate models between the zones defined in previous section. The resultant compartment model is independent from the CFD model and it is validated against this CFD model with the experiments showed in chapter 2.5. These experiments have different formulations (different density, particle size distribution), nozzle characteristics (different angle and velocity of the particles in the hollow cone formed by the nozzle), airflow temperatures and mass-flows of air and particles. The model is able to adapt the zones to each of these operating conditions and predict the internal distribution of the temperature with an average error below 8 K in all the regions.

Note: The supplementary material is attached in the physical version of the thesis and it is also available in: https://drive.google.com/drive/folders/1_EkYTjaqQYkP_okY1ckLG9DMSdbt8gRt?usp=sharing

3.2.1 INTRODUCTION

The modeling of spray dryers has been carried out following different approaches from simple well mixed assumption models to detailed rigorous models. An interesting review of all the approaches is available in Langrish [1]. He classified the approaches in three types: The coarsest scale consists of a model based only on mass and energy balances. This approach only provides a general understanding of the process implementing the kinetic by means of a simple empirical model (in either exponential or polynomial forms). Some examples of this approach can be found in [2-4]. In the most detailed work of this approach Ozmen and Langrish [4] were able to implement the glass transition temperature to estimate the sticky-point temperature at which particles can agglomerate in a previous studied case. A finer scale model includes the heat and mass transfer mechanisms as well as the momentum equations implemented within a reactor model, typically a parallel plug flow model in which the air and particles can interact in co-current or counter-current. This approach has been used in a wide range of studies [5-8] being even applicable to explore the glass transition temperature [6] and crystallization behavior [7] of the particles. The finest scale corresponds to the detailed CFD models and its extensive use has been shown in previous chapters. Apart from these models, an alternative solution is the use of CFD driven models. One of the first studies was developed by Pinto et al. [9] who extracted the residence time of the particles from a CFD model at the end of the dryer and implement the drying kinetics in gProms ®. The approach has been further developed by Process System Enterprise ®, integrating the system with the cell aggregation compartment procedure of Bezzo et al. [10]. However, as remarked in previous chapter, this type of approach requires the use of the CFD model every time a new operating conditions are defined.

In the area of counter-current spray dryers, most of the modelling studies have used CFD approaches since it allows to reproduce the complexity of the airflow patterns and their influence on the discrete phase. However, they are computationally very expensive. The modelling of the dryer with coarser approaches has been carried out with two types of models. On the one hand, the dryer has been modelled as a 1D plug flow reactor [11] considering the heat and mass transfer. The air was also modeled as a plug-flow and the particle momentum was computed in the axial axis based on the general equation of motion. On the other hand, a second study presented a CFD driven compartment model. The model was only validated under one operating condition and it was used for the same purpose than the one in which it was constructed. It was based on a CFD model with drying and validated with the same model, which is obvious that the model has to predict if the discretization is enough and the data is correctly driven [12]. An alternative to CFD driven compartment model with local description is the use of systematic compartment models. These models can be constructed to work under different operating conditions as shown in the previous chapter. All the models extracted for the flexibility of the zones, fluxes and momentum components are used in this work and extended introducing the heat and mass transfer mechanisms.

The chapter is structured in the following sections: Section 3.2.2 provides a description of the possible computational assessments to be used. Section 3.2.3 describes how the model for the heat and mass

transfer mechanisms have been implemented. Section 3.2.4 presents the results obtained and Section 3.2.5 summarizes the conclusions of the work.

3.2.2 COMPUTATIONAL ASSESMENTS.

The previous chapter has shown the modelling of the particle residence time distributions under a wide range of operating conditions. The model has been developed in an equation oriented software, gProms ®. For the modelling of the drying mechanism, a single droplet drying model has to be used. In chapter 1.1 the model developed was implemented in gProms ® and in chapter 2.5 it has been adapted for being implemented into a CFD code. The single droplet drying model was validated in chapter 1.1 under constant air conditions and the mass and energy balances were computed in gProms ® in 1-way coupling (the increase of moisture and losses of heat in the air were not updated after drying the droplet). However, in our case the 2-way coupling is needed since the contact between the air and particles occurs more than an instant. The contact takes place in counter-current in all the reactors and discretization steps (in the case of a plug flow such as the nozzle region) defined within each phenomenological region.

The integration of the single droplet drying model together with the momentum of the particles from the compartment model presented in chapter 3.1 can be carried out by integrating the kinetic between the different residence time steps as described by Pinto et al. [9]. By following this procedure, the results obtained from the kinetic model are highly influenced by the number of zones as presented in literature referred to CFD driven compartment models [13]. Alternatively, in systematic compartment models, which have been applied to simpler systems (typically where reactions between phases occur in co-current, with simpler kinetic mechanisms such simple diffusion models and also lower number of reactors); the kinetic models are implemented in the form of differential equations and integrated with standard methods (e.g. Runge-Kutta, Euler and their modifications) that are finer in the discretization step.

In the case under study in this thesis, the kinetic model is composed by different stages and to model the transitions between these stages it is required to capture very rough and discontinuous changes in the modification of the evaporating mass and particle temperature. Note that for the smallest bin of the particle size the second stage can be carried out in the order of 0.001 s and for the biggest the second stage can remain during all the residence time of the particle in the dryer. As a result from these changes, a discretization of the kinetics is necessary as presented in [9]. Here it is important to ensure that if the discretization is not fine enough, over-drying of the particles can occur in the transition from the 1st to 2nd stage or when the droplet gets dried. The error in the transition from the 1st to 2nd stage can be avoided by having a sufficient discretization near the injection. In the case of the transition when the droplet gets dried a correction can be included limiting the drying to not evaporate more than the moisture of the droplet. Taking into account all these considerations, in a first screening study the kinetic model presented in chapters 1.1 and 2.5 is implemented together with the momentum equations from section 3.2.3.1 in gProms ®. However, the model does not show to be feasible for more than 3 discretization steps when it is run in

transient and 4 when it is run in steady-state. The high number of non-linear functions (in the correlations of the momentum components, the intrinsic ones of the drying kinetics such as the vapor pressure, or in the use of arc-tangent functions to ensure the continuity in the transition between the stages) together with the number of loops to be closed between the air and the particles, see Eq. (1), make that equation oriented process simulators (which solve the equations and loops by optimization) cannot find a solution for more than 4 discretization steps (they can be either discretization steps of the PFR or CSTR's). In order to facilitate the convergence in equation-oriented process simulators, the strategy for closing these loops has been based on computing the particles first and then close the loops from the bottom to the top. However, the number of loops is still very high, see Eq. (1). A more detailed analysis for determining the number of loops of Eq. (1) is provided in the supplementary material. In this Eq. (1), N_{bins} is the number of bins and $N_{discret}$ is the number of CSTR's and discretized sections of the PFR reactor of the injection.

$$N_{recycles} = 2 \cdot (N_{bins} \cdot 2) \cdot (N_{discret} - 1) \cdot \frac{N_{discret}}{2} \quad (1)$$

In order to solve the model with equation-oriented modelling in a unique process, a simplification of the kinetics is necessary. These simplifications have been still computed in steady-state since the initial operating conditions in each of the internal parts of the dryer is not known and fixing them will not ensure the model to be adaptable to every case. The following alternative approaches have been evaluated taking into account the need for models with smother transitions in the drying kinetics:

- The use of a characteristic drying curve model such as the one proposed in [14]. This type of model still has discontinuities but less rough than the multi-stage model of chapter 2.5. The discontinuities can be smoothed by the use of arc-tangent functions. However, the solution of the system by optimization methods still shows limitations due to the high non-linearity of the equations (powers, arctangents, exponentials, etc.) and the high number of recycles in the system due to the counter-current behavior of the system. The total number of loops given by Eq. (1), where for the current case with 10 bins a maximum of 9 discretization steps obtained (with an optimization error of 0.1), is 1,440.
- The use of a simple diffusion based model without any transition and the diffusion modelled as a function of the temperature in the air (since it is the one that govern the drying of the particle in the boiling state which is the most relevant in the dryer) in the particles as presented in Eq. (2) has been also evaluated. Even though this method does not show any discontinuity, its solution is still limited to 19 discretization steps and it is by far not physically reliable. Highly non-linear terms are still intrinsic in the model with a high number of loops. Furthermore, it is necessary to adapt the drying model to every case where the airflow temperatures or a new detergent formulation is evaluated. Exploring the model in detail, it has been found that the vapor pressure equation, computed as in Eq. (3) involves the terms with highest changes. Assuming steady-state operating conditions and discretizing the vapor pressure equation into a mix-integer form, the solution has

shown stability for the system for at least 50 discretization steps and with 10 bins. However, this approach does not consider the transition to crust formation and boiling resulting in non-reliable results. The approach can be applied to other counter-current spray dryers with temperatures below boiling.

$$D = D_o \cdot \left(T_{air} + T_p\right)^n \quad (2)$$

$$P_w^o = 10^{8.07131 - \frac{1730.63}{T_{air} - 273.15 + 233.426}} \cdot \left(\frac{101325}{760}\right) \quad (3)$$

From this analysis it has been obtained that the use of equation oriented modeling tools (e.g. gProms®, Modelica) that use optimization based solvers for closing the loops does not allow to close all the loops of the current process with a multi-stage kinetic model. Better results can be obtained with transient simulations if the initial conditions in each of the reactors would be known. However, it is hardly difficult that the optimization still finds a feasible solution (especially if the model wants to be applied to new formulations, fluxes ratios or temperatures) since temperature in some regions have changes up to 50 ºC. Furthermore, the model that can be solved does not have a reliable physics. For example, the drying by boiling only takes place at sufficient temperatures increasing the drying rate. If the transition from drying by diffusion to boiling is not included, the physics are not adequately reproduced, since the diffusion is adapted to be only governed by temperature but not by particle structure. Other alternative that can be explored in future works with equation-oriented simulation tools is to divide the process in different sub-processes, run it independently and connect them externally for closing the loops.

Taking into account the non-feasibility of the kinetic model with equation-oriented modelling, the use of alternative numerical strategies and simulation tools are used to solve the system maintaining the physics. In this work the system has been modelled using sequential programing (Python is used for this task). The following procedure is followed to close the loops: First, each of the discretization is sequentially computed from the nozzle region to the product. Then, the air properties and elutriates are updated from the bottom to the top of the dryer. The iterative scheme finishes when the temperature above the nozzle region is stable. After that, the region of elutriates is computed since the drying there takes place in co-current.

The need of using sequential programming tools has significant implications in terms of model applicability since the new compartment model developed cannot be straightforward implemented into control or optimization models. It needs further reductions (some of them tested here but that do not allow the model to reproduce the physics and be robust enough) for such implementations. Furthermore, the presence of a very high number of loops and the need of reproducing a high complex kinetic model makes that the model cannot reproduce with low computational cost the dispersion by means of the equivalent number of tanks theory as in other simpler, co-current and with 1st order kinetics systems [17,18]. Finally, the systematic compartment model developed in this work can be also compared with the CFD driven compartment models and understand why those models allow a higher number of zones even that they use the same software.

In CFD driven compartment models such as the one developed by Process System Enterprise ®, the fluxes of mass and heat are fixed, which implies simpler equations (and specially in the loops) than in the current case where highly non-linear terms are used to adapt both the fluxes and different types of drying mechanism to every new operating condition.

3.2.3 MODEL DESCRIPTION

The computational analysis carried out has determined the need of using sequential programing to allow the use of the multi-stage kinetic mechanism used in previous systems and close all the loops generated by the counter-current flow of the particles and the air. As in the previous evaluation, in each of the discretization steps the operation is assumed to take place in steady-state, which does not allow to represent the dispersion determined in the previous sections of the thesis. Each of the discretizations, represented as a CSTR or combination of CSTR's plus a heat exchanger and a membrane or CSTR plus a separator in Figure 1, corresponds to a discretization step within the PFR (with a permeable wall) or the CSTR (plus heat exchanger or membrane). In the following subsections, a most detailed definition of the models used for heat and mass transfer in each of the phenomenological zones is presented.

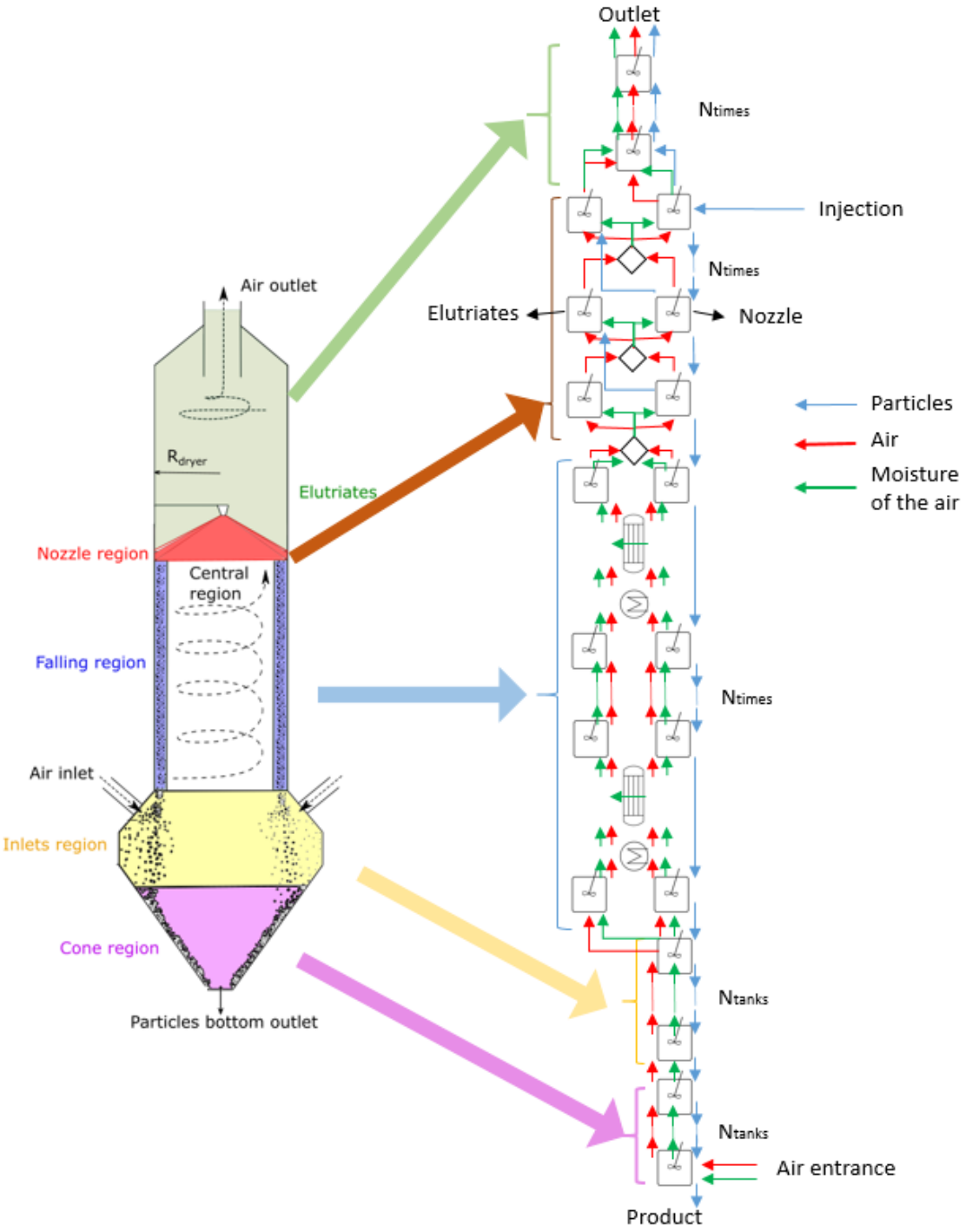

Figure 1. Structure of the model where the flux of each material is presented in arrows.

3.2.3.1 Input parameters.

The distribution of the material to be processed is computed before the mass and energy balances in the dryer. The injection is introduced in the form of a particle size distribution function (as a Rosin-Rammler or binomial function as defined in chapter 2.5), which is discretized in the same number of bins that the ones

used in the experiments. The inputs used in the nozzle are the same ones to be introduced here (velocity and angle of the injection, temperature, density, moisture content).

From the injection a multi-dimensional Particle Property Distribution (PPD) is defined as $f(t, d_p, n_1, \dots, n_n)$, where t is the residence time, dp is the particle diameter, and n_1 to n_n are different properties such as the particle moisture content, the temperature or the density of the particles. From the incoming mass flux of particles and integrating in the domain of particle diameters, the mass flux that is introduced in the nozzle in each of the bins can be computed from the definition of the Rosin-Rammler distribution, see Eq. (4):

$$for\ i = 0{:}\ N_{bins} \quad f(V_{cum\ bin}) = f\left(1 - \exp\left(-\frac{d_{bin}}{d_{mean}}\right)^n\right);\ f(V_{bin}) = f(V_{cum\ bin} - V_{cum\ bin-1}) \quad (4)$$

Once the mass flux in each of the bins is determined the following properties are maintained similar to the ones of the injection:

- Temperature of the particles.
- Density.
- Moisture content.
- Velocity at the injection.

From the characteristic particle diameter and density of each bin, one can compute the volume and mass of a single particle as presented in Eqs. (5) and (6):

$$f(V_p) = \frac{\pi}{6} f(d_{bin}^3) \quad (5)$$

$$f(m_p) = f(V_p \cdot \rho_p) \quad (6)$$

The number of particles in each of the bins defined is computed as presented in Eq. (7):

$$f(N_p) = f\left(\frac{F_{bin}}{m_p}\right) \quad (7)$$

Once the number of particles entering in the system is defined, the general population balance equation for each of the discretizations is defined as in Eq. (8). Due to the complexity of the kinetic model, the highly non-linear equations and the number of loops required for closing the mass and energy balances, the model is computed by means of sequential programming where the population balances in each of the discretization steps are solved in steady-state. The terms of Eq. (8) involve the accumulation, which is assumed to be zero in each of the discretization compartments since they are solved in steady-state. The two first terms of the right hand side of Eq. (8) present the inflow and outflow in each of the compartments. B represents the birth and D the deaths due to agglomeration and attrition. As presented in the first chapter of the current thesis, a step by step procedure is required in the validation of the model. In this chapter the validation only takes place for the heat and mass transport in the system. Thus, breakage and death terms,

generated by breakage and agglomeration, are assumed to be zero. In the following sections the special models, which complement the momentum models of chapter 3.1, used in each of the regions are defined.

$$\frac{df(N_i)}{d_t} = f(\dot{N}_{in}) - f(\dot{N}_{out}) + B - D \quad (8)$$

3.2.3.2 Modeling the cone section.

The air enters the dryer by the inlets region and it has a small contact with the particles in the cone region. A figure showing the streams followed by the air is presented in Figure S-2 of the supplementary material for further details. The contact between the air and the particles can then take place in the top part of this cone but it can be not significant enough to be considered. Furthermore, the particles are rolling along the cone and a large number of them can be covered by the remaining particles reducing the effect of drying. In the cone, the change of temperature in the air is highly relevant since the central part of the swirling flow shows a temperature drop as presented in Figure 2. In order to implement the drying, two studies have been carried out:

- First, the experimental cases of Chapter 2.5 have been computed taking into account that drying occurs in the cone at an average temperature between the air at the initial conditions (around 500 K) and the external one (300K).
- Second, drying has not been considered.

In the evaluation of these studies, the heat and mass transfer model is computed following the drying model presented in chapter 2.5. Furthermore, due to the presence of particles and also to the relevant drop of temperature due to the vortex flow that generates vacuum in the outlet, no heat losses are assumed through the wall. For further details about this issue, the cases taking into account the heat losses and kinetic considering are presented in Table S-1 and S-2 of the supplementary material. The temperature at the end of the inlets region when drying is considered in the cone is all the cases around 20 K (with a maximum error of 35 K) lower than the one obtained in the CFD model. However, if one considers that drying does not take place when the particles roll in the cone, the errors in the temperature predicted after the inlets are always below 8 K. The comparison for each of the cases studied is given with more detail in the supplementary material.

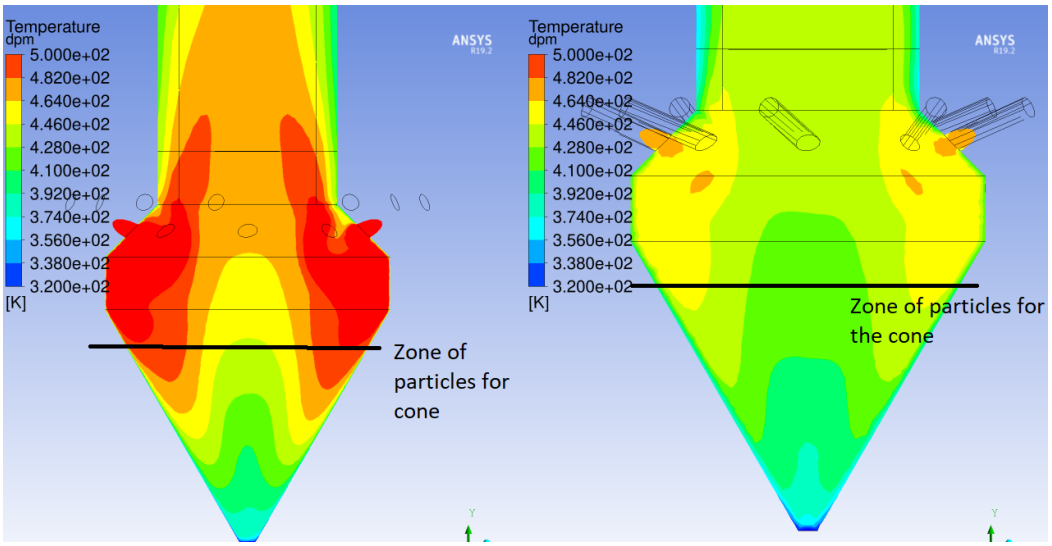

Figure 2. Distribution of temperature in the cone region.

Apart from the distribution of temperature, the air also suffers recirculation in the inlets region. For including this recirculation into the systematic compartment model, different reactors in parallel and with different loops must be included. These loops are then required to be closed for the airflow, which will even increase significantly more the computational cost of the model. Here it is also important to make a difference with data-driven compartment models. Those models are able to reproduce these loops for the air but the fluxes are still fixed, being necessary to generate a new compartment every new operating conditions.

3.2.3.3 Modeling the inlets section.

As presented in the previous chapter 3.1, the inlets region has a very unstable distribution of particle sizes. The distribution of the particles within the region is highly heterogeneous through the entire zone and general modeling conclusions cannot be obtained since some particles can be captured by eddies and displaced either to center of the dryer or to the wall. For an accurate modelling of the particles residence time, a CFD-driven model must be developed and the particles distribution will follow a different distribution within the zone for each case of study. Even the zones reported in [12] are far from being robust and not always observed as demonstrated in the previous chapter 3.1. If one desires to reproduce the distribution of particles in this region with further accuracy than the one reported in this work, a data-driven compartment model is necessary. Furthermore, it is recommended to discretize internally the zone as much as possible to have the concern of capturing the particles with low error.

Taking all these considerations into account, the section has been modelled as a single CSTR. In this region the transitions between the different stages of the drying mechanism of droplets rarely takes place and discretizing the zone in 200 sections is enough. In each of the discretizations, the structure presented in Figure 3 is followed for computing the momentum, mass and energy balances of the particles as follows:

- First, the properties of the air are computed with the inlet temperature.
- Then, taking into account the properties of the particles and the air, the equations for the momentum of the particles are computed based on the models presented in previous chapter 3.1.
- Using the momentum components (velocity that results in the Reynolds number and time in the zone), the drying model of Chapter 2.5 is computed. As a result, the moisture content, the evaporated mass and the heat transfer from the air to the particles is determined.
- Once the heat transfer from the particles to the wall has been computed. The energy balance for the particles is determined and in the case of particles it is computed as presented in Eq. (9), where the heat losses of the air are also taken into account. The heat losses through the wall of the inlets region is computed by the general heat transfer equation as presented in Eq. (10). In Eq. (10) U_{wall} is the global heat transfer coefficient of the wall used also in CFD simulations and based on [11], A_{cone} is the area of the wall, T_{air} is the inlet temperature of the air in each discretization and T_{atm} is the atmospheric temperature.

$$H_{out\ air} = H_{in\ air} - \dot{q_{drying}} - \dot{q_{loss}} \tag{9}$$

$$\dot{q_{loss}} = U_{wall} \cdot A_{cone} \cdot (T_{air} - T_{atm}) \tag{10}$$

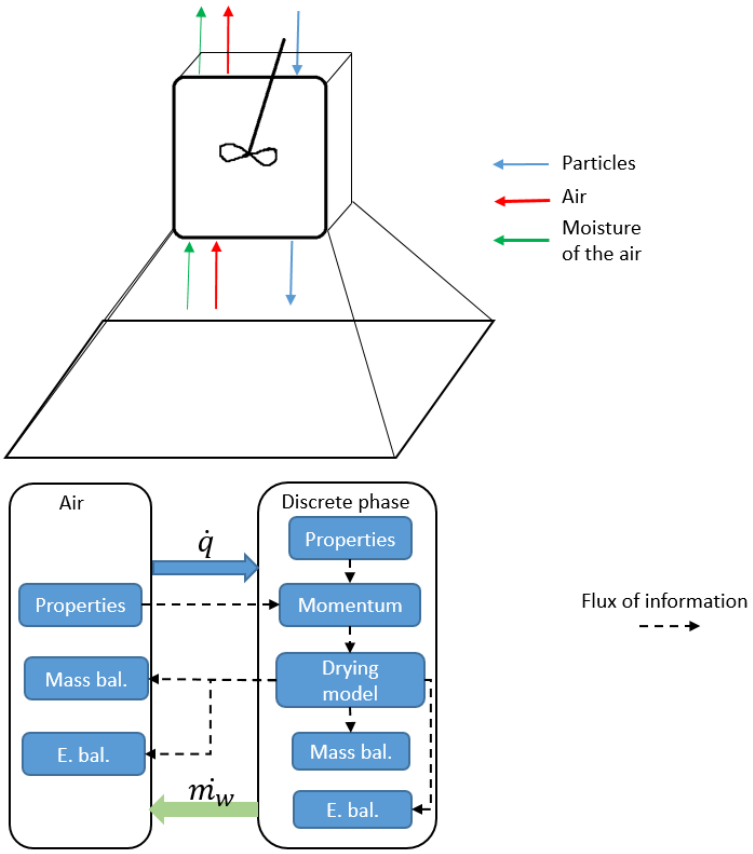

Figure 3. Structure of the model used in each discretization.

3.2.3.4 Modeling the falling and central regions.

The next zones to be computed correspond to the central and falling regions. In each of the axial discretizations of the cylinder both regions are computed in parallel considering the units given in Figure 4. The temperature in the region at which the particles tend to concentrate is smaller than the temperature in the center of the dryer since in this region drying is occurring. In the supplementary material a deeper analysis is provided for each of the cases showing that the radial temperature starts to drop at the same dimensionless radius of 0.77 r/R_{dryer} at which the particles are concentrated. The analysis also shows a second internal temperature drop where the log-law region is shaper at a relative radius of 0.96 $r/R_{dryer.}$ This section for the log-law has not been considered as an independent zone since it implies to generate a new set of discretizations where the drying model needs to be computed, increasing the computational cost. If more accuracy is desired in the region, it can be considered in future works. Similar to the temperature radial distribution, a study has been carried out for the moisture content. However, it shows a much more smother trend than the temperature, see supplementary material.

Taking into account the distribution of the properties, the process presented in Figure 4 is used in each of the discretizations. Here it is important to remark that the air is separated in the two regions as function of the swirl intensity, the Archimedes number of the particles and the angle of the nozzle as presented in previous chapter 3.1. One fraction of the air is sent to the central region and the remaining air is sent to the falling region. No transfer of air is considered between regions (they are assumed in a dynamic equilibrium). The first unit computed is the equivalent reactor (it can be a discretization of the PFR or the CSTR), which is computed following the procedure presented in Figure 3.

The only modification introduced in the reactor is the use of an equivalent Reynolds number for drying. The rotating behavior of the airflow pattern can generate that the particle move in the form of a spiral at a higher velocity than the one determined from the Reynolds number used for the residence time. For determining the Reynolds number of drying, different internal cuts in the falling region have been carried out in the momentum experiments and the velocity has been extracted. From the average velocity, a Reynolds number is computed. The ratio between the Reynolds number for drying and the one used for the residence time is determined as a function of the Reynolds number of the air, the characteristic Stokes number of the particles and the Swirl decay ratio due to roughness as presented in Eq. (11). The validation of the correlation is presented in the supplementary material.

$$\frac{Re_{p\,drying}}{Re_p} = 0.10762649 \cdot \left(\frac{S_1}{S_0}\right)^{0.3843244} \cdot St^{-0.41955} \cdot Re^{0.29552} \quad (11)$$

Then the air of the falling region is sent to a heat exchanger where it receives the energy from the air of the central region. The heat exchanger follows the general heat transfer equation where the area is computed with the radius used as a cut between the two regions and determined in the previous chapter. The heat transfer coefficient between the two regions has been determined from CFD experiments and it can be

computed from a modified Dittus-Boelter correlation as presented in Eq. (12). From the Nusselt number of this Dittus-Boelter correlation (assuming that the global heat transfer coefficient is governed by the convective coefficient) one can determine the heat transfer coefficient. The validation of this heat transfer coefficient is presented in Figure 5. Further details about how this correlation has been developed are given in the supplementary material.

$$Nu = 2.592 \cdot 10^{-3} \cdot Re^{1.07644} \cdot \left(\frac{S_1}{S_0}\right)^{-0.10223} \cdot Pr^{0.4} \quad (12)$$

In a similar way, the transport of moisture from the falling to central region has been also tried to be modelled in the form of a modified Dittus-Boelter correlation, see Eq. (13). However, the prediction of the mass transfer constant is not as good as for the heat transfer, see Figure 5, b). Therefore, a constant value has been assumed for the mass transfer as: k_m=0.048687 m/s.

$$Sh = 8.375179 \cdot Re^{-1.154154} \cdot \left(\frac{S_1}{S_0}\right)^{4.39729} \cdot Sc^{0.4} \quad (13)$$

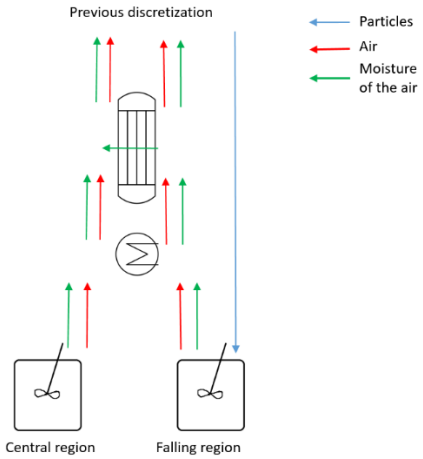

Figure 4. System of units in each discretization.

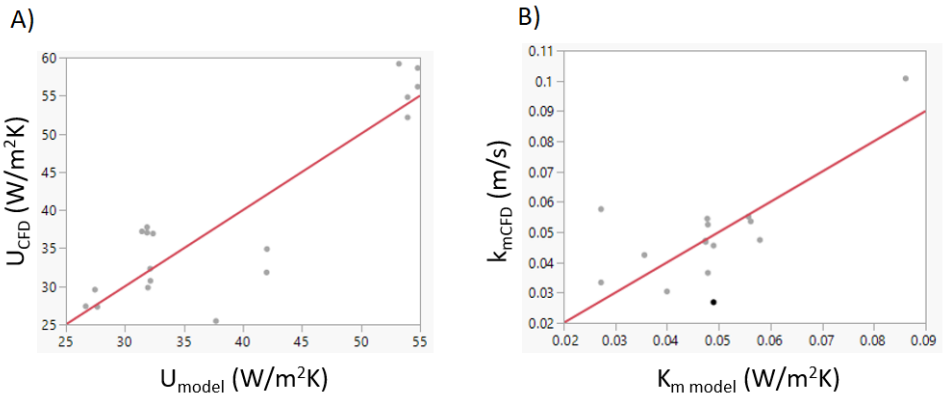

Figure 5. Comparison of A) the heat transfer coefficient extracted from CFD and the one of Eq. (11) and B), the mass transfer coefficient extracted from CFD and the one of Eq. (12).

3.2.3.5 Modeling the nozzle region.

The following region corresponds to the nozzle. This region has been modelled as a set of two reactors in parallel with an intermediate separator for the air components as presented in Figure 6. Even though the model can look like purely empirical with not physical meaning, it does not mean that other more complex have not been evaluated. In the supplementary material the reader is referred to other alternative approaches such as the one used between the falling and central region. The current approach assumes two reactors in parallel. The air is also assumed as a plug-flow and it is distributed in each of the discretizations by a separator, which distinguishes two regions: A central region where the flux is computed as presented in Eq. (14) and an external region that contains the remaining airflow.

$$F_{centre} = F_{in} \cdot \frac{A_{centre}}{A_{tot}} = F_{in} \cdot \frac{\pi \cdot r_{local}^2}{A_{tot}} = F_{in} \cdot \frac{\pi \cdot \left(tg(\alpha_{inj}) \cdot h_{local\ nozzle}\right)^2}{A_{tot}} \quad (14)$$

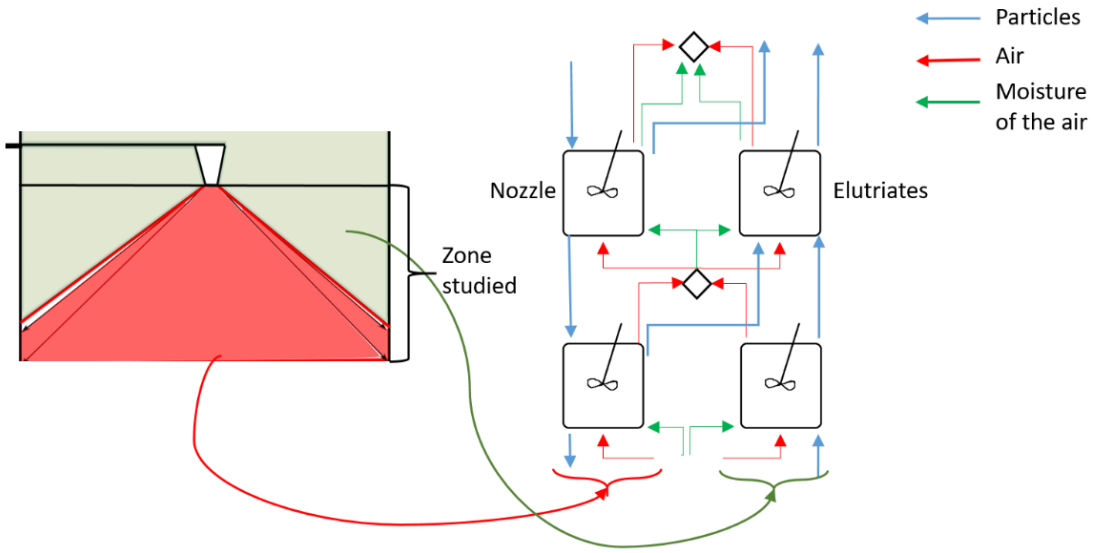

Figure 6. Equivalent system for the computation of each discretization within the nozzle region.

Once the air is divided, the water and temperature are also distributed between the two regions following the ratios determined from CFD. The equation that distributes the moisture between the central part of the nozzle and the external part is presented in Eq. (15) and the equation that distributes the enthalpies is based on a ratio of a ratio of temperatures as presented in Eq. (16). The validation of both models is presented in the supplementary material together other alternative approaches evaluated that have not been successful.

$$\frac{T_{wall}}{T_{centre}} = 1.0442 - 0.0817 \cdot \frac{h_{local\ nozzle}}{H_{total\ nozzle}} \quad (15)$$

$$\frac{w_{water\ wall}}{w_{water\ centre}} = 0.6527 + 0.3417 \cdot \frac{h_{local\ nozzle}}{H_{total\ nozzle}} \quad (16)$$

The modeling of the air is complemented with the particles where two regions can be distinguished:

- The region of the injected particles that are assumed to contact with the air located in the internal region (nozzle region in red from Figure 6) even though the sheet of liquid forms a hollow cone. The momentum in this section is computed as presented in the previous chapter where the Reynolds number of the particles and then a ratio of elutriated particles is computed. It is important to remark that the computation of the fraction of elutriates is limited only to those particles with diameters below $2.8 \cdot 10^{-4}$ m (it is the highest diameter recovered as elutriates in the CFD simulations) and velocity at the entrance of the discretization below 10m/s. Similar than in the falling region, the Reynolds number of the particles used in the drying model also needs to include the 3D components. In the current case, this Reynolds number is corrected with the angle of the nozzle region (note that this angle does not need to correspond with the one of the injection as defined in the previous chapter), see Eq. (17). The drying model is computed following the model of chapter 2.5.

$$Re_{p\ drying} = \frac{Re_p}{\cos(\alpha_{inj})} \tag{17}$$

- The parallel region of elutriated particles. In this region, the elutriated particles from the other zone move up to the region of elutriates. The velocity of the particles is assumed to be the same than in the elutriates region. No corrections are done for having a Reynolds number of the particles that accounts the 3D components in terms of drying. It is assumed to be the same than the one computed for the time. The single droplet drying model is also assumed to be the same than the one than in previous cases. After computing the drying model the outlet enthalpy of the zone is determined and the losses in the wall are computed as presented in Eq. (9) and (10).

Once the mass and energy balances have been computed in each of the two sub-regions, they are combined determining the global moisture content, enthalpy and temperature. After that, the fluxes of energy and mass are sent to the following discretization.

In this region the drying kinetic occurs very fast and the transition between the first and second stages takes place in most of the droplets. At least 800 discretizations are required to ensure that the smallest droplet (the one with the highest evaporation rate and subsequently the one that can involve highest error by over-estimation of drying) reports values in their 1st stage of drying for at least two steps of the discretization before changing to the 2nd stage of drying.

3.2.3.6 Modeling the elutriates region

The last region corresponds to the section of elutriated particles. This region is computed after the loop in the discretizations of the remaining counter-current regions presented before. The air is modeled assuming that it behaves as a plug-flow and the momentum of the particles is computed as presented in the previous

chapter without correction of the Reynolds number. The distribution of particles is also assumed homogeneous in the region since no radial distribution has been observed. The computation within each of the discretizations of this region is carried out as presented in Figure 3 and heat losses are also taken into account.

3.2.3.7 Computational set-up.

The model presented in the previous sections have been solved using sequential programming where the loops have been closed by a 2-way coupling iterative approach. In each of the iterations, the particle fluxes, momentum and drying are computed first from the nozzle to the bottom of the dryer and then the air is updated in counter-current from the bottom to the top of the dryer. In the current case, Python 3.6 has been used for this task and the model takes approximately 1h and 20 minutes to converge in an Intel Core ® i7-7700-3.6 GHz.

3.2.4 RESULTS

3.2.4.1 Results for the compartment model

The compartment model involving heat and mass transfer has been validated with the experiments showed in chapter 2.5. Furthermore, another 2 additional experiments have been added for intermediate flows (as for the bottom injection) at top and high levels of injection. It is important to note that the flexibility of the compartments and the models for the fluxes have only been developed for those cases with a single nozzle. A summary of the input of the experiments for validation is presented in Table 1.

Table 1. Experiments used for the validation of the compartment model.

Exp.	Formula	z_{inj}/Z	Re_{Air}	T_{in} (K)	F_{slurry}/F_{air}
A-HL-HF	A	0.7 (High Level)	6.61×10^4 (High Flow)	493	0.171
A-HL-MF			4.87×10^4 (Middle Flow)	530	0.214
A-HL-LF			4.06×10^4 (Low Flow)	564	0.254
A-ML-HF		0.5 (Middle Level)	5.97×10^4 (High Flow)	492	0.179
A-ML-MF			4.87×10^4 (Middle Flow)	530	0.214
A-ML-LF			3.95×10^4 (Low Flow)	564	0.247
A-LL-HF		0.3 (Low Level)	6.59×10^4 (High Flow)	493	0.166
A-LL-MF			4.87×10^4 (Middle Flow)	530	0.214
A-LL-LF			4.09×10^4 (Low Flow)	564	0.245

The first validation against the experiments is carried out for the general distribution of mass fluxes in order to evaluate if the model captures correctly the mass recovered at the bottom and the one as elutriates. In both the CFD and compartment models these elutriates are approximately to be the same. The average mass of elutriates is presented in Table 2. As it can be seen, the amount of elutriates is a bit higher in the compartment model than in the model of CFD. There is only a 2.5% more of elutriated particles predicted

by the compartment than by the CFD model. Here, the use of a threshold in terms of diameter helps to limit the amount of elutriates generated, which remarks a bit of weakness in the model used for the generation of elutriates in each of the layers of the nozzle. Specially, this model is a bit weak when the airflow in the dryer operates with low Reynolds numbers. In those cases where the Reynolds number is low, the amount of elutriated particles estimated by the compartment model can increase up to 29%. This amount of elutriates have also another implication in the temperature prediction, especially in the nozzle region. Some of the elutriated particles can be suspended in this region as well as they can move up or down. In the current compartment model, after the particles are moved up or down they are not allowed to return. The inclusion of those recirculation without fixing the fluxes (as in CFD driven compartment models) will increase a lot the computational cost of the model, which is actually significant enough. Even though, the errors in the prediction of the temperature are not that big as presented as follows.

Table 2. Comparison of the percentage of mass elutriated by the CFD model and the compartment model.

Average % of mass elutriated CFD (%)	Average % of mass elutriates compartment
6.93±0.02	9.28±0.01

The validation against the temperature profiles is presented in Figures 7 and the errors against the CFD model at the entrance and exit of the most relevant regions are given in Table 3. The temperature is selected as critical variable since it is more sensitive than other variables such as the moisture content. As it can be seen, the prediction of the temperature shows very small errors, in most of the cases below the 10ºC also reported in the experimental measurements of chapter 2.5. On average the region with highest error corresponds to the region of the elutriated particles. The prediction of the amount of elutriates can involve errors since some of the particles elutriated can be only suspended and then move back falling as final product. Furthermore, the momentum is also challenging even though in this work we are also using the mean value of the residence time as presented in the previous chapter. As also described in [15], the elutriated particles show uncertain patterns, which cannot be easily described within the zone.

Another region that also address significant uncertainty in the model is the inlets region. This region shows in particular a significant reduction of the model quality for the prediction of cases with low Reynolds numbers of the air. As described in the first chapters of the thesis (2.2 and 2.3), the swirl flow pattern of the air only shows to be stable in fully developed regime (Above $Re>1x10^5$). When this Reynolds number decreases the pattern starts to become more instable and it also starts to be deconstructed being much more difficult to predict its behavior. Those errors in the air can be transmitted into the momentum of the particles (which does not capture accurately the behavior at very those low Reynold numbers) and subsequently the drying. For further understanding of the inlets region, the following section is provided.

Table 3. Temperatures and errors at the entrance and outlet of each of the phenomenological regions. The error is defined as the temperature of the CFD model minus the temperature of the compartment model.

Experiment	After inlets (z/H=0.035)		Pre-nozzle (HL:z/H=0.664, ML: z/H=0.464, LL: z/H=0.2645)		After nozzle (HL:z/H=0.868, ML: z/H=0.668, LL: z/H=0.468)		Outlet (z/H=1)	
	T (K)	Error (K)	T(K)	Error (K)	T(K)	Error (K)	T(K)	Error (K)
A-HL-HF	422.7	3.9	359.2	-1.9	356.5	-8.2	350.5	-7.0
A-HL-MF	429.9	4.0	349.1	7.8	347.1	-0.7	340.7	0.8
A-HL-LF	433.3	9.1	344.4	11.1	340.9	3.8	334.5	6.5
A-ML-HF	423.1	1.3	373.2	-0.2	368.4	-5.2	351.9	1.6
A-ML-MF	432.0	2.2	368.7	1.3	362.8	-5.4	344.1	4.1
A-ML-LF	437.1	5.2	366.2	4.9	359.6	-1.7	339.7	8.5
A-LL-HF	426.8	-1.8	389.8	0.9	377.5	-4.1	348.7	11.2
A-LL-MF	432.7	-5.8	389.5	-0.3	375.7	-5.6	342.4	14.0
A-LL-LF	437.8	1.8	389.8	0.4	374.2	-4.1	338.4	16.9
Average RMSE (T)		3.9		3.2		4.4		7.8

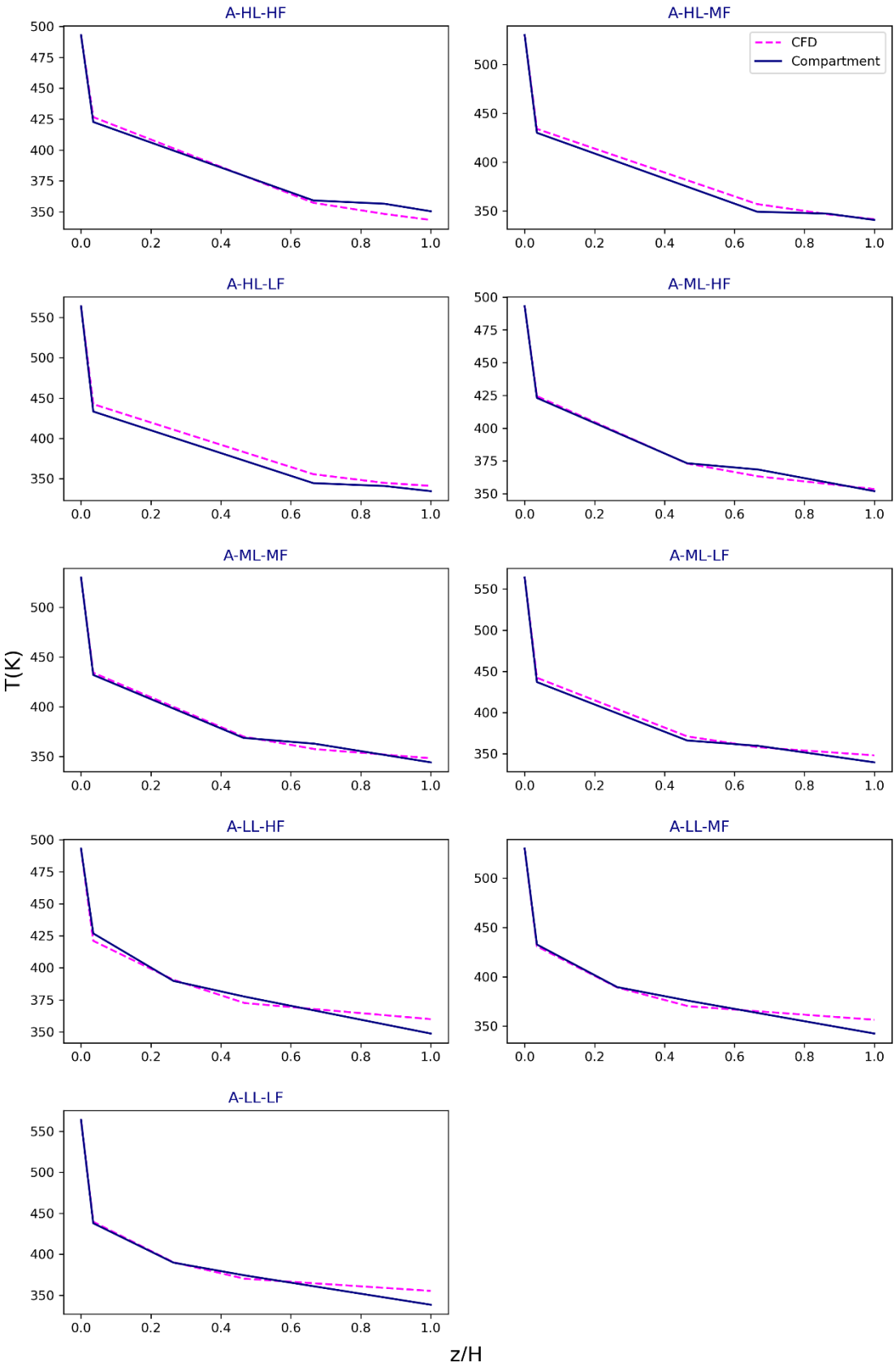

Figure 7. Comparison of temperature profiles predicted by the CFD and compartment models for formulation A.

Apart from the validation against the temperature distribution, the particles obtained by the model can be also validated with the moisture distribution content of the product obtained at the bottom of the dryer. As it can be seen in Figure 8, this moisture content shows to be very similar to the one obtained from CFD. The main changes can be observed in the smallest sizes where the compartment model shows smaller amounts of water content. In the CFD-DPM different parcels are tracked for every bin and it subsequently reproduces the dispersion. However, in this compartment model no stochastic distribution of the particles residence time has been included and all the particles are assumed to be dried. In future works stochastic functions can be used as alternative to the equivalent tanks reactor model for reproducing the dispersion as suggested in [16]. In the remaining particle sizes the same moisture content is obtained. In some few cases (A-HL-HF, A-HL-LF and A-ML-LF) the moisture content of the biggest bin of the particle size tends to be higher than the one predicted by the CFD model, which can be generated in order to balance the lower amount of water observed in the small particle sizes.

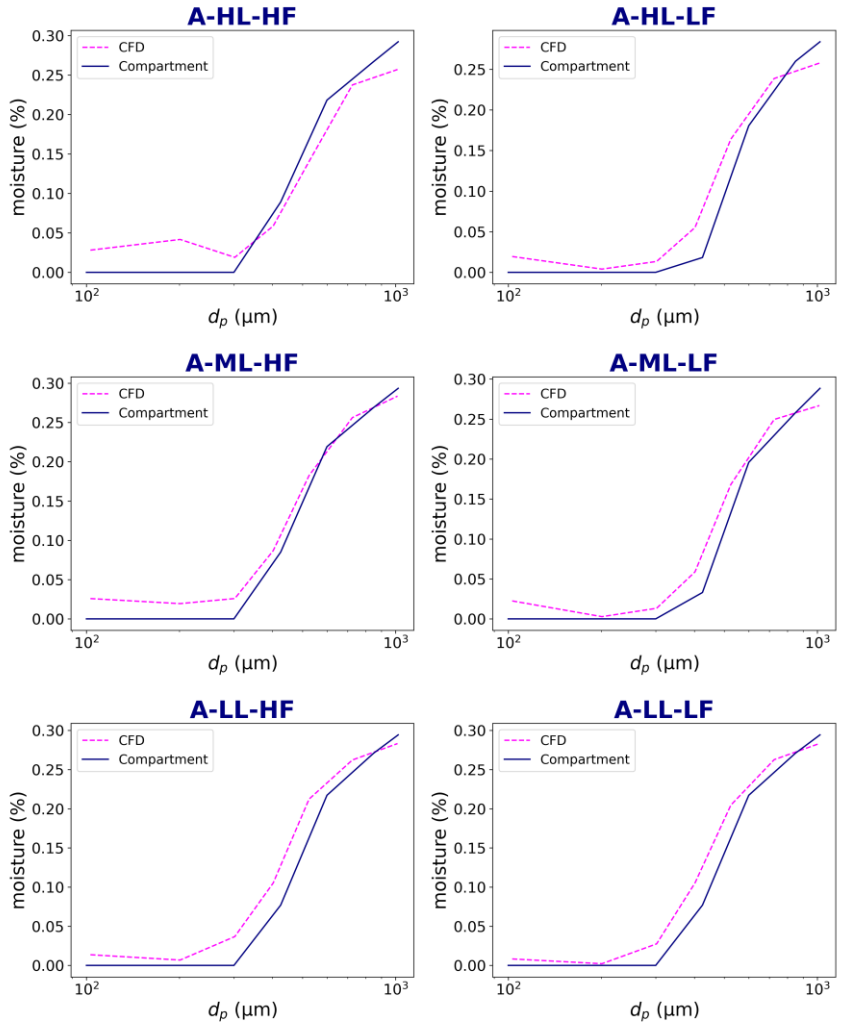

Figure 8. Comparison of the moisture distribution as function of the particle size predicted by the CFD and compartment models.

3.2.4.2 The role of the inlets.

One of the regions with higher uncertainties is the inlets region. As a result, significant errors in the prediction can be obtained. In some cases, the error involved in this region is accumulated with errors in the following regions resulting in significant differences at the top of the dryer. This fact particularly occurs in the case of the lowest Reynolds number as presented in the previous section. In order to check if any other regions can be defined in the inlets region, the temperature distribution and airflow streamlines are analyzed as presented in Figure 9. It can be seen that it is possible to characterize another region of low temperatures, where the particles are also concentrated. Furthermore, most of the patterns of the airflow show to remain in the heap section. Most of the streamlines that reach the cone do it after recirculation. This identification of the airflow streams and the temperature in the bottom section has a high impact on the final results (errors up to 30 K of difference can be obtained in the temperature). Even though the drying will not be considered in the cone, if one assumes that air gets there and there is also losses by heat transfer (with a significant area) there is a significant drop of temperature. This importance that the airflow has on the system distinguishes this system from other previous works on systematic compartment models applied to other systems where the air has impact on the particles momentum but none on the zone characterization [17, 18]. However, it has to be carefully used. As remarked in previous chapter and indicated in [19] the use of systematic compartment models can involve significant errors in describing the fluxes of fluid between the internal compartments of a unit. Especially, if one focuses on a compressible fluid system and in which the flow pattern suffers significant unstable changes as it is our current system. In these cases and if the purpose of the model is to be accurate, it is recommended to use CFD-driven compartment models even though the computational cost efficiency it is by far not as good as in the systematic approach. One compartmentalization is needed for every new operating conditions that modify the flow pattern, which occurs out of the fully developed turbulent regime for swirl flows.

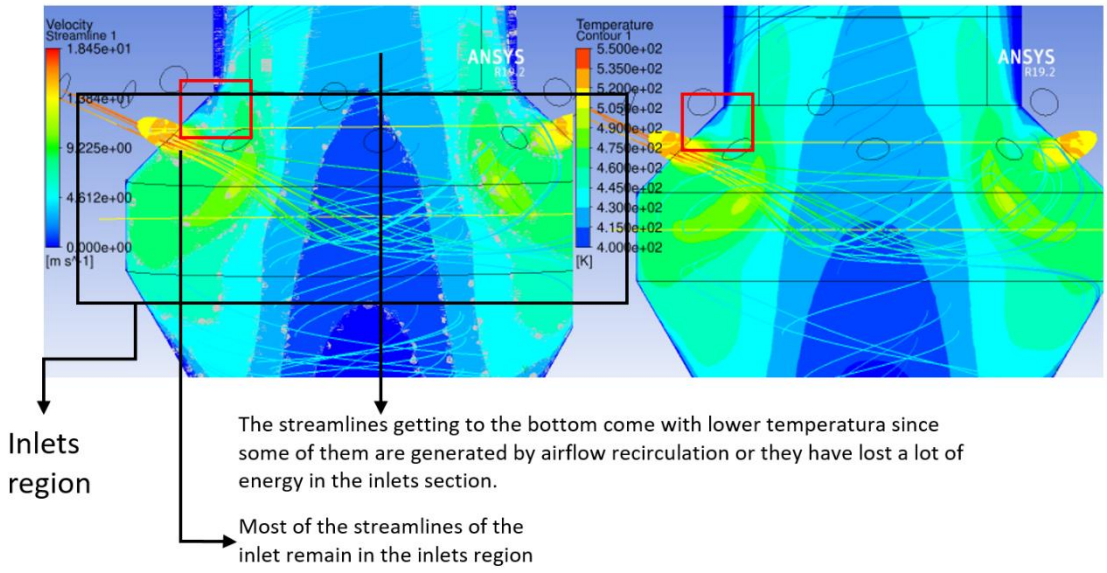

Figure 9. Streamlines of the airflow and temperature profiles in the inlets region.

In order to improve the accuracy in the inlets region and taking into account the stable observations of the air temperature distribution, a new zone can be defined for reducing the error of the model. The results obtained by including this zone are presented in Table 4. It can be seen that the final results does not show significant changes. The error in the inlets region is reduced but this error is then increased in the falling region and it is maintained above the nozzle region. The increase of the error in the falling region is generated because the falling region has a smaller under-prediction of the temperature and the introduction of the limitation in the inlets improve the prediction at the inlets (it shows a small over-prediction) but it reduces the accuracy at the exit of the falling region. In particular the experiment with worst accuracy, which is the one with lowest Reynolds number also shows a significant decrease on the temperature and it also reduces the errors. It can be seen in the last row of Table 4 that the average error has a significant decrease and below the nozzle the errors are below 5 ºC.

Table 4. Temperatures and errors at the entrance and outlet of each of the phenomenological regions with the introduction of low temperature zone in the inlets region. The error is defined as the temperature of the CFD model minus the temperature of the compartment model.

Experiment	**After inlets (z/H=0.035)**		**Pre-nozzle (HL:z/H=0.664, ML: z/H=0.464, LL: z/H=0.2645)**		**After nozzle (HL:z/H=0.868, ML: z/H=0.668, LL: z/H=0.468)**		**Outlet (z/H=1)**	
	T (K)	**Error (K)**	**T(K)**	**Error (K)**	**T(K)**	**Error (K)**	**T(K)**	**Error (K)**
A-HL-HF	426.3	0.3	359.9	-2.6	357.2	-8.9	351.1	-7.6
A-HL-MF	434.3	-0.3	348.9	8.0	346.8	-0.3	340.4	1.0
A-HL-LF	437.4	5.1	345.6	9.9	342.1	2.6	335.6	5.5
A-ML-HF	426.9	-2.5	374.1	-1.1	369.2	-5.9	352.5	1.0
A-ML-MF	432.2	1.9	370.0	0.1	363.8	-6.3	344.9	3.4
A-ML-LF	439.1	3.1	362.6	8.6	358.0	0.0	338.5	9.7
A-LL-HF	425.9	-4.9	390.8	-0.2	378.3	-5.8	349.0	10.9
A-LL-MF	432.6	-1.7	391.1	-1.8	376.3	-6.2	342.6	13.8
A-LL-LF	438.2	1.4	391.7	-1.6	375.1	-4.9	338.6	16.6
Average RMSE (K)		2.4		3.8		4.6		7.7

3.2.4.3 The role of the elutriated particles.

The results reported in the two previous studies show that in most of the cases the highest error corresponds to the region of elutriated particles. Furthermore, that region shows more drying in the compartment model in comparison to the CFD for all the cases (The error tends to increase and be positive in Tables 3 and 4 at the outlet.). This fact suggests that the drying of the elutriated particles is not captured very well. The error can be given by not capturing properly the momentum of the particles, which it still makes sense since the particles can be enrolled in eddied within this region; but it can also be given due to not capturing accurately the amount of elutritates generated.

For evaluating the role of elutriates, the threshold at which the particles can elutriate is modified. In the study we have obtained a bit higher elutriates that in the CFD model. For reducing the amount of elutriates, the cut is done at the diameter of the 66% of mass of elutriates. Using this smaller particle diameter as threshold for considering the elutriates it can be seen that the temperature in the regions below the nozzle suffers a drop and most of the cases tend to under-predict the temperature, see Table 5. These changes, up to 6 K below the nozzle (which are near the error that we are having in the model) and increasing the error in the temperature prediction up to 17 K, remark the influence that suspended and elutriated particles have on drying. In our case of study, the influence is not very high since the mass fraction sprayed between 200um and 300um represents less than 10% of the total mass. However, the uncertainty generated by this models can be more significant if higher mass fractions are sprayed in this range. In particular the suspended particles can play a significant error below the nozzle having substantial changes on the temperature that the air has when the particles get to the nozzle section and they subsequently dry in this region.

Table 5. Temperature at the entrance and outlet of the phenomenological regions considering smaller threshold for the elutriated particles.

Experiment	**After inlets (z/H=0.035)**		**Pre-nozzle (HL:z/H=0.664, ML: z/H=0.464, LL: z/H=0.2645)**		**After nozzle (HL:z/H=0.868, ML: z/H=0.668, LL: z/H=0.468)**		**Outlet (z/H=1)**	
	T (K)	**Error (K)**	**T(K)**	**Error (K)**	**T(K)**	**Error (K)**	**T(K)**	**Error (K)**
A-HL-HF	424.6	2.1	354.1	3.2	349.6	-1.3	348.7	-5.2
A-HL-MF	429.3	4.6	346.1	10.9	340.1	6.4	339.9	1.6
A-HL-LF	434.4	8.1	343.1	12.4	338.2	6.5	336.9	4.1
A-ML-HF	423.6	0.8	372.0	1.0	363.1	0.1	350.6	2.9
A-ML-MF	427.5	6.7	368.1	1.9	358.6	-1.1	348.1	0.2
A-ML-LF	435.1	7.2	360.2	11.0	347.9	10.1	337.6	10.6
A-LL-HF	421.1	-0.1	386.8	3.9	374.2	-1.6	348.8	11.2
A-LL-MF	428.2	2.7	388.1	1.1	374.5	-4.3	341.7	14.7
A-LL-LF	434.9	4.7	388.2	1.9	372.9	-2.7	338.4	16.9
Average RMSE (K)		3.6		4.1		3.1		7.3

3.2.4.4 Validation with the mass of droplets reaching the wall.

One of the benefits of the approach developed is the possible introduction of agglomeration and breakage kernels for determining the particle size of the particles with low computational cost. As defined in chapter 2.6, the transition from droplet to a particle can be modeled using the modified Fourier number of the single droplet drying model. In this case, the model used in Chapter 2.5 have been also implemented with a modified Fourier number of 12.5 (See Chapter 2.6). However, all the droplets suffer the transition within the nozzle region. The maximum relative distance of the nozzle region at which one can still find discrete phase in form of droplets is presented in Table 6. It can be seen that the maximum distance corresponds to those

systems at higher injection locations. These cases are the ones with highest possibilities to show agglomeration that results in the generation of particle sizes greater than the one introduced in the droplet size distribution. However, the model is not able to predict with sufficient accuracy the mass of droplets arriving to the wall and consequently the agglomerates generated by this interaction. In future works more studies can be developed re-calibrating the Fourier number, which will be valid for different formulations. However, it is important to remark that the residence time that the discrete phase spend as droplet in the best case is still below 1 s, which is by far much smaller than in other cases (fluidized bed [17] or granulator where the particles spend even hundreds of seconds in a bed of particles [18]) where this methodology has been applied. For including agglomeration into this approach, more detail models are still needed, which can focus on the following areas:

- The description of the elutriated particles. As it has been shown they play a significant role in the temperature distribution within the dryer and also in the moisture content of the air. The recirculation of them between the different discretizations of the reactors generating loops can increase significantly the computational time of the model and reduce the significant benefit of the current approach versus the CFD and subsequent data-driven approach.
- The generation of new models for the momentum description.
- The generation of new models for the distribution of the temperature and moisture in the air. These are the weakest models of this work. The models used have been re-fitted in the form of a power function but no improvement is obtained for the prediction of the relative distance at which the discrete phase arrives in the form of a droplet. In fact, in some cases a reduction is observed. See supplementary material for further details.

Table 6. Maximum relative height achieved by the droplets in the nozzle.

Experiment	Maximum distance covered by the droplets in the nozzle in terms of relative height, h/H_{nozzle}
A-HL-HF	0.656
A-HL-MF	0.758
A-HL-LF	0.761
A-ML-HF	0.451
A-ML-MF	0.473
A-ML-LF	0.438
A-LL-HF	0.306
A-LL-MF	0.275
A-LL-LF	0.256

3.2.5 CONCLUSIONS

In this chapter the heat and mass transfer mechanisms between the particles and the air as well as between the phenomenological regions have been addressed. The resultant model has been evaluated with experiments with different formulations (different density, particle size distribution), type of nozzles (different angle and velocity of the particles in the hollow cone formed by the nozzle), airflow temperatures and mass-flows and ratios between the amount of particles and air. The model has an average error below 8 K at the entrance and exit of all the phenomenological regions, which is lower than the one of the experimental measurement, 10 K. The model is also validated with the moisture content distribution of the particles, which is similar to the one determined by CFD, and the amount of elutriated particles generated, which is also similar.

The possible sources of error are also evaluated. The elutriated particles play a high significant role, being possible to reduce the accuracy of the temperature up to 20 K when the cut-diameter is selected to be the one that corresponds to 66% of the mass of elutriates from CFD instead of the maximum one obtained. In the case that the cut is not included, bigger diameters than the one obtained in the CFD model are determined by the compartment model. The second source of error identified is at low Reynolds numbers. When the air introduced in the dryer has the low Reynolds numbers within the operating space the accuracy in the prediction of the temperature at the entrance and exit of the regions shows a decrease in the accuracy. This fact it can be due to the stability of the airflow. As demonstrated in previous chapters, out of the fully developed turbulent regime ($Re=10^5$) the swirl pattern starts to be highly unstable. This instability increases when the Reynolds number is lower affecting significantly the momentum of the particles since the system is in two-way coupling. Even though the models for the compartment has been constructed using reduced models that show good accuracy in the falling region and they are robust enough since the operating space is covered, the stability of the flow can show significant oscillations that cannot be predicted without reproducing the complete swirl pattern either by solving Navier-Stokes equations or by reconstructions methods. It can be seen in Chapter 2.2 that even the widely and robust equation used to describe the decrease of the swirl intensity in a pipe shows oscillations of up to 20% of the stable in determining the swirl intensity from the CFD model for Reynolds below $1x10^5$.

To avoid these errors if further accuracy is desired, the alternative to be considered is the use of data-driven compartment models based on CFD. This models have been more suggested in [19] for systems govered by fluids. However, they will require to be run for every new operating conditions. Apart from the use of data-driven model, the model can be also improved in future works. Other open topics that can improve the model are the use of stochastic functions that allow the introduction of dispersion since with the current single droplet dying model the characteristic equivalent reactor network cannot be used. The introduction of the stochastic functions can improve the prediction of the moisture content of the smaller particles since now they are fully dried and some of them could have low residence times increasing the final average moisture content per bin. The last area in which the current model can be further developed is for the inclusion of

agglomeration. The agglomeration and breakage mechanisms developed in Chapter 2.6 needs to be re-adapted before the integration into the current model. In this work the temperature before the nozzle is accurately predicted but the distribution within the nozzle cannot be accurately captured. Small changes on the elutriated particles as well as the distance covered by them in the nozzle and the distribution of temperature and moisture within the nozzle regions can play a significant impact. These models can need to be improved but even with that the prediction of the mass of droplets that arrive as droplets to the wall is still challenging since the discrete phase only remains as droplet up to 0.7 s in the easiest case to be captured, which is by far much brief than other units where systematic compartment models have been used for modeling agglomeration [17, 18].

NOMENCLATURE

d_{bin}	Characteristic diameter of the bin (m).
d_{mean}	Mean diameter of the Rosin-Rammler distribution (m).
D	Diffusion coefficient of the detergent powder (m^2/s).
D_o	Parameter used for determining the diffusion coefficient of the detergent.
F_{bin}	Mass of particles per bin (kg).
$h_{local\ nozzle}$	Axial distance from the nozzle (m).
H	Enthalpy (J/s).
$H_{total\ nozzle}$	Total height of the nozzle (m).
m_p	Mass o single particle (kg).
n	Spread parameter of the Rosin-Rammler distribution.
N_{bins}	Number of bins defined for reproducing the particle size distribution.
N_p	Number of particles per bin.
$N_{recycles}$	Number of loops in the model.
Nu	Nusselt number.
P_w^o	Saturation pressure of water.
Pr	Prandtl number.
q_{drying}	Drying enthalpy (J/s).
q_{loss}	Heat losses (J/s).
r_{local}	Radial distance of the nozzle sheet (m).
Re	Reynolds number of the air in the dryer.
Re_p	Reynolds number of the particle used for reproducing the residence time.
$Re_{p\ drying}$	Reynolds number of the particle used for drying.
S	Swirl intensity.
Sc	Schmidt number.
Sh	Sherwood number.
St	Stokes number.
T_{air}	Temperature of the air (K).
T_{atm}	Ambient temperature (K).
T_{centre}	Temperature of the air in a central region (K).
T_{wall}	Temperature of the air in the region near to the wall (K).
T_p	Temperature of the powder (K).
U	Heat transfer coefficient (W/m^2K).
$V_{cum\ bin}$	Cumulative volume of particles per bin (m^3).

V_{bin}	Volume of particles per bin (m^3).
V_p	Volume of a single particle (m^3).
w_{water}	Moisture content of water (kg_{water}/kg_{air}).
α_{inj}	Angle of the nozzle.
ρ_p	Density of the particles (kg/m^3).

REFERENCES

[1] Langrish, T.A.G. (2009) Multi-scale mathematical modelling of spray dryers. J. of Food Engineering. Vol. 93 (2), 218-228.

[2] Keey, R.B. (1978) Introduction to Industrial Drying Operations. Pergamon, Oxford, pp. 15-99.

[3] Strumillo, C. Kudra, T. (1986) Drying: Principles, Application and Design, Gordon and Breach, New York, pp. 45-54.

[4] Ozmen, L. Langrish, T.A.G. (2002) Comparison of glass transition temperature and sticky-point temperature for skim milk powder. Drying Technology, 20 (6), 1177-1192.

[5] Zbicinski, I. (1995) Development and experimental verification of momentum, heat and mass transfer model in spray drying. The Chemical and the Biochemical Engineering Journal, 58, 2, 123-133.

[6] Truong, V. Bhandari, B.R. Howes, T. (2005) Optimization of co-current spray drying process of sugar-rich foods. Part I – Moisture and glass transition temperature profile during drying. Journal of Food Engineering, Vol. 71, 1, 55-65.

[7] Chiou, D. Langrish, T.A.G. Braham, R. (2008) Partial Crystallization Behaviour during Spray Drying: Simulations and Experiments. Drying Technology, 26, pp. 27-38.

[8] Bassani, A. Rossi, F. Fiorentini, C. Garrido, G.D. Reklaitis, G.V.R. Bonadies, Spigno, G. (2020) Model of Spray-Drying for Encapsulation of Natural Extracts. 30th Symposium on Computer Aided Process Engineering.

[9] Pinto, M. Kemp, I. Bermingham, S. Hartwig, T. Bisten, A. (2014) Development of an axisymmetric population balance model for spray drying and validation against experimental data and CFD simulations. Chemical Engineering Research and Design, Vol. 92, 4, 619-634.

[10] Bezzo, F. Macchietto, S. 2004b, A general methodology for hybrid multizonal-cfd models: Part II. Automatic zoning. Comp. Chem. Eng. 23 (4), 513-525.

[11] Ali, M. Mahmud, T. Heggs, P.J. Ghadiri, M. Djurdjevic, D. Ahmadian, H. Martín de Juan, L. Amador, C. Bayly, A. (2014) A one-dimensional plug-flow model of a counter-current spray drying tower. Chemical Engineering Research and Design, 92, 5, 826-841.

[12] Ali, M. Mahmud, T. Heggs, P.J. Ghadiri, M. (2020) Zonal modelling of a counter-current spray drying tower. Chemical Engineering Research and Design, 155, 180-199.

[13] Yang, S. Kiang, S. Farzan, P. Ierapetritou, M.G., 2019, Optimization of Reaction Selectivity using CFD-Based Compartmental Modeling and Surrogate-Based Optimization. Processes, 7(1), 9.

[14] Woo, M.W. Daud, W.R.W. Mujumdar, A.S. Taib, M.Z.M. Hua,W.Z. Tasirin, S.M. (2008) Comparative study of droplet drying models for CFD modeling. Chemical Engineering Research and Design, Vol. 86, 9, 1038-1048.

[15] Francia, V. (2015) Spray drying of detergents in counter-current towers: a study of turbulent swirling flows, fouling and agglomeration. Eng. D. Thesis. University of Birmingham.

[16] Gao, Y. Muzzio, F.J. Ierapetritou, M.G. (2012) A review of the Residence Time Distribution (RTD) applications in solid unit operations. Powder Technology, 228, 416-423.

[17] Li, J. Freireich, B. Wassgren, C. Litster, J.D. (2011) A general compartment-based population balance model for particle coating and layered granulation. AIChE Journal, 58,5, 1397-1408.

[18] Peglow, M. Kumar, J. Heinrich, S. Warnecke, G. Tsotsas, E. Mörl, L. Wolf, B. (2007) A generic population balance model for simultaneous agglomeration and drying in fluidized beds. Chemical Engineering Science, 62,1-2,513-532.

[19] Jourdan, N. Neveux, T. Potier, O. Kanniche, M. Wicks, J. Nopens, I. Rehman, U. Le Moullec, Y. (2019) Compartmental Modelling in Chemical Engineering: A critical review. Chemical Engineering Science, 210, 115196.

PART B. OPTIMIZATION OF PROCESSES INVOLING FORMULATED PRODUCTS.

BIOPROCESSING OF WASTES TO VALUE-ADDED PRODUCTS.

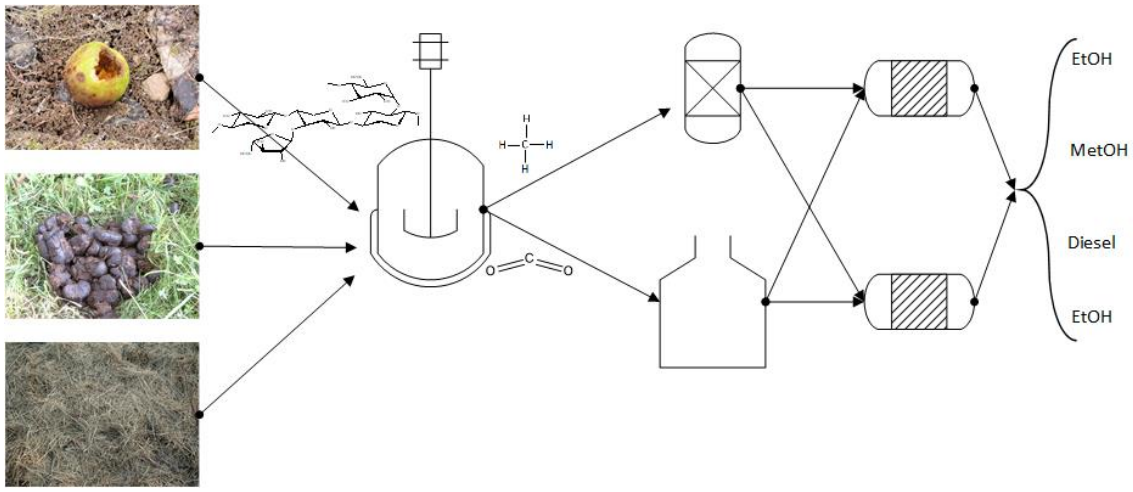

PART B. INTRODUCTION TO THE PROCESSING OF ORGANIC WASTES.

B.1 INTRODUCTION

The use of fossil fuels represents the primary energy source nowadays with a contribution around 80% in the energy consumption [1]. These resources are limited and they also have negative effects such as the emission of harmful gases (e.g. nitrogen and sulfur oxides, CO and CO_2). The emissions of some gases like NOx and SO_2 are limited in some countries [2]. However, the emissions of CO_2 are not. They have only been regulated by the implementation of carbon taxes [3]. Despite these penalties, CO_2 is the major greenhouse gas emitted by human activities representing 82% of the total greenhouse gas emissions in 2015 [4]. Its concentration in the atmosphere has increased from 317 ppm to 400 ppm in the last century [5]. The continuous increase in the concentration of CO_2 promotes the accumulation of heat in the atmosphere and it is responsible for the climate change. This climate change contributes to generate respiratory diseases, environmental problems (increase of wildfires, extreme weather or food supply disruptions) and the reduction of the animal species [6]. Because of these undesired effects, the reduction of CO_2 emissions has become a major issue for most of the countries [7]. Different alternatives have been proposed in the reduction and mitigation of CO_2 such as the use of renewable energies [8], its storage [9], its use in other industries (e.g. beverage [10], chemical [11-13]) or the design of more sustainable production processes [11]. One of the alternatives proposed for designing more sustainable production processes is based on the use of bioresources dedicated to the production of energy or chemicals. The use of bioresources presents an indirect way of using the solar energy and carbon without the need of extracting fossil fuels [14, 15].

The facilities dedicated to the transformation of bioresources into energy, chemicals or food have been named biorefineries [16, 17]. These biorefineries are classified in the following groups depending on the feedstock [18-20]:

- 1st generation biorefineries use edible and agricultural crops such as sugar sources, vegetable oils or cereals. Two examples can be found in biorefineries based on the fermentation of sugars or the ones dedicated to the production of biodiesel from vegetable oil. Even though the processing of some of these resources has advantages (e.g. easy fermentation of sugars [18]), the use of this type of resources for biorefineries competes with the food market. This food market has to be covered first for the population and it can be even more profitable. To avoid these ethical and economic issues, the use of alternative resources has been encouraged promoting the following types of biorefineries.
- 2nd generation biorefineries use the by-products obtained from the harvesting of agricultural or wood resources (e.g. wood residues, waste cooking oil). The use of these by-products, which are

mainly lignocellulose based, allows improving the profitability of the processing facilities by process integration. The residues can be used to produce energy used in the process or they can be also used to produce the desired products. Some of the processes used in this type of biorefineries are the fermentation of hydrolyzed cellulose, the gasification of cellulose or the anaerobic digestion of wastes [20].

- 3rd generation biorefineries are based on the use of microalgae as feedstock. This type of feedstock is interesting due to the fast growing rate and the low cost in the cultivation. However, they are difficult to control and they also require high consumption in the drying and component extraction. The improvement of the yield and the stability in the growing algae are still a challenge where genetic modification can propose promising alternatives [19].
- 4th generation biorefineries combine the use of algae and CO_2 for intensifying the capture of it by metabolic engineering. This type of biorefineries are still in development and there are no facilities operating nowadays [19].

From the previous types of biorefineries, the most common ones correspond to the 1st and 2nd generation. In particular, the second ones have received special attention in the last years. They do not only produce power or chemicals from a renewable source, but they can also be used to treat organic wastes as part of a circular economy [21-23]. The treatment of these organic wastes is not only mandatory in most of the countries [24, 25], but it is also an opportunity in many cases because the large amount that they suppose (approximately 0.5 t/year*person in Europe [26]). In order to treat these wastes, different technologies are available. In the following section B.2, a summary of those technologies is presented.

B.2 WASTE TREATMENT METHODS

For years, the most recurrent technology used for treating the wastes was incineration for the production of heat and power. However, in the last years other thermochemical and biochemical methods that allow generating other chemical compounds have been also taken into account. The different technologies that can be used are summarized in Figure 1. Each of them are described with more detail in the following sections. [18, 27].

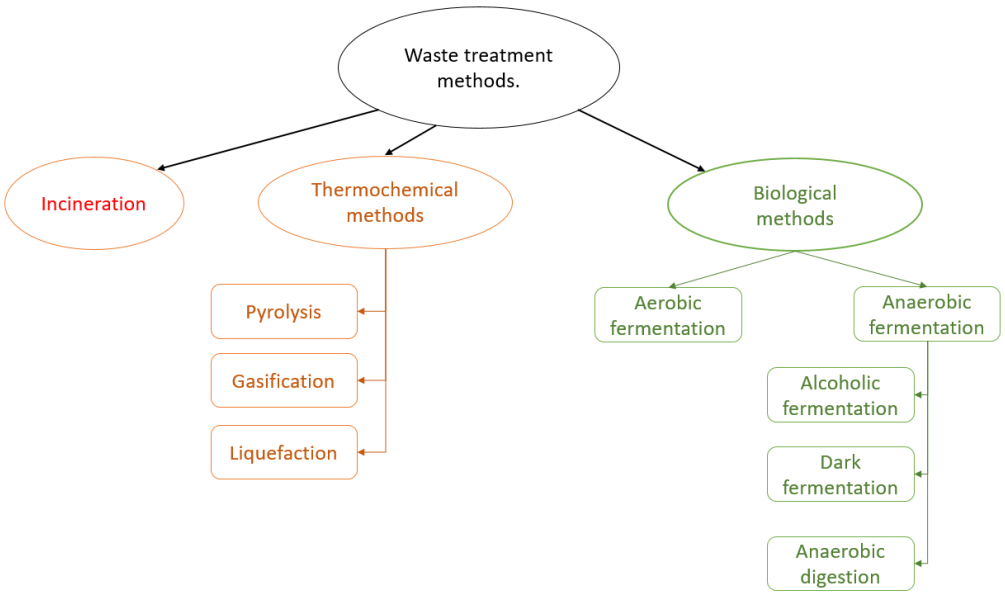

Figure 1. Possible treatment methods for wastes.

B.2.1 Thermochemical methods.

Thermochemical methods are based on the use of heat and/or catalysts for the transformation of different types of biomass into power or chemicals. Most of the technologies used in these transformations have been developed for years in the carbon industry and they are stablished at industrial scale. These thermochemical methods can be classified in two groups. One the one hand, it is possible to find the ones dedicated to the production of power, mainly covered by combustion. On the other hand, there are technologies that allow the production of chemical compounds such as pyrolysis, gasification and liquefaction. The current thesis mainly focuses on the production of chemicals from the treatment of waste resources. Thus, the following sub-chapters focus on providing a brief description of pyrolysis, liquefaction and gasification technologies [27].

Pyrolysis.

Pyrolysis, used for the decomposition of the biomass, takes place at high temperatures and in absence of oxygen. Under these operating conditions, the structure of the polymers is broken generating several products such as charcoal, biocrude, tars or gases (methane, hydrogen, CO, CO_2). The favored products and their generation ratios are dependent on the operating conditions of the reactor. Lower temperatures and longer residence times favor the conversion to charcoal. Higher temperatures and longer residence times increase the conversion to gas products and high temperatures with short residence times favor the production of liquid products. Different types of pyrolysis processes can be used in the processing of biomass [27]:

- Slow pyrolysis process has been traditionally used for making charcoal. The process is carried out at low heating rates (typical temperatures are below 700 K) and long residence times (in the order of days).
- Fast pyrolysis uses high operating temperatures (850 K and 1250 K) producing liquid and gas products. However, this process is far to be ideal. It has the cons of the large content of water simultaneously produced (approximately 20%), the low heating value of the products or their high oxygen content. The high proportion of oxygenated compounds reduces the value of the final product [27]. In order to solve this problem, different methodologies have been adopted. On the one hand, fast pyrolysis process has been intensified by integrating it with hydroconversion. The resultant hydropyrolysis process allows the direct production of transportation fuels. On the other hand, the bio-oil produced can be upgraded by treating it with a combination of steam reforming and hydrocracking. Techno-economic studies have evaluated this process, estimating a production cost between $2 and $3 per gallon. [28].
- Between the temperatures of 700 K to 850 K intermediate pyrolysis takes place. This process typically use low residence times, focusing in the production of condensable products.

Liquefaction

As presented in the previous section, one of the alternatives to reduce the presence of oxygenated compounds in pyrolysis is the integration with hydrothermal conversion. Hydrothermal treatment is based on the processing of biomass in water slurries. The typical hydrothermal processing conditions range from 523 K to 647 K and between 4 and 22 MPa. Under these conditions direct liquefaction takes place since the water is still in liquid phase and the high temperature allows the decomposition of the polymeric chains of the biomass. Apart from the use of water, other solvents have also been studied to improve the process proficiency. On the one hand, the use of alkali compounds have showed to catalyze the condensation reaction favoring the production of aromatic compounds [28]. On the other hand, solvents based on polar compounds have substituted the water leading to higher rates since they favor the solubility of biomass [18].

Gasification

In this treatment method the carbon of a dried biomass is converted into a gaseous fuel by entering in contact with a controlled amount of oxygen and/or steam. This process takes place between 1050 K and 1300 K under different gasifying mediums such as air, oxygen or steam. The reactions that occur during the process are: the partial oxidation of carbon, Eq. (1), the water gas shift reactions of carbon (Eq. (2)) and CO (Eq. (3)), the Boudouard equilibrium (Eq. (4)), the methanation reaction (Eq. (5)) and the steam reforming of methane (Eq. (6)) [29].

$$C + \frac{1}{2}O_2 \rightarrow CO \quad (1)$$

$$C + H_2O \leftrightarrows CO + H_2 \quad (2)$$

$$CO + H_2O \leftrightarrows CO_2 + H_2 \quad (3)$$

$$C + CO_2 \leftrightarrows 2CO \quad (4)$$

$$C + 2H_2 \leftrightarrows CH_4 \quad (5)$$

$$CH_4 + H_2O \leftrightarrows CO + 3H_2 \quad (6)$$

The resultant product of this gasification is mainly composed by CO_2, CO, CH_4, H_2 and traces of other gaseous hydrocarbons. These gases can be burned in gas turbines for the production of power or they can be applied for the production of chemicals. In the second case, the composition of the raw syngas is tuned up to obtain the syngas with the desired composition of hydrogen and CO. The final syngas is used in the synthesis of different products such as methanol, ethanol, dimethyl ether, Fischer-Tropsch fuels or synthetic natural gas. Apart from the gases, char and tars are also generated as by-products from the gasification. The tars are not desired in the gasification since they can generate corrosion and blockage in the equipment. However, the char can be used as a domestic fuel or it can be also transformed into fertilizers or activated carbon [30].

B.2.2 Biological methods

The transformation of biomass is not exclusively limited to the use of thermochemical methods. Biological methods, can also be used. In this area, fermentation has shown to be the most recurrent method in the treatment of bioresources. In this process, microorganisms act under certain operating conditions producing relevant biocompounds such as fuels (ethanol, butanol, etc.), biopolymers (polyols, poly-3-hydroxybutyrate) or beverages (beer, wine) [18, 31]. The microorganisms are very sensitive to the operating conditions being not able to process some of the raw materials (e.g. cellulose). In these cases, pretreatment methods such are required before fermentation. A common example is the use of hydrolysis, which is based on breaking the long chains of biomass molecules into simpler components like sugars or fatty acids. This rupture is promoted by the use of acids, bases or enzymes [32]. Furthermore, the characteristics of the microorganisms also have a significant impact on the treatment method. Depending on the oxygen accepted by the microorganisms, the biological processes can be classified in aerobic and anaerobic. In subsection B.2.2. 1 aerobic fermentation is presented and in subsection B.2.2.2, the two most popular anaerobic methods, anaerobic digestion and dark fermentation, are presented.

B.2.2.1 Aerobic Fermentation

Aerobic fermentation is a process where the microorganisms in presence of oxygen transform starches or sugars into several products such as alcohols, biopolymers, organic acids or antibiotics. The supply of oxygen to the microorganisms supposes one of the limiting factors in the process because of the low solubility in aqueous medium. The oxygen requirements represent high energy consumptions by either

agitation or aeration, limiting the use of this type of microorganisms in the processing of low valuable products. [31, 33].

B.2.2.2 Anaerobic Fermentation

In anaerobic fermentation, the microorganisms do not require oxygen for growing and producing different value added products such as fuels, organic acids or biopolymers. Focusing on the processing of biomass for the production of chemicals, the three following processes attract most of the attention.

Alcoholic fermentation

This process is based on the transformation of sugars to alcoholic compounds such as ethanol and butanol. In some cases, the raw material is a cellulosic biomass that needs to be ground and hydrolyzed. Hydrolysis (acid or enzymatic) breaks the chains of carbohydrates into monosaccharides that can be processed in the fermentation. In the case of ethanol production, see Eq. (7), the fermentation typically takes place between 30ºC and 40ºC and yeasts such as *Saccharomyces cerevisiae* or *Saccharomyces bayanus* are used. The tolerance of the yeasts to ethanol limit the final concentration of the broth below 17% [34, 35]. Apart from ethanol, other components such as glycerol and organic acids (acetic, lactic) are also obtained. This product is then separated and purified by the sequential use of distillation, rectification and molecular sieves [36].

$$C_6H_{12}O_6 \rightarrow 2C_2H_6O + 2\,CO_2 \quad (7)$$

Anaerobic digestion

A second biochemical process that has attracted a lot of attention in the processing of wastes is anaerobic digestion. Despite this treatment has been mainly applied to wet wastes such as wastewater, animal slurries and manure; other dried feedstocks such as agricultural residues or grass dissolved in water have also been evaluated. These residues have different concentrations of volatile solids, carbon, oxygen and nitrogen that result in different yields to methane and digestate [37]. The steps for the generation of methane from the biomass fed are presented in Figure 2. The hydrolysis step decomposes the chains of carbohydrates, lipids and proteins in monomers such as sugars, fatty acids and amino-acids. Then, the acidogenesis step generates intermediate products that can be inorganic such as H_2, NH_4^+ or H_2S or organic such as alcohols or acids with long chain (propionic, butyric, etc.). The third stage is acetogenesis where the acids are decomposed to acetic acid, CO_2, and H_2. The fourth step is methanogenesis where the acetic acid, CO_2 and H_2 react to form methane and CO_2. This methanogenesis can occur following two paths: By acetotrophic methanogenesis, where methane is formed by the decomposition of acetic acid, Eq. (8); or by hydrotrophic methanogenesis, where methane can be generated by the reaction between CO_2 and H_2, Eq. (9) [38].

$$CH_3COOH \rightarrow CH_4 + CO_2 \quad (8)$$

$$CO_2 + H_2 \rightarrow CH_4 + H_2O \quad (9)$$

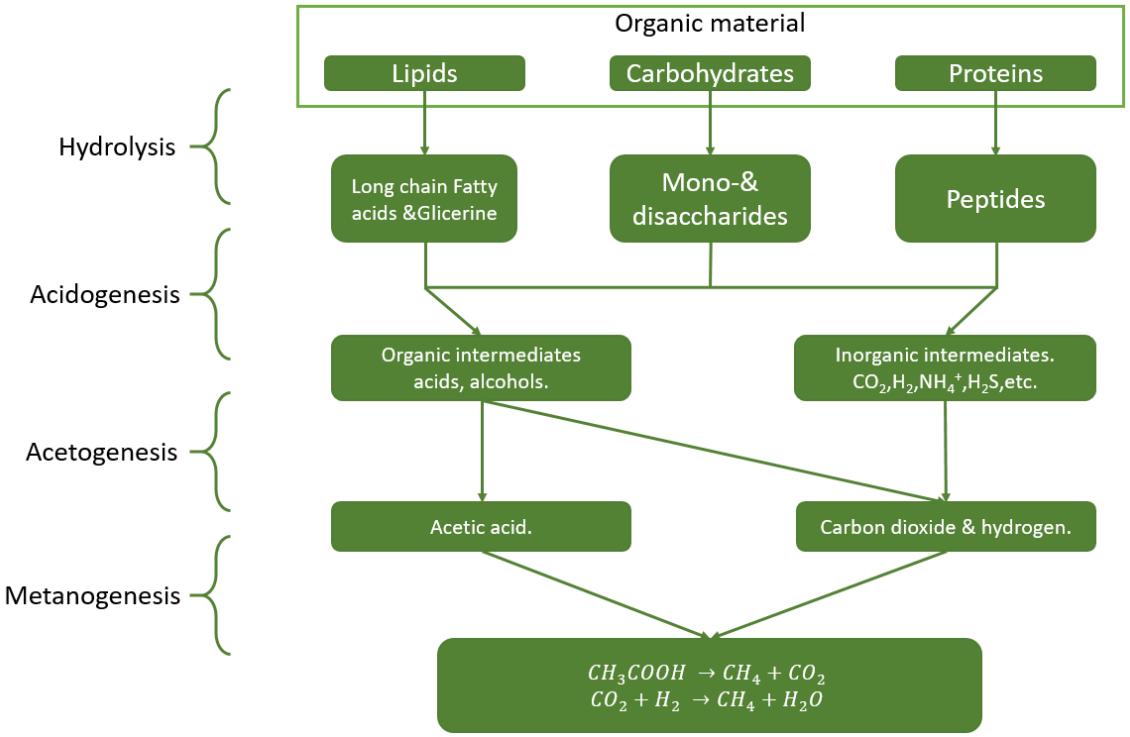

Figure 2. Steps in anaerobic digestion. Adapted from [38].

Apart from the composition, the yield in the anaerobic digestion process is also affected by the temperature. Three operating modes can be distinguished based on the temperature [37]:

- Psychrophilic conditions take place below a temperature of 20ºC. This operating mode is rarely found because of the large residence times are required, over 40 days.
- Mesophilic conditions between 30ºC and 50ºC (typically around 37ºC) have a high yield to methane and avoid de decomposition of nitrogen compounds that can be recovered as bio-fertilizers. Even though the residence time required in this mode is still high (in the order of days), it is the most used because of the high yields.
- Thermophilic conditions, between 50ºC and 70ºC, have a significant reduction of the residence time, until 1h at 70ºC. Thus, these thermophilic conditions allow achieving higher yields to methane for the same residence time, especially they show very good performance around 55ºC. However, these systems are very susceptible to variations in operating and environmental conditions as well as they are more likely to accumulate volatile fatty acids. As a result, the operating units of this type at large scale are scarce.

The treatment of wastes by anaerobic digestion results in two streams. On the one hand, the biogas stream that is generated following the steps presented in Figure 2. On the other hand, the digestate stream that is mainly composed by non-volatile organic and inorganic compounds (Nitrogen and phosphorous compounds). The biogas generated has been mainly used for the production of power, part of it to cover the production facility. The remaining biogas has been traditionally upgraded for its injection into the natural gas

network [37, 39]. Apart from this use, other studies has alternatively propose the production of syngas via dry reforming [40]. The other product, digestate, has been mainly used as fertilizer. The use has been done by a direct application of the recovered digestate or by the production of a concentrated form [41]. The processing for generation of concentrate forms is recommended since the direct application can be limited due to chemical and microbiological hazards [42].

Dark fermentation

A more immature technology is dark fermentation. This technology has been applied for treating a large number of organic components and mixtures such as sugars (glucose, xylose [43], lactose [44]), food waste, sludge or manure [45, 46]. Dark fermentation has received a lot of attention because of the generation of a high valuable product, hydrogen. However, it has the inconvenience of the very low yield achieved. This low yield and the difficulties in controlling the process have limited its use in large scale systems. In particular, the pH level, which is reduced by the generation of protons, can deactivate the microorganisms. The production of acids as well as the main product, hydrogen, is presented for glucose from Eq. (10) to (12). Eq. (10) and (11) present the decomposition of glucose for the generation of CO_2, H_2 and acids. Together with Eq. (10) and (11), the metabolic reaction presented in Eq. (12) is also required. In this reaction, glucose is consumed, resulting in pyruvate and nicotinamide adenine dinucleotide (NAD) [47].

$$C_6H_{12}O_6 + 2H_2O + H_2O \rightarrow 2\,CH_3COO^- + 2H^+ + 2CO_2 + 4\,H_2 \quad (10)$$

$$C_6H_{12}O_6 \rightarrow CH_3CH_2CH_2COO^- + H^+ + 2\,CO_2 + 2H_2 \quad (11)$$

$$C_6H_{12}O_6 + 2NADH \rightarrow 2\,CH_3CH_2COO^- + 2H_2O + 2\,NAD^+ \quad (12)$$

B.3 MODELING AND OPTIMIZATION OF PROCESSES FOR THE DESIGN OF WASTE TO VALUE-ADDED PRODUCTS. AIMS OF THIS PART

The use of mathematical modeling and optimization techniques applied to the processing of bioresources have been widely reviewed by several authors [48-51]. The studies have been applied from the detailed modeling of some waste treatment units [51] to the optimization at supply chain scale [49]. This part of the thesis focuses on the modeling and optimization of processes considering each of the units as a single entity. In this area, the use of process optimization techniques have mainly applied to the synthesis, design and integration of novel processes for biorefineries. The development of methodologies regarding the design have been widely covered by the group of Professor Gani [52, 53]. The steps that compose a generic methodology in the design of a biorefinery are presented in Figure 3 [52-54]. In the first stage, a conceptual analysis of the feedstocks available and the products that wants to be obtained is performed. In this literature analysis, the yields of the units and the stages that compose the process are defined. As a result from these analysis, it is possible to propose a superstructure in the second stage. The formulated superstructure addresses the mass and energy balances of every unit as well as reduced models that include the

efficiencies in each of the units. These efficiencies can be defined as non-linear models but in most of the cases they tend to be linear since there is also a large number of integer variables for the selection of the technologies. Once the technologies are selected, a more detailed modeling and optimization is performed. The units defined in the process are modelled with more detailed nonlinear models that describe the effect of the material properties and operating conditions on the unit efficiency. This optimization problem is highly non-linear and the optimal operating conditions in each unit can be optimized attending not only to economic criteria, but also to sustainability indexes. Once the process has been optimized, an improvement of it as well as other analysis regarding the optimal heat and water integration networks or the integration with other processes can be performed.

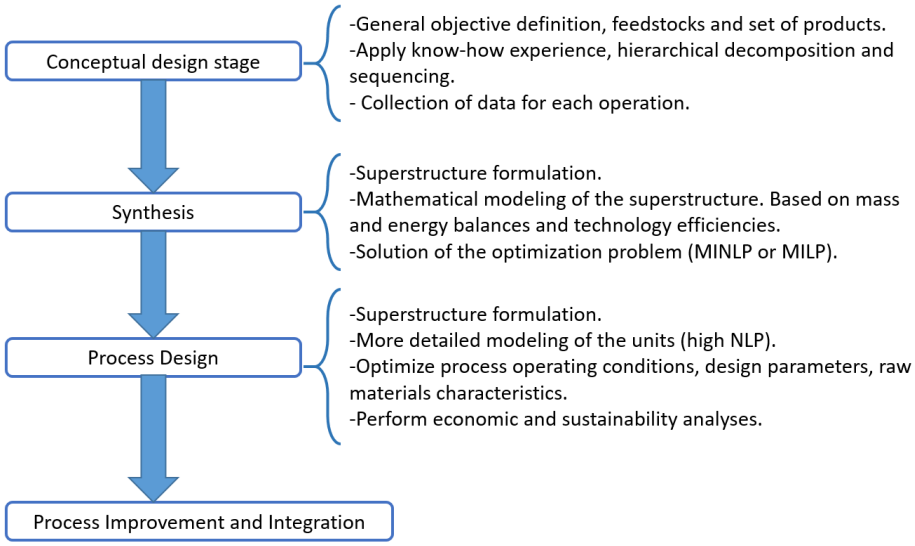

Figure 3. Stages in the design of processes for a biorefinery. Combination of [53] and [54].

As it can be seen in the general description of this methodology, 2 optimization problems (synthesis and process design) have to be solved in the definition of the process and another two optimization problems regarding the heat integration network and the integration of process are derived from it. In the current thesis, the studies are mainly focused on the development of process design problems. Each of the units of the processes are assumed as a single entity and they are modeled combining different types of the models presented in the introduction of the thesis. These models used for reproducing the influence of the operating conditions on the yield or consumptions in each unit are typically non-linear. Thus, the optimization studies addressed are formulated as non-linear programing problems (NLP). In particular, the optimization of the processes is applied for the production of fuels from wastes via biochemical methods. Despite these treatments have been showed to be less profitable [55], they are mandatory in the processing of some wastes [56] generating by-products that can be revalorized. The design of these revalorization processes is divided in the following three groups according to the type of problem and the treatment method used.

The first group of studies focuses on the optimization of anaerobic digestion and biogas uses for the production of fuels. The studies of this area are structured as follows.

- The first study is based on the modeling and optimization of the anaerobic digestion process using the digestate as fertilizer and the biogas for the production of power and syngas. The models addressed in this study are based on mass and energy balances and thermodynamic equilibriums. The formulation of the mass balances is done per components allowing to determine the optimal composition of the feedstock, which can be produced by a single raw material or by a blend of different materials.
- The second study focuses on the use of the biogas produced in the anaerobic digester. In this case, biogas is used for the production of Fischer-Tropsch fuels. The production of the fuels is carried out considering different reforming technologies (dual steam-dry reforming and tri-reforming) and two Fischer-Tropsch reactor modes (At low and high temperature). The total optimization problem is divided in two sub-problems depending on the reactor mode. Furthermore, another multi-parametric optimization study is performed to evaluate the role of oxygen on the operation of biogas tri-reforming for the production of syngas with different H_2:CO ratios.
- The third process optimization study evaluates the selection of different reforming technologies for the production of syngas. The technologies are evaluated under different CO_2 taxes. As a result, it is possible to determine the taxes at which a transition in the technology used is suggested. The study is performed using biogas and natural as raw materials, different H_2:CO ratios in the syngas and three reforming technologies: dual steam-dry, super dry and tri-reforming.

The second group focuses on the use of an alternative method to the treatment of wastes, dark fermentation. This method has been less studied than anaerobic digestion being necessary to develop a model for the process before addressing it into the optimization problem. In this context, a comparison of different kinetic models is provided in the work. These models are then addressed optimizing the production of two fuels: hydrogen and methanol.

The third area of these optimization studies presents a process integration problem towards self-sustainable production of chemicals/fuels. In the process optimization problem for an anaerobic digester it has been obtained that the economy of the process is highly governed by the digestate. This digestate can be directly applied in the agriculture or it can be processed [41]. On the one hand, the direct application in agriculture involves environment and safety hazards that can be relevant if the product harvested is used in the food market. On the other hand, the manufacture of the fertilizer can be more expensive than the direct application. The remanufacture implies the consumption of other resources (e.g. energy) that can generate other wastes and it is typically more expensive [57, 58]. Thus, it is suggested in later stages within zero waste and circular economy concepts, see Figure 4. Taking into account previous concerns, a direct controlled use of the digestate for improving the growth of algae is proposed before its later treatment. In

the production of biodiesel, alcohol is also needed for the transesterification of the oil extracted from the algae. This alcohol, methanol, can be produced from the biogas generated in the anaerobic digester. In order to determine the operating conditions involved in the integration of these processes, an optimization problem is formulated in that chapter.

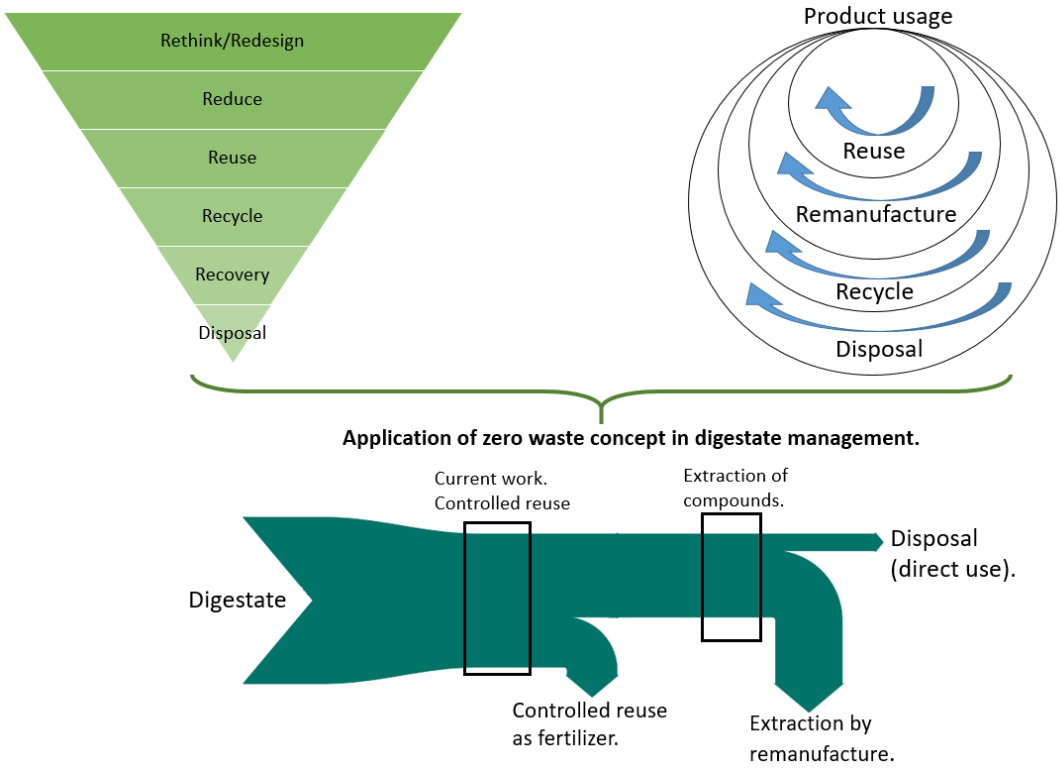

Figure 4. Zero waste concept [57], levels in the circular economy by demands of resources [58] and formulation for the digestate management, indicating where the current work is located.

REFERENCES

[1] International Energy Agency, (2020), Data and statistics. Total energy supply by source. World. Available in: https://www.iea.org/data-and-statistics?country=WORLD&fuel=Energy%20supply&indicator=Total%20primary%20energy%20supply%20(TPES)%20by%20source

[2] European Union, (2010), Directive 2010/75/EU of the European Parliament and of the Council of 24 November on industrial emissions (integrated pollution prevention and control. Available in: https://eur-lex.europa.eu/legal-content/en/TXT/?uri=CELEX:32010L0075

[3] Carbon Tax Centre, (2020), Where carbon is Taxed. Available in: https://www.carbontax.org/where-carbon-is-taxed/

[4] Environmental Protection Agency, (2018), Overview of greenhouse gases. Available in: https://www.epa.gov/ghgemissions/overview-greenhouse-gases

[5] CO2 Earth, (2020), NOAA Monthly CO2 Data. Available in: https://www.co2.earth/monthly-co2

[6] Nunez, C. (2019), Carbon dioxide levels are at a record high. Here's what you need to know. National geographic, Available in: https://www.nationalgeographic.com/environment/global-warming/greenhouse-gases/

[7] United Nations. (2015). The Paris Agreement. Available in: https://unfccc.int/process-and-meetings/the-paris-agreement/the-paris-agreement

[8] Leung, D.Y.C. Caramanna, G. Maroto-Valer, M.M. (2014) An overview of current status of carbon dioxide capture and storage technologies. Renewable and Sustainable Energy Reviews, 39, 426-443.

[9] Celia, M.A. Nordbottena, J.M. (2009) Practical modelling approaches for geological storage of carbon dioxide. Ground Water, 47, 627-638.

[10] Aresta, M. (2003) Carbon Dioxide Recovery and Utilization. Springer. ISBN: 798-90-481-6335-9.

[11] Davis, W. Martín, M. (2014) Optimal year-round operation for methane production from CO2 and water using wind and/or solar energy. Journal of Cleaner Production, 80, 252-261.

[12] Dooley, J.J. Davidson, C.L. Dahowski, R.T. (2009) An assessment of the commercial availability of carbon dioxide capture and storage technologies as of June 2009. Report for the US Department of Energy under a contract no. DE-AC05-T6RL01830, PNNL-18520.

[13] Sánchez, A. Gil, LM. Martín, M. (2019) Sustainable DMC production from CO2 and renewable ammonia and methanol. Journal of CO2 Utilization, 33, 521-531.

[14] Zhu, X-G. Long, S.P. Ort, D.R. (2008) What is the maximum efficiency with which photosynthesis can convert solar energy into biomass. Current Opinion in Biotechnology, 19, 153-159.

[15] Gaurav, N. Sivasankari, S. Kiran, G.S. Ninawe, A. Selvin, J. (2017) Utilization of bioresources for sustainable biofuels: A review. Renewable and Sustainable Energy Reviews, 73, 205-214.

[16] Kamm, B. Kamm, M. (2007) International biorefinery systems, Pure Appl. Chemistry, 79, 1983-1997.

[17] International Energy Agency (2009) Biorefineries: Adding value to the sustainable utilization of biomass. IEA Bioenergy, 1, 1-16.

[18] Cardona Alzate, C.A. Moncada Botero, J. Aristizábal Marulanda, V. (2019) Biorefineries. Design and Analysis. CRC Press. ISBN: 978-1-138-08002-7.

[19] Dutta, K. Daverey, A. Lin, J.G. (2014) Evolution retrospective for alternative fuels: First to fourth generation. Renewable Energy, 69, 114-122

[20] Escobar, J.C. Lora, E.S. Venturini, O.J. Yáñez, E.E. Castillo, E.F. Almazan, O. (2009) Biofuels: Environment, technology and food security. Renewable and Sustainable Energy Reviews, 13, 1275-1287.

[21] Nizami, A.S. Rehan, M. Waqas, M Naqvi, M. Ouda, O.K.M. Shahzad, K. Miandad, R. Khan, M.Z. Syamsiro, M. Ismail, I.M.I. Pant, D. (2017) Waste biorefineries: Enabling circular economies in developing countries. Bioresource Technology, 241, 1101-1117.

[22] Mohan, S.V. Nikhil, G.N. Chiranjeevi, P. Nagendranatha Reddy, C. Rohit, M.V. Naresh Kumar, A. Sarkar, O. (2016) Waste biorefinery models towards sustainable circular bioeconomy: Critical review and future perspectives. Bioresource Technology, 215, 2-12.

[23] Bhaskar, T. Pandey, A. Rene, E. Tsang, D.C.W. (2020) Waste Biorefinery. Integrating biorefineries for Waste Valorisation. 1st Edition. Elsevier. ISBN: 9780128182291

[24] European Union, (2018) European Directive 2018/851. Available in: https://eur-lex.europa.eu/legal-content/EN/TXT/?uri=CELEX:32018L0851

[25] European Union (1991) European Directive 91/271/EEC concerning urban waste-water treatment. Available in: https://ec.europa.eu/environment/water/water-urbanwaste/index_en.html

[26] Eurostat, Waste Statistics, (2017) ; Available in: https://ec.europa.eu/eurostat/statistics-explained/index.php?title=Waste_statistics (Accessed December 2019).

[27] Pandey, A. Bhaskar, T. Stöcker, M. Sukumaran, R.K. (2015) Recent advances in Thermochemical Conversion of Biomass. 1st Edition. Elsevier. ISBN: 978-0-444-63289-0.

[28] Brown, R.C. (2011) Thermochemical Processing of Biomass. Conversion into Fuels, Chemicals and Power. 1st Edition. John Wiley and Sons. ISBN: 978-0-470-72111-7.

[29] Sadhukhan, J. Ng, K.S. Martinez Hernández, E. (2014) Biorefineries and Chemical Processes. Design, Integration and Sustainability Analysis. John Wiley and Sons. ISBN: 978-1-119-99086-4.

[30] De Andrés, J.M. Roche, E. Narros, A. Rodríguez, M.E. (2016) Characterisation of tar from sewage sludge gasification. Influence of gasifying conditions: temperature, throughput, steam and use of primary catalysts. Fuel, 180, 116-126.

[31] Kreyenschulte, D. Emde, F. Regestein, L. Büchs, J. (2016) Computational minimization of the specific energy demand of large-scale aerobic fermentation processes based on small-scale data. Chemical Engineering Science, 153, 270-283.

[32] Binod, P. Janu, K.U. Sindhu, R. Pandey, A. (2011) Chapter 10. Hydrolysis of Lignocellulosic Biomass for Bioethanol Production. Biofuels. Alternative Feedstocks and Conversion Processes. ISBN: 978-0-12-385099-7.

[33] Cazzulo, J.J. de Cazzulo, B.M.F. Engel J.C. Cannata, J.J.B. (1985) End products and enzyme levels of aerobic glucose fermentation in trypanosomatids. Molecular and Biochemical Parasitology, 16,3, 329-343.

[34] Zoecklein, B. Fugelsang, K. Gump, B. Nury, F. (1999) Wine Analysis and Production. Springer US. ISBN: 978-1-4757-6967-8.

[35] Jacques, K.A. Lyons, T.P. Kelsall, D.R. (1995) The Alcohol Textbook. Nottingham University Press. 4th Edition. ISBN: 1-897676-13-1.

[36] Karuppiah, R. Pescles, A. Grossmann, I.E. Martín, M. Martinson, W. Zullo, L. (2008) Energy optimization for the design of corn-based ethanol plants. AIChE Journal, 54 (6), 1499-1525.

[37] Wellinger, A. Murphy, J. Baxter, D. (2013) The biogas handbook. Science, production and applications. Woodhead Publishing Limited. ISBN: 978-0-85709-498-8.

[38] Madsen, M. Holm-Nielsen,J.B. Esbensen, K.H. (2011) Monitoring of anaerobic digestion processes: A review perspective. Renewable and Sustainable Energy Reviews, 15 (6), 3141-3155.

[39] León, E. Martín, M. (2016) Optimal production of power in a combined cycle from manure based biogas. Energy Conversion and Management, 114, 89-99.

[40] Hernández, B. Martín, M. (2016) Optimal process operation for biogas reforming to methanol: effects of dry reforming and biogas composition. Industrial & Eng. Chem. Res. 55 (23), 6677-6685.

[41] Martín-Hernández, E. Sampat, A. Zavala, V.M. Martín, M. (2018) Optimal integrated facility for waste processing. Chemical Engineering Research and Design, 131, 160-182.

[42] Govasmark, E. Stäb, J. Holen, B. Hoornstra, D. Nesbakk, T. Salkinoja-Salonen, M. (2011) Chemical and microbiological hazards associated with recycling of anaerobic digested residue intended for agricultural use. Waste Management, 31, 12, 2577-2583.

[43] Ren, N. Cao, G. Wang, A. Lee, D. Guo, W. Zhu, Y. (2008) Dark fermentation of xyloxe and glucose mix using *Thermoanaerobacterium thermosaccharolyticum* W16. Int. J. Hydrogen Energy; 33 (21): 6124-6132.

[44] Calli, B. Schoenmaekers, K. Vanbroekhoven, K. Diels, L. (2008) Dark fermentative H2 production from xylose and lactose – Effects of on-line pH control. Int. J. Hydrogen Energy ; 33 (2): 522-530.

[45] Ntaikou, I. Antonopoulou, G. Lyberatos, G. (2010) Biohydrogen production from biomass and wastes via dark fermentation: A review. Waste Biomass Valorization; 1:21-39

[46] Guo, X.M. Trably, E. Latrille, E. Carrere, H. Steyer, J. (2010) Hydrogen production from agricultural waste by dark fermentation: A review. Int. J. Hydrogen Energy; 35: 10660-10673.

[47] Nandi, R. Sengupta, S. (1998) Microbial production of hydrogen: An overview. Critical reviews in microbiology; 24 (1): 61-84.

[48] Martín, M. Grossmann, I.E. (2016) Biomass as Source for Chemicals, Power and Fuels. Alternative Energy Sources and Technologies. Process Design and Operation. Springer International. ISBN: 978-3-319-28750-8.

[49] Ng,D.K.S. Tan, R.R. Foo, D.C.Y. El-Halwagi, M.M. (2016) Process Design Strategies for Biomass Conversion Systems. John Wiley & Sons. ISBN: 9781118699157.

[50] Sadhukhan, J. Ng, K.S. Martínez, E. (2014) Biorefineries and Chemical Processes. John Wiley & Sons. ISBN: 978-1-119-99086-4.

[51] Laurent, J. Samstag, R. Nopens, I. Wicks,J. (2020) CFD Modelling for Wastewater Treatment Processes. ISBN: 9781780409023.

[52] Cheali, P. Quaglia, A. Gargalo, C.L. Gernaey, K.V. Sin, G. Gani, R. (2016) Early-Stage Design and Analysis of Biorefinery Networks. Process Design Strategies for Biomass Conversion Systems. John Wiley & Sons. ISBN: 9781118699157.

[53] Bertran, M-O. Frauzem, R. Sanchez-Arcilla, A-S. Zhang, L. Woodley, J.M. Gani,R. (2017) A generic methodology for processing route synthesis and design based on superstructure optimization. Computers & Chemical Engineering, 106, 892-910.

[54] Aristizábal-Marulanda, V. Cardona Alzate, C.A. Martín, M. (2019) An integral methodological approach for biorefineries design: Study case of Colombian coffee cut-stems. Computers and Chemical Engineering, 126, 35-53.

[55] Martín, M. Grossmann, I.E. (2012) On the Systematic Synthesis of Sustainable Biorefineries. Industrial & Engineering Chemistry Research, 52, 3044-3064.

[56] European Parliament and Council (2010) Directive 2010/75/EU on industrial emissions (integrated pollution prevention and control). Available in: https://eur-lex.europa.eu/legal-content/ES/ALL/?uri=CELEX%3A32010L0075

[57] European Commision (2008) Directive 2008/98/EC. Available in: https://ec.europa.eu/environment/waste/framework/

[58] Korhonen, J. Honkasalo, A. Seppälä, J. (2018) Circular economy: The Concept and its Limitations. Ecological Economics, 143, 37-46.

CHAPTER 4.1. BIO-WASTE SELECTION AND BLENDING FOR THE OPTIMAL PRODUCTION OF POWER AND FUELS VIA ANAEROBIC DIGESTION.

ABSTRACT

This chapter presents a process optimization problem. The optimal waste or waste blend is determined for the production of chemicals, including DME, methanol, ethanol and FT fuels, and as drop-in fuel via biogas dry or hybrid reforming. Detailed models for biogas production and processing are used to compute the optimal mixture of biomass wastes among cattle and pig slurry, cattle and pig manure, sludge, urban food waste and urban green waste to be digested to obtain the required biogas. Even though the H_2 to CO ratio required by each chemical is different, the biogas composition suggested is similar, 50% methane, 47% CO_2. As a source of energy, 70% methane content is targeted. The optimal blend of biomasses is highly dependent on the price of the digestate, an important asset. Two approaches have been used to compute the cost of digestate obtaining different results. On the one hand, if the price is computed as the summation of each component, only sludge is suggested. On the other hand, the price of the digestate is computed determining how far the composition is from a commercial fertilizer. In this case, the biomass blend is suggested to have 65% of cattle slurry and 35% urban food waste.

4.1.1 INTRODUCTION

Biogas is a source of energy produced from wastes via anaerobic digestion. However, it can also be considered as a carbon source for chemicals. Its composition is mainly methane with a certain amount of carbon dioxide and other species in smaller quantities like H_2S or NH_3 [1, 2]. The composition of such a gas depends on the biomass sources and determines its further use [1, 3, 4]. In previous papers a power plant based on two different wastes was optimized evaluating various steam generation schemes [5]. For the electricity produced to be competitive, a credit from the digestate must be obtained. Later, Hernández and Martín [6] evaluated the possibility of using the biogas as a source for the production of methanol, taking into account that biogas already contains all the species required for dry reforming. The process consisted on producing syngas out of the biogas and with it, methanol was synthesized. Syngas and, in particular, biosyngas is the building block for a number of other chemicals such as dimethyl ether, DME [7], ethanol [8], FT fuels [9]. The difference is the H_2 to CO ratio required at the reactor, typically from 1, for the direct synthesis of DME and ethanol, to 2 in the case of methanol. We can produce such a syngas via dry reforming of biogas and, if necessary, by adding steam at different points of the process. Therefore, the goal is to select the waste or the mixture of wastes that produces the proper biogas for obtaining a syngas with the appropriate H_2 to CO ratio for further synthesis of various chemicals. In case the biogas is intended for power, the aim is the highest composition in methane. Typical wastes are manure and slurry from pigs and cattle, green and food wastes and wastewater treatment plants sludge, due to their wide availability. The problem involves process and product design simultaneously. Process design is related to the anaerobic digestion and the use of biogas for power or to produce chemicals via reforming. The products designed are the fertilizer obtained from the undigested biomass, with a composition suitable for selling it to the market, and the bio-syngas. Thus, the problem incorporates concepts of systematic process design and optimization for biogas processing to syngas and biomass blending for the proper biogas composition. The idea of biomass mixing is related to blending, that has been extensively studied in the literature from the design of polymer blends [10], refrigerant mixtures [11], and formulated products such as repellent lotions [12], detergents [13, 14] or surfactant design [15]. But above all, coal and crude blending have been the most studied cases in order to secure the appropriate composition in terms of sulphur content and combustion properties [16, 17]. Lately a linear approach has also been used to optimize the substrate blends in anaerobic co-digestion [18]. However, neither mixing is linear and nor are the operating stages to process the biogas. Furthermore, the production of biogas and digestate composition are also key for the profitability and environmental impact of the processing of wastes. Apart from blending, product design is sometimes related to the selection of components from a list. Computer aided molecular design includes not only the development of new molecules, but to select molecules out of the ones already available, and that problem is also related to the one at hand in the sense that we are selecting a biomass type [19-21].

Thus, in this work we determine the optimal waste type or mixture for the production of fuels and chemicals and the biogas composition used. We organize the paper as follows. In section 4.1.2 a brief description of the processes is presented. The section is divided into process design for biogas production from waste anaerobic digestion and

bio-syngas production from that biogas via dry reforming. The solution procedure is presented in section 4.1.3. In section 4.1.4 the results of the optimal operation of the facility are shown together with an economic evaluation. Finally, in section 4.1.5 we draw some conclusions.

4.1.2 MODELLING ISSUES

The process consists of four main stages. First a number of wastes are mixed and anaerobically digested to obtain raw biogas. This gas contains other species such as H_2S, NH_3 and CO_2. While CO_2 can be useful in further stages, the other species must be removed. Then, if the biogas is to be used as fuel, CO_2 can be removed or not, but else, no further processing is required after biogas clean-up. Otherwise, if we intend to use it as a source for chemicals, the presence of CO_2 is interesting as a source of carbon. Thus, we consider dry reforming of the mixture to produce raw syngas, a mixture of CO and H_2 with a small amount of CO_2. The production of different chemicals such as DME, ethanol, methanol or FT liquids requires a proper H_2 to CO ratio and, in some cases, certain amount of CO_2 [7-9]. Thus, a final step to adjust the composition is required before synthesis. Figure 1 shows the general scheme of the process. Therefore, the aim is to select the waste or a mixture of wastes that allows for the production of biogas as fuel and as a source for chemicals. We can consider this as a product design problem, since we aim at a proper composition of the syngas. Furthermore, for the process to be profitable we need to produce a digestate that must have an NPK index that complies with the minimum values established by norms and regulations in order to be sold as fertilizer. Basic models for units such as heat exchangers, compressors, stoichiometric reactors, splitters, etc are described in detail in [22]. Here we comment on the equations and only in some cases we present them for the sake of the length of the paper and we refer the reader to literature for further explanation.

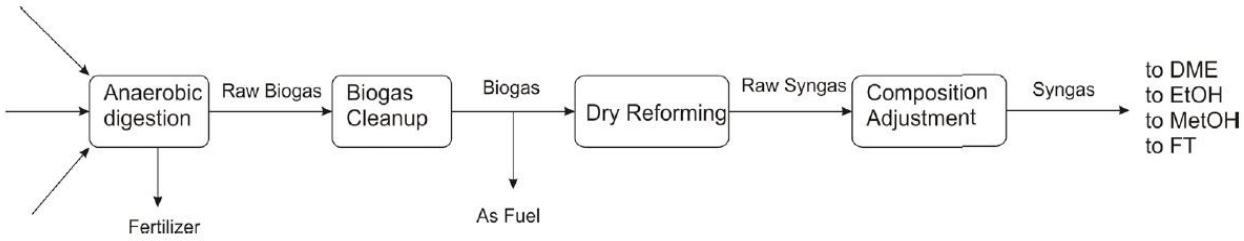

Figure 1. Scheme of biomass waste processing to fuels and chemicals.

4.1.2.1.-Waste blending

The use of different wastes to produce biogas is somehow a blending problem, similar to operations in food industry or other consumer goods production as well as gasoline manufacturing. The different wastes have different compositions that can lead to a variety of biogas compositions. The idea is to select the optimal waste or wastes blend to produce the appropriate biogas for certain applications. We must point out the fact that experimental validation of the anaerobic digestion of the suggested mixtures of biomass is required due to the differences in biomass structure and composition of the biomass samples that we mix. Although the mass balance holds, a number of experimental studies are available on co-digestion of substrates for adjusting the biogas yield (i.e. [23]).

The basic problem formulation is given by the biogas production model shown below and its further usage via dry reforming towards syngas with a proper H_2 to CO ratio.

4.1.2.2.-Biogas production

The anaerobic fermentation of biomass, wastes and other organic residues generates methane and carbon dioxide, biogas, through a series of reactions such as hydrolysis, acidogenesis, acetogenesis and methanogenesis [24]. The biogas produced shows a variable composition in methane and CO_2 depending on the composition of the biomass used and the operating conditions. The lower the temperature, the longer the retention time. We can operate below 20 ºC for 70 to 80 days under psychrophilic conditions, from 30 to 42ºC from 30 to 40 days under mesophilic conditions and finally from 43 to 55ºC under thermophilic conditions from 15 to 20 days. We select 55 ºC as the operating temperature for its highest yield to methane. A part from methane and CO_2, nitrogen, H_2S and NH_3 are produced [2]. Thus, in order to compute the biogas composition a mass balance is performed considering the composition of the different manure sources:

$$MW_{dry\text{-}biogas} = \sum_{a'} Y_{a'/biogas\text{-}dry} MW_{a'} \quad (1)$$

Where the typical composition, $Y_{i,}$ of the biogas is given by the following bounds:

$$0.7 \leq Y_{CH4} \leq 0.5$$

$$0.3 \leq Y_{CO2} \leq 0.5$$

$$0.02 \leq Y_{N2} \leq 0.06 \quad (2)$$

$$0.005 \leq Y_{O2} \leq 0.16$$

$$Y_{H2S} \leq 0.002$$

$$9 \cdot 10^{-5} \leq Y_{NH3} \leq 1 \cdot 10^{-4}$$

We assume that the gas leaving the reactor is saturated with water. Antoine correlation is used to determine the saturating pressure and specific humidity, Eq. (3). The flow of biogas is determined using Eq (4), while the accompanying water is computed using the specific moisture before. To compute the power in the compressor, we need to determine the molar mass of the biogas as in Eq. (5). The mass flow rate of each component is computed from its molecuar weight and the total flow rate, Eqs. (6) and (7).

$$y_{biogas} = \frac{MW_{H_2O}}{MW_{biogas\text{-}dry}} \frac{Pv(T)}{P\text{-}Pv(T)} \quad (3)$$

$$F_{biogas} = \rho_{biogas} \sum_{waste} w'_{SV/waste\_i} w_{MS/waste\_i} F_{waste\_i} \cdot V_{biogas/waste\_i} \quad (4)$$

$$fc(H_2O)_{biogas} = y_{biogas} \cdot \sum_{a'} fc(a')_{biogas} \quad (5)$$

$$fc_{(a',Bioreactor,Compres1)}/MW_{a'} = \frac{Y_{a'/biogas\text{-}dry}}{MW_{biogas\text{-}dry}}(F_{(Bioreactor,Compres1)} - fc_{(H_2O,Bioreactor,Compres1)}) \quad (6)$$

$$MW_{biogas}\sum_a \frac{x_{a/biogas}}{MW_a} = \sum_a x_{a/biogas} \quad (7)$$

Where the lower and upper limits for the potential generation of biogas is given by [24]:

$$0.20 \leq V_{biogas,waste} \leq 0.50;$$

$$0.10 \leq w_{MS,Waste} \leq 0.20; \quad (8)$$

$$0.50 \leq w_{VSB,Waste} \leq 0.80;$$

The rest of the waste constitutes the digestate whose composition is computed as follows [24]:

$$w'_{C/k} = R_{C\text{-}N/k}\left(w'_{Norg/k} + w'_{Nam/k}\right) \quad (9)$$

Where the typical composition of the waste is bounded as given in [25]. For the sake of simplicity we no longer use the subindex k for each waste type. All the following equations are applied to each waste.

$$6 \leq R_{C-N/Waste} \leq 20$$

$$0.005 \leq w_{N/Waste} \leq 0.047;$$

$$0.005 \leq w_{Norg/\,Waste} \leq 0.036;$$

$$0.008 \leq w_{P/\,Waste} \leq 0.013; \quad (10)$$

$$0.033 \leq w_{K/\,Waste} \leq 0.1;$$

$$w_{C/\,Waste} + w_{Norg/\,Waste} + w_{Nam/\,Waste} + w_{P/\,Waste} + w_{K/\,Waste} + w_{Rest/\,Waste} = 1 \quad (11)$$

The flow of each component leaving the reactor, either in the form of biogas or digestate is computed performing balances to carbon, to organic nitrogen (Norg), inorganic nitrogen (N), phosphate and potassium. The carbon either leaves in the form of CO_2 or CH_4 with the gas or as part of the waste in the digestate, Eq. (12). The organic nitrogen in the digestate is given by the fraction of organic nitrogen in the digestate minus the nitrogen releases as gas, Eq (13). Similarly, the inorganic nitrogen that is not used to produced ammonia that accompanies the gas or is left as residue computed using the values above, Eq. (14). P and K directly leave the reactor as part of the digestate, Eqs. (15)-(16). The rest that is not accounted for is assumed to be a residual part leaving the reactor with the digestate.

$$fc(C)_{digestate} = w'_{C/Waste} \cdot w_{MS/Waste} \cdot F_{Waste} - fc(CH_4)\frac{MW_C}{MW_{CH_4}} - fc(CO_2)\frac{MW_C}{MW_{CO_2}} \quad (12)$$

$$fc(Norg)_{digestate} = w'_{No/Waste} \cdot w_{MS/Waste} \cdot F_{Waste} - fc(N_2)\frac{MW_N}{MW_{N_2}} \quad (13)$$

$$fc(N)_{digestate} = w'_{N/Waste} \cdot w_{MS/Waste} \cdot F_{Waste} - fc(NH_3)\frac{MW_N}{MW_{NH_3}} \quad (14)$$

$$fc(P)_{digestate} = w'_{P/Waste} \cdot w_{MS/Waste} \cdot F_{Waste} \quad (15)$$

$$fc(K)_{digestate} = w'_{K/Waste} \cdot w_{MS/Waste} \cdot F_{Waste} \quad (16)$$

$$fc(Rest)_{digestate} = w'_{rest/Waste} \cdot w_{MS/Waste} \cdot F_{Waste} + fc(CH_4)_{biogas}\frac{4 \cdot MW_H}{MW_{CH_4}} - fc(CO_2)_{biogas}\frac{2 \cdot MW_O}{MW_{CO_2}} - fc(NH_3)_{biogas}\frac{3 \cdot MW_H}{MW_{NH_3}} - fc(H_2S)_{biogas} - fc(O_2)_{biogas} \quad (17)$$

$$fc(H_2O)_{digestate} = (1 - w_{MS/Waste}) \cdot F_{Waste} - fc(H_2O)_{biogas} \quad (18)$$

The energy balance to the digester is as follows:

$$Q_{digestor} = \Delta H_{reaction} - Fcp(T_{digestor} - T_{in})$$
$$\Delta H_{reaction} = \sum_{prod} \Delta H_{combus} - \sum_{reactants} \Delta H_{combus} \quad (19)$$

The digestate is further conditioned. To compute the evaporated water, the model is given by Eqs. (20) to (28):

We first compute the bubble point as in Eq. (20):

$$1 = K_{NH3}(T_{bubble}) \cdot x_N + K_{H2O}(T_{bubble}) \cdot x_{H2O}$$
$$Ki(T_{bubble}) = P_{sat}/P_T \quad (20)$$

The average temperature is computed as follows:

$$T_{m1} = \frac{T_{bubble} + T_{(HX2,Snk)}}{2} \quad (21)$$

With T_{m1}. and the following equation, we compute $R_{V/F}$

$$1 = y_{NH3} + y_{H2O} = \frac{x_N \cdot K_{NH3}(T_{m1})}{1 + R_{V/F} \cdot (K_{NH3}(T_{m1}) - 1)} + \frac{x_{H_2O} \cdot K_{H2O}(T_{m1})}{1 + R_{V/F} \cdot (K_{H2O}(T_{m1}) - 1)} \quad (22)$$

Next, we compute the bubble point with no ammonia

$$1=K_{H2O}(T'_{bubble})\frac{n_{H_2O}-n_{H_2O}\big|_{vapor}}{\sum_{i=1}^{n} n_i - n_{H_2O} - n_N} \qquad (23)$$
$$Ki(T'_{bubble})=P_{sat}/P_T$$

With that we compute the corresponding average temperature:

$$T_{m1}'=\frac{T_{bubble}'+T_{(HX2,Snk)}}{2} \qquad (24)$$

And

$$1=\frac{\left(\frac{n(Wa,Bio,HX2)-n_{H_2O}\big|_{vapor}}{n_{Total}-n(N,Bio,HX2)-n_{H_2O}\big|_{vapor}}\right)\cdot K_{H_2O}(T_{m1}')}{1+R_{V/F}'\cdot(K_{H_2O}(T_{m1}')-1)} \qquad (25)$$

Using the results above, we compute the mass and energy balances as follows:

$$\begin{aligned}
&fc_{(Wa,Snk6)}=fc(Wa)\big|_{vapor}+fc(Wa)\big|_{vapor'}\\
&fc(Wa)\big|_{vapor}=M(Wa)\cdot y(Wa)R_{V/F}\cdot n_{Total}\\
&fc(Wa)\big|_{vapor}=M(Wa)\cdot n_{H_2O}\big|_{vapor}\\
&fc(Wa)\big|_{vapor'}=M(Wa)\cdot R_{V/F}'\cdot(n_{Total}-n_N-n_{H_2O}\big|_{vapor})\\
&fc(Wa)\big|_{vapor'}=M(Wa)\cdot n_{H_2O}\big|_{vapor'}\\
&fc_{(Wa,Bio,HX2)}=fc_{(Wa,HX2,Snk6)}+fc_{(Wa,HX2,Snk7)}
\end{aligned} \qquad (26)$$

The ammonia that enters is generated out of the nitrogen:

$$fc_{(NH_3,HX2,Snk6)}=fc_{(N,HX2,Snk6)}\frac{M(NH_3)}{M(N)} \qquad (27)$$

The digestate is comprised of the water that is not evaporated and C, No, K , P and the mixture we defined as Rest

$$fc_{(i,Bio,HX2)}=fc_{(i,HX2,Snk7)} \qquad \forall i=\{C,No,K,P,Rest\} \qquad (28)$$

The energy balance accounts for the evaporation of water.

<u>H_2S removal. ZnO</u>

H_2S is removed using a reactive bed of Fe_2O_3 that operates at 25-50 ºC. The chemical reaction that takes place is the following [26].

$Fe_2O_3 + 3H_2S \rightarrow Fe_2S_3 + 3\,H_2O$

Thus, the model for this purification stage is written in accordance with the stoichiometry of this reaction by performing a mass balance. The bed can be regenerated using oxygen [26].

$2Fe_2S_3 + 3O_2 \rightarrow 2\,Fe_2O_3 + 6S$

Digestate composition

In order for the digestate to be accepted as fertilizer, it has to meet a certain composition defined by N, P and K indexes as below [24]:

$$K_{index} = \frac{fc(K)\dfrac{MW_{(K_2O)}}{2\cdot MW_{(K)}}}{fc(C)+fc(N)+fc(Wa)+fc(rest)+fc(K)\dfrac{MW_{(K_2O)}}{2\cdot MW_{(K)}}}\cdot 100$$

$$P_{index} = \frac{fc(P)\dfrac{MW_{(P_2O_5)}}{2\cdot MW_{(P)}}}{fc(C)+fc(N)+fc(Wa)+fc(rest)+fc(K)\dfrac{MW_{(K_2O)}}{2\cdot MW_{(K)}}+fc(P)\dfrac{MW_{(P_2O_5)}}{2\cdot MW_{(P)}}}\cdot 100$$

$$N_{index} = \frac{fc(N)}{fc(C)+fc(N)+fc(Wa)+fc(rest)+fc(K)\dfrac{MW_{(K_2O)}}{2\cdot MW_{(K)}}+fc(P)\dfrac{MW_{(P_2O_5)}}{2\cdot MW_{(P)}}}\cdot 100 \qquad (29)$$

$$K_{index}+N_{index}+P_{index} \geq 6$$

$$0 \leq \frac{n(C)}{n(N)} \leq 10$$

4.1.2.3.-Biogas for power production.

Once the biogas has been produced and cleaned, if we intend to use it as a fuel we can remove the CO_2 to reduce the unit size downstream. The removal of CO_2 is carried out using Zeolite 5A. Adsorbing beds of PSA systems operate at low temperatures (25 ºC) and moderate pressures (4.5 bar). Thus, the gas is compressed and cooled down.The compressor is modeled using a mass balance to determine the exiting flow, while the outlet temperature and pressure and the work involved are computed using Eqs. (30) and (31) where k =1.4 and the efficiency is assumed to be 0.85:

$$T_s = T_e + T_e\left(\left(\frac{P_s}{P_e}\right)^{\frac{k-1}{k}} - 1\right)\frac{1}{\eta_s} \qquad (30)$$

$$W(Compressor) = (F)\cdot\frac{8.314\cdot k\cdot(T)}{((MW)\cdot(k-1))}\frac{1}{\eta_c}\left(\left(\frac{P_{out}}{P_{in}}\right)^{\frac{k-1}{k}} - 1\right); \qquad (31)$$

The system is modelled as two beds in parallel, one operating and the second one in regeneration to allow for continuous operation of the plant. The removal efficiency is assumed to be 95% for CO_2 and 0% for any other species of the mixture [27, 28].

4.1.2.4.-Biogas reforming for chemicals production.

After biogas clean-up, see Figure 1, it is reformed to produce raw syngas. Part of the gas is needed to heat up the furnace since dry reforming is highly endothermic. The splittter is modeled using a mass balance where the split fraction determines the flow of biogas required to maintain an adiabatic operation in the reformer, see [22] for basic models for process synthesis. Since the first equilibrium depends on the pressure, see Eqs. (32)-(34), we use compressor 1 as polytropic, to adjust the pressure for the synthesis reaction. We use Eqs. (30)-(31) and a mass balance to model this unit. He1 is modeled using a mass and an energy balance.

The model of the methane reformer is based on the chemical equilibrium given by Eqs. (32) - (34):

$$CH_4+CO_2 \leftrightarrow 2CO+2H_2 \tag{32}$$

$$CH_4+H_2O \rightarrow CO+3H_2 \tag{33}$$

$$CO_{(g)}+H_2O_{(g)} \leftrightarrow CO_{2(g)}+H_{2(g)} \tag{34}$$

Only two of the equations are independent. Thus, the reformer is modeled using the equilibrium constants given in Eq. (35) to (37) [29, 30].

$$kp=e^{\left[31.447-\frac{29580}{T[K]}\right]}=\frac{P_{CO}\cdot P_{H_2}}{P_{CH_4}\cdot P_{CO_2}} \tag{35}$$

$$kp=10^{\left[-\frac{11650}{T[K]}+13.076\right]}=\frac{P_{CO}\cdot P_{H_2}^3}{P_{CH_4}\cdot P_{H_2O}} \tag{36}$$

$$kp=10^{\left[\frac{1910}{T[K]}-1.784\right]}=\frac{P_{CO_2}\cdot P_{H_2}}{P_{CO}\cdot P_{H_2O}} \tag{37}$$

Together with the atomic mass balance to C, H and O as per Eq. (38).

$$\begin{aligned} &n_{CH_4}+n_{CO_2}+n_{CO}\big|_{in}=n_{CH_4}+n_{CO}+n_{CO_2}\big|_{out} \\ &4\cdot n_{CH_4}+2\cdot n_{H_2O}\big|_{in}=4\cdot n_{CH_4}+2\cdot n_{H_2}+2\cdot n_{H_2O}\big|_{out} \\ &n_{H_2O}+2\cdot n_{CO_2}+n_{CO}\big|_{in}=n_{H_2O}+n_{CO}+2\cdot n_{CO_2}\big|_{out} \end{aligned} \tag{38}$$

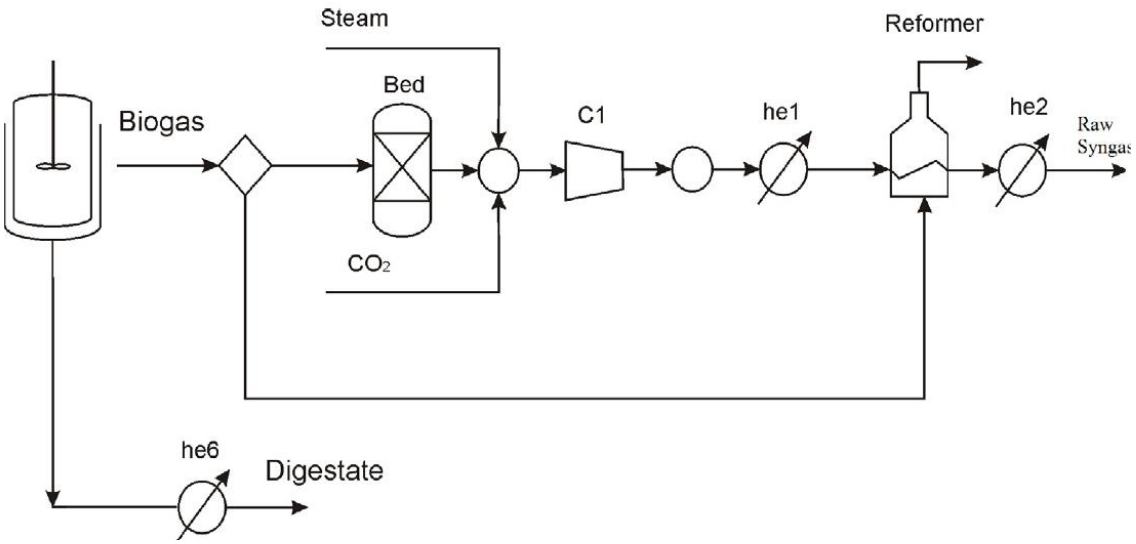

Figure 2. Biogas processing

The reforming reactions are endothermic. Thus, part of the biogas is used as fuel, diverted in splitter 1, see Figure 2, to provide for the energy required for the operation. The amount of natural gas burned is computed assuming that the energy required, $Q_{(\text{Methane reformer})}$, is provided as lower heating value (LHV) of the natural gas.

$$Q_{prod} = \sum_{i} fc_{(i,Reformer,Mix2)} \cdot (\Delta H_f + \int_{T_{ref}}^{T_{out}} CpdT) \tag{39}$$

$$Q_{reac} = \sum_{i=in} fc_{(i,Reformer,Mix2)} \cdot (\Delta H_f + \int_{T_{ref}}^{T_{in}} CpdT) \tag{40}$$

$$Q_{(\text{Methane reformer})} = \left(Q_{prod} - Q_{reac}\right); \tag{41}$$

$$fc_{(CH4,Spl3,Reformer)} \cdot LHV_{gas} = Q_{(\text{Methane reformer})} + Q_{(He1)}; \tag{42}$$

The gas coming out of the reformer is sent to the purification stage to remove hydrocarbon traces, see Figure 3. A PSA system that operates at 25 ºC and 4.5 bar using silica gel as adsorbent is used to remove the last traces of hydrocarbons and ammonia. For this unit, we compress the gas assuming polytropic behaviour, see Eqs. (30)-(31) for the model, and cool it down. Due to the low temperature, water condenses before the PSA adsorption beds and it is discharged. Antoine correlation is used to compute the specific moisture that the biogas can carry at 25ºC and 4.5 bar as in Eqs. (3) and (5) above. The heat exchanger is modelled using a mass balance and an energy balance considering the condensation of water.

The PSA system is modelled as two beds, one operating and the second one in regeneration to allow continuous operation of the plant. The pressure drop is assumed to be 10% of the operating pressure. We model the adsorbing bed as a component separator where an efficiency for the removal of hydrocarbon traces, NH_3 and H_2S is assumed to be 1.

Next, the biogas composition may need to be adjusted to a molar ratio of H_2:CO required by the product to be obtained, methanol, ethanol - DME, or FT fuels. Three alternatives are considered: water gas shift (WGS) reactor with a feed of steam, bypass and hybrid metal membrane and a PSA system with a bed of oxides for H_2 production. The split fraction depends on the performance of the reformer which may make this composition adjustment redundant. The hydrogen separation section consists of a compressor to reach 4.5 bar, a heat exchanger to cooldown the mixture to 25 ºC and a membrane-PSA system. Compressor and heat exchanger are modelled in previous instances while the membrane –PSA system is modelled as a component separator assuming that 100% of the hydrogen in the stream that is processed through this system can be recovered.

The WGS reactor is modelled based on an elementary balance to H, C and O and using Eq. (37) for computing the gas composition at the equilibrium. We may need to add steam to the reactor.

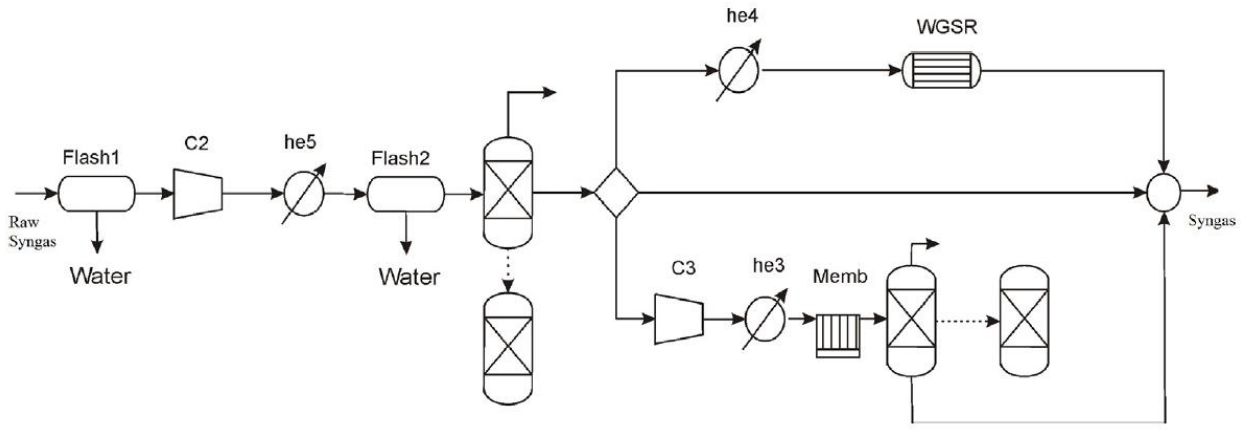

Figure 3. Syngas composition adjustment

Finally, the third section corresponds to the removal of sour gases, namely CO_2 . The operating conditions for this PSA system are 4.5 bar and 25 ºC. We assume 10% pressure drop in the bed and a system of two beds in parallel to secure continuous operation, see Figure 4. The units involved, compressors, heat exchanger and PSA systems are modelled as described above.

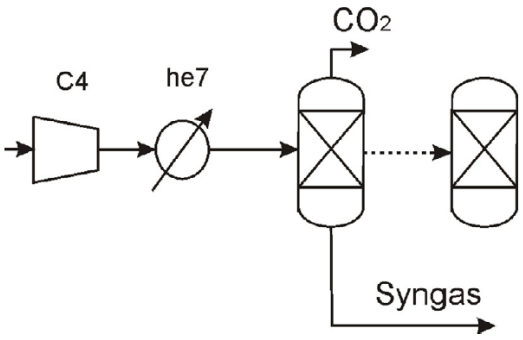

Figure 4. Sour gases removal.

4.1.3 SOLUTION PROCEDURE

The process consists of two sections, the production of biogas and its further processing to be used for synthesis. The first problem is to define the proper biogas required for each application, whether we aim at producing chemicals or fuels. The production of fuel aims at maximum methane production. Thus, there is only need to focus on the first section of the problem. Therefore, we split the problem in two for simplicity and clarity in the presentation of the results. P1 refers to the biogas processing into the syngas required by each application. This allows defining the proper biogas composition in terms of the proportion of methane and CO_2. P2 corresponds to the section of the facility dealing with the blending of wastes. This section of the facility produces fertilizers, with a composition that must be within market standards, and biogas, with the composition required for syngas production. Thus, The optimal biogas composition for the production of different chemicals is computed by solving problem (P1) consisting of an objective function given by Eq. (43):

$$Z=\left(fc\left(H2\right)\right)\cdot P_{H2} - P_{elec}\cdot \sum_{i\hat{I}compressors} W(Compressor)-P_{CH4}\cdot\left(fc\left(CH4\right)\right) -P_{Steam}\sum_{j\hat{I}HX} Q(HX) -P_{H2O}fc\left(H2O\right); \quad (43)$$

The model for the biogas processing stages given by Eqs. (30) to (40). The problem is an NLP with 770 variables and 678 equations. The analysis of the equations show bilinear terms in energy balances and equilibrium equations, exponentials, power and inverse functions leading to a non convex problem. However, in spite of the complexity, these equations allow representing the phenomena.

However, to obtain such a biogas, the aim is to determine the mixture of wastes that generates the required composition. (P2) consists of Eqs. (1-29) and the objective function in this case becomes:

$$Z=fc\left(CH4\right)-\sum_{i\hat{I}waste} Waste_i\cdot P_{Waste}+F\left(Fertilizer\right)\cdot Credit; \quad (44)$$

It corresponds to an NLP problem consisting of 311 variables and 178 equations. Similarly, bilinear terms, powers, exponential and inverse functions are part of the equations leading to a non convex problem.

The problems are written in GAMS® and solved with CONOPT using a multi-start approach. Thus, the solution expected is a local optimum. However, the solutions reported correspond to the best of the local solutions found and therefore, in spite of being local, it is not the first solution found bear in mind that we could have integrated both problems into a single NLP mathematical formulation. However, the fuels production does not need further biogas composition adjustment.

4.1.4 RESULTS

4.1.4.1.-Optimal biogas composition

We optimize the dry reforming of biogas for the production of different chemicals such as DME, ethanol, methanol, FT fuels and as a fuel. While the use of biogas as fuel targets maximun methane content, its use for chemicals production needs to target the H_2 to CO ratio needed for the synthesis stage. Thus, for biogas as a source of power we optimized (P2) subject to Eqs. (1)-(29). Otherwise, for chemicals production, the proper biogas composition actually comes from optimizing (P1) subject to Eqs. (30)-(40) where the proper H_2 to CO ratio for each chemical is imposed as a constraint in the formulation. Table 1 shows the results. We see that the composition required for chemicals production is always very similar. The major difference is the use of water at the WGS reactor to tune the H_2 to CO ratio. If the biogas is intended for energy production, mostly methane is produced and the rest is CO_2.

Table 1.- Composition of biogas for different applications.

	DME/Ethanol (H_2/CO=1)	**Methanol (H_2/CO=2)**	**FT (H_2/CO=1.7)**	**Energy (Max Methane)**
CO_2	0.465	0.468	0.464	0.3
CH_4	0.504	0.501	0.505	0.7
SH_2	0.0002	0.0002	0.0002	0.0
N_2	0.0001	0.0001	0.0001	1E-7
H_2O	0.031	0.031	0.031	
Obj	13.9	23.25	21.29	--
%CH_4 as fuel	4.17/14.17	4.082/14.082	4.074/14.073	--
Added H_2O per kmol gas in systhesis	0	1.51/10	1.145/10	--

4.1.4.2.-Optimal biomass composition.

Biogas composition depends on the feedstock and the operating conditions at the digestor. Basically we target two biogas compositions, one as fuel and one for chemicals. By solving P2 for such biogas composition leaving the biomass composition as a variable we can compute the features of the ideal biomass required for each application. Those features are given in Table 2. We see that the main difference is the composition of C in the biomass. As a source for chemicals, the biogas requires that the source has a larger carbon fraction. In both cases we aim at high dry mass fraction and volatile solids. The digestate properties are presented in Table 3 for each of the compositions.

Table 2. Composition of biogas for different applications

		Fuel	Chemical
wDM	Mass fraction of dry mass	0.1	0.1
wVS	Dry mass fraction of volatilized solids	0.8	0.8
wC	Dry mass fraction of element C	0.177	0.377
wN	Dry mass fraction of element N	0.009	0.044
wNorg	Dry mass fraction of element Norg	0.030	0.031
wP	Dry mass fraction of element P	0.008	0.008
wK	Dry mass fraction of element K	0.033	0.1
wRest		0.677	0.439
Rcn	Molar relation between C and N	5.76	5.835

Table 3. Digestate properties.

	Fuel	Chemical
K index	1.002	1.036
P Index	1.904	1.968
N index	2.95	3.063

4.1.4.3.-Optimal waste blending

The biomass composition presented in Table 2 is purely theoretical. However, a number of sources of biomass can be processed to obtain biogas. By solving a blending problem with different biomass sources we aim to determine the optimal mixture.

Thus, we optimize (P2) for a number of biomasses, i.e. cattle slurry, pig slurry, farm manure, sludge, with different compositions, see Table 4. The ranges of the variables and compositions are left as such, instead of using an average value, we leave them as variables. We target both uses, biogas as a source for chemical or as a source of energy. The selection of the biomasses depends not only on its cost but also on the credit that can be obtained from the digestate. For pricing the biomass, two alternatives are evaluated. In the first case we assume a cost for N of 0.45€/kg, for P, 0.32€/kg and for K, 0.24€/kg based on the values presented on the web page [31]. Thus, for the average composition of each of the main nutrients, the relative cost of the biomass sources is estimated considering the mass of each ingredient:

$$\text{Cost} = \text{fc(N)}\cdot P_N + \text{fc(P)}\cdot P_P + \text{fc(K)}\cdot P_K \quad (44)$$

Furthermore, we estimate the credit out of the digestate based on the N, P and K indexes. The typical fertilizers have a composition of 9, 18 and 13 % of N, P and K respectively. Considering a base price for the typical fertilizer using historic data in Spain, this price is considered to be 521 €/t. Thus the credit from the digestate can be estimated as how far it is from typical ones in the market, penalizing if any of the indexes is below the typical one.

$$\text{Credit}=\text{Price}_{\text{base}}\,\frac{1}{3}\left[\frac{\text{N}_{\text{index}}}{9}+\frac{\text{P}_{\text{index}}}{18}+\frac{\text{K}_{\text{index}}}{13}\right] \quad (45a)$$

Alternatively, we can estimate the digestate price based on the value for the fertilizes as a function of the nutrient [32]:

$$\text{Credit}=(10/0.454)\cdot(0.55\cdot\text{N}_{\text{index}}+0.69\cdot\text{P}_{\text{index}}+0.48\text{K}_{\text{index}}) \quad (45b)$$

In the first scenario for digestate pricing, the credit of the digestate is given by Eq. (45a). Using this pricing model, the optimal mixing of biomass types for the production of chemicals and fuels is provided in Table 5. Cattle slurry and food residues are selected with almost 65% cattle slurry and 35% urban food waste. Both biogas uses present also similar digestate composition. The composition of each of the biomasses is shown in Table 6. The C to N ratio (R_{cn}) aims to be the lower bound for cattle slurry and sludge and the upper bound for the Urban food waste. In terms of the composition, for the cattle slurry the values of nitrogen, phosphorous and potassium are to be at their upper bounds, due to the further use of the residue as fertilizer. In case of the sludge, organic nitrogen, and potassium are found to be at the lower bounds while phosphorous is expected at the upper bound.

Table 4.- Biomass properties.

	Biomass 1		**Biomass 2**	**Biomass 3**		**Biomass 4**	**Biomass 5**		**Biomass 6**	**Biomass 7**
	Cattle slurry [33]		**Pig Slurry [33]**	**Cattle Manure**		**Pig Manure**	**Sludge (Wastewater) [33]**		**Urban Food Waste**	**Urban Green Waste**
	LOW	UP	LOW	UP			LOW	UP		
Vbiogas (m3/kg)	0.2	0.5	0.25	0.5	0.25	0.38	0.25	0.60	0.44	0.23
wDM	0.1	0.2	0.03	0.08	0.25	0.25	0.08	0.25	0.31	0.25
wVS	0.5	0.7	0.7	0.8	0.80	0.75	0.3	0.5	0.85	0.88
wC						0.420			0.468	0.418
wN	0.005	0.047	0.005	0.095	0.004	0.006	0.024	0.320	0.001	0.001
wNorg	0.005	0.036	0.005	0.030	0.020	0.022	0.001	0.002	0.031	0.030
wP	0.008	0.013	0.019	0.022	0.006	0.010	0.009	0.063	0.005	0.005
wK	0.033	0.100	0.039	0.083	0.027	0.027	0.008	0.015	0.009	0.027
Rcn	3	20	3	10	20	15	6	24	15	13
Cost (€/kg)	0.031		0.043	0.010		0.012	0.091		0.004	0.0084

Table 5.- Biomass mixture and digestate properties using Eq. 45a.

	Chemicals	Fuel
Cattle slurry	6.522	6.454
Pig Slurry		
Cattle Manure		
Pig Manure		
Sludge		
Urban Food Waste	3.478	3.546
Urban Green Waste		
Digestate		
K index	1.064	1.017
P Index	2.023	1.932
N index	2.913	3.051
C/N	10	10

Table 6.- Biomass mixture and digestate properties using Eq. 45a.

	Chemicals		Fuels	
	Cattle slurry	Urban Food W	Cattle slurry	Urban Food W
Vbiogas (m3/kg)	0.5	0.44	0.5	0.44
wDM	0.2	0.31	0.2	0.31
wVS	0.7	0.85	0.7	0.85
wC	0.249	0.48	0.249	0.48
wN	0.047	0.001	0.047	0.001
wNorg	0.036	0.031	0.036	0.031
wP	0.013	0.005	0.013	0.005
wK	0.060	0.009	0.033	0.009
Rcn	3	15	3	15

However, if we price the fertilizer per component, as given by Eq. (45b), a different solution is obtained. In this case, sludge is the only biomass recommended for both applications. Tables 7 and 8 show the results. The digestate features whether we produce chemicals or fuel is similar. The main difference is the carbon to nitrogen ratio (R_{cn}). When biogas is aimed at chemical production, the R_{cn} ratio is larger. Furthermore, the NPK index differs from the one in case study 1.Table 8 presents the suggested composition of the biomass for the production of fuels and chemicals. The R_{cn} ratio of the biomass required is larger for fuels production

Table 7.- Biomass mixture and digestate properties using eq. 45b

	Chemicals	Fuel
Cattle slurry		
Pig Slurry		
Cattle Manure		
Pig Manure		
Sludge	10	10
Urban Food Waste		
Urban Green Waste		
Digestate		
K index	2.055	2.050
P Index	3.906	3.896
N index	0.038	0.054
C/N	9.12	8.041

Table 8.- Biomass mixture and digestate properties using eq. 45b

	Chemicals	Fuels
	Sludge	Sludge
Vbiogas (m3/kg)	0.25	0.6
wDM	0.25	0.25
wVS	0.3	0.5
wC	0.577	0.392
wN	0.070	0.041
wNorg	0.002	0.002
wP	0.063	0.063
wK	0.008	0.012
Rcn	7.972	9.146

4.1.5 CONCLUSIONS

In this work we have use mathematical optimization techniques to compute the optimal mixture of waste from the production of biogas as a source of chemicals and as fuel. The biogas processing problem determines the optimal composition of the biomass for a certain application and the digestate properties. Next, a mixture of biomass is suggested by solving the biogas production subproblem . This formulation can also help within the waste supply chain to determine the optimal mixture as a function of waste availability. The solutions found are local optimum, therefore, further research is needed to find global solutions for which specific algorithms are to be developed.

However, for different chemicals production, the syngas composition required is different, based on the H_2 to CO ratio. A biogas consisting of 50% methane, and 48% CO_2 is the most appropriate biogas for dry reforming to syngas. When the biogas is intended as fuel, the maximum allowable methane fraction is targeted.

In order to obtain the biogas with that composition, we process different waste types via anaerobic digestion. The estimation of the digestate price determines the selection of the mix of biomass. If the price of the fertilizer is given by components, sludge is the only source recommended for further use. If we aim to obtain the most typical fertilizer composition, it turns out that for chemicals production, 65% of cattle slurry and 35% urban food waste is the optimal blend. Experimental validation is required so as to validate the possibility of processing such a biomass mixture simultaneously.

Nomenclature

a': {CH4}, {CO2},{NH3},{H2S},{O2} or {N2}
a: {H2O}, {CH4}, {CO2},{NH3},{H2S},{O2} or {N2}
b: {C}, {Nam}, {Norg}, {P}, {K} or {Rest}
K_i*: (T): Ratio between vapour pressure at T and total pressure*
k: Polytropic index
K_{index} : Potassium index eq. (29)
kp: Equilibrium constant
$K_i(T)$ Defined in eq. (23).
F_j: Total flow of stream j (kg/s)
fc(i): Mass flow of component i (kg/s)
$fc_{(i,unit,unit1)}$: Mass flow of component i from unit to unit1 (kg/s)
LHV: lower heating value (kJ/kg)
MW: Molar mass (kg/kmol)
n_i: Molar flow of species i (kmol/s)
N_{index}: Nitrogen index eq. (29)
P_{index} Phosphorous index eq. (29)
P_v:Vapor pressure (bar)
P_i: Partial pressure of component I (bar)
P_j: Price of component j (€/kg)
$P_{out/in}$: Outlet / inlet total pressure (bar)
Q_i: Thermal energy associated to unit i (kW)
$V_{biogas,\ waste}$ = Biogas volume produced per unit of volatile solids (SV) ($m^3_{biogas}/kg_{SV/i}$).
$R_{V/F}$ = Molar ratio between the vapor and feed phases
$R_{C\text{-}N,\ waste}$ = Mass ratio between the carbon and nitrogen in waste
T: Temperature (ºC o K)
W: Work (kW)
Waste: Type of residude processed.
$w_{MS/waste}$: dry mass fraction ($kg_{MS/\ waste}$ /kg).
$w'_{SV/\ waste}$: dry mass fraction of volatile solids out of the dry waste ($kg_{SV/\ waste}$ /$kg_{MS/\ waste}$).
$w'_{C/\ waste}$: dry mass fraction of C in waste ($kg_{C/\ waste}$ /$kg_{MS/\ waste}$).
$w'_{Nam/\ waste}$: dry mass fraction of ammonia nitrogen in waste ($kg_{Nam/\ waste}$ /$kg_{MS/\ waste}$).
$w'_{Norg/\ waste}$: dry mass fraction of organic nitrogen in waste ($kg_{Norg/\ waste}$ /$kg_{MS/\ waste}$).
$w'_{P/\ waste}$: dry mass fraction of P nitrogen in waste ($kg_{P/\ waste}$ /$kg_{MS/\ waste}$).
$w'_{K/\ waste}$: dry mass fraction of K nitrogen in waste ($kg_{K/\ waste}$ /$kg_{MS/\ waste}$).
$w'_{Rest/\ waste}$: dry mass fraction of the rest nitrogen in waste ($kg_{K/\ waste}$ /$kg_{MS/\ waste}$).
$Y_{a'/biogas\_dry}$: molar fraction of the dry gas
$x_{a/biogas}$= mass fraction of the gas
y_{biogas}= specific saturated moisture of biogas
Z: Objective function (€/s)
ΔH: Enthalpy (kW)
η: Compressor efficiency.

References

[1] Nallathambi Gunaseelan, V.N., 1997 Anaerobic digestion of biomass fro methane production: A review. Biomass Bioener.. 13 (12), 83-114

[2] Japaraju, P., Rintala, J., 2013. 17 - Generation of heat and power from biogas for stationary applications: boilers, gas engines and turbines, combined heat and power (CHP) plants and fuel cells 404-427, In The Biogas Hand book

[3] http://www.biogas-info.co.uk/biogas-biogas-yields.html. Last access on: 11/31/2015

[4] Steffen R., Szolar, O., Braun, R., 1998 Feedstocks for anaerobic digestion. *Q:\RODL\PROJEKTE\AD-NETT\FEEDNEW.DOC*

[5] León, E., Martín, M., 2016. Optimal production of power in a combined cycle from manure based biogas Energ. Conv. Manag. 114, 89–99

[6] Hernández, B, Martín, M. 2016. Optimal composition of the biogas for dry reforming in the Production of Methanol Ind. Eng. Chem. Res. 10.1021/acs.iecr.6b01044

[7] Peral, E. Martín, M , 2015. Optimal production of DME from switchgrass based syngas via direct synthesis. Ind. Eng. Chem. Res. 54 (30) 7465-7475

[8] Martín, M., Grossmann, I.E., 2011- Energy Optimization of Bioethanol Production via Gasification of Switchgrass AIChE J. 57, 12, 3408, 3428

[9] Martín, M., Grossmann, I.E., 2011. Process optimization of FT- Diesel production from biomass. Accepted Ind. Eng. Chem Res, *50* (23),13485–13499

[10] Vaidyanathan, R., El-Halwagi, M., 1996. Computer-Aided Synthesis of Polymers and Blends with Target Properties. Ind. Eng. Chem. Res.. 35(2), 627-634.

[11] Churi, N., Achenie, L. E. K. 1997. The Optimal Design of Refrigerant Mixtures for a Two-Evaporator Refrigeration System. Comp. and Chem. Eng. 21, 349-354.

[12] Conte, E., Gani, R. Chemicals-Based Formulation Design: Virtual Experimentations. 21st European Symposium on Computer Aided Process Engineering. 2011.

[13] Martín, M., Martínez. 2013. A Methodology for simultaneous process and product design in the consumer products industry: The case study of the laundry business. *Chem. Eng. Res. Des.* 91, 795–809

[14] Martín, M., Martínez. 2015. Addressing Uncertainty in Formulated Products and Process Design. Ind. Eng. Chem. Res. 54, 5990-6001

[15] Mattei, M., Kontogeorgis, G. M., Gani, R., 2014. A Comprehensive Framework for Surfactant Selection and Design for Emulsion based Chemical Product Design. Fluid Phase Equil. 362, 288-299.

[16] Shih, J..S., Frey, H.C., 1995. Coal blending optimization under uncertainty. *Eur. J. Oper. Res.,* 83, 3(22), 452-465.

[17] Zhao, X., Wang, Y., 2009. Gasoline blending scheduling based on uncertainty. Proceedings of the 2009 International Conference on Computational Intelligence and Natural Computing, CINC 2009, 2, 5231039, 84-87

[18] García-Gen, S., Rodríguez, J., Lema, J.M., 2014 Optimization of substrate blends in anaerobic co-digestion using adaptive linear programming. Bioresource Technology. 173, 159-167

[19] Gani, R. . 2004, Computer-aided methods and tools for chemical product design." Chemical Engineering Research and Design 82(11), 1494-1504.

[20] Ng, L.Y., Chong, F.K., Chemmangattuvalappil, N.G. 2015 Challenges and opportunities in computer-aided molecular design. Computers & Chemical Engineering 81, 115-129.

[21] Austin, N.D., Sahinidis, N.V., Trahan, D.W. 2016. Computer-aided molecular design: An introduction and review of tools, applications, and solution techniques." Chemical Engineering Research and Design 116 (2016): 2-26.

[22] Martín, 2016. Industrial Chemical Process. Analysis and Design. Elsevier, Oxford.

[23] Xu, F., Wang, Z.W., Li, Y., 2014. Predicting the methane yield of lignocelullosic biomass in mesophillic solid-state anaerobic digestion based on feedstock characteristics and process parameters. Bioresor. Technol. 173, 168-176.

[24] Al Seadi, T., Rutz, D., Prassl, H., Köttner, M., Finsterwalder, T., Volk, S., Janssen, R. 2008 Biogas Handbook University of Southern Denmark Esbjerg, Esbjerg, Denmark

[25] Defra (2011) Fertilizer manual.
http://adlib.everysite.co.uk/adlib/defra/content.aspx?id=2RRVTHNXTS.88UF9N65FWLCJ.Last access on: 11/31/2016

[26] Rykebosch, E., Brouillon, M., Vervaeren, H., 2011. Techniques for trasnformation of biogas to biomethane. Biomass Bioenergy. 35, 1633-1645

[27] GPSA 2004. Engineering_Data_Book FPS VERSION 21-10, 2004

[28] Nexant Inc., 2006. Equipment Design and Cost Estimation for Small Modular Biomass Systems, Synthesis Gas Cleanup, and Oxygen Separation Equipment Task 2: Gas Cleanup Design and Cost Estimates – Black Liquor Gasification Subcontract Report NREL/SR-510-39944 May 2006

[29] Luyben, W.L., 2014 Design and Control of the Dry Methane Reforming Process *Ind. Eng. Chem. Res.*, 53, 14423−14439.

[30] Roh, H-S., Lee, D.K., Koo, K.Y., Jung, U.H., Yoon, W.L., 2010. Natural gas steam reforming for hydrogen production over metal monolith catalyst with efficient heat-transfer. Int J Hydrogen, 35(3), 1613-1619

[31] (http://adlib.everysite.co.uk/adlib/defra/content.aspx?doc=245926&id=246003)

[32] Year-end fertilizer prices. Available in: https://www.canr.msu.edu/news/year-end-fertilizer-prices Last access: 11/31/2016.

[33] European Commission (2001) Available in: http://ec.europa.eu/environment/waste/studies/compost/landspreading_4-6.pdf Last access: 11/31/2016.

CHAPTER 4.2. OPTIMIZATION FOR BIOGAS TO CHEMICALS VIA TRI-REFORMING. ANALYSIS OF FISCHER-TROPSCH FUELS FROM BIOGAS.

ABSTRACT

This chapter presents an optimization approach for studying the production of syngas from biogas via tri-reforming. The optimization, formulated as a NLP problem, is performed for three syngas ratios according to the desired product: methanol, ethanol or Fischer-Tropsch (FT) fuels. As a result, the optimal operating conditions and biogas composition are defined. For the production of ethanol, a biogas composed by a CH_4:CO_2 ratio of 0.52:0.48 is desired, requiring 0.035 mol of O_2 per mol of Biogas in the reformer. For the production of methanol and FT, biogas with the largest content of methane is suggested to be reformed with 0.275 molO_2/mol biogas. The largest H_2:CO ratio required for methanol is achieved by feeding steam in a WGS reactor after the reformer. The syngas optimization study is completed by evaluating tri-reforming for the production of FT fuels from biogas via high and low temperature FT synthesis. The production cost for a plant fed with 12 MMm^3/y of biogas results in $3/gal for biodiesel via HTFT and $1.7/gal via LTFT.

Note: The supplementary material is available in:
https://www.sciencedirect.com/science/article/pii/S0196890418309336

4.2.1 INTRODUCTION

Developed societies generate large volumes of organic wastes such as sludge from water treatment, urban and forest residues or manure [1]. Most of these organic wastes require treatment before disposal. Anaerobic digestion represents a technology that allows not only processing and stabilizing the waste, but that also generating additional value in the form of biogas and digestate, as part of the circular economy initiative [2-4]. For decades, these products were the only ones obtained, being the biogas applied for the production of power [5, 6] and/or as a source of methane for natural gas networks [5,7,8]. However, biogas is an interesting source of carbon not only because of the methane, but also due to its CO_2 content. Initially, biogas was upgraded transforming the methane into syngas and hydrogen via steam reforming (SR) [9-12] and auto-thermal reforming (ATR) [13, 14]. However, the inherent CO_2 within the biogas can be also used to produce syngas via dry reforming (DR) [15]. Hernandez and Martin evaluated the possibility of using biogas for the production of methanol via combined SR and DR [15]. Dry reforming does not only upgrade the biogas [16], but it also reduces CO_2 emissions of the process [15]. The syngas produced from the reformer was also evaluated by Hernandez et al. [17] for the production of other chemicals such as DME, ethanol or F-T fuels. However, the study was conceived as a product design problem for the selection of waste type and the evaluation focused on determining the H_2:CO ratio required, and no process design beyond syngas production was been performed for each of the chemicals produced except for methanol. The production process of methanol defined by Hernandez and Martin [15] was thermodynamically evaluated by Vita. et al. [18] proposing upgrades such as the use of tri-reforming (TR) and providing a range of profitability for the process. This process has been also more recently optimized by Oliveira dos Santos et al. [19] for different biogas sources.

TR is a technology that combines three methane reforming processes [20]: SR (Eq. (1)), partial oxidation (POX) (Eq. (2)) and DR (Eq. (3)). The synergetic combination of these three technologies has the merit of the high economical advantage of SR [21,22], the high energy efficiency of the exothermal POX [23,24], and the environmental advantage of carbon dioxide reforming [9,25-27] .

$$CH_4 + H_2O \leftrightarrow CO + 3H_2 \qquad \Delta H^0_{298K} = +206\frac{kJ}{mol} \tag{1}$$

$$CH_4 + \frac{1}{2}\,O_2 \leftrightarrow CO + 2H_2 \qquad \Delta H^0_{298K} = -36\frac{kJ}{mol} \tag{2}$$

$$CH_4 + CO_2 \leftrightarrow 2CO + 2H_2 \qquad \Delta H^0_{298K} = +247\frac{kJ}{mol} \tag{3}$$

Kinetic models have been proposed and optimized for the study of TR from methane [28, 29, 30], natural gas [31, 32] and biogas [33]. The integration of tri-reforming in process optimization and design has been only recently addressed by Balasubramanian et al. [34]. They performed an MINLP optimization selecting the optimal reformer, including tri-reforming, for different H_2: CO syngas ratios and using natural gas as raw material [34]. However, to the best of authors' knowledge the only study concerning to the optimization of biogas TR does not consider the cleaning of the biogas as well as the tune-up of the syngas produced, being the optimization only performed to the

kinetic of reformer [33]. No optimization studies have been performed integrating the biogas TR in process design and complete process design of fuels production is not available either. Thus, in this work we propose a parametric optimization approach evaluating different O_2:Biogas ratios. The optimization is first applied for the production of syngas with different H_2:CO ratios depending on the syngas application: for the production of methanol, DME, ethanol or F-T. The study allows identifying the optimal type of reformer, the optimal biogas composition and if external supply of CO_2, steam or oxygen are required.

The manuscript is completed with a second study. A novel integrated process is designed for the production of FT-fuels from biogas as raw material. The integration of tri-reforming has been performed for the production of different chemicals such as methanol, using natural gas [35] and biogas [18, 19] as raw material, DME, using natural gas as raw material [36], or fuel for SOFC [37]. Meanwhile for the production of FT fuels via tri-reforming, processes have been also recently presented using natural gas [38] or biomass as raw material [39]. However, no process has been defined for biogas to FT fuels via tri-reforming. To the best of author´s knowledge, the only two studies concerning biogas to FT fuels uses auto-thermal reforming for the processing of biogas [40, 41] or natural gas [42]. Therefore, a new process for the production of FT-fuels from biogas is also presented in this work. For the first time, the biogas is not only used for the direct production of FT-fuels, but it is also considered in the operation of complementary units such as the burner, where it is used as fuel, or the hydro-treatment unit, where the hydrogen used to enhance the yield from the wax obtained at low temperature FT (LTFT) is obtained from biogas reforming.

The rest of the paper is structured as follows. In Section 4.2.2, the modelling issues for the process optimization of biogas to syngas via tri-reforming are described. In Section 4.2.3, the modelling issues for the process design of syngas to Fischer-Tropsch fuels are defined. In Section 4.2.4, the results are presented. Finally, remarks and conclusions are drawn in Section 4.2.5.

4.2.2 MODELLING ISSUES. BIOGAS TO SYNGAS

The process section of syngas production from biogas is presented in Figure 1. The biogas generated from anaerobic digestion is mainly composed by methane and CO_2, apart from other species in small quantities such as nitrogen, H_2S, steam or NH_3. These components of the biogas together with the rest of the components of the tri-reforming system belong to the set $J = \{CH_4, CO_2, N_2, H_2S, H_2O, NH_3, H_2, CO, O_2\}$. Before processing the biogas, some of its components need to be removed since they can reduce the catalyst efficiency. Thus, a clean-up stage is initially introduced in the process in order to prepare the biogas to be fed to the reformer. After the reforming stage, it may be necessary to clean and tune-up the H_2:CO ratio of the syngas. A cleaning process to absorb the unreacted and impurities is initially proposed. It is followed by a hydrogen tuned-up section consisting of a PSA membrane unit for H_2 recovery, a by-pass and a water gas shift (WGS) reactor. Finally, a CO_2 removal section composed by a PSA membrane and a by-pass is considered.

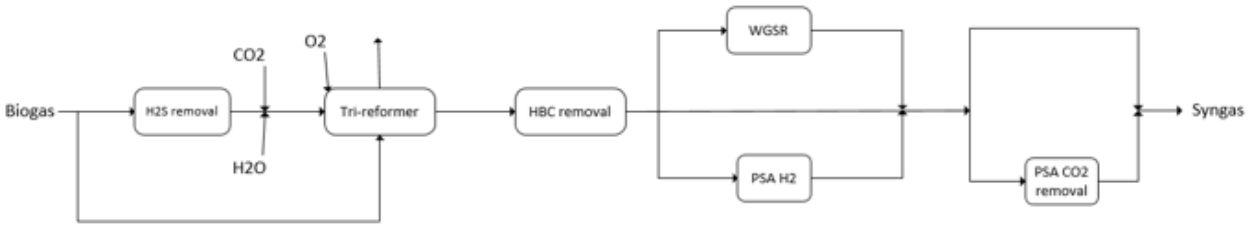

Figure 1. Syngas processing.

4.2.2.1 Biogas cleaning section.

Biogas is a complex mixture of gases with a wide range of components and different compositions that are dependent on the biogas source [5, 6, 43, 44]. For simplification, in the present work the ranges of composition provided in Table 1 are taken [44]. This ranges are global enough to consider different biogas sources such as sludge, pig or cattle manure as well as their blend to obtain intermediate mixtures. In the same way, if external requirements of methane, CO_2 or steam are needed; their presence is considered with the cost involved for each component as presented in Figure 2.

Table 1. Ranges of concentration for components of the biogas [44].

Component (%vol)	Minimum	Maximum
CH_4	0.37	0.75
CO_2	0.25	0.50
N_2	0.01	0.17
H_2S	$2•10^{-5}$	$2•10^{-3}$
H_2O	0	0.031
NH_3	$1•10^{-6}$	$3.5•10^{-6}$

The biogas is fed to a mixed-packed bed of Fe_2O_3 and zeolites for the removal of H_2S and ammonia. The bed can operate at 298-323 K and the capture of the ammonia is carried out by the zeolite bed, meanwhile H_2S capture is performed as follows [8]:

$$Fe_2O_3 + 3\,H_2S \rightarrow Fe_2S_3 + 3H_2O \quad (4)$$

The removal of ammonia is modelled assuming an efficiency of 100% and the removal of H_2S is modelled following the stoichiometry of the reaction assuming complete conversion of the sour gas. The Fe_2O_3 of the bed can be regenerated using oxygen [8].

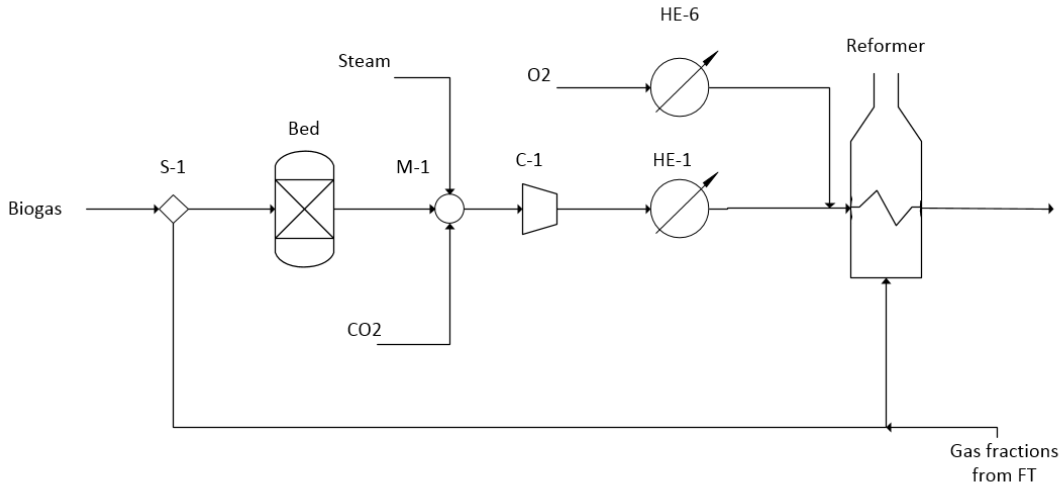

Figure 2. Biogas cleaning and reforming.

4.2.2.2 Biogas Tri-reforming.

As previously presented, TR combines the highly endothermic steam and dry reforming reactions with the exothermic partial oxidation of methane, improving the energy efficiency of the process [24]. Apart from these three reactions, the competitive WGS reaction needs to be taken into account during the reforming processes [15, 32], see eq. (5).

$$CO + H_2O \leftrightarrow CO_2 + H_2 \qquad \Delta H^0_{298K} = -41 \frac{kJ}{mole} \tag{5}$$

The reformer is modelled based on chemical equilibria. The kinetic studies of Arab Aboosadi et al. [45] and Chein et al. [29] showed that oxygen reacts with methane at the beginning of the reactor and then the components are distributed according to the equilibriums achieved. Thus, TR is implemented in the optimization as follows. The mass balances in the tri-reformer are decomposed in two stages and one energy balance is carried out for the entire unit. In the first stage, the oxygen reacts as in eq. (2) and a conversion of 100% is assumed with the O_2:biogas ratio as an optimization parameter. In the second stage, DR, SR and WGS occur until the equilibria given by eqs. (6) to (8) is achieved [46,47].

$$k_p = e^{\left[31.447 - \frac{29580}{T}\right]} = \frac{P_{CO} P_{H_2}}{P_{CH_4} P_{CO_2}} \tag{6}$$

$$k_p = 10^{\left[-\frac{11650}{T} + 13.076\right]} = \frac{P_{CO} P_{H_2}^3}{P_{CH_4} P_{H_2O}} \tag{7}$$

$$k_p = 10^{\left[\frac{1910}{T} - 1.784\right]} = \frac{P_{CO_2} P_{H_2}}{P_{CO} P_{H_2O}} \tag{8}$$

The atomic balances are also performed in this second stage as follows:

$$mol_{CH_4}\big|_{in} = mol_{CH_4} + mol_{CO} + mol_{CO_2}\big|_{out} \quad (9)$$

$$4 \cdot mol_{CH_4} + 2 \cdot mol_{H_2O}\big|_{in} = 4 \cdot mol_{CH_4} + 2 \cdot mol_{H_2} + 2 \cdot mol_{H_2O}\big|_{out} \quad (10)$$

$$mol_{H_2O}\big|_{in} = mol_{H_2O} + mol_{CO} + 2 \cdot mol_{CO_2}\big|_{out} \quad (11)$$

The energy balance in the reactor is computed from eq. (12):

$$Q('reformer') = Q_{prod} + Q_{react} = \sum_i fc(i, reformer, HE2) \cdot \left(\Delta H_f + \int_{T_{ref}}^{T_{out}} C_p dT\right) - \sum_i fc(i, HE1, reformer) \cdot \left(\Delta H_f + \int_{T_{ref}}^{T_{out}} C_p dT\right) - \sum_i fc(i, HE6, reformer) \cdot \left(\Delta H_f + \int_{T_{ref}}^{T_{out}} C_p dT\right) \quad (12)$$

The amount of fuel required to be burned is computed assuming that the energy in Q('reformer') is provided by lower heating value (LHV) of the fuels fed in the burner. The LHV is determined as function of the outgas composition recycled from the F-T and the biogas fed following eq. (13). For the parametric optimization of biogas to syngas described in this section, the recycling of gases from FT is set to zero.

$$Q('reformer') = LHV_{CH_4} \cdot \left(m_{CH_4\ Biogas} + m_{CH4\ FT}\right) + LHV_{H_2} m_{H_2\ FT} + LHV_{CO} m_{CO\ FT} \quad (13)$$

4.2.2.3 Syngas cleaning and composition adjustment.

The gas coming out of the reformer is sent to a purification stage, Figure 3, where the H_2:CO ratio is tuned-up according to the product that wants to be synthesized. First, water is removed in a two-step process using a flash (Flash-1) before compression and a dephlegmator (Flash-2) right after. Next, a PSA system is used to remove the last traces of hydrocarbons and nitrogen (HCB bed) in order to avoid the deposition of carbon on the catalyst surface [48]. It operates at 298 K and 4.5 bar using silica gel as adsorbent with an assumed efficiency of 100% [49]. Thus, the gas coming out from the reformer needs to be compressed (C-2) and cooled down (HE-3). The compressors are modelled assuming polytrophic behaviour (k_c=1.4, η_c=0.8). During the cool down, the water condensates and it is discharged. The PSA system is modelled as two beds, one operating and other one in regeneration to allow the continuous operation of the plant.

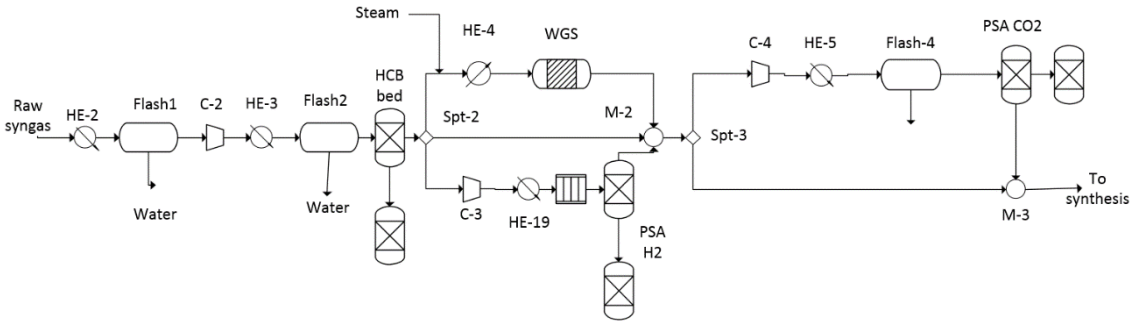

Figure 3. Syngas purification.

Next, the syngas H_2:CO ratio is adjusted. Three technologies are allowed to modify this ratio: A WGS reactor to increase the amount of hydrogen, a bypass and a hybrid membrane-PSA system to recover the excess of hydrogen [49].

The last cleaning stage consists of the removal of CO_2 for the preparation of the syngas as it can be seen in Figure 3. CO_2 can be fully or partially removed depending on the composition required for synthesis. For methanol production, the CO_2 composition is required to be from 2% to 8% in volume [50]. In the production of ethanol and Fischer-Tropsch fuel the CO_2 content is limited up to 6% in volume to avoid the reduction of the conversion of CO [51]. To achieve this concentration, only a fraction of the gas stream needs to be treated in the PSA system (PSA CO_2). The PSA adsorbs the excess of CO_2 using Zeolite 5A or 13X. It works at 298 K and 5 bar with an adsorption capacity of around 0.1 kg of CO_2 per kg of zeolite that allows the removal of 95% of the CO_2 [52]. Thus, the stream coming from the previous stage needs to be compressed and cooled down. In this section, the water also condensates and it needs to be separated before feeding it to the PSA membrane by means of Flash-4.

4.2.2.4 Solution procedure.

The problem addressed in this section is divided in three cases according to the final use of syngas. The H_2:CO ratios are fixed to 2.5 for methanol [53], 1 for ethanol and 1.7 for FT fuels [34]. The following objective function, eq. (14), is evaluated for the three cases. The values for the prices of the components involved in the objective function are \$3.3/1000 ft^3 for methane [54], \$0.021/kg for the O_2 [31], \$26 per tonne of CO_2 [55]. The utilities are assumed to have a price of $\$5.7 \cdot 10^{-5}$/kg for cooling water, \$0.019/kg for steam and \$0.06/kWh for electricity [56]. Finally, the operating cost of the Fe_2O_3 bed to remove H_2S is \$90 per kg of H_2S removed [15].

$$Profit = C_{H_2}F_{H_2} - C_{elec}\sum_{i\epsilon Compressors} W_i - C_{CH_4}\sum_{i\epsilon CH_4 inlets} F_{CH_4} - C_{O_2}F_{O_2' Triref'} - C_{CO_2}\sum_{i\epsilon CO_2 inlets} F_{CO_2} - C_q\sum_{j\epsilon Q_{heat}} Q + C_w\sum_{k\epsilon Q_{refrig}} Q - C_{H_2S}F_{H_2S} - C_{H2O}F_{H2O} \quad (14)$$

The equations involved in the problem show non-linearities such as logarithmic, exponential and inverse functions of the equilibrium equations. Therefore, the problem formulated as an NLP optimization is applied to each syngas ratio evaluating a range of O_2:biogas ratios from 0:1 to 0.3:1. It consists of 866 variables and 678 equations.

4.2.3 MODELLING ISSUES. FT PROCESS DESIGN.

In this section we present the modelling issues for the design of the biogas to FT fuels integrated process. FT synthesis produces alkanes that need to be introduced in the component set as follows: $J = \{CH_4, CO_2, N_2, H_2S, H_2O, NH_3, H_2, CO, O_2, LPG, Gasoline, Diesel, Heavy\}$. We consider 4 more fractions of alkanes as it will be presented in section 4.2.3.2.

The process superstructure is presented in Figure 4. It addresses the two possible modes of operation in FT synthesis. On the one hand, FT-fuels production can be carried out at high temperature, between 590 K and 630 K. On the other hand, the operation can be performed at low temperature, between 440 K and 530 K [57]. Depending on the mode of operation selected in the FT synthesis, the design of the reactor is different and the product distribution obtained is also different [57], which modifies the separation and purification operations required accordingly.

In high temperature Fischer-Tropsch (HTFT) only traces of waxes are obtained together the rest of the products in the same stream, requiring a separation performed in two stages [57, 58]: First, the most valuable liquid organic products, gasoline and diesel, are separated from the gases and water obtained in the FT synthesis. Second, fuels are separated and purified by means of a distillation column.

Low temperature Fischer-Tropsch (LTFT) is carried out in a fixed bed reactor, obtaining a stream composed of two phases: A liquid phase composed by the heavy fractions (waxes) and a gas phase with the rest of FT products [57, 58]. The amount of waxes obtained in this synthesis is more significant and a recovery of diesel and gasoline is also considered in the modelling of the process. The recovery is performed using a hydro-cracking reactor, which uses the hydrogen previously separated from the syngas and produces gasoline and diesel that are lately separated in a distillation column such as in HTFT.

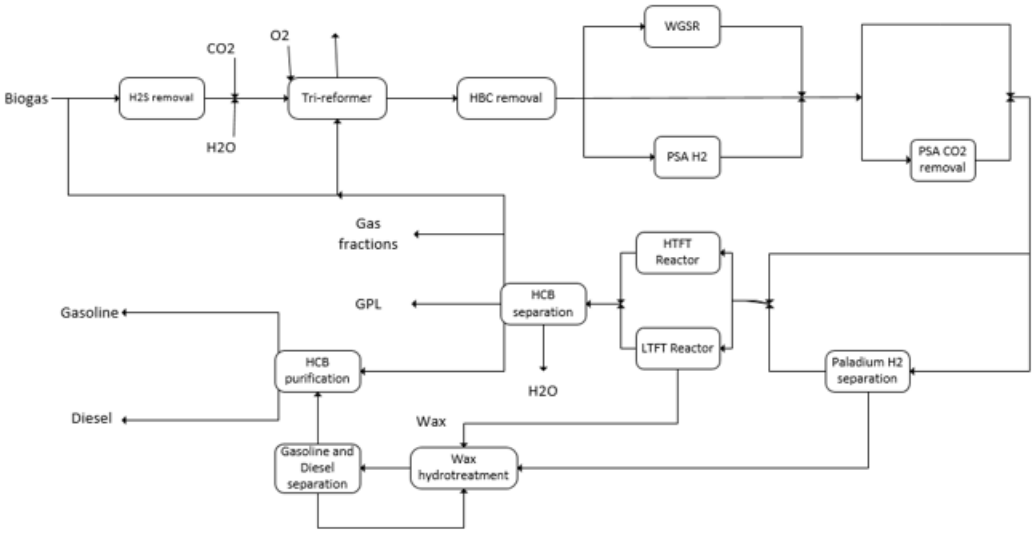

Figure 4. Integrated process of biogas to FT-fuels via tri-reforming.

In the following sections, the models of each of the process stages are defined. We start from the definition of the syngas previously presented in Section 4.2.2. Its generation is not presented again but it is also included in the processes. The only difference to be noticed is that the H_2:CO ratio of the syngas is not fixed as before. Now, the boundaries are provided in the feed of the reactor, allowing the separation of hydrogen. Thus, in section 4.2.3.1 the hydrogen separation and FT reactants adjustment are discussed. Then, in section 4.2.3.2 the FT reactor is described in its two modes of operation. Finally, in section 4.2.3.3, the separation, purification and hydro-treatment stages are presented in two parts: first, the separation of products involved in the HTFT and second, those products from the LTFT.

4.2.3.1. Hydrogen generation and adjustment for Fischer-Tropsch

The syngas is initially fed to a palladium membrane where hydrogen may be separated. The separation efficiency of the membrane is assumed to be 100%, working at 12 bar and 298 K [59]. Thus, the syngas needs to be compressed and cooled down before reaching the membrane. To avoid the presence of liquid water, a dephlegmator (Flash-3) is defined before splitter Spt-4, see Figure 5. Two streams are obtained from the membrane. The hydrogen permeated is recovered at 1 bar of pressure and the stream that contains the rest of components is assumed not to have suffered any pressure drop [59].

Since H_2:CO ratio between 1 and 2 needs also to be secured for the later FT reactor, a splitter is previously required to separate the proper amount of hydrogen. Splitter Spt-4 divides the flow in two streams that are later mixed. One stream goes to the membrane and the other stream is a bypass sent to mixer M-4.

After the mixer, the syngas with a H_2:CO ratio between 1 and 2 needs to be compressed up to 30 bar; and a temperature between 440 K and 530 K for the LTFT reactor or between 590 K and 630 K for the HTFT reactor [58]. Thus, a compressor (C-6) followed by a heat exchanger (HE-7) are defined before the reactor.

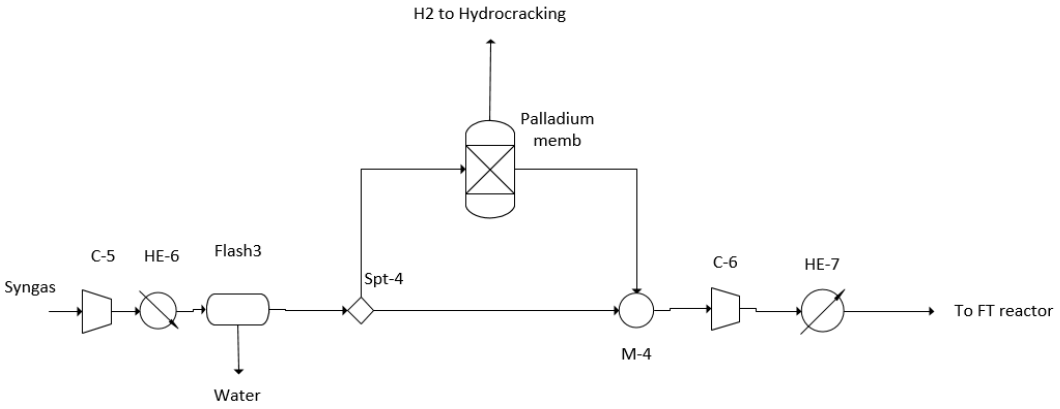

Figure 5. H_2 separation and synthesis.

4.2.3.2 Fischer-Tropsch reactor.

The reactions taking place in a Fischer-Tropsch reactor are equivalent to a polymerization where larger chains are achieved thanks to the dissociation of CO over the catalyst. The main reactions can be seen in eqs. (15) and (16). The first reaction in eq. (15) corresponds to methanation, the second is the water gas shift and the third reaction is the Boudouard reaction. The methanation reaction and the Boudouard are undesirable [60, 61].

$$CO + 3H_2 \rightarrow CH_4 + H_2O \qquad \Delta H^0_{298K} = 247\ kJ/mol$$

$$CO + H_2O \rightarrow CO_2 + H_2 \qquad H^0_{298K} = -41\ kJ/mol \tag{15}$$

$$2CO \rightarrow C + CO_2 \qquad \Delta H^0_{298K} = -172\ kJ/mol$$

The reaction given in eq. (16) is desired, and is the most dominant reaction when applying cobalt-based catalyst. When using iron-based catalyst, the WGS reaction also occurs.

$$ncCO + \left(nc + \frac{nh}{2}\right) H_2 \rightarrow C_{nc}H_{nh} + ncH_2O \tag{16}$$

The operating conditions depend on the types and quantities of Fisher-Tropsch products desired. Two operating modes can be selected: HTFT (590-630 K) with pressures between 10 bar and 40 bar and iron based catalyst, or LTFT (440-530 K) with iron or cobalt catalyst [60, 62]. The iron catalyst working around 30 bar provides high selectivity for C_{10}-C_{18}, which means high selectivity for diesel production [58, 60, 62]. The H_2:CO ratio shows an

optimal for H_2:CO=1.3:1 when the reactor is optimized individually [60], but limits between 1:1 and 2:1 are used as boundaries [62, 63].

To determine the operating conditions in each of the two modes proposed, Anderson-Schulz-Flory distribution is assumed to model the products distribution [64]. The fraction of mass of the hydrocarbons, w_i, depends on the probability of chain growth, α. A conversion of 0.9 in CO is considered based on the results by Park & Norbeck [65]. According to the studies of Song [66], α is a function of the temperature, and the ratio CO to H_2 through eqs. (17)-(18) determine w_i. The effect of α on the distribution of products obtained in the reaction is presented in Figure S1.

$$w_i = \alpha^{nc-1}(1-\alpha)^2 \cdot nc \tag{17}$$

$$\alpha = \left(0.2332 \cdot \left(\frac{y_\infty}{y_{H_2}+y_\infty}\right) + 0.633\right) \cdot \left(1 - 0.0039 \cdot \left(\left(T_{Synthesis} + 273\right) - 533\right)\right) \tag{18}$$

Figure S1 also includes the range of products obtained for HTFT and LTFT when eqs. (17) and (18) are analyzed. It can be seen that the products obtained are different and the modelling strategies proposed in this work are also different since the low concentration of some products results in numerical issues during the optimization. Thus, the design problem is divided in two problems, one for the integration and optimization of the HTFT process and another for the LTFT process. The model to compute the distribution of products for the LTFT mode is presented in section 4.2.3.2.1 and for the HTFT is presented in section 4.2.3.2.2.

4.2.3.2.1 Modeling the LTFT reactor

The distribution of the different fractions for LTFT can be seen in Figure S1 and are computed by numerical integration. The integration for light fractions is performed straightforward since the number of components is low. However, a simplification is required when more components are included in the fraction. The approach defined by Martin and Grossmann [67] is used for calculating the fractions as a function of α, see eq. (19) to (24).

$$frac_{CH_4} = (1-\alpha)^2 + \alpha \cdot (1-\alpha)^2 \cdot 2 \tag{19}$$

$$frac_{LPG} = \alpha^2 \cdot (1-\alpha)^2 \cdot 3 + \alpha^3 \cdot (1-\alpha)^2 \cdot 4 \tag{20}$$

$$frac_{gasoline} = 3 \cdot (\alpha^4(1-\alpha) \cdot 5 + \alpha^9 \cdot (1-\alpha)^2 \cdot 10) \tag{21}$$

$$frac_{Diesel} = 5 \cdot (\alpha^{10} \cdot (1-\alpha)^2 \cdot 11 + \alpha^{19} \cdot (1-\alpha)^2 \cdot 20) \tag{22}$$

$$frac_{Heavy} = 1 - frac_{CH_4} - frac_{C_3C_4} - frac_{gasoline} - frac_{Diesel} \tag{23}$$

$$fc(j, HE7, FT\ reactor)) = fc(j, FT\ reactor, HE8) \tag{24}$$

The mass balance per fraction is given by eqs. (25) to (34). The configuration of this reactor is also considered since it contains an internal separator as defined in Figure S2. It separates the products in liquid, mainly waxes, and gas fractions, the rest of components [57, 58].

$$fc(Wa, FT\ reactor, HE8) = fc(Wa, HE7, FT\ reactor) + \left(\frac{MW_{Wa}}{MW_{CO}}\right) \cdot X_{CO} \cdot fc(CO, HE7, FT\ reactor) \quad (25)$$

$$fc(CO, FT\ reactor, HE8) = (1 - X_{CO}) \cdot fc(CO, HE7, FT\ reactor) \quad (26)$$

$$fc(H_2, FT\ reactor, HE8) = (1 - X_{CO}) \cdot fc(CO, HE7, FT\ reactor) \quad (27)$$

$$fc(CO_2, FT\ reactor, HE8) = fc(CO_2, HE7, FT\ reactor) \quad (28)$$

$$Mass\ Product = X_{CO} \cdot \left(fc\ (H_2, HE7, FT\ reactor) + \left(1 - \frac{MW_{Wa}}{MW_{CO}}\right) fc(CO, HE7, FT\ reactor) \right) \quad (29)$$

$$fc(CH_4, FT\ reactor, HE8) = frac_{CH_4} \cdot Mass\ Product \quad (30)$$

$$fc(LPG, FT\ reactor, HE8) = frac_{C_3C_4} \cdot Mass\ Product \quad (31)$$

$$fc(Gasoline, FT\ reactor, HE8) = frac_{Gasoline} \cdot Mass\ Product \quad (32)$$

$$fc(Diesel, FT\ reactor, HE8) = frac_{Diesel} \cdot Mass\ Product \quad (33)$$

$$fc(Heavy, FT\ reactor, HE8) = frac_{Heavy} \cdot Mass\ Product \quad (34)$$

4.2.3.2.2 Modeling the HTFT reactor

HTFT generates products of lower chain length. Experimental results show that the product of HTFT contains waxes up to 5% and diesel between 5-10% [58]. Performing the analysis of eqs. (17) and (18), the content is even lower: Only traces of waxes (up to 0.05%) and diesel fractions up to 3% are obtained [64]. Thus, the waxes content in the product are assumed to be zero and no recovery of them by hydrocracking is needed in the subsequent separation section. The computational resources required to model the production of diesel and waxes as well as for waxes recovery can be applied to provide a more accurate prediction of the product distribution, in particular of the gasoline fraction. Now, the integrals are not reduced and they are computed following eqs. (19) and (20) for C_1-C_2 fraction and LPG. Meanwhile gasoline and diesel fractions are computed as in eqs. (35) and (36):

$$frac_{gasoline} = \alpha^4 \cdot (1-\alpha)^2 \cdot 5 + \alpha^5 \cdot (1-\alpha)^2 \cdot 6 + \alpha^6 \cdot (1-\alpha)^2 \cdot 7 + \alpha^7 \cdot (1-\alpha)^2 \cdot 8 + \alpha^8 \cdot (1-\alpha)^2 \cdot 9 + \alpha^9 \cdot (1-\alpha)^2 \cdot 10 \quad (35)$$

$$frac_{Diesel} = 1 - frac_{CH4} - frac_{LPG} - frac_{Gasoline} \quad (36)$$

Hence, the mass balances for HTFT reactor are given as eqs. (37) to (46). The reactor is a fluidized bed where products are obtained in the same stream, as presented in [58].

$$fc(Wa, FT\ reactor, HE20) = fc(Wa, HE7, FTreactor) + \left(\frac{MW_{Wa}}{MW_{CO}}\right) \cdot X_{CO} \cdot fc(CO, HE7, FT\ reactor) \quad (37)$$

$$fc(CO, FT\ reactor, HE20) = (1 - X_{CO}) \cdot fc(CO, HE7, FT\ reactor) \quad (38)$$

$$fc(H_2, FT\ reactor, HE20) = (1 - X_{CO}) \cdot fc(CO, HE7, FT\ reactor) \quad (39)$$

$$fc(CO_2, FT\ reactor, HE20) = fc(CO_2, HE7, FT\ reactor) \quad (40)$$

$$Mass\ Product = X_{CO} \cdot \left(fc\ (H_2, HE7, FT\ reactor) + \left(1 - \frac{MW_{Wa}}{MW_{CO}}\right) fc(CO, HE7, FT\ reactor) \right) \quad (41)$$

$$fc(CH_4, FT\ reactor, HE20) = frac_{CH_4} \cdot Mass\ Product \quad (42)$$

$$fc(LPG, FT\ reactor, HE20) = frac_{C_3C_4} \cdot Mass\ Product \quad (43)$$

$$fc(Gasoline, FT\ reactor, HE20) = frac_{Gasoline} \cdot Mass\ Product \quad (44)$$

$$fc(Diesel, FT\ reactor, HE20) = frac_{Diesel} \cdot Mass\ Product \quad (45)$$

$$fc(Heavy, FT\ reactor, HE20) = frac_{Heavy} \cdot Mass\ Product \quad (46)$$

4.2.3.3 Separation and purification

The separation section depends on the products obtained from the FT reactor. In previous section 4.2.3.2, two modes of operation are defined resulting in two different product distributions. Therefore, this section is structured in two parts: In section 4.2.3.3.1, the separation and wax hydro-treatment sections for the LTFT products are presented and in section 4.2.3.3.2, the purification of HTFT products is presented.

4.2.3.3.1 Separation and purification of LTFT products.

The LTFT reactor produces two outlet streams as presented in Figure S2. One liquid containing the waxes and another one in gas phase, composed by the rest of components. The fractions obtained in the gas stream from the LTFT reactor need to be separated since diesel and gasoline are desired to be obtained as purified products from the plant. The outlet stream of the reactor is composed by the organic fractions generated and water. The separation is presented in Figure 6 and it is carried out by a flash, a three phase separator and a distillation column [67, 68].

Flash-5 separates the lightest components (H_2, CO, CO_2 and C1-C2 fraction) from the other LTFT reactor products. The separation efficiency is assumed to be 1 and it is carry out by cooling down the reactor outlet stream until 303K. The gas stream composition is complex and further separation is not preferred since it involves larger costs

and the stream can be used as substitute for the biogas in the burner of the reformer. It saves the biogas raw material used for heating the burner.

After Flash-5, the liquid products are sent to a three-phase separator, which may work at different pressures depending on the gas-liquid equilibrium [69-71]. This case works at atmospheric pressure to allow for LPG recovery from the gas fraction. The pressure reduction is performed by means of Valve-1. Furthermore, two liquid streams are also obtained from the three-phase separator: One of organic components (Gasoline and Diesel) and another of water, see Figure 6.

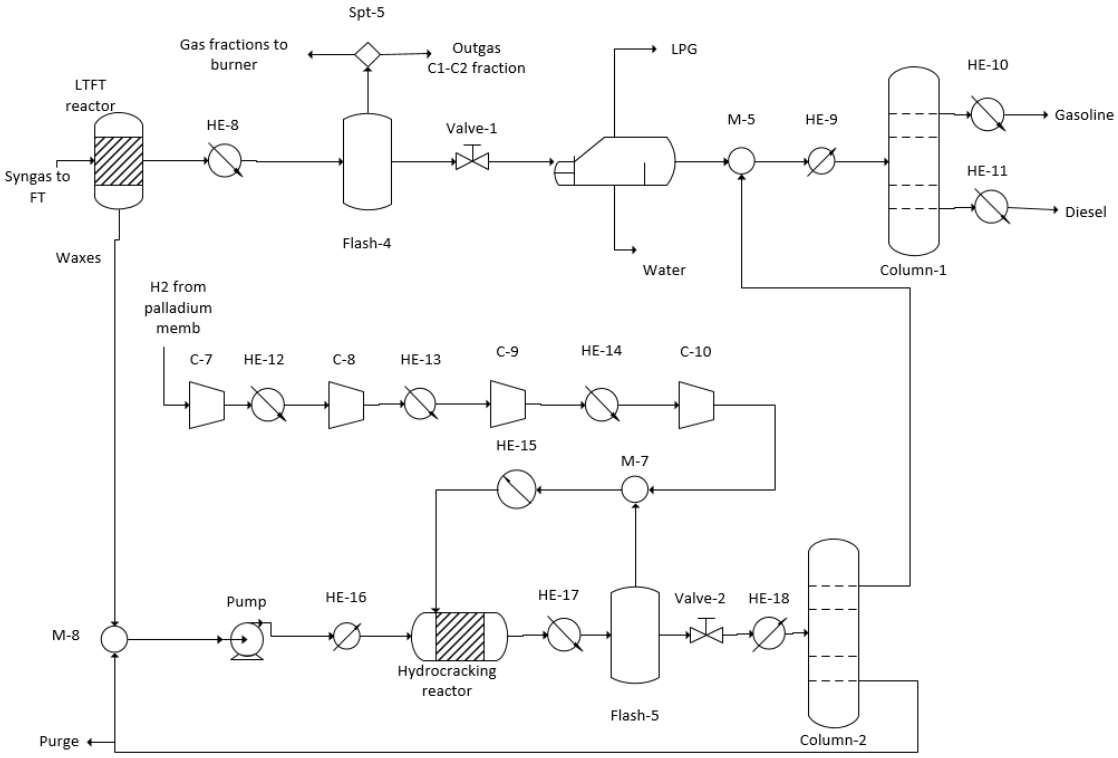

Figure 6. Separation, purification and wax recovery.

The water stream is sent to treatment and the rest of hydrocarbons go to the next stage of purification. The two liquid fractions are separated in a distillation system. The distillation tower for the oil mixture, Column-1, operates at 120ºC for the top light fractions, gasoline, and 250ºC for the heavier ones, diesel.

Apart from the diesel separated in the outlet gas stream of the LTFT reactor, the liquid wax produced in the LTFT reactor can also be recovered to enhance the production of diesel and gasoline. The wax reacts with hydrogen in a hydrocracker. Hydrocracking reactor works at 140 bar and a range of temperatures between 570 K and 670 K is assumed [72, 73]. Therefore, the hydrogen previously separated by a palladium membrane needs to be compressed up to the hydrocracker pressure and the wax is also pumped. The conversion and the selectivity to diesel is dependent on the temperature following eq. (47) and (48) [67, 73]:

$$X_{Hydro_{react}} = 0.000185714 \cdot \left(T_{Hydro_{reactor}}\right)^2 - 0.128829 \cdot T_{Hydro_{reactor}} + 22.6931 \quad (47)$$

$$S_{Diesel} = -0.00014286 \cdot \left(T_{Hydro_{reactor}}\right)^2 + 0.099514 \cdot T_{Hydro_{reactor}} - 16.383 \quad (48)$$

The input of hydrogen and heavy fraction to the reactor are modelled as from Eq. (49) to (52). It is assumed that the hydrogen that exits the reactor is 600 ft^3 per bbl of products, which represents around 7.5 % of the total hydrogen fed in the hydrocracker [67, 73, 74].

$$fc(Diesel, Hydro\ reactor, HE17) = X_{Wax} \cdot S_{Diesel} \cdot mass_{Hydro} \quad (49)$$

$$fc(Gasoline, Hydro\ reactor, HE17) = X_{Wax} \cdot (1 - S_{Diesel}) \cdot mass_{Hydro} \quad (50)$$

$$fc(Heavy,\ Hydro\ reactor, HE17) = (1 - X_{Wax}) \cdot mass_{Hydro} \quad (51)$$

$$fc(H_2,\ Hydro\ reactor, HE17) = 0.15 \cdot mass_{Hydro} \quad (52)$$

The products obtained from the reactor are separated in Flash-6 where hydrogen is recovered in the gas stream and sent back to the hydrocracker. The other products are sent to a distillation column. Column-2 separates diesel and gasoline from wax fractions. The distillation is carried out at atmospheric pressure. The feed pressure is reduced by mean of Valve 2. The temperature given by the light fractions in the top of the tower is 220 ^oC and in the bottom the wax is recovered at 300 ^oC. The light fractions composed by diesel and gasoline are sent to the mixer Mix-7 where they are separated from each other in Column-1.

4.2.3.3.2 Separation and purification of HTFT products

Products from the HTFT reactor are obtained in the same outlet [57, 58]. The stream is composed by different organic fractions and water that need to be separated. The separation is carried out by a successive flash, three phase separator and distillation column as it can be seen in Figure 7.

Each of the units is modelled as presented in section 4.2.3.3.1. Flash-7 works at 30 bar and 303 K, separating H_2, CO, CO_2 and C1-C2 fractions in the gas stream. The three phase separator works at atmospheric pressure, removing LPG and Water from the rest of organics liquids. Finally, a distillation column (Column-3) is used to separate and purify Diesel and Gasoline fractions.

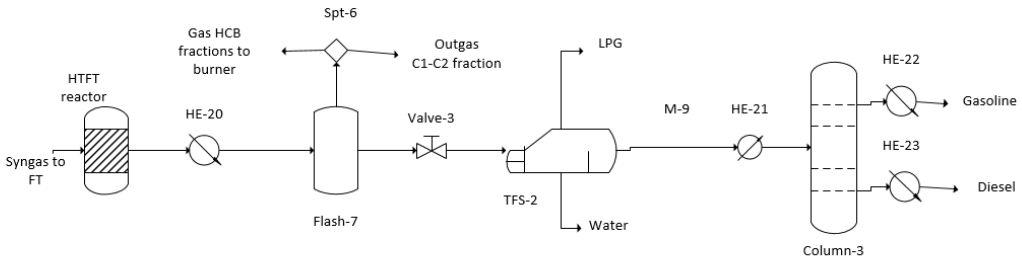

Figure 7. Separation and purification of HTFT products.

4.2.3.4 Solution procedure.

The integration and process design problem defined in this section is optimized in order to maximize the profit of the process. The MINLP problem has been divided in two NLP sub-problems, for each reactor mode of operation.

Five objective functions, eqs. (53) to (57), are defined in order to evaluate the weight of each product on the final result and if the biogas fed as fuel has any influence on the final objective function. Eq. (53) includes the profit generated by all the products and the cost of biogas as a methane source in the burner. In eq. (54) the price of the biogas sent to the burner is not included. Eq. (55) is similar to eq. (53) but the price of diesel is not included. The same sensitivity analysis is performed in eq. (56), where the price of gasoline is not included, or in eq. (57), where butane price is not included. The values for the prices involved in the objective function for O_2, CO_2, and utilities are the same that defined in section 4.2.2.4. The products are assumed to have a price of \$1.7/gal for crude gasoline, \$1.9/gal for crude diesel [75] and \$580 per tonne for LPG [76].

$$Profit = C_{gasoline}F_{gasoline} + C_{diesel}F_{diesel} + C_{LPG}F_{LPG} - C_{elec}\sum_{i\epsilon Compressors} W_i - C_{CH_4}\sum_{i\epsilon CH_4 inlets} F_{CH_4} - C_{O_2}F_{O_2' Triref'} - C_{CO_2}\sum_{i\epsilon CO_2 inlets} F_{CO_2} - C_q\sum_{j\epsilon Q_{heat}} Q + C_{c-w}\sum_{k\epsilon Q_{refrig}} Q - C_{H_2S}F_{H_2S} - C_{H2O}F_{H2O} \quad (53)$$

$$Profit = C_{gasoline}F_{gasoline} + C_{diesel}F_{diesel} + C_{LPG}F_{LPG} - C_{elec}\sum_{i\epsilon Compressors} W_i - C_{O_2}F_{O_2' Triref'} - C_{CO_2}\sum_{i\epsilon CO_2 inlets} F_{CO_2} - C_q\sum_{j\epsilon Q_{heat}} Q + C_{c-w}\sum_{k\epsilon Q_{refrig}} Q - C_{H_2S}F_{H_2S} - C_{H2O}F_{H2O} \quad (54)$$

$$profit = C_{gasoline}F_{gasoline} + C_{LPG}F_{LPG} - C_{elec}\sum_{i\epsilon Compressors} W_i - C_{CH_4}\sum_{i\epsilon CH_4 inlets} F_{CH_4} - C_{O_2}F_{O_2' Triref'} - C_{CO_2}\sum_{i\epsilon CO_2 inlets} F_{CO_2} - C_q\sum_{j\epsilon Q_{heat}} Q + C_{c-w}\sum_{k\epsilon Q_{refrig}} Q - C_{H_2S}F_{H_2S} - C_{H2O}F_{H2O} \quad (55)$$

$$profit = C_{diesel}F_{diesel} + C_{LPG}F_{LPG} - C_{elec}\sum_{i\epsilon Compressors} W_i - C_{CH_4}\sum_{i\epsilon CH_4 inlets} F_{CH_4} - C_{O_2}F_{O_2' Triref'} - C_{CO_2}\sum_{i\epsilon CO_2 inlets} F_{CO_2} - C_q\sum_{j\epsilon Q_{heat}} Q + C_{c-w}\sum_{k\epsilon Q_{refrig}} Q - C_{H_2S}F_{H_2S} - C_{H2O}F_{H2O} \quad (56)$$

$$profit = C_{gasoline}F_{gasoline} + C_{diesel}F_{diesel} - C_{elec}\sum_{i\epsilon Compressors} W_i - C_{CH_4}\sum_{i\epsilon CH_4 inlets} F_{CH_4} - C_{O_2}F_{O_2'Triref'} - C_{CO_2}\sum_{i\epsilon CO_2 inlets} F_{CO_2} - C_q\sum_{j\epsilon Q_{heat}} Q + C_{c-w}\sum_{k\epsilon Q_{refrig}} Q - C_{H_2S}F_{H_2S} - C_{H2O}F_{H2O} \quad (57)$$

Each objective function of the integration problem is set independently as an NLP problem with over 2,500 variables and 2,000 equations for the LTFT process. Meanwhile for the HTFT process the NLP problem is composed of 1,700 equations and 2,000 variables. Both modes of operation are modelled in GAMS and solved using a multi-start approach with CONOPT 3.0. After the process optimization, a heat integration is performed externally defining the heat exchanger network. Finally, an economic evaluation is accomplished to estimate the production cost of diesel and gasoline and the investment required for the plant. They are performed from the optimization that uses eq. (54) as objective function for HTFT and LTFT processes.

4.2.4 RESULTS

The results of the two studies performed are presented in this section. In section 4.2.4.1 for the parametric optimization of biogas to syngas via tri-reforming and in section 4.2.4.2 for the process design problem of biogas to FT fuels.

4.2.4.1. Parametric optimization of syngas production.

The results for the parametric optimization of biogas to syngas via tri-reforming are presented in this section. Three H_2:CO ratios are analysed according to the further use of the syngas: methanol (2.5:1), ethanol (1:1) or FT-fuels (1.7:1) production. Figure 8 presents the values of the objective function, eq. (14), under different O_2:Biogas ratios. The maximum profit obtained per 10 mol/s of biogas fed in the process is \$0.015/s when syngas is applied to methanol production, \$0.007/s when it is applied to ethanol and \$0.016/s to FT synthesis. The optimal values are achieved when the O_2:biogas ratio feed in the process is 0.275 for methanol production, 0.035 for ethanol and 0.275 for FT fuels production. Attending to these requirements of oxygen, the tri-reforming is preferred than a combined steam and dry reforming even when the oxygen to be fed supposes a cost. As it has been also presented by previous authors [18,33], tri-reforming is the best technology not only for the processing of biogas into syngas for methanol production, but also for other products such as ethanol, DME and FT fuels. Thus, this technology is recommended to be used versus the other reforming technologies presented.

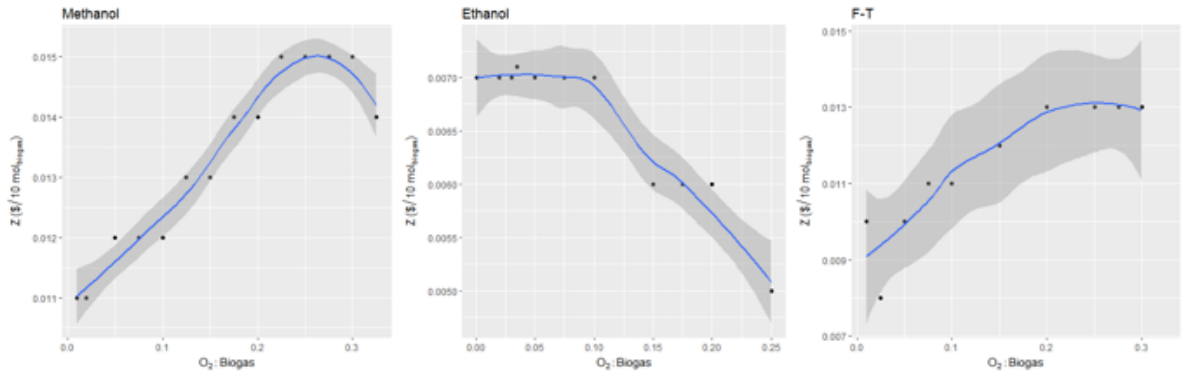

Figure 8. Parametric optimization results for the objective function.

However, O_2:biogas ratio does not only influences the profit but also the optimal composition of the biogas as well as the process operating conditions. Figure 9 presents the influence of O_2:biogas ratio on the biogas composition in the process feed and Table 2 summarizes the compositions when the largest credit is obtained. It can be seen that as the O_2:biogas ratio in the tri-reformer increases, the CO_2 composition in the biogas decreases. At small O_2:biogas ratios, the oxygen of CO_2 is used as a substitute of O_2 in the reformer, allowing a larger production of syngas. The behavior of the methane content in the biogas as a function of the O_2:biogas ratio used is opposite to the behavior of the CO_2 content, showing an increase of methane for larger O_2:biogas ratios. Meanwhile the water content shows a step just before achieving the optimal for the three syngas products studied. The water content always takes the minimum value when the profitability optimum is achieved since no further value is assumed to this product. Methane is preferred since it contains more atoms of hydrogen per mol.

In Table 2, it can be seen that for methanol and FT production the biogas composition obtained is the same. In both cases, the maximum methane content is desired. However, for ethanol production a different biogas composition is suggested since the ratio H_2:CO required is not that large. Methane is taken as a source of hydrogen being larger quantities required for methanol and FT than for ethanol.

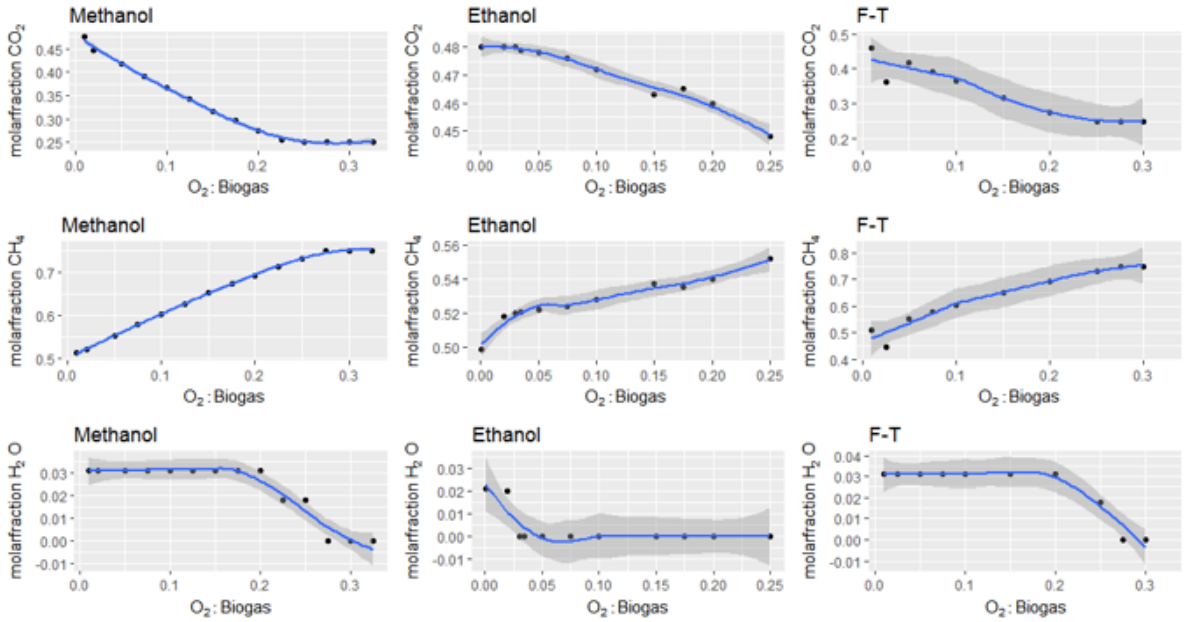

Figure 9. Influence of O_2:Biogas ratio on biogas composition.

Table 2. Global optimal composition of biogas.

Component	Methanol (H_2:CO=2.5)	Ethanol (H_2:CO=1)	F-T (H_2:CO=1.7)
CO_2	0.25	0.479	0.25
CH_4	0.75	0.521	0.75
H_2O	$1•10^{-10}$	$1•10^{-10}$	$1•10^{-10}$
N_2	$1•10^{-4}$	$1•10^{-4}$	$1•10^{-4}$
SH_2	$2•10^{-5}$	$2•10^{-5}$	$2•10^{-5}$
NH_3	$1•10^{-6}$	$1•10^{-6}$	$1•10^{-6}$

Despite the fact that the same compositions of biogas are obtained for methanol and FT syngas production, the process conditions are different, as presented in Table 3. To achieve the H_2:CO ratio required for methanol and FT production, another source of hydrogen is required. It can be seen in Table 3 that the second source of hydrogen, after adjusting the composition, is the addition of water in the WGS reactor of the syngas composition adjustment stage. It is preferred to add water after the reforming than before. For all the cases, the addition of steam and CO_2 before the reforming is not selected. The reformer works at 1273 K for methanol and FT production and 1231 K for ethanol production in the optimum of each case. Contrary to the larger temperature in the production of methanol and FT, the biogas required to be burned is lower because energy is produced from the POX of the biogas involved in the process. In Figure 10 it is shown how the O_2:biogas ratio modifies the reformer operating conditions: For methanol, the biogas sent to the burner decreases until the optimal is achieved and then it increases again and the temperature decreases for O_2:Biogas ratios larger than 0.275. For ethanol production, a slight decrease is observed in the amount of biogas sent to burner when the O_2:biogas ratio increases; meanwhile the temperature shows a minimal for O_2:Biogas ratio of 0.1. For FT production, the biogas sent to burner behaves similar than for methanol production and the temperature achieved at the reformer is always the maximum allowed.

The WGS reactor requires more water for methanol production, 0.21 mol per mol of biogas, than for FT fuels production, 0.06 mol per mol of biogas when the process works in its optimum due to the larger H_2 to CO ration required; meanwhile for ethanol, the WGS reactor does not need to be included in the process. The analysis under different O_2:biogas ratios is also shown in Figure 10. It can be seen that for methanol production the steam fed to the WGS reactor decreases when the O_2:biogas ratio increases and the temperature achieved is always the maximum since hydrogen generation is promoted. However, for FT and ethanol production a similar behavior is observed, the use of a WGS reactor is never required.

Table 3. Optimal process variables.

Process variable	**Methanol**	**Ethanol**	**F-T**
Biogas sent to burner (mol/mol Biogas fed to process)	0.092	0.302	0.092
O_2:Biogas	0.275	0.035	0.275
$T_{reformer}$ (K)	1273	1231	1273
Fraction to WGS	1	0	1
Fraction to PSA CO_2	0.66	0	0
H_2O WGS (mol/mol Biogas fed in the process)	0.206	0	0.062
Heat required (kJ/mol Biogas fed in the process)	70.4	51.9	63.9
Refrig required (kJ/mol Biogas fed in the process)	105	71.2	91.1

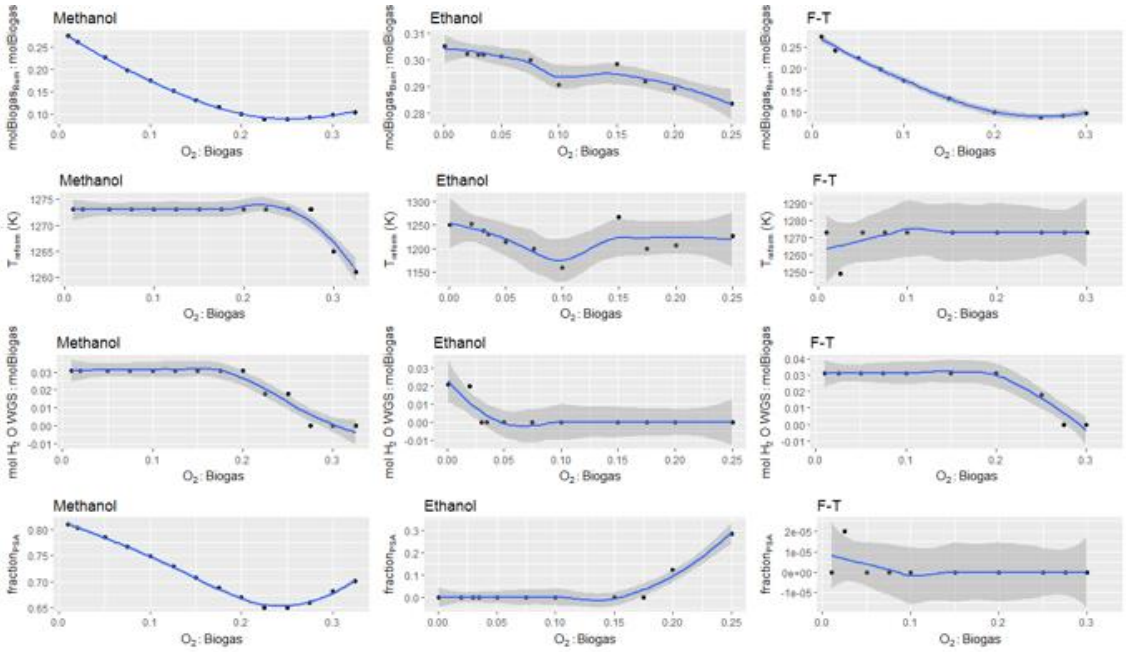

Figure 10. Effect of O_2:Biogas ratio on process variables.

In Table 3 the fraction of flow sent to PSA membranes for CO_2 removal is also presented. It can be seen that only methanol production requires PSA treatment, being necessary to treat 66% of the syngas obtained when the credit obtained by eq. (14) is maximized. In Figure 10 it can also be seen that for methanol production, the flow fraction sent to the PSA decreases before the optimal and then increases. For FT fuels, it is never required to use the PSA unit and for ethanol it is only required for O_2:biogas ratios larger than 0.175.

The utilities consumption is also presented in Table 3. It can be seen that the production of syngas when intended to produce ethanol requires the lowest consumption of utilities. In the production of ethanol the reformer works at lower temperature and no WGS reactor is required. Thus, less heat and refrigeration are required. Opposite, the production of syngas for methanol requires the largest quantities of steam in the WGS reactor. Therefore, more heat and refrigeration are involved than in the other two cases.

4.2.4.2 Results of optimal biogas to F-T Diesel production processes

4.2.4.2.1 Process operation

The results for the optimal operation of FT production process using biogas as raw material are presented in this section. The results of the two modes of operation, HTFT and LTFT, are compared. The results for the economic optimization are presented in Table 4 comparing the five objective functions defined in section 4.2.3.4. It can be seen that LTFT provides larger profitability than the HTFT process. Table 4 also presents the contribution of each of the terms and a sensibility analysis using the definitions from eq. (54) to (57).

Table 4. Economic Results for optimal HTFT and LTFT processes.

Objective function		HTFT	LTFT
Z ($/mol of Biogas fed) Eq. (53)		$7•10^{-4}$	$2.2•10^{-3}$
	Diesel ($/mol of Biogas fed)	$1•10^{-4}$	$1.8•10^{-3}$
	Gasoline ($/mol of Biogas fed)	$1•10^{-3}$	$1.4•10^{-3}$
	Butane ($/mol of Biogas fed)	$9•10^{-4}$	$4•10^{-4}$
	Electricity ($/mol of Biogas fed)	$-4•10^{-4}$	$-5•10^{-4}$
	Steam ($/mol of Biogas fed)	$-6•10^{-4}$	$-6•10^{-4}$
	Ref. water ($/mol of Biogas fed)	$-3•10^{-4}$	$-3•10^{-4}$
Z ($/mol of Biogas fed) Eq. (54)		$7•10^{-4}$	$2.3•10^{-3}$
	Diesel ($/mol of Biogas fed)	$1•10^{-4}$	$1.8•10^{-3}$
	Gasoline ($/mol of Biogas fed)	$1•10^{-3}$	$1.5•10^{-3}$
	Butane ($/mol of Biogas fed)	$9•10^{-4}$	$4•10^{-4}$
	Electricity ($/mol of Biogas fed)	$-4•10^{-4}$	$-5•10^{-4}$
	Steam ($/mol of Biogas fed)	$-6•10^{-4}$	$-6•10^{-4}$
	Ref. water ($/mol of Biogas fed)	$-3•10^{-4}$	$-3•10^{-4}$
Z ($/10mol of Biogas fed) Eq. (55)		$6•10^{-4}$	$8•10^{-4}$
	Diesel ($/mol of Biogas fed)	0	0
	Gasoline ($/mol of Biogas fed)	$1•10^{-3}$	$1.5•10^{-3}$
	Butane ($/mol of Biogas fed)	$9•10^{-4}$	$6•10^{-4}$
	Electricity ($/mol of Biogas fed)	$-4•10^{-4}$	$-4•10^{-4}$
	Steam ($/mol of Biogas fed)	$-6•10^{-4}$	$-6•10^{-4}$
	Ref. water ($/mol of Biogas fed)	$-3•10^{-4}$	$-3•10^{-4}$
Z ($/10mol of Biogas fed) Eq. (56)		$-2•10^{-4}$	$9•10^{-4}$
	Diesel ($/mol of Biogas fed)	$1•10^{-4}$	$1.9•10^{-3}$
	Gasoline ($/mol of Biogas fed)	0	0
	Butane ($/mol of Biogas fed)	$8•10^{-4}$	$4•10^{-4}$
	Electricity ($/mol of Biogas fed)	$-4•10^{-4}$	$-6•10^{-4}$
	Steam ($/mol of Biogas fed)	$-5•10^{-4}$	$-6•10^{-4}$
	Ref. water ($/mol of Biogas fed)	$-2•10^{-4}$	$-3•10^{-4}$
Z ($/10mol of Biogas fed) Eq. (57)		$-2•10^{-4}$	$1.9•10^{-3}$
	Diesel ($/mol of Biogas fed)	$1•10^{-4}$	$2•10^{-3}$
	Gasoline ($/mol of Biogas fed)	$9•10^{-4}$	$1.4•10^{-3}$
	Butane ($/mol of Biogas fed)	0	0
	Electricity ($/mol of Biogas fed)	$-4•10^{-4}$	$6•10^{-4}$
	Steam ($/mol of Biogas fed)	$-5•10^{-4}$	$6•10^{-4}$
	Ref. water ($/mol of Biogas fed)	$-3•10^{-4}$	$3•10^{-4}$

In Table 4 it can be also seen that the optimal value of the objective function is not modified for the HTFT process when the cost of methane contained in the biogas is included. The amount of Outgas produced in the HTFT is large enough and no requirement of extra biogas supply is required as energy source. For LTFT process, a small change is observed from the result of the objective function, eq. (53), to the one without methane, eq. (54).

Evaluating the contribution of each component to the final profit, the following observations are found: Gasoline and butane are the two components that generate more added value to the HTFT process. The maximum profit is never positive when one of both is not included as valuable product in the objective function since the amount produced is larger than that of diesel. For the LTFT process, the diesel is the one that provides the largest profit and butane the lowest. The lower temperatures achieved in the FT reactor promote the generation of large amount of products with larger chains such as diesel and waxes.

The contributions of each component also modify the biogas composition and process operating parameters. The optimal biogas composition is presented in Table 5 and the main operating conditions of the process are presented in Table 6. It can be seen that larger amounts of methane are produced in the LTFT mode compared to the HTFT one. This is due to the need for larger hydrogen quantities required in the process. Instead a lower H_2:CO ratio is observed at the entrance of LTFT reactor (see Table 6), more hydrogen is required in LTFT process to recover the wax via hydro-cracking. Opposite to the methane composition, the CO_2 shows lower concentration for LTFT and the rest of the components achieve their minimum value.

Table 5. Optimal biogas composition for HTFT and LTFT processes.

Component	HTFT	LTFT
Methane	0.622	0.69
CO_2	0.378	0.31
SH_2	$2•10^{-5}$	$2•10^{-5}$
N_2	$1•10^{-4}$	$1•10^{-4}$
H_2O	$1•10^{-10}$	$1•10^{-10}$
NH_3	$1•10^{-6}$	$1•10^{-6}$

The results of the main operating parameters for the optimization of both processes following eq. (53) are presented in Table 6. It can be seen that tri-reforming is preferred than a combined dry and steam reforming as it has been suggested in previous works for syngas [34] or methanol production [18]. Larger amounts of oxygen are required for the LTFT compared to the HTFT process that allow achieving also higher temperatures at the reactor. However, the conversion in the reformer is larger for the HTFT process since lower quantities of methane are desired to be contained in the biogas fed.

The cleaning section of the syngas does not require a WGS reactor to generate large quantities of H_2 as it H_2:CO ratios of 1 are aimed (ethanol production in section 4.2.4.1). However, CO_2 removal by means of PSA membranes is desired not only because of ensuring a CO_2 concentration lower than the maximum allowed, but also to improve the FT reactor efficiency since large quantities of CO and H_2 are ensured. After the membrane, a 32% of the syngas needs to be sent to a palladium membrane where hydrogen is recovered in the LTFT process.

The results obtained for the parameters of the FT reactor in Table 6 show that HTFT reactor requires to operate with an H_2:CO ratio larger than LTFT. The rest of the parameters are in agreement with the model defined. Larger temperatures results in lower chain lengths for the HTFT reactor. The products obtained from the HTFT reactor

contain higher quantities of light products such as methane and LPG and low compositions of diesel and waxes. Opposite, the LTFT reactor promotes the generation of products with larger chains. The fraction with higher production corresponds to gasoline (0.036 mol per mol of biogas fed in the process). Furthermore, LTFT reactor also generates waxes that are treated to improve the process profitability and the gasoline production up to 0.037 mol per mol of biogas fed in the process and the diesel production changes from 0.019 to 0.021 mol/mol of biogas fed. The hydrocracking of the waxes is performed at 623 K, resulting in a conversion of 0.567 and a selectivity to diesel of 76%.

The optimization based on eq. (53) is considered the most typical since credit can be obtained from selling all the products. However, by performing the sensitivity analysis by deleting the credit from each of the products, different results are obtained. The results when any of the products are not included in the objective function as presented in Table 7. The two first columns of Table 7 show the parameters of the optimal solution when the biogas fed to the burner is considered as a valuable product since the methane can be used for other facilities. As a result, it can be seen that no biogas is suggested to be burned in the reformer. All the fuel come from the outgas. The rest of the process parameters are not affected for the HTFT process and are slightly affected for the LTFT process. The main changes observed are a decrease of the fraction of hydrogen separated in the palladium membrane and slight increase in the FT-reactor temperature and H_2:CO ratio. The hydrocracking reactor works at lower temperature, resulting in lower conversions. However, the products obtained are roughly the same.

Based on the sensitivity analysis performed for the products, it can be seen in Table 7 that the oxygen required in the tri-reformer decreases in HTFT and LTFT processes when gasoline is not included in the objective function, eq. (56). The reformer also shows differences in the operating parameters when diesel is not included in the objective function, requiring to work at lower temperatures and resulting in larger conversions. Once the syngas is produced, the tune-up and cleaning section never requires the use of a WGS reactor for hydrogen generation in the HTFT process. PSA membranes are required to capture the CO_2 when butane (eq. (57)) and gasoline (eq. (56)) are not included in the objective function. The next stage in the process is the FT reactor, which also modifies its operating conditions in order to promote the generation of fuels defined in the objective function. The reactor does not show changes of temperature when it works in HTFT mode (the maximum reactor temperature is always achieved), using the H_2:CO ratio to promote the generation of the products desired. However, in LTFT mode the generation of products defined by the objective functions is given by modifying both parameters, the temperature and the H_2:CO ratio. In both modes of operation, the H_2:CO ratio is always larger when diesel is not included in the objective function, helping to reduce the length of the chain. The following stage in the LTFT mode is the recovery based on hydro-treatment. It can be seen in Table 7 that the temperatures are larger when components with larger chains are not included in the objective function. For example, the exclusion of diesel, eq. (55), requires large temperatures, not only to have waxes conversion but also to obtain a low selectivity to diesel and promote gasoline production.

Table 6. Main operating parameters for economic optimization, eq. (53).

OPERATING VARIABLE	HTFT	LTFT
Dry reforming reactor temperature (K)	1234	1273
Biogas burned (mol /mol Biogas fed in the process)	0.176	0.0376
O_2 fed in tri-reforming (mol /mol Biogas fed in the process)	0.1434	0.2715
X_{CH4}	0.92	0.9
Fraction sent to WGS	0	0
CO_2 removed in PSA per mol of biogas fed in the process	0.022	0.018
Fraction sent to Palladium membrane	-	0.317
$T_{SynthesisFT}$ (K)	590	507.3
H_2:CO in synthesis reactor	1.203	1
CO_2 in synthesis reactor (% vol)	0.05%	0.9%
α	0.575	0.844
$T_{Hydrothermal}$ (K)	-	623
X_{Wax}	-	0.567
$S_{Wax\ to\ diesel}$	-	0.759
Fraction of outgas sent to burner	0.003	0.844
Outgas produced from reactor (mol /mol Biogas fed in the process)	0.468	0.264
Butane produced in the process (mol/mol Biogas fed in the process)	0.058	0.024
Gasoline produced (mol /mol Biogas fed in the process)	0.025	0.037
Diesel produced (mol /mol Biogas fed in the process)	0.001	0.022
Cooling water (kg/mol of biogas fed in the process)	4.69	5.73
Steam required (kg/mol of biogas fed in the process)	0	0.0025
Electricity required (kW/mol of biogas fed in the process)	265.9	359.1

Table 7. Main operating variables results for optimal solution of eqs. (54), (55), (56) and (57).

OPERATING VARIABLE	HTFT eq. (54)	LTFT eq. (54)	HTFT eq. (55)	LTFT eq. (55)	HTFT eq. (56)	LTFT eq. (56)	HTFT eq. (57)	LTFT eq. (57)
T dry reforming (K)	1234	1273	1245	1242	1253	1273	1273	1273
Biogas burned (mol/mol of Biogas)	0	0	0.167	0.1188	0	0.0455	0.1798	0.0495
O_2 in tri-reforming	0.1434	0.275	0.1526	0.163	0.1402	0.275	0.055	0.275
X_{CH4} reformer	0.92	0.9	0.911	0.917	0.936	0.9	0.9	0.9
Fraction sent to WGS	0	0	0	0	0	0	0	0
CO_2 removed in PSA per mol of biogas fed in the process	0.022	0	0	0	0.019	0	0.0039	0
Fraction sent to Palladium memb.	-	0.172	-	0	-	0.317	-	0.317
$T_{SynthesisFT}$ (K)	590	509	590	519	590	508	590	507
H_2:CO in synthesis reactor	1.203	1.212	1.24	1.2447	1.202	1	1.203	1
CO_2 in synthesis reactor (%vol)	0.05	1.5	0.8	1	0.05	0.9	0.07	0.9
α	0.575	0.805	0.573	0.774	0.575	0.825	0.575	0.825
$T_{Hydrothermal}$ (K)	-	654	-	673	-	647	-	623
X_{Wax} Hydrotreatment	-	0.567	-	0.876	-	0.491	-	0.567
S_{Diesel}	-	0.795	-	0.565	-	0.85	-	0.795
Fraction of outgas sent to burner	0.594	0.401	0.012	0.898	0.595	0.427	0.991	0.391
Outgas produced from reactor (mol per mol of biogas fed in the process)	0.4683	0.2979	0.4923	0.3217	0.472	0.2636	0.364	0.2636
Butane produced in the process (mol per mol of biogas fed in the process)	0.0578	0.0284	0.0584	0.0343	0.0544	0.0235	0.0449	0.0235
Gasoline produced (mol per mol of biogas fed in the process)	0.0254	0.0378	0.0255	0.0401	0.0257	0.0354	0.0198	0.0342
Diesel produced (mol per mol of biogas fed in the process)	0.0013	0.0212	0.0013	0.0161	0.0013	0.0243	0.001	0.024

4.2.4.2.2 Economic evaluation.

An economic evaluation of the two plants for HTFT and LTFT process has been carried out in order to estimate the main costs of the plant and the final price that the fuel can reach following the economic optimization variables achieved in previous optimization. The plant size has been designed to be fed with a flow of 12 M m^3/y of biogas, which is a tenth of the maximum potential biogas in the region of Madrid [15]. Despite the population density in the region is large (805 inhabitants/km^2) and the waste generation is concentrated, the region is small, 8,030 km^2 [78] and larger plants can be designed for other locations. Therefore, a scale-up study is also presented in this section.

Investment Cost

The factorial method is used to estimate the investment cost of the facility [79]. It is based on the cost estimation for the units involved in the process that is performed as follows:

- H_2S iron foam has been estimated following the cost per kg of SH_2 removed [15]. A cost of $260 per year is estimated for the optimal composition of biogas obtained when 12 M m^3/y of biogas are processed.
- The cost of hydrocarbon and CO_2 removal beds has been estimated considering two components. First, the cost of the vessel using the Matche's cost estimator [80] and, second, the cost of the molecular sieves following the correlations presented by Almena and Martin [81].
- Flash separators and tri-phase separator have been estimated using the cost of the vessel given by the weight of the metal [81].
- The cost of pump and compressors is estimated as a function of the power consumption required per unit [81].
- Fired heater cost has been estimated as a cylindrical fired heater, with the heat requirements given by the optimization and using Matche correlations [80].
- Heat exchangers cost, that also includes FT and hydro-treatment reactors and evaporator and condenser from distillation columns, has been computed by the heat exchanger area following the correlations presented in Almena and Martin [81].
- Distillation columns cost are estimated considering the cost of the vessel and the trays as presented in Almena and Martin [81]. The number of trays is computed from the optimization results and using short-cut methods with an efficiency of 80% per tray. The distillation column of HTFT process is composed of 10 trays, the distillation column of LTFT that separates gasoline and diesel is composed of 13 trays and the distillation column after hydro-treatment is composed of 12 trays.

Figure 11 shows the contribution to the investment cost per type of unit. It can be seen that the cost involved in heat exchanger processes is larger than the other equipment required in both HTFT and LTFT processes.

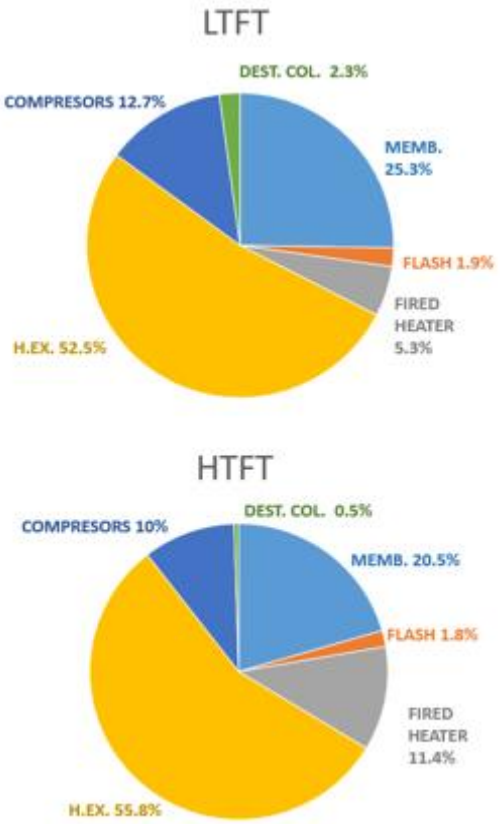

Figure 11. Unit Cost distribution.

Using the factorial method [79] for plants that process fluids and considering a feed of 12 M m^3/y of biogas, the capital cost of the plant adds up to $8 M for the HTFT plant and $19 M for the LTFT plant.

Production Cost

Production Cost is estimated considering maintenance, labor, administration and management, other expenses and units amortization, except for the membranes, which must be replaced annually. All these items are estimated based on Silla´s method [82]. The cost of the raw materials and utilities are computed using the prices presented in the description of the objective function. The distribution of costs per year for HTFT and LTFT plants are shown in Figure 12. It can be seen that they are highly determined by the equipment cost, which represents more than 60% of the production costs in both cases.

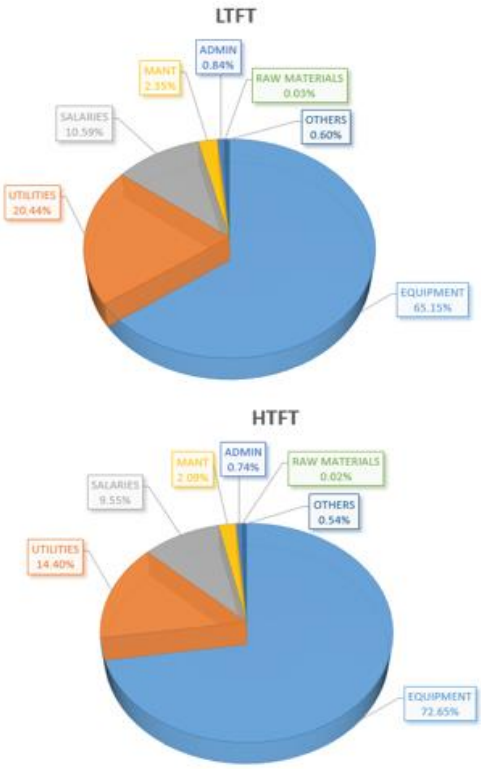

Figure 12. Cost distribution.

The costs are distributed between the production of LPG, gasoline and diesel maintaining the current ratios of prices per kg. The price of each component is computed using a factor as presented in eq. (58). Where $\$_{avg}$ is the average price, which is computed following eq. (59).

$$factor_i = \frac{\$_i}{\$_{avg}} \tag{58}$$

$$\$_{avg} = \frac{\$_{LPG}+\$_{gasoline}+\$_{diesel}}{3} \tag{59}$$

Thus, for the HTFT process the production cost of LPG is \$610/ton, for gasoline a production cost of \$2.57/gal is obtained and for diesel it is \$3.02/gal. The prices with this technology are close but still higher than the current selling price: \$580/ton for LPG, \$2.5/gal for gasoline and \$2.9/gal for diesel. Therefore, the production of the fuels following the current process and the size designed for a 10% of potential biogas is not profitable.

The LTFT process shows lower production costs. A production cost of \$520/ton is obtained for LPG. For gasoline a production cost of \$1.25/gal is obtained and for diesel a value of \$1.67/gal results. The LTFT process reduces the production costs, resulting in a more competitive process with prices lower than the current selling price but not much lower than the current production cost, which is estimated to be \$1.7/gal for gasoline and \$1.9/gal for diesel (taxes, distribution and marketing costs have been discounted from [62]). Thus, this current process might be competitive with current prices if a taxes to promote sustainability are defined.

The current processes can be also evaluated with other processes that produce biodiesel from wastes. A production cost of €0.31/gal of diesel was obtained for a plant that produces 90 Mgal of diesel [83]. To allow the production of such as diesel quantities, the processes need to be scale-up and the cost of the anaerobic digester needs to be included in the economic analysis of both processes. The cost of anaerobic digester is computed as presented in [83]. The production prices of both modes of operation, HTFT and LTFT, with and without the cost of anaerobic digester are summarized in Figure 13. To produce 90 Mgal of fuels (diesel, gasoline and LPG), LTFT plant requires to treat 60 M m^3/y and HTFT requires 85 M m^3/y. As result, the average price of the fuels produced are $1.03/kg for LTFT and $1.8/kg for HTFT.

Focusing on diesel, the production prices obtained are $3.3/gal for LTFT and $5.4/gal for HTFT. Thus, the new processes are less competitive than the developed previously in [83] and the production costs are larger than the current selling price when the anaerobic digester cost is included in the CAPEX. Figure 13 also presents a scale-up study for the 4 processes proposed. A breakeven point is observed between LTFT and HTFT processes, showing that LTFT process is more profitable than HTFT for plants smaller than 450 Mm^3/y of biogas.

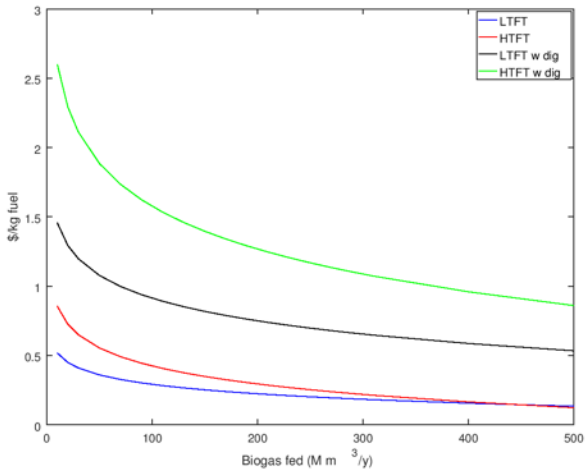

Figure 13 –Scale up of production costs for FT facilities.

A second comparison can be also performed with the FT process presented in [40]. In that work the process was not optimized and a selling price of $5.79/gal was obtained when the process was fed with 2,000 Nm^3/h, meanwhile a selling price of $2.06/gal when it is fed with 20,000 Nm^3/h. If we scale-up our results to that biogas fed, a selling price of $2.05/gal is obtained with the LTFT and $3.65/gal with the HTFT process when it is fed with 2,000 Nm^3/h. In the case of a feed of 20,000 Nm^3/h, our estimated selling prices will decrease up to $1.2/gal for LTFT process and $2.05/gal for the HTFT process. Therefore, instead of the selling prices are computed using different models, the differences obtained in the final are so different so that we can consider that one part is given thanks to the optimization of the process. However, the current work still has larger production cost than the work presented in [83], which is the recommended to be followed in the case of diesel want to be produced.

4.2.5 CONCLUSIONS

In this work, an optimization approach has been performed to evaluate the biogas tri-reforming for the production of different syngas ratios. As result, the work provides the optimal process conditions and optimal biogas composition for three different syngas applications. The optimization selects a biogas mainly composed of 52% of methane and 48% of CO_2 when syngas is later applied to ethanol production. Meanwhile for methanol and FT fuels production the biogas with the largest content of methane is selected, 75%. The largest H_2:CO ratio required for methanol is achieved by introducing more steam in a WGS reactor after the reformer. Apart from the WGS reactor, which is only required for the production of methanol and FT, a PSA system is also needed to capture the CO_2 when syngas is applied to methanol production.

The work is completed with a second section where the tri-reformer model is defined within a process integration problem for the production of FT fuels from biogas at high and low temperatures of operation. The integration did not only apply the biogas as raw material for the process, but it also used it as fuel or for the production of extra hydrogen in the reformer when it needs to be used in the hydro-treatment of the waxes. This hydrogen is endogenously generated in the process, avoiding the external demand and ethical issues because of the use of fossil based hydrogen as well as allowing the implementation of the LTFT plant in isolated locations. The study applied to a plant fed directly with biogas, considering it as a waste with zero cost and from a plant fed with wastes, which requires treatment via anaerobic digestion. For the plant fed with 12 MMm^3/y of biogas results in a production cost of \$3/gal for diesel via HTFT and \$1.7/gal via LTFT. The production cost obtained are larger than the current production cost of fuel but lower than the final selling price, in the case of LTFT process. Therefore, LTFT might become a sustainable solution if taxes promoting sustainability are implemented. In the case of the same plants (producing 12 MMm^3/y of biogas via anaerobic digestion) fed with wastes, the production costs increases up \$4.6/gal for LTFT and \$9/gal for HTFT, which are not profitable comparing with the current selling prices of diesel.

NOMENCLATURE

C_i: Cost of the material/product i.
Cp: Specific heat capacity at constant pressure (J/mol K)
fc(i,j,k): molar flow rate of component i, from unit j to k (mol/s)
$frac_i$: Mass fraction corresponding to the group of components defined in i.
F: Global molar flow rate (mol/s).
ΔH^0_{298K}: Reaction enthalpy at 298 K.
Hf_i: enthalpy of formation of component i (J/mol)
J: Set of components.
k_p: Equilibrium constant defined as ration between vapour pressures.
K_c: Polytrophic constant for compressors.
LHV_i: Low heating value of component i. (J/kg)
m_i: mass flow rate of component i (kg/s)
mol_i: mol of component i.
MW_i: Molar mass of component i (kg/kmol)
nc: Number of carbon atoms in the formula of a component.
nh: Number of hydrogen atoms in the formula of a component.
P_i: Partial pressure of component i (bar)
Q: Heat flux (J/s)

S_i: Selectivity to component i.
T: Temperature (K)
w_i: mass fraction of component i.
W: Electricity (W)
y_i: molar fraction of component i.
X_i: Conversion of component i.
Z: Profit ($/mol of biogas)
α: chain growth from Anderson-Schulz-Flory distribution.
η_c: Compressor efficiency.
$\$_i$: Price of component i.

REFERENCES

[1] Eurostat Waste statistics. 2017. Available in: http://ec.europa.eu/eurostat/statistics-explained/index.php?title=Waste_statistics Last acceded: May 2018.

[2] Masullo, A. Organic wastes management in a circular economy approach: Rebuilding the link between urban and rural areas. Ecological engineering; 2017, 101, 84-90.

[3] Stambasky, J. Introduction to EBA and the Circular Economy. 6th April 2016. EBA's Circular Economy Workshop. 2016. Available in: http://european-biogas.eu/members-only/presentations-reports/circular-economy-workshop/

[4] Ellen MacArthur Foundation. Towards the circular economy I. 2012. Available in: https://www.ellenmacarthurfoundation.org/assets/downloads/publications/Ellen-MacArthur-Foundation-Towards-the-Circular-Economy-vol.1.pdf

[5] Wellinger, A. Murphy, J. Baxter, D. The biogas handbook: Science, production and applications. Edt. Woodhead Publishing. 2013.

[6] Leon, E. Martin, M. Electricity production from manure based biogas. Energy Convers. Manage. 2016, 114, 89.

[7] Tippayawong, N. Thanompongchart,P. Biogas quality upgrade by simultaneous removal of CO2 and H2S in a packed column reactor. Energy. 2010, 35, 4531-4535.

[8] Ryckebosch, E. Drouillon, M. Vervaeren, H. Techniques for transformation of biogas to biomethane. Biomass and bioenergy. 2011, 35 1633-1645.

[9] Braga, L.B. Silveira, J.L. da Silva, M.E. Tuna, C.E. Marchin, E.B. Pedroso, D.T. Hydrogen production by biogas steam reforming: A technical, economic and ecological analysis. Renewable and sustainable Energy Reviews. 2013, 28, 166-173.

[10] Cipiti, F. Barbera, O. Briguglio, N. Giacoppo, G. Italiano, C. Vita, A. Design of a biogas steam reforming reactor: A modelling and experimental approach. International Journal of Hydrogen Energy. 2016, 41 (27), 11577-11583.

[11] Avraam, D.G. Halkides, T.I. Liguras, D.K. Bereketidou, O.A. Goula,M.A. An experimental and theoretical approach for the biogas steam reforming reaction. Int. J. Hydrogen Energy. 2010, 35, 9818-9827.

[12] Kolbitsch, P. Pfeifer, C. Hofbauer, H. Catalytic steam reforming of model biogas. Fuel. 2008, 87, 701-706.

[13] Araki, S. Hino, N. Mori, T. Hikazudani, S. Autothermal reforming of biogas over a monolithic catalyst. Jounal of Natural Gas Chemistry. 2010, 19, 477-481.

[14] Xuan, J. Leung, M.K.H. Leung, D.Y.C. Ni, M. Integrating chemical kinetics with CFD modelling for autothermal reforming of biogas. Int. J. Hydrogen Energy. 2009, 34, 9076-9086.

[15] Hernandez, B. Martin, M. Optimal Process operation for biogas reforming to methanol: effects of dry reforming and biogas composition. Ind. Eng. Chem. Res., 2016, 55 (23), 6677-6685.

[16] Lau, C.S. Tsolakis, A. Wyszynski, M.L. Biogas upgrade to syn-gas (H2-CO) via dry and oxidative reforming. Int. J. of Hydrogen Energy, 2011, 36, 397-404.

[17] Hernandez, B. Leon, E. Martin, M. Bio-waste selection and blending for the optimal production of power and fuels via anaerobic digestion. Chemical Engineering Research and Design, 2017, 121, 163-172.

[18] Vita, A. Italiano, C. Previtali, D. Fabiano,C. Palella, A. Freni, F. Bozzano, G. Pino, L. Manenti,F. Methanoll synthesis from biogas: A thermodynamic analysis. Renewable Energy. 2018, 118, 673-684.

[19] Oliveira dos Santos, R. Sousa Santos, L. Martinez Prata, D. Simulation and optimization of a methanol synthesis process from different biogas sources. J. Cleaner Production, 2018, 186, 821-830.

[20] Song, C. Tri-reforming of methane: A novel concept for catalytic production of industrially useful synthesis gas with desired H2/CO ratios. Catal. Today 2004, 98, 463-484.

[21] Bartels, J.R. Pate, M.B. Olson, N.K. An economic survey of hydrogen production from conventional and alternative energy sources. Int. J. Hydrogen energy. 2010, 35, 8371-8384.

[22] Shu, J. Grandjean, B.P.A. Kaliaguine, S. Methane steam reforming in asymmetric Pd- and Pd-Ag/porous SS membrane reactors. Applied Catalysis A: General. 1994, 119, 305-325.

[23] Souza, M.V.M. Schmal,M. Autothermal reforming of methane over Pt/ZrO2/Al2O3 catalysts. Applied Catalysis A: General. 2005, 281, 19-24.

[24] Solovev, SA. Kurilets, Y. Orlik, S.N. Tri-reforming of methane on structured Ni-containing catalysts. Theor. Exp. Chem. 2012, 48, 199-205.

[25] Challiwala, M.S. Ghouri, M.M. Linke, P. El-Halwagi, M.M. Elbashir, N.O. A combined thermos-kinetic analysis of various methane reforming technologies: Comparison with dry reforming. Journal of CO2 Utilization. 2017, 17, 99-111.

[26] Gangadharan, P. Kanchi, K.C. Lou, H. Evaluation of the economic and environmental impact of combining dry reforming with steam reforming of methane. Chemical Engineering Research and Design. 2012, 90, 11, 1956-1968.

[27] Afzal, S. Sengupta, D. Sarkar, A. El-Halwagi, M. Elbashir, N.O. An Optimizaton Approach to the Reduction of CO_2 Emissions for Syngas Production Involving Dry Reforming. ACS Sustainable Chem. Eng., 2018, 6 (6), 7532-7544.

[28] Wu, KT. Yu, CT. Chein, RY. Numerical modelling on catalytic Tri-reforming Reaction of Methane for Syngas Production. Energy Procedia. 2017, 105, 4198-4203.

[29] Chein, RY. Wang, CY. Yu, C. Parametric study on catalytic tri-reforming of methane for syngas production. Energy. 2017, 118, 1-17.

[30] Challiwala, M.S. Ghouri, M.M. Sengupta, D. El-Halwagi, M. Elbashir, N.O. A Process Integration Approach to the Optimization of CO_2 Utilization via Tri-Reforming of Methane. Computer Aided Chemical Engineering, Vol. 40, 2017, 1993-1998.

[31] Noureldin, M.B. Elbashir, N.O. El-Halwagi, M. Optimization and selection of Reforming Approaches for Syngas Generation form Natural/Shale gas. Ind. Eng. Chem. Res., 2004, 53 (5), 1841-1855.

[32] Cho, W. Song, T. Mitsos, A. McKinnon, J.T. Ko, G.H. Tolsma, J.E. Denholm, D. Park, T. Optimal design and operation of a natural gas tri-reforming reactor for DME synthesis. Catalysis Today. 2009, 139, 261-267.

[33] Chein, R. Hsu, W. Analysis of Syngas Production from Biogas via the Tri-Reforming Process. Energies, 2018, 11, 1075.

[34] Balasubramanian, P. Bajaj,I. Hasan, M.F. Simulation and optimization of reforming reactors for carbon dioxide utilization using both rigorous and reduced models. Journal of CO2 Utilization, 2018, 23, 80-104.

[35] Zhang, Y. Cruz, J. Zhang, S. Lou, H.H. Benson, T.J. Process simulation and optimization of methanol production coupled to tri-reforming process. Journal of Hydrogen Energy, 2013, 38, 13617-13630.

[36] Zhang, Y. Zhang, S. Benson, T. A conceptual design by integrating dimethyl ether (DME) production with tri-reforming process for CO_2 emission reduction. Fuel Processing Technology, 2015, 131, 7-13.

[37] Manenti, F. Pelosato, R. Vallevi, P. Leon-Garzon, A.R. Dotelli, G. Vita, A. Lo Faro, M. Maggio, G. Pino, L. Arico, A.S. Biogas-fed solid oxide fuel cell (SOFC) coupled to tri-reforming process: Modelling and simulation. International Journal of Hydrogen Energy, 2015, 40, 14640-14650.

[38] Graciano, J. E.A., Carreira, A.D. Giudici, R. Alves, R.M.B. Production of Fuels from CO2-rich Natural Gas using Fischer-Tropsch Synthesis Coupled to Tri-reforming Process. Computer Aided Chemical Enginering, 2017, 40, 2659-2664.

[39] Peduzzi, E. Boissonnet, G. Haarlemmer, G. Maréchal, F. Thermo-economic analysis and multi-objective optimisation of lignocellulosic biomass conversion to Fischer-Tropsch fuels. Sustainable Energy & Fuels, 2018, 2, 1069-1084.

[40] Okeke, I.J. Mani, S. Techno-economic assessment of biogas to liquid fuels conversion technology via Fischer-Tropsch synthesis. Biofuels, Bioproducts and Biorefining, 2017, 11, 472-487.

[41] Design and evaluation of a Fischer-Tropsch process for the production of waxes from biogas. Energy, 2017, 132, 370-381.

[42] Martinez, D.Y. Jimenez-Gutierrez,A. Linke, P. Gabriel, K.J. Noureldin, M. M. B. El-Halwagi, M.M. Water and Energy Issues in Gas-to-Liquid Processes: Assessment and Integration of Different Gas-Reforming Alternatives. ACS Sustainable Chem. Eng. 2,2, 216-225.

[43] Japaraju, P. Rintala,J. 17-Generation of heat and power from biogas for stationary applications: boilers, gas engines and turbines, combined heat and power (CHP) plants and fuel cells 404-427. Biogas Handbook 2013, 404. DOI: 10.1533/9780857097415.3.404#

[44] Jahn, M. Heddrich, M. Weder,A. Reichelt, E. Lange,R. Oxidative dry-reforming of biogas: Reactor design and SOFC. Syst. Integ. Energ. Technol. 2013, 1 (1) 48-58 DOI: 10.1002/ente.201200007

[45] Arab Aboosadi, Z. Jahanmiri, A.H. Rahimpour, M.R. Optimization of tri-reformer reactor to produce synthesis gas for methanol production using differential evolution (DE) method. Appl. Energy 2011; 88:2691-701.

[46] Luyben, W.L. Design and Control of the Dry Methane Reforming Process. Ind. Eng. Chem. Res. 2014, 53 (37), 14423-14439.

[47] Roh, H.-S. Lee, D.K. Koo,K.Y. Jung, U.H. Yoon, W.L. Natural gas steam reforming for hydrogen production over metal monolith catalyst with efficient heat-transfer. Int. J. Hydrogen Energy, 2010, 35 (3), 1613-1619.

[48] Bader, A. Bauersfeld, S. Brunhuber, C. Pardemann, R. Meyer, B. Modelling of a chemical reactor for simulation of a methanisation Plant Presentation 063:064. Proceedings of the 8th International Modelica Conference, March 20th-22nd , 2011, Technical University, Dresden, Germany. https://modelica.org/events/modelica2011/Proceedings/pages/papers/44_4_ID_202_a_fv.pdf Last accessed: May, 2018.

[49] Martin, M. Grossmann, I.E. Energy optimization of bioethanol production via gasification of switchgrass. AIChE. J. 2011, 57 (12) 3408-3428. DOI: 10.1002/aic. 12544.

[50] Lee, S. Methanol Synthesis from Syngas. Handbook of alternative Fuel Technologies; Taylor and Francis: Boca Raton. FL, 2007; Chapter 9.

[51] Phillips, S. Aden,A. Jechura, J. Dayton, D. Eggeman, T. Thermochemical ethanol via indirect gasification and mixed alcohol synthesis of lignocellulosic biomass. Technical Report, 2007, NREL/TP-510-41168.

[52] Riboldi, L. Bolland, O. Overview on Pressure Swing Adsorption (PSA) as CO2 capture technology: state-of-the-art, limits and potentials. Energy Procedia. 2017, 114, 2390-2400.

[53] Lee, S. Methanol synthesis from Syngas. Handbook of alternative Fuel Technologies; Taylor and Francis: Boca Raton. FL, 2007; Chapter 9. ISBN: 0-8247-4096-6

[54] EIA Natural Gas Prices. 2017 Last Access: February 2018. Available in: https://www.eia.gov/dnav/ng/ng_pri_sum_dcu_nus_m.htm.

[55] Global CCS Institute. The CO_2 market. 2018. Available in: https://hub.globalccsinstitute.com/publications/accelerating-uptake-ccs-industrial-use-captured-carbon-dioxide/2-co2-market

[56] Franceschin, G. Zamboni, A. Bezzo, F. Bertucco,A. Ethanol from corn: a technical and economical assessment based on different scenarios. Chem. Eng. Res. Des. 2008, 86 (5) 488-498. DOI: 10.1016/j.cherd.2008.01.001

[57] De Klerk, A. Fischer-Tropsch Refining; Wiley-VCH: Weinheim, 2011

[58] Rodriguez Vallejo, D.F. de Klerk, A. Improving the interface between Fischer-Tropsch Synthesis and Refining. Energy & Fuels. 2013, 27, 3137-3147. DOI: dx.doi.org/10.1021/ef400560z

[59] Acquaviva, J. High-Performance, Durable, Palladium Alloy Membrane for Hydrogen Separation and Purification. 2009. Available in: http://www.hydrogen.energy.gov/pdfs/review09/pd_07_acquaviva.pdf

[60] Dry, M. E. The FischerTropsch process: 19502000. Catal. Today 2002, 71, 227–241

[61] Brown, R. C.; Wright, M. Biomass conversion to fuels and electric power. In Biofuels: Environmental Consequences and Interactions with Changing Land Use. Proceedings of the Scientific Committee on Problems of the Environment (SCOPE)

International Biofuels Project Rapid Assessment, 2225 September 2008, Gummersbach Germany. Howarth, R. W., Bringezu, S., Eds.; Cornell University, Ithaca, NY, USA, pp 5364. http://cip.cornell.edu/biofuels/ (accessed month day, year).

[62] Li, C. Modeling and optimization of industrial Fischer-Tropsch synthesis with the slurry bubble column reactor and iron-based catalyst. Chinese J. of Chem. Eng. 2018, 26, 5, 1102-1109.

[63] Weng, L. Men, Z. Multiphase Reactor Engineering for Clean and Low-Carbon Energy applications. Chp. 7 Fischer-Tropsch Processes and reactors. 2017, DOI: 10.1002/9781119251101.ch7

[64] Schulz, H., Schaub, G. Claeys, M. Riedel, T. Transient initial kinetic regimes of Fischer-Tropsch synthesis, App. Cat. A, 1999, 186, 215-227.

[65] Park, C.S. Norbeck, J.M. Synthetic diesel production from Carbonaceous Feed Stocks. 2009. www.eri.ucr.edu/ISAFXVCD/ISAFXVAF/SyDPCFS.pdf

[66] Song Hyun-Seob, S. Ramkrishna,D. Wright, H. Operating Strategies for Fischer-Tropsch Reactors: A model-directed Study, Korean J. Chem., 2004, 21, 308-317.

[67] Martin, M. Grossmann, I.E. Process optimization of FT-Diesel production from biomass. Ind. Eng. Chem. Res., 2011, 50 (23), 13485-13499.

[68] Gebreslassie, B.H. Slivinsky, M. Wang,B. You,F. Life cycle optimization for sustainable design and operations of hydrocarbon biorefinery via fast pysolysis, hydrotreating and hydrocracking. Computers and Chem. Eng., 2013, 50 (2013) 71-91.

[69] Yuan, Z. Eden, M.R. Superstructure optimization of integrated Fast Pyrolysis-Gasification for Production of Liquid Fuels and propylene. AIChE J. 2016, 62; 3155-3176.

[70] PetroWiki. Oil and gas separators. 2018. Available in: http://petrowiki.org/Oil_and_gas_separators#Separator_performance

[71] Sayda, A.F. Taylor, J. H. Modeling and control of three-phase gravity separators in oil production facilities. American Control Conference. 2007.

[72] Bezergianni, S., Kalogianni, A., Vasalos, I. A. Hydrocracking of vacuum gas oil-vegetable oil mixtures for biofuels production. *Bioresour. Technol*. 2009, 100, 3036–3042

[73] Berzergianni, S. Kalogianni, A. Hydrocracking of used cooking oil for biofuels production. Bioresource Technol. 2009, 100, 3927-3932.

[74] Speight, J.G. The Chemistry and Technology of Petroleum. 2nd Edition. Marcel Dekker Inc., New York. 1991.

[75] EIA. Gasoline and Diesel Fuel Update. 2018. Available in: https://www.eia.gov/petroleum/gasdiesel/ Last accessed March 2018.

[76] GlobalPetrolPrices.com LPG prices, liter. 2018. Avilable in: https://www.globalpetrolprices.com/lpg_prices/ Last accessed March 2018.

[77] Bailon, L. Hinge, J. Biogas Upgrading. Evaluation of Methods for H2S Removal. Danish Technological Institute, 2014. Available in: http://www.teknologisk.dk/_/media/60599_Biogas%20upgrading.%20Evaluation%20of%20methods%20for%20H2S%20removal

[78] Wikipedia. Comunidad Autonoma de Madrid. 2018. Available in: https://es.wikipedia.org/wiki/Comunidad_de_Madrid

[79] Sinnot, R.K. Coulson and Richardson´s Chemical Engineering, 3rd ed. Butterworth Heinemann: Singapore, 1999.

[80] Matches cost estimator. http://www.matche.com/ 2015.

[81] Almena, A. Martín, M. Techno-economic analysis of the production of epiclorhidrin from glycerol. Ind. Eng. Chem. Res. 2015, 55, 3226.

[82] Silla, H. Chemical Process Engineering. Design and Economics; Marcel Dekker Inc.: New York, 2003; ISBN: 0-8247-4274-5.

[83] Hernández, B. Martín, M. Optimal Integrated Plant for Production of Biodiesel from Waste. ACS Sustainable Chem. Eng., 2017, 5 (8), 6756-6767.

CHAPTER 4.3. OPTIMAL PRODUCTION OF SYNGAS VIA SUPER-DRY REFORMING. ANALYSIS FOR NATURAL GAS AND BIOGAS UNDER DIFFERENT CO_2 TAXES.

ABSTRACT

This chapter presents a mathematical optimization approach that evaluates the use of super-dry reforming (SDR) together other reforming technologies, water–gas-shift and hydrogen from electrolysis. The aim is to produce syngas with different H_2:CO ratios, several CO_2 taxes and two methane sources: natural gas and biogas. A superstructure is developed and optimized using an economic objective function that considers carbon taxes as parameter to determine the most profitable technology or the combination of them. As a result from this analysis, the use of SDR is less profitable than the use of tri-reforming when only one technology can be used for all the range of carbon taxes studied. SDR is only selected when it operates in parallel with a tri-reformer to produce syngas with a H_2:CO ratio of 1 for any of the raw materials used. For a ratio of 1.7, SDR is only selected in parallel to tri-reforming to process biogas and with CO_2 taxes of at least \$60/t. Meanwhile for a H_2:CO ratio of 2.5 it is never selected. In the case that the reformers do not generate enough H_2, WGS is selected to adjust the H_2:CO ratio for all the carbon taxes studied.

Note: The supplementary material of this chapter is available in:
https://www.sciencedirect.com/science/article/pii/S0263876219303211

4.3.1 INTRODUCTION

CO_2 is the major greenhouse gas emitted by human activities representing 82% of the total greenhouse gas emissions in 2015 [1]. Its concentration in the atmosphere has increased during the last century from 317 ppm in 1958 up to 409 ppm in 2018 [2]. Energy and industry sectors were estimated to contribute about 50% of these worldwide anthropogenic emissions of CO_2 in 2014, which implied two thirds of the stationary emissions [3]. The reduction and mitigation of these emissions have become a major issue for most of the countries, as declared in the 21st United Nations Climate Change Conference in Paris, 2015 [4]. According to the pledges defined in this agreement, it is desired that the warming will stabilized below 2ºC, requiring an estimated reduction of the CO_2 emissions between 30 Gt/y and 48 Gt/y [5].

Different solutions have been proposed to mitigate and capture the CO_2 in processes such as the use of renewable energies [6], the absorption of CO_2 with amines [7,8], the use of Pressure Swing Adsorption (PSA) [9, 10] and Temperature Swing Adsorption beds [11, 12], the introduction in chemical looping systems [13, 14] or by cryogenic distillation [15]. The capture and storage [16] is not only desired, an added value using that CO_2 is also preferred. Different ways have been also presented including the production of rock [17] and organic carbonates [18, 19], the production of basic organic compounds [20, 21] or within the food and beverage industries [22]. Apart from the previous examples, another promising route to convert CO_2 is producing syngas. The use of dry reforming (DR) of methane is a technology that does not only convert CO_2, but also another greenhouse gas, methane, see Eq. (1).

$$CH_4 + CO_2 \leftrightarrow 2CO + 2H_2 \qquad \Delta H^0_{298K} = +247 \frac{kJ}{mol} \tag{1}$$

DR has been widely studied for the production of different syngas ratios and using various raw materials such as methane [23, 24], natural gas [25], shale gas or biogas [26, 27]. A comparative study between DR and other reforming technologies was carried out by Noureldin et al. [25]. They suggested that the combined operation of DR with other reforming technologies benefits the CO_2 fixation as well as the profitability of the process. Baltrusaitis and Luyben [23] compared five reforming routes, evaluating their annual cost. As a result, the combined steam reforming (SR), Eq. 2, and DR showed to be the technology with lowest cost. A solution for the reduction of the reforming cost was also suggested by Lim et al. [28]. They proposed recirculating the CO_2 of flue gases for the production of syngas using a combined SR and DR. In a recent study, Afzal et al. [29] performed a comparison integrating the capture of CO_2 and different reforming technologies. Such work presented an analysis of the carbon footprint of different processes. As a result, the use of a single DR shows the lowest CO_2 footprint when it operates only with a syngas ratio, H_2:CO, up to 1. The combination of SR and DR shows the lowest footprint for syngas ratios between 1 and 2.5. For all of them, an estimated production cost of $1/kmol syngas was estimated.

$$CH_4 + H_2O \leftrightarrow CO + 3H_2 \qquad \Delta H^0_{298K} = +206 \frac{kJ}{mol} \tag{2}$$

The integration of DR has not only been performed with SR. A more profitable solution has been found combining these two reforming technologies with the partial oxidation of methane (POX), Eq. (3). The resulting technology,

tri-reforming (TR), becomes promising since it combines the high economical advantage of SR and the environmental advantage of DR with the energy efficiency of the exothermal POX [30, 31].

$$CH_4 + \frac{1}{2}\, O_2 \leftrightarrow CO + 2H_2 \qquad \Delta H^0_{298K} = -36\,\frac{kJ}{mol} \tag{3}$$

TR was thermodynamically evaluated by [32] varying the mole ratio of the feed and proposing an optimal ratio of CH_4:CO_2:H_2O:O_2=1:0.291:0.576:0.088 to maximize H_2 yield and CO_2 conversion. This ratio was also studied by Challiwala et al. [24] considering the carbon deposition by CO_2 fixation and changing the recommended ratio of CH_4:CO_2:H_2O:O_2 to 1:1:0.4:0.3. As suggested in these works, the composition of the feed is shown to be the most relevant parameter on the TR process of methane. This importance was also observed in the TR of biogas. The syngas production from biogas was thermo-kinetically analysed by Chein and Hsu [30] suggesting a ratio CH_4:CO_2:H_2O:Air = 1:0.5:1:2 based on the reactor optimization performed by Chein et al. [33]. This optimization was only carried out including the reforming reactor. However, if a tune-up stage is applied to the syngas after the reforming, the optimal Biogas:H_2O:O_2 ratio of 1:0:0.035 is suggested by Hernández and Martín [31] for ethanol production (H_2:CO=1). For FT (H_2:CO=1.7) and methanol (H_2:CO=2.5) production, the desired Biogas:H_2O: O_2 ratio was 1:0: 0.275 with an addition of steam in a water gas shift (WGS) reactor in the tune up section of 0.062 mol of H_2O per mol of Biogas for FT and 0.206 mol of H_2O per mol of Biogas for methanol. The parametric optimization involved in this study also included the comparison with a combined SR and DR for biogas showing more profitable results for TR since oxygen is desired for all the syngas ratios. Another study comparing different technologies was carried out by Balasubramanian et al. [34] for natural gas. Their study evaluated SR, DR, POX and the possible combinations between them, being the combination of POX and DR selected when the CO_2 use is maximized for syngas ratios between 1 and 1.7. For ratios between 1.7 and 2.4 they suggested the parallel processing using a DR, a combined SR-DR and a TR. For H_2:CO ratios larger than 2.4 they suggested the parallel production with a SR, TR and a WGS reactor.

Apart from all the attention paid to compare the possible reforming types, none of the previous modelling studies have evaluated super-dry reforming (SDR), Eq. (4). SDR was recently obtained by intensifying the DR with the objective of increasing the conversion of CO_2 [35]. This improvement in the conversion is achieved by eliminating the reverse WGS reaction with a combined process composed by a Ni/$MgAl_2O_4$ catalyst for CH_4 reforming, a Fe_2O_3/$MgAl_2O_4$ support that acts as oxygen carrier and a CaO/Al_2O_3 sorbent for CO_2. The continuous operation of the process was described in the supplementary material of [35] and it is based on 8 parallel reactors that operate in 2 steps. 4 reactors are oxidizing the methane and the remaining 4 reactors are in CO_2 reduction mode. The global reaction taking into account both modes is presented in Eq. (4).

$$CH_4 + 3\,CO_2 \leftrightarrow 4\,CO + 2H_2O \qquad \Delta H^0_{298K} = +330\,\frac{kJ}{mol} \tag{4}$$

Several studies have recently been published evaluating the looping materials involved in the development of catalysts for SDR technology [36, 37]. However, the analysis of processes involving SDR has been only evaluated in the work of Verbeeck et al. [38]. They performed a comparative economic analysis based on simulations carried

out in Aspen and using biogas as raw material for producing CO and syngas. Three reforming technologies (SR, DR and SDR) were compared using the OPEX that included CO_2 emission taxes. As a result, they obtained that only SDR and DR ensure a positive profit for CO and syngas production. An economic analysis was also presented showing an estimated financial support of 130€/t of CH_4 for producing CO via SDR, 420€/t of CH_4 for producing syngas via DR and a support between 250 and 950 €/t for producing syngas via SR. However, the study used a simulation based approach without considering integration and optimization. Furthermore, the work also described some possible applications of the CO obtained via SDR but it does not provide a comparison for the most profitable technology for hydrogen production and if it is competitive with other technologies such as TR. Thus, in the current work we propose the production of syngas using different reforming technologies and including additional supply of H_2 from a WGS reactor and an electrolyzer. As a result from the optimization, the most profitable technologies for reforming and hydrogen production are selected. The selection is evaluated under different CO_2 taxes for three common H_2:CO ratios: 1:1, typical in the production of for ethanol and DME production, 1.75 for FT fuels and 2.5 for methanol production. These evaluations are also performed taking into account two type of raw materials: biogas and natural gas. The rest of the paper is structured as follows. Section 4.3.2 describes the models involved in each of the process sections. In section 4.3.3, the optimization results under the different taxes, raw materials and ratios are presented. Finally, the conclusions are described in Section 4.3.4.

4.3.2. MODELLING ISSUES.

4.3.2.1 Superstructure formulation

The superstructure proposed to carry out the analysis of the reforming technologies is presented in Figure 1. Natural gas (assumed to be 100% CH_4) and biogas are fed in the system by means of three streams: two of them are used as fuels to heat-up the reformer and the other one is processed. In the case of biogas, a first section is included to remove the impurities that reduce the catalyst efficiency [39]. The cleaned biogas or natural gas are mixed before the reformers with other gases that allow optimizing the composition desired in the reactor. Three types of reforming technologies defined in two units are considered in this work. Two of the possible reforming types (combined DR-SR and TR) can be carried out in the same unit but the other type, SDR, is not integrated since it is not compatible with the WGS and SR presented in combined SR-DR and TR.

After reforming, cleaning and tune-up sections are taken into account for the production of syngas. Once the traces of hydrocarbons are removed during cleaning, two options are considered for the syngas post-processing of both reformers. First, the syngas from both reformers can be mixed and sent to the tune-up section together. Second, it is not desired to mix the syngas streams at the beginning of the tune-up section and they can be mixed later.

Once the syngas is cleaned, two treatments are considered in the following tune-up stage: First, the H_2:CO ratio is modified by increasing the H_2 content with a WGS reactor, keeping the same composition with a bypass or reducing the H_2 by removing it with a membrane-PSA system. Second, the CO_2 is removed since it promotes carbonation on the catalyst of the synthesis reactors at large compositions [40, 41]. Between these stages and at

the end of them, the syngas coming out from the SDR is allowed to be mixed depending on the treatments that it requires, see Figure 1.

After performing the cleaning and tune-up of the syngas, additional hydrogen can be added from electrolysis in a last stage. This hydrogen added at the end of the process helps to achieve the desired H_2:CO ratio of the syngas, competing with the previous WGS reactor. The modelling regarding to each of these stages is deeply described in the next sections.

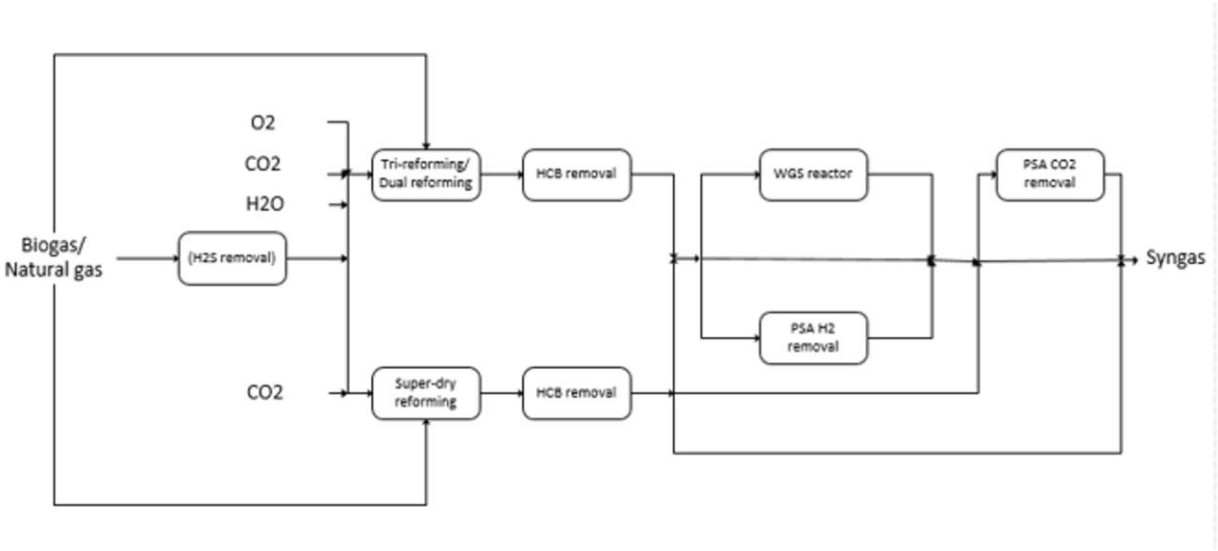

Figure 1. Superstructure of the problem.

4.3.2.2 Methane sources evaluated

Two types of feeds are evaluated in this work. On the one hand, natural gas is evaluated considering to be composed only by methane and requiring to be mixed with other components before the reformers. On the other hand, biogas is also taken into account for the reforming. Biogas is a mixture of gases involving different components as it is presented in Table 1. In the two cases, the methane source is assumed to be fed at 298K and 1atm.

Table 1. Ranges of concentration for each of the components of the biogas [42].

Component (%vol)	Minimum	Maximum
CH_4	0.37	0.75
CO_2	0.25	0.50
N_2	0.01	0.17
H_2S	$2 \cdot 10^{-5}$	$2 \cdot 10^{-3}$
H_2O	0	0.031
NH_3	$1 \cdot 10^{-6}$	$3.5 \cdot 10^{-6}$

4.3.2.3 Cleaning and raw materials preparation for reforming.

The H_2S ammonia traces of biogas damage the catalyst in the reforming section and reducing its efficiency. Thus, a pretreatment is required as presented in Figure 4,a. The biogas fed is sent to a mixed packed-bed of Fe_2O_3 and zeolites that operates between 298 K and 323 K. The capture of the ammonia is carried out by the zeolites, which are assumed to have an efficiency of 100%., while the removal of H_2S is assumed to follow Eq. (5) with a conversion of 100% [39]:

$$Fe_2O_3 + 3\,H_2S \rightarrow Fe_2S_3 + 3H_2O \quad (5)$$

After removing the H_2S and the ammonia, the purified biogas is sent to splitter S-1 that separates two fractions for each reformer. Before processing the biogas in the reformers, a modification of the composition is also allowed by adding some required reactants such as steam, CO_2 and O_2. The mixture obtained as feed of the TR reactor (R-1) is sent to a compressor and a heat exchanger in order to achieve the operating conditions of reactor R-1. In the case of the SDR reactor (R-2), the same structure is followed using a compressor that ensures the atmospheric pressure in the reactor and the heat exchanger HE-2. Lower pressures in SDR reactor improve the yield of the reaction (Le Chatelier's principle) but the operation in vacuum conditions increases the cost of the unit.

The preprocessing of natural is similar to the biogas but it is directly introduced into the splitter, S-1, as presented in Figure 2-b.

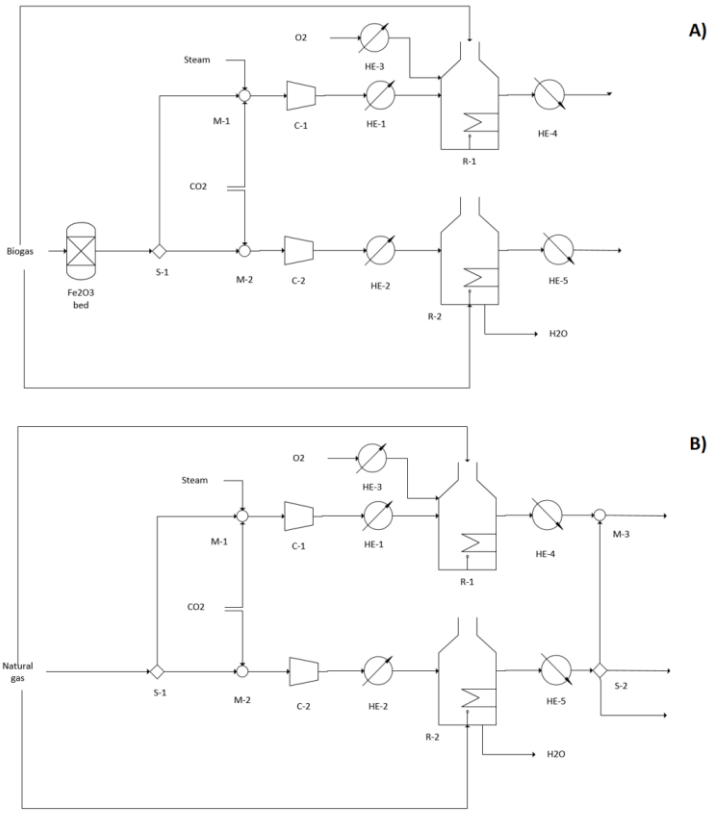

Figure 2. Preprocessing and reforming for biogas (a) and natural gas (b).

4.3.2.4 Reforming

Three types of reformers are defined in the superstructure modelled in this work. Two of these reforming types (combined SR-DR and TR) are carried out in the same unit and the other reforming type, SDR, is carried out in a parallel reactor as presented in Figures 2-a and 2-b. The models involved in each of these types are presented in the following paragraphs.

4.3.2.4.1 Modeling of dual SR-DR and TR.

The papers analyzing the kinetic of TR have shown that the reaction occurs in two steps: First, the methane is oxidized. Second, the species reach thermodynamic equilibria [33]. According to the kinetics observed in such works, Hernández and Martín [31] proposed a parametric optimization approach dividing the TR in two stages: a first stage where oxidation occurs, and a second stage where the combined SR-DR and the competitive WGS, Eq. (6), takes place.

$$CO + H_2O \leftrightarrow CO_2 + H_2 \qquad \Delta H^0_{298K} = -41\,\frac{kJ}{mole} \tag{6}$$

The first stage is modelled assuming that the POX takes place with an oxygen conversion of 100%. In the second stage, the equilibria given by Eqs. (7) to (9) is achieved. These equations correspond respectively to the SR, DR and WGS reactions and are taken from the literature [43, 44].

$$k_p = e^{\left[31.447-\frac{29580}{T}\right]} = \frac{P_{CO}P_{H_2}}{P_{CH_4}P_{CO_2}} \tag{7}$$

$$k_p = 10^{\left[-\frac{11650}{T}+13.076\right]} = \frac{P_{CO}P^3_{H_2}}{P_{CH_4}P_{H_2O}} \tag{8}$$

$$k_p = 10^{\left[\frac{1910}{T}-1.784\right]} = \frac{P_{CO_2}P_{H_2}}{P_{CO}P_{H_2O}} \tag{9}$$

The atomic balances are also computed in the second stage following Eq. (10) to (12):

$$mol_{CO_2} + mol_{CO} + mol_{CH_4}\big|_{in} = mol_{CH_4} + mol_{CO} + mol_{CO_2}\big|_{out} \tag{10}$$

$$4 \cdot mol_{CH_4} + 2 \cdot mol_{H_2O}\big|_{in} = 4 \cdot mol_{CH_4} + 2 \cdot mol_{H_2} + 2 \cdot mol_{H_2O}\big|_{out} \tag{11}$$

$$mol_{CO} + 2mol_{CO2} + mol_{H_2O}\big|_{in} = mol_{H_2O} + mol_{CO} + 2 \cdot mol_{CO_2}\big|_{out} \tag{12}$$

The energy balance for the entire reactor is computed as presented in Eq. (13):

$$Q('R1') = Q_{prod} + Q_{react} = \sum_i fc(i,'R1','HE4') \cdot \left(\Delta H_f + \int_{T_{ref}}^{T_{out}} C_p dT\right) - \sum_i fc(i,'HE1','R1') \cdot \left(\Delta H_f + \int_{T_{ref}}^{T_{out}} C_p dT\right) - \sum_i fc(i,'HE3','R1') \cdot \left(\Delta H_f + \int_{T_{ref}}^{T_{out}} C_p dT\right) \tag{13}$$

From the approach proposed, note that in the case that no oxygen is introduced into the reformer, the first stage does not play any role and the final model only follows the second stage, which corresponds to a combined SR-DR with a competitive WGS reaction.

In both cases, the energy required in the reformer is supplied by burning a fraction of the biogas or natural gas fed in the process. This amount is computed as function of the low heating value of the methane, see Eq. (14).

$$Q('R1') = LHV_{CH_4} \cdot m_{CH_4\ Biogas} \quad (14)$$

4.3.2.4.2 Modeling of SDR process.

As presented, SDR is a novel technology that achieves higher yields in CO_2 utilization. To the best of author's knowledge, there is none kinetic model and only one thermodynamic analysis has been performed using the EkviCalc software package. This thermodynamic analysis resulted in the iso-conversion lines that show to be dependent on the CO_2:CH_4 ratio, pressure and temperature as reported in [35].

Analyzing Eq. (4) it can be seen that the number of moles produced in the reaction is larger than the reactants. Taking into account LeChatelier's principle, for smaller pressures larger conversions are achieved. However, the operation in vacuum conditions increases the cost of the reactor. Thus, the pressure in this SDR reactor is fixed at 1 atm. The reactor operating temperatures can range from 773 K to 1237 K and the CO_2 ratio is assumed to be between 3 and 10 according to results presented in Buelens et al. [35]. The thermodynamic data at 1 atm has been fitted in a two-stage procedure to determine a reduce order model that shows a good trade-off between accuracy and low computational cost. First, the Bayesian Information Criterion is minimized with ALAMO [45], obtaining the main terms from a set composed by ratios, logarithmic functions, monomial terms with powers up to x^2 and the single interaction of all of these terms, eg. (Log(x)·x, $x \cdot x^2$, etc). The reduced order model obtained by this minimization is still so complex, see supplementary material. Thus, a statistical analysis is performed in a second stage. The P-values are analyzed in order to obtain the most relevant terms that are fitted in a simpler model. The predictor plot obtained from that fitting is presented in Figure S-2 of the supplementary material. It compares the data obtained from Eq. (15) with the thermodynamic results presented by Buelens et al. [35] and showing an R^2 of 0.96. Another two alternative models for the reactor are presented in the supplementary material. However, the Proposal 3 of the supplementary material involves the interaction of two logarithmic terms that introduce highly non-linear terms in the optimization and the Proposal 4 introduces an additional term to be computed. Apart from this two proposals, another two ones are presented when the model is reduced to the three (Proposal 5) and the two most significant terms (Proposal 6). In such cases, the R^2 is subsequently reduced to 0.94 and 0.86 without removing so much complexity since one logarithmic term and the inverse of temperature are still involved.

$$X_{CH_4} = 8.130458975 + 0.76543 * \ln\left(\frac{mol_{CO_2}}{mol_{CH_4}}\right) - \frac{4746.37}{T(K)} - 0.00259 * T(K) - 0.000629 * T * \ln\left(\frac{mol_{CO_2}}{mol_{CH_4}}\right) \quad (15)$$

The model of the reactor also reduces the mass balances as in Eq. (4) and taking into account that the water is captured by the CaO/Al_2O_3 bed and then removed in other stream that leaves the reactor [35]. The energy balance is computed as follows, see Eq. (16):

$$Q('R2') = Q_{prod} + Q_{react} = \sum_i fc(i,'R2','HE5') \cdot \left(\Delta H_f + \int_{T_{ref}}^{T_{out}} C_p dT\right) - \sum_i fc(i,'HE2','R2') \cdot \left(\Delta H_f + \int_{T_{ref}}^{T_{out}} C_p dT\right) \quad (16)$$

The energy computed by this Eq. (16) is also supplied by burning the source of methane as presented in Eq. (14).

4.3.2.5 Syngas cleaning and composition tune-up

The syngas produced in the reformers needs to be cleaned and treated before sending it to the synthesis reactors. The first treatment presented in Figure 3 corresponds to the removal of water that comes out from the TR reactor. This removal is carried out by means of Flash-1, after cooling down the products of the reactor and a deplhegmator (Flash-2) located after the syngas compression.

Then, a bed is used to remove the traces of hydrocarbons and, in the case of biogas, the traces of nitrogen. This system is required in each of the syngas streams that comes out from the two reformers since it is necessary to avoid the deposition of carbon on the catalysts involved in the WGS or subsequent synthesis reactors [46]. The bed system uses silica gel as adsorbent and it includes a regenerating bed to allow for the continuous operation of the process. The system works at 298 K and 4.5 bar with an assumed efficiency of 100%. Thus, the syngas generated in the reformers is compressed (C-2 and C-3) and cooled down (HE-6 and HE-7) before the bed. The modelling of the compressors is carried out assuming polytrophic behaviour (K_c=1.4, η_c=0.8).

After cleaning, the H_2:CO ratio of the syngas is tuned-up. Three technologies are taken into account to adjust the ratio: First, a WGS reactor that increases the concentration of hydrogen and it is modelled following the equilibrium presented in Eq. (9). Second, a bypass. Third, a hybrid membrane-PSA system that removes the hydrogen [47]. This PSA-system is also assumed to be composed by two membranes that allow the continuous operation of the process, working with a pressure of 5 bar and a temperature of 298K.

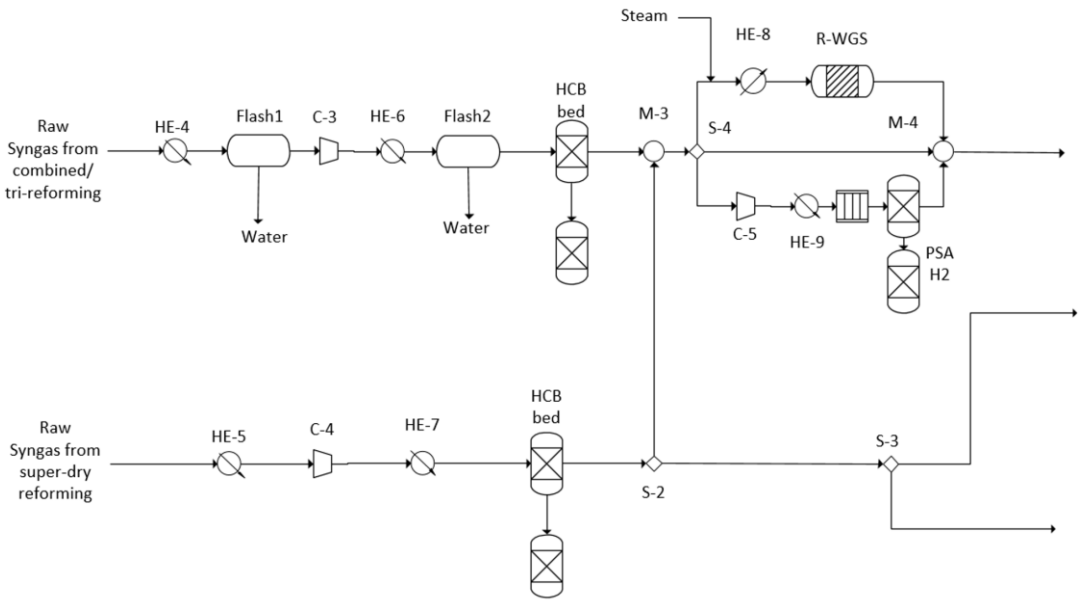

Figure 3. Syngas cleaning and H_2 tune-up stage.

The last stage of the cleaning section consists of the CO_2 removal for the production of the final syngas, see Figure 4. This treatment is applied to the syngas coming from the previous section and to the syngas stream that left the SDR reactor. Thus, these two streams are mixed in M-3. The CO_2 present in the stream that lefts M-5 can be fully or partially removed depending on the composition allowed for each synthesis: Between 2% and 8% in volume for the production of methanol [40] and up to 6% in volume for the production of ethanol and FT fuels [41].

To achieve this concentration of CO_2, the stream that comes out M-5 is divided in two streams. One is used as a by-pass and the other stream is treated in the PSA system (PSA CO_2). The PSA system absorbs the CO_2 by means of a bed composed by Zeolite 5A or 13X. It operates at 298 K and 5 bar with a removal of 95% of the CO_2 [10]. Therefore, the syngas coming out from mixer M-5 is compressed and cooled down when it is sent to the PSA system. In this section, the water generated in the WGS reactor also condensates and it has to be removed by means of Flash-3 before sending it to the PSA system for CO_2 capture.

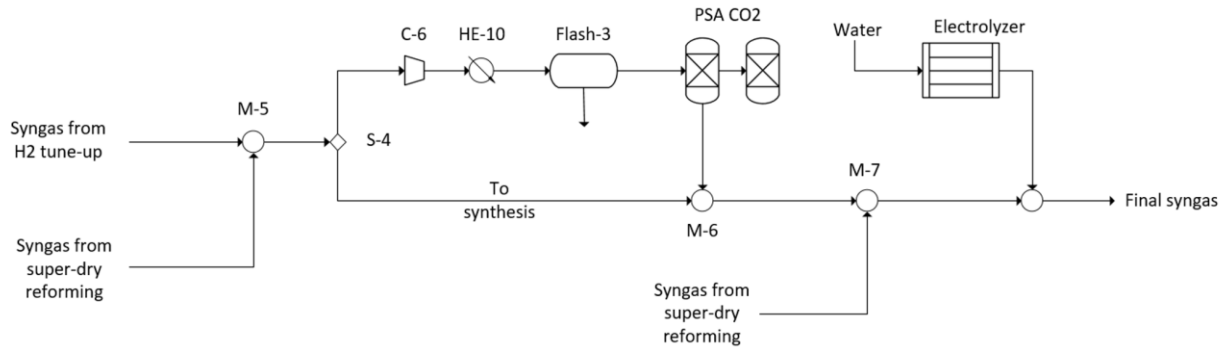

Figure 4. CO_2 removal and electrolysis section.

4.3.2.6 H_2 production from electrolysis

Since SDR does not produce H_2, another technology is required to obtain this component. The previous section has presented the use of other reforming technologies and WGS for producing H_2. However, it can also be obtained with an electrolyzer from electricity as described by Verbeeck et al. [38]. The generation of H_2 via electrolysis follows Eq. (17) and it takes place using a solution of 25% of KOH at 80 ^oC and 1atm. It generates 0.0124 kg H_2/s with a power consumption of 53.15 kWh_e/kg H_2 [48]. This technology is presented in Figure 4 where it can be seen that the hydrogen is introduced at the end of the syngas production and it competes the production of H_2 with the WGS reactor.

$$2H_2O \rightarrow 2H_2 + O_2 \quad (17)$$

4.3.2.7 Solution procedure

The problem presented in this work is optimized in order to determine if SDR or the parallel operation of this technology with TR or the combined SR-DR is more competitive than the use of single TR for the production of syngas with different H_2:CO ratios: 2.5:1 for methanol, 1.7:1 for FT fuels and 1:1 for ethanol and DME. Each of these ratios is evaluated using biogas and natural gas as raw materials and under different CO_2 taxes. It is expected that the technologies selected depends on the CO_2 emission taxes, being SDR preferred in economies with higher taxes since it at least absorbs three more times of CO_2 than DR.

The study is carried out with the objective of maximizing the profit (Z) of Eq. (18). The prices of the components described in the objective function, Eq. (18), are: \$2/kg for hydrogen [49], \$3.67/1000 ft^3 for methane (assumed to be natural gas) [50], \$0.021/kg for the O_2 [28], \$26 per tonne of CO_2 [51]. The utilities are assumed to have a cost of $\$5.7 \cdot 10^{-5}$/kg for cooling water and \$0.019/kg for steam and \$0.06/kWh_e for electricity [52]. The last term takes

into account the CO_2 emission taxes of the process. The optimization is performed under zero carbon taxes and the taxes presented in Table 2 that correspond to the current taxes of different countries. The CO_2 emissions in the process are computed from the mass and energy balances of the process as presented in Eq. (19).

$$Z = C_{H_2}F_{H_2} - C_{elec}\sum_{i\epsilon Compressors} W_i - C_{CH_4}\sum_{i\epsilon CH_4 inlets} F_{CH_4} - C_{O_2}F_{O_2'Triref'} - C_{CO_2}\sum_{i\epsilon CO_2 inlets} F_{CO_2} - C_q\sum_{j\epsilon Q_{heat}} Q + C_w\sum_{k\epsilon Q_{refrig}} Q - C_{H2O}F_{H2O} - C_{CO2Taxes}Emissions_{CO_2} \quad (18)$$

$$Emmisions_{CO_2} = MW_{CO_2}\cdot\left[\sum_{i\epsilon CO_2 outlets} F_{CO_2} - \sum_{i\epsilon CO_2 inlets} F_{CO_2}\right] + CO_{2kWhe}\cdot\sum_{i\epsilon Compressors} W_i + CO_{2kWhe}\cdot(4.914882\cdot 10^{-8})\cdot\sum_{k\epsilon Q_{refrig}} Q + CO_{2Heating}\cdot m_{steam} + CO_{2Pur_{Water}}\cdot MW_{H2O}\cdot\sum_{i\epsilon CO_2 inlets} F_{H_2O} \quad (19)$$

The first term of Eq. (19) corresponds to the CO_2 absorbed by the process as raw material and the CO_2 emitted by the process as wastes (e.g. fuel burned in the reformers and CO_2 separated).

The following terms correspond to the indirect emissions involved in the process:

- The second term are the emissions associated to the power consumption. To estimate this term the CO_2 produced per electric kWh_e is computed from the correlation presented by Hernández and Martín [53], see Eq. (20).

$$\frac{m_{CO_2}}{kWh_e} = -0.0131(year) + 26.719 \quad (20)$$

- The third term corresponds to the emissions generated by the cooling water. It is computed taking into account the emissions generated in the processing of water. A power consumption of 7.775 kWh_e/Mgal is assumed as an average from supply and distribution values reported in [54].
- The fourth term corresponds to the water used as raw material. This water does not only need to be transported, but it also needs to be treated. Therefore, a power consumption of 15825 kWh_e/Mgal are assumed according to [54].
- The last term are the CO_2 emissions generated by the use of steam. A close cycle for steam is considered. The computation of that CO_2 generated by burning the methane that produces the steam is performed using a value of 0.204 $kgCO_2/kWh_t$ [55].

As described, the superstructure proposed in this work is evaluated with the taxes defined in Table 2 and the condition of zero taxes for CO_2 emissions. Apart from evaluating the effect of these carbon taxes on the operation of the entire super-structure, sensitivity analysis of these taxes are also performed:

- Evaluating the use of profitable renewable energies to determine if the use of electrolyzers for H_2 production is enough profitable and compare it with the process defined by Verbeeck et al. [38]. In order to check if the operation of electrolyzers presents any opportunity on the integration, the best case of renewables energies is studied. It involves the use of geothermal energy that it not only supposes zero emissions in Eq. (20), but also the cost of the electricity is reduced to \$0.04/kWh_e [56].

- Evaluating the single operation of TR and SDR in order to determine how the optimal operating parameters are modified by the carbon taxes with each reforming reactor and if SDR is more profitable than TR for the range of taxes studied.

Therefore, for performing these sensitivity analysis, the optimization problem defined is solved 80 times for each raw material, biogas and natural gas. This problem is composed of 1,200 equations and 1,400 variables that are solved with CONOPT 3.0 using a multi-start approach in GAMS ®.

Table 2. Carbon taxes in different countries [57].

Country/ Region	CO_2 taxes ($/t)
New Zealand, Canada, California (USA)	13
UK, France, Denmark, Ireland	24
Finland	60
Switzerland	86
Sweden	131

4.3.3. RESULTS

4.3.3.1 Optimization results using natural gas as raw material

4.3.3.1.1 Results considering parallel reforming operation

The process described in previous sections has been optimized under different CO_2 taxes in order to determine the optimal operating conditions and the cut-off point where SDR becomes a profitable technology to be taken into account in the process. As a result from the optimizations performed using natural as raw material, Figure 5,a) is obtained for the economic objective function and Figure 5,b) for the CO_2 generated by the process. In Figure 5,a) it is shown that the largest profitability of the process is achieved when a syngas with a H_2:CO ratio of 2.5 is produced without carbon taxes. This ratio is the most profitable to be produced in most of the countries nowadays. Only in the cases of Finland, Switzerland and Sweden lower H_2:CO ratios are preferred. The larger carbon taxes of these countries make the process with a ratio of 2.5 unprofitable. The H_2:CO ratio of 1.7 also shows a similar behavior than the ratio of 2.5. Both of them become less profitable when the taxes are increased but the ratio of 1.7 decreases much slower since it emits less CO_2, see Figure 5,b). Finally, the production of a syngas with a H_2:CO ratio of 1 is the only one that becomes more profitable for higher CO_2 taxes. This ratio is the one that emits lowest carbon taxes and its profitability decreases up to a minimum when the CO_2 taxes are $24/t and it increases again with larger taxes. For taxes larger than $60/t, the process absorbs CO_2 and it receives profit because of producing the syngas and absorbing CO_2. The last plot, Figure 5,c), shows a comparison between the CO_2 emissions and the profit obtained by the process. In the case of a H_2:CO ratio of 1 it can be seen that there is a

minimum profit according to the emissions. From such minimum, the process follows two behaviors: On the one hand, it tends to increase the profit when more CO_2 is absorbed because of the larger carbon taxes. On the other hand, operating with low taxes, it is preferred to emit more CO_2. In the cases of H_2:CO ratios of 1.7 and 2.5, the increase of the taxes, reduces the profit since the process does not prefer to capture more CO_2. As a consequence, a limit of lower emissions for such ratios can be seen in Figure 5-c.

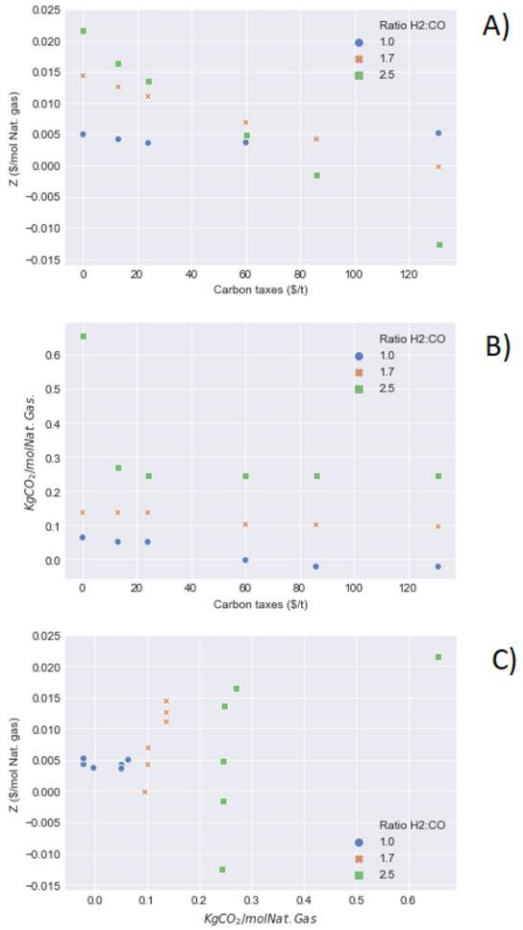

Figure 5. Economic objective function (Z), CO_2 generated by the processes and relation between the results of both for H_2:CO ratios of the syngas of 1, 1.7 and 2.5, and using natural gas as raw material.

Apart from the economic and environment results presented, the optimization also provides the desired operating conditions of the process. The most relevant parameters are presented in Figure 6 and another operating conditions are presented in Table S-1 of the supplementary material. It can be seen in Figure 6 that with zero carbon taxes SDR is only selected when a syngas with a H_2:CO ratio of 1 is produced. The fraction of the feed processed through the SDR increases when the carbon taxes increase for the production of a ratio of 1 and 1.7 since SDR process absorbs more CO_2 than TR. However, for producing syngas with a ratio of 2.5 the fraction remains zero for all the taxes studied. The SDR is desired to operate between 1044 K and 859 K and the TR reforming reactor is always desired to operate with a temperature of 1273 K as it is showed in Table-S1 of the supplementary material. Both reactors require another feedstocks apart from natural gas:

- SDR requires an amount of CO_2 that goes from 0.3mol_{CO2}:$mol_{Natural\ gas}$ up to 1mol_{CO2}:$mol_{Natural\ gas}$. This feed of CO_2 is desired to be larger when a syngas with a H_2:CO ratio of 1 is desired since it has large percentage of carbon monoxide. This SDR also requires to be heated-up with fuel, which is natural gas, and it requires an amount around 0.215 mol $Nat.gas_{Fuel}$:mol $Nat.gas_{process}$ when a H_2:CO ratio of 1 is desired and a value of 0.014 mol $Nat.gas_{Fuel}$:mol $Nat.gas_{process}$ when a a H_2:CO ratio of 1.7 and the operation of SDR are desired.
- In the case of TR, the system needs CO_2, O_2 and fuel. The CO_2 added is desired to be between 0.23 up to 0.28 molCO_2:mol $Nat.gas_{process}$. The oxygen added goes from 0.33 up to 0.39 molO_2:mol $Nat.gas_{process}$ and the fuel required is always around 0.7 mol $Nat.gas_{Fuel}$:mol $Nat.gas_{process}$, as presented in Table S-1 of the supplementary material.

The total contributions of the CO_2 and fuel sent to both reformers are summarized in Figure 6. It can be seen that the largest quantity of fuel is required for producing a syngas with a ratio of 2.5 when the carbon taxes are zero. Nevertheless, after introducing the carbon taxes, the requirements of fuel drop down to 0.08 mol $Nat.gas_{Fuel}$:mol $Nat.gas_{process}$, having similar values to the required by a ratio of 1.7. Finally, the process with the lowest fuel required is the one for producing a syngas ratio of 1. Contrary to the fuel requirements, the CO_2 consumption is larger for lower H_2:CO ratios. Only for zero taxes, the requirements are shown to be larger for the H_2:CO ratio of 2.5.

After generating the syngas from both reformers, it is sent to a cleaning and tune-up stage. The most characteristic parameters of this section are the decisions taken for the tune-up of the syngas. The first equipment selection to be taken is the fraction to be sent to the WGS reactor. In the case of producing a syngas with a H_2:CO ratio of 1 (Ethanol), none of the syngas treatments are desired to be included. In the case of a syngas with a H_2:CO ratio of 1.7 (F-T), only the WGS reactor is desired. The fraction sent to this WGS increases with the CO_2 taxes, having a maximum with a taxes of \$60/t as presented in Figure 6. The steam added in this reactor has a value of 0.057 molH_2O:molNat.gas when the taxes are lower than \$60/t. This value increases with the taxes up to a maximum of 0.2 molH_2O:molNat.gas for the largest carbon taxes studied. The last case for producing a syngas with a H_2:CO ratio of 2.5 requires the use of the WGS reactor and the PSA membranes for the removal of CO_2. The fraction sent to the WGS reactor is around 0.36 except in the case with zero taxes, which is desired to be 0.61. The WGS reactor also needs to be fed with steam that takes a value of 0.26 mol_{H2O}:mol $Nat.gas_{process}$ for most of the cases except the one with zero carbon taxes that requires 0.6 mol_{H2O}:mol $Nat.gas_{process}$. The second decision regards +to the use of the PSA membrane for removing CO_2, the fraction sent is always around 0.65, except in the case with zero taxes where a fraction of 0.84 is desired to be sent. The last unit to be selected in the superstructure are the electrolyzers that produce H_2. However, this technology is never selected for all the H_2:CO ratios of the syngas and ranges of carbon taxes studied. In order to evaluate if this technology would be used with lower electricity costs, a sensitivity analysis has been performed assuming that the electricity is generated from the cheapest source, \$0.04/kWh_e for geothermal plants [56]. However, even in that case the electrolyzers are not selected for generating hydrogen as it can be seen in Table S-2 of the supplementary material.

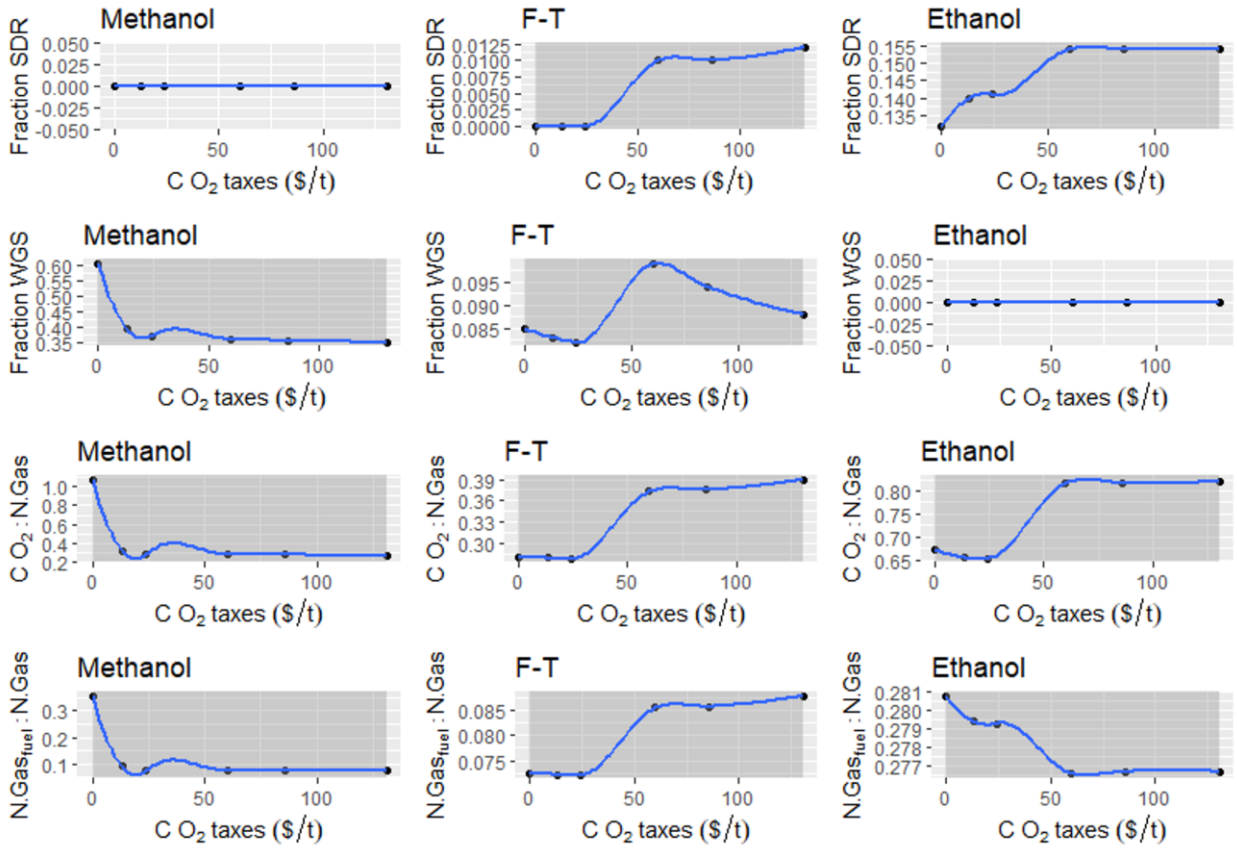

Figure 6. Optimal operating parameters under different carbon taxes for the production of syngas with a ratio of 2.5 (methanol), 1.7 (FT) and 1 (ethanol), and using natural gas as raw material.

4.3.3.1.2 Results for single operation of SDR and TR

Previous results have shown the optimal operating conditions when TR and SDR operate in parallel. However, it can be desired to have only one reactor. Therefore, a sensitivity analysis of the CO_2 taxes is also performed comparing the individual operation of TR versus the individual operation of SDR. The economic results of this sensitivity analysis are presented in Figure 7. It can be seen that the single use of SDR is never more profitable than the single use of TR. SDR improves the profitability of the process when it is introduced in parallel with the TR for the production of a syngas with a H_2:CO ratio of 1 for any carbon taxes and it also improves the profitability for ratios of 1.7 when the carbon taxes are larger than $60/t.

The rest of the results involving the operating conditions of the single operation of the SDR and TR reactors are subsequently presented in tables S-3 and S-4 of the supplementary material. In these tables it can be seen that the operating conditions with the single TR reactor are similar to the operating conditions that when SDR and TR

are allowed to operate in parallel. The most relevant changes occur with the operation of a single SDR and they are summarized in the following paragraphs.

Comparing the CO_2 emissions, it can be seen that the emissions generated by single SDR process perform differently according to the H_2:CO ratio of the syngas. In this case of single SDR, with carbon taxes larger than \$24/t, the largest emissions are generated for producing a syngas with a H_2:CO ratio of 1.7 (around 0.8kgCO_2/mol Nat.gas). The following ratio with more emissions is 2.5 (around 0.67kgCO_2/mol Nat.gas) and for a syngas with a ratio of 1 is around 0.58kgCO_2/mol Nat.gas.

Analyzing the utilities of the SDR process, it can be seen that the amount of natural gas used for heating-up the reformer and the amount of CO_2 fed are always around 1.5 mol Nat gas_{Fuel}: mol Nat. $gas_{process}$ and 3 mol CO_2:molNat. Gas. Only the cases for producing a syngas with a H_2:CO ratio of 1 and 1.7 with zero carbon taxes, consume more CO_2 with subsequent ratios of 8.3 and 3.2 mol Nat gas_{Fuel}: mol Nat. $gas_{process}$. The low level in most of the cases suggests that instead of obtaining benefits for consuming CO_2, the processing of it is expensive enough to result profitable. It can be seen that large amounts of fuel are used to heat-up the reformer.

Another relevant result is the selected source of hydrogen. The work of Verbeeck et al. [38] proposed a process based on an electrolyzer. However, the current optimization prefers the use of a WGS reactor instead of an electrolyzer for producing hydrogen. This WGS reactor does not only generate H_2, but it also generates CO_2 that is removed with the PSA system. This PSA membrane is required for all the cases after the WGS reactor.

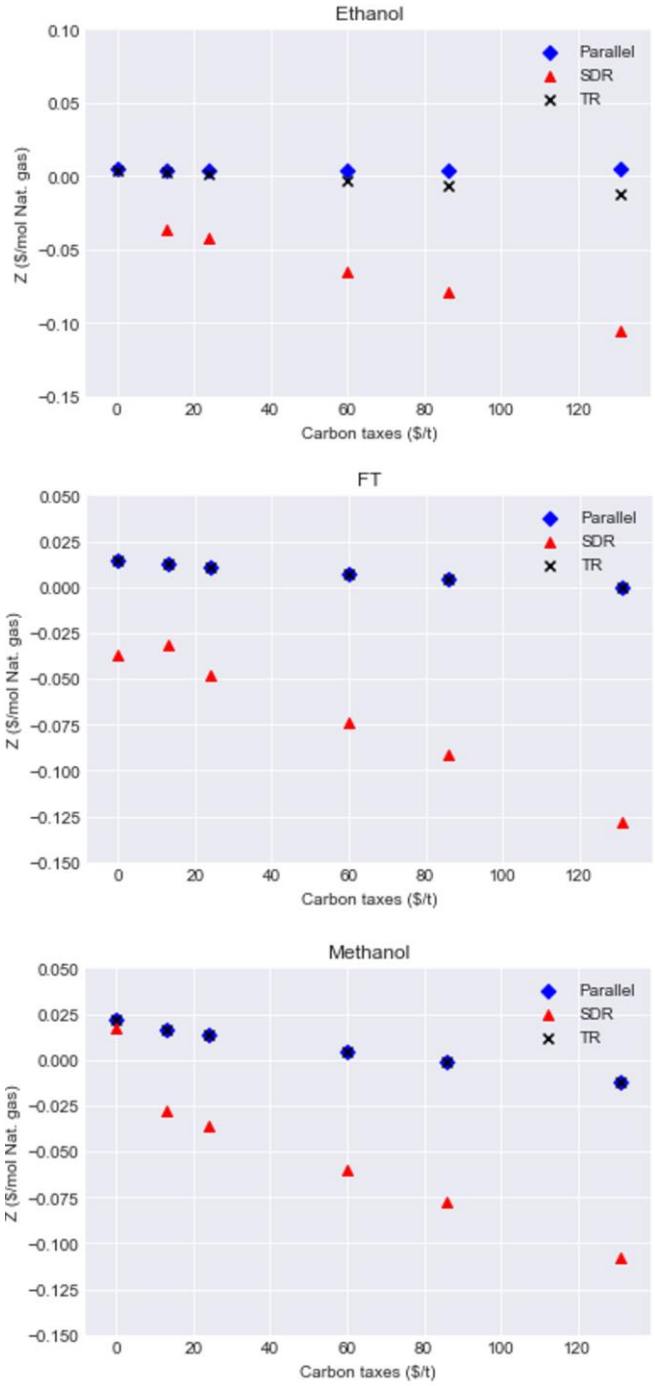

Figure 7. Comparison of the economic function using single SDR and TR and their parallel use for syngas production with a H_2:CO ratio of 1, 1.7 and 2.5 using natural gas as raw material.

4.3.3.2 Optimization results using biogas as raw material

4.3.3.2.1 Results considering parallel reforming operation

This second section presents the results when biogas is fed as raw material. Figure 8 presents the economic and environment results of the optimizations under the CO_2 taxes defined in section 4.3.2.6 and another two cases where the taxes are assumed to be 10 times larger than most of the current ones, \$200/t_{CO2} and \$300/t_{CO2}. It can be seen in Figure 8,a that the production of a syngas with a H_2:CO ratio of 1 becomes more profitable when the carbon taxes increase. For the production of syngas with a ratio of 1.7, the process reduces its profit up to a minimum when the taxes are \$24/t and then this profit is governed by the negative carbon taxes that increase the benefit obtained when they are larger. In the last case for a syngas with a H_2:CO ratio of 2.5, the process always has positive emissions, see Figure 8,b. As a result, a reduction of the profit is observed when the carbon taxes increase. Comparing the syngas ratios studied in the work, it can be seen that the production of syngas for methanol is recommended for economies with carbon taxes lower than \$60/t_{CO2} and the production of syngas for ethanol is recommended for economies with larger carbon taxes. In Figure 8,c, a comparison between the emissions and the profit obtained is presented. It can be seen that to achieve a syngas with a H_2:CO ratio of 2.5 is the case with largest emissions of CO_2 for all the taxes studied. The emissions of this process are always positive until reaching a minimum of approximately 0.07 $kg_{CO2}/10mol_{Natural\ gas}$, and resulting in a reduction of the profit. However, in the case of producing a syngas with H_2:CO ratios of 1 or 1.7, a Pareto plot is obtained. It can be seen in Figure 8,c that the profit of the process increases when more CO_2 is absorbed. The absorption of CO_2 represents a benefit in these two cases, being more significant in the case of the production of a syngas with a ratio of 1 since it contains larger percentage of carbon in its composition.

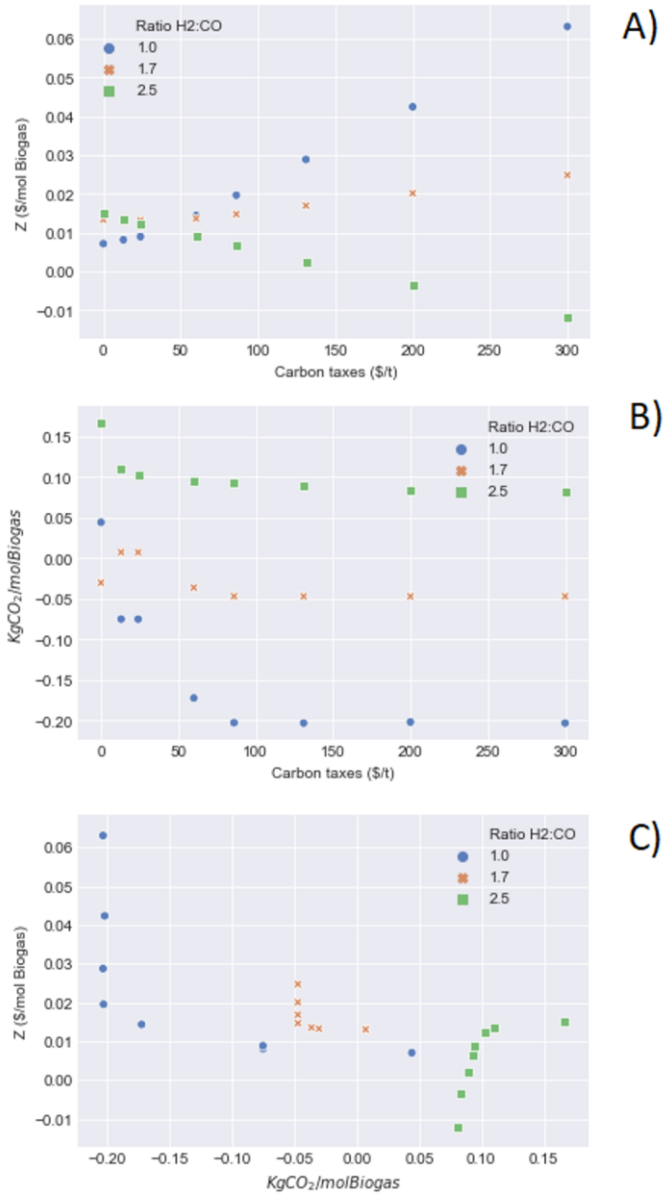

Figure 8. Economic objective function (Z), CO_2 generated by the processes and relation between the results of both for H_2:CO ratios of the syngas of 1, 1.7 and 2.5, and using biogas as raw material.

The following lines present the main operating conditions of the superstructure when it is optimized using biogas as raw material. The first decision to be taken in the process is the specification of the optimal composition of the biogas fed in the system. This composition is presented in Table S-5 of the supplementary material. It can be seen that the desired biogas always desires large contents of methane for the production of syngas with a ratio of 1.7 or larger. However, in the case of a H_2:CO ratio of 1 the desired biogas is composed by 52%CH_4 and 48%CO_2 when the carbon taxes are zero, increasing the methane content up to get a maximum when the taxes are \$60/t or larger. A relevant change in the composition is the increase of the moisture content. For lower carbon taxes, a biogas is desired to have the lower bound of the moisture content and for taxes of \$24/t or larger, the moisture content increases until it gets the upper bound for all the syngas ratios when the taxes are of \$131/t.

The next decision corresponds to the fraction of biogas sent to the SDR reactor. Figure 9 shows that the inclusion of SDR is not desired for carbon taxes up to \$24/t, which is the case of most of the countries nowadays. In the case of taxes of \$60/t, SDR starts to be taken into account in the production of syngas with a ratio of 1 and for taxes of \$86/t it is desired to be included in the processing of syngas with a H_2:CO ratio of 1.7. The operating conditions of these reactors are desired to be as follows:

- The TR reactor is always desired to operate at 1273K except for the cases where a syngas with a H_2:CO ratio of 1 is produced with carbon taxes up to \$13/t. The operation of this reactor is carried out by adding oxygen as reactant and part of the biogas as fuel to heat-up the reformer. The desired oxygen for the processing of syngas with a H_2:CO ratio of 1 is around 0.03mol O_2:mol biogas when the carbon taxes are \$24/t or lower and around 0.2 mol O_2:mol biogas when the taxes are larger. Opposite, the fuel required is the reactor is higher for lower taxes, around 0.3 mol biogas fuel: mol biogas process, and lower for higher carbon taxes, around 0.06 mol biogas fuel: mol biogas process. The processing of syngas with H_2:CO ratios of 1.7 and 2.5 suggests an addition of O_2 that is between 0.28 and 0.21 mol O_2:mol biogas and an addition of biogas that it is between 0.09 and 0.07 mol biogas fuel: mol biogas process.
- In the case of the SDR reactor, an addition of extra CO_2 and fuel are also suggested. For the production of a syngas with a ratio of 1, the amount of CO_2 added increases up to 0.47 mol CO_2: mol biogas processed and the biogas sent as fuel also increases up to 0.38 mol biogas fuel:mol biogas process. For producing a syngas with a ratio of 1.7, the lower content of carbon results in a lower addition of CO_2, 0.1 mol CO_2: mol biogas processed, and subsequently in a lower amount of biogas used as fuel, 0.08 mol biogas fuel:mol biogas processed.

The sum of the contribution of the biogas sent as fuel and the CO_2 fed to both SDR and TR reactors is presented in Figure 9 showing that the largest global consumption is required for producing a syngas with a H_2:CO ratio of 1.

The subsequent decision to be taken in the superstructure is the amount of syngas sent to the WGS reactor. It can be noticed that the production of a syngas for methanol requires a larger fraction to be sent to the WGS reactor since the final syngas has larger content of H_2. This reactor is always selected for methanol and FT production but with an opposite behavior as function of the carbon taxes. On the one hand, for producing a syngas with a H_2:CO ratio of 2.5, methanol, the fraction sent to the WGS increases with the carbon taxes until the taxes are \$86/t. Then, it decreases up to get a constant value of 0.3 for taxes of \$131/t or larger. On the other hand, the production of syngas with a ratio of 1.7, FT, increases with the carbon taxes going from a ratio of 0.1 up to 0.2. The case involving the production of a syngas with a ratio of 1 does not require the use of a WGS reactor when the taxes are \$60/t or less. For larger carbon taxes, the ratio sent to the WGS reactor increases having a maximum of 0.3 when the taxes are \$200/t. The second treatment to be performed in the system is the capture of CO_2 by means of a PSA system. It can be seen in Table S-5 of the supplementary material that the PSA membrane is only desired for the production of a syngas with a ratio of 2.5. All the cases with this ratio require to treat about 65% of the syngas produced. After removing the CO_2, the production of H_2 via electrolysis is also allowed. However, this technology is not desired for

any of the cases studied. In order to evaluate if this technology would take place with lower electricity costs, a sensitivity analysis has been performed assuming the cheapest electricity cost, \$0.04/kWh$_e$ for geothermal plants [56], but in none of the cases the electrolyzers are selected for generating hydrogen, see Table S-6 of the supplementary material.

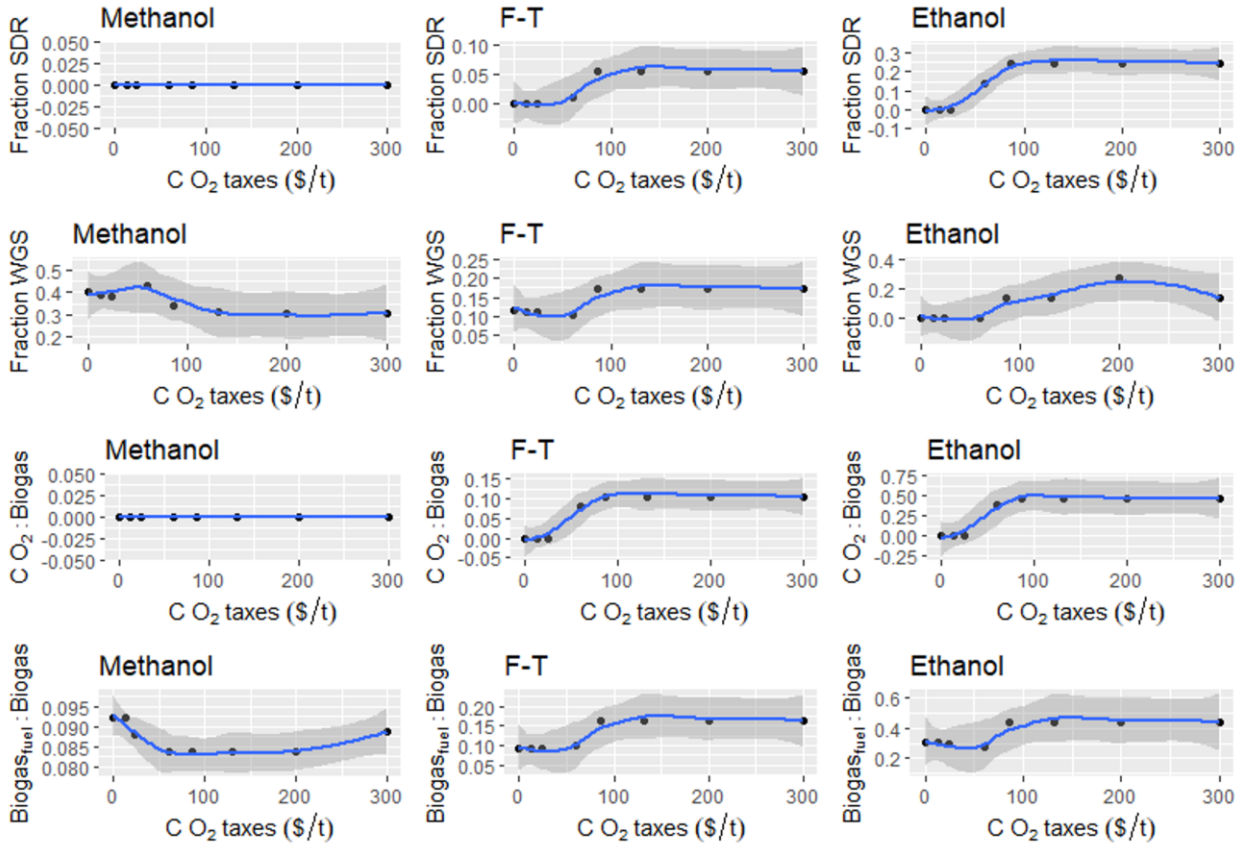

Figure 9. Optimal operating parameters under different carbon taxes for the production of syngas with a ratio of 2.5 (methanol), 1.7 (FT) and 1 (ethanol), and using biogas as raw material.

4.3.3.2.2 Results for single operation of SDR and TR

The results presented in this section has shown that SDR can be an option for the production of syngas when the CO_2 taxes are large enough. However, the use of TR and SDR at the same time involves larger investment than the use of a single technology. Therefore, the following lines present an evaluation using a single reforming technology.

The economic results presented in Figure 10 show that the single use of SDR is always less profitable than the single use of a TR reactor. In fact, for producing a syngas with a H_2:CO ratio larger than 1 the process with a single SDR reactor becomes less profitable than the TR when the taxes increase. Analyzing these profits, it can be seen that the only profitable application for SDR is the production of a syngas with a H_2:CO ratio of 1 and with carbon taxes of at least \$60/t.

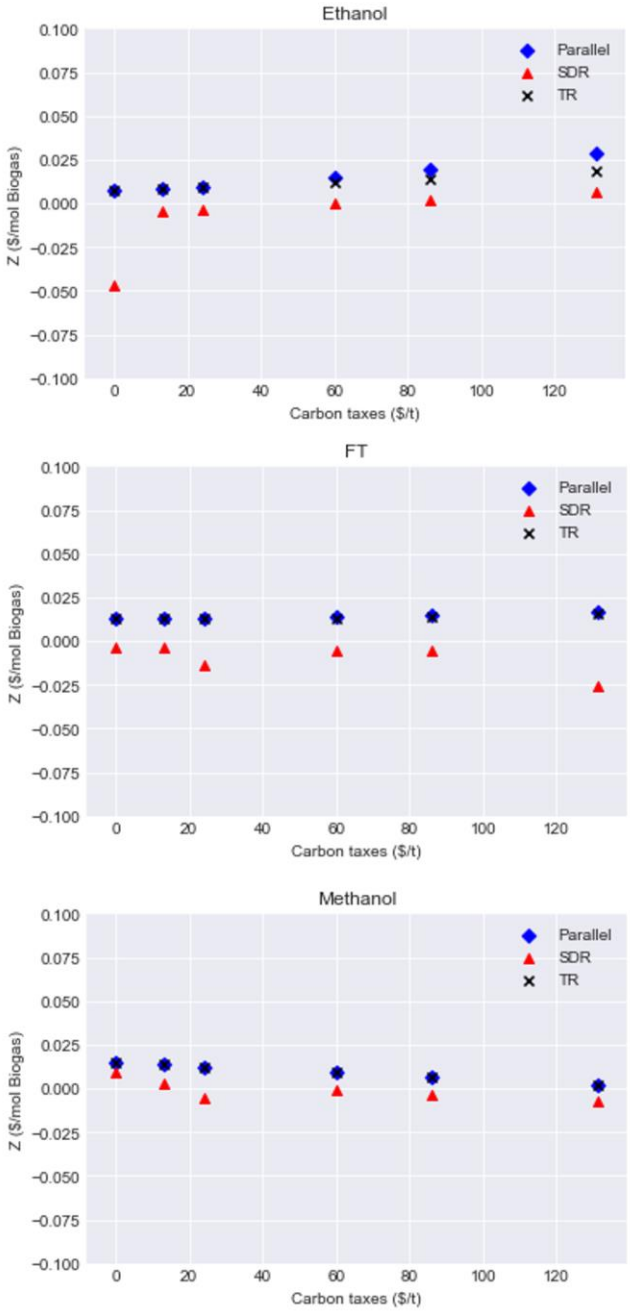

Figure 10. Comparison of the economic results comparing SDR, TR and the parallel use of both.

The CO_2 emissions and optimal operating conditions of the single processes are presented in Tables S-7 and S-8 of the supplementary material. These emissions always tend to decrease when the carbon taxes are larger. Furthermore, when the ratio is 1, the emissions are negative and part of the benefit is obtained by absorbing the CO_2. In the case of a ratio of 1.7 and 2.5, the emissions are roughly constant with a reduction when the carbon taxes increase.

Analyzing the operating conditions, one of the most relevant changes is observed in the biogas composition. Contrary to the case with parallel reformers, in the case of a single SDR reactor the biogas is desired to have the

lowest content of methane. The process is not profitable and the material consumption tends to be reduced. Even in the case when the process is profitable for a syngas ratio of 1, the optimization still suggests a biogas with low content of methane. This behavior is explained in this case because the main credit is obtained thanks to the consumption of CO_2. Apart from this difference in the biogas composition, the two following relevant changes are observed. First, the WGS reactor is always desired to produce all the H_2 required in the syngas. The fraction sent to the WGS is larger than 0.8 in most of the cases, being this technology preferred versus the electrolyzers. Second, the PSA system to capture the CO_2 is also desired for all the cases studied with fractions always larger than 0.9.

4.3.4. CONCLUSIONS

This works has presented a mathematical optimization approach for the evaluation of the opportunities to use super-dry reforming for producing syngas. As a result from this study, it is obtained that the single use of SDR is not more profitable than the use of TR when biogas, natural gas is used as raw materials for all the carbon taxes studied. This SDR technology is only desired to be integrated in the processing of syngas by operating in parallel with a TR reactor for H_2:CO ratios of 1.7 and 2.5 when the taxes are large enough. Using natural gas as raw material for producing a syngas with a ratio of 1.7, SDR is only desired for carbon taxes of at least 60$/t and for producing a syngas with a ratio of 2.5, SDR reforming is desired for all the taxes. In the case of using biogas as raw material, SDR is suggested to be included when the carbon taxes are at least of 60$/t for a syngas ratios of 1.7 and 2.5. Apart from studying the economic feasibility of SDR, the work also provides the optimal source that has to support the generation of H_2 for the syngas. It has been obtained for all the cases studied that the preferred technology is the use of a WGS reactor. The use of electrolyzers is never desired for all the cases studied.

NOMENCLATURE

C_j: Price of the material/product j.
Cp: Specific heat capacity at constant pressure (J/mol K)
fc(i,j,k): molar flow rate of component i, from equipment j to k (mol/s)
F: Total molar flow rate (mol/s).
ΔH^0_{298K}: Reaction enthalpy at 298 K (kJ/mol)
Hf_i: Formation enthalpy of component i (J/mol)
i: Set of components.
K_c: Polytrophic coefficient for compressors.
k_p: Equilibrium constant.
kWh_e: kWh for electricity.
kWh_t: kWh for thermal energy.
LHV_i: Low heating value of component i. (J/kg)
m_i: mass flow rate of component i (kg/s)
mol_i: mol of component i.
MW_i: Molar mass of component i (kg/kmol)
P_i: Partial pressure of component i (bar)
Q: Heat flux (J/s)
T: Temperature (K)
W: Electricity (W)
X_i: Conversion of component i.

Z: Profit ($/mol of natural gas)
η_c: Compressor efficiency.

REFERENCES

[1] EPA. 2018. Overview of Greenhouse Gases. Available. in: https://www.epa.gov/ghgemissions/overview-greenhouse-gases [Last access: September, 2018].

[2] CO_2 – Earth. 2018. NOAA Monthly CO2 Data. Available in: https://www.co2.earth/monthly-co2 Last access: October 2018.

[3] Ottmar, E. Pichs-Madruga, R. Sokona, Y. Minx, J. C. Farahani, E. Kadner, S. Seyboth, K. Adler, A. Baum, I. Brunner, S. 2014. *Working Group III Contribution to the Fifth Assessment Report of the Intergovernmental Panel on Climate Change (IPCC)*.

[4] United Nations Climate Change. 2015. The Paris Agreement. Available in: https://unfccc.int/process-and-meetings/the-paris-agreement/the-paris-agreement [Last access: October 2018].

[5] Our World in Data. 2018. Future greenhouse gas emission scenarios. Available in: https://ourworldindata.org/grapher/future-greenhouse-gas-emission-scenarios. [Last access: October 2018].

[6] Leung, D. Y. C., Caramanna, G. Maroto-Valer, M.M. 2014. An overview of current status of carbon dioxide capture and storage technologies. Renewable and Sustainable Energy Reviews, 39, 426-443.

[7] Bhown, AS. Freeman, BC. 2011. Analysis and status of post-combustion carbon dioxide capture technologies. Environ. Sci. Technology; 45:8624–32.

[8] Boot-Handford, M.E. Abanades, J,C. Anthony, E.J. Blunt, M.J. Brandani, S. Mac Dowell, N. Fernández, J.R. Ferrari, M.C. Gross, R. Hallett, J.P. Haszeldine, R.S. Heptonstall, P. Lyngfelt, A. Makuch, Z. Mangano, E. Porter, T.J. Pourkashanian, M. Rochelle, G.T. Shah, N. Yao, J.G. Fennell, P.S. 2014. Carbon capture and storage update. Energy & Environmental Science, 7,130.

[9] Takamura, Y. Narita, S. Aoki, J. Uchida, S. 2001. Application of high-PSA process for improvement of CO2 recovery system. Can J Chem. Eng.;79:812–6.

[10] Riboldi, L. Bolland, O. 2017. Overview on Pressure Swing Adsorption (PSA) as CO2 capture technology: state-of-the-art, limits and potentials. Energy Procedia. 2017, 114, 2390-2400.

[11] Hedin, N. Andersson, L. Bergstrom, L. Yan, J. 2013. Adsorbents for the post-combustion capture of CO2 using rapid temperature swing or vacuum swing adsorption. Applied Energy, Vol. 104, 2013, 418-433.

[12] Vogtenhuber, H. Sonnleitner, E. Helmenger, F. Hofmann, R. Schöny, G. Wilk, V. Lauermann, M. Werner, A. Hofbauer, H. 2018. Innovative Temperature Swing Adsorption Simulation Model for Biogas Upgrading. Computer Aided Chemical Engineering, Vol. 43, 1377-1382.

[13] Lyngfelt, A. Mattisson, T. 2011. Materials for chemical-looping combustion. In: Stolten D,Scherer V, editors. Efficient carbon capture for coal power plants. Weinheim: Wiley-VCH Verlag GmbH&Co. KGaA;.p.475–504.

[14] Adánez, J. Abad, A. Garcia-Labiano, F. Gayan, P. Diego, L., 2012. Progress in chemical-looping combustion and reforming technologies. Prog. Energy Combust Sci. ;38:215–82.

[15] Tuinier, MJ. Annaland, MVS. Kramer, GJ. Kuipers, JAM. 2010. Cryogenic CO2 capture using dynamically operated packed beds. Chem. Eng. Sci. 65:114–9.

[16] Celia, MA. Nordbottena, JM. 2009. Practical modelling approaches for geological storage of carbon dioxide. Ground Water;47:627–38.

[17] Blamey, J. Anthony, E.J. Wang, J. Fennell, P.S. 2010. The calcium looping cycle for large-scale CO2 capture. Progress in Energy and Combustion Science, 36, 260-279.

[18] Kumar, P. With, P. Srivastava, V.C. Shukla, K. Gläser, R. Mishra, I.M. 2016. Dimethyl carbonate synthesis from carbon dioxide using ceria-zirconia catalysts prepared using a templating method: characterization, parametric optimization and chemical equilibrium modeling. RSC Advances. 6, 110235.

[19] Jarvis, S.M. Samsatli, S. 2018. Technologies and infrastructures underpinning future CO2 value chains: A comprehensive review and comparative analysis. Renewable and Sustainable Energy Reviews 85, 46-68.

[20] Dooley, J.J. Davidson, C.L. Dahowski, R.T. 2009. An assessment of the commercial availability of carbon dioxide capture and storage technologies as of June 2009. Report for the US Department of Energy under a contract no. DE-AC05-T6RL01830, PNNL-18520.

[21] Davis, W., Martín, M. 2014. Optimal year-round operation for methane production from CO_2 and Water using wind and/or Solar energy. J. Cleaner Prod. 80, 252-261.

[22] Aresta, M. 2003. Carbon Dioxide Recovery and Utilization. Ed. Springer. ISBN: 978-90-481-6335-9.

[23] Baltrusaitis, J. Luyben, W.L. 2015. Methane Conversion to Syngas for Gas-to-Liquids (GTL): Is Sustainable CO2 Reuse via Dry Methane Reforming (DMR) Cost Competitive with SMR and ATR Processes? ACS Sustainable Chemistry & Engineering, 3, 9, 2100-2111.

[24] Challiwala, M.S. Ghouri, M.M. Linke, P. El-Halwagi, M.M. Elbahir, N.O. 2017. A combined thermo-kinetic analysis of various methane reforming technologies: Comparison with dry reforming. J. of CO2 Utilization, 17, 99-111.

[25] Noureldin, M.M.B. Elbahir, N.O. El-Halwagi, M.M. 2014. Optimization and selection of reforming approaches for syngas generation from natural/shale gas. Ind. Eng. Chem. Res. 53 (5) 1841-1855.

[26] Löfberg, A. Kane, T. Guerrero-Caballero, J. Jalowiecki-Duhamel,L. 2017. Chemical looping dry reforming of methane: toward shale-gas and biogas valorization. Chemical Engineering & Processing: Process Intensification 122, 523-529.

[27] Hernández, B. León, E. Martín, M. 2017. Bio-waste selection and blending for the optimal production of power and fuels via anaerobic digestion. Chem. Eng. R. and D. Vol. 121, 163-172.

[28] Lim, Y. Lee, C. Jeong, Y.S. Song, I.H. Lee, C.J. Han, C. 2012. Optimal Design and Decision for Combined Steam Reforming Process with Dry Methane Reforming to Reuse CO2 as a Raw Material. Ind. Eng. Chem. Res., 51, 4982-4989.

[29] Afzal, S. Sengupta, D. Sarkar, A. El-Halwagi, M.M. Elbashir, N.O., 2018. An Optimization Approach to the Reduction of CO2 Emissions for Syngas Production Involving Dry Reforming. ACS Sustainable Chem. Eng., 6, 6, 7532-7544.

[30] Chein, R.Y. Hsu, W. 2018. Analysis of Syngas Production from Biogas via the Tri-Reforming Process. Energies, 11, 1075; DOI: 10.3390/en11051075.

[31] Hernandez, B. Martín, M. 2018. Optimization for biogas to chemicals via tri-reforming. Analysis of Fischer-Tropsch fuels from biogas. Energy Conversion and Management. Vol. 174, 998-1013.

[32] Zhang, Y. Zhang, S. Gossage, J.L. Lou, H.H. Benson, T.J. 2014. Thermodynamic Analyses of Tri-reforming Reactions to Produce Syngas. Energy & Fuels, 28, 4, 2717-2726.

[33] Chein, R.; Wang, C.; Yu, C. 2017. Parametric study on catalytic tri-reforming of methane for syngas production. Energy, 118, 1–17.

[34] Balasubramanian, P. Bajaj, I. Hasan, M.M.F. 2018. Simulation and optimization of reforming reactors for carbon dioxide utilization using both rigorous and reduced models. Journal of CO2 Utilization, Vol. 23, 80-104.

[35] Buelens, L.C. Galvita, V.V. Poelman, H. Detavernier, C. Marin, G.B. 2016. Super-dry reforming of methane intensifies CO2 utilization via Le Chatelier´s principle. Science, 354, 449-452.

[36] Hu, J. Galvita, V.V. Poelman, H. Marin, G.B. 2017a. Advanced Chemical Looping Materials for CO2 Utilization: A Review. Materials, 11, 1187. doi:10.3390/ma11071187

[37] Hu, J. Galvita, V.V. Poelman, H. Detavernier, C. Marin, G.B. 2017b A core-shell structured Fe2O3/ZrO2@ZrO2 nanomaterial with enhanced redox activity and stability for CO2 conversion. Journal of CO2 Utilization 17 20-31.

[38] Verbeeck, K. Buelens, L.C. Galvita, V.V. Marin, G.B. Van Geem, K.M. Rabaey, K. 2018. Upgrading the value of anaerobic digestion via chemical production from grid injected biomethane. Energy & Enviromental Science, 7, DOI: 10.1039/c8ee01059e

[39] Ryckebosch, E. Drouillon, M. Vervaeren, H. 2011. Techniques for transformation of biogas to biomethane. Biomass and bioenergy. 35 1633-1645.

[40] Lee, S. 2007. Methanol Synthesis from Syngas. Handbook of alternative Fuel Technologies; Taylor and Francis: Boca Raton. FL; Chapter 9.

[41] Phillips, S. Aden,A. Jechura, J. Dayton, D. Eggeman, T. 2007. Thermochemical ethanol via indirect gasification and mixed alcohol synthesis of lignocellulosic biomass. Technical Report, NREL/TP-510-41168.

[42] Jahn, M. Heddrich, M. Weder,A. Reichelt, E. Lange,R. 2013. Oxidative dry-reforming of biogas: Reactor design and SOFC. Syst. Integ. Energ. Technol., 1 (1) 48-58 DOI: 10.1002/ente.201200007

[43] Luyben, W.L. 2014. Design and Control of the Dry Methane Reforming Process. Ind. Eng. Chem. Res. 53 (37), 14423-14439.

[44] Roh, H-S. Lee, D.K. Jung, U.H. Yoon, W.L. 2010. Natural gas steam reforming for hydrogen production over metal monolith catalyst with efficient heat-transfer. Int. J. Hydrogen 35 (3): 1613:1619.

[45] Cozad, A. Sahinidis, N.V. Miller, D.C. 2014. Learning Surrogate Models for Simulation-Based Optimization. AIChE. Journal, Vol. 60, No.6, 2211-2227.

[46] Bader, A. Bauersfeld, S. Brunhuber, C. Pardemann, R. Meyer, B. 2011. Modelling of a chemical reactor for simulation of a methanisation Plant Presentation 063:064. Proceedings of the 8th International Modelica Conference, March 20th-22nd, Technical University, Dresden, Germany. https://modelica.org/events/modelica2011/Proceedings/pages/papers/44_4_ID_202_a_fv.pdf [Last access: May, 2018].

[47] Martin, M. Grossmann, I.E. 2011. Energy optimization of bioethanol production via gasification of switchgrass. AIChE. J. 57 (12) 3408-3428. DOI: 10.1002/aic. 12544.

[48] Ivy, J. 2004. Summary of Electolytic Hydrogen Production. Milestone Completion Report. NREL.

[49] Philibert, C. 2017. Producing ammonia and fertilizers: new oportunities from renewables. October 2017. International Energy Agency. Available in: https://www.iea.org/media/news/2017/Fertilizer_manufacturing_Renewables_01102017.pdf [Last access: October 2018].

[50] Energy Information Administration. 2018a. Natural Gas Prices. August 2018. Available in: https://www.eia.gov/dnav/ng/ng_pri_sum_dcu_nus_m.htm. [Last Access: November 2018].

[51] Global CCS Institute. 2018. The CO_2 market. 2018. Available in: https://hub.globalccsinstitute.com/publications/accelerating-uptake-ccs-industrial-use-captured-carbon-dioxide/2-co2-market [Last access: October, 2018].

[52] Martin, M. Grossmann, I. E. 2014. Design of an optimal process for enhanced production of bioethanol and biodiesel from algae via glycerol fermentation. Applied Energy 135, 108-114.

[53] Hernández, B. Martín, M. 2016. Optimal Process Operation for Biogas Reforming to Methanol: Effects of Dry Reforming and Biogas Composition. Ind. Eng. Chem. Res. 55, 23, 6677-6685.

[54] Griffiths-Satenspiel, B. Wilson, W. 2009. The Carbon Footprint of Water, River Network. Available in: https://www.rivernetwork.org/wp-content/uploads/2015/10/The-Carbon-Footprint-of-Water-River-Network-2009.pdf [Last access: October 2018].

[55] IDAE, 2014. Factores de emision de CO2 y coeficientes de paso a energía primaria de diferentes fuentes de energía final consumidas en el sector de edificios en España. Available in: https://www.mincotur.gob.es/energia/desarrollo/EficienciaEnergetica/RITE/propuestas/Documents/2014_03_03_Factores_de_emision_CO2_y_Factores_de_paso_Efinal_Eprimaria_V.pdf [Last access: October 2018].

[56] Energy Information Administration. 2018b. Levelized Cost and Levelized Avoided Cost of New Generation Resources in the Annual Energy Outlook 2018. March 2018. Available in: https://www.eia.gov/outlooks/aeo/pdf/electricity_generation.pdf [Last access: December 2018].

[57] Carbon tax center. 2018. Where Carbon Is Taxed. Available in: https://www.carbontax.org/where-carbon-is-taxed/ [Last access: October 2018].

CHAPTER 4.4. PRODUCTION OF H_2 AND METHANOL VIA DARK FERMENTATION. A PROCESS OPTIMIZATION STUDY.

ABSTRACT

This work presents a process optimization study of the production of H_2 and methanol via dark fermentation. A kinetic model is developed for dark fermentation and it is implemented in the process optimization by means of orthogonal collocation. As a result from the entire process optimization, the optimal operating conditions of the process are determined. The investment in the process is estimated to be $18.2 M and has a production cost of $37.6 per kg of H_2 produced when 1 kg/s of biomass is treated. The second process optimization study is developed for the production of methanol via hydrogenation of CO_2. This process is estimated to require an investment of $ 16.4 M and the production cost is $6.9/kg of methanol when 1kg/s of biomass is treated. In both cases, the amounts of H_2, 8 g/s, and methanol produced, 38 g/s, are very low in comparison with the resource treated.

Note: Supplementary material is available in: https://pubs.acs.org/doi/abs/10.1021/acs.iecr.0c03336

4.4.1 INTRODUCTION

The transformation of bio-resources into valuable products has been a widely covered topic in the last years. Specially, the use of organic waste is receiving a lot of attention due to its potential. In Europe the total amount of waste generated is estimated to be approximately 0.5 t/year*person [1]. Approximately, 15% of that amount corresponds to organic wastes from different sectors such as agriculture, forest, food or waste water treatment plants [2]. The treatment of these organic wastes is not only mandatory in most of the countries [3, 4], but in many cases it is also an opportunity since further value can be generated from them. For years, the most recurrent technology used for treating the waste was incineration for the production of heat and power. Later, other thermochemical methods such as gasification and pyrolysis were taken into account [5]. However, in the last years bio-chemical methods such as anaerobic digestion and fermentation have focused most of the research attention because they generate products with added value as well as they can also operate at ambient temperatures and pressures [6]. In this context, the use of dark fermentation is another bio-chemical technology that does not only treat the waste but it also has additional benefits such as the production of a high valuable chemical, hydrogen [7], and the possibility of using several types of biomass sources [8].

The modelling of this process has been carried out following different approaches [9] from the most detailed CFD models to artificial neural networks [10]. Even though CFD models provide the most detailed description within the unit, these models are very complex to be introduced into process simulation and optimization, being mainly replaced by several kinetic models applied to the entire reactor [11]. Among these models, two have been the most commonly used. The Gompertz model proposed by Zwietering et al. [12] has been widely used for the analysis of batch operations, reproducing with high fidelity the substrate degradation and the H_2 generated. Alternatively to Gompertz model, Monod´s equation and its extensions or adaptations to include the presence of inhibitors, the influence of pH, temperature or the level of substrate [11] have been applied to describe the dark fermentation kinetics not only in batch reactors [13] but also in continuous reactors [14]. Analyzing the influence of several properties on the kinetic model, optimization of the dark fermentation process by means of genetic algorithms has been carried out in order to maximize the production of hydrogen in the process [15]. However, the costs involved in purifying such hydrogen as well as other factors such as the type of hydrolysis selected have not been addressed in the optimization.

Furthermore, in spite of hydrogen is considered to be one of the most promising fuels due to environmental and energy concerns [16], its storage still presents a challenge [17]. These difficulties make interesting the development of other compounds such as methanol or ethanol that are easy to store and transport. These compounds are typically synthesized from carbon and hydrogen sources via syngas. The syngas can be generated using different types of raw materials and processes. On the one hand, syngas can be produced from bio-resources by means of gasification of dry biomass [18]. This method provides a high yield for the transformation of waste but the high temperatures achieved result in the generation of compounds such as H_2S, NH_3 or HCl that are difficult to separate and damage catalysts [19]. On the other hand, syngas can be also produced by processing intermediate

compounds, such as biogas, generated in the treatment of wet wastes [20]. In either gasification or biogas reforming, high temperatures are required, usually above 1000 K. As a result, part of the raw material is dedicated to produce energy, being the process difficult to integrate with other renewable resources such as solar energy and generating higher CO_2 emissions. Alternatively to the synthesis route, the hydrogenation of CO_2 is studied since it represents a high suitable technology for the integration with dark fermentation because the products required in the hydrogenation process correspond with the ones generated in the fermentation.

In this work a cleaner process for the production of methanol is studied since all the technologies work at a maximum temperature of 573 K, which is lower than the temperature required for reforming or gasification while it is possible to process wet biomass [21]. The process combines dark fermentation and methanol production via CO_2 hydrogenation. It is designed and optimized as presented in the following sections. The paper is structured as follows. Section 4.4.2 describes the modelling of the units involved in the processes for H_2 and methanol production. Particular attention is paid to the model of the kinetics of dark fermentation. Section 4.4.3 presents the optimization results. The last section 4.4.4 draw the conclusions of this work.

4.4.2 PROCESS MODELING

This section presents the stages that constitute the process, see Figure 1, and the models developed for all the units. The waste introduced into the process is first hydrolyzed to obtain glucose and xylose. These sugars are then transformed into H_2 via dark fermentation. The H_2 produced from the reactor is not pure and other compounds such as H_2S, CO, methane and CO_2 are also produced. Thus, the production of purified hydrogen or methanol requires of a cleaning stage where H_2S and methane are removed. After removing those gases, the next stage is the tune-up of the CO_2 content. The CO_2 can be fully or partially removed depending on the desired product. In the case of producing methanol, the gas mixture is fed to a Pressure Swing Adsorption (PSA) system and then to the CO_2 hydrogenation reactor. Since the reactor has a low yield to methanol, recirculation of the unreacted gases is also taken into account. Finally, this methanol is separated and purified.

All the units are modelled using mass and energy balances, thermodynamics such as the case of compression steps, rules of thumb and experimental data. In the following sections we pay attention to the major units involved in the process.

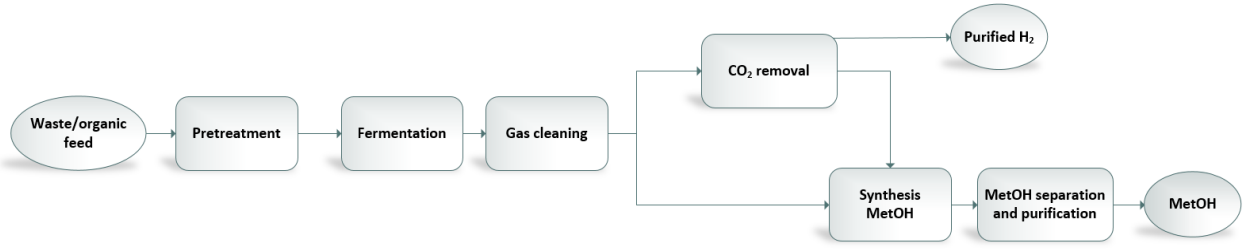

Figure 1. Process stages for the production of Methanol and Hydrogen from organic waste via dark fermentation.

4.4.2.1 Pre-treatment of the waste.

Before dark fermentation, the organic feed needs to be hydrolyzed to increase the sugar content. Hydrolysis can be carried out following two technologies: On the one hand, enzymatic hydrolysis shows the advantage of not requiring the consumption of energy or chemicals. However, the yield achieved in the generation of sugars is low and the enzymes require a higher cost. On the other hand, acid hydrolysis allows achieving higher yields in the process but it consumes energy and chemicals. Despite the two technologies can be independently used, the combination of both allows achieving even higher yields [22]. Thus, the process combining them is taken into account for the production of glucose as presented in Figure 2. Apart from the hydrolysis method, the yield achieved is highly dependent on the composition of the feed, its particle size and the residence time of such processes. In this work corn has been used as basis for the computation of hydrolysis yields due to the availability of kinetic data. The formulation is general to be applied to other raw material or waste if the experimental results become available. The models developed for the hydrolysis of corn are based on the work of Lloyd and Wyman [22]. This work showed that the two main sugars promoters of corn are glucan, which is 36.4% of the corn composition, and xylan, which is a 21.4%. The acid hydrolysis is assumed to achieve a yield of 33 %. However, the time required to achieve that yield depends on the operating conditions of the process, see Eq. (1). It is determined by Bayesian Information Criteria (BIC) minimization with ALAMO [23] and it addresses the influence of pH, which is between 5 and 7, and temperature, typically between 90ºC and 200ºC [24], in the residence time required in the reactor. The pH reduction is carried out using H_2SO_4 with 98% of concentration.

$$t_{Hydro1} = -5231.66 - 443.419662 * w_{H2SO4} + 828.653273 * \log(T - 273) + \frac{170159.9565}{T-273} \quad (1)$$

After acid hydrolysis, the pH needs to be increased again before the enzymatic hydrolysis process. $Ca(OH)_2$ is used for that purpose. The outlet can be sent straight to the dark fermentation reactor or it can be partially sent to the enzymatic hydrolysis if the yield achieved by this technology is high enough. In the enzymatic hydrolysis the pH is assumed to remain constant at 6 and the temperature required is 50 ºC [22]. For carrying out the hydrolysis, two type of enzymes are assumed:

- On the one hand, Novozyme 188, cellobiase, with an assumed load of 15 FPU/g of glucan can be used as proposed by Lloyd and Wyman [22]. In that work, the sensitivity analysis shows that for this concentration the yield achieved in the transformation of glucan and xylan to glucose and xylose is similar to the case with a load of 60 FPU/g of glucan. The activity of the enzyme is assumed to be the one of cellulose, resulting in a desired concentration of 0.000125 g of cellobiase per g of glucan for such load of 15 FPU/g of glucan [25].
- On the other hand, enzymes such as glucoamylase and protease can also be used with a consumption of 0.005kg per kg of biomass [26]. The production of these enzymes can be integrated in the process as presented by Han et al. [26], being necessary 9.22×10^{-3} kg of biomass per kg of biomass fed in the enzymatic hydrolysis reactor and 4.29×10^{-4} L of *A. awamori* and *A. oryzae* per kg of biomass fed in the reactor [26].

Even though that each type of enzyme result in different yields, the rate of degradation is highly influenced by other parameters such as the pH, the type of raw material and, specially, the particle size [27]. Since corn is used in the current work, the modelling of the rate is based on the work of Lloyd and Wyman [22], where the yield is a function of the residence time as presented in Eq. (2). Note that Eq. (2) is valid for residence times up to 40 min.

$$yield = 0.8267902 - \frac{1.72173913}{t_{enz}} - 0.0577078 * \log(t_{enz}) \quad (2)$$

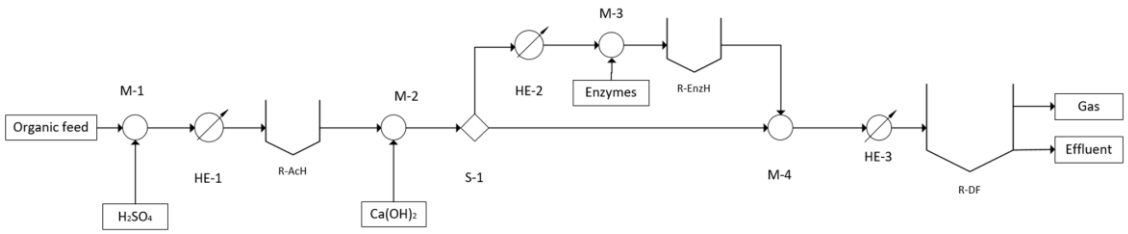

Figure 2. Pre-processing and dark fermentation stages.

4.4.2.2 Modelling the dark fermentation reactor.

Dark fermentation is the limiting stage of the process in terms of reaction rate since it is orders of magnitude slower than hydrolysis. Hydrolysis is in the order of hundredths of minutes while dark fermentation is in the order of tenths of hours [28]. As a result, it is expected that the volume required in the reactor is higher than in other units and a good definition of the kinetic behavior of the unit is desired. For the kinetic modelling of the process, Andrew's model, which has been typically applied to model the hydrogen production of Eq. (3), has been extended to include the other two competitive reactions of dark fermentation, Eq. (4) and (5). Eq. (4) presents the decomposition of glucose to butyrate compounds such as butyric acid and Eq. (5) presents the metabolic reaction. In this metabolic reaction, glucose is consumed, resulting in pyruvate and nicotinamide adenine dinucleotide (NAD) [29].

$$C_6H_{12}O_6 + 2H_2O + H_2O \rightarrow 2\,CH_3COO^- + 2H^+ + 2CO_2 + 4\,H_2 \quad (3)$$

$$C_6H_{12}O_6 \rightarrow CH_3CH_2CH_2COO^- + H^+ + 2\,CO_2 + 2H_2 \quad (4)$$

$$C_6H_{12}O_6 + 2NADH \rightarrow 2\,CH_3CH_2COO^- + 2H_2O + 2\,NAD^+ \quad (5)$$

These kinetic equations are modelled as defined from Eq. (6) to (11), where the following assumptions are considered since no data is available:

- An efficiency term is included, $\eta_{gluctogas}$. It accounts for the fraction of substrate that is decomposed following the reaction of Eqs. (3) and (4). The remaining fraction is assumed to follow Eq. (5).
- The concentration of bacteria is assumed constant. Thus, a single parameter combining the maximum yield, μ_{max}, and the microorganism concentration, X_o, is determined.

These parameters and the characteristic constants are determined based on data from the literature [28] by means of the parameter estimation tool from gProms ® v.5.0. The validation of the model and the comparison with other models is deeply described in the supplementary material. The validated model is then implemented in the optimization formulation by means of an orthogonal collocation scheme [30]. The volume of the reactor is computed from the residence time and the volumetric flux. The investment cost that corresponds to this volume is computed as presented in the supplementary material. Apart from the initial investment, the reactor requires agitation for homogenizing the liquid mixture. Based on the rules of thumb for anaerobic digesters, a power consumption of 0.018 kW/m^3 is used [31].

$$\frac{d[S]}{dt} = \frac{-\mu_{max1}\cdot X_o\cdot[S]}{k_{s1}+[S]+[S]^2/K_{s1}} + \frac{-\mu_{max2}\cdot X_o\cdot[S]}{k_{s2}+[S]+[S]^2/K_{s2}} \quad (6)$$

$$\frac{d[H_2]}{dt} = \eta_{gluctoH2}\left(4\cdot\frac{\mu_{max1}\cdot X_o\cdot[S]}{k_{s1}+[S]+[S]^2/K_{s1}} + 2\cdot\frac{\mu_{max2}\cdot X_o\cdot[S]}{k_{s2}+[S]+[S]^2/K_{s2}}\right) \quad (7)$$

$$\frac{d[CO_2]}{dt} = \eta_{gluctoH2}\left(2\cdot\frac{\mu_{max1}\cdot X_o\cdot[S]}{k_{s1}+[S]+[S]^2/K_{s1}} + 2\cdot\frac{\mu_{max2}\cdot X_o\cdot[S]}{k_{s2}+[S]+[S]^2/K_{s2}}\right) \quad (8)$$

$$\frac{\mathrm{d}[CH_3COO^-]}{\mathrm{dt}} = \eta_{gluctogas}\left(\frac{2*\mu_{max1}\cdot X_o\cdot[S]}{k_{s1}+[S]+[S]^2/K_{s1}}\right) \quad (9)$$

$$\frac{\mathrm{d}\,[CH_3CH_2CH_2COO^-]}{\mathrm{dt}} = \left(1-\eta_{gluctogas}\right)\left(\frac{\mu_{max1}\cdot X_o\cdot[S]}{k_{s1}+[S]+[S]^2/K_{s1}} + \frac{\mu_{max2}\cdot X_o\cdot[S]}{k_{s2}+[S]+[S]^2/K_{s2}}\right) \quad (10)$$

$$\frac{\mathrm{d}[\mathrm{H_2}O]}{\mathrm{dt}} = 2\cdot\left(1-\eta_{gluctogas}\right)\left(\frac{\mu_{max1}\cdot X_o\cdot[S]}{k_{s1}+[S]+[S]^2/K_{s1}} + \frac{\mu_{max2}\cdot X_o\cdot[S]}{k_{s2}+[S]+[S]^2/K_{s2}}\right) - \eta_{gluctogas}\left(\frac{2*\mu_{max1}\cdot X_o\cdot[S]}{k_{s1}+[S]+[S]^2/K_{s1}}\right) \quad (11)$$

Once the glucose has been processed via dark fermentation, two streams leave the reactor: On the one hand, a gas stream, composed mainly by CO_2 and H_2. On the other hand, a liquid stream with the remaining effluent. Furthermore, it is important to remark that the current work only focuses on the conceptual design of the process and the control structures have not been added. In the implementation of that systems, the control of the pH in this reactor is critical. pH is modified by the generation of acid compounds and they reduce the efficiency of the microorganism that generate H_2.

4.4.2.3 Modelling the H_2 purification and CO_2 removal stages.

The gases produced in the dark fermentation reactor are mainly H_2 and CO_2 and traces of other compounds such as H_2S and methane [32]. The first stage of this purification is dedicated to remove those traces of H_2S and methane since they poison the catalyst in the methanol synthesis reactor and the PSA beds in the removal of CO_2 [33]. This task is carried out by means of a PSA system composed by 2 beds (one in operation and another in regeneration) of silica since it allows the selective adsorption of H_2S and methane without trapping the two most relevant gases, H_2 and CO_2.The system is assumed to work at 120 kPa, 298 K and with a pressure drop of 10% [34], being necessary to compress and cool down the feeding stream. The compressor is modelled as polytrophic with a coefficient, K_c=1.4 and an efficiency, ε=0.8.

Once methane and H_2S are removed, the gases are sent to a CO_2 removal section. Two options are considered depending on the desired product. For the production of pure H_2 with a minimum concentration of 99.9% a PSA system with a minimum operating pressure is required. In particular, the one selected for this objective requires an operating pressure of 500 kPa and a temperature of 298 K. The bed is assumed to present a pressure drop of 10%. The H_2 obtained has a concentration of 99.98% of H_2, being 20% of the mass flow rate of this components removed with the other stream [34]. Thus, a two-stage compression system with intercooling is required before the PSA system, see Figure 3, a). This PSA system is also assumed to be composed of 2 beds for operation and regeneration.

Alternatively to the production of H_2, the production of methanol is also studied in this work. It is carried out by means of CO_2 hydrogenation. The minimum ratio defined by Eq. (12) equal to 2 is allowed [35]. Therefore, the CO_2 of the gases generated in the dark fermentation reactor can be partially removed by sending a fraction to a PSA system. In this case the PSA system does not need to remove all the CO_2 and systems operating at lower pressure can be used. In the current case, 150 kPa is assumed and only one compressor followed by a heat exchanger is needed, see Figure 3, b). The system at this pressure is assumed to have a CO_2 removal efficiency of 90% and a pressure drop of 10% of the feeding pressure [34]. Contrary to the removal by means of PSA system, the gases produced in the dark fermentation can be almost free from CO_2. In such a case, additional CO_2 is to be fed. This CO_2 is introduced in mixer M-5.

$$\frac{y_{H2}-y_{CO2}}{y_{CO}+y_{CO2}} \geq 2 \qquad (12)$$

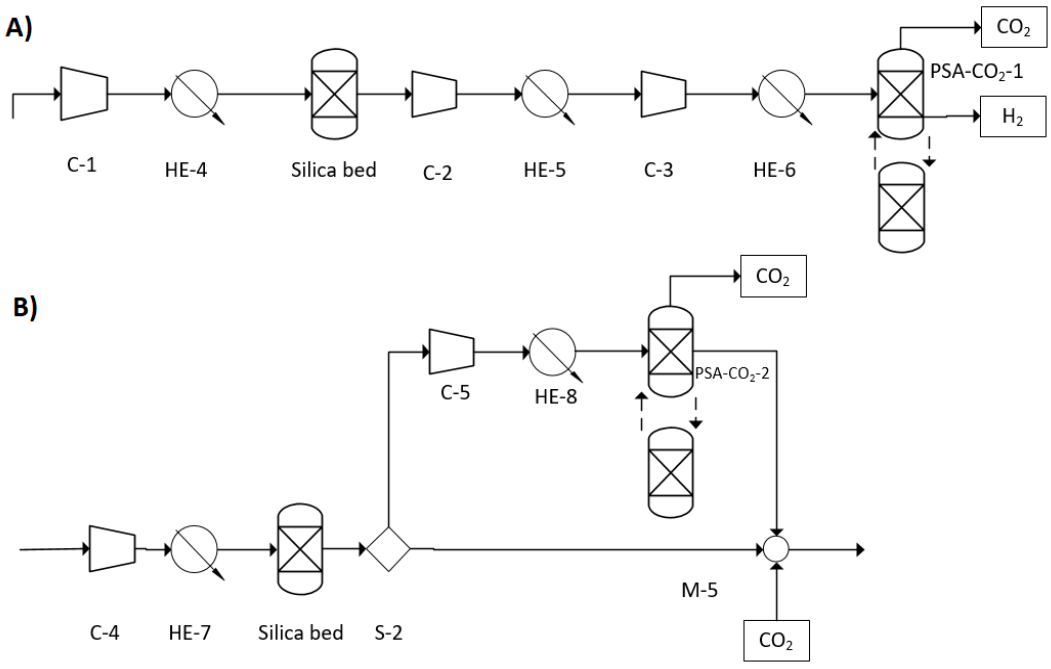

Figure 3. Purification and cleaning of the gases from dark fermentation for hydrogen production, A), and for methanol production, B).

4.4.2.4 Modelling of methanol production and purification.

The gases cleaned in the previous stage are sent to the methanol production stage, see Figure 4. Methanol is generated following the three reactions presented in Eq. (13) to Eq. (15). The first two reactions are highly exothermic and correspond to the hydrogenation of CO_2 and CO to methanol and water. The third reaction is endothermic and corresponds to the competitive reverse water-gas-shift equilibrium. Only two of the reactions are linearly independent. Therefore, only the CO_2 hydrogenation and the water-gas-shift equilibrium, defined by the constants of Eq. (16) and (17), are considered in the model [36].

$$CO_2 + 3H_2 \leftrightarrows \quad CH_3OH + H_2O \tag{13}$$

$$CO + 2H_2 \leftrightarrows \quad CH_3OH \tag{14}$$

$$CO_2 + H_2 \leftrightarrows \quad CO + H_2O \tag{15}$$

$$\log_{10} K_{MetOH\,1} = \frac{3066}{T} - 10.592 \tag{16}$$

$$\log_{10} K_{MetOH\,3} = -\frac{2073}{T} - 2.029 \tag{17}$$

Once methanol is produced in the hydrogenation reactor, the mixture is cooled down and then separated by means of flash F-1. On the one hand, the unreacted gases are recycled to the reactor to improve the process yield, allowing a purge of gases in case that impurities will be present. On the other hand, the liquid fraction containing methanol is obtained. The CO_2 in the stream that leaves the heat exchanger is under gas-liquid equilibrium conditions. Part of the CO_2 is in the gas phase and the remaining fraction is absorbed in the liquid phase. In order to determine the fraction recovered as liquid after the cool down, offline simulations have been performed in ChemCAD® for pressures between 5,000 and 7,500 kPa, temperatures between 298 and 325 K and mass fractions between 80%-50% of H_2, 1%-5% of CO, 10% to 30% of CO_2, 2%-5% of H_2O and 3% to 9% of Methanol. From these studies with ChemCAD®, the CO_2 absorbed in the liquid methanol has never been higher than 0.5% of the total CO_2. This value is very small and a constant value of 0.5% of the total CO_2 fed in the flash is assumed to be absorbed in the liquid stream of methanol and water.

Finally, the methanol separated at flash F-1 requires further purification. The fraction of CO_2 absorbed in the liquid stream is separated by a sequential depressurization and separation with a valve and flash F-2. Then the methanol-water mixture is separated in a distillation column where the mixture is assumed to be fed at liquid saturated conditions, being necessary a heat exchanger, HE-13, to heat up the stream. See the supplementary material for the details of the modeling of the distillation column.

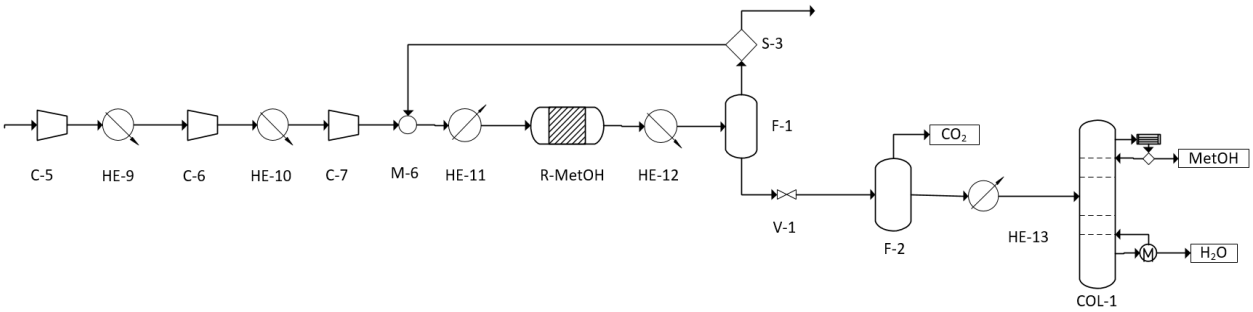

Figure 4. Methanol production and separation stages.

4.4.2.5 Objective function

The models proposed in this work are to put together into a process flowsheet. It is optimized using the return of investment (ROI) as objective function, see Eq. (18). The ROI is selected instead of other methods such as net present value due to the high non-profitability of the process. In those cases where the investment is added as negative, the volumes of the hydrolysis and dark fermentation reactors tend to be zero. The income generated by selling the hydrogen or methanol produced is computed as presented in Eq. (19). Prices of \$1.6/kg for hydrogen [37] and \$0.367/kg in the production of methanol [38] are assumed. The total costs of the process, C, are computed as presented in Eq. (20) and included the following terms:

- The chemicals used in the pretreatment stage such as the sulfuric acid, with a cost of \$0.4/kg [39], and the $Ca(OH)_2$ with a cost of \$0.12/kg [40]. The cost of cellobiase in the hydrolysis is assumed to be \$42/kg [41]. The cost of *A. awamori* and *A. oryzae* is assumed to be \$1.61/L [26]. The cost of the CO_2 is assumed to be \$23/t [42] and the cost of corn has a price of \$0.146/kg [43].
- The utilities involved in the process. The cost of the power involved in the agitation of the system and the compressors is assumed to have a cost of \$0.06/kWh. The cooling water is assumed to have a price of \$5.7x10^{-5}/kg and the steam is assumed to have a cost of \$0.025/kg [44].

$$\max\left(ROI = \frac{B - C_T}{I}\right) \tag{18}$$

$$B = P_{prod} \cdot F \tag{19}$$

$$C_T = C_{H2SO4} \cdot F_{H_2SO_4} + C_{NaOH} \cdot F_{NaOH} + C_{Enz} \cdot F_{Enz} + C_{Co2} \cdot F_{CO2} + C_{corn} \cdot F_{corn} + C_{elec} \cdot \left[\sum_{i \in Compressors} W + W_{DF}\right] + C_q \cdot \sum_{i \in HE_{heat}} Q - C_w \cdot \sum_{i \in HE_{cooling}} Q \tag{20}$$

Finally, the investment cost of the process is computed. The investment costs of each unit are determined per unit of time and they have been computed as follows: The correlations of most of the units have been previously developed by Hernández and Martín [45] except for the distillation column and the hydrolysis and dark fermentation reactors. The cost of the column is developed based on the assumptions reported in the supplementary material

and the estimated costs from Almena and Martín [46]. The volume of the hydrolysis and dark fermentation reactors, is determined as proposed by Taifouris and Martín [47]. The final equations used for the costs of the units are summarized from Eq. (S-9) to (S-16) of the supplementary material. The estimated life expectancy of the units is assumed to be 30 years for the tanks, 20 years for the heat exchangers, flash separators and compressors [48] and 4 years for the membranes [49]. The costs of each unit is multiplied by an installation factor, which is assumed to be 1.4. Furthermore, the total investment cost is also computed by a factor of 3.15 to include the cost of piping and instrumentation systems, electrical, utilities, land plot and buildings [48].

4.4.2.6 Case studies

The two processes studied in this work are independently optimized in GAMS. The H_2 production process is composed by 1300 equations and 1400 variables and the methanol production process consists of 1700 equations and 1800 variables. Both of them are solved using CONOPT using a multi-start initialization approach. A first base case with the assumptions defined in previous sections has been studied. Furthermore, the following sensitivity and numerical analysis have been carried out:

- The price of the raw material has been modified in order to evaluate not only the economy of the process with corn, but also with wastes, assuming them with a similar efficiency in the yields of hydrolysis but with zero cost as raw materials.
- A scale-up study has been evaluated, performing the optimization for treating different amounts in the feed.

4.4.3 RESULTS

4.4.3.1 Process optimization results for the production of H_2

The optimization carried out for the production of H_2 has resulted in a negative ROI of -767%, indicating the non-profitability of the process even under the best operating conditions. An analysis of the operating costs, the income generated by selling the hydrogen and the investment costs of the process is provided in Figure 5, a). It can be seen that the income is $\$9 \cdot 10^{-3}$/s, which exclusively due to the H_2 generated. On the contrary, the costs involved in the operation of the process are approximately three times more, with a value of \$0.263/s. Due to all these costs and the depreciation costs, the resultant production cost for H_2 is estimated to be \$37.6/kg, which is approximately 30 times higher than current price for hydrogen [37]. Among the operating costs, the highest ones correspond to the raw material, corn, suggesting the low yield in the production of H_2 from dark fermentation. Only 8 g/s of H_2 are produced per 1 kg/s of bio-resource, corn.

The yield in the hydrolysis, where both technologies are selected and the integrated production of enzymes proposed by Han et al.[26] is suggested, is 520 g/s of glucose and xylose per 1 kg/s of corn, which is a conversion of 92% of the total glucan and xylan in the corn. Meanwhile, in the dark fermentation process only 8 g/s of H_2 are produced from the 520 g/s of glucose. This low yield in the generation of H_2 is the limiting stage in the process

economy. In order to improve the yield to H_2 and the profitability of the process, dark fermentation can be integrated together with other treatment technologies such as anaerobic digestion [50] or gasification [51]. In future works the optimal operation of these integrated processes can be evaluated. The time required to achieve that yield in the dark fermentation process is suggested to be 69h and the volume of that reactor is estimated to be 5790 m^3. Apart from these characteristic values in the operation of the process, further results such as the power required, the flux of chemicals, utilities, etc. are provided in table S-3 attached in the supplementary material.

The investment costs determined for this optimal process are $18.2M. The distribution of the investment costs required in the units is presented in Figure 5, b). It can be seen that the terms with the highest investment costs are the bed and membranes term and the tanks required for hydrolysis and dark fermentation. Concretely, the tanks for dark fermentation represent a much higher cost (37.2% of the total) than the tanks for hydrolysis (0.75% of the total). It is important to remember that the residence time required in the dark fermentation process is between 10 and 70 times larger than in both hydrolysis processes.

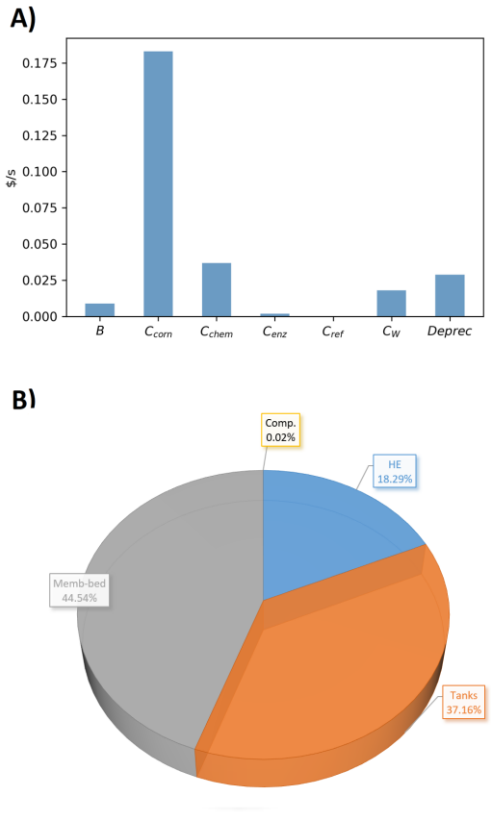

Figure 5. Summary of operating costs and income for the production of H_2 A) and distribution of investment costs of the units B).

The role of the raw material

As it has been observed in the previous results, the term that represents the highest operating costs is the raw material. In the current work we have used corn due to the data available in literature. However, this resource can be substituted by waste. Even if waste results in lower yields, better economic results are expected because the

cost of corn is very high. In this evaluation the yields have been assumed to be equal to the case with corn but the cost of the raw material is assumed to be zero (no transportation costs are assumed to be charged in the processing plant). As a result from this study, the same optimal operating conditions have been obtained for the process, see Table S-3 of the supplementary material. Despite the operating conditions remain similar, better economic results are obtained for the process. The ROI increases up to -166% due to the zero cost of the waste. The remaining costs maintain similar values since the operating conditions are the same as it can be read with more detail in the supplementary material. The production cost obtained for the hydrogen is \$11.9/kg, which supposes to reduce the cost of the corn nearly to a third. Thus, to ensure the profitability of the process (fixing the production cost of H_2 equal to \$1.6/kg to be competitive with the reforming of methane [37]) a minimum credit of \$0.011 is required for treating every kg of wastes.

Scale-up study.

The last study performs an optimization analysis under different scales. As a result from such evaluation, no relevant changes have been obtained in the suggested operating conditions and economic results. All the operating costs show an increase when the feed is increased. The optimal ROI is also very similar for all the scales studied (from treating 0.01kg/s to 5kg/s), with a light decrease for feeds lower than 0.1 kg/s. These economic results for the ROI and the production costs are presented in Figure 6. The economic terms and the optimal operating conditions under different scales are deeply described in Table S-4 of the supplementary material.

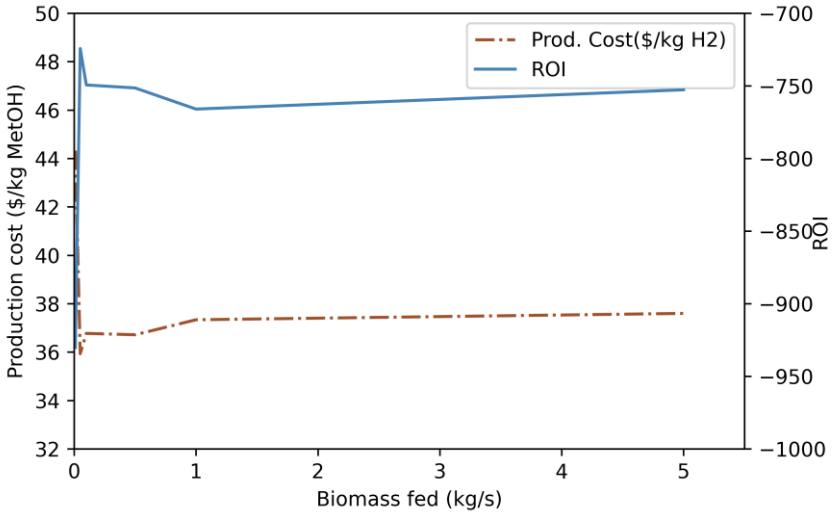

Figure 6. Return of Investment (ROI) and production cost of hydrogen under different scales.

4.4.3.2 Process optimization results for the production of methanol via hydrogenation of CO_2.

The process presented in the previous section is extended for the production of methanol via CO_2 hydrogenation. In this case the ROI obtained from the process is -920%. This ROI is lower than the one obtained for H_2, suggesting that H_2 is more profitable to be produced than methanol. However, the storage and transportation of methanol is easier than for H_2. In future works a comprehensive analysis involving the production and supply chain of both fuels can be studied. The income and cost terms used for computing that ROI are presented in Figure 7. The income generated by selling the methanol is very low, \$0.014/s. However, the profit obtained by selling methanol is higher than the one obtained for hydrogen since the quantity produced is higher, 38 g/s of methanol per 1 kg/s of corn treated with a production cost of \$6.9/kg. The reason behind is the better use of the raw materials since part of the CO_2 is transformed in methanol. However, the estimated production cost is nearly 20 times higher than the original cost of methanol, which is similar to the comparison between the production price of hydrogen and its current price.

The computation of the ROI does not only takes into account the operating costs and income, the investment is also considered. The total initial investment cost of the plant is estimated to be \$16.36M and the distributions among the units is presented in Figure 7, b). This investment cost is lower than in the case for the production of H_2 since the beds and membranes do not require to capture that much CO_2 and they represent a high percentage of the investment. As it also happened for the production of H_2, most of the investment is required for beds, 36 %, and the tanks, 46 %. The remaining units in the process do not represent a high cost since they are mainly used in the processing of gases into methanol and the quantity produced is very low. The suggested operating conditions of the units for the processing of the gases are summarized in Table S-5 of the supplementary material. The most remarkable results apart from the residence time required in the tanks are summarized in Table 1. It can be seen in this table that the removal of CO_2 by means of a PSA system is suggested to achieve high H_2:CO_2 ratios in the methanol reactor. These ratios are much higher than the minimum needed with a value of 18.78. The methanol reactor is also suggested to operate at low pressures, 5,000 kPa, and temperatures, 473 K.

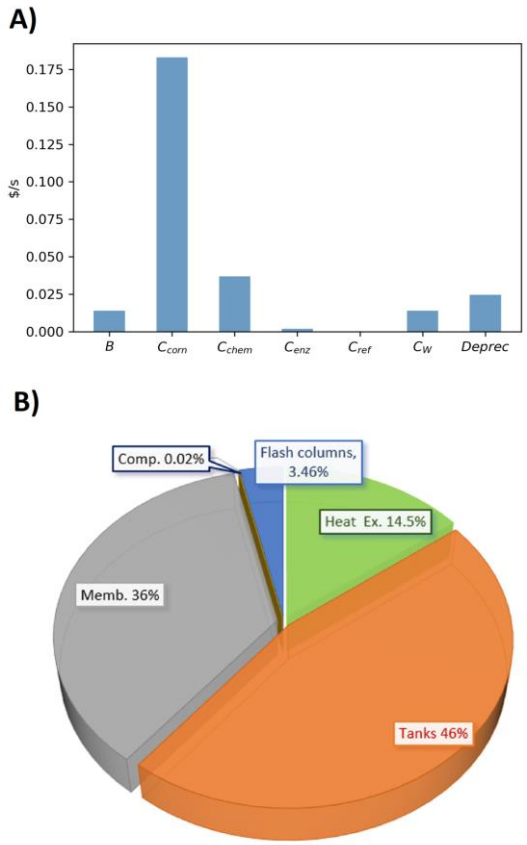

Figure 7. Summary of operating costs and income A) and distribution of investment costs B) for the production of Methanol.

Table 1. Optimal operating parameters for the production of methanol.

Operating Parameter	Value
Residence time in enzymatic hydrolysis (min)	29.9
Residence time in dark fermentation (h)	69.3
Fraction to PSA system for CO_2 capture	0.737
$T_{MetOH\ reactor}$ (K)	473
$P_{MetOH\ reactor}$ (kPa)	5,000
$\frac{y_{H2}-y_{CO2}}{y_{CO}+y_{CO2}}$	18.78
Reflux ratio in the distillation column	4.67

The role of the raw material

Similar to the production of H_2, a sensitivity analysis is also carried out for the raw material used in the methanol production process. The use of wastes with zero cost results in a more profitable process with a ROI of -175 %. As it was also occurring in the processing of H_2, none of the operating parameters and producing cost terms are modified, see Table S-5 of the supplementary material. The only change observed is in the cost of the raw material, whose reduction exclusively modifies the ROI and the production cost that in the current case drops to \$2.12/kg. If this methanol production process is considered as a waste treatment process, an income of \$0.068 per kg of waste treated is required to make the process profitable and ensure a methanol production cost of \$0.367/kg.

Scale-up study

The last analysis focuses on the process optimization under different scales. The ROI and the production costs from this analysis are presented in Figure 8. The remaining results from this analysis are summarized in Table S-6 of the supplementary material. These results show that the ROI remains similar when the amount is higher than 0.1 kg/s and it tends to decrease for lower amount of raw material.

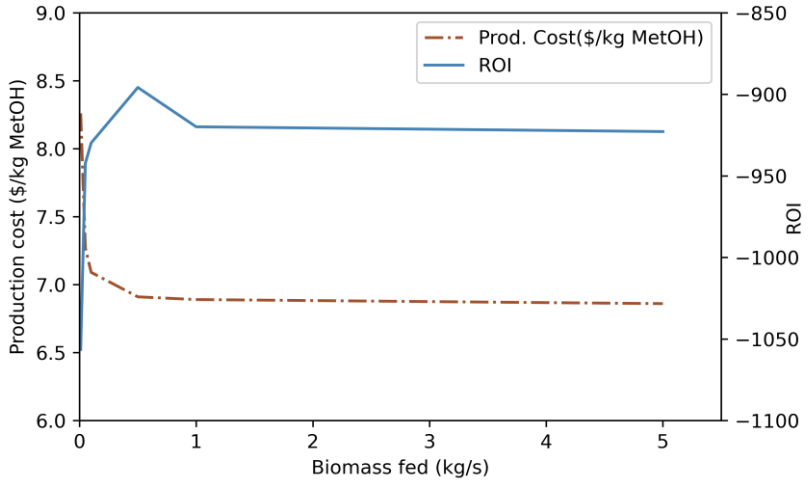

Figure 8. Return of Investment (ROI) and production cost of methanol under different scales.

4.4.3.3 Process comparison

Apart from the sensitivity and numerical analysis presented in previous sections, the processes studied can be compared with other studies for the production of H_2 and methanol. The production cost of H_2 with wastes (most profitable case), \$11.9/kgH_2, has been determined to be more expensive than the production cost by the reforming of natural gas, \$1.6/kgH_2 or by electrolysis, \$2-7/kgH_2 [37]. The economic comparison is carried out together with an comparison of the emissions. The emissions in the current work have been determined by including the mass balance of CO_2 and the ones generated by power and utilities consumption as presented by Hernández and Martín [42]. Note that supplementary raw materials such as the enzymes, acid and base are not considered since the production method and location is not known. These emissions for the production of H_2 are determined to be 27.9

$kgCO_2/kgH_2$. These emissions are a bit lower than the one produced from the reforming of natural gas. Based on a previous work [45], the emissions for the tri-reforming of natural gas are determined to be 33.9 $kgCO_2/kgH_2$. Thus, comparing with reforming the process only shows a slight improvement in the reduction of emissions.

In the production of methanol, the process can be compared with the production via reforming of methanol and via anaerobic digestion. For that purpose, the optimal process developed by Hernández and Martín [42] has been scaled down for processing 1 kg of waste per second and adapted including a cost for the biogas based on amortizing the cost anaerobic digesters and their power consumption. As a result, the production cost of the methanol from waste via anaerobic digestion is estimated to be $1.23/kg. This production cost is still higher than the one of reforming, $0.367/kgMetOH, but lower than the process developed in this work, $2.12/kgMetOH. Even in the most profitable case for dark fermentation where waste is used as raw material, the production cost is still the double than the one obtained by anaerobic digestion and reforming of biogas. The analysis of the emissions neither show a better performance in the process developed in the current work. The emissions of the process developed in this work via dark fermentation are determined to be 4.09 $kgCO_2/kgMetOH$ and in the process via biogas reforming those emissions account for 1.29 $kgCO_2/kgMetOH$. In the case of reforming of natural gas studies have reported emissions between 7 and 30 $kgCO_2/kgMetOH$ [52]. The higher emissions in the current case in comparison with the reforming of methanol is given by two reasons: First, the low yield achieved in the methanol synthesis by CO_2 hydrogenation. Low amount of CO is supplied to the reactor, being the synthesis of H_2 with CO_2 less efficient than with CO. Second, the CO_2 absorbed for producing such CO via dry reforming, which is able to balance the emissions generated for burning the gas that allow to achieve the high temperatures of the reformer.

Therefore, the use of dark fermentation is not recommended for the production of methanol since it is less profitable and with higher emissions than other methods. The only advantage offered by the dark fermentation process is its possible integration with other processes at low temperature. In the production of H_2, the method is still highly non-profitable but it can provide a slight reduction of the emissions, which make it a bit interesting in future works. However, there are still big challenges associated to this technology. The processing of waste involves high uncertainty due to its composition, physical characteristics (e.g. particle size) and controllability in the dark fermenter since acid compounds can be generated there. Thus, for a final decision the experimental characterization of the waste to be treated is to be performed and there is a need to validate the integrated production of enzymes process proposed by Han et al. [26] at pilot scale as well as the yield achieved in the dark fermentation and enzymatic reactors.

4.4.4 CONCLUSIONS

This work has evaluated the dark fermentation process to methanol and H_2 using a mathematical optimization approach. To evaluate the yield and performance of the dark fermentation stage an extension Andrew's kinetic models has been proposed. In the extension the three parallel reactions that simultaneously occur in dark fermentation has been taken into account and used for determine the optimal operating conditions and the economics of the two following processes:

- First, the process for the production of H_2 from corn via dark fermentation has been optimized. The platform developed is able to determine the optimal operating conditions, production costs and volume of the units. The resultant process does not show to be profitable with a ROI of --767 % for treating 1 kg/s of corn and an estimated production cost of $37.6/kg for producing H_2 from that corn. In the case of using waste as raw material, the ROI is improved to be -166% and the production cost of hydrogen is estimated to be $11.9/kg.
- Second, a novel integrated process for the production of methanol has been optimized obtaining also the optimal operating conditions in the process. However, the process neither result profitable. In the current case a ROI of -920 % and a production cost of $6.9/kg are obtained when corn is used as raw material. This process is even less profitable than the one for the production of H_2. Similarly than for the production of H_2, the economy of the process can be improved by using waste as raw material. In that case the ROI increases up to -175% and the production cost is estimated to be $2.12/kg of methanol. However, it should be remarked the consumption and production of the integrated enzymes is based on laboratory data and the scale-up to industrial scale may even involve a reduction of the process profitability.

Therefore, neither the production of H_2 or methanol are profitable under their optimal conditions since the yield in the dark fermentation process is very low. In best case, only 8 g/s of H_2 are produced for treating 1 kg/s of bio-resource.

NOMENCLATURE

Sets

i	Set of units.
j	Set of components

Parameters

k_{sn}	1st Kinetic constant of reaction n from Andrew's model (mol/L)
K_{sn}	2nd Kinetic constant of reaction n from Andrew's model (mol/L)
K_c	Polytrophic coefficient for compressors.
Xo	Original concentration of microorganisms in dark fermentation process.
ε	Compressor efficiency.
$\eta_{j1\ to\ j2}$	Reaction efficiency in the transformation of component j1 to component j2.
μ_{maxn}	Maximum yield in dark fermentation reaction (h^{-1})
χ^2	Chi square statistic parameter.

Variables

[j]	Concentration of component j [mol/L].
C_k	Cost corresponding to term k ($/s)
Deprec	Depreciation costs ($/s)
F	Total mass flow rate (kg/s)
fc_j	Flux of component j (kg/s)
$K_{i\,n}$	Equilibrium constant of reaction n in unit i
Q_i	Heat flux in unit i (J/s).
S	Concentration of substrate in dark fermentation reaction (mol/l).
t_i	Residence time in unit i (h).
T_i	Temperature of unit i (K).
V_i	Volume of unit i (m^3).
W	Power consumption (J/s).
w_j	Mass fraction of component j.

Subscripts

corn	cost of the raw material
chem	cost of the chemicals in acid hydrolysis.
enz	cost of the enzymes.
ref	cost in refrigeration.
w	cost of the power consumption.

REFERENCES

[1] Eurostat, Waste Statistics, 2017; Available in: https://ec.europa.eu/eurostat/statistics-explained/index.php?title=Waste_statistics (Accessed December 2019).

[2] European Environment Agency, Waste generation, 2018; Available in: https://www.eea.europa.eu/airs/2018/resource-efficiency-and-low-carbon-economy/waste-generation

[3] European Directive 2018/851. Available in: https://eur-lex.europa.eu/legal-content/EN/TXT/?uri=CELEX:32018L0851

[4] European Directive 91/271/EEC concerning urban waste-water treatment. Available in: https://ec.europa.eu/environment/water/water-urbanwaste/index_en.html

[5] Aristizabal-Marulanda V, Botero Gutierrez C, Cardona Alzate C, Chapter 4- Thermochemical, Biological, Biochemical and Hybrid Conversion Methods of Bio-derived Molecules into Renewable Fuels. Advanced Bioprocessing for Alternative Fuels, Biobased Chemicals and Bioproducts. 2019; DOI: https://doi.org/10.1016/B978-0-12-817941-3.00004-8.

[6] Chu, S. Majumdar, A. Opportunities and challenges for a sustainable energy future. Nature, 2012; 488: 294-303.

[7] Singh, A. Sevda, S. Abu, Reesh,I.M. Vanbroekhoven, K. Rathore, D. Pant, D. Biohydrogen production from Lignocellulosic Biomass: Technology and Sustainability. Energies. 2015; 8 (11): 13062-13080.

[8] Argun, H. Kargi, F. Bio-hydrogen production by different operational model of dark and photo-fermentation: An overview. Int. J. Hydrogen Energy 2011; 36: 7443-7459.

[9] Trad, Z. Fontaine, J. Larroche, C. Vial, C. Multiscale mixing analysis and modeling of biohydrogen production via dark fermentation. Renewable energy. 2016; 98: 264-282.

[10] Sewsynker, Y. Gueguim Kana, E.B. Intelligent models to predict hydrogen yield in dark microbial fermentations using existing knowledge. Int. J. Hydrogen Energy. 2016; 41: 12929-12940.

[11] Wang, J. Wan, W. Kinetic models for fermentative hydrogen production: A review. Int. J. Hydrogen Energy. 2009; 34: 3313-3323.

[12] Zwietering, MH. Jongenburger, I. Rombouts FM, van´t Riet K. Modeling of the bacterial growth curve. Appl. Environ. Microbiology. 1990; 1875-1881.

[13] Pradhan, N. Dipasquale, L. d'Ippolito, G. Fontana, A. Panico, A. Lens, P.N.L. Pirozzi, F. Esposito, G. Kinetic modeling of fermentative hydrogen production by *Thermotoga neapolitana*. Int. J. Hydrogen Energy. 2016; 41 (9): 4931-4940.

[14] Lin, CN, Wu, SY. Chang, J.S. Fermentative hydrogen production with a draft tube fluidized bed reactor contining silicone-gel-immobilized anaerobic sludge. Int. J. Hydrogen Energy. 2006; 31 (15): 2200-2210.

[15] Nath, K. Das, D. (2011) Modeling and optimization of fermentative hydrogen production. Bioresource Technology. 2011; 102: 8569-8581.

[16] Marbán, G. Valdés-Solís, T. Towards the hydrogen economy? Int. J. Hydrogen Energy. 2007; 32 (12): 1625-1637.

[17] Levin, D.B. Chahine, R. Challenges for renewable hydrogen production from biomass. Int. J. Hydrogen Energy. 2010; 35(10): 4962-4969.

[18] Sanchez, A. Martín, M. Vega, P. Biomass Based Sustainable Ammonia Production: Digestion vs Gasification. ACS Sustainable Chem. Eng. 2019; 7(11): 9995-10007.

[19] Asadullah, M. Biomass gasification gas cleaning for downstream applications: A comparative critical review. Renewable and Sustainable Energy Reviews. 2014; 40: 118-132.

[20] Hernandez, B. Martín, M. Optimization for biogas to chemicals via tri-reforming. Analysis of Fischer-Tropsch fuels from biogas. Energy Conversion and Management. 2018; 174: 998-1013.

[21] Saeidi, S. Amin, N.A.S. Rahimpour, M.R. Hydrogenation of CO2 to value-added products – A review and potential future developments. Journal of CO2 Utilization. 2014; 5: 66-81.

[22] Lloyd, T. A. Wyman, C.E. Combined sugar yields for dilute sulfuric acid pretreatment of corn stover followed by enzymatic hydrolysis of the remaining solids. Bioresource Technology. 2005; 96: 1967-1977.

[23] Cozad, A. Sahinidis, N.V. Miller, D.C. Learning surrogate models for simulation-based optimization. AIChE J. 2014; 60 (6): 2211-2227.

[24] Sagnak, R. Kargi, F. Kapdan, I.K. Bio-hydrogen production from acid hydrolyzed waste ground wheat by dark fermentation. Int. J. Hydrogen Energy. 2011; 36: 12803-12809.

[25] Adney, B. Baker, J. Measurement of Cellulase Activities. National Renewable Energy Laboratory. 2008; Available in: https://www.nrel.gov/docs/gen/fy08/42628.pdf

[26] Han, W. Fang, J. Liu, Z. Tang, J. Techno-economic evaluation of a combined bioprocess for fermentative hydrogen production from food waste. Bioresource Technology. 2016; 202: 107-112.

[27] Yeh, A. Huang, y. Chen, S.H. Effect of particle size on the rate of enzymatic hydrolysis of cellulose. Carbohydrate Polymers, 2010; 79 (1): 192-199.

[28] Han, W. Yan, Y. Shi, Y. Gu, J. Tang, J. Zhao, H. Biohydrogen production from enzymatic hydrolysis of food wate in batch and continuous systems. Scientific reports. 2016; 6: 38395. DOI: 10.1038/srep38395

[29] Nandi, R. Sengupta, S. Microbial production of hydrogen: An overview. Critical reviews in microbiology. 1998; 24 (1): 61-84.

[30] Flores Tlacuahuac, A. S. Terrazas Moreno, S. Biegler, L.T. On global optimization of Highly Nonlinear Dynamic Systems, Industrial and Engineering Chemistry Research. 2008; 47 (8): 2643-2655.

[31] Woods, D.R. Rules of thumb in Engineering Practice. 2007; Ed. Wiley. ISBN: 9783527312207.

[32] Martínez-Merino, V. Gil, M.J. Cornejo, A. Chapter 5 – Biomass sources for Hydrogen Production. Renewable Hydrogen Technologies. Production, Purification, Storage, Applications and Safety. 2013.

[33] Augelletti, R. Conti, M. Annesini, C. Pressure swing adsorption for biogas upgrading. A new process configuration for the separation of biomethane and carbon dioxide. Journal of Cleaner Production. 2016; DOI: 10.1016/j.jclepro.2016.10.013.

[34] Riboldi, L. Bolland, O. Overview on Pressure Swing Adsorption (PSA) as CO2 capture technology: state-of-the-art, llimits and potentials. Energy Procedia. 2017; 114: 2390-2400.

[35] Kiss, A.A. Pragt, J.J. Vos, H.J. Bargeman, G. de Groot, M.T. Novel efficient process for methanol synthesis by CO2 hydrogenation. Chemical Engineering Journal. 2016; 284: 260-269.

[36] Graaf, G.H. Sijtsema, P.J.J.M. Stamhuis, E.J. Joosten, G.E.H. Chemical equilibria in methanol synthesis. Chem. Eng. Sci. 1986; 41: 2883.

[37] Philibert, C. Producing Ammonia and Fertilizers: New Oportunities from renewables. October 2017; Available in: https://www.iea.org/media/news/2017/Fertilizer_manufacturing_Renewables_01102017.pdf

[38] Methanex Methanex posts regional contract methanol prices for North America, Europe and Asia. 2019; Available in: https://www.methanex.com/our-business/pricing

[39] Alibaba Sulfuric Acid, degree 98%. 2019; https://www.alibaba.com/showroom/sulfuric-acid-price.html

[40] Alibaba Hydrate lime Ca(OH)2 95%. 2019; Available in: https://www.alibaba.com/product-detail/low-price-China-manufacturer-95-Hydrated_60223145397.html?spm=a2700.7724857.normalList.40.324a2171xAAKVa

[41] Bauer, N. Gibbons, W.R. Saccharification versus simultaneous saccharification and fermentation of kraft pulp. Int. J. Agricultural & Biological. Engineering. 2012; 5 (1): 48-55.

[42] Hernández, B. Martín, M. Optimal Process Operation for Biogas Reforming to Methanol: Effects of Dry Reforming and Biogas Composition. Ind. Eng. Chem. Res. 2016; 55 (23): 6677-6685. DOI: 10.1021/acs.iecr.6b01044

[43] Indexmundi. Maize corn daily price. October 2019; Available in: https://www.indexmundi.com/commodities/?commodity=corn

[44] Perez-Uresti, S. Martín, M. Jiménez-Gutierrez, A. Estimation of renewable-based steam costs. Applied Energy, 2019; 250: 1120-1131.

[45] Hernández, B. Martín, M. Optimal production of syngas via super-dry reforming. Analysis for natural gas and biogas under different CO2 taxes. Chemical Engineering Research and Design. 2019; 148: 375-392.

[46] Almena, A. Martín, M. Technoeconomic Analysis of the Production of Epichlorohydrin from Glycerol. Ind. Eng. Chem. Res. 2016; 55 (12): 3226-3238.

[47] Taifouris, M. R. Martín, M. Multiscale scheme for the optimal use of residues for the production of biogas across Castile and Leon. 2018; 185: 239-251.

[48] Sinnott, R.K. Coulson and Richardson's Chemical Engineering, Volume 6, Chemical Engineering Design, 2nd Edition, Butterworth-Heinemann, Oxford, 1999.

[49] Sholz, M. Alders, M. Lohaus, T. Wessling, M. 2015. Structural optimization of membrane-based biogas upgrading processes. J. Membr. Sci. 474, 1-10.

[50] Nathao, C. Sirisukpoka, U. Pisutpaisal, N. Production of hydrogen and methane by one and two stage fermentation of food waste. Int. J. Hydrogen Energy. 2013; 38 (35): 15764-15769.

[51] Garcia, CA. Betancourt, R. Cardona, CA. Stand-alone biorefinery pathways to produce hydrogen through gasification and dark fermentation using *Pinus Patula*. Journal of Environmental Management. 2017; 203: 695-703.

[52] Matzen, M. Alhajji, M. Demirel, Y. Chemical storage of wind energy by renewable methanol production: Feasibility analysis using a multi-criteria decision matrix. Energy. 93; 1: 343-353.

CHAPTER 5.1. OPTIMAL INTEGRATED PROCESS FOR THE PRODUCTION OF BIODIESEL FROM WASTE VIA ANAEROBIC DIGESTION.

ABSTRACT

This chapter presents the optimization of an integrated facility for the production of biodiesel from waste via anaerobic digestion. The treatment of wastes via anaerobic digestion generates two products: biogas and digestate. On the one hand, the biogas produced can be treated by mean of reforming technologies for producing syngas and methanol. On the other hand, the digestate is used as a nutrient to improve the yield in the growth of algae. The oil of the algae is extracted and then transesterified with the produced methanol. The problem for solving this superstructure is formulated as a large non-linear problem. The optimal operating conditions or the various reactors as well as the biogas composition and the content of nutrients in the digestate are determined. Optimal heat exchanger and water networks are designed afterward. A total of 3110 kt/yr of manure is processed for the production of 90 Mgal/yr of biodiesel and 46.7 kt/yr of methanol. The process also uses a fraction of the biogas to provide energy required in the reformer unit. Furthermore, the process also requires 1.5 MJ/gal and 1.22 gal of water per gal of biodiesel. The production cost of biodiesel is competitive with previous work, 0.31 €/gal, but the investment is higher due to the need to process the waste into biogas, 193 M€. A scaled-down study is also carried out to evaluate the production and investment cost as a function of the farm size.

5.1.1 INTRODUCTION

Current developed societies generate large volumes of waste. The major types are the sludge produced in water treatment, urban residues, forest residues and manure. Apart from the volume, their composition is complex and dangerous. Anaerobic digestion represents a technology to stabilize the waste while generating added value in the form of methane and a digestate that can be used as fertilizer. For decades, the aim of processing waste has focused on power production. León & Martín [1] optimized a facility for the use of manure to produce power using a gas and a steam turbine. The facility was only profitable if the digestate was used a fertilizer and sold as such. However, biogas is an interesting carbon source, not only because of the methane, but also due to the amount of CO_2 available. Hernández and Martín [2] evaluated the possibility of using the biogas as a source for the production of methanol, taking into account that its composition already contains all the species required for dry reforming. The process consisted on producing syngas out of the biogas. Next, methanol was synthesized. Lately, Hernández et al. [3] evaluated the use of different wastes towards the production of power and chemicals. They found that the price of the digestate as an asset determined the selection of the waste or the mix of wastes.

Algae production requires a source of carbon and nutrients. We realize that both can be obtained from the processes presented above. The digestate contains nutrients that can allow algae growth. Xin et al. [4] evaluated the effect of the nutrient concentration on the growth rate of algae. Furthermore, in the production of methanol, CO_2 is captured while adjusting the composition of the syngas before feeding the reactor. Even if the CO_2 is not enough, we have all the ingredients for the production of biodiesel with no need for fossil based chemicals and with the opportunity of additional CO_2 capture. This facility can be compared to previous work where various integrated designs are presented for the production of biodiesel with no fossil based raw material such as Martín and Grossmann [5], where algae was used to produce both the alcohol, ethanol, and the oil needed for biodiesel production. Recently Martín and Grossmann [6] suggested the simultaneous production of the alcohol and the oil by using switchgrass and algae. Furthermore, other alternatives proposed in the literature involve the use of solar energy and CO_2 as the raw materials for the production of both, the algae and methanol using electrolytic hydrogen and CO_2 [7]. In both cases, nutrients for the algae were bought, but not fossil raw material is required since the oil and the methanol come from renewable sources. Process integration has provided means to mitigate the lack of resources, improve the economics or the environmental impact by putting together chemical complexes from the renewables such has solar, wind and biomass [8, 9] by integrating nuclear energy and water management [10] or upgrading sections of refineries with utilities plants [11].

Thus, in this work we propose and optimized an integrated facility that produces biodiesel from waste. Waste is digested to produce biogas and digestate. While digestate is used for algae growing, providing the required nutrients, biogas is used to produce the methanol required for the transesterification of the algae. This facility does not need to use non-renewable intermediates such as methanol or nutrients via the proper integration of the sub processes involved avoiding ethical issues such as the use of fossil alcohol to produce a biofuel or environmental problems typically related to the discharge of the digestate in already nitrogen or phosphorous rich areas. We

organize the paper as follows. First we provide a brief description of the process. Next the modelling issues related to each section of the process are presented. Subsequently, the results of the optimal operation of the facility are shown together with an economic evaluation. Finally, we draw some conclusions.

5.1.2 PROCESS DESCRIPTION

Biogas and digestate are produced via anaerobic digestion of wastes. The digestate is used as nutrients for algae growing. The biogas is further processed for methanol production. After its cleanup, it is reformed with the CO_2 already available in the gas and steam, if necessary. Next, the syngas composition is adjusted for methanol production where CO_2 has to be partially captured before feeding the synthesis reactor. In order not to emit this greenhouse gas, we use it as carbon source for algae production. Algae are grown using CO_2 as a carbon source and the nutrients provided by the digestate. Water is added to the ponds. Most of it can be recycled or waste water, but there is a fraction lost by evaporation from the ponds. The oil accumulated in the algae is extracted using a solvent, c-hexane, and mechanical action. The solvent is recovered by distillation and the oil is sent to transesterification. We use the methanol produced from the biogas to produce biodiesel, fatty acid methyl ester, FAME. In this way we have an integrated facility from biomass wastes to biodiesel production with no need for purchasing methanol to be compared with other integrated facilities where methanol was also produced from renewable based resources.[6,7] Figure 1 shows a scheme of the process. In section three we present the modeling issues related to the process.

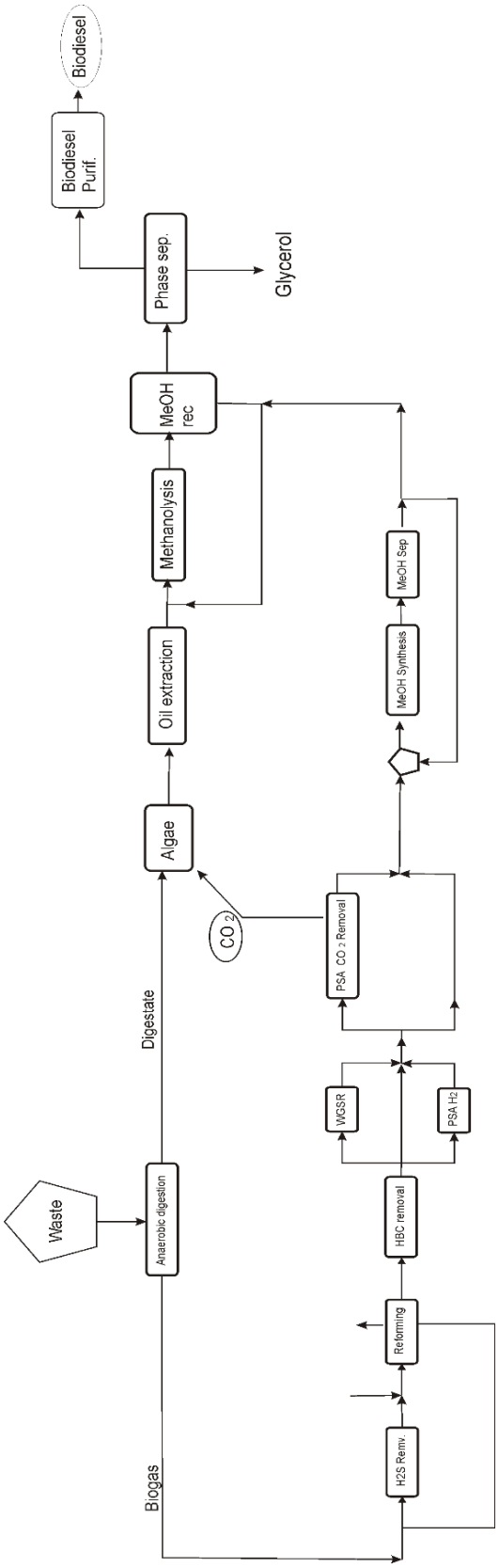

Figure 1. Integrated process for biodiesel production from biomass wastes.

5.1.3 MODELLING ISSUES

5.1.3.1 Biogas production

Figure 2 shows the detail for the section of biogas production and gas clean-up. The anaerobic digestion of waste consists of a series of reactions including hydrolysis, acidogenesis, acetogenesis and methanogenesis that break carbohydrates, lipids and protein of the feedstock into methane and CO_2 [12]. Following the results of previous papers, we consider the operation of the digester under thermophilic conditions for 15 to 20 days. However, the composition of the biogas required for further stages may change the actual operating conditions. A part from methane and CO_2, nitrogen, H_2S and NH_3 are produced [13]. Thus, the biogas needs cleanup before further use.

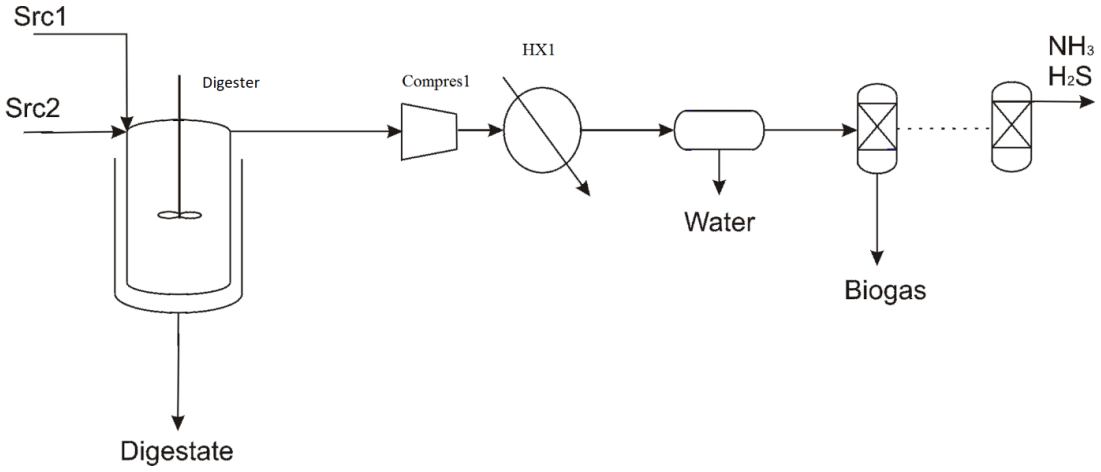

Figure 2. Detail of the biogas production section of the flowsheet.

The yield from waste to biogas depends on the type of raw material [14-16]. Thus, in order to compute the biogas composition, a mass balance is performed considering the composition of the different manure sources such as pig and cattle slurry [1]:

$$MW_{dry-biogas} = \sum_{a'} Y_{a'/biogas-dry} MW_{a'} \quad (1)$$

The gas composition is bounded by typical results in the literature [6] and it exits the reactor saturated with water. The composition is computed as per eqs. (2) to (7):

$$0.7 \leq Y_{CH4} \leq 0.5$$

$$0.3 \leq Y_{CO2} \leq 0.5$$

$$0.02 \leq Y_{N2} \leq 0.06 \quad (2)$$

$$0.005 \leq Y_{O2} \leq 0.16$$

$$Y_{H2S} \leq 0.002$$

$$9 \cdot 10^{-5} \leq Y_{NH3} \leq 1 \cdot 10^{-4}$$

$$y_{biogas} = \frac{MW_{H_2O}}{MW_{biogas-dry}} \frac{Pv(T)}{P - Pv(T)} \quad (3)$$

$$F_{biogas} = \rho_{biogas} \left[w'_{SV/cattle}\, w_{MS/cattle} F_{cattle} \cdot V_{biogas/cattle} + w'_{SV/pork}\, w_{MS/pork} F_{pork} \cdot V_{biogas/pork} \right] \quad (4)$$

$$fc(H_2O)_{biogas} = y_{biogas} \cdot \sum_{a'} fc(a')_{biogas} \quad (5)$$

$$fc_{(a',Bioreactor,Compres1)} / MW_{a'} = \frac{Y_{a'/biogas-dry}}{MW_{biogas-dry}} (F_{(Bioreactor,Compres1)} - fc_{(H_2O,Bioreactor,Compres1)}) \quad (6)$$

$$MW_{biogas} \sum_{a} \frac{x_{a/biogas}}{MW_a} = \sum_{a} x_{a/biogas} \quad (7)$$

Where the lower and upper limits for the potential generation of biogas are given by eq (8) [8]:

$0.20 \leq V_{biogasbiomass} \leq 0.50;$

$0.10 \leq w_{MSBiomass} \leq 0.20;$ (8)

$0.50 \leq w_{VSBiomass} \leq 0.80;$

A mass balance determines the composition of the digestate consisting of the residue once the biogas is produced [12]. Defra's studies [17] show the typical composition of the digestate for the two manure types considered. The digestate composition is computed as eqs. (9) to (18):

$$w'_{C/k} = R_{C-N/k} \left(w'_{Norg/k} + w'_{Nam/k} \right) \quad (9)$$

$6 \leq R_{C-N/CS} \leq 20$

$0.005 \leq w'_{Nam/CS} \leq 0.047;$

$0.005 \leq w'_{Norg/CS} \leq 0.036;$

$0.008 \leq w'_{P/CS} \leq 0.013;$

$0.033 \leq w'_{K/CS} \leq 0.1;$ (10)

$3 \leq R_{C-N/PS} \leq 10$

$0.005 \leq w'_{Nam/PS} \leq 0.095;$

$0.005 \leq w'_{Norg/PS} \leq 0.030;$

$0.019 \leq w'_{P/PS} \leq 0.022;$

$0.039 \leq w'_{K/PS} \leq 0.083;$

$w_{C/Biomass}+w_{Norg/Biomass}+w_{Nam/Biomass}+w_{P/Biomass}+w_{K/Biomass}+w_{Rest/Biomass}=1$ (11)

$$fc(C)_{digestate} = w'_{C/Biomass} \cdot w_{MS/Biomass} \cdot F_{Biomass} - fc(CH_4)\frac{MW_C}{MW_{CH_4}} - fc(CO_2)\frac{MW_C}{MW_{CO_2}} \quad (12)$$

$$fc(Norg)_{digestate} = w'_{No/Biomass} \cdot w_{MS/Biomass} \cdot F_{Biomass} - fc(N_2)\frac{MW_N}{MW_{N_2}} \quad (13)$$

$$fc(N)_{digestate} = w'_{N/Biomass} \cdot w_{MS/Biomass} \cdot F_{Biomass} - fc(NH_3)\frac{MW_N}{MW_{NH_3}} \quad (14)$$

$$fc(P)_{digestate} = w'_{P/Biomass} \cdot w_{MS/Biomass} \cdot F_{Biomass} \quad (15)$$

$$fc(K)_{digestate} = w'_{K/Biomass} \cdot w_{MS/Biomass} \cdot F_{Biomass} \quad (16)$$

$$fc(\mathrm{Re}\,st)_{digestate} = w'_{rest/Waste} \cdot w_{MS/Waste} \cdot F_{Waste} - fc(CH_4)_{biogas}\frac{4 \cdot MW_H}{MW_{CH_4}} - fc(CO_2)_{biogas}\frac{2 \cdot MW_O}{MW_{CO_2}} - fc(NH_3)_{biogas}\frac{3 \cdot MW_H}{MW_{NH_3}} - fc(H_2S)_{biogas} - fc(O_2)_{biogas} \quad (17)$$

$$fc(H_2O)_{digestate} = (1 - w_{MS/Biomass}) \cdot F_{Biomass} - fc(H_2O)_{biogas} \quad (18)$$

The energy balance to the digester is as follows:

$$Q_{digestor} = \Delta H_{reaction} - Fcp(T_{digestor} - T_{in})$$
$$\Delta H_{reaction} = \sum_{prod} \Delta H_{combus} - \sum_{reactants} \Delta H_{combus} \quad (19)$$

The digestate is sent to the ponds and, if needed, more water is added.

The traces of NH_3 and H_2S in the biogas are removed using packed bed columns that operate at 50 ºC. A mixed bed made of Fe_2O_3 and zeolites is assumed since it is up to the zeolites to adsorb the NH_3, while the Fe_2O_3 removes the H_2S. In this last case, the following chemical reaction takes place [18].

$Fe_2O_3 + 3H_2S \rightarrow Fe_2S_3 + 3\,H_2O$

While the removal of ammonia is modelled just assuming an efficiency of 100%, the removal of H_2S is modelled following the stoichiometry of the reaction assuming complete conversion of the sour gas. The bed of Fe_2O_3 can be regenerated using Oxygen [18].

$2Fe_2S_3 + 3O_2 \rightarrow 2FeO_3 + 6S$

5.1.3.2 Biogas reforming and purification.

The production of methanol is carried out from syngas that is obtained via dry or hybrid dry and steam reforming of the biogas. This is an endothermic process. Therefore, part of the biogas is required to provide the energy to heat up and maintain the operating temperature at the furnace, see Figure 3. The fraction of biogas burned is computed assuming that the energy required to heat up and to perform the reforming reaction isothermally, is provided as the lower heating value of the methane within the biogas.

$$Q_{prod} = \sum_{i} fc_{(i,\text{Reformer},Mix2)} \cdot (\Delta H_f + \int_{T_{ref}}^{T_{out}} CpdT) \tag{20}$$

$$Q_{reac} = \sum_{i=in} fc_{(i,\text{Reformer},Mix2)} \cdot (\Delta H_f + \int_{T_{ref}}^{T_{in}} CpdT) \tag{21}$$

$$Q_{reformer} = Q_{prod} - Q_{reac} \tag{22}$$

$$fc_{(CH_4,Spl3,Reformer)} \cdot LHV_{gas} = Q_{reformer} + Q_{HE1} \tag{23}$$

We can oversize the biogas production section to produce the biogas needed for the production of biodiesel. However, economically this is not even promising due to the large cost of the digester. Simple energy balances are used to model the heat exchanger and the compressors are modelled as polytropic. The model of the methane reformer is based on the chemical equilibria given by eqs. (24) - (26):

$$CH_4 + CO_2 \leftrightarrow 2CO + 2H_2 \tag{24}$$

$$CH_4 + H_2O \leftrightarrow CO + 3H_2 \tag{25}$$

$$CO_{(g)} + H_2O_{(g)} \leftrightarrow CO_{2(g)} + H_{2(g)} \tag{26}$$

Out of the three equations, only two are independent. Since the first equilibrium depends on the pressure, we use compressor 1 to adjust the pressure for the reaction. We model the reactor to compute the syngas composition based on atomic balances as follows:

$$\begin{aligned} &mol_{CH_4} + mol_{CO_2}\big|_{in} = mol_{CH_4} + mol_{CO} + mol_{CO_2}\big|_{out} \\ &4 \cdot mol_{CH_4} + 2 \cdot mol_{H_2O}\big|_{in} = 4 \cdot mol_{CH_4} + 2 \cdot mol_{H_2} + 2 \cdot mol_{H_2O}\big|_{out} \\ &2 \cdot mol_{CO_2} + mol_{CO} + mol_{H_2O}\big|_{in} = mol_{H_2O} + mol_{CO} + 2 \cdot mol_{CO_2}\big|_{out} \end{aligned} \tag{27}$$

And the chemical equilibrium, where the equilibrium constants are given by eqs. (28-29) as follows [19, 20]:

$$kp = e^{[31.447 - \frac{29580}{T}]} = \frac{P_{CO} \cdot P_{H_2}}{P_{CH_4} \cdot P_{CO_2}} \tag{28}$$

$$kp = 10^{\left[-\frac{11650}{T}+13{,}076\right]} = \frac{P_{CO}\cdot P_{H_2}^3}{P_{CH_4}\cdot P_{H_2O}} \tag{29}$$

$$kp = 10^{\left[\frac{1910}{T}-1{,}784\right]} = \frac{P_{CO_2}\cdot P_{H_2}}{P_{CO}\cdot P_{H_2O}} \tag{30}$$

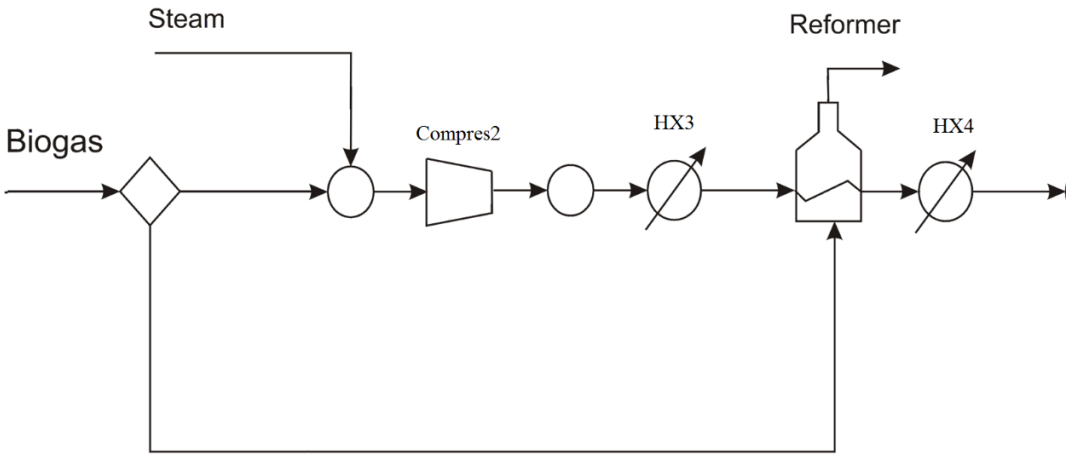

Figure 3. Biogas reforming stage.

The traces of hydrocarbons are removed using pressure swing absorption, PSA, see Figure 4. A bed of silica gel is selected for this task. The operating conditions are 25 ºC and 4.5 bar. Two units operate in parallel to secure continuous operation of the downstream process. One of the beds is operating and the second one is in regeneration. To adjust the pressure and temperature of the raw syngas, the gas stream is compressed and cooled down. As before, the compressors are modeled as polytropic ones and the heat exchangers assume saturated gas after water condensation. Thus, the condensed water is removed. We use Antoine correlations to compute the water that remains with the gas after condensation. The pressure drop across the bed is assumed to be 10% of the operating pressure as a design condition based on previous work [1].

The composition of the syngas may need to be further tuned in terms of the H_2 to CO ratio for methanol production. We consider the use of three technologies. Two of them can operate in parallel simultaneously. The first one is a water gas shift reactor. We model this reactor assuming molar mass balances and the equilibrium as given by eq. (26). The second technology is a bypass and the third one consists of a hybrid membrane / PSA for H_2 recovery. The bed of this adsorbent unit is made of oxides. For this technology the gas is recompressed up to 4.5 bar. The adsorbent bed operates at 25ºC. The hydrogen separation section is modelled assuming that 100% of the hydrogen in the stream that is processed through this system can be recovered by means of using a palladium membrane that is permeable to hydrogen alone and the PSA system to retain any other gas that may accompany it. The split fraction depends on the performance of the reformer which may make this composition adjustment redundant. See Hernández and Martín [2] for further details.

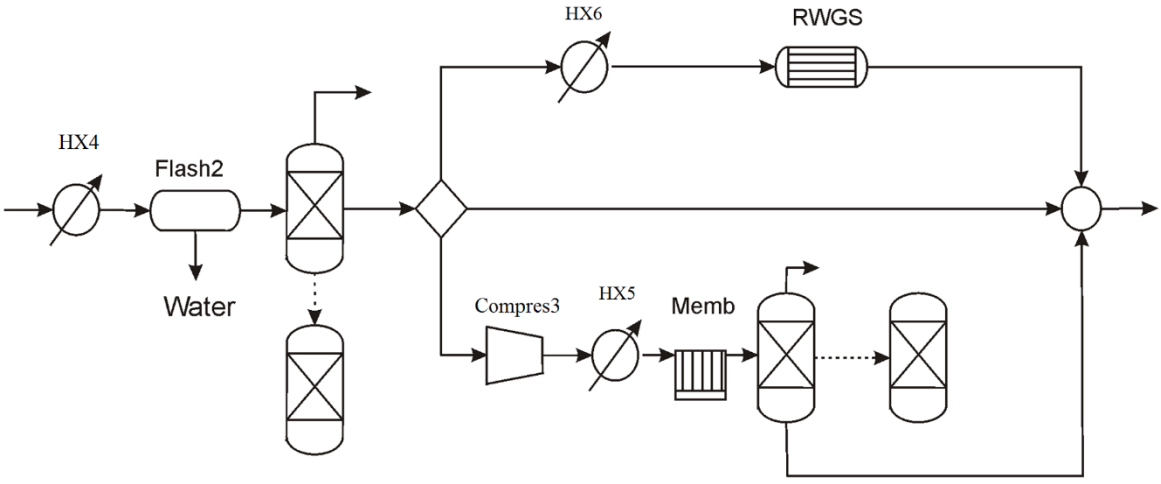

Figure 4. Syngas composition adjustment.

The last gas purification stage consists of the removal of CO_2. However, the role of the CO_2 in the synthesis of methanol results in the need to maintain a certain amount in the syngas, typically from 2% to 8% in volume [21]. Therefore, a bypass system is also considered. A fraction of the syngas is processed through a PSA system to remove the excess of CO_2 using Zeolite 5A or 13X. This bed operates at 25ºC and 4.5 bar. Thus, the gas is cooled down and compressed before being fed to the PSA system. The water condensed, if any, is removed from the system. The bed adsorbs 0.1 kg of CO_2 per kg of zeolite. We assume a removal efficiency of 95%, see Figure 5 [22, 23]. The unprocessed syngas is mixed with the stream exiting the adsorbing system.

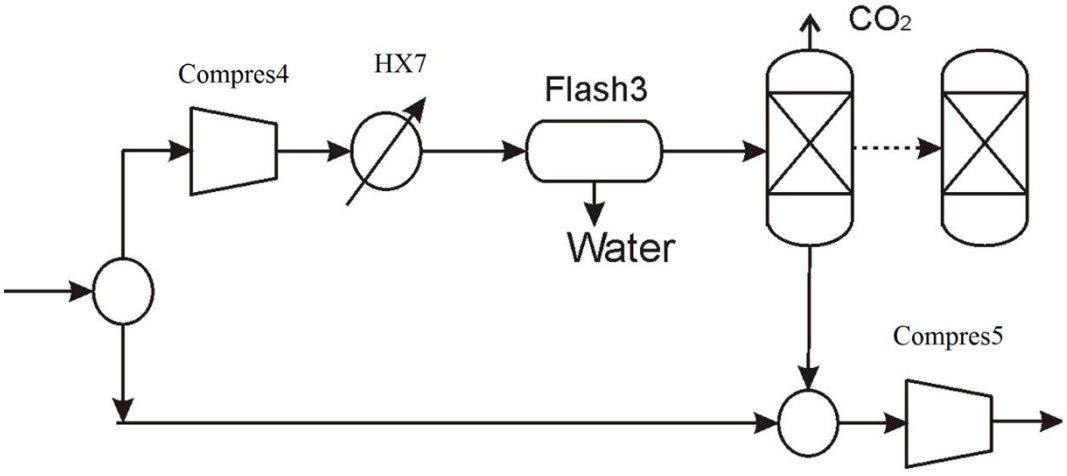

Figure 5. CO_2 removal stage [2].

5.1.3.3 Methanol Synthesis

Figure 6 presents the detail of the synthesis loop for methanol production. The syngas is fed to a reactor that uses a catalysis comprised of *CuO −ZnO −Al O* to produce methanol. The reactor considers the equilibria described by the following reactions:

$$CO + 2H_2 \leftrightarrow CH_3OH$$
$$CO_2 + H_2 \leftrightarrow CO + H_2O \quad (31)$$

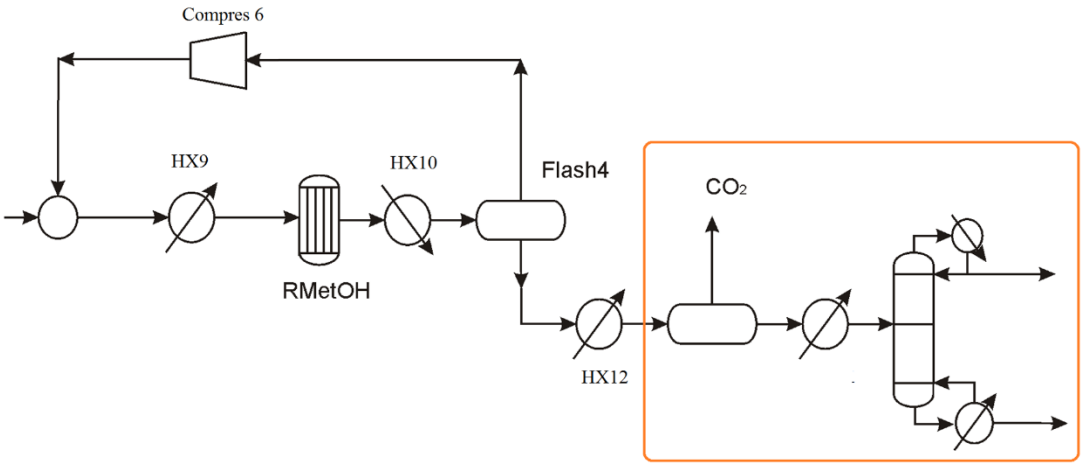

Figure 6. Methanol synthesis section.

The reaction is favored by low temperatures and high pressures, but lately pressures about 50-100 bar and temperatures in the range of 200-300 ºC are the most common. For the reactor to operate properly there are a few constrains in the composition of the feed such as the ratio between hydrogen and CO, given by eq. (32) [24].

$$1.75 \le \frac{H_2}{CO} \le 3 \quad (32)$$

As well as the fact that the concentration of CO_2 should be between 2% to 8% [21, 25] and the ratio of the syngas components involving CO_2 [24, 26] given by eq. (33):

$$1.5 \le \frac{H_2 - CO_2}{CO + CO_2} \le 2.5 \quad (33)$$

The operation of the reactor is modeled considering the mass balance to the species involved, eqs. (34)-(36) and the equilibrium constants given by the experimental results [27,28] with P in bars and T in K as presented by eqs. (37)-(38).

$$\text{H: } 2\cdot n_{H_2} + 2\cdot n_{H_2O}\Big|_{in} - \left(2\cdot n_{H_2} + 2\cdot n_{H_2O} + 4\cdot n_{CH_3OH}\right)\Big|_{out} = 0; \quad (34)$$

C: $n_{CO} + n_{CO_2}\big|_{in} - \left(n_{CO} + n_{CO_2} + n_{CH_3OH}\right)\Big|_{out} = 0;$ (35)

O: $n_{CO} + 2 \cdot n_{CO_2} + n_{H_2O}\big|_{in} - \left(n_{CO} + 2 \cdot n_{CO_2} + n_{H_2O} + n_{CH_3OH}\right)\Big|_{out} = 0;$ (36)

$$\frac{\left[P_{CH_3OH}\right]}{\left[P_{CO}\right]\left[P_{H_2}\right]^2} = 10^{\left[\frac{3971}{T} - 7.492 Log T + 1.77x10^{-3}T - 3.11x10^{-8}T^2 + 9.218\right]} \quad (37)$$

$$\frac{\left[P_{CO}\right]\left[P_{H_2O}\right]}{\left[P_{CO_2}\right]\left[P_{H_2}\right]} = Exp\left[13.148 - \frac{5639.5}{T} - 1.077\ln T - 5.44x10^{-4}T + 1.125x10^{-7}T^2 + \frac{49170}{T^2}\right] \quad (38)$$

The unreacted gases are separated in a flash, recycling the syngas and recovering methanol and water. Methanol may need to be further purified depending on the performance of the reactor. In such a case, a system of molecular sieves can be used to remove the water formed in the synthesis. Part of the methanol will be used for the transesterification of the oil while the rest is sold to the market. Alternatively, if no enough methanol is produced out of the biogas, it has to be injected in the system at a cost.

5.1.3.4 Oil production

Figure 7 presents a detail of the algae growing section of the flowsheet.

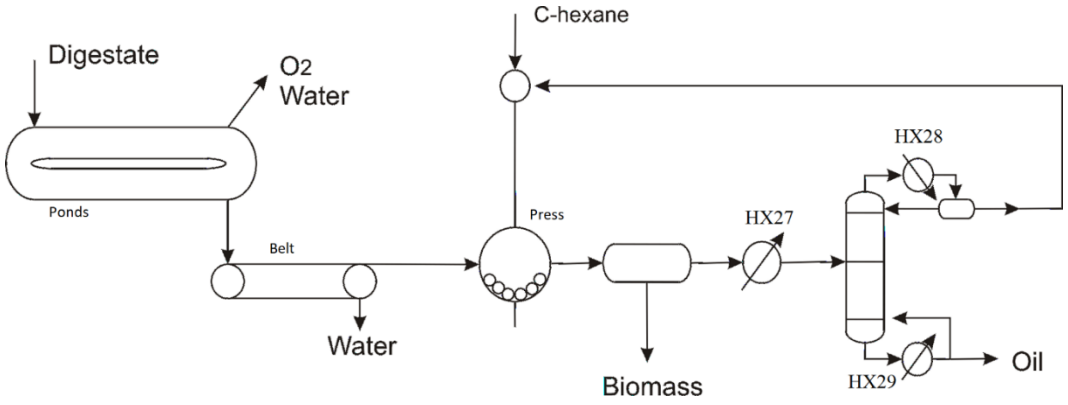

Figure 7. Algae oil section.

Algae growth depends on a number of parameters such as carbon source, water, nutrients or light. In particular, nutrients concentration in terms of total nitrogen and total phosphorous determine the growth rate. We first develop a correlation for the effect of the nutrients concentration on algae growth using data from several studies. Most of the data come from Xin et al. [4] but also results from the work by Amini et al. [29] are also included. The total phosphorus and the total nitrogen are given in mg per L.

$$\text{Growth}\left(\frac{g}{m^2 d}\right) = 0.418528 \cdot \text{TotP} + 0.52762 \cdot \text{TotN} + 0.225013 \cdot \text{TotN} \cdot \text{TotP} - 0.20754 \cdot \text{TotP}^2 - 0.03026 * \text{TotN}^2; \quad (39)$$

Apart from nutrients, CO_2 is also consumed. The consumption rate depends on the growth-rate of the algae as given by eq. (40) [30]:

$$CO_2\left(\frac{m^3}{d}\right) = 0.6565 \cdot \text{Growth}\left(\frac{g}{m^2 d}\right) + 5.0784 \quad (40)$$

The amount of water required can be provided by two sources. The digestate from the bioreactor carries water and additional source may also be needed to meet an algae concentration of 0.006kg per kg of biomass [31]. The energy consumed for the operation of the ponds is computed following Sazdanoff's data [30]. Next, algae are harvested and dried up to 5% moisture content using Univenture's design. The energy consumption of this stage is 40W for 500L/h of flow [32]. We assume that the water can be recycled to the pond so that the water is lost only by evaporation. The nutrients are provided by the liquid digestate.

The oil, representing 55% of the dry biomass is extracted using a solvent, c-hexane, and mechanical press, and the solvent and the oil are separated in vacuum distillation column. Starch is considered to be 35% of the algae dry mass and the rest protein. Next, the solvent and the oil are separated in a vacuum distillation column so that the bottoms are below 350ºC to avoid oil decomposition. The oil is further sent to transesterification and the solvent is recycled. The oil is sent to transesterification and the solvent is recycled.

5.1.3.5 Biodiesel synthesis and transesterification

Martín & Grossmann [16] showed that the use of heterogeneous catalysis was promising due to the easier product separation. There is no need for biodiesel washing, reducing consumption of process water. Furthermore, the use of heterogeneous catalysis provides flexibility to use different oil sources. A surface response model from previous work is used to compute the yield of the reaction eq. (41). Table 1 shows the lower and upper bounds of the operating conditions.

$$\begin{aligned}\text{yield} = {} & -73.6 + 2.5 \cdot T_{Trans} + 24.9 \cdot \text{Cat} + 8.8 \cdot \text{ratio\_met} - 0.01 \cdot T_{Trans}^2 - \\ & 1.29 \cdot \text{Cat}^2 - 0.39 \cdot \text{ratio\_met}^2 - 0.26 \cdot T_{Trans} \cdot \text{Cat}\end{aligned} \quad (41)$$

Table 1.-Range of operation of the variables. Heterogeneous catalysed.

Variable	Lower bound	Upper bound
Temperature (ºC)	40	60
Ratio methanol (mol/mol)	6	12
Cat (%)	1	4

The excess of methanol is recovered using a distillation column. Short cut methods are used to model this column, taking into account the presence of two liquid phases, a polar and a non-polar one. To avoid that the bottoms reaches 150ºC, a temperature that can decompose glycerol, the column must operate under vacuum. A variable reflux ratio from 2 to 3 is allowed based on offline simulations using ChemCAD ®. Next, polar and non-polar phases are separated at 40ºC. The glycerol phase may not need further purification, but biodiesel requires further treatment before being sold. A distillation column operating under vacuum is used to avoid reaching temperature above 250ºC in the distillate. Figure 8 shows a flowsheet for this section of the facility.

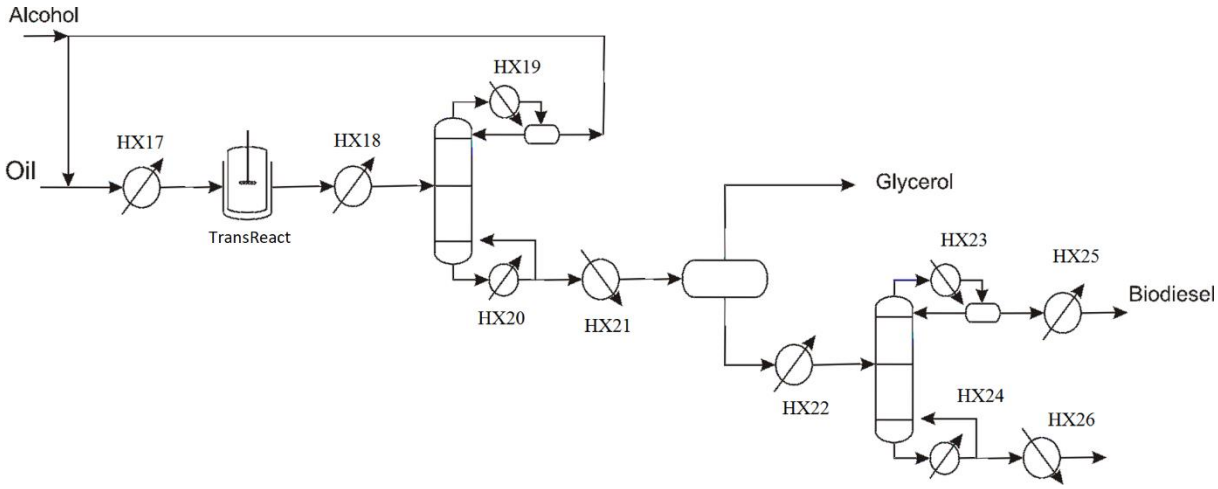

Figure 8.- Biodiesel production section [39].

5.1.4 SOLUTION PROCEDURE

The problem for the conceptual design of the integrated facility that produces biodiesel with no need for fossil intermediates is formulated as a large NLP with 5000 var and 3500 eqs writen in GAMS®. The objective function includes the credit from biodiesel, that of the methanol in case an excess is produced and we need to pay for utilities such as power or steam for certain heat exchangers. Note that HX-3 is also minimized as a cost, however, the energy for the reformer and for this heat exchanger comes from the use of part of the biogas. The idea of adding a cost for methanol is simply in case the system cannot produce enough methanol, to reduce the external need for it.

$$Z = \mathrm{fc}(\mathrm{FAME}) - C_{Power} \sum_i W_{compres\_i} - C_{steam} \sum_j Q_{HX\_j} \quad -C_{MetOH} \cdot \mathrm{fc}(\mathrm{MetOH}_{added}) \tag{37}$$

The problem solved to optimality using a multistart optimization approach with CONOPT 3.0 as the preferred solver. The model is solved in a Windows 7 professional machine, Intel Core i7. 25 CPU min where needed to find convergence. Next, we design the heat exchanger network using Yee and Grossmann's model [33] and a water network [34].

5.1.5 RESULTS

5.1.5.1 Mass and energy balances

The plant processes 100kg/s of waste, 50% cattle manure and 50% pig manure, producing 88Mgal/yr of biodiesel and 46.7 kt/y of methanol, a typical size of algae based biodiesel facilities in the literature [5]. Note that the farm size to produce such a waste means is quite large which involves a logistic problem that is not considered in this work. 45% of the methane needs to be used to provide energy for the reforming process. As a result, the recommended biogas composition is 67.5% methane, 30% CO_2 and the rest nitrogen, H_2S, ammonia and oxygen. A summary of the remaining most relevant operating conditions is provided in Table 2 and 3. Table 4 shows the power required by the units across the flowsheet while Table 5 presents the themal energy involved before integration. Note that the reformer actually uses a fraction of the biogas as fuel. Furthermore, the amount of energy required, after heat integration and the development of a HEN is, 4.25 MJ/s, 1.5 MJ/gal of FAME. In terms of cooling, 27MJ/s, that, together with the energy result in the consumption of 1.22 $gal_{Water}/gal_{Biodiesel}$ by developing the corresponding water network, where we consider a boiler and a cooling tower as a units that require water and generate also wastewater as presented in previous work [34]. Figure 9 shows the T-Q curve for the integrated system. 17MW were integrated by means of the formulation and the development of the heat exchanger network. Furthermore, the process captures 3kg of CO_2 per kg of Biodiesel produced. Tables 2 and 3 show the operating conditions of the major equipment such as reactors, including the ponds, the furnace for the production of syngas, the methanol synthesis reactor and the transeterification reactor. In all cases, the temperatures and pressures are within typical operating limits. For instance, the transesterification reactor requires a molar ratio of methanol to oil close to 6, and the operating temperature is 60ºC, close to the ones presented in previous works [32]. For the production of methanol, low temperatures and pressures are suggested, 200ºC and 50 bar, to reduce the costs related to preparing the feed before synthesis. However, in this case, the fraction of methane required to provide for energy for the reforming is larger than usual, in the range of 10 to 25 %. It is related to the high hydrogen to CO ratio required and the added value that the methanol brings to the process.

Table 2. Main operating variables of selected units (T: TOP; B: Bottom)

Unit/Op. COndition	Pond
Number	15000
N(mg/L)	56
P (mg/L)	45
T(ºC)	amb

Table 3. Main operating variables of selected units (T: TOP; B: Bottom)

Unit/Op. COndition	Dry reform	Transesterification Reactor	Oil Column	MeoH Column	Biodiesel Column	MeOH Purification	MetOH Synthesis
T (ºC)	1000	60	T: 31 B:350	T: 41.5 B:150	T: 243 B:274	T: 63 B: 101	200
P (bar)	1.084	4	135/760	300/760	45/760	1	50
H_2/CO_2							2.5
MeOH/Oil		6.541					
CH4 fuel %	45						

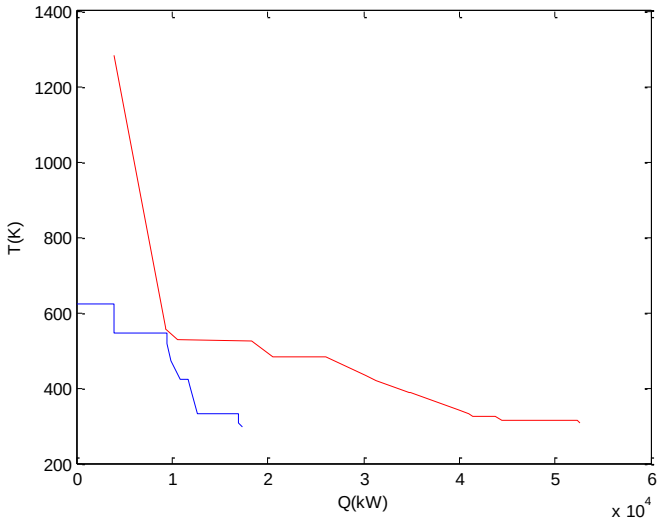

Figure 9-. T-Q Curve for the integrated facility.

Table 4.- Power consumption of the units involved.

Unit	W (kW)
Ponds	1500
Belt	838
Press	3813
Compres1	564
Compres2	-605
Compres3	1146
Compres4	58
Compres5	1666
Compres6	691

Table 5.- Thermal energy involved in the units

Unit	kW		Unit	kW
Digester	9.460		HX20	680
HX1	-562		HX21	-1.059
HX3	4.623		HX22	1.748
HX4	-5.245		HX23	-7.773
HX5	-435		HX24	5.455
HX6	54		HX25	-1.983
HX7	-360		HX26	-95
HX8	-688		HX27	343
HX9	464		HX28	-7905
HX10	-2.782		HX29	3983
HX11	-403		Reformer	6.978
HX17	-6.270		Rwgs	-118
HX18	-177		RMetOH	-2.983
HX19	-2.318		TransReact	4.276

5.1.5.2 Economic evaluation

For the evaluation of the investment cost we use the factorial method [35]. The Matche web page [36] is used to estimate the cost of the chemical processing equipment. The correlation for estimating the cost of the digester can be found in the appendix below and the ones for the rest of the units are available in the supplementary material of Almena and Martín [37]. Figure 10 shows the distribution of the cost among the three major sections of the process. We see that biogas production, and in particular the digester represents the major contribution to the investment cost. Other sections such as methanol and biodiesel show similar share, around 11-17%. Biodiesel involves algae growing and harvesting as well as oil transesterification, while methanol section includes reforming, gas cleanup and composition adjustment followed by synthesis and purification stages. To estimate the investment cost, the installed equipment represents 1.5 times the equipment cost. Piping, insulation, instrumentation and utilities represent 20%, 15%, 20% and 10% of the equipment cost respectively. The CAPEX adds up to 193 M€.

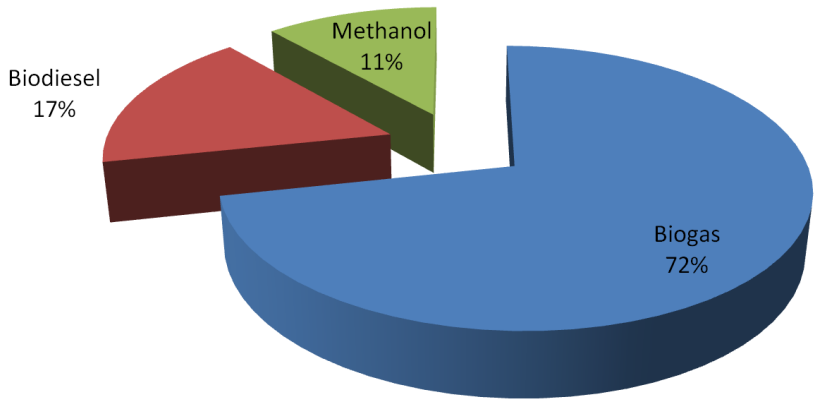

Figure 10. Breakdown of the contribution of the different sections to the overal CAPEX.

To estimate the production cost of the fully renewable FAME, we consider labour, taxes, administration, utilities and equipment maintenance [35]. Figure 11 presents the breakdown of the production costs. Note that most of the cost is related to amortization and maintenance (equipment in Figure 11). Utilities represent the second contribution. Cooling water and steam add up to 2.5 M€/yr. The total production cost is 40.5M€ /y. By selling the excess of methanol at 0.3€/kg we can obtain a credit of 13M€/y. Thus, the production costs for the 88Mgal/yr is $0.31/gal.

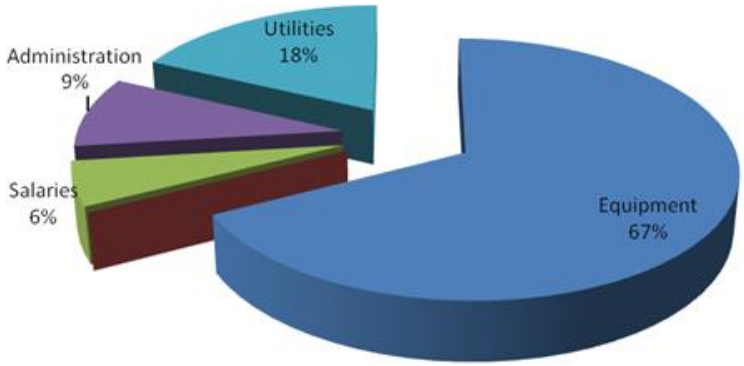

Figure 11. Breadown of the production costs excluding credits.

5.1.5.3 Comparison with other integrated processes.

The first comparison is with a conceptual design by Martín and Grossmann [7]. That facility produces biodiesel using solar and/or wind energy and carbon dioxide. Microalgae are grown to accumulate lipids that are extracted. The methanol needed for the transesterification is synthesized from carbon dioxide and electrolytic hydrogen. The electricity for the complex is produced using solar panels or wind turbines. The flowsheet is formulated as a multi-period mixed integer nonlinear programming problem whose solution provides the optimal source of energy and the operating conditions over a year for an average production of 60 Mgal/yr of biodiesel. The facility requires an investment of 120 M€ for a production cost of 0.79€/gal (0.25 €/kg). However, that facility production capacity is smaller than the one in this study. To scale-up the cost we make use of the fact that the investment cost is computed using the factorial method [35]. This method relies on the equipment cost where the investment cost is computed using factors to account for installation, pipping, isolation, etc. Therefore, if the cost estimation of the units is a function of the mass or energy flows and account for rules of thumb such as the fact that if a flow larger than a standard the unit must be duplicated, i.e. heat exchanger larger than 2000m^2 are not commercial, the entire plant cost can estimate the effect of the scale. In our studies, the equipment cost is estimated using the correlations developed in previous work as a function of the production capacity [37]. By increasing the production capacity, we easily recomputed the units cost and the investment of the scaled-up facility. The procedure is explained in detail in previous work [40]. By scaling this facility to the same size as this work, the production cost decreases to 0.76€/gal and the investment increases to 144 M€. The energy consumption is 3.2 MJ/gal of biodiesel capturing 4.05 kg of carbon dioxide per kg of biodiesel and consuming 1L/L of water including the operation of the cooling tower and the boiler. As we see, there are a number of trade-offs since this process is cheaper than the one in this work and consumes less freshwater, but with a larger energy consumption.

The second comparison consists of the use of switchgrass to produce methanol and algae for the biodiesel (FAME). A superstructure optimization approach is used to select the optimal integrated topology, gasification and reforming technologies, that provides the thermal energy and the methanol that biodiesel production requires. The

excess of methanol can be sold as biofuel or it can be further processed to gasoline. The optimal integrated process involves indirect gasification followed by steam reforming based on the need for high H_2 to CO ratio to produce methanol and avoiding the use of oxygen. The integrated process produces 776ML/yr (205 Mgal/yr) of biofuels, 34% FAME, at 0.14€/L (0.53 €/gal). The plant does not emit CO_2, but captures 1.27 kg of CO_2 per kg of methanol produced. The investment costs adds up to 180 M€. By scaling this size to the one in this work, the production costs goes up to 1€/gal and the investment decreases to 134M€ [6].

Finally, although it works with ethanol instead of methanol, the process proposed in Martín and Grossmann [5] produces ethanol from the starch in the algae and oil from the lipids. In that work, for the production of 90Mgal/yr of biodiesel, FAEE, the production cost results in 0.35 $/gal, using enzymes, with energy and water consumption values (4.00 MJ/gal & 0.59 gal/gal). The investment cost is close to the one in this work, 180MM$. Table 6 summarizes the comparison.

In all cases the nutrients were bought while the use of the digestate as a source for fertilizers reduces not only the cost but also the actual impact.

Table 6. Comparison among self-sufficient processes for biodiesel production

Process	**Investment (M€)**	**Production cost (€/gal)**	**Kg CO_2 captured per kg produced of biofuel**	**Energy consumed (MJ/gal of biodiesel)**	**Water consumed (gal/gal biodiesel)**
This work	193	0.31	3	1.5	1.22
Martin and Grossman[7] (2017)	144	0.76	4.05	3.2	1
Martin and Grosssmann[5] (2016)	180	0.53	1.27	1.94	NA . High cooling needs.
Martin and Grossmann[5] (2013)	170	0.33	2.81	4	0.59

5.1.5.4 Scale-up and down of the facility: Manure availability.

The facility evaluated tried to reach a production capacity of biodiesel comparable to typical sizes in the literature. However, the feedstock required represents the manure produced by around 300000 animals [41]. Therefore, in this section we evaluate the economics and scale down of the facility to 3000 animals, around 1 kg/s of manure. The same procedure presented above on plant scale up and down is used [35]. Figure 12 shows the production (A) and production (B) costs as a function of the farm size required. We see that for the fuel to have a price below 1 €/gal a farm above 35000 animals is required. Eq. (38) shows the correlation for the production cost as a function

of the animals. No good correlation as a function of the scale can be obtained from the results of the investment cost.

$$\text{Biodiesel prod cost} = 1160.3(\text{Animals})^{-0.664} \quad (38)$$

However, even though in the US there has been an increase in the typical farms size, most farms do not reach 100 [42] cows resulting in the fact that a detail supply chain study is required to evaluate the actual production of fully renewable diesel. However, instead of transporting manure as fertilizer, recently Sampat et al. [41] evaluated the production of struvite, a solid fertilizer easy to transport that provides an interesting option towards the use of manure as fertilizer.

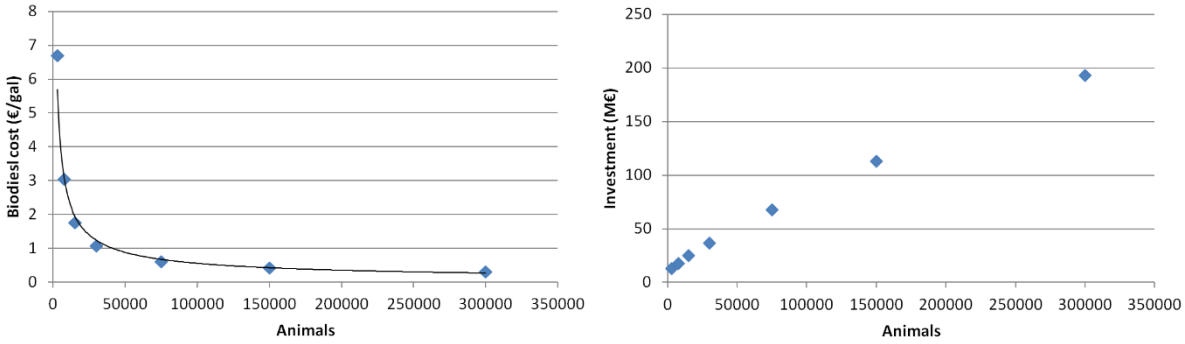

Figure 12.- Scale down on the biodiesel facility.

5.1.6 CONCLUSIONS AND FUTURE CHALLENGES

In this work we have developed an integrated process for the production of renewable diesel from manure via anaerobic digestion in search for making full use of the two main products, biogas and digestate. On the one hand, biogas is produced and further used to obtain renewable methanol via dry reforming. On the other hand, the digestate is used as nutrients to increase the algae yield. This point has two main implications, to reduce the need for input from other sources and therefore the cost, but also the fact that the discharge of digestate can generate an environmental problem due to the high nitrogen and phosphorus content in farm regions. Thus, FAME is produced by transesterifying the algae oil with biogas based methanol.

The problem is formualted as a large NLP for the optimization of the operating conditions at the various reactors such as the dry reformer, the methanol sysntesis, the FAME production and the algae growing where a model for the growth rate as a function of the nutrients has also beed developed. This framework exploits the integration of up to four different sections that are typically evaluated separately such as biogas production, methanol production, algae growing and biodiesel production but that they are strongly linked.

The production of biodiesel from manure is promising from the production cost and enviromental points of view, since it is competitive with other integrated processes that simultaneously produce methanol and oil. The investment cost is larger, at least 30% more, due to the digestion and gas reforming processes. However, the large

amount of feedstock may jeopardize the implementation of this kind of facilities. Most of the biogas plants are actually built and with smaller scale that the one proposed here. In this case, the process can be also applied if the biogas and digestate are fed externally. Thus, it opens a new research topic about the supply chain of biogas and nutirents where further studies can be carried out.

Appendix

The cost of the digester is computed as [34]:

$C_{Digester}$ (€)= 1475100·(Flow Manure (kg/s)$^{0.82227}$

Nomenclature

a'= {CH4}, {CO2},{NH3},{H2S},{O2} or {N2}
a= {H2O}, {CH4}, {CO2},{NH3},{H2S},{O2} or {N2}
b= {C}, {Nam}, {Norg}, {P}, {K} or {Resto}
n_i: Molar flow rate of component I (kmol/s)
P_i: Partial pressure of component i
$V_{biogas,k}$= Biogas volume produced per unit of volatile solids (SV) ($m^3_{biogás}/kg_{SV/i}$).
$R_{C\text{-}N,k}$ = Mass ratio between the carbon and nitrogen in the biomass
$w_{MS/k}$= dry mass fraction ($kg_{MS/k}/kg$).
$w'_{SV/k}$= dry mass fraction of volatile solids out of the dry biomass ($kg_{SV/k}/kg_{MS/k}$).
$w'_{C/k}$= dry mass fraction of C in biomass ($kg_{C/k}/kg_{MS/k}$).
$w'_{Nam/k}$= dry mass fraction of ammonia nitrogen in biomass ($kg_{Nam/k}/kg_{MS/k}$).
$w'_{Norg/k}$= dry mass fraction of organic nitrogen in biomass ($kg_{Norg/k}/kg_{MS/k}$).
$w'_{P/k}$= dry mass fraction of P nitrogen in biomass ($kg_{P/k}/kg_{MS/k}$).
$w'_{K/k}$= dry mass fraction of K nitrogen in biomass ($kg_{K/k}/kg_{MS/k}$).
$w'_{Rest/k}$= dry mass fraction of the rest nitrogen in biomass ($kg_{K/k}/kg_{MS/k}$).
$Y_{a'/biogás\_seco}$= molar fraction of the dry gas
$x_{a/biogás}$= mass fraction of the gas
$y_{biogás}$= specific saturated moisture of biogas
MW: Molar mass (kg/kmol)
T: Temperature (ºC)
HEN: Heat Exchanger Network.
FAME: Fatty acid methyl ester.

REFERENCES

[1] León, E.; Martín, M. Optimal production of power in a combined cycle from manure based biogas *Energy. Convers. Manage.* **2016,** 114, 89–99

[2] Hernández, B.; Martín, M. Optimal Process Operation for Biogas Reforming to Methanol: Effects of Dry Reforming and Biogas Composition *Ind. Eng. Chem. Res*. **2016**, 55, 6677-6685

[3] Hernández, B.; León, E.; Martín, M. Bio-waste selection and blending for the optimal production of power and fuels via anaerobic digestion. *Chem. Eng. Res. Des*. **2017**, 121, 163-172

[4] Xin, L.; Hong ying, H.; Ke, G.; Ying-xue, S. Effects of different nitrogen and phosphorus concentrations on the growth, nutrient uptake, and lipid accumulation of a freshwater microalga Scenedesmus sp. *Biores. Technol*., **2010**, 101, 5494–5500

[5] Martín, M.; Grossmann, I.E. Optimal engineered algae composition for the integrated simultaneous production of bioethanol and biodiesel *AIChE J*., **2013**, 59 (8) , 2872–2883

[6] Martín, M.; Grossmann, I.E. Optimal Integration of Algae−Switchgrass Facility for the Production

of Methanol and Biodiesel ACS Sustainable Chem. Eng. **2016**, 4, 5651−5658

[7] Martín, M.; Grossmann, I.E.. Optimal integration of a self sustained algae based facility with solar and/or wind energy. *J. Cleaner Prod.* , **2017**, 10.1016/j.jclepro.2017.01.051

[8] Elsholkami, M.; Elkamel A.; Vargas F Optmizaed integration of renewavle energy technologies into Alberta's oil Sands industry. Comp. Chem Eng **2016**, 90, 1-22

[9] Shahandeh, H., Li, Z Design of Bitumen Upgrading and utility plant through integrated optimization. Ind. Eng. Chem Res. **2017**; 56 (8), 2017-2126

[10] Martín, M, Davis, W. Integration of wind, solar and biomass over a year for the constant production of CH_4 from CO_2 and water *Comp Chem Eng* . **2015**, 84, 314-325**,**

[11] Betancourt-Torcat, A., Elkamel, A., Ricardez-Sandoval L Optimal integration of nuclear energy and water management into the oil sands operations. *AIChE J*. **2012**, 58 (11) 3433-3454

[12] Al Seadi, T., Rutz, D., Prassl, H., Köttner, M., Finsterwalder, T., Volk, S., Janssen, R.. Biogas Handbook University of Southern Denmark Esbjerg, Esbjerg, Denmark. 2008.

[13] Japaraju, P., Rintala, J. (2013) 17 - Generation of heat and power from biogas for stationary applications: boilers, gas engines and turbines, combined heat and power (CHP) plants and fuel cells 404-427, In The Biogas Hand book

[14] http://www.biogas-info.co.uk/biogas-biogas-yields.html

[15]Steffen R., Szolar, O., Braun, R (1998) Feedstocks for anaerobic digestion. *Q:\RODL\PROJEKTE\AD-NETT\FEEDNEW.DOC*

[16] Gunaseelan, V.N. Anaerobic digestion of biomass for methane production: A review. *Biomass Bioenergy*.**1997**, 13 (12), 83-114

[17] Defra. Fertilizer manual. **2011**
http://adlib.everysite.co.uk/adlib/defra/content.aspx?id=2RRVTHNXTS.88UF9N65FWLCJ
http://adlib.everysite.co.uk/adlib/defra/content.aspx?doc=262994&id=263068

[18] Rykebosch, E.; Brouillon, M.; Vervaeren, H. Techniques for transformation of biogas to biomethane. Biomass Bioenergy. **2011,** 35, 1633-1645

[19] Luyben, W.L. Design and Control of the Dry Methane Reforming Process *Ind. Eng. Chem. Res.* **2014**, 53 (37), 14423−14439.

[20] Roh, H-S.; Lee. DK.; Koo, KY.; Jung, UH.; Yoon, WL. Natural gas steam reforming for hydrogen production over metal monolith catalyst with efficient heat-transfer.*Int J Hydrogen* **2010**;35(3):1613-1619

[21] Lee, S. Methanol Synthesis from Syngas. Handbook of alternative Fuel Technologies; Taylor and Francis: Boca Raton. FL, 2007; Chapter 9.

[22] Nexant Inc. Equipment Design and Cost Estimation for Small Modular Biomass Systems, Synthesis Gas Cleanup, and Oxygen Separation Equipment Task 2: Gas Cleanup Design and Cost Estimates – Black Liquor Gasification Subcontract Report NREL/SR-510-39944 May 2006

[23] GPSA Engineering_Data_Book FPS VERSION 21-10, 2004

[24] Ribeiro, A.; Santos, J.C.; Rodrigues, A .E. PSA design for stoichiometric adjustment of bio-syngas for methanol production and co-capture of carbon dioxide, Chemical Engineering . 2010.

[25] Tijm, P.J.A.; Waller,F.J.; Brown, D.M. Methanol technology developments for the new millennium Applied Catalysis A: General , **2001**, 221, 275–282

[26] Marechal, F.; Heyen, G.; Kalitventzeff, B. Energy Saving in Methanol Synthesis: Use of Heat Integration Techniques and Simulation Tools. Comp. Chem. Eng., **1997,** 21, S511-S516

[27] Cherednichenko, V. M. Dissertation, Karpova, Physico Chemical Institute, Moscow, U.S.S.R., 1953.

[28] Bissett, L. Equilibrium Constants for Shift Reactions. *Chem. Eng.***1977**, 84 (21), 155−156.

[29] Amini, H.; Wang, L.; Shahbazi, A. Effects of harvesting cell density, medium depth and environmental factors on biomass and lipid productivities of Chlorella vulgaris grown in swine wastewater Chem. Eng. Sci. **2016**, 152, 403–412

[30] Sazdanoff, N. Modeling and Simulation of the Algae to Biodiesel Fuel Cycle. Undegraduate Thesis. The Ohio State University, Columbus, OH, 2006.

[31] Pate, R. Biofuels and the Energy-Water Nexus AAAS/SWARM April 11, 2008 Albuquerque, NM. 2008

[32] Martín, M.; Grossmann, I.E. Simultaneous optimization and heat integration for biodiesel production from cooking oil and algae. Ind. Eng. Chem Res. **2012**. 51 (23), 7998–8014

[34] Yee, T.F.; Grossmann, I.E. Simultaneous optimization models for heat integration – II. Heat exchanger networks synthesis. *Comp. Chem. Eng*., **1990**, 28, 1165-1184.

[34] Ahmetović, E.; Grossmann, I. E. Global superstructure optimization for the design of integrated process water networks. *AIChE J.*, **2011,** 57 (2), 434-457

[35] Sinnot, R.K. (1999). Coulson and Richardson, Chemical Engineering, 3rd ed.Butterworth Heinemann, Singapur,

[36] Matche (2014) http://www.matche.com/equipcost/EquipmentIndex.html

[37] Almena, A.; Martín, M. Techno-economic analysis of the production of epiclorhidrin from glycerol. Ind. Eng. Chem. Res. **2016**, 55 (12) 3226-3238

[38] http://anaerobic-digestion.com/anaerobic-digestion-plants/cost-of-anaerobic-digestion-plant/

[39] Martín, M (2016) Industrial chemical process analysis and design. Elsevier Oxford.

[40] Martín, M. Artifical vs natural reuse of CO2 for DME production. Are we getting any close? Engineering. **2017** http://dx.doi.org/10.1016/J.ENG.2017.02.002

[41] Sampat, A.S., Martín, E., Martín, M., Zavala, VM (2017) Optimization Formulations for Multi-Product Supply Chain Networks. Comp Chem .Eng. 104, 296-310

[42] Zoetis (2017) http://blog.especialistasennovillas.es/posts/tamano-granjas-lecheras.aspx. Last accessed June 2017